CONFIDENTIAL
RESTRICTED DATA

RECORD COPY

SNPO-C

Subcontract NP-1

MASTER

March 1967

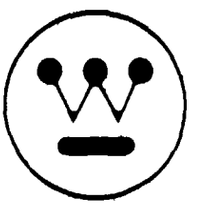

Westinghouse Astronuclear Laboratory

NOTICE
This report was prepared as an account of work sponsored by the United States Government. Neither the United States nor the United States Energy Research and Development Administration, nor any of their employees, nor any of their contractors, subcontractors, or their employees, makes any warranty, express or implied, or assumes any legal liability or responsibility for the accuracy, completeness or usefulness of any information, apparatus, product or process disclosed, or represents that its use would not infringe privately owned rights.

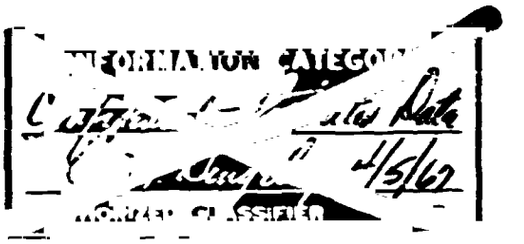

Classification cancelled (or changed to _____)
by authority of Doc
by _____ T.I.C. date SEP 10 1973

WANL-TNR-219

NRX-A5 REACTOR TEST ANALYSIS REPORT

(Title Unclassified)

DISTRIBUTION OF THIS DOCUMENT IS UNLIMITED

Subcontract NP-1

W. L. Knecht
Technical Editor

Prepared By:
Thermal and Nuclear
Design Department

CONFIDENTIAL
RESTRICTED DATA

RECORD COPY

MAJOR CONTRIBUTORS

The following contributors were primarily responsible for the specified chapters of this report:

Chapter	Editor
1, 2, 3	W. L. Knecht
4	A. Y. Lee
5	E. Cort, J. Guzek
6	S. L. Davidson
7	L. Ortenberg
8	M. A. Capo, R.N. Nassano
9	R. Doncals

TABLE OF CONTENTS

Chapter		Page
1	INTRODUCTION	1-1
2	SUMMARY	2-1
	2.1 Performance Analysis	2-1
	2.2 Reflector Seal System, and Filler Strips	2-2
	2.3 Core Temperatures	2-2
	2.4 Corrosion	2-3
	2.5 Nuclear Analysis	2-4
	2.6 Dosimetry	2-5
3	PERFORMANCE ANALYSIS	3-1
	3.1 Summary	3-1
	3.2 Background Data	3-3
	3.2.1 Test Cell "A" Feedsystem	3-3
	3.2.2 Reactor Geometry and Flow Path	3-3
	3.2.3 Reactor Scram Shutdown Procedures	3-4
	3.3 Pre-Power Tests	3-9
	3.3.1 EP-I Ambient Hydrogen Flow Test	3-9
	3.3.2 Low Power - Zero Flow (Neutronic Calibration) Test	3-14
	3.3.2.1 Description of Test Profile and Data	3-14
	3.3.2.2 Analysis of Test Data	3-15
	3.4 Power Tests	3-26
	3.4.1 Description of Power Tests	3-26
	3.4.1.1 Background	3-26
	3.4.1.2 Test Profile: EP-III	3-27
	3.4.1.3 Test Profile: EP-IV	3-36

Chapter			Page
	3.4.2	Best Estimated Chamber Temperature, Reactor Power, and Flow Rate	3-44
		3.4.2.1 Summary of Results	3-44
		3.4.2.2 Description of Calculation Procedure	3-47
	3.4.3	Comparison of Transient and Steady State Test Data With TNT Calculations	3-51
		3.4.3.1 TNT Reactor Model for Calculations	3-52
		3.4.3.2 Transient Comparisons	3-53
		3.4.3.3 Discussion of Performance	3-55
		3.4.3.4 Discussion of Performance Parameter Comparisons	3-57
	3.4.4	Decay Power Analysis	3-73
		3.4.4.1 Summary	3-73
		3.4.4.2 Description of Cooldown	3-73
		3.4.4.3 Description of Calculation Procedure	3-74
		3.4.4.4 Decay Power Comparison	3-77
		3.4.4.5 Recommended Changes to Data Recording Intervals	3-77
	3.5	NRX Performance Results	3-82
	3.5.1	Summary of NRX Testing	3-82
		3.5.1.1 General Summary of Tests	3-82
		3.5.1.2 Summary of Environmental Conditions	3-85
	3.5.2	Reflector Heating in NRX/EST and NRX-A5	3-92
	3.5.3	Comparison of Core Station 26 with Chamber Temperature	3-97
	3.6	References	3-100
4	REFLECTOR SYSTEM, SHIELD AND FILLER STRIPS THERMAL AND FLUID FLOW ANALYSIS		4-1
	4.1	Summary	4-1
	4.2	Description of the Reflector System	4-4

Chapter			Page
	4.3	Steady State Thermal and Hydraulic Conditions	4-7
		4.3.1 Reflector System	4-7
		4.3.2 Lateral Support Systems	4-10
	4.4	Reflector and Lateral Support Component Material Temperature	4-16
		4.4.1 Outer Reflector Sector Material Temperature	4-16
		4.4.2 Inner Reflector Graphite Barrel Material Temperature	4-17
		4.4.3 Control Drum Assembly	4-19
		4.4.4 Core Support Plate	4-21
		4.4.5 Shield and Reflector Tie Bolt Material Temperatures	4-21
		4.4.6 NRX-A6 Experimental Lateral Support Spring Temperature	4-21
	4.5	Hot Buffer Filler Strips Transient Thermal Analysis During EP-IV Shutdown	4-36
	4.6	Filler Strip Thermal Capsule Measurements	4-48
5	CORE THERMAL ANALYSIS		5-1
	5.1	Introduction	5-1
	5.2	Summary	5-2
	5.3	Core Pressure Drop	5-4
	5.4	Core Temperatures	5-9
		5.4.1 Placement of Sensors	5-9
		5.4.2 Radial Core Temperature Distributions	5-11
		5.4.2.1 Radial Temperature Profiles for EP-III and EP-IV	5-11
		5.4.2.2 TRACK Analysis	5-17
		5.4.3 Axial Temperature Distributions	5-21
		5.4.4 Perturbations on Core Temperature Distributions	5-33
		5.4.4.1 Control Drum Position	5-33
		5.4.4.2 Effects of Corrosion	5-37

Chapter				Page
		5.4.4.3	Hot Buffered Periphery	5-41
		5.4.4.4	Effects of Shims	5-46
	5.4.5		Azimuthal Temperature Distribution	5-49
	5.4.6		Thermal Capsule Measurements	5-57
	5.4.7		Tie Rod Temperatures	5-62
	5.4.8		Peripheral Fuel Element During EP-IV Shutdown	5-64
	5.4.9		Statistical Analysis of Core Temperatures	5-76
		5.4.9.1	Analysis of Variance of Core Temperatures	5-76
		5.4.9.2	Multiple Regression Analysis	5-77
		5.4.9.3	Maximum Measured and Calculated Temperatures and Element to Element Variations	5-78
	5.5	Appendix		5-83
	5.5.1		Analysis of Variance Method	5-83
	5.5.2		Results of NRX-A5 Analysis of Variance	5-85
6	CORROSION			6-1
	6.1	Summary		6-1
	6.2	Introduction		6-2
	6.3	Fuel Element Corrosion		6-3
	6.3.1		Fuel Element Overall Weight Losses	6-3
	6.3.2		Fuel Element Incremental Weight Losses	6-14
	6.3.3		Fuel Element External Surface Weight Losses	6-22
		6.3.3.1	Data Acquisition	6-22
		6.3.3.2	Data Reduction	6-23
		6.3.3.3	Results of Surface Regression Measurements	6-23
		6.3.3.4	Fuel Element Bore Weight Losses Deduced from Incremental and Surface Corrosion Measurements	6-30

Chapter				Page
		6.3.3.5	Surface Regression Maximum Point Frequency	6-35
	6.3.4		Peripheral Fuel Element Evaluations	6-44
		6.3.4.1	Hot Buffer Region	6-44
		6.3.4.2	Fuel Loading Effect	6-56
		6.3.4.3	Element Location Effect	6-56
		6.3.4.4	Comparison of NRX-A3, NRX/EST, and NRX-A5 Peripheral Fuel Element Performance	6-57
	6.3.5		Pinholes and Channel Exposure	6-65
		6.3.5.1	Background	6-65
		6.3.5.2	NRX-A5 Pinholes and Channel Exposure	6-67
		6.3.5.3	Comparison of NRX-A3, NRX/EST, and NRX-A5 Pinholes and Channel Exposure	6-78
		6.3.5.4	"Zero Defect" Pinhole and Channel Exposure Elements	6-82
	6.4		Filler Strip Corrosion	6-84
	6.5		Fuel Element Hot End Condition	6-88
	6.6		Support Block Corrosion	6-90
		6.6.1	Mechanical Performance	6-90
		6.6.2	Corrosion Performance	6-90
		6.6.3	J-9 Peripheral Support Block Temperature Responses During NRX-A5, EP-IV Startup	6-91
	6.7		Correlation of Weight Loss in the NRX-A5 and NRX/EST	6-94
		6.7.1	Correlation of Total Weight Loss Data for the NRX-A5 Elements Having As Leached Body Porosity Data	6-94
		6.7.2	Correlation of Average Orifice Diameter versus Total Weight Loss	6-99

Chapter			Page
	6.7.3	Effect of Hole Location	6-101
	6.7.4	Correlation of the NRX/EST Total Weight Loss with Gross Ionization Measurements	6-101
	6.8	Analytical Techniques	6-107
	6.8.1	Bore Corrosion	6-107
	6.8.2	Surface Corrosion	6-108
	6.8.3	Pinholing Effects	6-109
	6.9	Conclusions	6-116
7	NUCLEAR ANALYSIS		7-1
	7.1	Summary	7-1
	7.2	Approach to Criticality	7-2
	7.2.1	Peripheral Poison Wire Removal	7-2
	7.2.2	Central Poison Wire Removal	7-13
	7.2.3	Conclusion	7-29
	7.3	Control Drum Worth	7-30
	7.3.1	Single Drum Withdrawal and Insertion Measurements	7-30
	7.3.2	Drum Bank Differential Worth Measurements	7-32
	7.3.3	Drum Bank Integral Worth Measurements	7-32
	7.3.4	Feedback Reactivity in GH_2 Test	7-32
	7.3.5	Cold-to-Hot Swing to Full Power	7-35
	7.3.6	Individual Drum Uniformity Measurements	7-35
	7.3.7	Conclusion	7-36
	7.4	Temperature Coefficients from Near Ambient Testing	7-40
	7.4.1	Station 8 Temperature Coefficient of Reactivity	7-40
	7.4.2	Beryllium Reflector Temperature Coefficient of Reactivity	7-41
	7.4.3	Conclusions	7-44

Chapter			Page
	7.5	Operating Reactivity Changes Due to Corrosion	7-45
		7.5.1 Summary of Pre-Test and Post-Test Criticality Measurements	7-45
		7.5.2 Observed Reactivity Loss	7-45
		7.5.2.1 Reactivity Loss from Ambient Criticality Data	7-48
		7.5.2.2 Reactivity Loss During Operation	7-48
		7.5.2.3 Comparison of KIWI B-4E, PHOEBUS 1A, NRX-A3 and NRX/EST Reactivity Loss Rate Information	7-65
		7.5.2.4 Conclusions	7-68
	7.6	Nuclear Analysis of Power Runs	7-69
8	DOSIMETRY		8-1
	8.1	Summary	8-1
	8.2	Experimental Program	8-2
	8.3	Analytical Methods	8-9
	8.4	Gamma Ray Dose Rate Data	8-11
	8.5	Fast Neutron Flux Data	8-28
	8.6	Thermal Neutron Flux Data	8-45
	8.7	Heating Rates From Calorimetric Data	8-58
	8.8	Compilation of Radiation Environment Data for NRX Reactors at Test Cell "A"	8-69
	8.9	Conclusions	8-74
	8.10	References	8-77
9	POST-OPERATIVE RADIOCHEMISTRY		9-1
	9.1	Summary	9-1
	9.2	NRX-A5 Power Distribution Predictions	9-3

Chapter		Page
9.3	Effective Drum Angle for the NRX-A5 Hot Test	9-5
9.4	Comparison of the NRX-A5 Experimental Power Distribution with Predictions	9-7
9.5	Fission Product Loss during Testing	9-11
9.6	Comparison of Adjusted NRX-A5 Experimental Power Distribution with Predictions	9-19
9.7	Measured Cold-to-Hot Power Change	9-27
9.8	Comparison of the NRX Experimental and Predicted Axial Power Distributions	9-29
9.9	Comparison of the NRX/EST and NRX-A5 Gross Ionization Measurements	9-31

LIST OF ILLUSTRATIONS

Figure		Page
1-1	NRX-A5 Test Assembly Mated to Test Cell "A"	1-5
1-2	NRX-A5 Test Assembly at Test Cell "A" During EP-IV (Second Full Power Test)	1-6
3-1	Simplified Schematic of Test Cell "A" Feed System	3-6
3-2	NRX-A5 Reactor Flow Path	3-7
3-3	NRX-A5 Flow Shutdown Nozzle Torus Pressure Demand as a Function of Core Station 26 Temperature	3-8
3-4	NRX-A5 EP-I Ambient Hydrogen Flow Test: Flow Rate and Control Drum Position	3-11
3-5	NRX-A5 EP-I Ambient Hydrogen Flow Test: Nozzle Manifold and Chamber Pressure	3-12
3-6	NRX-A5 EP-II Neutronic Calibration Test: Power and Core Temperatures versus Time	3-30
3-7	NRX-A5 EP-II Neutronic Calibration Test: Station 0.5 and [illegible] Core Radial Temperature Profiles	3-21
3-8	NRX-A5 EP-II Neutronic Calibration Test: Station 8 Core Radial Temperature Profiles	3-22
3-9	NRX-A5 EP-II Neutronic Calibration Test: Comparison of Computed Core and Inner Reflector Temperatures with Test Data	3-23
3-10	NRX-A5 EP-II Neutronic Calibration Test: Axial Core Temperature Profiles	3-24
3-11	NRX-A5 EP-II Neutronic Calibration Test: Radial Core Temperature Profiles	3-25
3-12	NRX-A5 EP-III Power Test Description: Chamber Temperature, Flow Rate, Power and Control Drum Position	3-30
3-13	NRX-A5 EP-III Power Test Description: Average Chamber and Core Station 26 Temperatures and Time Rate of Change of Chamber Temperatures	3-31

Figure		Page
3-14	NRX-A5 EP-III Power Test Description: Tie Rod Material and Plenum Temperatures	3-32
3-15	NRX-A5 EP-III Power Test Description: Plenum Pressures	3-33
3-16	NRX-A5 EP-III Power Test Description: Component Pressure Drops	3-34
3-17	NRX-A5 EP-III Power Test Description: Core Unfueled Element Temperature (Electrical Averages)	3-35
3-18	NRX-A5 EP-IV Power Test Description: Chamber Temperature, Flow Rate, Power and Control Drum Position	3-38
3-19	NRX-A5 EP-IV Power Test Description: Average Chamber and Core Station 26 Temperatures and Time Rate of Change of Chamber Temperature	3-39
3-20	NRX-A5 EP-IV Power Test Description: Tie Rod Material and Plenum Temperatures	3-40
3-21	NRX-A5 EP-IV Power Test Description: Plenum Pressures	3-41
3-22	NRX-A5 EP-IV Power Test Description: Component Pressure Drops	3-42
3-23	NRX-A5 EP-IV Power Test Description: Core Unfueled Element Temperatures (Electrical Averages)	3-43
3-24	NRX-A5 EP-III Startup Comparison: Power Flow and Chamber Temperature	3-60
3-25	NRX-A5 EP-III Startup Comparison: Tie Rod and Plenum Temperatures	3-61
3-26	NRX-A5 EP-III Startup Comparison: Plenum Pressures	3-62
3-27	NRX-A5 EP-III Startup Comparison: Pressure Drops	3-63
3-28	NRX-A5 EP-III Startup Comparison: Core Station Temperatures	3-64

Figure		Page
3-29	NRX-A5 EP-III Startup Comparison: Control Drum Position	3-65
3-30	NRX-A5 EP-IV Startup Comparison: Control Drum Position, Power, Flow and Chamber Temperature	3-66
3-31	NRX-A5 EP-IV Shutdown Comparison: Power Flow and Chamber Temperature	3-67
3-32	NRX-A5 EP-IV Shutdown Comparison: Tie Rod and Plenum Temperatures	3-68
3-33	NRX-A5 EP-IV Shutdown Comparison: Core Station Temperatures	3-69
3-34	NRX-A5 EP-IV Shutdown Comparison: Plenum Pressures	3-70
3-35	NRX-A5 EP-IV Shutdown Comparison: Pressure Drops	3-71
3-36	NRX-A5 EP-IV Shutdown Comparison: Control Drum Bank Position	3-72
3-37	NRX-A5 EP-III Cooldown: Typical Radial Core Temperature Profiles	3-79
3-38	NRX-A5 EP-III Cooldown: Typical Axial Temperature Profiles	3-80
3-39	NRX-A5 EP-III: Decay Power	3-81
3-40	Comparison of Nozzle Chamber Profiles During NRX Testing	3-86
3-41	Summary of Power Profiles During Fixed Control Drum Testing	3-87
3-42	Percentage of Total Power Generated in Peripheral Components for All Reactors	3-95
3-43	Azimuthal Temperature Distributions in Core Inlet and Reflector Inlet Plenums: NRX/EST, EP-IV	3-[illegible]5
3-44	Ratio of Core Station 26 Temperature to Nozzle Chamber Temperature: NRX-A5 and NRX/EST	3-99
4-1	Reflector, Shield and Core Support Flow Schematic	4-6
4-2	Azimuthal Reflector Inlet, Dome End and Core Inlet Plenums Temperatures, NRX-A5, EP-III, EP-IV	4-12

Figure		Page
4-3	NRX-A5 Time History of the Inner Reflector Dome End Plenum and Core Inlet Plenum Pressures	4-13
4-4	NRX-A5 Normalized Seal Chamber Pressure Profiles	4-14
4-5	NRX-A5 Seal Chamber as a Function of Time	4-15
4-6	NRX-A5 Axial Temperature Profile of Outer Reflector Sector at Full Power	4-23
4-7	NRX-A5 Outer Reflector Sector Temperature Rise During Steady State Full Power Holds	4-24
4-8	NRX-A5 Axial Temperature Profiles of Inner Reflector Graphite Barrel at Full Power	4-25
4-9	NRX-A5 Inner Reflector Graphite Barrel Temperature Rise During Full Power Holds at R = 19.25"	4-26
4-10	NRX-A5 Inner Reflector Graphite Barrel Temperature Rise During Full Power Holds at R = 18.25", STA = 32.5"	4-27
4-11	Control Drum Transient Temperature Difference During NRX-A5 EP-III Startup	4-29
4-12	Control Drum Transient Temperature Difference During NRX-A5 EP-IV Startup	4-30
4-13	NRX-A5 Axial Temperature Profile of Control Drum at Full Power	4-32
4-14	NRX-A5 Core Support Plate and Core Inlet Plenum Temperature	4-34
4-15	NRX-A5 Experimental Lateral Support Spring Temperature in NRX-A5 EP-IV Full Power Hold	4-35
4-16	NRX-A5 Hot Buffer Filler Strip Model (30° Sector)	4-40
4-17	Temperature Differences Between Average and Coldest Hot Buffer Filler Strip During NRX-A5 EP-IV Shutdown	4-41
4-18	Temperature Difference Between Hottest and Coldest Hot Buffer Filler Strip During NRX-A5 EP-IV Shutdown	4-42
4-19	NRX-A5 Hot Buffer Filler Strip Temperatures at E L - Steady State	4-43
4-20	NRX-A5 Hot Buffer Filler Strip Temperatures 40 Seconds After Start of EP-IV Shutdown (Worst Condition)	4-44

Figure		Page
4-21	Temperature Difference Between Hot Buffer Filler Strip and Average Core Element during NRX-A5 EP-IV Shutdown	4-45
4-22	Axial Temperature Variation of NRX-A5 Hot Buffer Filler Strips - EOL	4-46
4-23	NRX-A5 End of Life Hot Buffer Periphery Gaps	4-47
4-24	Core Orientation and Cluster Identification	4-51
4-25	NRX-A5 Thermal Capsule Data in Hot Buffer Filler Strips - F.S. 4-8 and F.S. 4-18	4-52
4-26	NRX-A5 Thermal Capsule Data in Hot Buffer Filler Strips - F.S. 3-2 and F.S. 4-2	4-53
4-27	NRX-A5 Thermal Capsule Data in Hot Buffer Filler Strips - F.S. 4-25 and F.S. 4-2	4-54
4-28	NRX-A5 Thermal Capsule Distribution in Nominal Filler Strip - F.S. 6-18	4-[illegible]
5-1	NRX-A5 EP-III CRT 25242.5 Drum Angle = 97 Degree Temperature versus Radius	5-13
5-2	NRX-A5 EP-III SOL CRT 25400 Drum Angle = 109 Degree Temperature versus Radius	5-14
5-3	NRX-A5 SOL EP-IV CRT-13002.5 Drum Angle = 114.8 Degree Temperature versus Radius	5-15
5-4	NRX-A5 EOL EP-IV CRT-13812.5 Drum Angle = 145 Degree Temperature versus Radius	5-16
5-5	NRX-A5 EP-IV SOL CRT-13002.5 Comparison of Calculated and Measured Temperature	5-19
5-6	NRX-A5 EP-IV EOL CRT-13812.5 Comparison of Calculated and Measured Temperature	5-20
5-7	Quarter Cross Section of Core Regions of Discussion and NRX-A5 Nominal Radial Power Distribution	5-23
5-8	Axial Temperature Profile NRX-A5 EP-IV SOL CRT-13002.5 Central Region	5-24
5-9	Axial Temperature Profile NRX-A5 EP-IV EOL CRT-13812.5 Central Region	5-25

Figure		Page
5-10	Axial Temperature Profile NRX-A5 EP-IV SOL CRT-13002.5 Trough Region	5-26
5-11	Axial Temperature Profile NRX-A5 EP-IV EOL CRT-13812.5 Trough Region	5-27
5-12	Axial Temperature Profile NRX-A5 EP-IV SOL CRT-13002.5 Peripheral Region	5-28
5-13	Axial Temperature Profile NRX-A5 EP-IV EOL CRT-13812.5 Peripheral Region	5-29
5-14	Axial Sensor Temperature Profile in the AIA Elements at SOL NRX-A5 EP-IV SOL CRT-13002.5	5-30
5-15	Axial Sensor Temperature Profile for J9Q Elements at EOL NRX-A5 EP-IV EOL CRT-13812.5	5-31
5-16	Axial Sensor Temperature Profile for J3 Cluster Elements at EOL NRX-A5 EP-IV EOL CRT-13812.5	5-32
5-17	Comparison of the Measured and Predicted Fuel Temperature Change per Change of Drum Angle	5-36
5-18	NRX-A5 EP-IV EOL Station 20 Core Material Temperatures	5-38
5-19	NRX-A5 EP-IV EOL Station 26 Core Material Temperatures - R<8 Inches	5-39
5-20	NRX-A5 EP-IV EOL Station 32 Core Material Temperatures - R< 8 Inches	5-40
5-21	Azimuthal Temperature Variation in NRX-A5 Inlet EP-IV CRT-13002.5	5-43
5-22	Azimuthal Temperature Variation in NRX-A5 Inlet EP-IV CRT-13812.5	5-44
5-23	Radial Temperature Distribution Across J9H Adjacent to NRX-A5 Hot Reflector Periphery - Steady State EP-IV EOL for Station 32	5-45
5-24	NRX-A5 Shimming Distribution and Instrumentation Placement	5-47
5-25	NRX-A5 Average Core Temperature and Shim Density versus Radius	5-48
5-26	NRX-A5 EP-III CRT 25247.5 Station 26 Temperature versus Azimuthal Position	5-52

Figure		Page
5-27	NRX-A5 EP-IV SOL CRT-13002.5 Station 26 Temperature versus Azimuthal Position	5-23
5-28	NRX-A5 EP-IV EOL CRT-13812.5 Station 26 Temperature versus Azimuthal Position	5-54
5-29	NRX-A5 Core Material Temperatures versus Normalized Azimuthal Position	5-55
5-30	NRX-A5 Station 36 Thermal Capsule Temperatures versus Azimuthal Position	5-56
5-31	NRX-A5 Thermal Capsule Data versus Core Radius	5-60
5-32	NRX/EST Thermal Capsule Data versus Core Radius	5-61
5-33	NRX-A5 Tie Rod Material Temperatures versus Radius for EP-III and EP-IV	5-63
5-34	J9 Cluster Model	5-67
5-35	J9 Cluster Element Temperatures during NRX-A5 EP-IV Shutdown	5-68
5-36	J9 Cluster Element Temperatures during NRX-A5 EP-IV Shutdown	5-69
5-37	J9 Cluster Element Temperatures during NRX-A5 EP-IV Shutdown	5-70
5-38	J9 Cluster Element Temperatures Variations NRX-A5 EP-IV Shutdown	5-71
5-39	J9 Cluster Element Temperatures Variations NRX-A5 EP-IV Shutdown	5-72
5-40	J9 Cluster Element Temperatures Variations during NRX-A5 EP-IV Shutdown	5-73
5-41	Peripheral Element Temperature Difference NRX-A5 EP-IV Shutdown Station 26	5-74
5-42	Peripheral Element Temperature Difference for Station 52 NRX-A5 EP-IV Shutdown	5-75

Figure		Page
6-1	Radial Distribution of NRX-A5 Overall Fuel Element Weight Loss	6-8
6-2	Radial Distribution of Overall Weight Losses in the NRX-A3, NRX/EST, and NRX-A5	6-9
6-3	Azimuthal Variation of NRX-A5 Overall Weight Loss for WAFF Fuel Elements	6-10
6-4	Azimuthal Variation of NRX-A5 Overall Weight Loss for Y-12 Fuel Elements	6-11
6-5	Distribution of the Fraction of Broken Elements in the NRX-A5 Reactor	6-12
6-6	Comparison of the Fraction of Broken Elements in the NRX/EST and NRX-A5 Reactors	6-13
6-7	NRX-A5 Incremental Weight Losses in Three Radial Regions	6-15
6-8	NRX/EST Incremental Weight Losses in Three Radial Regions	6-16
6-9	NRX-A5 Average Incremental Weight Losses for all WAFF and Y-12 Fuel Elements	6-17
6-10	Radial Distribution of Peak NRX/EST and NRX-A5 Weight Losses	6-18
6-11	External Surface Corrosion Measuring Apparatus	6-19
6-12	Block Diagram of Digitized Surface Corrosion Measuring System	6-20
6-13	Location of Trace Data	6-21
6-14	Central Region Surface Corrosion in the NRX-A3, NRX/EST, and NRX-A5	6-25
6-15	Mid-Radial Region Surface Corrosion in the NRX-A3, NRX/EST, and NRX-A5	6-26
6-16	Peripheral Region Surface Corrosion in the NRX-A3, NRX/EST, and NRX-A5	6-27
6-17	Calculated and Measured Surface Regression for NRX/EST, A Cluster	6-28
6-18	Calculated and Measured Surface Regression, for NRX/EST, G Cluster	6-29

Figure		Page
6-19	External Surface Weight Loss Distribution for NRX-A5 Fuel Element 3A1D	6-31
6-20	Axial Distribution of NRX-A5 Incremental Weight Loss	6-32
6-21	External Surface Weight Loss Distribution for NRX-A5 Fuel Element 2H6G	6-33
6-22	External Surface Weight Loss Distribution for NRX-A5 Fuel Element 2J7F	6-34
6-23	Axial Distribution of Incremental Weight Loss NRX-A3	6-37
6-24	Axial Distribution of Incremental Weight Loss NRX/EST	6-38
6-25	NRX-A3 Estimated Division of Fuel Element Bore and Surface Weight Losses	6-39
6-26	NRX/EST Estimated Division of Fuel Element Bore and Surface Weight Losses	6-40
6-27	NRX-A5 Estimated Division of Fuel Element Bore and Surface Weight Losses	6-41
6-28	NRX-A5 Average Surface Regression Region 4-D	6-42
6-29	Frequency of Points in the Maximum NRX-A5 Surface Regression Curves for Region 4-D	6-43
6-30	Sketch of NRX-A5 Hot Buffer Region	6-49
6-31	Location of Surface Regression Measurements	6-50
6-32	NRX-A5 Average Corner Surface Corrosion	6-51
6-33	NRX-A5 Corner Surface Corrosion in the Hot Buffer Region	6-52
6-34	NRX-A5 Surface Corrosion Outermost Uncoated Row, Location D, Normal Buffer Region	6-53
6-35	NRX-A5 Surface Corrosion Outermost Uncoated Row, Location C, Normal Buffer Region	6-54
6-36	NRX-A5 Surface Corrosion Outermost Uncoated Row, Location B, Normal Buffer Region	6-55
6-37	NRX/EST and NRX-A5 Weight Loss versus Code	6-58
6-38	NRX/EST and NRX-A5 Percent Broken Elements versus Loading Code	6-59

Figure		Page
6-39	Location Rating Factor for the NRX-A5 Core	6-60
6-40	Peripheral Element Breakage Pattern for the NRX-A5 Core	6-61
6-41	Location Rating Factors versus Average Power Factor for the NRX-A5 Core	6-62
6-42	Average Surface Regression all NRX-A3 Elements, First Row Uncoated	6-63
6-43	Average Surface Regression all NRX/EST Elements, First Row Uncoated	6-64
6-44	NRX-A5 Axial and Radial Distribution of Number of Pinholes per Element	6-72
6-45	NRX-A5 Axial and Radial Distribution of Inches of Channel Exposed per Element	6-73
6-46	NRX-A5 Axial Distribution of the Pinhole and Channel Exposure Characteristics of Row A	6-74
6-47	NRX-A5 Axial Distribution of the Pinhole and Channel Exposure Characteristics of Row J	6-75
6-48	NRX-A5 EP-IV EOL Surface Corrosion Depth due to Pinholes, Core Center Region	6-76
6-49	NRX-A5 EP-IV EOL Surface Corrosion Depth due to Pinholes, Core Mid-Radial Region	6-77
6-50	Comparison of NRX-A3, NRX/EST and NRX-A5 Radial Distribution of Pinholes per Element	6-79
6-51	Comparison of NRX/EST and NRX-A5 Radial Distribution of Channel Exposure per Element	6-80
6-52	Comparisons of the Axial Distribution of the Average No. of Pinholes per Element and the Inches of Channel Exposure for the NRX-A3, NRX/EST, and NRX-A5	6-81
6-53	NRX-A5 Filler Strip Surface Regression in Hot Buffer Region	6-86
6-54	NRX-A5 Filler Strip Surface Regression Outside Hot Buffer Region	6-87

Figure		Page
6-55	Fueled Element Hot End Design	6-89
6-56	Temperature Difference in J-9 NRX-A5 Support Block Cluster EP-IV Startup	6-93
6-57	NRX/EST WAFF Fuel Elements Total Weight Loss versus Average Orifice Size	6-100
6-58	NRX-A5 Mid-Band Core Characterization	6-111
6-59	Calculated NRX-A5 Bore Weight Loss Distributions Normalized to Measured Data - Core Central Region	6-112
6-60	Calculated NRX-A5 Bore Weight Loss Distributions Normalized to Measured Data-Core Mid-Radial Region	6-113
6-61	Calculated NRX-A5 Bore Weight Loss Distributions Normalized to Measured Data-Core Peripheral Region	6-114
6-62	Equations used in CAPING Code	6-115
7-1	Typical Poison Wire Loading Pattern for NRX-A5 Core Sectors	7-3
7-2	Source and Detector Locations for NRX-A5 Peripheral Poison Wire Removal	7-5
7-3	Inverse Multiplication during Peripheral Poison Wire Removal	7-9
7-4	Inverse Multiplication during Last Five Steps of NRX-A5 Peripheral Poison Wire Removal	7-10
7-5	Source and Detector Location for NRX-A5 Central Poison Wire Removal	7-15
7-6	Inverse Multiplication Plot for Detector C-1* during Central Poison Wire Removal	7-20
7-7	Inverse Multiplication Plot for Detector C-2* during Central Poison Wire Removal	7-21
7-8	Inverse Multiplication Plot for Detector C-3* during Central Poison Wire Removal	7-22
7-9	Average Inverse Multiplication Plot during Central Poison Wire Removal	7-23
7-10	Comparison of Various Techniques of Computing Shutdown	7-27
7-11	Relative Drum Worth Uniformity Comparison	7-39

Figure		Page
7-12	Variation of Control Drum Position during EP-III	7-49
7-13	Variation of Control Drum Position during EP-IV	7-50
7-14	NRX/EST and NRX-A5 Control Drum Position during Operation above 3800°R Chamber Temperature	7-51
7-15	NRX-A5 Reactivity Loss in EP-III	7-54
7-16	NRX-A5 Reactivity Loss in EP-IV	7-55
7-17	NRX-A5 Reactivity Loss Rate in EP-III	7-56
7-18	NRX-A5 Reactivity Loss Rate in EP-IV	7-57
7-19	Time Behavior of Reactivity Loss Rate	7-58
7-20	Variation with Drum Position of Radial Fuel Channel Coolant Density-MCAP Calculation	7-63
7-21	Summary of Reactivity Loss Rate Experience to Date	7-67
7-22	NRX/EST Performance Map	7-70
8-1	Cross Sectional View of NRX-A5 Showing Dosimeter Locations	8-6
8-2	Elevation View of Test Cell Wall Showing NRX-A5 Dosimeter Locations	8-7
8-3	Plan View of Test Cell Pad Showing NRX-A5 Dosimeter Locations	8-8
8-4	This Figure is Intentionally Deleted	
8-5	Axial Distribution of the Gamma Ray Dose Rate on the Surface of the Pressure Vessel	8-14
8-6	Gamma Ray Dose Rate Distribution on the Dosimeter Role	8-17
8-7	Gamma Ray Dose Rate on the Reactor Midplane versus Distance from Reactor Axis	8-18
8-8	Gamma Ray Dose Rate Distribution on the Top Surface of the Privy Roof Shield	8-19
8-9	Gamma Ray Dose Rate Distribution Under the Privy Roof (Horizontal Traverse at Approximately Station-108)	8-20
8-10	Gamma Ray Dose Rate Distribution on the Test Cell Wall (Horizontal Traverse in the Core Midplane)	8-23

Figure		Page
8-11	Gamma Ray Dose Rate Distribution on the Test Cell Wall (Vertical Traverse Five Feet North of Reactor)	8-24
8-12	Gamma Ray Dose Rate on the Test Pad (Traverse Parallel to the Wall and 3 Feet from the Wall)	8-25
8-13	Gamma Ray Dose Rate Distribution on the Test Pad (Traverse Normal to Wall and 5 Feet North of Reactor)	8-26
8-14	Axial Distribution of the Fast Neutron Flux (E > 2.9 Mev) on the Surface of the Pressure Vessel)	8-31
8-15	Fast Neutron Flux (E > 2.9 Mev) Distribution on the Dosimeter Pole	8-33
8-16	Fast Neutron Flux (E > 2.9 Mev) Distribution on the Top Surface of the Privy Roof Shield	8-34
8-17	Fast Neutron Flux (E > 2.9 Mev) Distribution Under the Privy Roof (Horizontal Traverse-Station-108)	8-36
8-18	Fast Neutron Flux (E > 2.9 Mev) Distribution on the Reactor Axis under the Privy Roof	8-37
8-19	Fast Neutron Flux (E > 2.9 Mev) Distribution on the Test Cell Wall (Horizontal Traverse in the Core Midplane)	8-39
8-20	Fast Neutron Flux (E > 2.9 Mev) Distribution on the Test Cell Wall (Vertical Traverse Five Feet North of the Reactor)	8-40
8-21	Fast Neutron Flux (E > 2.9 Mev) Distribution on the Test Pad (Traverse Parallel to the Wall and 3 Feet from the Wall)	8-41
8-22	Fast Neutron Flux (E > 2.9 Mev) Distribution on the Test Pad (Traverse Normal to the Wall and 5 Feet North of the Reactor)	8-42
8-23	Axial Distribution of the Thermal Neutron Flux (E < 0.4 ev) on the Surface of the Pressure Vessel	8-48
8-24	Thermal Neutron Flux (E < 0.4 ev) Distribution on the Dosimeter Pole	8-49
8-25	Thermal Neutron Flux (E < 0.4 ev) Distribution on the Top Surface of the Privy Roof Shield	8-50
8-26	Thermal Neutron Flux (E < 0.4 ev) Distribution Under the Privy Roof (Horizontal Traverse-Station-108)	8-51

Figure		Page
8-27	Thermal Neutron Flux (E<0.4 ev) Distribution on the Reactor Axis Under the Privy Roof	8-52
8-28	Thermal Neutron Flux (E<0.4 ev) on the Test Cell Wall (Horizontal Traverse in the Core Midplane)	8-53
8-29	Thermal Neutron Flux (E<0.4 ev) Distribution on the Test Cell Wall (Vertical Traverse Five Feet North of the Reactor)	8-54
8-30	Thermal Neutron Flux (E<0.4 ev) Distribution on the Test Pad (Traverse Parallel to the Wall and 3 Feet from the Wall)	8-55
8-31	Thermal Neutron Flux (E<0.4 ev) Distribution on the Test Pad (Traverse Normal to Wall and 5 Feet North of the Reactor)	8-56
8-32	Schematic Diagram of NRX-A5 Calorimeter	8-59
8-33	View of Test Facility Showing Calorimeter Locations for the Various NRX Test Series	8-61
8-34	Gamma Ray Isodose Pattern Around a Typical NRX Reactor in Test Cell A	8-71
8-35	Fast Neutron (E>2.9 Mev) Isoflux Pattern Around a Typical NRX Reactor in Test Cell A	8-72
8-36	Isoheating Rate Contours for Aluminum Around a Typical NRX Reactor in Test Cell A	8-73
9-1	NRX-A5 Experimental Fissions per Gram Values as Derived from Gross Radiation Measurements, Uncorrected for Fission Product Loss	9-8
9-2	Comparison of Theoretical and Uncorrected Experimental Fissions/ Gram Uranium	9-9
9-3	The Effect of Corrosion on Fission Product Activity by Various Methods	9-13
9-4	Loss of Fission Product Activity Due to Corrosion (Scintillation Detector Measurements)	9-15
9-5	Loss of Fission Product Activity Due to Corrosion (Scintillation Detector Measurements)	9-16

Figure		Page
9-6	Loss of Fission Product Activity Due to Corrosion (Scintillation Detector Measurements)	9-17
9-7	NRX-A5 Experimental Fission per Gram Values, Corrected for Fission Product Loss	9-20
9-8	Comparison of the Theoretical and Experimental Fissions/Gram Uranium (Experimental Values Adjusted for Corrosion Effects)	9-21
9-9	Ratio of the NRX-A5 Experimental (Adjusted for Fission Product Loss) to Calculated Fissions per Gram, Each Fission Distribution Being Normalized to Unity in the Center-Most Cluster	9-22
9-10	Ratio of the NRX-A5 Experimental (Adjusted for Fission Product Loss) to Calculated Fissions per Gram, Each Fission Distribution Being Normalized to a Unity Average Factor in the Core	9-23
9-11	Ratio of NRX-A5 Hot to PAX-D Cold Experimental Fission Densities	9-28
9-12	Comparison of the Measured and Predicted Axial Power Distributions for Low Weight Loss Elements in NRX-A5	9-30
9-13	Comparison of NRX/EST and NRX-A5 Radiochemical Power Measurements	9-32

LIST OF TABLES

Table		Page
1-1	Summary of NRX-A5 Test Series	1-4
3-1	Comparison of Measured and Computed Reactor Pressures and Pressure Drops for the Ambient Hydrogen Flow Test	3-13
3-2	Power Computed from Rate of Core Temperature Increase - Results of Simplified Analysis	3-17
3-3	NRX-A5 Steady State Power and Flow Data	3-45
3-4	Comparison of Measured Nuclear with Computed Thermal Power	3-46
3-5	Steady State Comparison of Test Data with Calculated Results	3-56
3-6	NRX-A5 EP-111 Cooldown : Comparison of Decay Power Computed from Test Data with Predictions	3-76
3-7	Summary of Cold Flow Runs, Power Runs, and Aborts during NRX Testing	3-83
3-8	NRX Key Environmental Conditions	3-88
3-9	Detailed Breakdown of Times above Chamber Temperature for NRX/EST and NRX-A5	3-89
3-10	Detailed Breakdown of Times above Core Station 20 Temperature for NRX/EST and NRX-A5	3-90
3-11	Detailed Breakdown of Times above Core Station 26 Temperature for NRX/EST and NRX-A5	3-91
4-1	NRX-A5 Full Power Hold Reflector Hydraulic Conditions	4-11
4-2	Rate of Temperature Increase during Full Power Holds	4-28
4-3	Comparison of NRX-A3, NRX/EST, and NRX-A5 Control Drum Material Temperature Responses	4-31
4-4	NRX-A5 Calculated Shield and Tie Bolt Material Temperature	4-33
4-5	NRX-A5 Hot Buffer Filler Strip Breakage Tabulation	4-39
5-1	NRX-A5 Comparison of Measured and Calculated Pressure Drops	5-6

Table		Page
5-2	Core Pressure Drop Comparison between NRX-A5 and NRX/EST	5-7
5-3	NRX-A5 Comparison of Measured and Calculated Core Flow and Power for Measured Pressure Drop and Chamber Conditions	5-8
5-4	Instrumentation for Analysis of Variance in NRX-A5	5-10
5-5	NRX-A5 Core Operating Conditions in EP-IV and Comparison with Design Values	5-18
5-6	Temperature Increase due to Control Drum Rotation	5-35
5-7	Equations of Multiple Regression Fit to Thermal Capsule Temperatures Core Station 44 Inches	5-59
5-8	Comparison of Radial Temperatures in NRX/EST and NRX-A5	5-80
5-9	Factors Considered in Analysis of Element-to-Element Temperature Variations	5-81
5-10	Tabulation of Maximum Temperatures in NRX-A2, NRX-A3, NRX/EST and NRX-A5	5-82
5-11	NRX-A5 Temperature - EP-III (4 Holds)	5-88
5-12	NRX-A5 Temperature - EP-III (25400)	5-89
5-13	Summary of Results of Analysis of Variance on NRX-A5 Thermocouples	5-90
6-1	NRX-A5 Total Fuel Element Weight Loss	6-4
6-2	Comparison of the NRX/EST and NRX-A5 Fuel Element Weight Loss	6-7
6-3	NRX-A5 First Row Elements, WAFF, Code 39 Overall Weight Loss	6-45
6-4	NRX-A5 Second Row Elements, WAFF, Overall Weight Loss	6-46
6-5	Comparison of Percent Elements Broken in Normal Periphery and Hot Buffer Periphery	6-47
6-6	Location Rating Factor	6-56
6-7	Pinholing and Channel Exposure	6-66
6-8	NRX-A5 Summary Data for Pinholing and Channel Exposure	6-71
6-9	NRX-A5 Fuel Elements with Zero Pinholes and Zero Channel Exposure	6-83

Table		Page
6-10	Summary of Coating Batches in Elements Used for the NRX-A5 Multiple Regression on Total Weight Loss	6-96
6-11	Correlation Parameters	6097
6-12	Results of Correlation on the NRX-A5 Total Weight Loss Measurements	6-99
6-13	Comparison of Weight Losses in Elements with Hole Location VR's	6-103
7-1	Peripheral Poison Wire Removal Increments	7-6
7-2	NRX-A5 Peripheral Poison Wire Removal Data	7-7
7-3	Effect of Axial Positioning on Detector Response during NRX-A5 Peripheral Wire Removal	7-11
7-4	Central Poison Wire Removal Data (All Drums at Zero)	7-16
7-5	Central Poison Wire Removal Data (One Drum at 180 Degrees)	7-17
7-6	Central Poison Wire Removal Data (Extrapolation Using Recent and Next-Most-Recent Data Points)	7-18
7-7	Calculated Shutdown Margin Data	7-26
7-8	Summary of Shutdown Data	7-28
7-9	Analysis of Drum No. 2 Calibration Data by R-102	7-31
7-10	Analysis of Drum Bank Bumps by R-102	7-33
7-11	Summary of Selected EF-1 Reactivity Measurements	7-34
7-12	Drum Printout Data for Relative Integral Drum Worth Measurements	7-38
7-13	Summary of Selected NRX-A5 Post-Test Criticality Data	7-42
7-14	Summary of Critical Control Drum Positions	7-46
7-15	Predicted versus Experimental Cold Critical Drum Positions of NERVA Reactors	7-47
7-16	Statistical Fit of NRX-A5 Reactivity Loss and Loss Rate Data	7-61
7-17	Summary of Reactivity Effects Resulting from Propellant Flow Redistribution	7-64

Table		Page
7-18	Hydrogen Worth Calculations	7-66
7-19	Selected NRX-A5 Cold-to-Hot Swing Calculations	7-71
8-1	Location of NRX-A5 Dosimetry	8-5
8-2	Comparison of Experimental with Calculated NRX-A5 Gamma Ray Dose Rate Data	8-12
8-3	Comparison of Experimental with Calculated NRX-A5 Fast Neutron Flux (E > 2.9 Mev) Data	8-29
8-4	NRX-A5 Thermal Neutron Flux Measurements	8-44
8-5	NRX-A5 Heating Rates from Calorimeter Measurements	8-62
8-6	NRX-A5 Calorimeter Heating Rates Adjusted to 100 Percent Power (1[illegible] MW)	8-65
8-7	Comparison of Calculations with Measurements of Calorimeter Data for NRX-A5	8-67
8-8	Comparison of Calorimeter Data from All NRX Reactor Tests	8-68

CHAPTER I
INTRODUCTION

This report presents the results of the thermal and nuclear analysis of the NRX-A5 reactor test. The NRX-A5 test series which extended from the initial criticality on 26 May 1966 to the final endurance test on 23 June 1966, is summarized in Table 1-1. Included in this table are the accumulated times above specified chamber temperature levels and the integrated thermal power for each experimental test plan. Sinusoidal transfer function tests were not performed and only 125 seconds of cross correlation measurements were taken during EP-III. The total integrated power was 2.16×10^6 MW-sec or 36,000 MW-min which is the equivalent to 32.1 minutes at the design power of 1120 MW.

Two secondary test objectives were successfully accomplished as part of the two endurance runs. A startup with fixed control drums was performed from 30 KW to near design power. This startup covered the greatest power range to date for this mode of startup. A new controller, the "no-flux loop" temperature controller, was successfully used during startup, steady state, and shutdown operations. The specific objectives of each experimental plan together with data on whether or not they were met are given in the Three Day Reports[1,2,3] and the Site Test Report.[4]

Two photographs are included to show the NRX-A5 reactor both prior to the test series and during the second power run. Figure 1-1 shows the NRX-A5 Test Assembly mated to Test Cell "A". A good view of Test Cell "A" and the reactor during power operation is shown in Figure 1-2.

The purpose of this report is to present the NRX-A5 test data that are most significant from a thermal and nuclear standpoint, to describe the analysis that have been performed on these data, and to present the conclusions drawn from these analyses. Companion test analysis reports have been prepared for the NRX-A2[5], NRX-A3[6], and NRX/EST.[7] An additional objective of this report is to compare the results of the NRX-A2, NRX-A3, NRX/EST, and NRX-A5 test analyses. Therefore this report also contains a comprehensive discussion of the important conclusions in each technical area from the NRX test series to date.

The principal thermal, fluid flow, corrosion, nuclear, and radiation characteristics of the NRX-A5 reactor are given in the NRX-A5 Data Book.[8] Similar key characteristics of the NRX-A2, NRX-A3, and NRX/EST reactors are given respectively in References 9, 10, and 11.

This report is divided into nine chapters, the first two are the Introduction and Summary. Chapters 3, 4, and 5 are concerned with thermal analysis, chapter 6 with the corrosion analysis, chapters 7 and 9 with nuclear analysis, and chapter 8 with radiation environment analysis. Each of these last seven chapters contains either a summary or conclusions section in greater detail than is given in Chapter 2.

Chapter 3 contains a detailed description of the power test profiles including time history plots of all major performance parameters. Best estimated chamber temperature, flow rate, and power are determined for 10 steady state points. Post test calculations are made for four steady state points and three transients and the major performance parameters are compared with test data. The relationship between reactor temperatures and power during low power-no flow operation is examined to determine the feasibility of using the sensible heat method to calibrate neutronic power. Reactor decay power computed from test measurements is compared with S-4 (Fission Product Energy Release Code) predictions. A comparison of station 26 and chamber temperature as primary temperature control feedback is made for the NRX/EST and NRX-A5 tests. An evaluation of the effect of the Privy Roof Mounted Shield on NRX/EST reflector heating is presented.

In Chapter 4, steady state and transient temperatures and pressures in the inner and outer reflectors, control drums, lateral support system and filler strips are presented and discussed. Comparison of pertinent results are made with previous NRX tests.

Chapter 5 contains a discussion of the core pressure drop and core thermocouple and thermal capsule temperature measurements. The change in core temperature distribution resulting from control drum movement, inlet temperature asymmetry, and the shim pattern are discussed. A transient analysis of a peripheral element during shutdown is included. Comparisons are made with previous NRX tests.

Chapter 6 contains a discussion of the fuel element corrosion performance in the NRX-A5. The corrosion characteristics considered, include overall fuel element weight losses, incremental and surface weight losses, pinholing and channel exposure. In addition, an assessment of the filler strip, support block, and fuel element hot end condition is made. The analytical techniques for predicting corrosion are presented. Comparisons are made with NRX-A3 and NRX/EST corrosion performance.

Chapter 7 contains a discussion of the inherent reactivity of the reactor, control drum worth, reactivity feedback of the fuel temperature and hydrogen propellant, low power temperature coefficients of reactivity and reactivity loss resulting from corrosion.

Chapter 8 presents the analysis of data obtained from the radiation measurements program on the nuclear environment surrounding the reactor. Included are gamma ray dose rates, neutron fluxes, and heating rates external to the reactor. Typical radiation patterns around an NRX reactor at Test Cell "A" are presented.

Chapter 9 presents the radial and axial fission distributions established by post-test gross radiation measurements and radiochemical analysis. These are corrected for fission product loss and compared with calculated values. Comparisons with previous NRX tests are also included.

TABLE 1-1

SUMMARY OF NRX-A5 TEST SERIES

Experimental Plan		Type of Test	Time Above Chamber Temperature (Minutes) 1900°R	3600°R	3900°R	Integrated Thermal Power (MW-Sec)
I	1	Initial Criticality	--	--	--	7.5
	2	Control Drum Bank Worth Measurements				
	3	Phase I Neutronic Calibration				
	4	Ambient GH_2 Flow Test				
	5	Cold GN_2 Flow Test				
	6	LH_2 Flow Decay Tests (Flow bypassed reactor)				
II	1	Phase II Neutronic Calibration	--	--	--	53
	2	Power Limiter Checkout at Low Power				
	3	Low Power Dosimetry Irradiation				
III	1	Engine Endurance Test	18.7	16.1	11.9	1.10×10^6
	2	Power and Temperature Limiter Checkout				
	3	Cross Correlation Measurements n RPM Loop at Rated Conditions				
	4	Operation with No-Flux Loop Temperature Controller				
IV	1	Engine Endurance Test	16.5	14.8	14.6	1.06×10^6
	2	Fixed Drum Startup from 30 KW to 850 MW				

Astronautics Laboratory

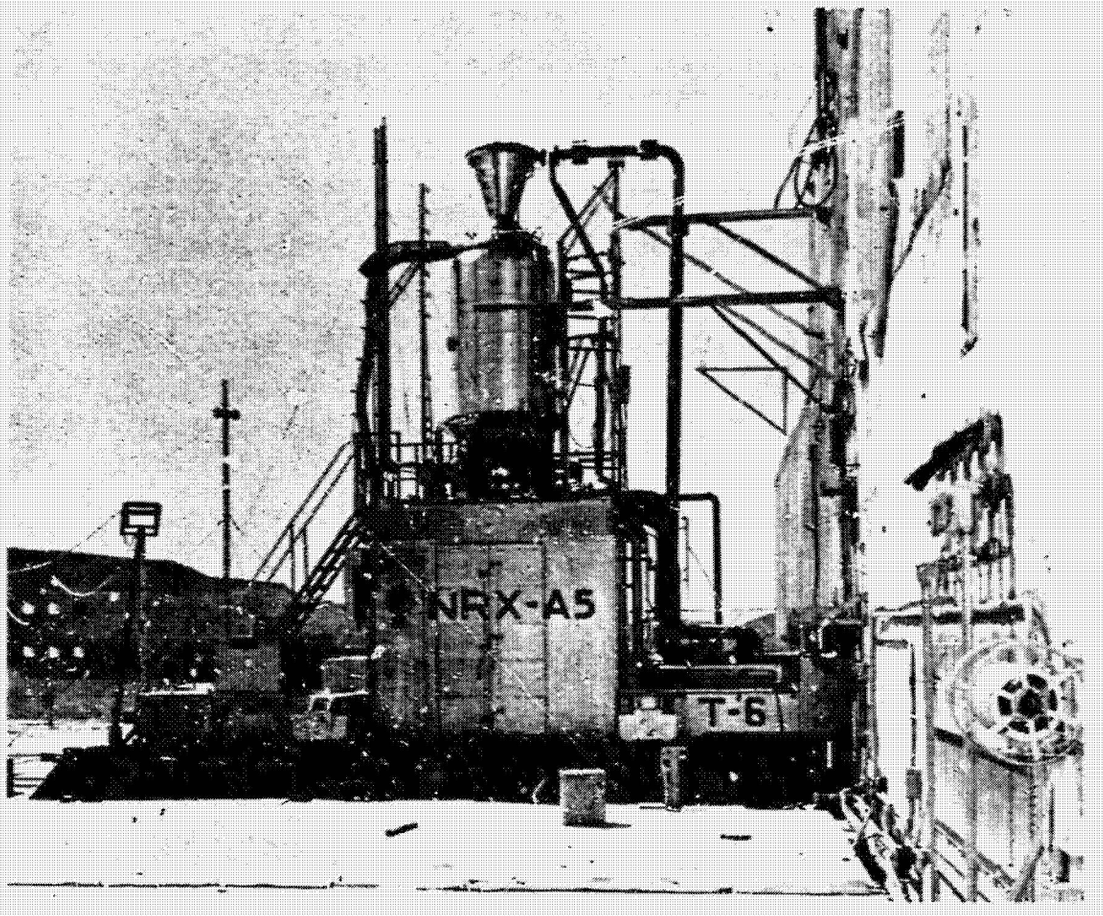

Figure 1-1 NRX-A5 Test Assembly Mated to Test Cell "A"

Figure 1-2 NRX-A5 Test Assembly at Test Cell "A" During EP-IV (Second Full Power Test)
(smoke at right of hydrogen plume is from JATO motors used as Effluent Cloud Marker)

REFERENCES

1. NTO-R-0076, NRX-A5, EP-I Test Report, Initial Criticality, Neutronic Calibration, Control Drum Worth Measurements and Flow Tests, 2 June 1966.

2. NTO-R-0078, NRX-A5, EP-II and EP-III Test Report, First Power Test, 14 June 1966.

3. NTO-R-0080, NRX-A5, EP-IV Test Report, Second Power Test, 28 June 1966.

4. NTO-R-0084, NRX-A5, Site Test Report, 28 July 1966.

5. WANL-TNR-199, "Analysis of NRX-A2 Reactor Test Results," April 1965.

6. WANL-TNR-202, "NRX-A3 Reactor Final Test Report," December 1965.

7. WANL-TNR-216, "NRX/EST Reactor Test Analysis Report," December 1966.

8. WANL-TME-1389, "NRX-A5 Reactor Analysis Data," 15 April 1966.

9. WANL-TME-1210, "NRX-A4/EST Reactor Analysis Data," 30 August 1965.

10. WANL-TME-840A, "NRX-A3 Reactor Analysis Data."

11. WANL-TME-840, "NRX-A2 Reactor Analysis Data."

CHAPTER 2

SUMMARY

2.1 PERFORMANCE ANALYSIS

Two full power endurance tests were performed during the NRX-A5 test series. The second test featured a fixed control drum startup over the greatest power range for this mode of startup (approximately 30 KW to 850 MW) in the NRX test program to date. The startup was extremely smooth with a peak chamber temperature ramp rate of 55°R/sec and minimum reactor period of 1.8 seconds. The accumulated run time for both endurance tests was 30.1 minutes above 3700°R chamber temperature.

Detailed steady state and transient comparisons of thermal performance parameters were made with TNT (Thermal and Transient Computer Code) post test calculations. The comparisons between test data and calculations are reasonably good and indicated that the TNT code is adequate for the purpose of test prediction calculations.

The decay power was computed from test data for the cooldown following EP-III. The experimental power compares satisfactorily with the decay power predicted by Revision 1 of the S-4 (Fission Product Energy Release) code.

The relationship between power and rate of core temperature increase during low power - no flow operation was determined. This analysis indicated that thermal power calibration during low power - no flow operation is a feasible means for the calibration of the nuclear power measuring instruments.

A comparison of heat generation in the peripheral reactor components for NRX/EST and NRX-A5 indicated that an accurate evaluation of the increased heating resulting from the external shield could not be made because the uncertainties in the data were of the same order of magnitude as the calculated shield effect.

A comparison of average station 26 temperature with average chamber temperature for both NRX/EST and NRX-A5 indicated that either measurement could be used as the primary control temperature.

2.2 REFLECTOR AND SEAL SYSTEM, AND FILLER STRIPS

The reflector, lateral support system, and other peripheral reactor components performed satisfactorily during the power tests; however, broken filler strips were discovered in the hot buffer region during disassembly. The reflector pressure drop showed good agreement with calculations. The performance of the lateral support seal system was similar to NRX/EST. The normalized seal pressure distribution decreased with operation as a result of core periphery corrosion which perturbs the coolant flow in the seal chambers. The maximum measured temperature difference across the diameter of the redesigned control drums was about 15°R which is considerably less than for previous reactors. Consequently control drum rubbing did not occur during the test series. This significant reduction in the temperature difference is due to the addition of a cooling slot in the control drum opposite the vane.

Continuous gradual temperature increases in the beryllium and graphite reflector components similar to previous tests were observed. The rates of temperature rise at station 32 for the NRX reactors were 1.2°R/minute for the beryllium sector, and 7.2 and 18.5 °R/minute depending on radial location for the graphite barrel.

The maximum measured filler strip temperatures were 4400°R in the hot buffer region and 2350°R in the nominal region. The maximum temperatures measured in the nominal filler strips were in agreement with calculations. The hot buffer strip temperatures were also in agreement except at the hot end where the measured temperatures were lower than predicted. The lower predicted temperatures were attributed to higher than calculated radial inflow of seal coolant. The hot buffer filler strip breaks were attributed to bridging of the strips during the shutdown transients.

2.3 CORE TEMPERATURES

Agreement between core temperatures indicated by thermocouples and by thermal capsules was good. The agreement of these measurements with predictions was also good, ±50°R on the radial average and ±200°R at any core location, except in the core center after the development of extensive corrosion. The maximum measured material temperature

in the core central region, determined from a thermal capsule in an unfueled element, was 4700°R at the start of EP-III with a control drum position of 109 degrees. The maximum measured temperature in the core peripheral region was 4840°R at the end of EP-IV with a control drum position of 145 degrees. The average fuel element exit gas temperatures that correspond to these maximum thermal capsule temperatures were calculated to be 4277°R and 4275°R, respectively.

Analysis of variance on the core thermocouple temperatures near full power design conditions indicated less than ±60°R radial and circumferential temperature variations. Also, no azimuthal temperature variation as a result of power scalloping caused by change in control drum position was detected.

During the full power hold of EP-IV, a number of thermocouples located in the unfueled elements in the core central region, experienced sudden decreases in temperature at various times during otherwise steady state conditions. This behavior was attributed to corrosion of the adjacent fuel elements resulting in coolant flow in the interelement region.

Tie rod material temperatures at the initial full power condition varied from 760°R at the core center to 620°R at the periphery. The maximum difference at any location between the measured and calculated tie rod material temperatures was 60°R.

2.4 CORROSION

The average NRX-A5 fuel element weight loss was 27 grams per element, based on measurements taken on 1551 elements (925 unbroken, 626 broken). For comparison, the average fuel element weight loss of the NRX/EST was 32.4 grams per element. The overall weight loss performance of the NRX-A5 Y-12 fuel elements was better than the WAFF fuel elements. Between 15 and 30 percent of the total fuel element weight loss was attributed to loss of material from the external surfaces of the elements and the remainder to loss of material from the coolant channel surfaces.

The overall integrated incremental weight loss was highest (42.3 grams) in the core central region and lowest (16.3 grams) in the mid-radial region. The NRX-A5 exhibited a

well-defined peak midband weight loss at approximately core station 20.0 inches and a relatively lower hot end weight loss from core stations 30 to 52 inches.

The number of pinholes and lengths of channel exposure were measured for the NRX-A5 fuel elements. The Y-12 fuel elements exhibited an average of 7.3 pinholes per element and an average channel exposure length of 6.1 inches per element compared to an average of 12.5 pinholes and 33.9 inches of channel exposure for the WAFF fuel elements.

The condition of the fuel element hot ends was excellent as a result of the reduced undercut depth at the aft end of the NRX-A5 elements.

The mechanical and corrosion performance of the support blocks was better than for previous reactors. This was attributed to slower startups and to the absence of extended low power operation.

2.5 NUCLEAR ANALYSIS

The initial ambient critical control drum position of 99.3 degrees compares well with the final prediction of 95.0 ±7 degrees and reasonably well with the 93 degree aim position.

The final ambient critical position following the test series was 137.3 degrees, indicating that 2.36$ reactivity loss resulted from corrosion. The changing critical angle during operation indicated that the rate of reactivity loss increased exponentially with elapsed time at full power.

The analysis of drum worth data indicated a control drum span of 8.2$, as compared to the predicted 8.5$, and confirmed the uniformity of the individual drum worths.

The measured reactivity swings to full power proved to be well represented by the NRX/EST empirical reactivity feedback model.

The actual power distribution was inferred from NTO fuel element radiochemistry after correction for the effects of corrosion on fission product activity. When the result was compared with predictions for the effective average control drum position of 119 degrees over the test series, the largest difference was 4.7 percent. These errors are attributed mainly to fuel loading changes between the NRX-A5 and the NRX-A3 reactor, on which the hot power predictions were based.

The derived radial power shape at full power proved to be identical to the power distribution measured in the PAX reactor at room temperature, except in the peripheral fuel elements, where the power density was slightly higher at operating conditions.

2.6 DOSIMETRY

Typical radiation patterns around an NRX reactor in Test Cell "A" were determined on the basis of NRX-A2, NRX-A3, and NRX-A5 dosimetry test data, and supplementary calculated data. The data are presented in the form of iso-flux contours for fast neutrons, iso-dose rate contours for gamma rays, and iso-heating rate contours for radiation heating. These radiation levels are generally considered to be accurate within a factor of two.

Six calorimeters were employed during the NRX-A5 high power test to measure heating rates outside the reactor. These calorimeters provided useful heating rates on the privy roof, at the aluminum shield flange, and at a radii of 25 feet from the core center on the midplane.

CHAPTER 3

PERFORMANCE ANALYSIS *

The performance analysis of the NRX-A5 reactor test is described in this chapter. The scope of the analysis is summarized below:

1) A detailed description of each power test including time history plots of all major performance parameters.
2) Detailed steady state and transient performance comparisons between calculations and test data.
3) Best estimated chamber temperature, power, and flow rate data.
4) Comparison of decay power computed from test data with predictions.
5) An analysis to determine the feasibility to calibrate neutronic power from a heat capacity test utilizing the rate of core temperature increase.
6) A performance summary of NRX test results. Included is reflector heating in NRX/EST and NRX-A5, and a comparison of core station 26 with chamber temperature for NRX/EST and NRX-A5.

3.1 SUMMARY

Two full power endurance tests were performed during the NRX-A5 test series. The second test featured a fixed control drum startup over the greatest power range for this mode of startup (30 KW to near full power) to date in the NRX testing program. The startup was extremely smooth with a peak rate of change of chamber temperature of 55°R/sec and a minimum reactor period of 1.8 seconds. The accumulated run time for both endurance tests was 30.1 minutes above 3700°R nozzle chamber temperature, and 26.5 minutes above 3900°R nozzle chamber temperature.

Best estimated chamber temperature, flow rate, and thermal power were computed for 10 steady state points. Steady state comparisons between test data and TNT (Thermal and Nuclear Transients program) calculations were made for four of these points; two points for

---

* Major contributors to this chapter were R. R. Burghardt, J. Homan, W. L. Knecht, G. R. Reithmiller, and R. P. Vijuk.

each EP. In addition transient comparisons for both startups and the EP-4 shutdown were made. The comparisons between test data and calculations are reasonably good for all performance parameters. The input parameters for the EP-IV startup calculation were control drum position and flow rate. The calculated power based on these inputs is in good agreement up to 400 MW; at higher power the computed power is about 10 percent low.

The decay power was computed from test data obtained during the cooldown following the first power run, EP-III. The experimental power compares satisfactorily with the decay power predicted by Revision 1 of the S-4 (Fission Product Energy Release) code. As part of this analysis, modifications to the data recording intervals were defined to increase the scope of the decay power calculation for future tests.

Data obtained during the neutronic calibration test of EP-II was used to determine the relationship between rate of core temperature change and power without coolant flow. This analysis indicated that a detailed multi-node model of the core and reactor is required to adequately simulate this relationship. The computed temperatures showed good agreement with test data for a power 10 percent above measured nuclear power. During EP-III, the measured nuclear power (linear No. 1) was also 10 percent greater than the best estimated thermal power. Therefore, on a qualitative basis thermal power calibration is feasible for calibrating the nuclear power measuring instruments.

A comparison of heat generation in the peripheral reactor components (reflector system, pressure vessel, shield, core support plate) was made for NRX-A5 and NRX/EST, primarily to determine the effect of the external shield on the NRX/EST. Thermal data was analyzed in several ways but since the uncertainties were of the same order of magnitude as the calculated shield effect, it was concluded that an accurate evaluation of the increased heating resulting from the external shield could not be made from the available temperature data.

A comparison of average station 26 temperature with average chamber temperature for both NRX/EST and NRX-A5 indicates that either measurement could be used as the primary control temperature.

3.2 BACKGROUND

This section describes the feedsystem of Test Cell "A" at the Nevada Nuclear Rocket Development Station (NRDS), the NRX-A5 reactor geometry and propellant flow path, and the two implemented reactor scram shutdown procedures.

3.2.1 Test Cell "A" Feedsystem

A detailed schematic of the Test Cell "A" feedsystem is given in Reference 1. The simplified schematic in Figure 3-1 shows only the primary pipes, valves, venturis and other components which are required for a basic understanding of its operation during power testing. Liquid hydrogen propellant flows from the dewars to the reactor through a path consisting of the pump suction line, the pump, and the pump discharge line. The pump is driven by a turbine which is powered by high pressure ambient hydrogen. Liquid hydrogen flow is measured by two venturis. The FE-4 venturi measures pump inlet flow and the FE-7 venturi measures pump discharge flow. Liquid hydrogen may be vented from the pump discharge line at two locations. The ACV-6 valve controls flow vented between the pump and the pump discharge venturi. The main purpose of this valve is to keep the pump within its operating region. The AVV-2 valve controls flow vented downstream of the pump discharge venturi. The purpose of this valve is to chill the propellant line to cryogenic temperatures prior to the initiation of a run. The main propellant shutoff valve, ACV-3, is located downstream of the pump discharge venturi. Flow to the reactor during a power run is generally initiated by simultaneously closing AVV-2 and opening ACV-3.

Ambient gas is supplied to the reactor from the high pressure gas bank by a line which connects to the pump discharge line between the nozzle manifold and ACV-3. Ambient gas flow is controlled by the PCV-10 valve and measured by the FE-10 venturi. Ambient hydrogen supplied through this line is the primary source of emergency coolant (see Section 3.2.3).

3.2.2 Reactor Geometry and Flow Path

A detailed description of the NRX-A5 reactor geometry and flow path is given in the NRX-A5 Reactor Analysis Data Book.[2] The overall reactor flow path from the nozzle manifold to the core exit (nozzle chamber) is illustrated on a longitudinal section of the reactor in

Figure 3-2. The major assemblies are the core, lateral support, core support plate, reflector, aluminum replacement shield, pressure vessel, and nozzle. The propellant flow enters through the nozzle manifold and passes through the nozzle, reflector, simulated shield, core support plate, and core before exhausting through the nozzle throat. A small part of the inner reflector exit flow bypasses the shield and core by flowing through the lateral support seal system. This seal flow discharges into the core exit chamber. The seal system is composed of 18 equally spaced graphite load and seal segment rings. The core is composed of two types of channels, fuel and tie rod channels. The tie rods are part of the core structural support system. Approximately 6 percent of the core flow passes through the tie rod channels.

3.2.3 Reactor Scram Shutdown Procedures

Providing adequate protection for the reactor and engine components during a scram from full or part power is important to safeguard the test assembly. The rapid transients caused by a reactor scram or loss of the primary coolant necessitate extensive and careful analysis to assure adequate protection. The two scram shutdown procedures which were implemented for the NRX-A5 power tests are described in the following paragraphs.

3.2.3.1 FLOW Shutdown

The FLOW shutdown is the major emergency shutdown procedure for the case of loss of liquid hydrogen flow. Initiation can be accomplished either by manual or automatic control. Typical automatic initiation is through a turbopump overspeed trip or in case of complete loss of electric power at the Control Point. See Table II.C.3 in the NRX-A5 Test Specification[3] for a complete list of conditions that result in automatic activation of a FLOW shutdown. A FLOW shutdown consists of the following essentially simultaneous events:

1) Reactor scram at maximum control drum speed.
2) Closing of the urbine control valve.
3) Closing of ACV-3 and opening of vent valves to stop liquid hydrogen flow.
4) Opening of PCV-41 to initiate ambient hydrogen flow to the reactor. PCV-41 is automatically controlled to maintain a nozzle torus pressure which is determined as a function of measured core

station 26 temperature. The function is called a "tracking function" and is shown in Figure 3-3.

3.2.3.2 SCRAM Shutdown

A SCRAM shutdown consists of the following events:

1) Reactor scram at maximum control drum speed.
2) Liquid hydrogen flow is reduced exponentially to 25 lb/sec on a 1 second time constant. Flow of 25 lb/sec is maintained until manual control is initiated. The flow prior to SCRAM is maintained if it was less than 25 lb/sec.

3.2.3.3 Scram Shutdown Procedure During NRX-A5 Shutdowns

Both the SCRAM and FLOW shutdowns were used as part of the normal shutdown sequence for the two power runs. The normal shutdown sequence starts from full power, and the flow and temperature profiles are the mirror image of the startup profiles. At 2500°R the SCRAM shutdown was manually activated. This was followed by a manual FLOW shutdown when the chamber temperature had decreased to 1500°R. From this time on all further control of coolant flow was by manual control.

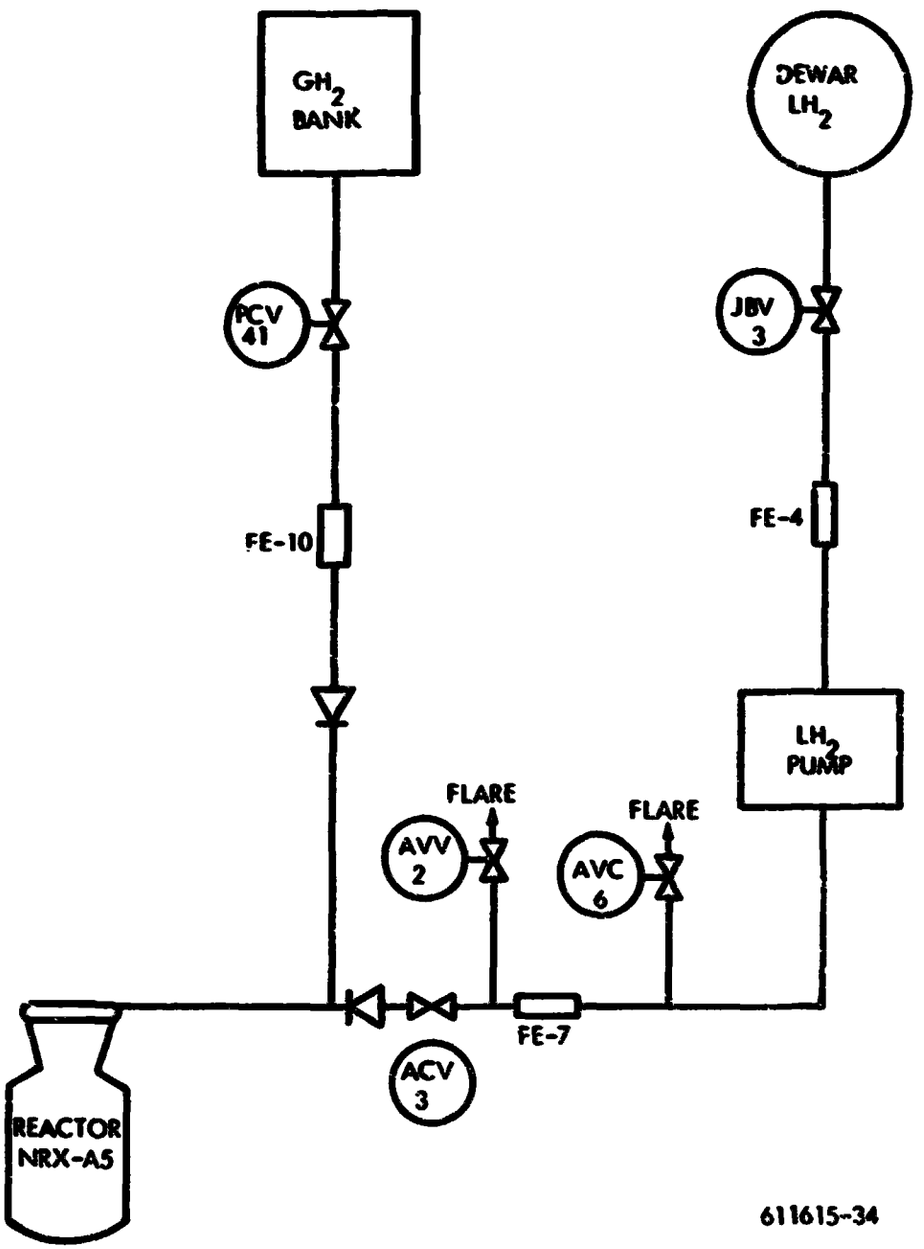

Figure 3-1. Simplified Schematic of Test Cell "A" Feed System

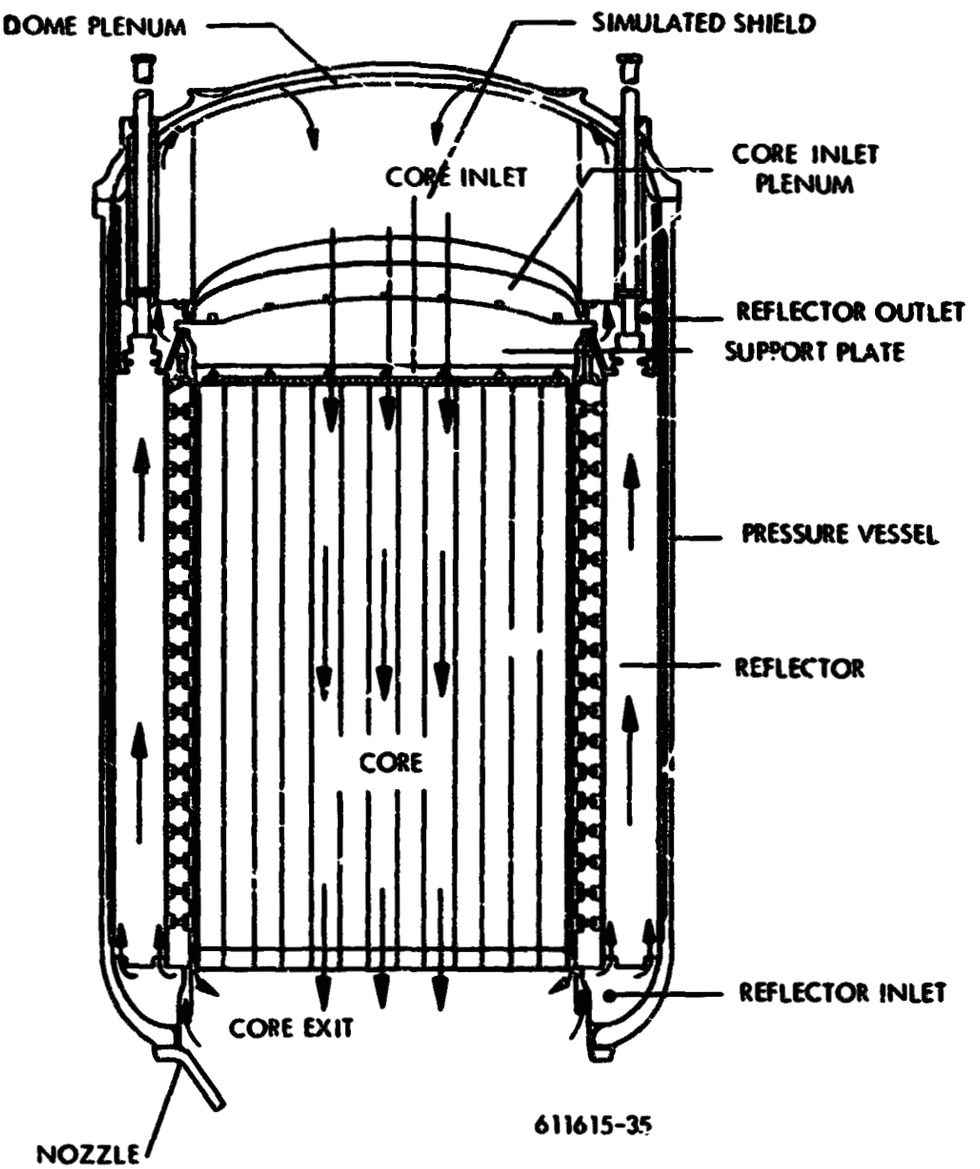

Figure 3-2. NRX-A5 Reactor Flow Path

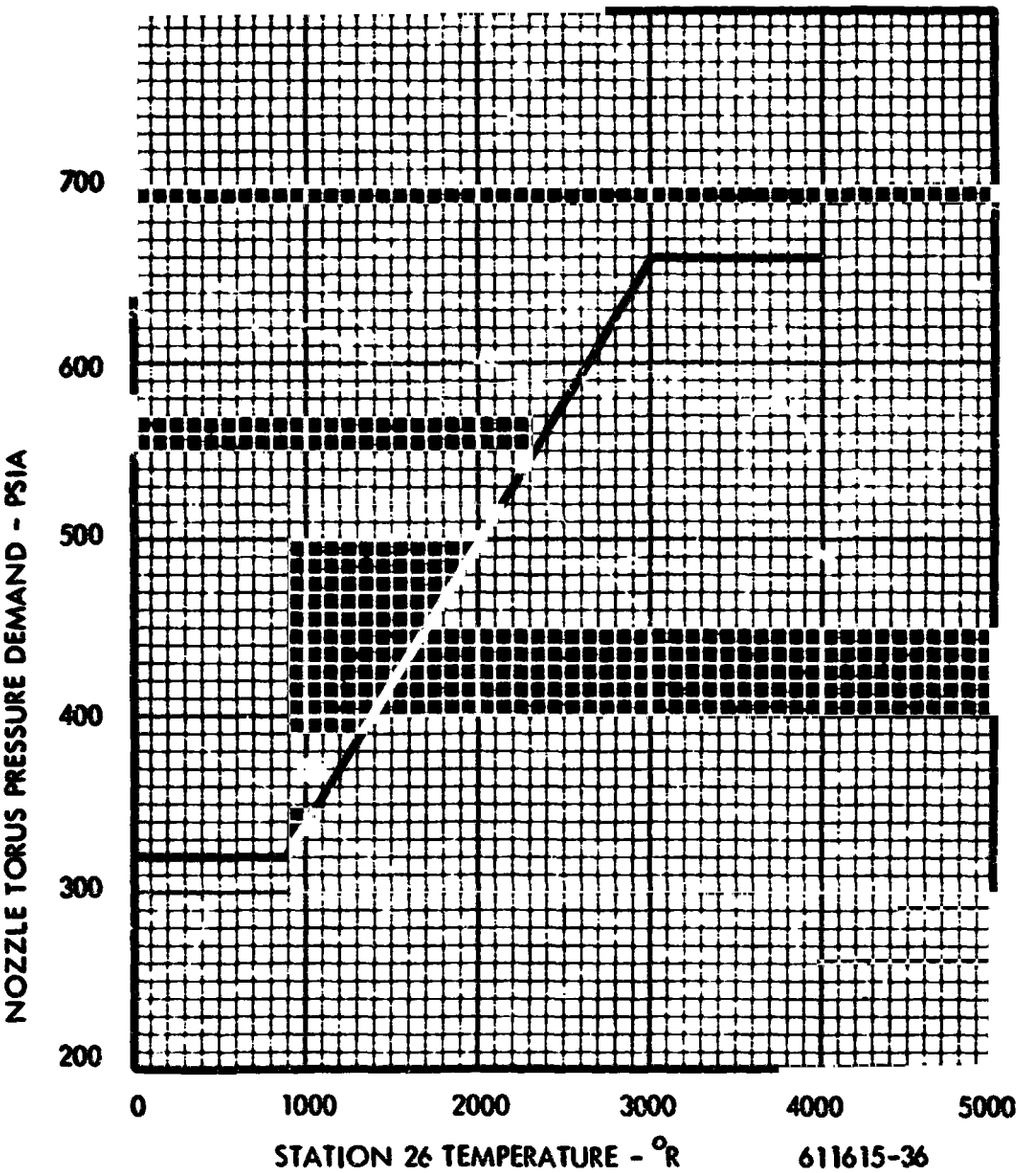

Figure 3-3. NRX-A5 Flow Shutdown Nozzle Torus Pressure Demand as a Function of Core Station 26 Temperature

3.3 PRE-POWER TESTS

The primary objectives of the pre-power tests during EP-I and EP-II were to assure that the reactor and facility were ready for the subsequent high power tests. In addition, data of interest for increasing the understanding of reactor operation were obtained from the ambient hydrogen flow test, EP-I, and the rem set neutronic calibration test, EP-II. Reactor plenum pressures and pressure drops measured during the ambient hydrogen flow test are compared with TNT (Thermal and Nuclear Transient program)* calculations. The comparison indicates that TNT adequately simulates reactor pressures and pressure drops during ambient gas flow. Data obtained during the neutronic calibration test was used to determine the relationship between rate of core temperature increase and power during low power and zero flow conditions. The results indicate that power can be computed from the rate of core temperature increase and that neutronic power can be calibrated using reactor sensible heat.

3.3.1 EP-I Ambient Hydrogen Flow Test

3.3.1.1 Test Profile

Two objectives of EP-I were to evaluate the integrity of the test assembly and to check the pressure instrumentation. The test to accomplish these objectives consisted of ramping ambient GH_2 flow at a rate of 2 lb/sec/sec to 22.3 lb/sec and holding there for a period of 16 seconds; then, the flow was programmed down to 11.4 lb/sec and held for 88 seconds before terminating the test. During the latter hold, data system and control system step response measurements were made. Profiles of flow rate, drum position, chamber pressure and nozzle torus pressure are shown in Figures 3-4 and 3-5. Reactor power was held at a nominal 1 KW level during this test.

3.3.1.2 Comparison with Predictions

The calculation of system pressures and component pressure drops at the two steady-state holds of this test was made using flow rates calculated from test measurements as input to the TNT (Thermal and Nuclear Transient) code. Ambient hydrogen flow was supplied through the FE-10 venturi (see Figure 3-1). The equation used for the flow calculation

* See Section D.5 of Reference 2 (NRX-A5 Reactor Analysis Data Book)

is,

$$W = 0.418 \frac{P_{10}}{\sqrt{T_{10}}}$$

where,

W = flow rate (lb/sec)

P_{10} = pressure upstream of FE-10 (psia)

T_{10} = temperature upstream of FE-10 ($^{\circ}R$)

A comparison of TNT calculations with test measurements is given in Table 3-1. The comparison shows that the TNT calculation results agree reasonably well with test measurements, although about half of the calculated parameters fall just outside of the 2σ variation of the test measurements. However, this criteria does not take into consideration the large uncertainty in the flow rates which were used as input for the TNT calculation. The maximum deviation of core and reflector pressure drops, and the reactor plenum pressures was less than 6 percent. In view of this agreement, it may be concluded that TNT adequately predicts reactor pressures and pressure drops during ambient hydrogen flow tests.

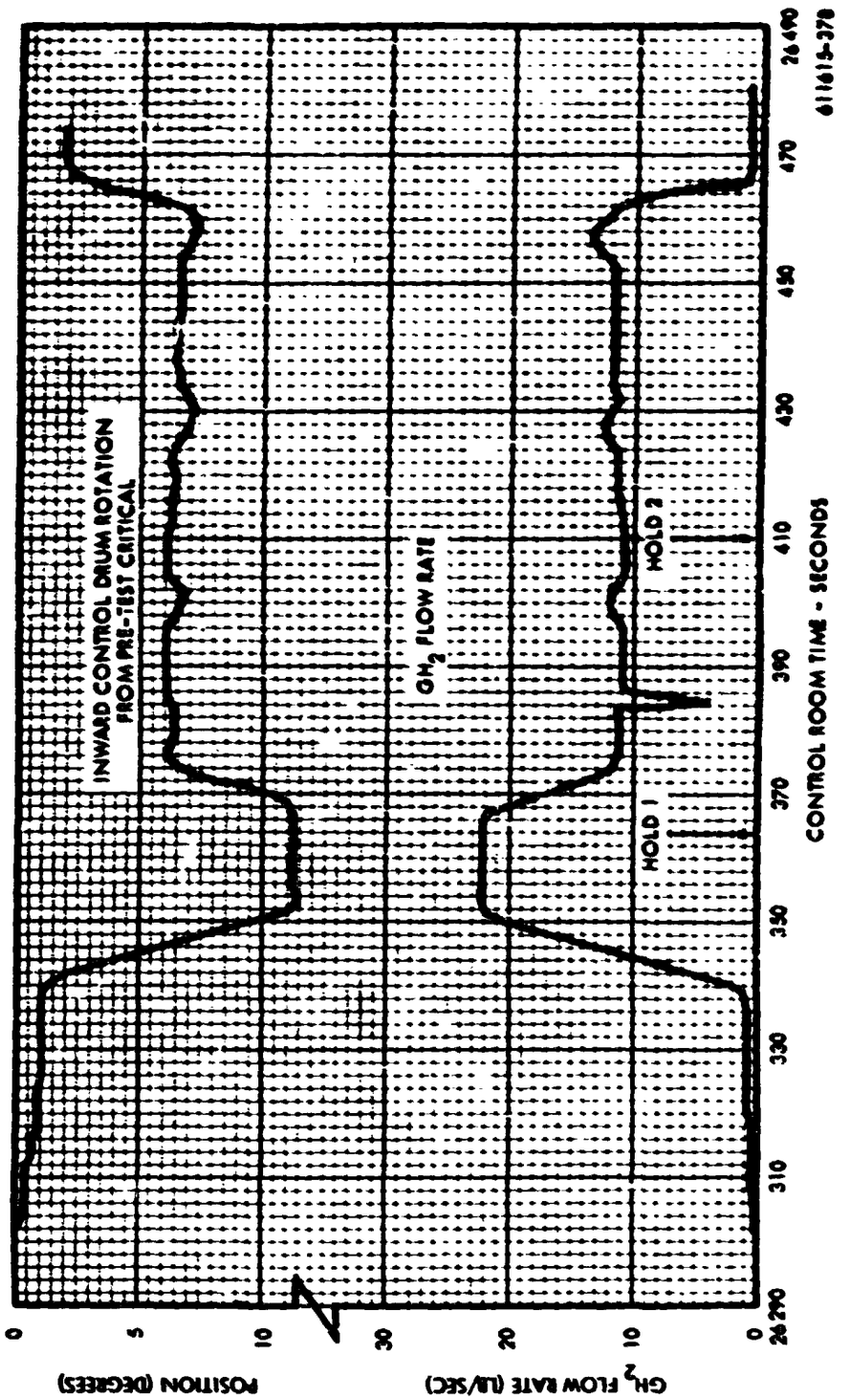

Figure 3-4. NRX-A5 EP-1 Ambient Hydrogen Flow Test: Flow Rate and Control Drum Position

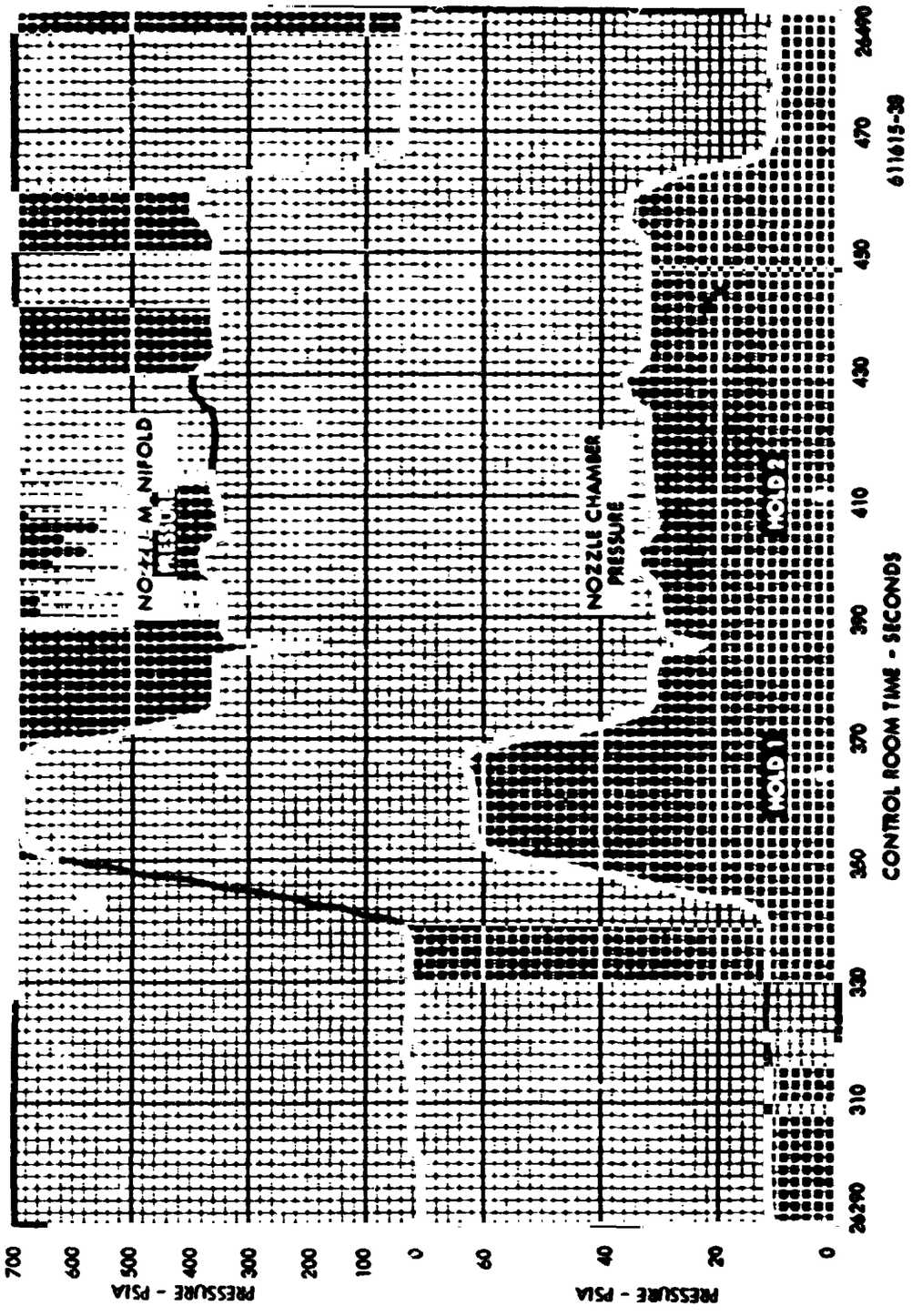

Figure 3-5. NRX-A5 EP-1 Ambient Hydrogen Flow Test: Nozzle Manifold and Chamber Pressure

TABLE 3-1

COMPARISON OF MEASURED AND COMPUTED REACTOR PRESSURES AND PRESSURE DROPS FOR THE AMBIENT HYDROGEN FLOW TEST

Parameter	Hold 1		Hold 2	
Flow Rate, lb/sec	22.3 ±3.7		11.4 ±1.9	
FE-10 Venturi,				
Inlet Temperature, °R	574.		569.	
Inlet Pressure, psia	1275.		650.	
Average Temperature of Hydrogen in Reactor, °R	565.		570.	
Pressure Drops, psi	Test ±2σ	TNT	Test ±2σ	TNT
Nozzle Tube	489.7 ± 22.0	457.8	247.7 ± 22.0	234.4
Outer Reflector	41.0 ± 1.6	38.4	21.5 ± 1.6	20.2
Inner Reflector	39.5 ± 2.0	----	20.5 ± 2.0	----
Simulated Shield and Support Plate	14.5 ± 0.8	11.6	7.5 ± 0.8	6.1
Core	92.4 ± 3.6	87.7	48.35 ± 3.6	45.6
Reflector Inlet/ Core Exit	148.5 ± 4.0	137.6	78.5 ± 4.0	71.9
Plenum Pressures, psia	Test ±2σ	TNT	Test ±2σ	TNT
Nozzle Manifold	700.2 ± 22.0	661.7	358.7 ± 22.0	339.7
Reflector Inlet	210.5 ± 15.4	203.9	111.0 ± 15.4	105.3
Reflector Outlet	168.0 ± 12.3	165.5	88.0 ± 12.3	85.2
Core Inlet	155.5 ± 5.5	154.0	79.5 ± 5.5	79.0
Nozzle Chamber	63.0 ± 2.8	66.3	32.0 ± 2.8	33.4

3.3.2 Low Power - Zero Flow (Neutronic Calibration) Test

Data obtained from the ram set neutronic calibration test, EP-II, was used to determine the relationship between rate of core temperature change and power with no coolant flow. This information is of interest for the following major reasons:

1) To evaluate the sensible heat method for calibrating neutronic power.
2) To provide data for the development of a no flow, low power computer model of the reactor. This model could be used to study proposed temperature autostart schemes, to calculate decay power during the no flow phase of pulse cooling, and to predict power for the sensible heat calibration method.

The test analysis is divided into: (1) a description of the test profile and data, (2) an analysis of the test using a simple model, and (3) an analysis of the test using a detailed model.

3.3.2.1 Description of Test Profile and Data

The neutronic calibration test was performed during EP-II, prior to full power operation. The test was initiated from ambient temperature by bringing power up to 52.4 KW. Approximately constant power was then maintained for 17 minutes before the reactor was scrammed. The three primary test objectives; ram set neutronics calibration, cross correlation measurements on the power control loop, and the irradiation of the low power dosimeter were successfully achieved.

The measured nuclear power and measured core temperatures at stations 1 and 8 are shown in Figure 3-6. The measured power varied between 52.3 to 58.4 KW. The core temperatures are shown in the original reduced form without any attempt to average or smooth the data. Each temperature trace exhibits an approximate $10^{\circ}R$ spread. Core temperature data was not available during the initial three minutes of the test. The average core temperature at the start of the test (6320 CRT Time) was estimated to be $535^{\circ}R$ by extrapolating the temperature traces.

High temperature thermocouples are used at core stations 20, 26, and 32. These are inaccurate for the low temperatures (less than $700^{\circ}R$) of EP-II. Consequently all analyses are based only on the core station 0.5, 1.0, and 8.0 temperatures.

The core temperature traces in Figure 3-6 indicate the existence of a

significant temperature gradient from the center to the periphery. The measured radial core temperature profiles at station 1 and 8 are shown in Figures 3-7 and 3-8 at various times during the test. The maximum radial gradients occur at the conclusion of the test when the core temperatures are greatest. The maximum gradients are 36°R at both stations 1 and 0.5 and 48°R at station 8. Figure 3-7 also shows that the temperatures at stations 0.5 and 1.0 are identical at each radial location.

3.3.2.2 Analysis of Test Data

Two calculation models were used to determine the relationship between core temperature and reactor power. The first model proved to be too simplified to adequately simulate test data and indicated the need for a more detailed model. A detailed reactor model consisting of 415 material nodes was then developed. The results of analyses with this model compared satisfactorily with test data. Both the models and the results obtained with each are described in the following paragraphs.

3.3.2.2.1 Simplified Analysis

A simple model was first developed to relate rate of core temperature increase and reactor power. This model neglects all axial and radial heat transfer by conduction and radiation. The following equation was used to compute reactor power:

$$W_c * C_p * \frac{\Delta T}{\Delta t} = 0.947 * Q * F_R * F_A * F_C \qquad (3\text{-}1)$$

where,

W_c = core weight (equivalent graphite), lb = 2460 lb

C_p = specific heat of graphite (evaluated as a function of temperature) Btu/lb°R

$\frac{\Delta T}{\Delta t}$ = rate of increase of temperature, °R/sec

Q = reactor power, KW

F_R = radial power factor

F_A = axial power factor

F_C = fraction of reactor power generated in core = 0.96

[redacted]

This equation may be rewritten and solved for reactor power directly.

$$Q = \left[\frac{W_c * C_p}{0.947 * F_R * F_A * F_C}\right]\left[\frac{\Delta T}{\Delta t}\right] \qquad (3\text{-}2)$$

Reactor power was evaluated with this equation using the slopes ($\Delta T/\Delta t$) of the temperature traces for all functioning core station 0.5, 1.0, and 8 thermocouples. The radial power factors were obtained from Reference 2, and the axial power factors were obtained from PAX* measurements.

Reactor power was computed with equation (3-2) using the measured core temperatures during a five minute time interval (6680 through 6970 CRT seconds) near the mid-point of this test. The measured nuclear power was a constant 58.4 KW during this interval. The reactor power computed with all available measurements is summarized in Table 3-2. A comparison of measured and computed power indicates the following three characteristics: One, the best agreement (within 11 percent) between measured and computed power exists when the station 8 thermocouples within 10 inches of the core center are used for the calculation. Two, the computed power for the station 0.5 and 1 thermocouples are considerably greater than measured (between 28 and 92 percent). And three, for each station the computed power is lower for thermocouples in the periphery compared to thermocouples near the center of the core. These characteristics are primarily caused by the effects of radial and axial conduction heat transfer. The power computed with the station 0.5 and 1.0 thermocouples is considerably greater than measured because of axial conduction. The contribution of axial conduction is probably small for station 8 since nearly equal energy is both gained and lost by conduction. However, station 1 experiences a net energy gain by conduction since the loss by radiation to the support plate is negligible for the temperatures experienced during the test. The reason for the lower computed power when the periphery thermocouples are used is primarily due to a net heat loss by radial conduction to the reflector region.

To summarize, station 8 temperature measurements located within 10 inches of the core center may be used to compute power in the range of 60 KW. Measurements at stations 0.5 and 1 and at station 8 in the core periphery are not useful for the calculation

* Experimental axial power distribution measured with a PAX mockup of NRX-A2 fuel elements.

TABLE 3-2

RESULTS OF SIMPLIFIED ANALYSIS-POWER COMPUTED FROM RATE OF CORE TEMPERATURE INCREASE

Station	Radius inches	Channel Name	$\frac{\Delta T}{\Delta t}$ $\frac{^{\circ}R}{sec}$	Power-KW	Power Computed / Power Measured
8	2.2	T.640.5A	0.107	56.3	0.96
8	2.3	T.641.5A	0.114	60.6	1.04
8	10.2	T.645.5A	0.103	64.7	1.11
8	14.7	T.646.5A	0.082	49.6	0.85
8	15.9	T.638.5A	0.069	42.8	0.73
8	16.6	T.643.5A	0.072	48.4	0.83
0.5	1.2	T.619.5A	0.094	112.2	1.92
1.0	1.1	T.666.5A	0.094	111.3	1.91
0.5	16.5	T.650.5A	0.048	75.0	1.28
1.0	16.5	T.624.5A	0.062	96.8	1.66
0.5	17.0	T.669.5A	0.094	94.1	1.61
1.0	17.0	T.627.5A	0.060	97.6	1.67

*Measured nuclear power is 58.4 KW

of power with this simplified model because axial and radial heat conduction are neglected.

Improved results may be expected for higher power since the contribution of axial conduction compared to generated power will decrease with increase in power. However, the complexity of the reactor indicates the need for a detailed model.

3.3.2.2.2 Detailed Analysis

A detailed reactor model consisting of 415 material nodes was developed to determine the relationship between rate of core temperature increase and power. The model was developed for solution with the TØSS[4] computer program. Following is a brief description of the reactor model and a comparison between test data and calculation results.

The core was represented by 286 material nodes arranged in nine radial sections. These sections were further subdivided into 26 axial nodes. The effect of core void, gaps between core elements, and channel spacing were considered in specifying conduction heat transfer resistances between nodes. The type of gas in the gaps between core elements has a considerable effect on the thermal resistance of the core to heat transfer in the radial direction. For example, the radial resistance of the core increases about four times for nitrogen compared to helium. A 30 SCFM helium purge was used during the neutronic calibration test and therefore helium was assumed in the gaps. The filler strips, pyrographite tiles, lateral support seals, inner reflector, and outer reflector and pressure vessel were represented to accurately simulate heat transfer from the core to the reflector region. Radiation heat transfer from both faces of the core was considered. The remaining components of the reactor were represented with less detail. Power generation was specified for all reactor material nodes; both radial and axial power factors were specified for the core nodes.

The temperatures computed with the detailed two-dimensional conduction model were compared against test data at two power levels; one equal to measured and the second 10 percent above measured power. Comparisons between test data and calculation results are shown in Figure 3-9 for core and inner reflector temperatures. Good agreement exists for a power 10 percent above the measured nuclear power. The slopes of the calculated temperatures are then nearly identical to measured. In addition, the computed temperatures are within 5 degrees of the measured temperatures except for station 8, radius 2.2 inches where the maximum

difference is about 8 degrees. The comparison for inner reflector temperatures is excellent. The good comparison for the inner reflector is a significant indication of the accuracy of the model since about 80 percent of the inner reflector temperature rise is the result of heat conduction from the core at a power of 60 KW. These good comparisons indicate that this TØSS model accurately simulates reactor temperatures during low power - no flow operation.

Additional results are shown in Figures 3-10 and 3-11. The computed axial temperature profiles at radii of 2.2 and 16.5 inches at the conclusion of the test are shown on Figure 3-10. These curves show considerable axial gradients, which re-emphasizes the requirement for a detail model to account for all internal heat transfer. The computed radial temperature profiles for core stations 1, 8, and 26 are shown in Figure 3-11. Good agreement exists between the computed and measured radial profiles.

The following conclusions are based on this analysis:

1) A detailed heat transfer model of the core and reactor is required to simulate reactor temperatures during low power, no flow conditions.
2) The EP-II power computed from reversible heat, based on the detailed model, was 10 percent greater than the measured nuclear power. Comparing measured nuclear power (linear No. 1) with thermal power for EP-III shows that best estimated thermal power was between 10 to 13 percent greater than nuclear power. If the nuclear power had been calibrated by the EP-II thermal power, the agreement of nuclear power with best estimated thermal power during EP-III would have been excellent.
3) The reactor purge gas has a significant effect on the radial core temperature gradients. Helium purge is preferred in place of nitrogen because of its greater thermal conductivity which minimizes the radial temperature gradients.
4) Significant radial temperature gradients can exist in the core even at a power of only 60 KW.

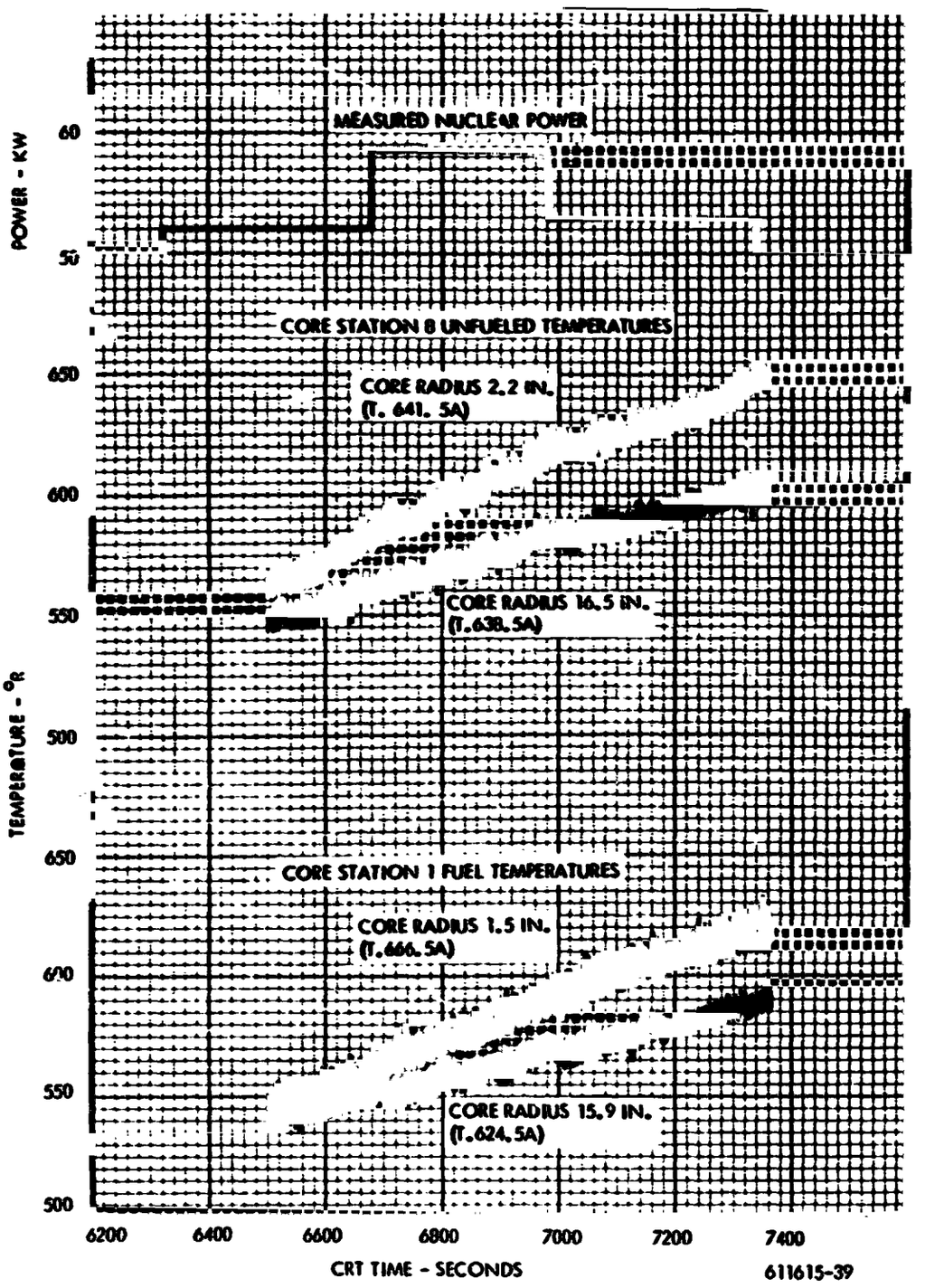

Figure 3-6. NRX-A5 EP-II Neutronic Calibration Test
Power and Core Temperatures versus Time

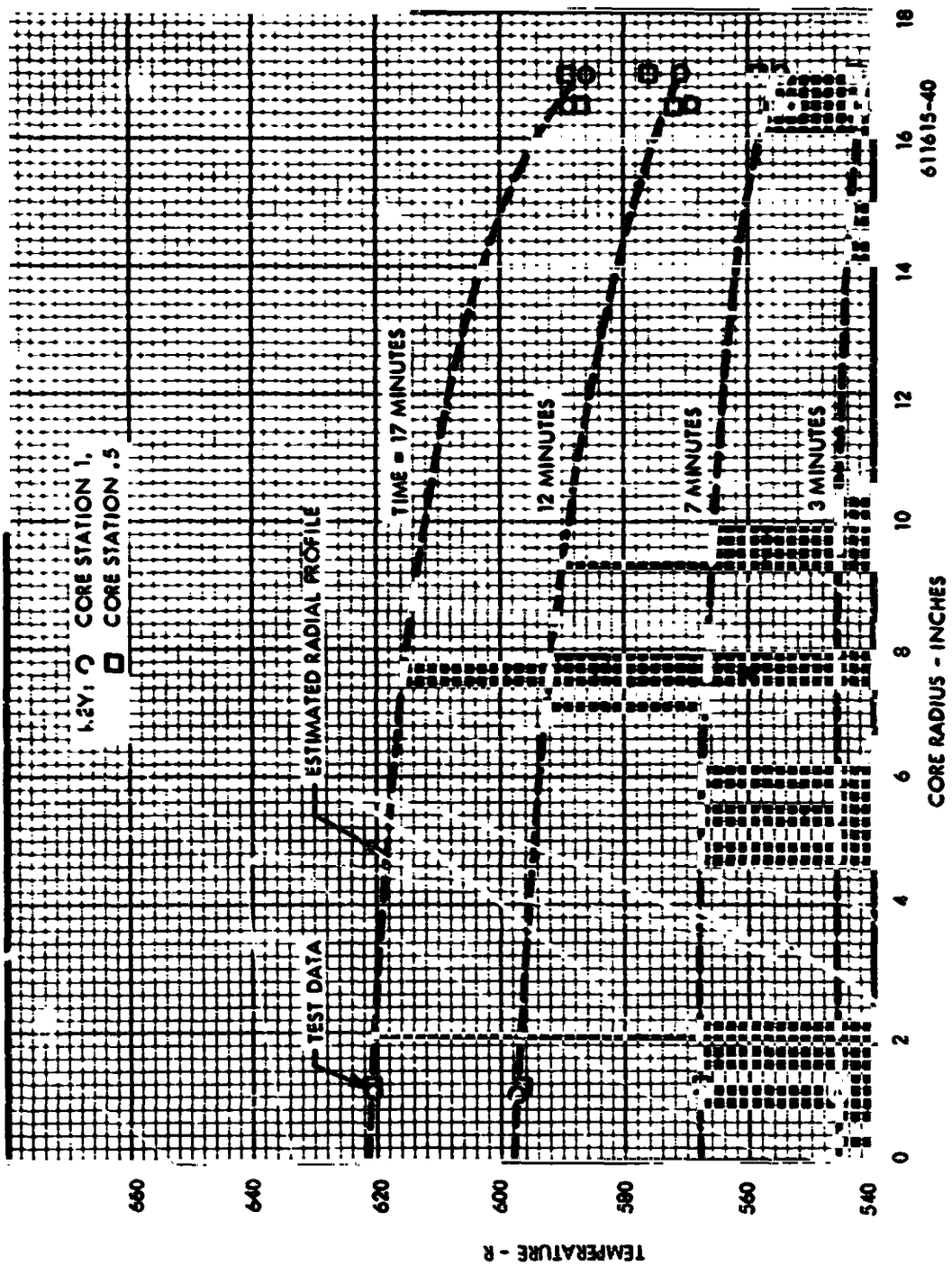

Figure 3-7. NRX-A5 EP-II Neutronic Calibration Test: Station 0.5 and 1.0 Core Radial Temperature Profiles

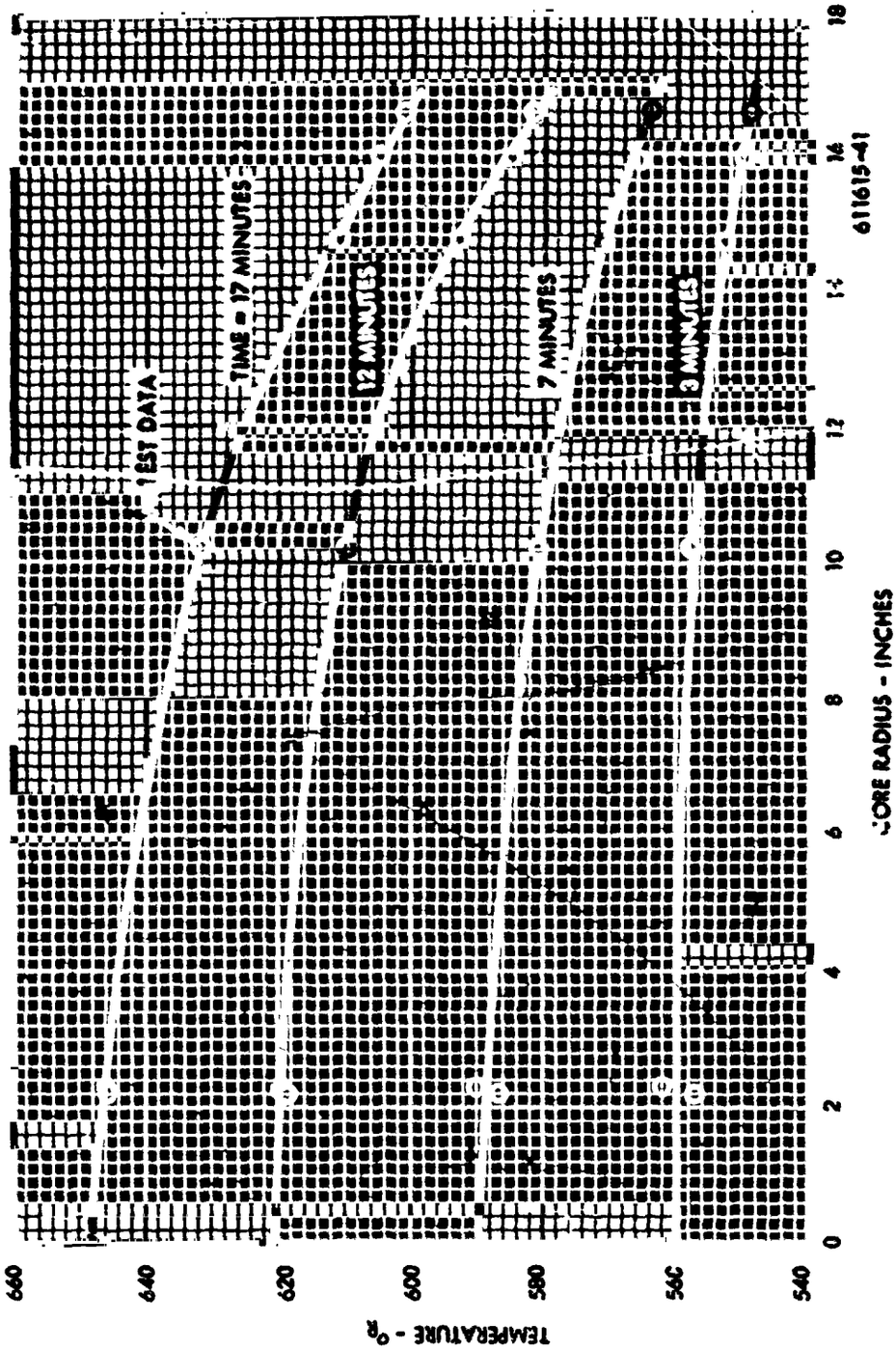

Figure 3-8. NRX-A5 EP-II Neutronic Calibration Test: Station 8 Core Radial Temperature Profiles

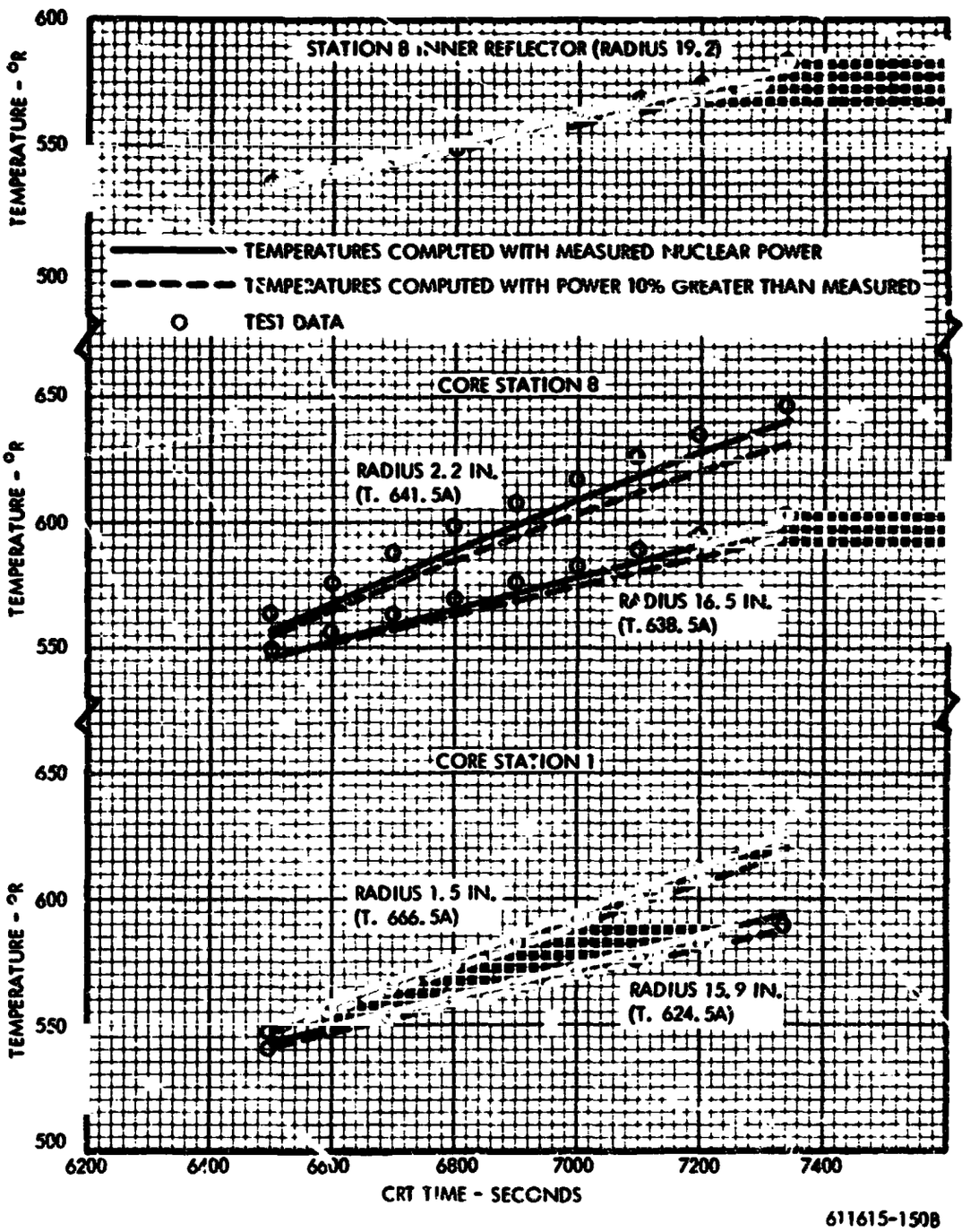

Figure 3-9. NRX A5 EP-II Neutronic Calibration Test: Comparison of Computed Core and Inner Reflector Temperatures with Test Data

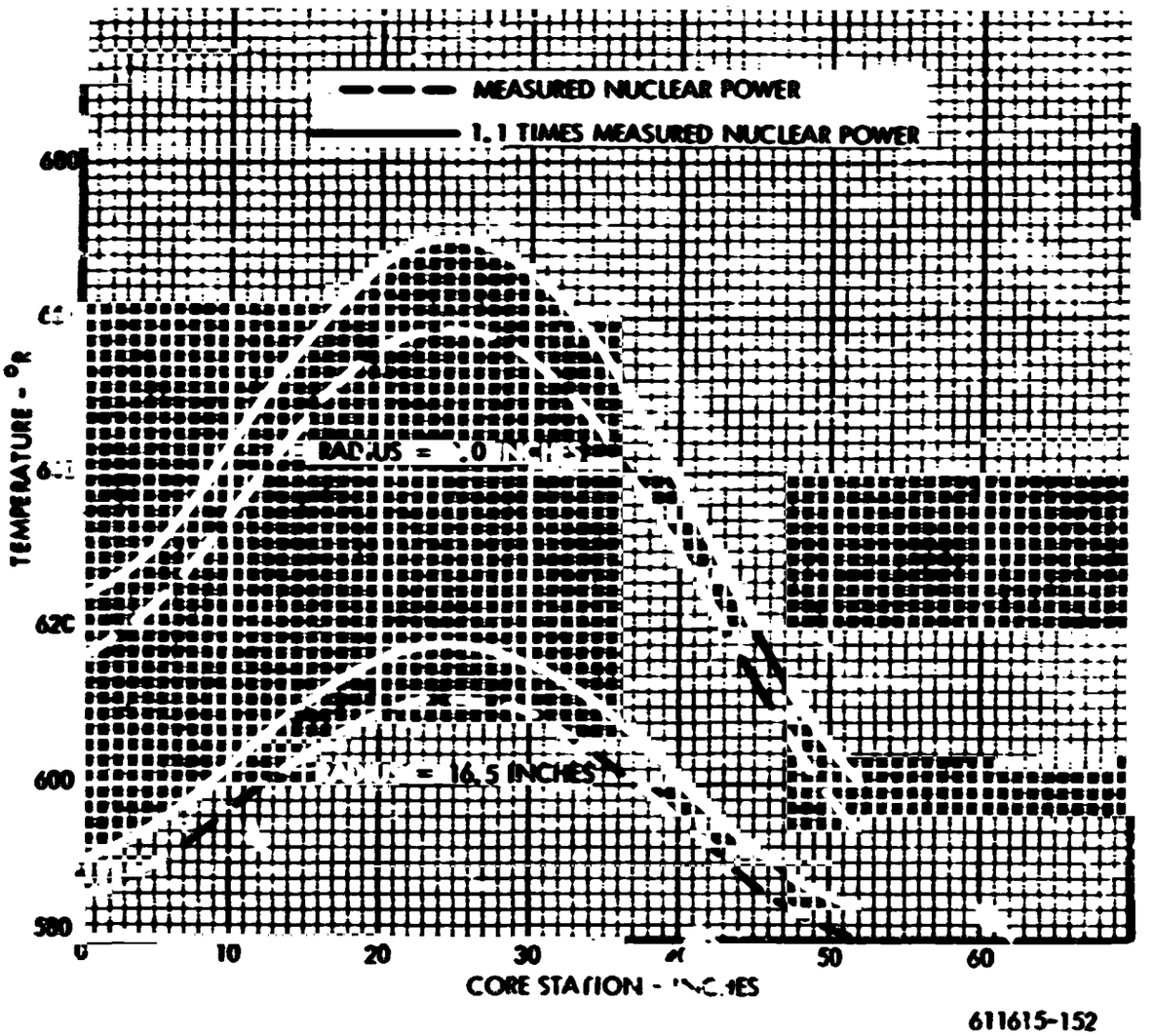

Figure 3-10. NRX-A5 EP-II Neutronic Calibration Test: Axial Core Temperature Profiles

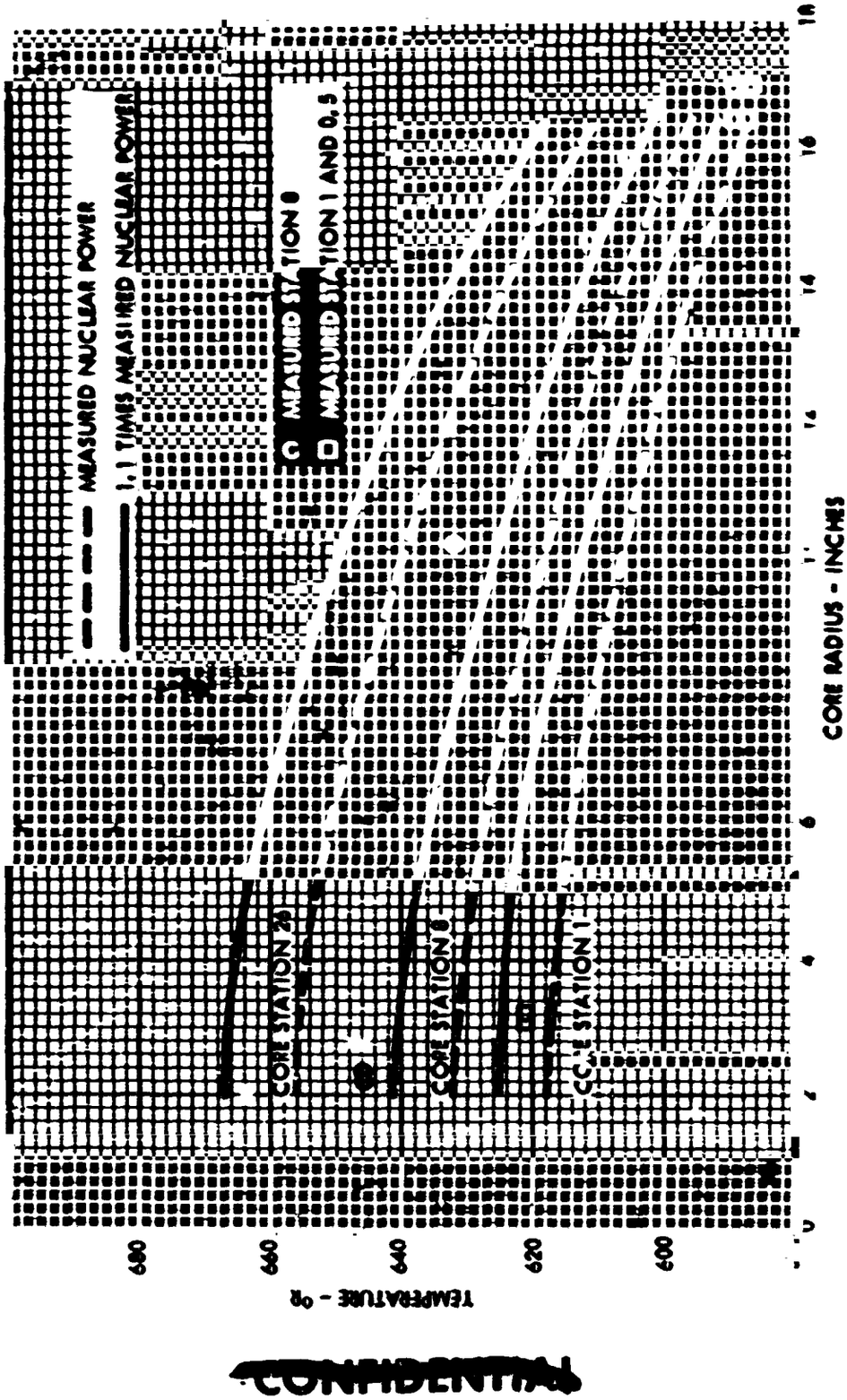

Figure 3-11. NRX-A5 EP-II Neutronic Calibration Test: Radial Core Temperature Profiles

3.4 POWER TESTS

The reactor power tests, EP-III and IV, are described in four subsections. In the first subsection, each test profile is described and time history figures are given for all major reactor performance parameters. This description is also intended to serve as background information for many of the analyses contained in the report.

The second subsection describes the procedure used to compute best estimated chamber temperature, flow rate, and power, and gives these data at five steady-state times for both EP-III and EP-IV. Detailed steady state and transient reactor performance comparisons of test measurements with post test calculations are presented in the third subsection. The last subsection compares calculated decay power for the EP-III cooldown with decay power predicted by the S-4 (Fission Product Energy Release).

3.4.1 Description of Power Tests

3.4.1.1 Background

The major objective of the NRX-A5 test series was to operate at design conditions for a total time of 40 minutes. Secondary objectives were to demonstrate a fixed drum startup from a low power subcritical condition to near full power and to evaluate the operation of a "no-flux loop" temperature controller. Other objectives were to evaluate the mechanical, nuclear, thermal, and control characteristics of the reactor.

The accumulated run time for two full power tests was 15.1 minutes above 4000°k nozzle chamber temperature and 30.1 minutes above 3700°R nozzle chamber temperature. The test was terminated by the control drum position limit of 145 degrees before completing 40 minutes of run time at design conditions. This control drum position limit corresponded to 2.2 dollars of corrosion reactivity loss. (See Reference 5 for limit justification.) A fixed control drum startup from 30 KW to near design power was successfully accomplished. The "no-flux loop" temperature controller also functioned satisfactorily during the test series.

The test profile descriptions will emphasize reactor thermal and nuclear performance. All significant performance parameters are displayed graphically as a function of time. The following group of figures is used for this purpose:

1) Power, flow rate, nozzle chamber temperature, and control drum position.
2) Nozzle chamber temperature, core station 26 control temperature, and nozzle chamber temperature ramp rate.
3) Tie rod material temperature (average, maximum, and minimum) and reactor plenum temperatures.
4) Reactor plenum pressures and seal chamber pressures.
5) Component pressure drops and pressure differences between seal chambers.
6) Electrical average core temperatures at stations 8, 20, 26, and 32.

These figures were prepared by the DAC* code using data from the N-3 (narrow band data) computer tapes. Averages of all measurements are shown for parameters where more than one measurement was available. Most of the same parameters are used in Section 3.4.3 for the transient and steady-state comparisons with calculations. The data for the steady-state comparisons were averaged over 5-second time intervals.

3.4.1.2 Test Profile for EP-III

The test was initiated by an autostart to 1 MW. The main pro. . valve, ACV-3 (See Figure 3-1) was then opened briefly to cool the outer reflector from 570°R to 540°R to insure meeting the reflector maximum temperature limit for startup. The ramp to the 2000°R hold was initiated by programming ACV-3 open and AVV-2 closed; and starting the power, flow rate, and station 26 temperature demand profiles. The station 26 limiter was set prior to startup to limit at about 1900°R chamber temperature. It functioned satisfactorily at 1850°R and reduced chamber temperature by 200°R. The limiter was reset to its design point value and the "no-flux loop" temperature controller was activated. The startup to full power was continued after a 130 second hold at approximately 1950°R. The setting of the power limiter caused unintentional power limiting to occur just prior to full power. The power limiter set point was therefore raised sufficiently to permit full power

* The DAC code designates a series of computer programs which are used to automate data analysis and plotting.

operation. The power then started to oscillate. These oscillations were evident on most neutronic channels. For example, the linear No. 1 measurement showed oscillations between 700 and 970 MW with a minimum period of 3 seconds. These oscillations lasted for about 25 seconds and disappeared just before control was switched to the control drum position control mode. These oscillations are completely discussed at the end of this section. The reactor was then brought to full power conditions.

With the reactor operating at nominal design conditions, the station 26 temperature and power limiters were checked first in the "no-flux loop" control mode and then in the control drum position control mode. Next, 125 seconds of cross correlation measurements were made on the turbine speed loop while the drums were in fixed position control. Nominal design conditions were then maintained with the "no-flux loop" station 26 temperature controller until the pre-determined shutdown point based on the liquid hydrogen level in the dewars was reached. Shutdown was programmed to 2500°R, followed by a SCRAM shutdown. A manual FLOW shutdown was initiated at 1500°R chamber temperature.

The time variation of the major reactor performance parameters throughout the test profile is shown in Figures 3-12 to 3-17. The temperature and power limiter checkouts, the power oscillations at the start of the high power hold, and the cross correlation measurements at the midpoint of the hold are clearly evident on all curves. As is shown in Figure 3-13, the peak rate of change of chamber temperature was 60°R/sec during startup, -85°R/sec during the programmed shutdown prior to scram, and -170°R/sec for a two second interval after scram. The reactor operated 15.4 minutes above 3700°R chamber temperature during EP-III.

Figure 3-14 shows the nearly constant tie rod material and very slightly increasing reactor plenum temperatures during the high power hold. The reactor plenum pressures shown in Figure 3-15 are essentially constant throughout the hold, except for a slight decrease in seal chamber No. 11 pressure. The pressure drops shown in Figure 3-16 also remained constant; except for the seal pressure differences. A change in the seal pressure distribution is an indication of the onset of corrosion in the outer regions of the core. A detailed analysis of the lateral support system showing the variation in the seal pressure

distribution with run time is given in Section 4.3.1. All core temperatures except station 20 remained essentially constant during the high power hold; station 20 increased about 50°R. This behavior is discussed further in Chapter 5.

Power oscillations occurred 20 seconds after nominal full power conditions were attained. These oscillations are very evident on the power and control drum position curves in Figure 3-12. The oscillations lasted for about 25 seconds, and ended just before control was switched from the "no-flux loop" station 26 temperature control to control drum position control. Post test analysis* indicated that the signal from one of the ten temperature measurements (T.679) in the station 26 average, had become noisy and was causing positive temperature spikes in the average. These then caused spikes in the feedback to the "no-flux loop" temperature controller. The oscillations were caused by the controller trying to maintain the demanded temperature. The T.679 thermocouple was automatically rejected 15 seconds after the oscillations ended, and the "no-flux loop" controller functioned properly during the remainder of the test. After the test, the controller was modified to prevent the recurrence of such oscillations.

---

* See Reference 6, Page 4-1.

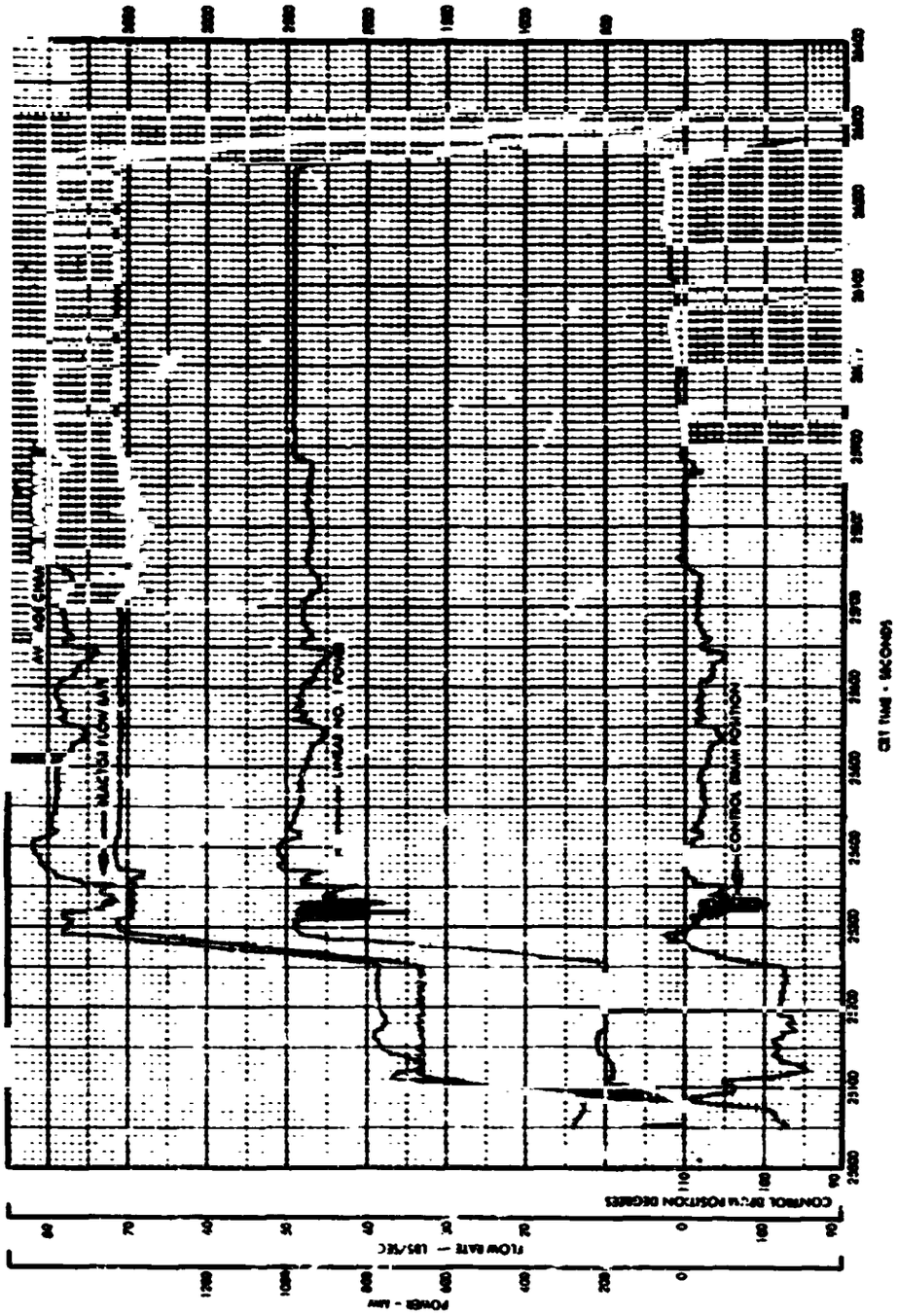

Figure 3-12. NRX-A5 EP-III Power Test Description: Chamber Temperature, Flow Rate, Power and Control Drum Position

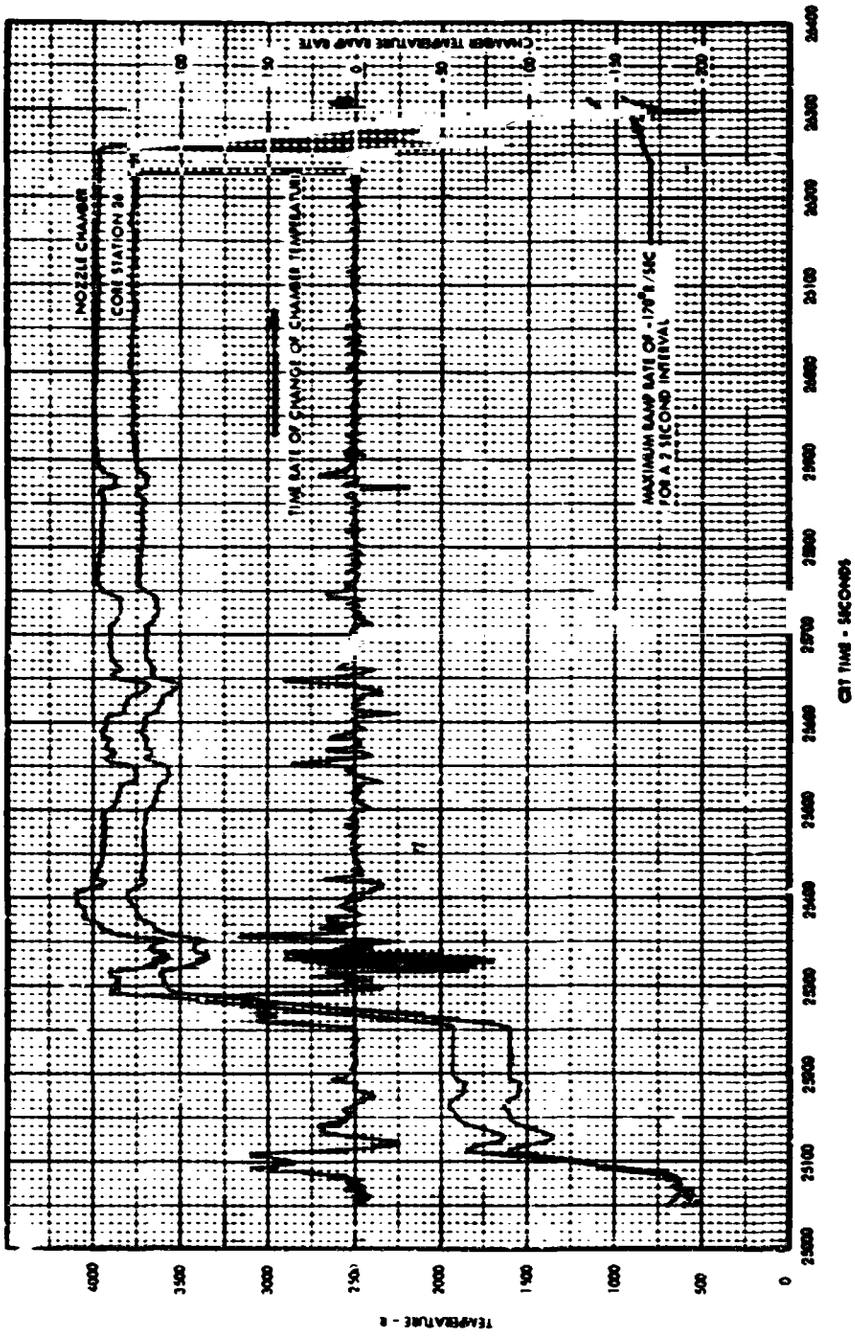

Figure 3-13. NRX-A5 EP-III Power Test Description: Average Chamber and Core Station 26 Temperatures and Time Rate of Change of Chamber Temperatures

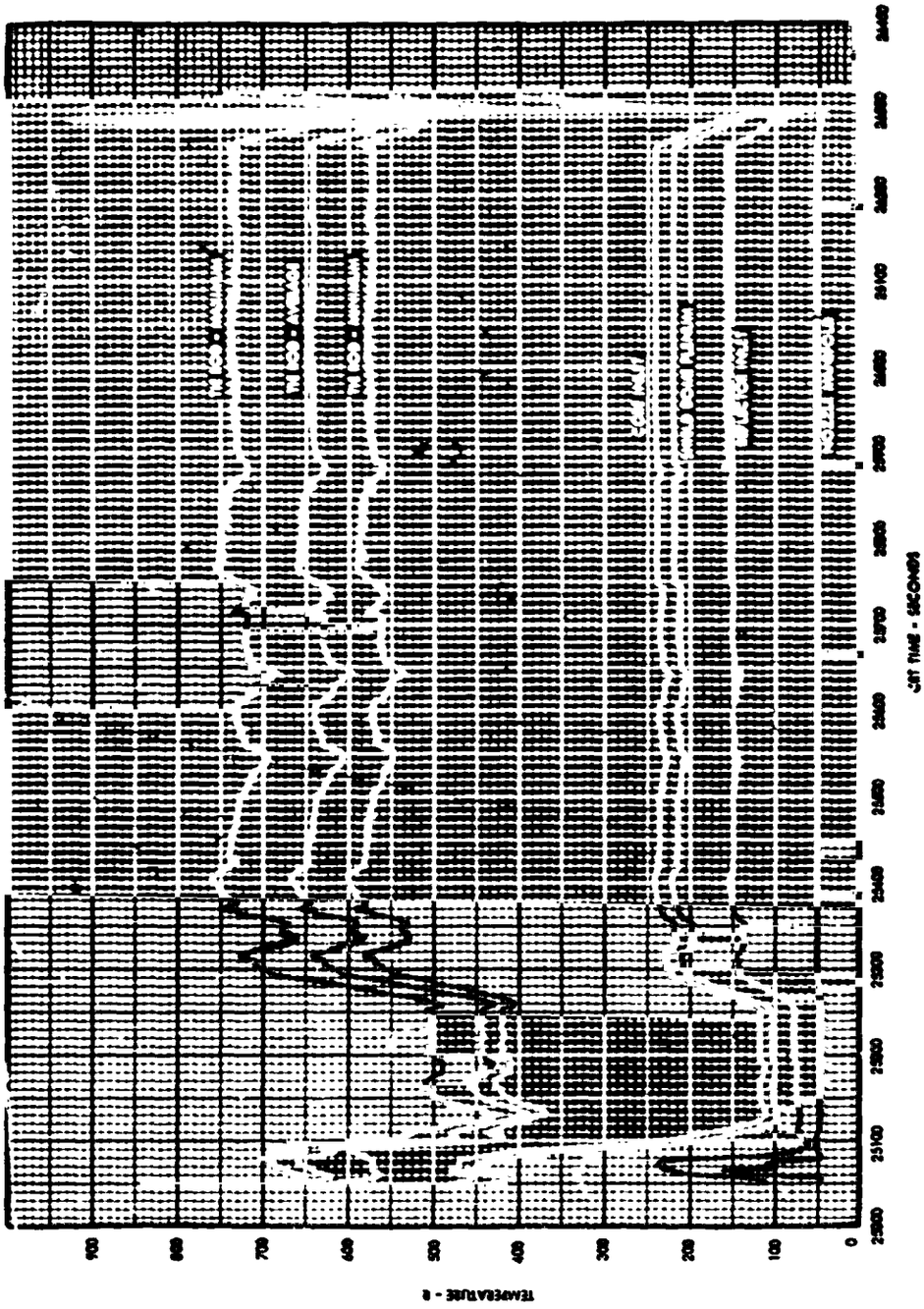

Figure 3-14. NRX-A5 EP-III Power Test Description: Tie Rod Material and Plenum Temperatures

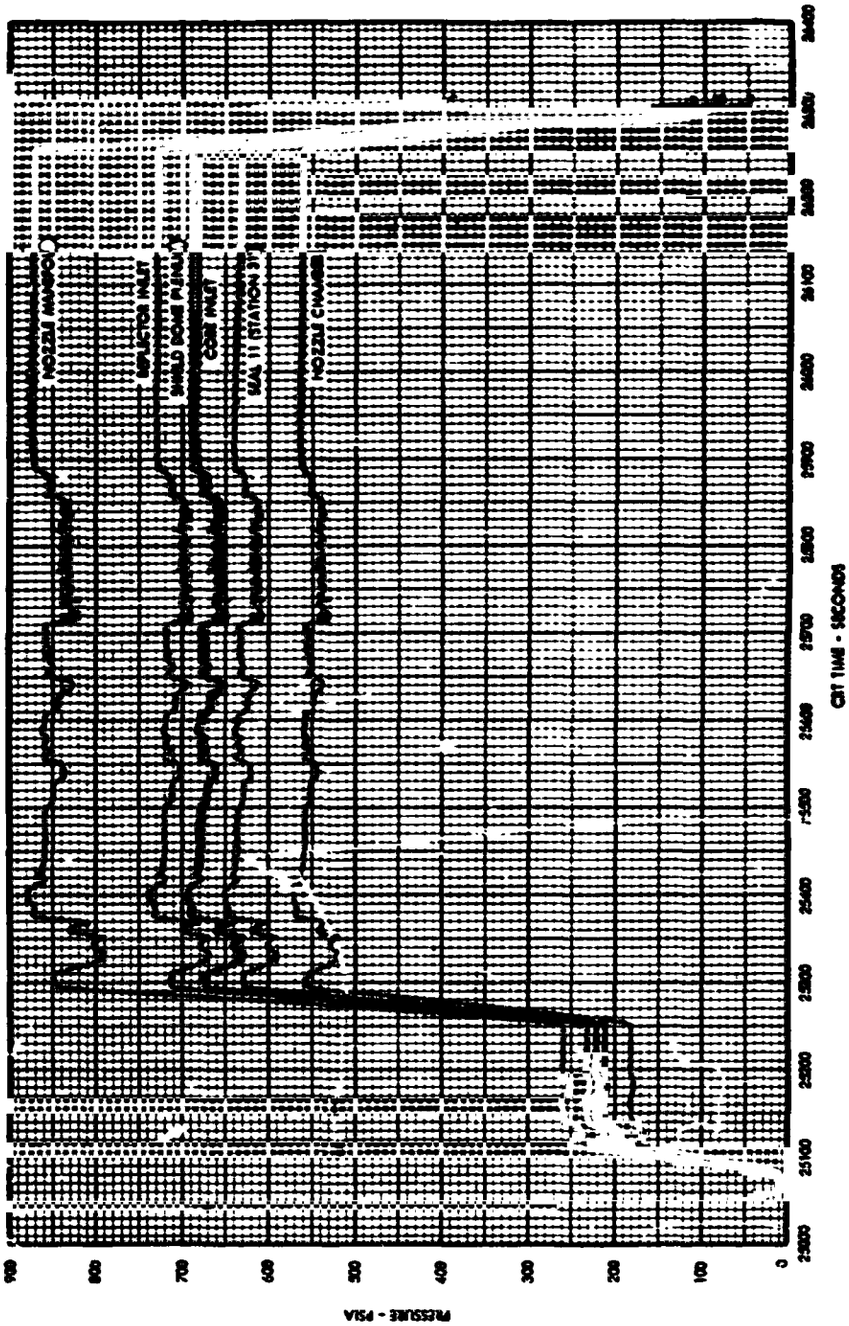

Figure 3-15. NRX-A5 EP-III Power Test Description: Plenum Pressures

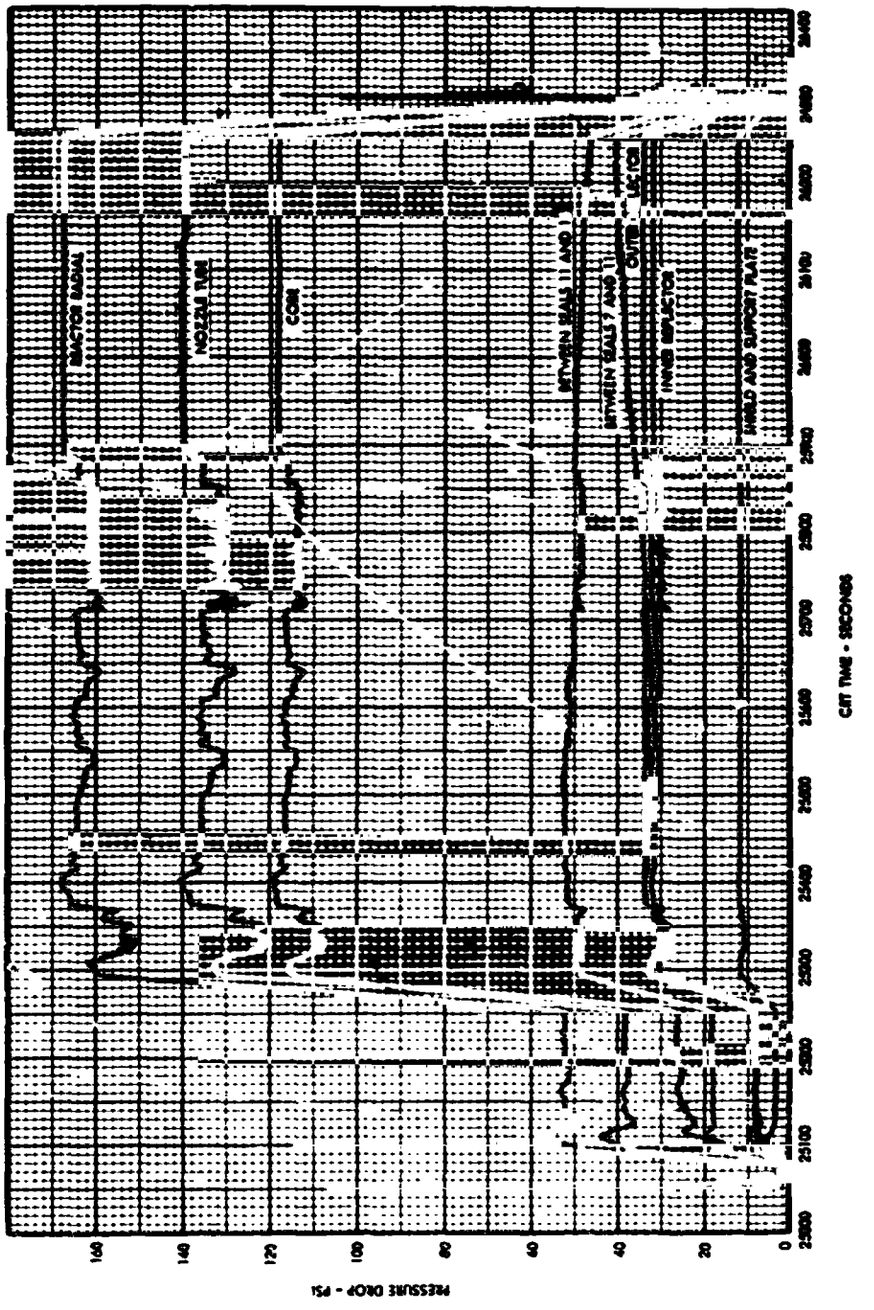

Figure 3-16. NRX-A5 EP-III Power Test Description: Component Pressure Drops

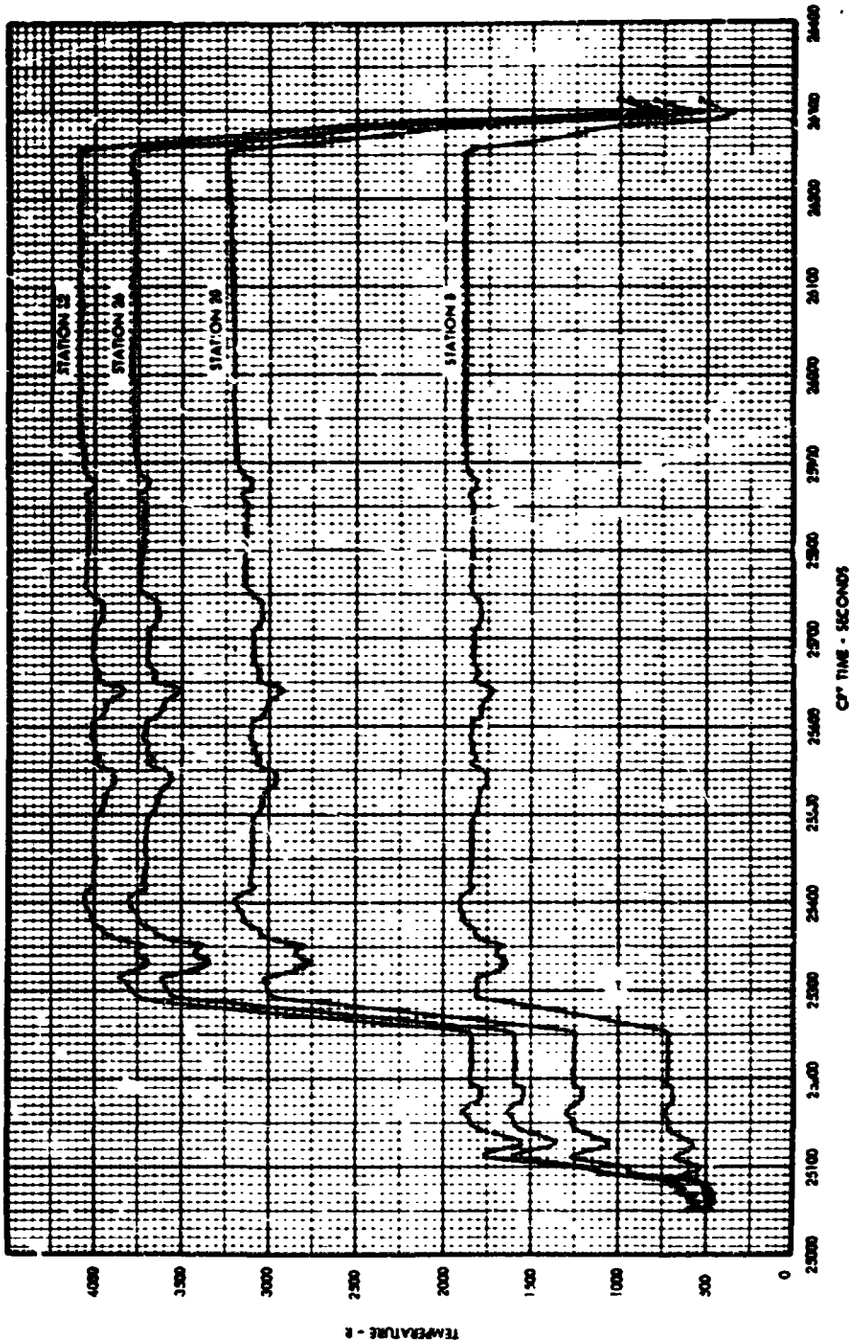

Figure 3-17. NRX-A5 EP-III Power Test Description: Core Unfueled Element Temperature (Electrical Averages)

3.4.1.3 Test Profile for EP-IV

The EP-IV startup consisted of a fixed drum startup from 30 KW to 850 MW power followed by a controlled ramp to full power conditions using the "no-flux loop" temperature controller. The run was initiated from 30 KW by first rotating the control drums inward by 2.0 degrees (102.7 to 100.7 degrees) from the pre-run critical drum position. The reactor was now slightly subcritical and consequently power decreased to approximately 20 KW during the 20 second interval which elapsed before liquid hydrogen flow was initiated. The flow was increased to 10 lb/sec using ACV-3 in position control. Power now started to increase as a result of the positive reactivity insertion caused by the liquid hydrogen flow. The minimum reactor period of 1.8 seconds (a minimum period of 2 seconds had been predicted prior to the test, see Reference 18) occurred at a power of 7 MW. When the power had increased to 20 MW, the pre-test power level selected to initiate the demand flow profile, the flow was ramped to 71.3 lb/sec at an average rate of 0.82 lb/sec^2. At the end of the flow ramp, the control drums were rotated outward to 101.4 degrees to increase chamber temperature to 3250°R. This operation was required to zero the temperature error before switching to the "no-flux loop" temperature controller. The "no-flux loop" controller was then activated and chamber temperature was ramped to design point conditions at about 50°/sec. The fixed drum startup was extremely smooth: the peak chamber temperature ramp rate was 55°R/sec.

Full power conditions were maintained using flow and station 26 temperature as control inputs. Two slight trim adjustments in temperature, (one 50°R negative and one 50°R positive) and one trim to increase flow rate were made during the hold. The run was terminated after 14.5 minutes above 4000°R chamber temperature at the pre-test determined shutdown limit of a 145 degree* control drum position. The shutdown profile was identical to the one used during EP-III (see Section 3.4.1.2 for the description).

The significant reactor performance parameters are shown in Figures 3-18 to 3-23 for the entire test profile. Figure 3-18 shows nozzle chamber temperature, flow rate, power, and control drum position. The figure clearly shows the two chamber temperature

* See Reference 5 for the justification of this limit.

trims and the flow rate trim near the start of the high power hold. Nozzle chamber temperature was nearly constant during the high power hold with a variation from mean of less than 50°R. The rate of change of nozzle chamber temperature is shown in Figure 3-19. The maximum rates were 60°R/sec during startup, -65°R/sec during shutdown before scram, and -100°R/sec during shutdown after scram.

The reactor plenum (reflector inlet, shield, and core inlet) temperatures in Figure 3-20 show a gradual increase during the high power hold. The net increase of about 10°R for each plenum is due to the unexplained increase in the reflector inlet temperature. The temperature of the central control rod decreased by about 90°R during the high power hold. This characteristic is as expected, and is due to the change in the core radial power distribution with control drum roll out. Figure 3-21 shows a gradual decrease in systems' pressures during this hold. The decrease is about 10 psi, for all pressures except for the decrease in seal chamber 11 pressure which is 20 psia. The system pressure drops are shown on Figure 3-22. The reflector, shield, and support plate pressure drops increased slightly (less than 2 psia) during the hold. The nozzle tube pressure drop increased about 8 psia during the hold. The cause of this increase is not completely known at this time; see Reference 7 for a detailed discussion of the increase in reflector pressure drop and reflector inlet temperature during the high power hold.

The pressure differences between seals changed by a maximum of 7 psi during the hold; the seal chamber 11 pressure also decreased more than the other plenum pressures (see Figure 3-21). A change in the seal pressure distribution is believed due to corrosion effects (see Section 4.3.1 for a more detailed explanation). The effects of control drum runout and core corrosion are evident in the electrical averages of core temperatures shown on Figure 3-23. The trace of the average station 32 temperature clearly shows two instances where measurements were rejected from the average.

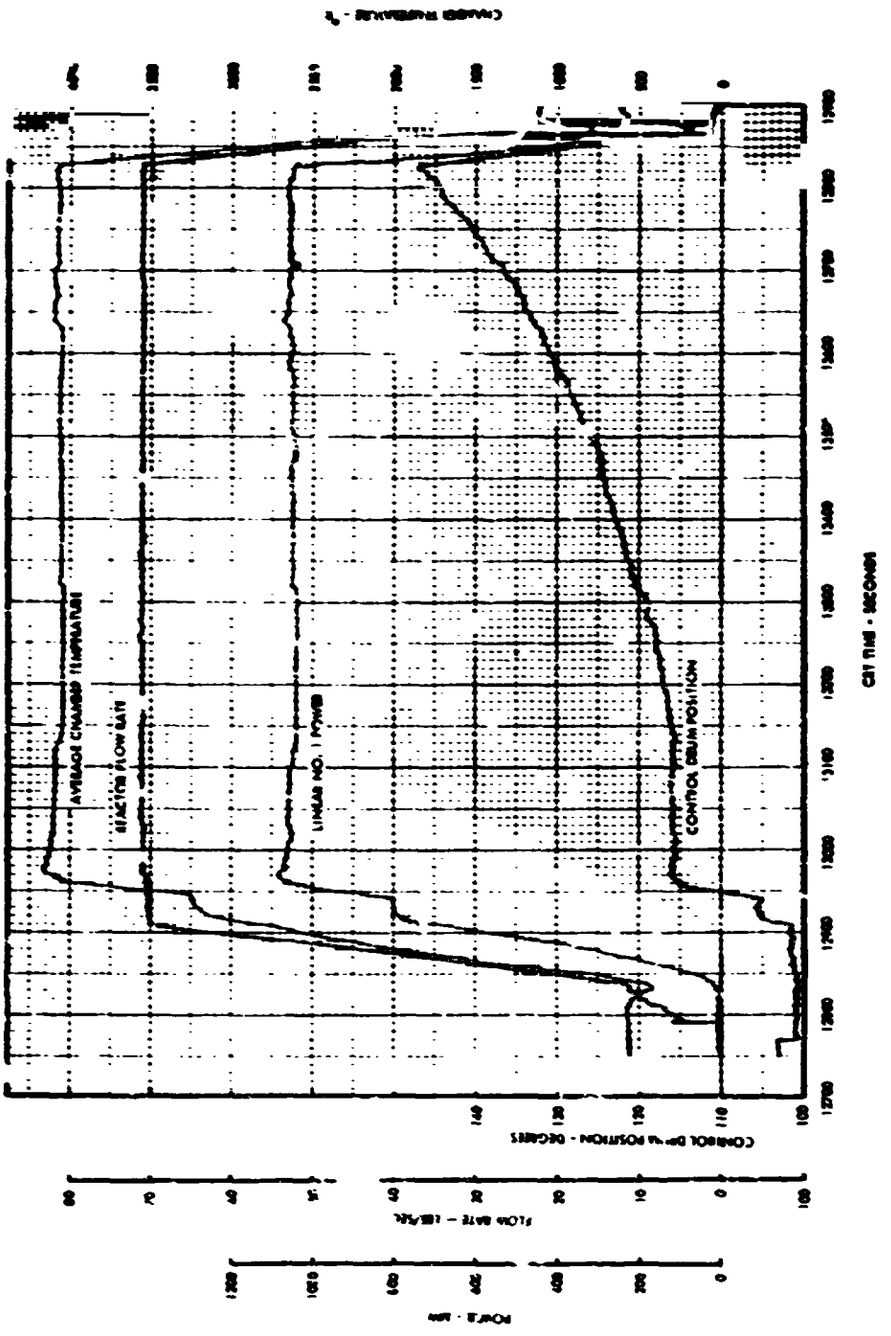

Figure 3-18. NRX-A5 EP-IV Power Test Description: Chamber Temperature, Flow Rate, Power and Control Drum Position

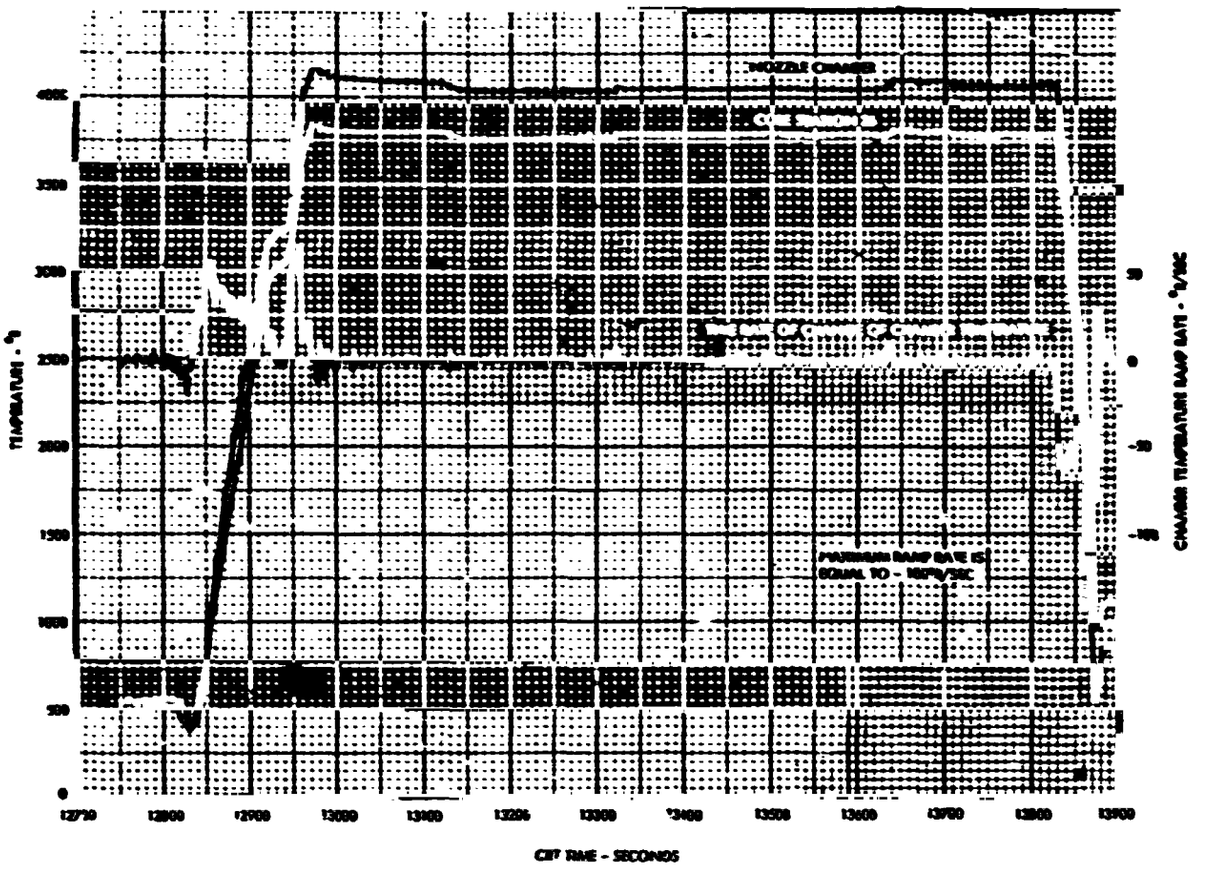

Figure 3-19. NRX-A5 EP-IV Power Test Description:
Average Chamber and Core Station: 26
Temperatures and Time Rate of Change of Chamber Temperature

CONFIDENTIAL

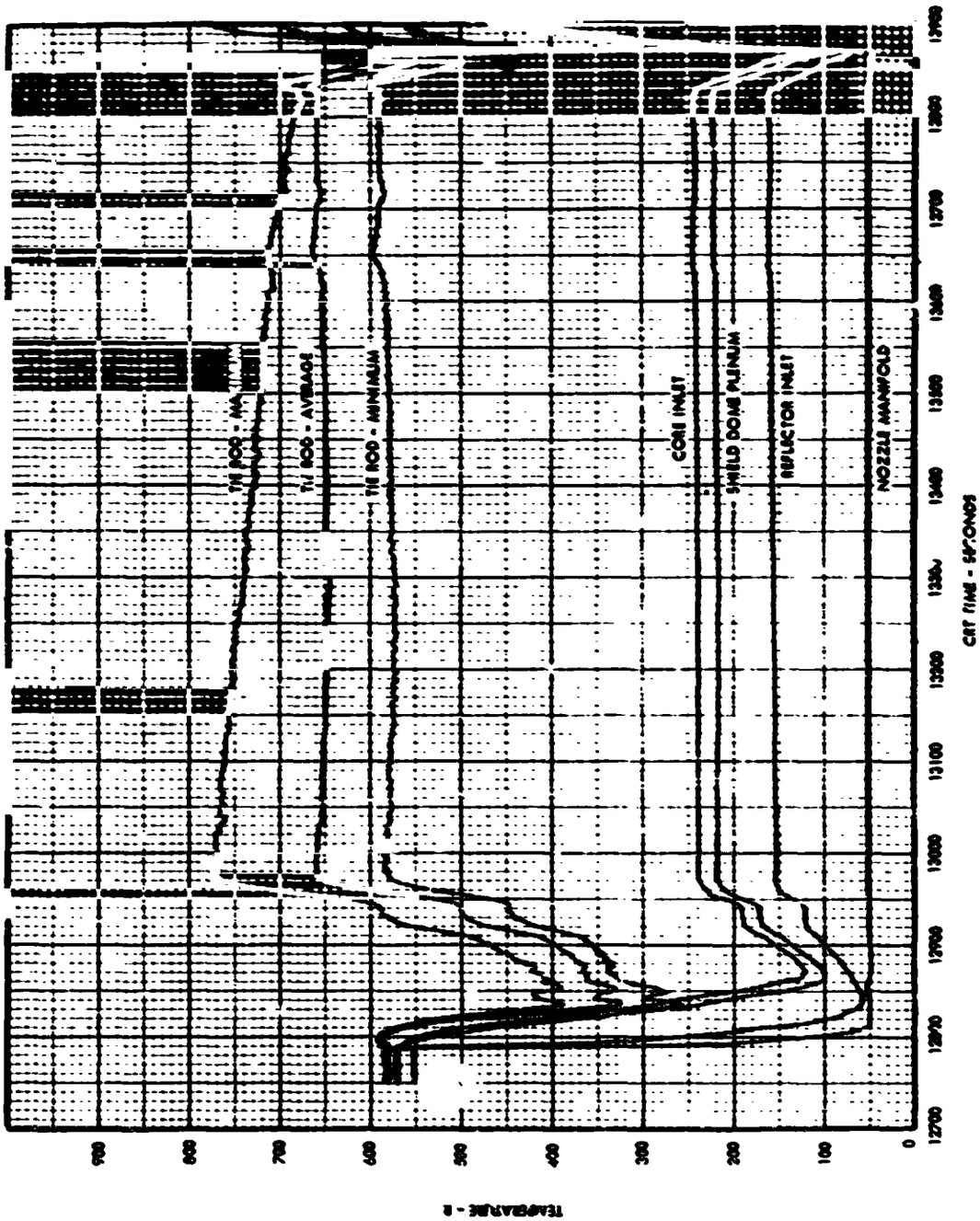

Figure 3-20. NRX-A5 EP-IV Power Test Description
Tie Rod Material and Plenum Temperatures

CONFIDENTIAL

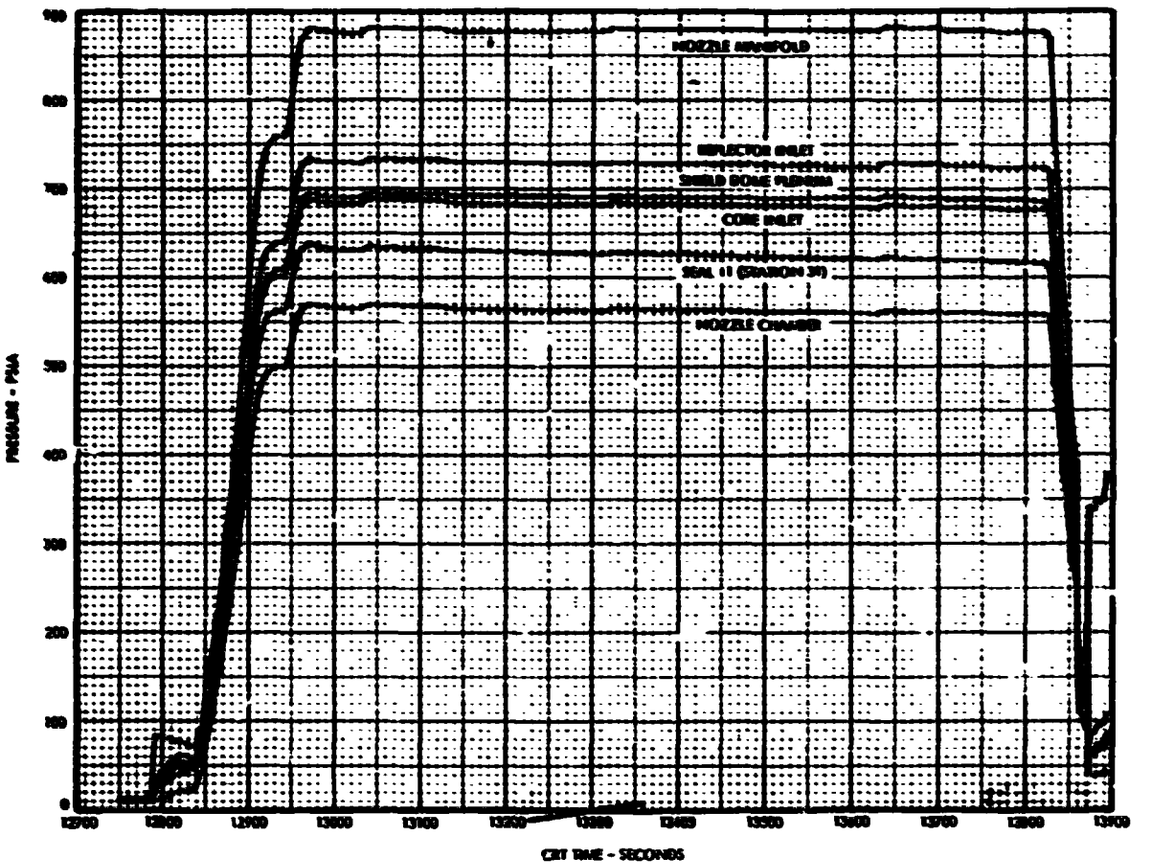

Figure 3-21. NRX-A5 EF-IV Power Test Description: Plenum Pressures

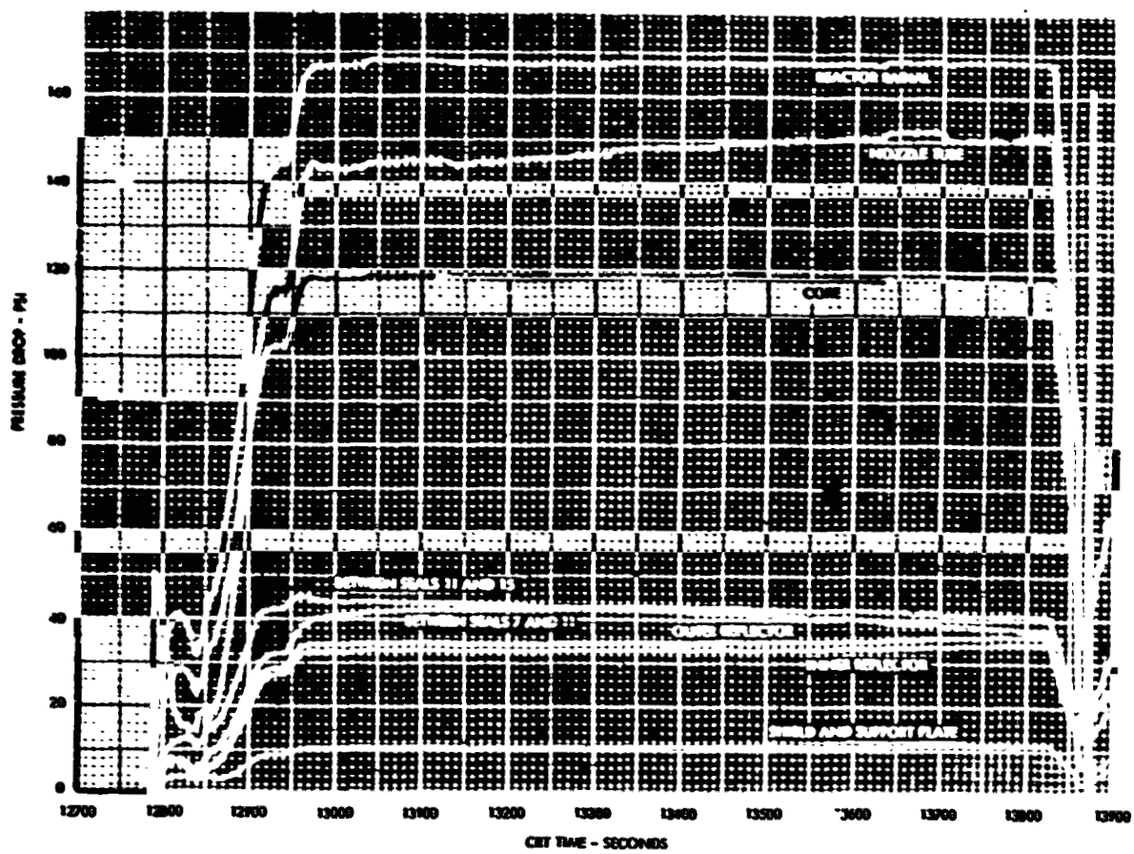

Figure 3-22. NRX-A5 EP-IV Power Test Description: Component Pressure Drops

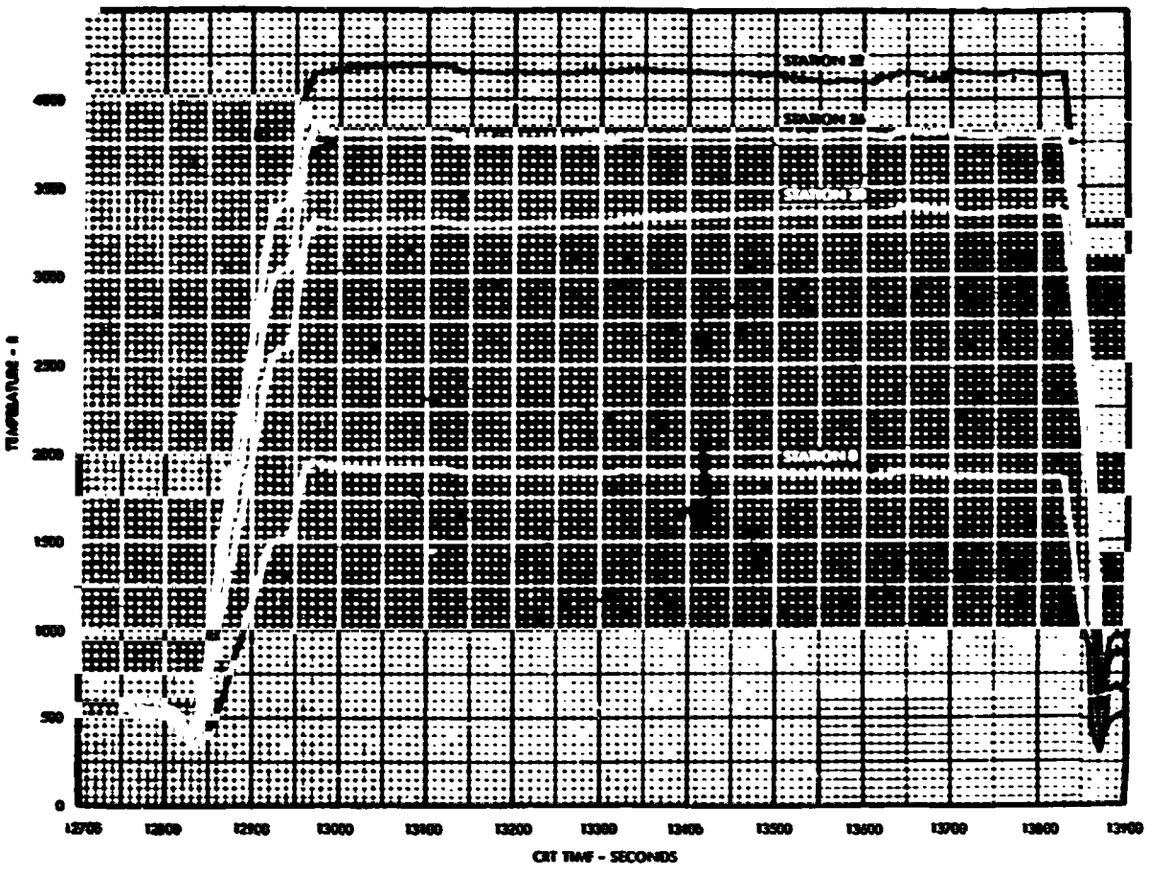

Figure 3-23. NRX-A5 EF-IV Power Test Description: Core Unfueled Element Temperatures (Electrical Averages)

3.4.2 Best Estimated Chamber Temperature, Reactor Power, and Flow Rate

3.4.2.1 Summary of Results

Calculations of best estimated chamber temperature, reactor power, and flow rate were made for ten steady-state points (five points for each power test). Table 3-3 summarizes the best estimates and the test data used for the calculction. The two standard deviations (2σ) for all parameters are also given in Table 3-3; two standard deviations define the 95 percent confidence level of the parameter.

The measured chamber temperatures were corrected for labline drift. The maximum required correction was plus 16°R. Table 3-3 shows that the accuracy of the measured chamber temperature is four times greater than the computed value, assuming that the measurement is a good indication of chamber temperature; consequently, the best estimated temperature is essentially equal to the average measured temperature.

The best estimated thermal power is compared with the measured linear No. 1 power in Table 3-4. The ratio of thermal to measured nuclear power is nearly constant for the full power points of each EP. The shift in this ratio from 1.10 for EP-III to 1.05 for EP-IV may be attributed to a change in the neutronic calibration adjustment between tests. The ratio decreased by about 4 percent going from the 229 MW hold at the start of EP-III to the full power hold.

TABLE 3-3
STEADY STATE NRX-A5 POWER AND FLOW DATA

EP	III	III	III	III	III	IV	IV	IV	IV	IV
TIME (sec)	25247.5	25400.0	25700.0	25930.0	26247.5	12940.0	13002.5	13242.5	13482.5	13812.5
FE-4 FLOW:										
Inlet Temperature (°R)	39.1 ± 1.0	39.1 ± 1.0	39.1 ± 1.0	39.2 ± 1.0	39.3 ± 1.0	39.3 ± 1.0	39.3 ± 1.0	39.3 ± 1.0	39.5 ± 1.0	39.2 ± 1.0
Inlet Pressure (psia)	95.1 ± 1.8	86.9 ± 1.8	86.6 ± 1.8	86.0 ± 1.8	79.2 ± 1.8	85.5 ± 1.8	85.6 ± 1.8	85.1 ± 1.8	84.1 ± 1.8	79.8 ± 1.8
Pressure Drops (psi)										
(1) P.210.AL	4.82 ± 0.92	23.6 ± 0.92	23.0 ± 0.92	23.4 ± 0.92	23.7 ± 0.92	22.5 ± 0.92	23.3 ± 0.92	23.3 ± 0.92	23.4 ± 0.92	23.3 ± 0.92
(2) P. 125.AL	5.20 ± 0.92	24.0 ± 0.92	24.0 ± 0.92	23.9 ± 0.92	24.0 ± 0.92	23.0 ± 0.92	23.7 ± 0.92	23.6 ± 0.92	23.6 ± 0.92	23.6 ± 0.92
Flow (lb/sec)										
(1) P.210.AL	32.1 ± 3.1	71.0 ± 2.0	70.1 ± 2.0	70.7 ± 2.0	71.1 ± 2.0	69.3 ± 2.0	70.5 ± 2.0	70.6 ± 2.0	70.6 ± 2.0	70.6 ± 2.0
(2) P. 125.AL	33.4 ± 3.0	71.6 ± 2.0	70.6 ± 2.0	71.4 ± 2.0	71.5 ± 2.0	70.1 ± 2.0	71.2 ± 2.0	71.0 ± 2.0	71.0 ± 2.0	70.9 ± 2.0
FE-7 FLOW:										
Inlet Temperature (°R)	41.1 ± 1.0	48. ± 1.0	48.5 ± 1.0	48.8 ± 1.0	49.0 ± 1.0	47.7 ± 1.0	48.9 ± 1.0	49.0 ± 1.0	49.2 ± 1.0	48.9 ± 1.0
Inlet Pressure (psia)	274.3 ± 18.0	917.6 ± 18.0	897.1 ± 18.0	911.8 ± 18.0	908.2 ± 18.0	798.8 ± 18.0	915.0 ± 18.0	916.4 ± 18.0	919.6 ± 18.0	916.5 ± 18.0
Pressure Drops (psi)										
(1) P.211.AL	5.36 ± 0.92	24	24.0 ± 0.92	24.3 ± 0.92	24.2 ± 0.92	23.7 ± 0.92	24.0 ± 0.92	24.2 ± 0.92	24.3 ± 0.92	24.3 ± 0.92
(2) P. 126.AL	5.31 ± 0.92	23.	23.1 ± 0.92	23.2 ± 0.92	23.1 ± 0.92	23.1 ± 0.92	23.1 ± 0.92	23.4 ± 0.92	23.3 ± 0.92	23.2 ± 0.92
Flow (lb/sec)										
(1) P.211.AL	33.9 ± 3.0	72.3 ± 2.0	72.1 ± .0	72.6 ± 2.0	72.4 ± 2.0	71.6 ± 2.0	72.1 ± 2.0	72.4 ± 2.0	72.5 ± 2.0	72.5 ± 2.0
(2) P. 126.AL	33.7 ± 3.0	71.2 ± 2.0	70.8 ± .0	70.9 ± 2.0	70.7 ± 2.0	70.6 ± 2.0	70.6 ± 2.0	71.1 ± 2.0	71.0 ± 2.0	70.9 ± 2.0
REACTOR FLOW (lb/sec)	33.3 ± 1.5	71 5 ± 1.0	70.9 ± 1.0	71.4 ± 1.0	71.4 ± 1.0	70.4 ± 1.0	71.1 ± 1.0	71.3 ± 1.0	71 3 ± 1.0	71.2 ± 1.0
CHAMBER TEMPERATURE (°R)	1922 ± 36	4088 ± 50	3907 ± 46	4033 ± 47	3977 ± 47	3240 ± 39	4116 ± 51	4040 ± 49	4063 ± 49	4089 ± 50
Computed	1955 ± 248	4058 ± 223	3910 ± 216	3982 ± 219	3931 ± 217	3251 ± 184	4045 ± 223	3995 ± 220	3977 ± 219	3923 ± 217
Measured	1921 ± 37	4090 ± 51	3907 ± 47	4004 ± 49	3979 ± 48	3239 ± 40	4118 ± 52	4042 ± 50	4068 ± 50	4098 ± 51
CHAMBER PRESSURE (psia)	180.6 ± 7.1	570.3 ± 7.1	553.9 ± 7.1	563.6 ± 7.1	560.0 ± 7.1	498.5 ± 7.1	565.9 ± 7.1	563.5 ± 7.1	562.4 ± 7.1	557.6 ± 7.1
REFLECTOR INLET:										
Temperature (°R)	76.2 ± 6.2	153.7 ± 4.3	150.4 ± 4.3	155.0 ± 4.3	156.1 ± 4.2	121.3 ± 6.9	153.2 ± 4.3	154.7 ± 4.3	158.2 ± 4.2	160.6 ± 4.2
Pressure (psia)	231.3 ± 10.6	735.6 ± 10.6	716.9 ± 10.6	729.0 ± 10.6	727.2 ± 10.6	639.1 ± 10.6	729.8 ± 10.6	728.7 ± 10.6	728.4 ± 10.6	725.6 ± 10.6
REACTOR THERMAL POWER (MW)	229 ± 11	1119 ± 23	1051 ± 21	.089 ± 22	1081 ± 22	847 ± 17	1120 ± 23	1099 ± [illegible]	1106 ± 22	1112 ± 23

TABLE 3-4

COMPARISON OF MEASURED NUCLEAR WITH COMPUTED THERMAL POWER

EP	Time	Best Estimated Thermal Power	Measured Power (Linear 1)	Thermal/ Measured
III	25247.5	229	201	1.139
III	25400.0	1119	1015	1.102
III	25700.0	1051	955	1.101
III	2593.0	1089	980	1.111
III	26247.5	1081	980	1.103
IV	12940.0	847	805	1.052
IV	13092.5	1120	1061	1.056
IV	13242.5	1099	1045	1.052
IV	13482.5	1106	1047	1.056
IV	13812.5	1112	1054	1.055

3.4.2.2 Description of Calculation Procedure

The procedure for the calculation of best estimated chamber temperature, flow rate, and power is described below. A computer program was written to perform these calculations. The latest parahydrogen properties (See Reference 8) were used in the calculation.

1) Standard Deviation of Computed Parameters

The standard deviation of all calculated parameters was computed using the following technique:

If the parameter Y is of the form

$$Y = f(X_1, X_2, X_3 \ldots\ldots X_n)$$

then the standard deviation of Y is defined by the equation,

$$S_y^2 = \sum_{i=1}^{n} \left(\frac{\partial Y}{\partial X_i}\right)^2 S_{x_i}$$

where,

S_y = standard deviation of computed parameter Y

X_i = parameters and constants used in the calculation of Y

S_{x_i} = standard deviation of parameters and constants used in the calculation of Y

The one standard deviation of constants was assumed to be one percent of the value of the constant.[9]

2) Best Estimates

The best estimate of parameters which had more than one independent measurement and/or calculation was computed using the following procedure:

$$Y_{BE} = \sum_{i=1}^{n} A_i Y_i$$

where,

Y_{BE} = best estimate of parameter Y

Y_i = independent indications of parameter Y

n = number of independent indications of Y

A_i = weighting factor for each independent indication of Y

The weighting factors are computed as,

$$A_i = \frac{\vdots}{S_i^2 \sum_{i=1}^{n} \left(\frac{1}{S_i^2}\right)}$$

where,

S_i = standard deviations of the independent indications of Y.

The standard deviation of the best estimate is then given by,

$$S_Y^2 = \frac{1}{\sum_{i=1}^{n} \left(\frac{1}{S_i^2}\right)}$$

where the symbols are as defined above. The standard deviations of measured parameters were obtained from the combined instrumentation and data system accuracies presented in References 10 and 11.

3) Reactor Flow Rate

Two venturis (FE-4 and FE-7) were used to measure reactor flow rate. The pressure drop across each venturi was measured by two independent transducers, so that there were four independent measurements of reactor flow rate. The equation used to relate venturi pressure drop to flow rate was,

$$W = K * (\rho * \Delta P)^{\frac{1}{2}}$$

where,

W = reactor flow rate (lb/sec)

K = 7.01 for FE-4

6.98 for FE-7

ρ = venturi inlet density evaluated from pressure and temperature measurements (lb/ft^3)

ΔP = venturi pressure drop (psi)

The best estimate of reactor flow rate was calculated by the equation,

$$W_B = \sum_{i=1}^{4} W_i * A_i$$

where,

W_B = best estimated reactor flow rate

W_i = individual flow rate measurement

A_i = weighting factor for each individual measurement (The method used to calculate weighting factors was discussed previously in item 2)

Another possible indication of reactor flow rate is the flow rate calculated using the choked nozzle equation with measured nozzle chamber temperature and pressure. However, this estimate of flow rate was not used in the best estimate calculation because the flow rate computed in this manner has a much greater standard deviation than the venturi calculations. For example, the standard deviation of flow rate calculated by the choked nozzle equation at the first full power hold of EP-III is 2.50 lb/sec compared to a standard deviation of 1.00 lb/sec for the average calculated venturi flow rate.

4) Nozzle Chamber Temperature

There were four independent measurements of nozzle chamber temperature. From these four measurements, an average measured chamber temperature was calculated by the equation,

$$T_c = \sum_{i=1}^{4} T_i * A_i$$

where,

T_c = average measured chamber temperature

T_i = individual measurements of chamber temperature (T. 138. 5A, T. 139. 5A, T. 140. 5A, T. 141. 5A)

A_i = weighting factors for each individual measurement

Another estimate of chamber temperature was computed using the best estimated reactor flow rate, measured chamber pressure and the nozzle choking equation,

$$T_{cc} = A_E^2 \left[\frac{g_c M k}{R}\left(\frac{2}{k+1}\right)^{\frac{k+1}{k-1}}\right]\left(\frac{P_c}{W_B}\right)^2$$

where,

T_{cc} = computed chamber temperature (°R)

P_c = statistical average measured chamber pressure (psia) (P. 152. 5A, P. 154. 5A, P. 156. 5A, P. 706. 5A)

A_E = effective throat area (58. 46 in^2)

g_c = gravitational constant (ft - lbm/lbf - sec^2)

M = molecular weight of gas (2. 016 lbm/lb mole for hydrogen)

k = specific heat ratio

R = universal gas constant (1545. 4 ft - lbf/R lb-mole)

W_B = best estimated reactor flow rate (lbm/sec)

The best estimate of chamber temperature was then calculated by the equation,

$$T_{CB} = A_1 T_C + A_2 T_{cc}$$

where,

T_{cB} = best estimated chamber temperature

A_1 = weighting factor for measured chamber temperature

A_2 = weighting factor for computed chamber temperature

T_c and T_{cc} are as above, and where the weighting factors are computed as described in item 2.

5) Reactor Thermal Power

The energy equation used to calculcte the reactor thermal power is:

$$Q_R = 1.054 \times 10^{-3} * W_B * (h_c - h_{RI})$$

where,

Q_R = reactor thermal power (MW)

W_B = best estimated reactor flow rate (lb/sec)

h_c = nozzle chamber enthalpy based on best estimates of chamber temperature and pressure (Btu/lb)

h_{RI} = reflector inlet enthalpy based on average reflector inlet temperature and pressure (Btu/lb)

3.4.3 Comparison of Transient and Steady State Test Data with TNT Calculations

The purpose of this section is to compare NRX-A5 reactor performance test measurements with post-test calculations. The comparison is made for both transient and steady state operation, and the parameters compared include reactor temperatures, pressures, pressure drops and either power or control drum position. This section is divided into four subsections:

1) reactor model used for the calculations
2) transient comparisons
3) steady state comparisons
4) discussion of performance parameter comparisons

In summary, the comparisons between test data and post test calculations are reasonably good for all parameters. Improvements in the core temperature calculations and the reactivity feedback calculations over some portions of the operating map are still required and are now being investigated.

3.4.3.1 TNT Reactor Model for Calculations

The TNT (Thermal and Nuclear Transient) code was used for the post test calculation of the performance parameters. The TNT reactor model used for the transient calculations is described in Reference 2.* Several revisions were made to this reactor model prior to the time at which the steady state calculations were made. These revisions included the following:

1) Revision of axial reactor power distribution to simulate that of Reference 2.**
2) Revision of the turbulent gas convective heat transfer correlation.
3) The fuel channel inlet loss coefficient was removed and the orifice pressure drop is computed according to the flow test data shown in Reference 12.***
4) The tie rod channel inlet loss coefficient was made a function of tie rod flow Reynold's number.

These revisions either improve the accuracy of the calculation or simplify the calculations; the improved accuracy is shown in the following discussion of parameter comparisons, Section 3.4.3.4.

---

* See Index D. 5. a. 2

** See Index E. 5. g. 12

*** See Index I. 4. e. 2

3.4.3.2 Transient Comparisons

Three transients of the NRX-A5 test series were selected for post-test calculation and comparison with test data. The table below describes these transients and the input to the calculation for each transient.

RUN DESCRIPTION	INPUT
EP-III Startup to full power	Reactor power, flow rate, and nozzle manifold inlet enthalpy
EP-IV Fixed drum startup	Control drum position, reactor flow rates and nozzle manifold inlet enthalpy
EP-IV Shutdown	Reactor power, flow rate and nozzle manifold inlet enthalpy

The reactor power inputs were taken from Linear Power No. 1 measurements and corrected to the best estimated thermal power at appropriate full power hold points. The reactor flow rate inputs were taken as the average of the post test computed FE-4 and FE-7 venturi flow rates for liquid flow and as the computed FE-10 venturi flow rate for gas flow. Only the FE-7 flow rate was used when ACV-6 was open (see Figure 3-1). The control drum position input was also obtained from test measurements (digital data). A brief description of the comparisons for each transient follows.

1) EP-III Startup to full power

The input to the calculations and the comparison of the calculations with test data for this transient are shown on Figures 3-24 to 3-29. As these figures show, the calculations agree reasonably well with test data for all parameters.

2) EP-IV Fixed drum startup

Figure 3-30 shows the input flow rate and control drum position, and the comparison between test data and calculations for reactor power and nozzle chamber temperature. During the first 120 seconds of this transient the control drums were fixed at 2.0 degrees in from the cold critical position, while the flow was ramped up to 70 lbs/sec. Then the drums were moved outward 3.7 degrees and held fixed for 20 seconds

until the "no flux loop" temperature controller was activated. Calculated power is in good agreement with measured power up to 35 percent of full power. However, above this power level the computed and measured power disagree by as much as ten percent. This poor agreement is the result of the inaccuracy of the reactivity feedback calculations in the portion of the operating map traversed during this startup. The accuracy of the reactivity feedback calculations varies significantly over the operating map as can be seen from Reference 13. * This reference shows a comparison between predicted and measured reactivity feedback over the operating map for the NRX/EST reactor; also, the reference shows that there is only one line on the operating map on which the predicted reactivity agrees with test data (zero error reactivity feedback line). This accounts for the difference in the accuracy of the reactivity feedback calculations between the EP-III and EP-IV startups since the EP-III startup traversed the operating map by a path which was nearer the zero error reactivity feedback line than the path traversed in the EP-IV startup. As a result of the poor accuracy of the reactivity feedback calculations for the EP-IV startup, the calculated chamber temperature is 250°R greater than measured at the conclusion of the fixed drum startup. Comparisons were not made for other performance parameters because the differences between computed and measured power would make such comparisons questionable.

3) EP-IV Shutdown

This transient is the shutdown following the second duration test of the NRX-A5 reactor. The input, power and flow rate, and the comparisons of calculations with test data are shown in Figures 3-31 to 3-36. The comparisons for all parameters are reasonably good until the switch from liquid to gaseous hydrogen flow occurs (about CRT 13871.0).

---

* See page 6-66 of Reference 13.

The difference between calculated and test values after the switch to gaseous flow may be attributed to the uncertainty in defining the exact time of the switch and to the uncertainty of the computed flow rate for several seconds after the switch. The computed flow rate at the FE-10 venturi was used; however, the cooling effect of the liquid downstream of this venturi at the time PCV-41 opened was neglected in the calculation. Hence, the measured temperatures are lower than calculated for several seconds after the switch.

3.4.3.3 Steady State Comparisons

Post test TNT calculations were made for four steady state times during the NRX-A5 test series. These consist of two points for each experimental plan; one partial power hold and one full power hold. The reactor conditions for the intermediate power hold of EP-IV (12940 second CRT time) are not completely steady state; however, this point was included because it is referenced in other chapters of this report. Comparisons for additional points were not considered necessary since the power and flow remained approximately constant for the duration of each hold; the only changes during each hold were corrosion effects which are not simulated by the TNT program. Best estimated reactor flow rate and calculated reactor thermal power based on best estimates of flow rate, nozzle chamber conditions, and reflector inlet conditions were input to the TNT calculation for these steady state points. Table 3-5 presents the comparisons between test data and calculations for all performance parameters. This table shows that the calculated results agree with test measurements remarkably well for all but a few parameters. The worst comparisons are for the unfueled element temperatures but even most of these calculations fall within ten percent of the measurements. In summary, the post test TNT calculations of the NRX-A5 steady state points agree satisfactorily with test measurements.

TABLE 3-5

STEADY STATE COMPARISON OF TEST DATA WITH CALCULATED RESULTS

EXPERIMENTAL PLAN		III		III		IV		IV	
CONTROL ROOM TIME		25247.5		25400.		12940.		13002.5	
		Measured	TNT	Measured	TNT	Measured	TNT	Measured	TNT
Reactor Power - MW		228.8		1118.5		847.0		1120.3	
Inlet Flow - LB/SEC		33.3		71.5		70.4		71.1	
Nozzle Torus:	T - °R	45.0	44.7	52.0	52.5	51.0	50.9	52.4	53.5
	P - psia	258.2	260.6	878.0	884.8	737.8	758.4	875.4	883.0
Reflector Inlet:	T - °R	76.2	65.8	153.7	148.2	121.3	116.5	153.2	149.2
	P - psia	231.2	229.8	735.3	739.6	638.8	640.8	729.4	736.0
Reflector Outlet:	P - psia	220.0	221.5	699.0	706.1	611.8	612.5	697.3	704.6
Shield Dome Plenum:	T - °R	103.7	102.0	221.4	233.6	171.3	185.2	217.5	235.2
Core Inlet:	T - °R	116.4	108.1	241.7	244.2	191.1	193.9	238.4	245.8
	P - psia	219.6	218.4	690.4	695.3	601.4	600.1	684.1	693.9
Core Exit:	T - °R	1922.2	1909.8	4088.2	4080.6	3229.8	3223.5	4 14.1	4107.7
	P - psia	171.3	179.2	570.3	574.4	498.4	499.1	566.7	573.1
Tie Rod Exit:	T - °R	442.5	443.3	644.9	675.5	502.7	506.7	657.4	682.8
Unfueled Element Temperatures: °R	Station 8	713.9	796.	1935.1	1894.	1535.6	1463.	1959.0	1906.
	Station 20	1277.3	1230.	3220.8	3093.	2683.5	2375.	3345.9	3118.
	Station 26	1501.9	1470.	3749.1	3684.	3044.4	2822.	3886.4	3708.
	Station 32	1816.4	1690.	4048.4	4152.	3291.9	3211.	4169.1	4178.
Pressure Drops: psid	Reactor	52.4	50.6	167.4	166.2	145.4	141.7	166.9	164.9
	Core	38.4	39.2	118.3	120.9	103.6	104.0	118.0	120.8
	Reflector	8.0	8.4	32.1	33.4	27.3	28.3	33.6	33.4
	Shield & SP	3.4	3.0	12.0	10.8	8.9	9.4	10.8	10.8
	Nozzle	26.4	30.8	140.0	148.2	114.9	114.6	143.1	148.0

CONFIDENTIAL

3.4.3.4 Discussion of Performance Parameter Comparisons

The following is a discussion of the comparison between test data and post test calculations for reactor performance parameters. The comparisons are for three steady state points in Table 3-5 the two for EP-III and the high power point for EP-IV, the EP-III startup transient in Figures 3-24 to 3-29 and the EP-IV shutdown transient (prior to CRT 13871.0) in Figures 3-31 to 3-36. The partial power steady state point of EP-IV (CRT 12940) was not considered in the following comparisons because the reactor had not reached a completely steady state condition.

a) Plenum Temperatures (Reflector Inlet, Shield Dome Plenum, and Core Inlet)

The agreement between calculated and measured plenum temperatures is good for nearly all of the comparison points considered. The only calculated plenum temperatures which are not within about five percent of the measured values are the reflector inlet and core inlet temperatures at the low power steady state point of EP-III (CRT 25247.5) and the reflector inlet temperature during the first forty seconds of the EP-IV shutdown. The low calculated reflector inlet temperature at low reactor power level has been noticed in previous tests and investigation of the calculations has been made; however, no satisfactory modification to the calculation to improve this situation has yet been found. During the full power hold of EP-IV, the reflector inlet temperature increased about ten degrees for unknown reasons. (see reference 7 for a detailed discussion). Part of the difference between computed and measured plenum temperatures during the EP-IV shutdown is due to this unexplained increase in the reflector inlet temperature. This increase in measured reflector inlet temperature is responsible for corresponding differences in the dome and core inlet comparisons.

b) Plenum Pressures (Nozzle Torus, Reflector Inlet, Reflector Outlet, Dome End, Core Inlet, Nozzle Chamber)

Calculated plenum pressures are in good agreement with test data except during the ten seconds of the EP-IV shutdown subsequent to the time at which the reactor was scrammed (CRT 13859.C). The calculated pressures are within about three percent of the test data for the steady state points and within about five percent of test data during all but ten seconds of the transients. In view of these good agreements it may be concluded that plenum pressure calculations are satisfactory.

c) Component Pressure Drops (Reflector, Core and Reactor)

The comparison between calculated and measured component pressure drops is good for both transients and the four steady state points considered. The calculated pressure drops agree within five percent of measured values for all data considered. For the steady state points the comparison for the reflector and core pressure drops are especially good; the worst comparisons are 33.4 psi computed and 32.1 psi measured for the reflector, and 120.8 psia computed and 118.0 psi measured for the core.

d) Core Unfueled Element Temperatures (Station 8, 20, 26, and 32)

The calculated core station temperatures show reasonable good agreement (better than 10 percent) with test data for the EP-III startup and for the two steady points at the start of EP-III. The differences are greater during the EP-IV shutdown which occurred after significant corrosion. The effect of corrosion on these temperatures is not considered in the TNT calculation. Base corrosion effects are evident by the differences of measured core temperatures between the two full power steady state points; that is, the measured unfueled element temperatures increased by 25 to 125 degrees from the start of the EP-III hold to the start of the EP-IV hold. For this reason, the comparison of calculated and measured station temperatures should be restricted to EP-III. In addition, the comparisons of these temperatures for the steady state points are better than for the transients. The revised axial power distribution and convective heat transfer correlation mentioned in Section 3.4.3.1 were used for the steady state calculations. These revisions have brought the calculated unfueled element temperatures into better agreement with

test data than they were previously. However, even with these new revisions, the calculated core temperatures are not of the same order of accuracy as other calculated parameters. Probably the major reason for these differences is the relatively simple model used to represent the unfueled and fuel elements in the TNT program. For example, the gap between fueled and unfueled elements varies with core axial location; however, a constant gap is used in the TNT program. In addition, the heat transfer correlation probably does not have the same accuracy over the entire range of conditions encountered in the core.

It should also be noted that some of the calculated unfueled element temperatures agree better with test data than others; for the steady state points, calculated station 8 and station 20 temperatures differ with test data by 3 to 10 percent, while station 26 differs by 3 to 8 percent and station 32 differs by 1 to 7 percent.

e) Tie Rod Exit Gas Temperature

The calculated tie rod exit gas temperature agrees within ten percent of test data over most portions of the transients and within five percent of test data for the steady state points. The better agreement for the steady state points is a result of the revision of the tie rod channel inlet loss coefficient as was mentioned in Section 3.4.3.1. This revision was used in the steady state calculations but was not available for the transient calculations. The revision allows the loss coefficient to vary with the Reynolds number of the tie rod channel flow; thus the tie rod channel flow and its exit temperature are more accurately calculated. In view of the good agreement between calculated and measured tie rod exit gas temperature using the revised loss coefficient, this calculation appears to be satisfactory.

f) Control Drum Bank Position

The calculated control drum position agrees reasonably well with test data. Comparisons for this parameter were made for the transients only. The maximum deviation of calculated results from test data is 4.5 degrees which occurs during the EP-IV shutdown (CRT 25125.0). The accuracy of the control drum position calculation will improve if better reactivity feedback equations are developed, as was mentioned in Section 3.4.3.2.

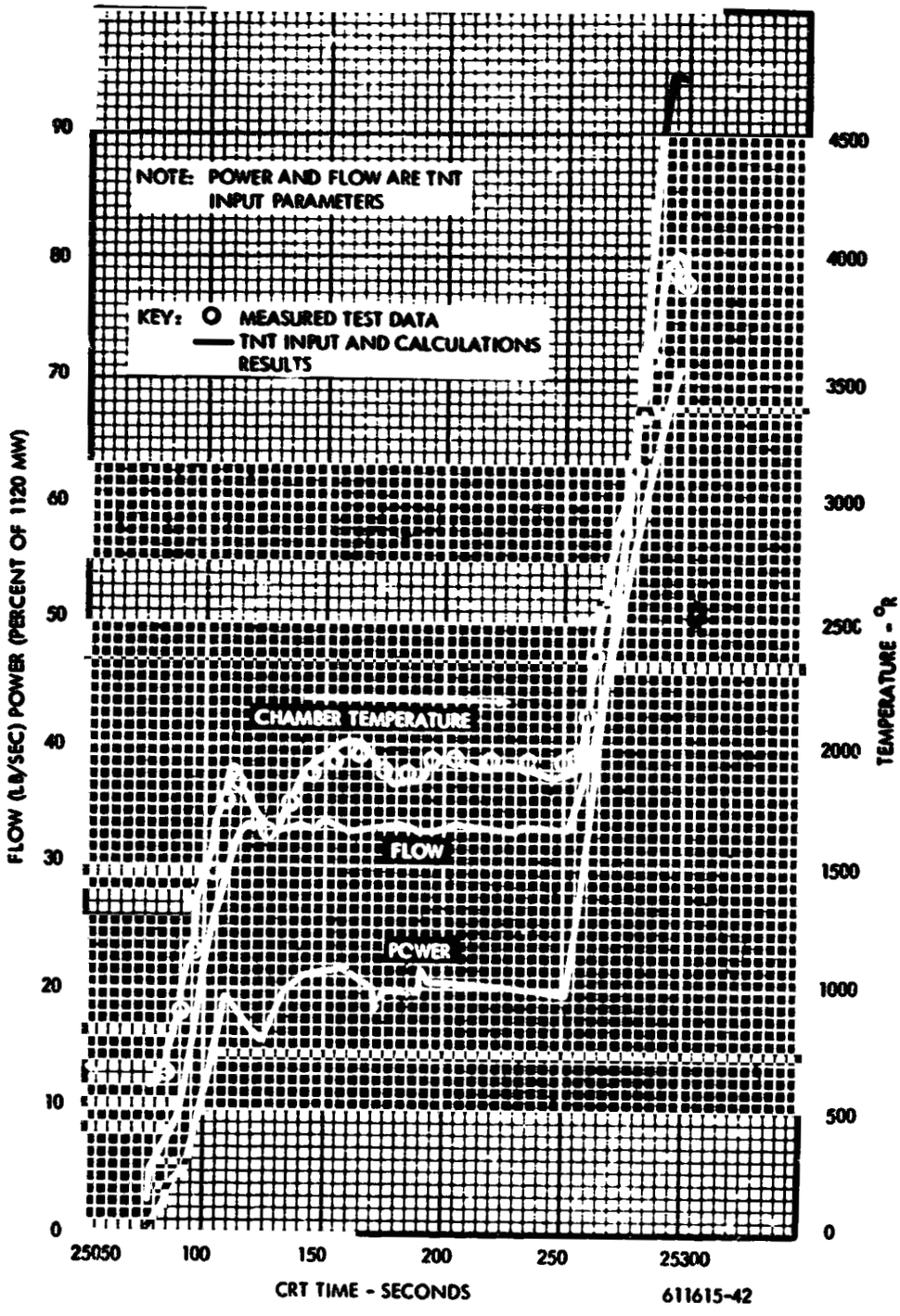

Figure 3-24. NRX-A5 EP-III Startup Comparison: Power Flow and Chamber Temperature

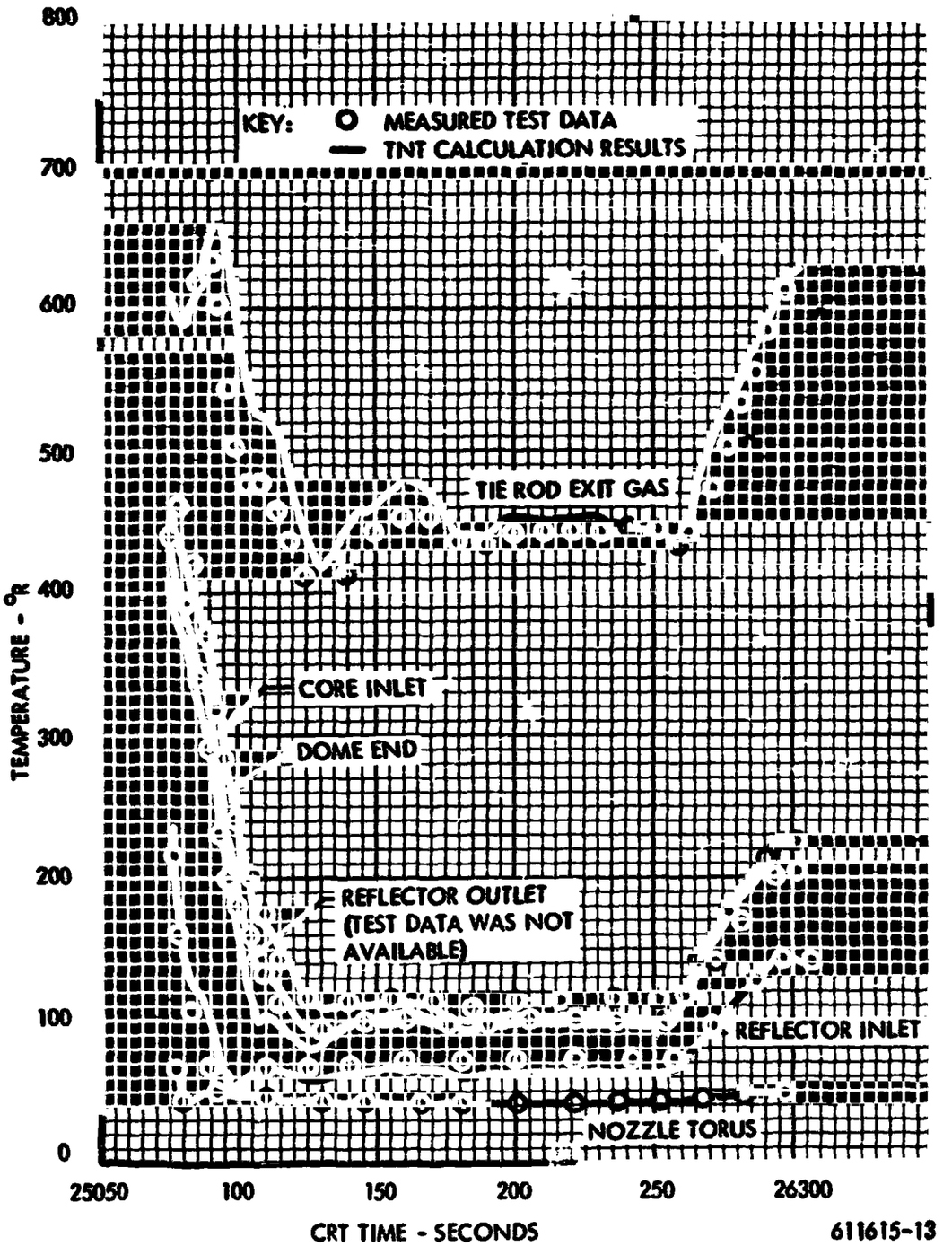

Figure 3-25. NRX-A[illegible]P-III Startup Comparison: Tie Rod and Plenum Temperatures

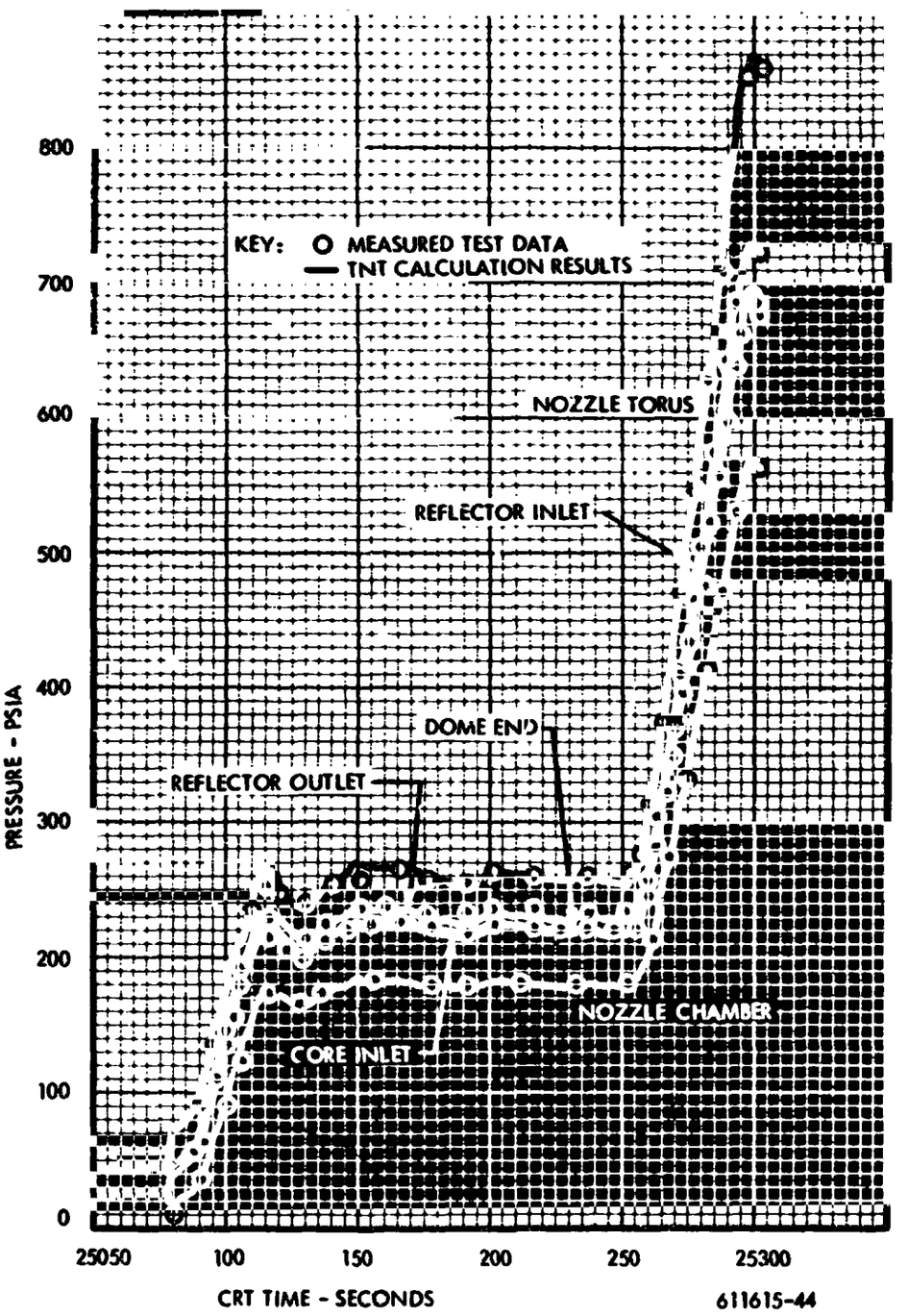

Figure 3-26. NRX-A5 EP-III Startup Comparison: Plenum Pressures

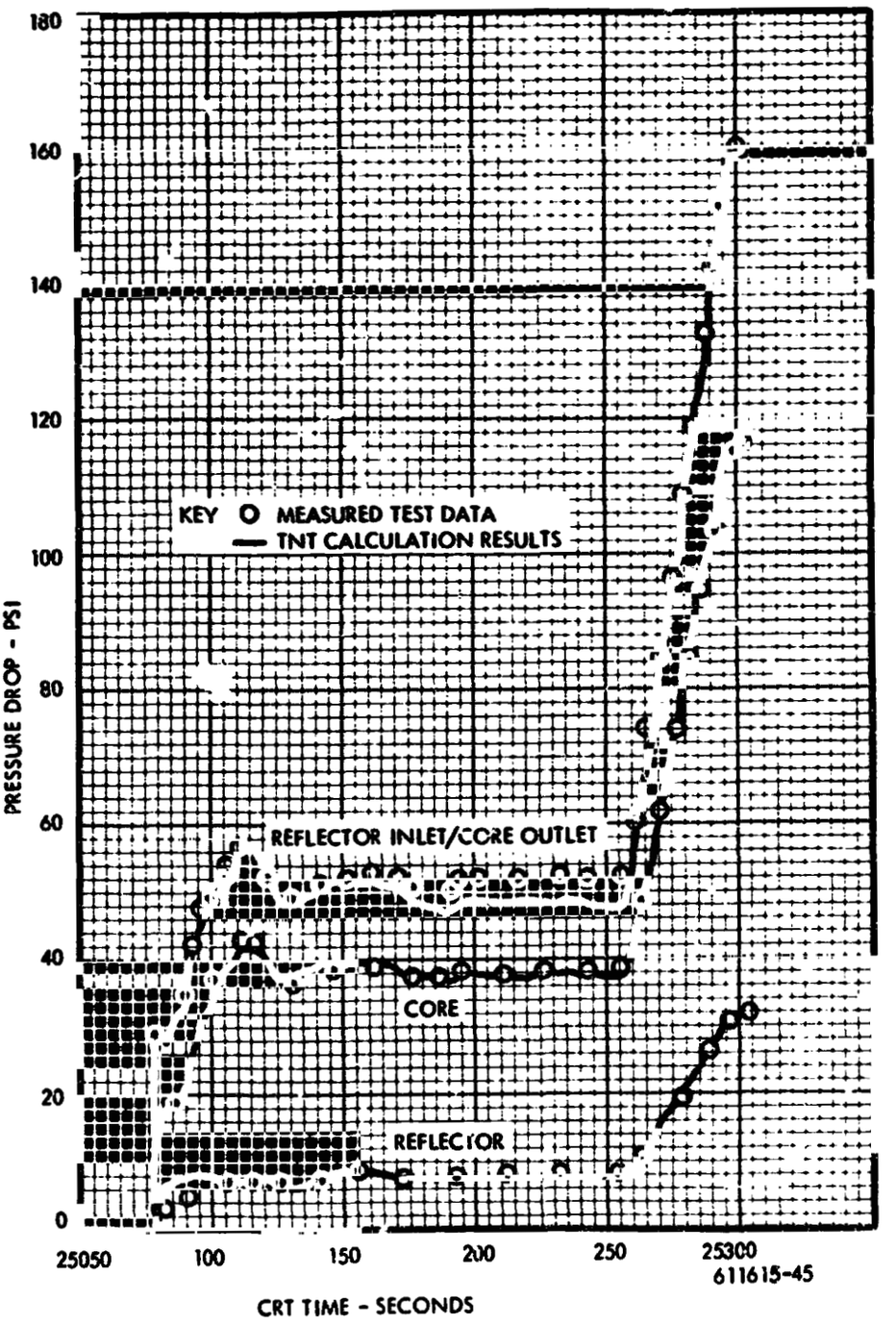

Figure 3-27. NRX-A5 EP-III Startup Comparison: Pressure Drops

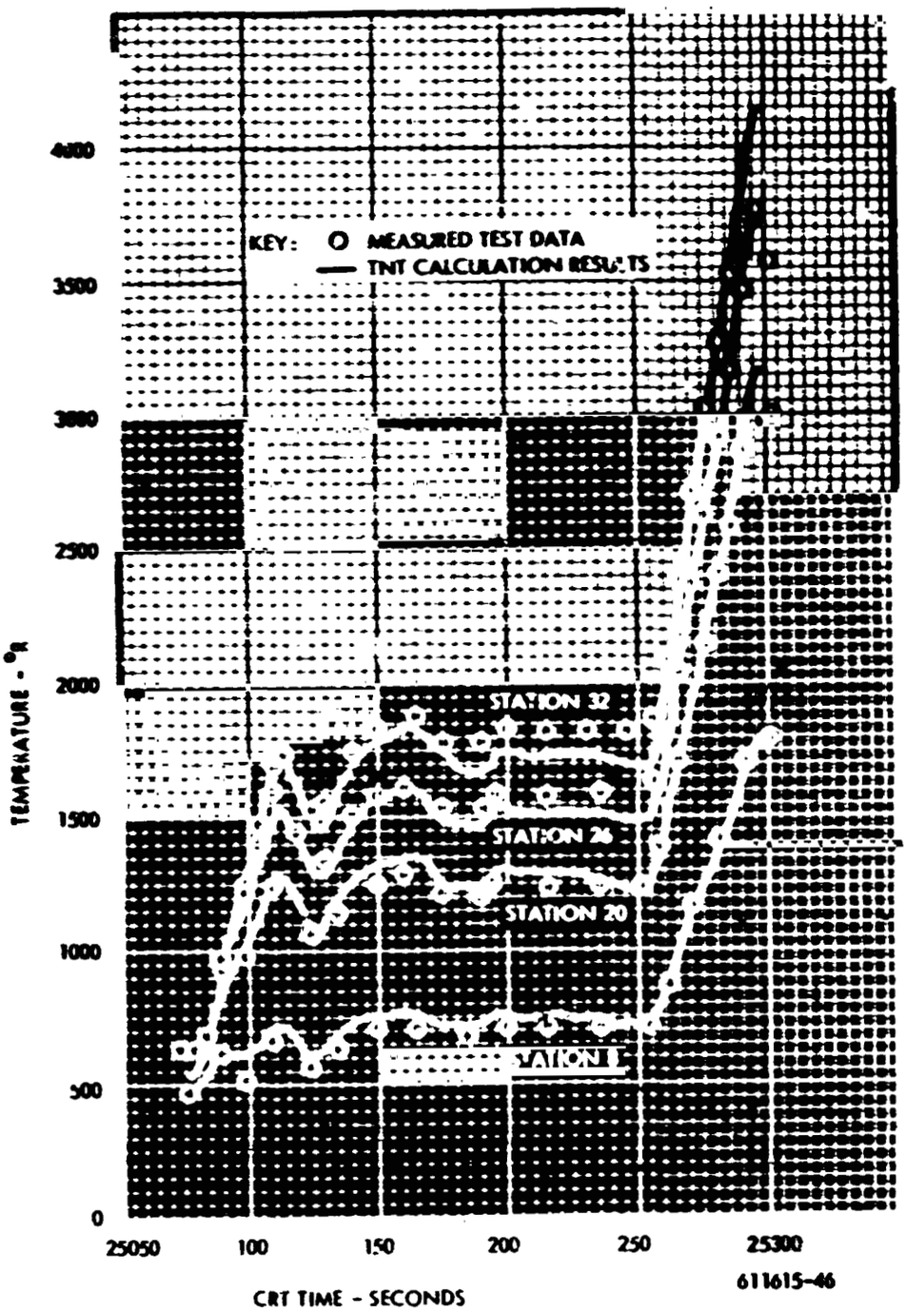

Figure 3-28. NRX-A5 EP-III Startup Comparison: Core Station Temperatures

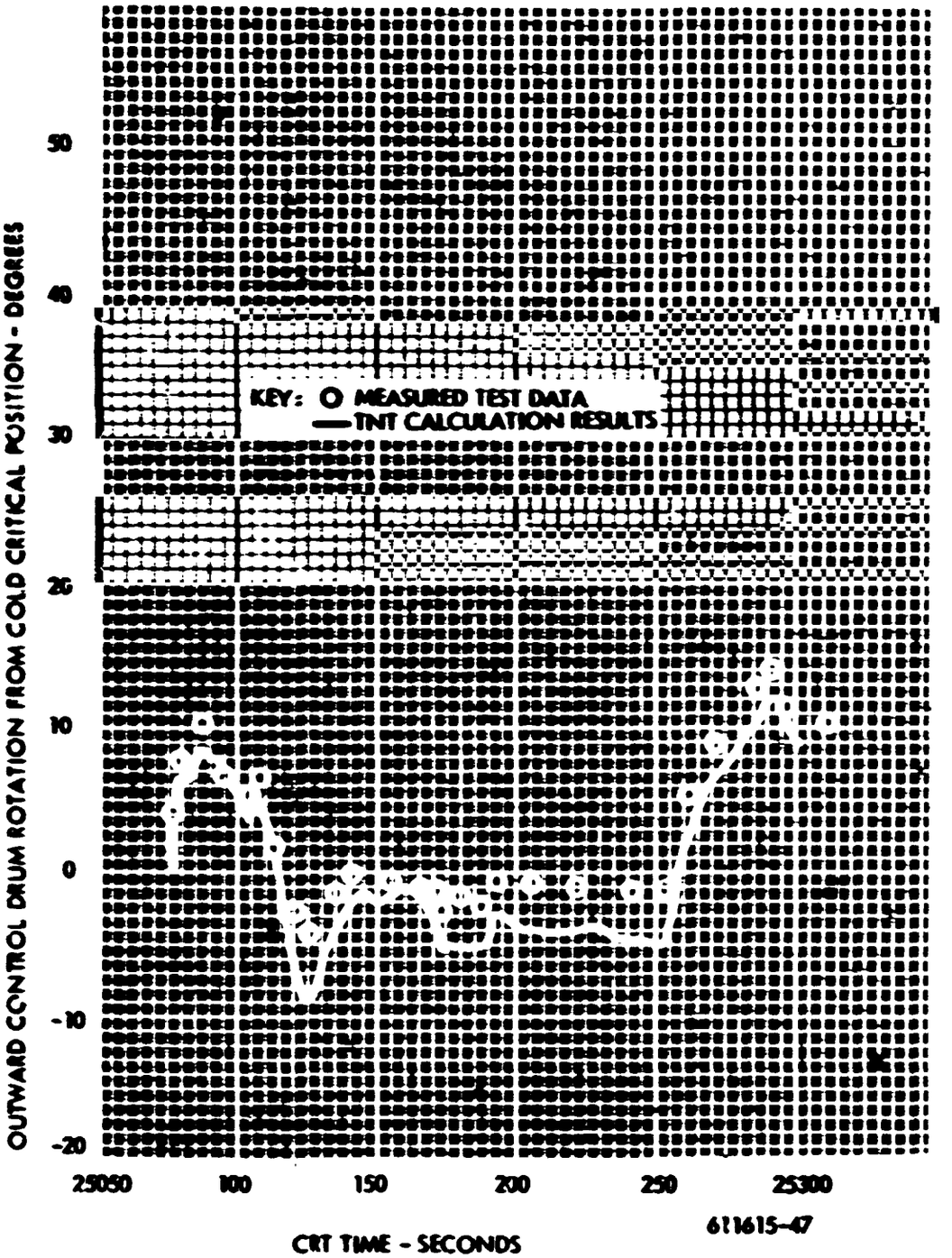

Figure 3-29. NRX-A5 EP-III Startup Comparison: Control Drum Position

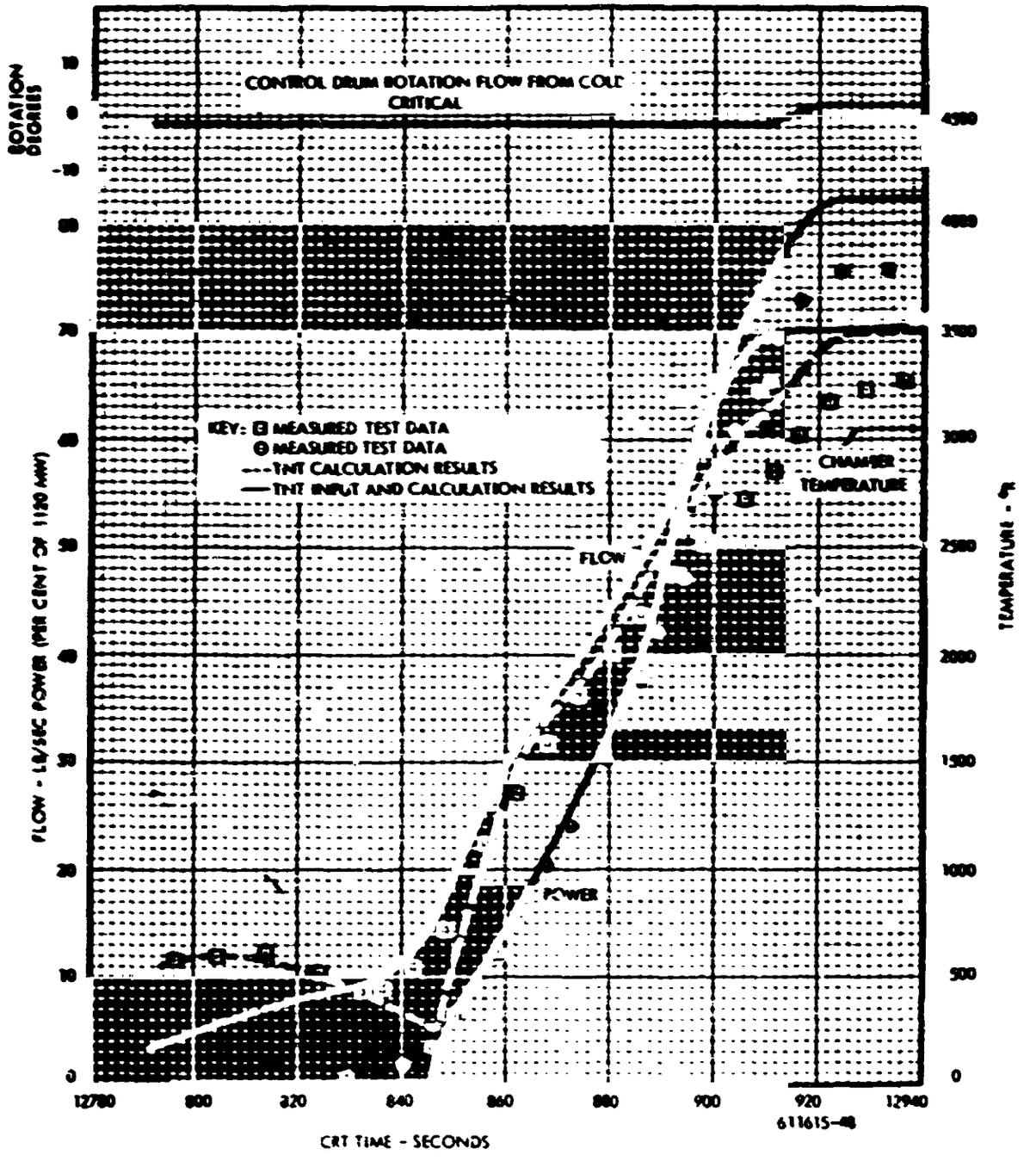

Figure 3-30. NRX-A5 EP-IV Startup Comparison: Control Drum Position, Power, Flow and Chamber Temperature

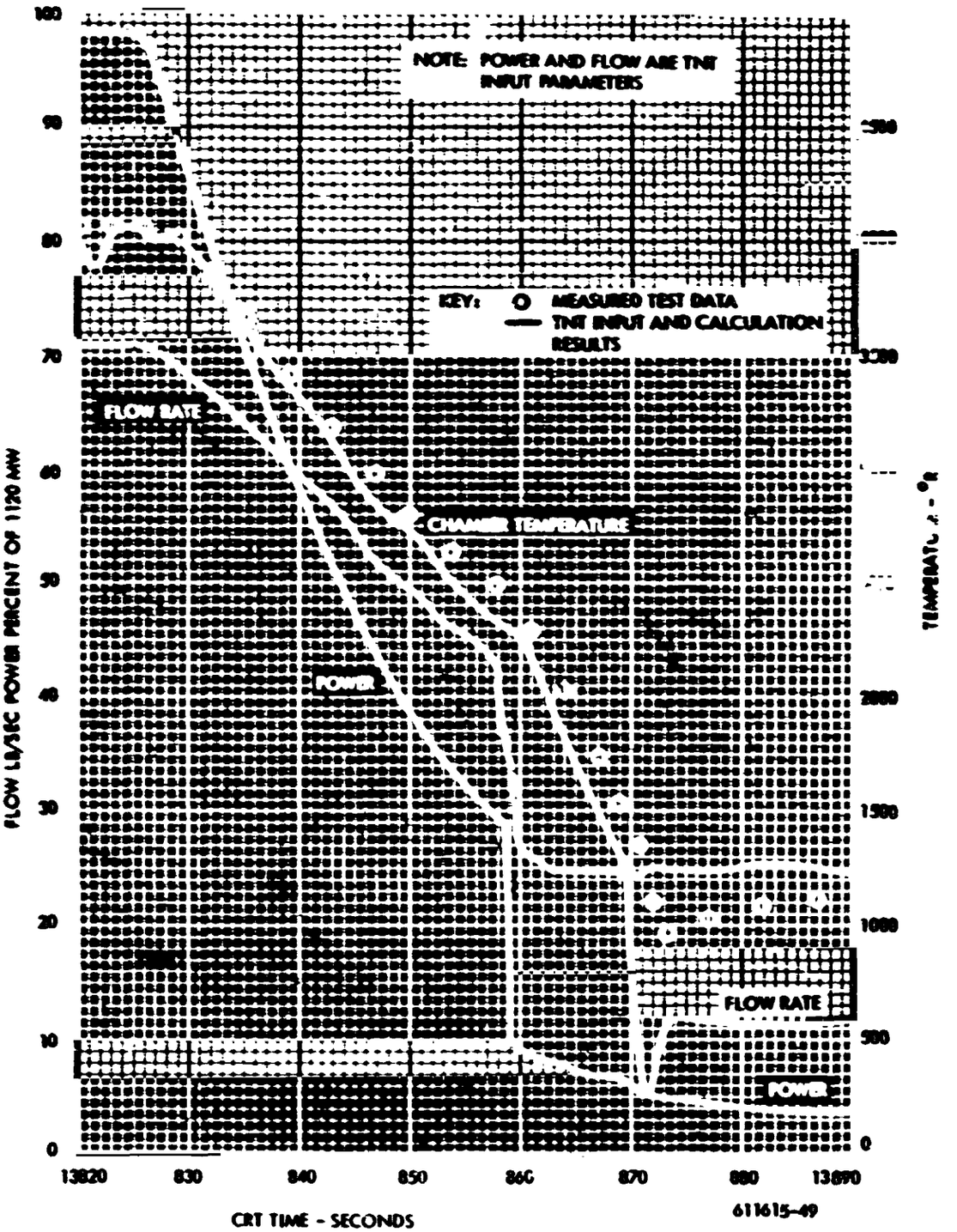

Figure 3-31. NRX-A5 EP-IV Shutdown Comparison: Power Flow and Chamber Temperature

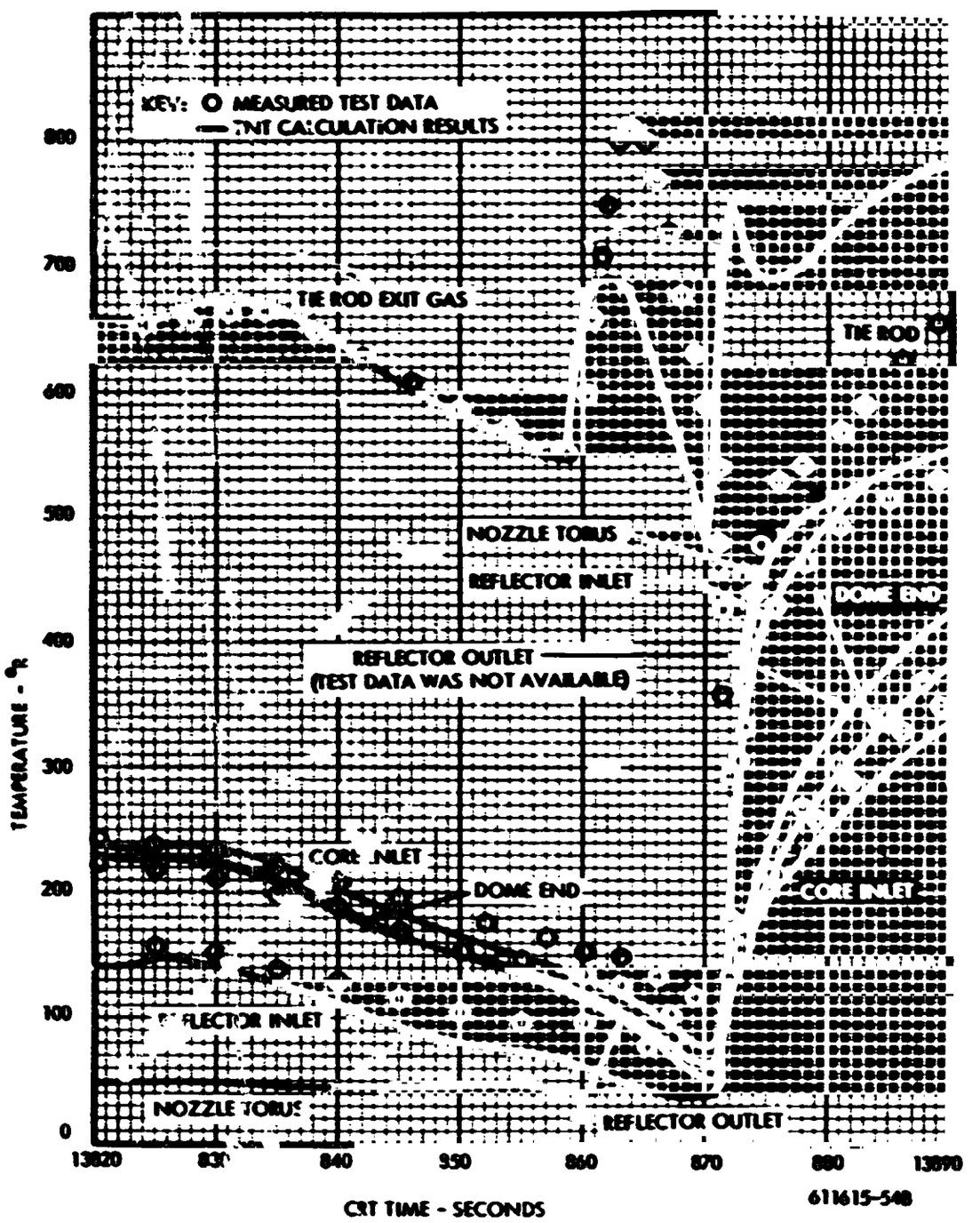

Figure 3-32. NRX-A5 EP-IV Shutdown Comparison: Tie Rod and Plenum Temperatures

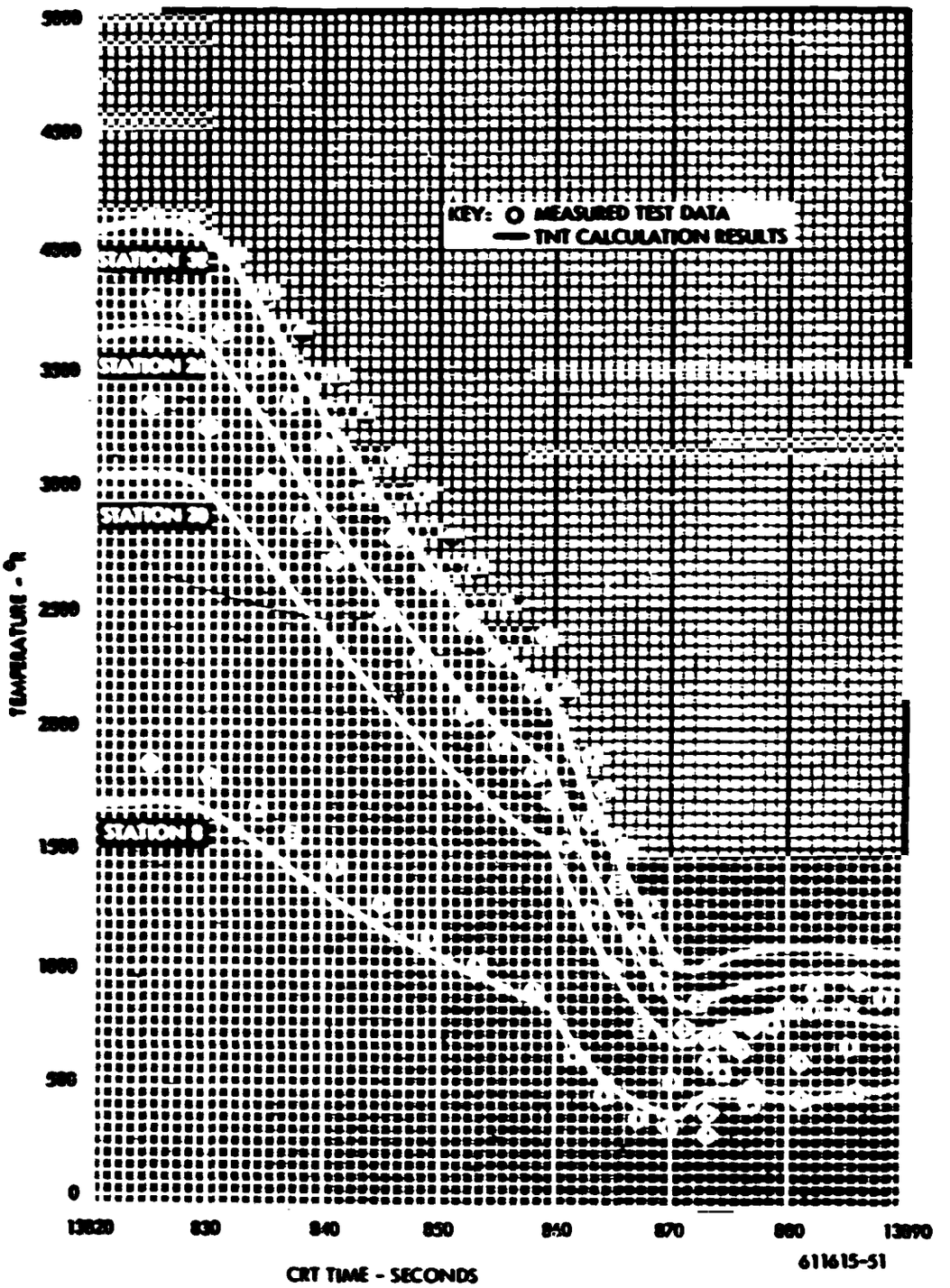

Figure 3-33. NRX-A5 EP-IV Shutdown Comparison: Core Station Temperatures

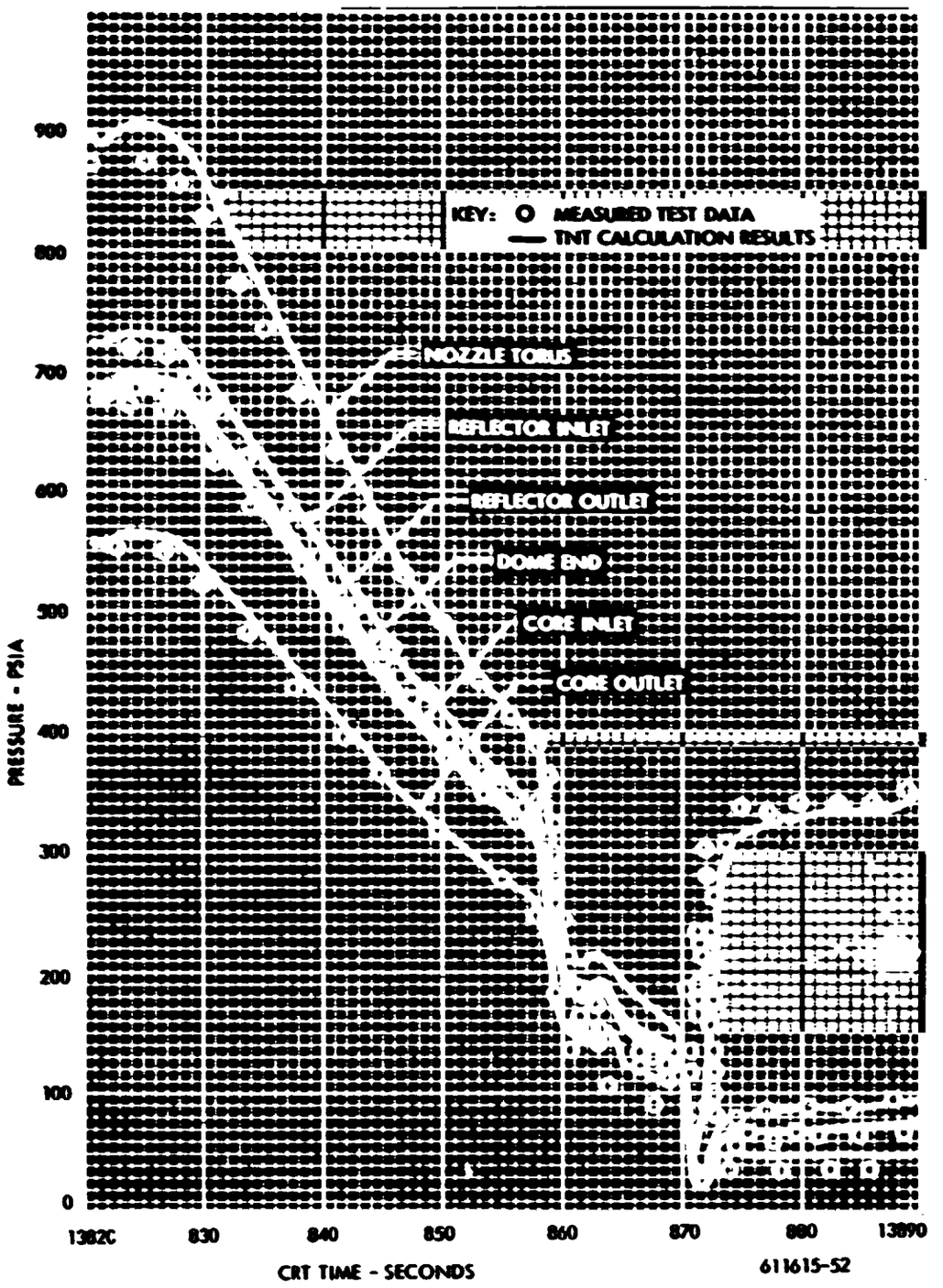

Figure 3-34. NRX-A5 EP-IV Shutdown Comparison: Plenum Pressures

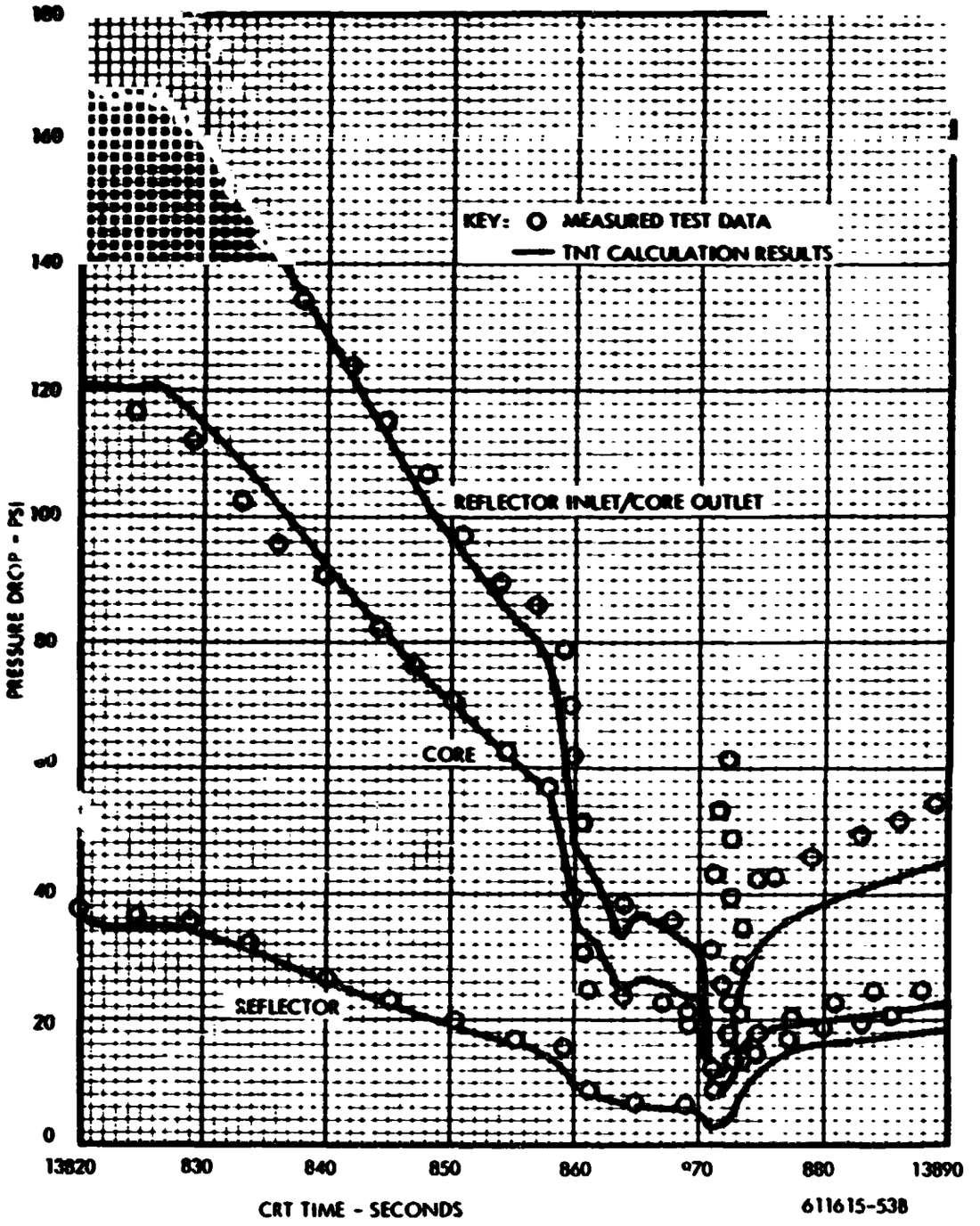

Figure 3-35. NRX-A5 EP-IV Shutdown Comparison: Pressure Drops

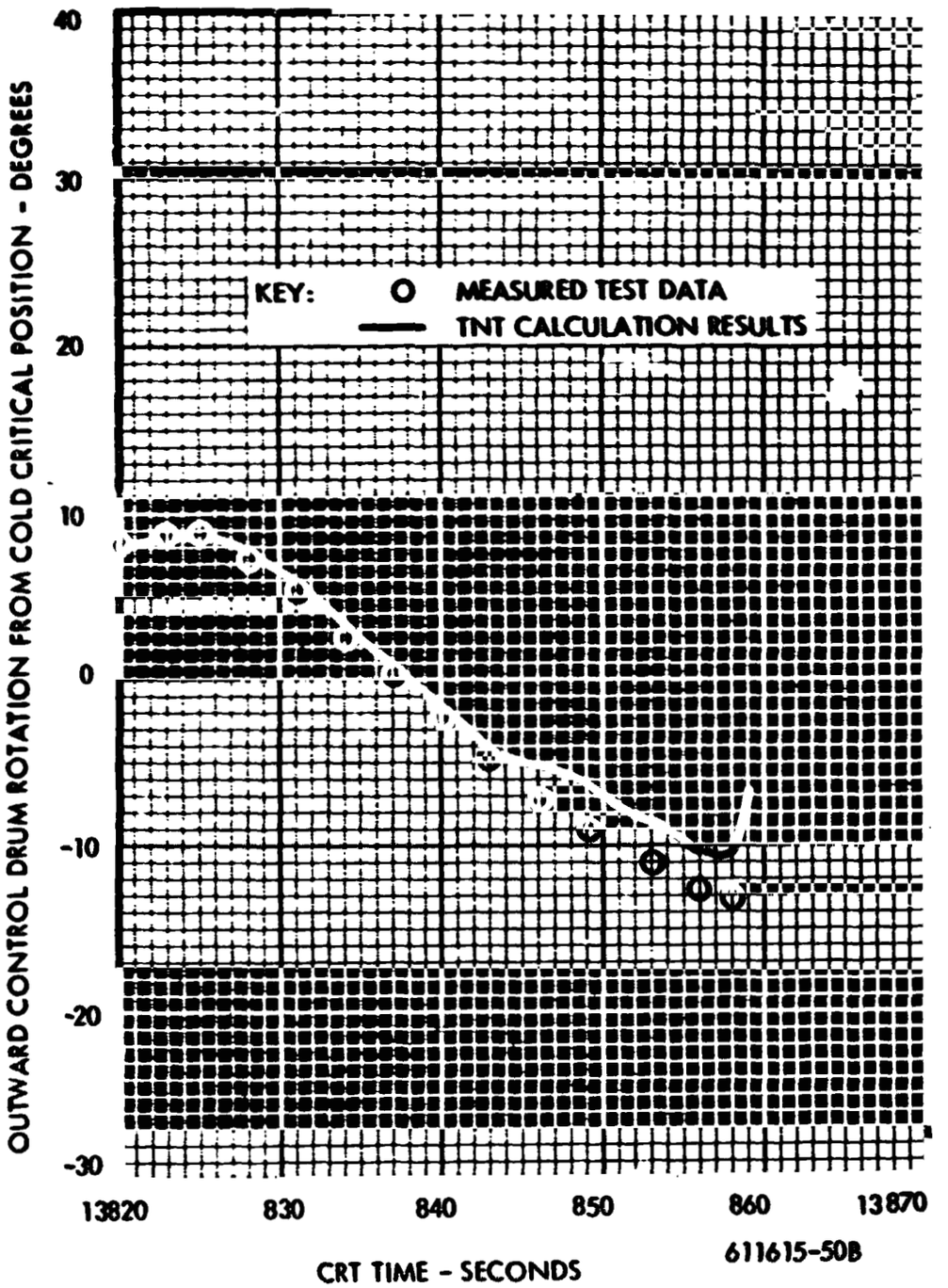

Figure 3-36. NRX-A5 EP-IV Shutdown Comparison: Control Drum Bank Position

3.4.4 Decay Power Analysis

3.4.4.1 Summary

The decay power was computed from test data obtained during the cooldown following the first power test, EP-III. The experimental decay power compares satisfactorily with the decay power computed by Revision 1 of the S-4 prediction code.* The scope and detail of the decay power calculation was restricted by a lack of usable test data. However, the analysis indicated several modifications to the data recording intervals which would greatly improve the scope of the decay power analysis.

The following data are contained in this section:

1) Description of the cooldown.
2) Description of the decay power calculation procedure.
3) Comparison of calculated (from test data) decay power with decay power predicted by Revision 1 of the S-4 (Fission Product Energy Release) code.*
4) Modifications of the data recording intervals to increase the scope of the analysis.

3.4.4.2 Description of Cooldown

The measured nuclear power profiles for each EP are shown on Figures 3-12 and 3-18. The integrated power (based on best estimated thermal power) is 1.10×10^6 MW-sec for EP-III and 1.06×10^6 MW-sec for EP-IV. The equivalent full power (1120 MW) operating times are 16.4 minutes for EP-III and 15.8 minutes for EP-IV. One of the reasons for restricting the analysis to EP-III was the similarity in the two power profiles.

---

* Two versions of the S-4 code are available. The original S-4 code assumes that the decay curve for the beta energy release rate following fission is the same as the decay curve for gamma rays; i.e. both have the same time dependence. Revision 1 uses separate time dependence for betas and gammas.

Following each power run the reactor was "pulse" cooled with liquid nitrogen. Approximately 20 pulses were required to complete each cooldown. Tabular summaries of the pulse cooldowns including reactor temperatures before and after pulse flow are included in the Three Day Reports.[9, 10] Flow was generally initiated when the average core station 8 temperature had increased to 900°R and was discontinued when the average tie rod material temperature had decreased to 450°R. The average flow rate during a pulse was about 5 lb/sec.

Approximately 900 pounds of liquid nitrogen remained in the line between the liquid nitrogen ON-OFF control valve and the nozzle manifold at the conclusion of each pulse. This quantity of liquid nitrogen slowly vaporized and cooled the reactor for several minutes after the conclusion of a pulse. Consequently the reactor was cooled to temperatures less than planned; after some pulses core temperatures were near 200°R.

3.4.4.3 Description of the Calculation Procedure

Data recorded during short time intervals before the initiation of liquid nitrogen flow were used to perform the decay power analysis. Core temperatures during these intervals were near their highest value during cooldown and consequently were the most accurate.

A three part calculation was performed to compute decay power from the measured reactor temperatures. One, the increase in core sensible heat was computed during intervals without coolant flow. Two, the energy loss from the core by radiation from the faces, by convection to the purge flow, and by conduction to the reflector region was computed for the same time interval and added to the sensible energy gain calculated for the core. The third part of the calculation consisted of dividing the net sensible energy gain of the core by the time interval used for part one, and by the fraction of core power to total reactor power. The calculation is described in more detail in the following paragraphs.

Average axial temperature profiles at two times during intervals without coolant flow were used to determine the heat stored in the core. All core and tie rod measurements were used to determine the average axial temperature profiles required for the calculation. As a first step, average radial material temperatures were computed at each instrumented core station. For core stations 8, 20,26, and 32 least square curve fits of the measured

temperatures as a function of radial location were determined and used to compute weighted average radial temperatures. Figure 3-37 shows typical radial temperature profiles for core stations 8 and 26. These radial temperature profiles were measured shortly before the start of a pulse. Relative to the EP-III power runs, these temperatures occurred 15766 seconds (4.5 hours) after scram and correspond to a computed decay power of 190 KW.

Average temperatures were computed by integrating the area under these radial curve fits. Arithmetic averages of the three core station 1 measurements were used to determine the average temperature at core station 1 and averages of all tie rod exit thermocouples were used to determine the average temperature at core station 52. A least square curve fit of third degree was then constructed as a function of core length using these average temperatures for stations 1, 8, 20, 26, 32, and 52. Two typical axial temperature profiles determined with this procedure are shown in Figure 3-38. These profiles are for the start and the end points of a 50 second interval without coolant flow. The temperatures occurred at 0.4 hours after scram and correspond to a computed decay power of 2237 KW. The increase in core sensible heat was determined by calculating the change in core enthalpy corresponding to two such axial temperature profiles.

The energy loss from the core by conduction to the reflector region, radiation from the end faces, and convection to the purge flow was computed for the same time interval and added to the sensible energy gain of the core. For the reactor temperatures experienced during cooldown the energy loss by radiation from the faces and convection to the purge flow was negligible. The energy loss to the reflector region was determined for the same time interval used for part one of this calculation by first computing the sensible energy gain of the inner reflector and then subtracting the generated energy. An inner reflector power fraction of 2.6 percent of total reactor power (see Reference 2) was used. The calculated energy loss from the core to the reflector with this procedure ranged between 70 and 30 KW depending on time during the cooldown.

TABLE 3-6

NRX-A5 EP-III COOLDOWN: COMPARISON OF DECAY POWER COMPUTED FROM TEST DATA WITH PREDICTIONS

Time After Scram, Seconds	Decay Power (MW)		Predicted / Computed
	* Predicted	Computed	
1661	2230	2237	1.00
2266	1650	1658	1.00
2966	1230	1372	0.90
3891	920	1015	0.91
7511	445	453	0.98
11216	270	270	1.00
15741	181	191	0.95

* Decay power predicted with "new" S-4 (Fission Product Energy Release) code.

The third part of the calculation consisted of dividing the net core energy gain during intervals without coolant flow by the corresponding time interval and by the fraction of core power to total reactor power. The fraction of core power to total reactor power is a function of time after scram; a value of 0.92 was used for the calculation which applies to the time range of this calculation (1500 to 1600 seconds after scram).

3.4.4.4 Decay Power Comparison

The decay power was predicted with the S-4 (Fission Product Energy Release) code. Two versions of this program are available. Decay power data for the S-4 code is given in the NRX/EST Data Book and for Revision 1 is given in the NRX-A5 Data Book (see References 12 and 2). The predicted decay power using both versions of the S-4 code Revision 1, (solid curve) is approximately 30 percent greater than the S-4 code (dashed curve) in the interval from 1000 to 10,000 seconds after scram. At 80,000 seconds both programs predict the same decay power. For greater times after scram Revision 1 predicts a lower decay power.

The computed decay power is compared against predicted decay power for EP-III in Figure 3-39. The computed decay power ranges from 2234 to 191 KW and covers a time range from 1660 to 15740 seconds (0.4 to 4.4 hours) after scram. A tabular comparison of the same data is shown on Table 3-6. The ratio of predicted to computed decay power ranges between 0.90 and 1.00 with a mean ratio of 0.96. The computed decay power is therefore an average of 4 percent greater than predicted. This comparison is satisfactory, and indicates that the S-4 code Revision 1, accurately predicts decay power over the range of conditions analyzed.

3.4.4.5 Recommended Changes to Data Recording Intervals

During the NRX-A5 cooldown, the data recorders were started 30 - 120 seconds before flow was initiated and stopped about 60 seconds after the valve was closed. Additional short recording intervals are recommended during the intervals between pulses.

Either station 20 or 26 should be monitored, and 10 to 20 seconds of data should be recorded after each 50 to 100°R increase in the monitored temperature. This data would permit 5 to 8 decay power calculations of the type described during the intervals between all pulses; which would greatly increase the scope of the calculation.

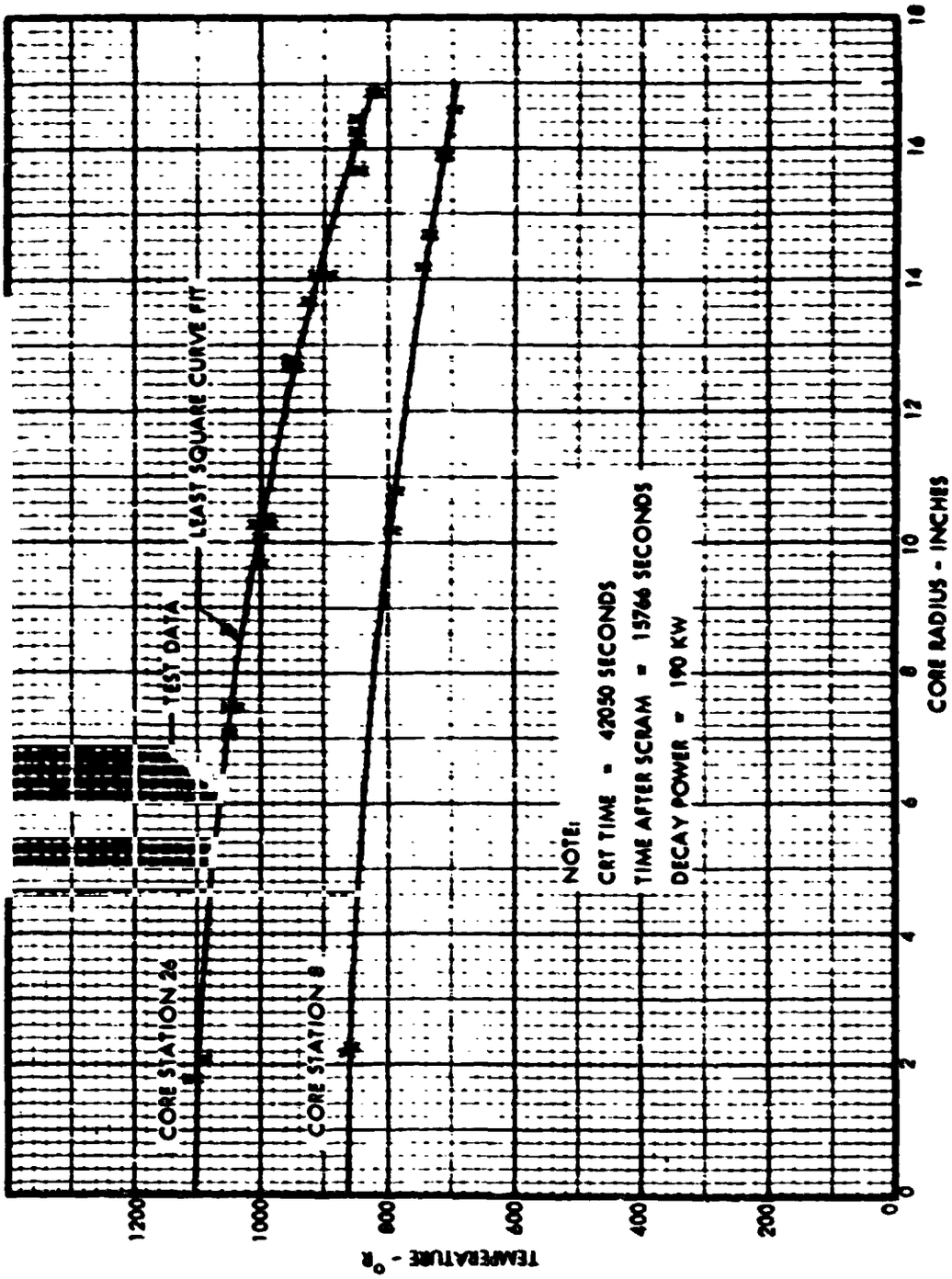

Figure 3-37. NRX-A5 EP-111 Cooldown: Typical Radial Core Temperature Profiles

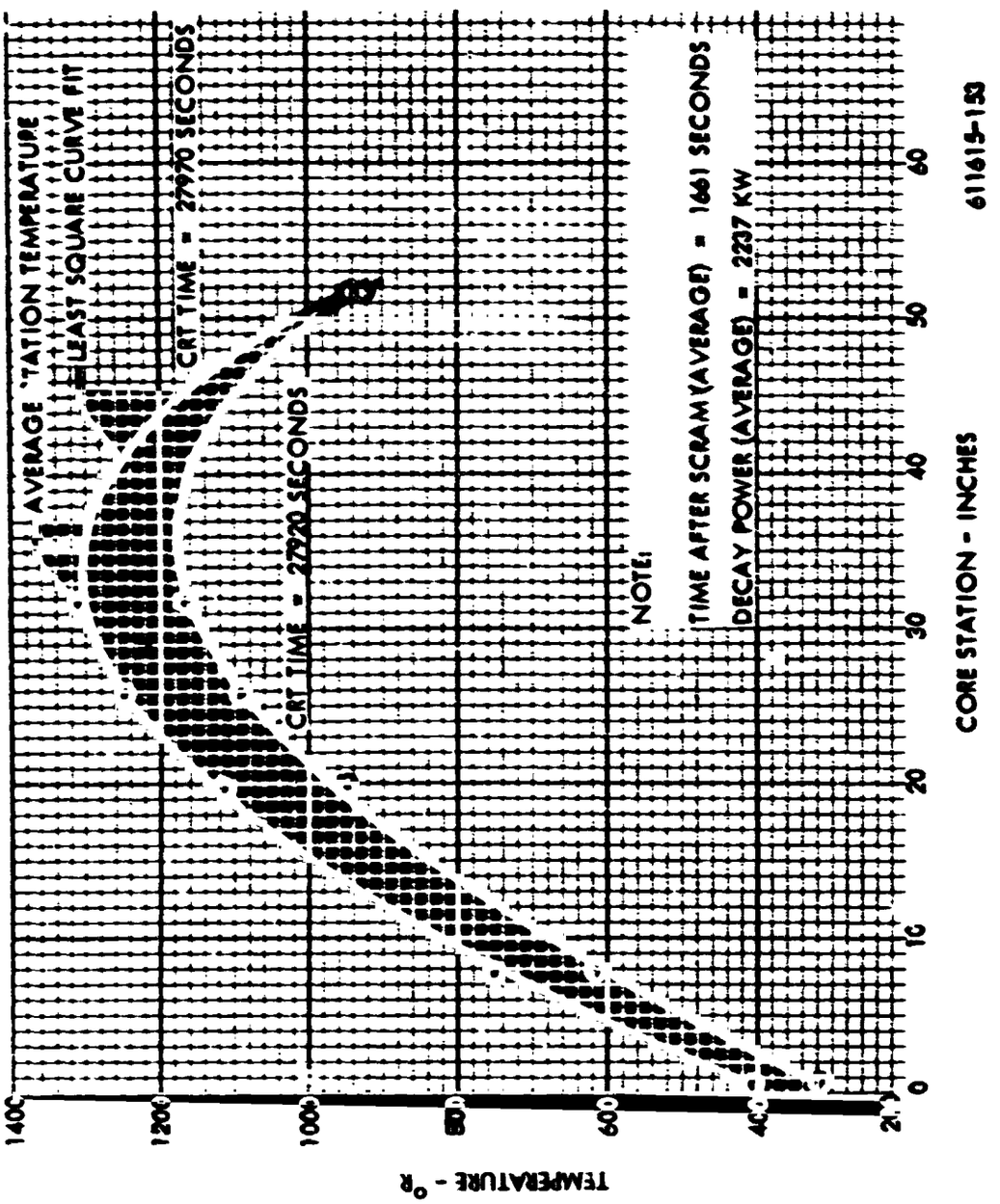

Figure 3-38. NRX-A5 EP-111 Cooldown: Typical Axial Temperature Profiles

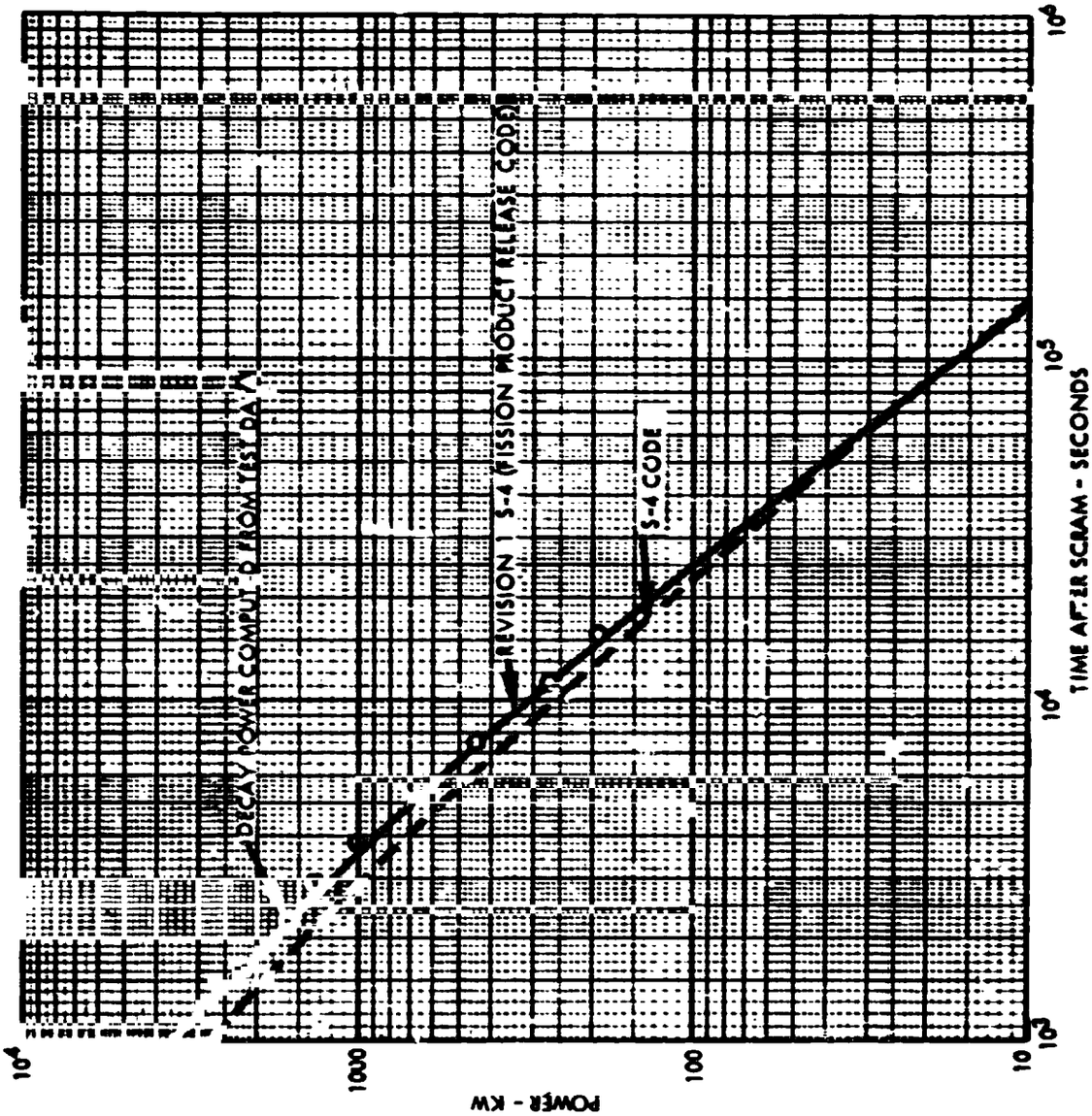

Figure 3-39. NRX-A5 EP-III: Decay Power

3.5 NRX PERFORMANCE RESULTS

3.5.1 Summary of NRX Testing

Data that summarizes reactor performance for the NRX test program are presented in this section. Detailed analysis of these tests are given in the corresponding test reports (References 14, 15, 16, and 13). This section presents some of the data and comparisons which were prepared for various presentations. Data are presented in two sub-sections.

1) General Summary of Test Performance
2) Key Environmental Conditions

3.5.1.1 General Summary of Test Performance

The number of cold flow runs, power runs, and aborts for the NRX test program are tabulated in Table 3-7. A total of 28 cold flow runs, 15 power runs, and 3 aborted runs have been performed to date. The three aborted runs occurred during NRX/EST while attempting low dewar pressure bootstraps. Chamber temperature profiles for the NRX-A3, NRX/EST, and NRX-A5 power tests are shown in Figure 3-40.

Significant accomplishments of the program included six fixed control drum tests. These are summarized below for each reactor test:

Fixed Control Drum Operation During NRX Testing Program

1) NRX-A2, EP-V Low Power Mapping Test

The major objectives of this EP were to map the low power operating region and to demonstrate operation in the fixed control drum mode. The entire EP was performed without operation of the liquid hydrogen pump; reactor flow was produced by dewar pressure and was controlled by the main propellant valve. The fixed drum mapping test was performed over a 23 - 56 MW range in power and a 5 - 13.5 lb/sec range in flow rate. Starting from 40 MW and 10.5 lb/sec, flow was slowly increased to 13.5 lb/sec, held for about 60 seconds, and then decreased to 5 lb/sec. The resulting power variation was from 40 MW, to 56 MW, and back to 23 MW.

TABLE 3-7

SUMMARY OF COLD FLOW RUNS, POWER RUNS, AND ABORTS DURING NRX TESTING

Test Series	No. of Cold Flow	No. of Aborts	No. of Power Startups
NRX-A1 EP-II	2 LHYD	---	---
NRX-A1 EP-IV	2 LHYD	---	---
NRX-A1 EP-II	4 Cold Hyd	---	---
NRX-A1 EP-IV	3 Cold Hyd	---	---
NRX-A2 EP-1B	2 LHYD	---	---
NRX-A2 EP-IV	---	---	1
NRX-A2 EP-V	---	---	1
NRX-A3 EP-I	2 LHYD	---	---
NRX-A3 EP-III	2 LHYD	---	---
NRX-A3 EP-IIIA	1 LHYD	---	---
NRX-A3 EP-IV	---	---	1
NRX-A3 EP-V	---	---	1
NRX-A3 EP-VI	---	---	1
NRX/EST EP-1AP	4 LHYD	---	---
NRX/EST EP-1APP	1 LHYD	---	---
NRX/EST EP-1A4	5 LHYD	---	---
NRX/EST EP-IIB	---	---	2
NRX/EST EP-IIC	---	1	2
NRX/EST EP-III	---	1	2
NRX/EST EP-IV	---	1	1
NRX/EST EP-IVA	---	---	1
NRX-A5 EP-III	---	---	1
NRX-A5 EP-IV	---	---	1
TOTAL	28	3	15

2) NRX-A3, EP-VI Mapping Test

The major objectives of EP-VI were to map the intermediate power operating region both in the power and the fixed control drum position control modes. Two fixed control drum tests were performed. The first one consisted of a fixed drum startup from 1 MW to 35 MW using a 0 to 7.5 lb/sec liquid hydrogen flow ramp. A fixed drum mapping test was performed near the end of EP-VI. Starting from approximate steady state conditions of 19 lb/sec and 50 MW, flow was ramped to 47 lb/sec, held for 40 seconds and then ramped down to 20 lb/sec. The resulting power variation was from 50 MW, to 310 MW, and back to 100 MW.

3) NRX/EST

The following two fixed control drum position tests are described with greater detail in Reference 13.*

a) EP-IIC Run 1 Startup

This run consisted of a bootstrap to intermediate power with fixed control drums. A flow ramp from near 0 to 37 lb/sec resulted in a power increase from 1 to 250 MW.

b) EP-IV Low Dewar Pressure Bootstrap

The bootstrap to the first hold was performed in the fixed control drum position mode. A flow ramp from near 0 to 39 lb/sec resulted in a power increase from 1 to 240 MW.

4) NRX-A5, EP-IV Startup

The EP-IV fixed drum startup is discussed in detail in Section 3.4.1. A flow ramp to 70 lb/sec resulted in a power increase from 30 KW to 870 MW.

The power profiles for five of these runs are summarized on Figure 3-41. Three of these profiles represent fixed drum startups, and the remaining two represent mapping with fixed control drums between steady state conditions. During all runs the power

---

* See pages 3-15 and 3-42.

responded smoothly and predictably to changes in flow rate. The maximum power attained during fixed drum startups was increased significantly during the testing program from 40 MW for A3, to 250 MW for EST, and to 870 MW for A5.

3.5.1.2 Key Environmental Conditions

A summary of key environmental conditions of the NRX-A3, NRX/EST, and NRX-A5 tests is shown on Table 3-8. The summary consists of accumulated run time between specified nozzle chamber, core station 20, and core station 26 temperature intervals, equivalent full power radiation times, maximum power and flow rates, maximum ramp rates, and maximum beryllium temperatures before startup. Tables 3-9, 3-10, and 3-11 present times above chamber temperature, and core station 20 and core station 26 temperatures in greater detail for the NRX/EST and NRX-A5 tests. In Table 3-9, the arithmetic average of the four chamber temperature measurements was used for NRX-A5 and the on line computed electric average was used for NRX/EST. The times given in Table 3-9 have not been corrected for the effect of labline drift on chamber temperature. The effect of labline drift is a decrease in the measured chamber temperature. Correction for labline drift would increase NRX/EST chamber temperature a maximum of 11°R, and NRX-A5 chamber temperature by a maximum of 16°R.

CONFIDENTIAL

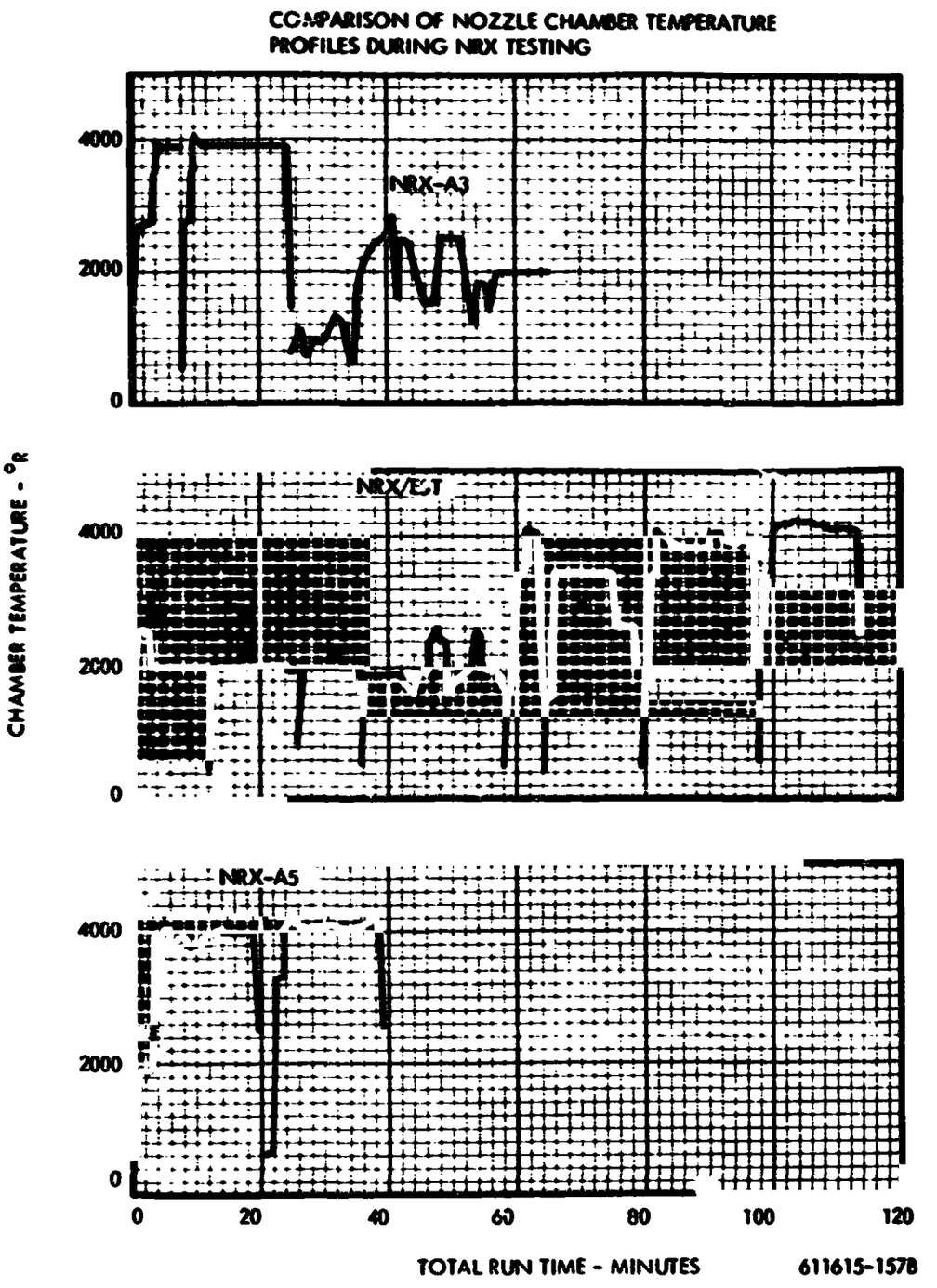

Figure 3-40. Comparison of Nozzle Chamber Profiles During NRX Testing

CONFIDENTIAL

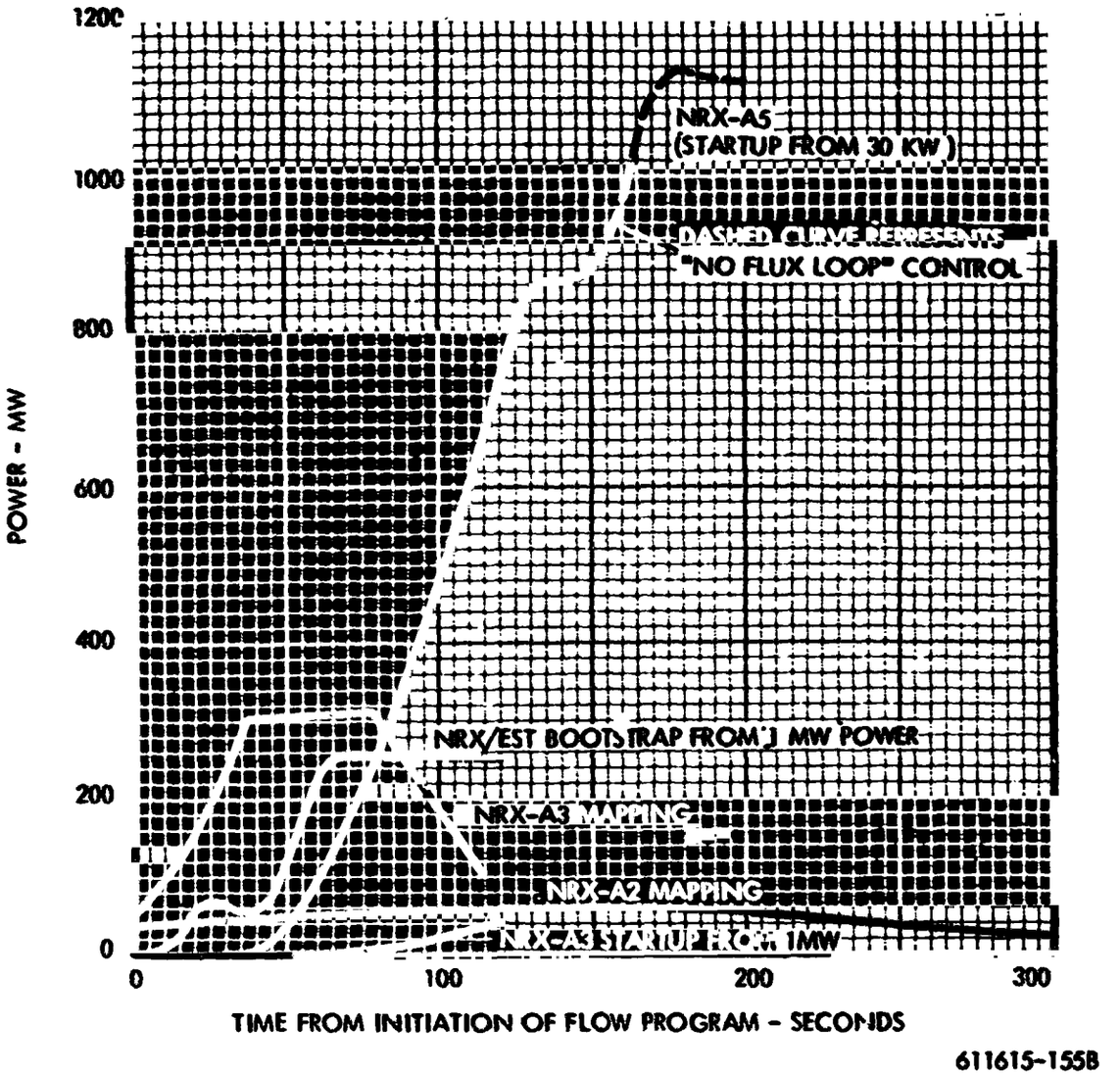

Figure 3-41. Summary of Power Profiles During Fixed Control Drum Testing

TABLE 3-8

NRX KEY ENVIRONMENTAL CONDITIONS

Time Within Temperature Interval (Minutes)	NRX-A3	NRX/EST			NRX-A5		
		Nozzle Chamber	Station 26	Station 20	Nozzle Chamber	Station 26	Station 20
1900-2000°R		29.3	1.3	1.5	1.5	0.1	0.2
2000-2500°R		15.5	9.7	4.9	0.7	0.7	0.9
2500-2900°R		7.7	2.1	13.7	0.7	0.6	1.5
2900-3200°R		0.6	10.6	14.0	0.5	0.7	11.9
3200-3400°R		7.0	2.4	12.8	0.6	0.6	18.5
3400-3600°R		6.0	8.6	-	0.4	1.7	-
3600-3700°R		0.2	7.1	-	0.7	4.4	-
3700-3800°R		3.6	0.7	-	0.7	18.2	-
3800-3900°R		6.1	12.8	-	3.0	6.4	-
3900-4000°R		5.3	-	-	11.3	-	-
4000-4100°R		7.3	-	-	12.8	-	-
4100-4200°R		7.8	-	-	2.3	-	-
Equivalent Full Power Radiation (Min.)	26.8		54.4			30.0	
Maximum Flow Rate (lb/sec)	73.5		87.9			71.9	
Maximum Power (MW)	1100		1155			1120	
No. of Startups and Shutdowns	3		11			2	
Maximum Startup Ramp (°R/sec)	80		+140			+70	
Maximum Shutdown Ramp (°R/sec)	-130		-141			-80	
Maximum Beryllium Temperature Before Startup (°R)	589		645			575	

TABLE 3-9

DETAILED TIMES ABOVE CHAMBER TEMPERATURE FOR NRX/EST AND NRX-A5

	NRX/EST						NRX-A5		
Chamber Temperature	IIB	IIC	III	IV	IVA	Total	III	IV	Total
4100			.2		7.6	7.8		2.3	2.3
4050			.6	.1	13.2	13.9	.5	14.2	14.7
4000			.7	.8	13.6	15.1	.6	14.5	15.1
3950			1.6	3.3	13.6	18.5	9.3	14.5	23.8
3900			1.3	5.5	13.7	20.6	11.9	14.6	26.5
3800			1.4	11.5	13.7	26.6	14.8	14.6	29.4
3700			1.4	15.1	13.7	30.2	15.4	14.7	30.1
3600			1.6	15.1	13.7	30.4	16.1	14.8	30.9
3500			3.6	15.2	13.8	32.6	16.3	14.8	31.1
3400			7.4	15.2	13.8	36.4	16.3	14.9	31.2
3300			12.8	15.8	14.2	42.8	16.4	14.9	31.3
3200			13.4	15.8	14.2	43.4	16.4	15.3	31.7
3100			13.5	15.9	14.2	43.6	16.5	15.4	31.9
3000			13.6	15.9	14.3	43.8	16.6	15.5	32.1
2900			13.7	16.0	14.3	44.0	16.7	15.6	32.3
2800			13.9	16.0	14.3	44.2	16.7	15.7	32.4
2700			14 0	16.1	14.6	44.7	16.8	15.8	32.6
2600		.3	16.3	16.4	14.7	47.7	16.9	15.9	32.8
2500	1.4	1.1	17.8	16.5	14.7	51.5	17.0	16.0	33.0
2400	2.1	1.6	18.4	16.5	14.7	53.3	17.0	16.1	33.1
2300	2.1	3.1	18.5	16.6	14.8	55.1	17.1	16.2	33.3
2200	2.1	3.3	18.6	16.6	14.8	55.4	17.1	16.3	33.4
2100	8.3	3.5	18.7	16.7	14.8	62.0	17.2	16.3	33.5
2000	11.9	4.5	18.8	16.7	15.0	66.9	17.2	16.4	33.6
1900	22.4	22.2	18.9	17.5	15.3	96.3	18.7	16.5	35.2
1800	24.5	27.2	18.9	17.7	15.3	103.6	19.3	16.5	35.8
1700	24.8	28.7	19.0	17.7	15.4	105.6	19.5	16.6	36.1
1600	24.9	47.2	19.3	17.8	15.4	124.6	19.8	16.7	36.5
1500	25.0	64.8	20.6	17.9	15.5	143.8	19.9	16.7	36.6

TABLE 3-10

DETAILED TIMES ABOVE CORE STATION 20 TEMPERATURE FOR NRX/EST AND NRX-A5

Chamber Temperature	NRX/EST				NRX-A5		
	III	IV	IVA	Total	III	IV	Total
3350						6.2	6.2
3300						12.7	12.7
3250			9.6	9.6		14.4	14.4
3200			12.8	12.8	4.0	14.5	18.5
3150			13.0	13.0	6.6	14.6	21.2
3100		0.1	13.6	13.7	9.2	14.6	23.8
3050		2.9	13.6	16.5	12.8	14.7	27.5
3000		4.7	13.7	18.4	14.5	14.7	29.2
2950	0.6	7.0	13.7	21.3	15.3	14.7	30.0
2900	1.2	11.9	13.7	26.8	15.6	14.7	30.3
2850	1.4	13.8	13.7	28.9	15.7	14.8	30.5
2800	1.4	14.1	13.7	29.2	16.0	14.8	30.8
2700	2.5	14.4	13.8	30.7	16.3	14.9	31.2
2600	4.6	15.0	13.8	33.4	16.4	15.1	31.5
25[illegible]	10.8	15.5	14.2	40.5	16.4	15.4	31.8
2400	12.4	15.6	14.2	42.2	16.5	15.5	32.0
2300	13.6	15.7	14.3	43.6	16.6	15.6	32.2
2200	13.8	15.8	14.3	43.9	16.7	15.7	32.4
2100	13.9	15.9	14.3	44.1	16.7	15.8	32.5
2000	15.2	15.9	14.4	45.5	16.8	15.9	32.7
1900	15.8	16.3	14.7	46.8	16.9	16.0	32.9

TABLE 3-11

DETAILED TIMES ABOVE CORE STATION 26 TEMPERATURE FOR NRX/EST AND NRX-A5

Chamber Temperature, °R	NRX/EST						NRX-A5		
	IIB	IIC	III	IV	IVA	Total	III	IV	Total
3800					12.9	12.9		6.4	6.4
3750					13.1	13.1	6.4	14.4	20.8
3700					13.5	13.5	10.1	14.5	24.6
3650				2.2	13.6	15.8	13.0	14.5	27.5
3600			0.9	6.1	13.6	20.6	14.3	14.6	28.9
3550			1.3	7.9	13.7	22.9	15.2	14.6	29.8
3500			1.3	12.0	13.7	27.0	15.6	14.7	30.3
3400			1.4	14.1	13.7	29.2	15.9	14.7	30.6
3300			1.5	14.4	13.8	29.7	16.3	14.8	31.1
3200			2.8	15.0	13.8	31.6	16.3	14.9	31.2
3100			5.0	15.1	13.8	33.9	16.4	14.9	31.3
3000			10.9	15.6	14.2	40.7	16.4	15.3	31.7
2900			12.3	15.7	14.2	42.2	16.5	15.4	31.9
2800			13.6	15.7	14.3	43.6	16.6	15.5	32.1
2700			13.7	15.8	14.3	43.8	16.6	15.6	32.2
2600			13.8	15.9	14.3	44.0	16.7	15.7	32.4
2500			14.0	15.9	14.4	44.3	16.8	15.8	32.6
2400			15.4	16.0	14.4	45.8	16.9	15.9	32.8
2300			16.9	16.3	14.7	47.9	16.9	15.9	32.8
2200			17.2	16.4	14.7	48.3	17.0	16.0	33.0
2100	1.4	1.8	18.4	16.4	14.7	52.7	17.0	16.1	33.1
2000	2.0	2.3	18.5	16.5	14.8	54.1	17.1	16.2	33.3
1900	2.1	3.3	18.6	16.5	14.8	55.3	17.1	16.3	33.4

CONFIDENTIAL

CONFIDENTIAL

Astronuclear Laboratory

3.5.2 Reflector Heating in NRX/EST and NRX-A5

Temperature asymmetries were observed in all plenu of the NRX/EST reactor with maximum temperature in the sector adjacent to the privy roof mounted shield (PRMS). An increase in temperatures in this sector was expected because of the additional heating from the PRMS* but the magnitude of the observed asymmetries was greater than predicted. Thermal data from all reactors were analyzed in an attempt to isolate the effect of the PRMS on the power generation in the peripheral components, i.e., all reactor components affected by the coolant between the reflector inlet plenum and the core inlet plenum (reflector system, pressure vessel, simulated shield, and core support plate).

Two approaches were used to determine the magnitude of the heating of peripheral components in the PRMS sector. The first approach used average temperatures in the reflector inlet and core inlet plena to calculate the power ratios for all reactors, i.e., the power generated in the peripheral components as a percentage of total reactor power. Ratioing the power ratio of NRX/EST to that of NRX-A5 gave the heating attributable to a 360 degree PRMS on NRX/EST. Adjustment for the actual shield sector of 135 degrees gave the heating attributable to the PRMS. Only NRX-A5 data was used for comparison with NRX/EST data because these two reactors had bare bead thermocouples in the core inlet plenum rather than the grounded junction thermocouples of A2 and A3 which required a substantial correction for gamma heating. The power ratios calculated for NRX-A5 and NRX/EST were corrected for the build-up of decay gammas to an equivalent of 15 minutes at full power and are shown in Figure 3-42 as a function of time after the start of each full power hold. The averages of these power ratios are 2.20 percent for NRX-A5 and 2.44 percent for NRX/EST. The average power ratios for NRX-A3 and NRX-A2, also shown in the figure, are 2.22 percent and 2.38 percent, respectively.

---

* See Reference 17, Index No. F.4.d.5.

One difference between the NRX-A5 and NRX/EST reactors which affected the reflector heating but which is not included in the above values or in Figure 3-42 was the 120 degree hot buffer periphery sector in NRX-A5. Predictions indicated that this sector would cause the total heat pickup in the reflector coolant to be reduced by about one percent.

This first approach does not take into consideration a possibly substantial bias between the power ratios of the two reactors. The second approach eliminated this bias by using only NRX/EST data. Azimuthal temperature distributions in the core inlet plenum were determined from 12 thermocouples located within a band from core radius 15.0 to radius 15.6 inches. Also the azimuthal temperature distributions in the reflector inlet plenum were determined from the four RTT's. These distributions are shown in Figure 3-43 for a time midway through EP-IV. The highest temperatures can be seen to have occurred within the region of the PRMS but are more nearly centered with the hot bleed port which may have contributed to the asymmetries.

Power was calculated from the temperatures in the sector 180 degrees away from the PRMS sector - normal power unaffected by the external shield. The average NRX/EST power was ratioed to this normal power and the result adjusted to a 135 degree shield as before. This approach eliminates the differences between reactors but has the disadvantages that it assumes that the flow is uniformly distributed and that no mixing occurs in the plena.

The first approach gave an increased heating in the PRMS sector of 29.3 percent $\pm$ 25.8 percent. Thus within the 95 percent confidence interval this value could be as high as 55.1 percent and as low as 3.5 percent. Inclusion of the one percent correction for the NRX-A5 hot buffer would reduce this value to 26.7 $\pm$ 25.8 percent. The second approach gave an increased heating in this sector of 15.3 percent $\pm$ 28.2 percent which means that within the 95 percent confidence interval this value could be as high as 43.5 percent and as low as minus 12.9 percent, i.e., the power could actually be lower in the PRMS sector than elsewhere.

The uncertainties in both approaches are of the same order of magnitude as the calculated PRMS effect. Therefore an accurate evaluation of the increased heating resulting from the PRMS cannot be deduced from the available temperature data. Analysis of critical experiment radiation environmental data has indicated a maximum increase in heating caused by the PRMS of only seven percent.

A best estimate of the heating in the peripheral components for a reactor unaffected by an external shield or by a hot buffer periphery can be obtained from NRX-A3 and corrected NRX-A5 data. With the NRX-A5 data adjusted by one percent to compensate for the effect of the hot buffer, the power ratios of A3 and A5 compare exactly, giving an average power generation of 2.22 ± 0.09 percent of total reactor power.

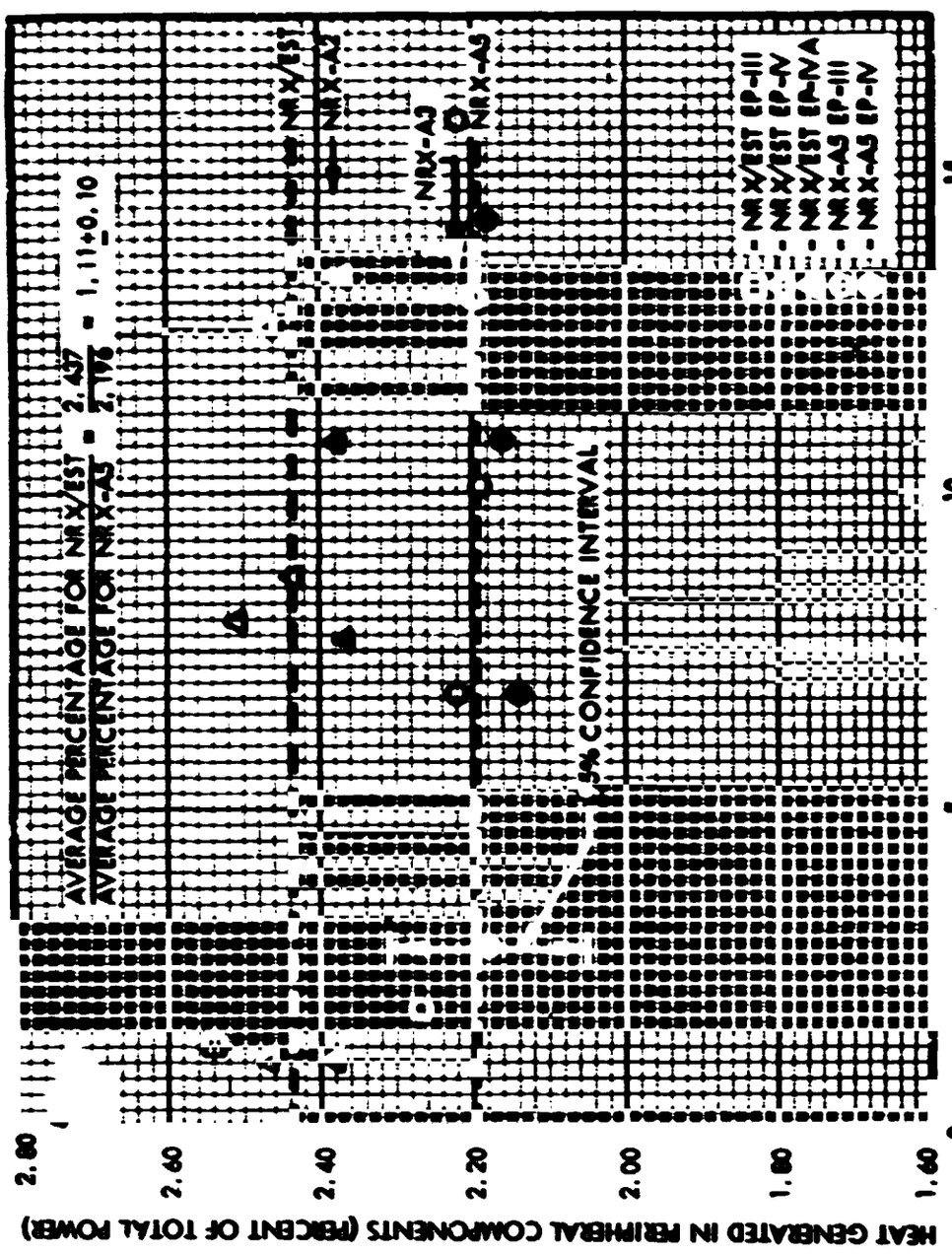

Figure 3-42. Percentage of Total Power Generated in Peripheral Components for All Reactors

Figure 3-43. Azimuthal Temperature Distributions in Core Inlet and Reflector Inlet Plenums: NRX/EST, EP-IV

3.5.3 Comparison of Core Station 26 with Chamber Temperature

A comparison was made between core station 26 temperature and nozzle chamber temperature for NRX-A5 and NRX/EST. The ratio of the two temperatures is shown in Figure 3-44 as a function of full power run times. The station 26 temperature input to this ratio was from the electrical averaging circuit which was the primary controller on NRX-A5 and the backup controller on NRX/EST. These circuits initially had 10 input thermocouples in each reactor but some were rejected as the tests progressed. The total number of thermocouples remaining at the end of each test was 9 on NRX-A5 and 8 on NRX/EST. The maximum deviation of the electrical average from the arithmetic average of the thermocouples was 20°R. The nozzle chamber temperature input to the ratio was the arithmetic average of the nozzle chamber thermocouples (4 in NRX-A5; 5 in NRX/EST). Both the chamber and station 26 average temperatures for each of the full power runs of NRX-A5 are shown in Figures 3-13 and 3-19. Average chamber temperature traces for NRX/EST are shown in Figures 3-31 and 3-36 of the NRX/EST Reactor Test Analysis Report (WANL-TNR-216).

The station 26 and chamber temperature traces show that station 26 temperature lagged chamber temperature during the first 2 or 3 minutes after the start of the power hold. The lag resulted in low ratios, Figure 3-44, for the same time interval. Thereafter, the ratios for longer run times were essentially constant and were generally within 1.4 percent of the average ratio. The 1.4 percent is the 95 percent confidence interval of the calculation based on the uncertainties of the average thermocouple measurements and the data system.

The average ratio of station 26 to chamber temperature was essentially the same for the two tests: 0.940 for NRX-A5 and 0.935 for NRX/EST. Data for the first 2.5 minutes of each run was not included in these averages. Also omitted in the calculation of the NRX/EST average were the last two points from EP-IVA. Corrosion had become extensive at that time and had introduced about 2 percent change in the ratio. The change is attributed to a change in the radial temperature shape which affects both station 26 and chamber temperature measurements. In contrast, near the end of NRX-A5 the temperature ratio decreased slightly but remained within the 1.4 percent uncertainty band.

The data in Figure 3-44 represent a range of operating conditions near the design point. The station 26 to chamber temperature ratio is expected to vary slightly as the operating conditions vary and a small correction would be required to adjust each point to a consistent set of conditions. However, the corrections were not applied to the data because the uncertainty on the correction was of the same order of magnitude as the correction itself and would have been well within the 1.4 percent uncertainty band.

In NRX-A5, the average ratio for EP-IV was 1.5 percent lower than the average ratio for EP-III (0.933 compared with 0.948). This difference appears to have been caused by a drift in the data acquisition system which has a 2σ uncertainty of about 1.8 percent.

The station 26 chamber temperature ratio was constant and independent of run time once station 26 temperature reached its steady state value. The test data indicated that approximately 2.5 minutes are required to achieve a steady state station 26 temperature. Although the station 26 temperature shows a thermal lag on startup, the lag effect could be accounted for in the scheduling of the demand station 26 profile. Therefore, either station 26 or chamber temperature can be used as the primary temperature control feedback.

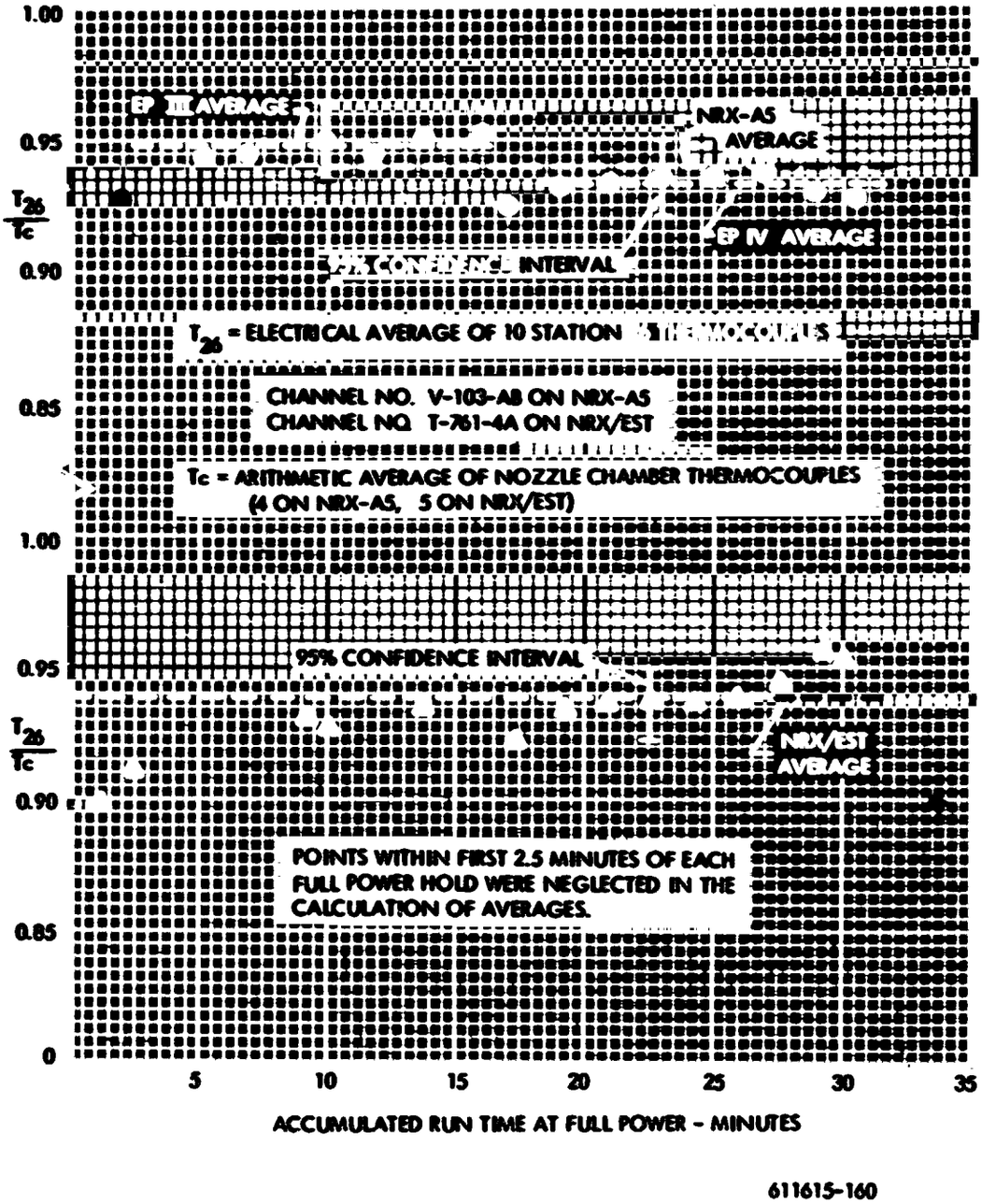

Figure 3-44. Ratio of Core Station 26 Temperature to Nozzle Chamber Temperature: NRX-A5 and NRX/EST

3.6 REFERENCES

1. NTO-R-0084, "NRX-A5 Site Test Report", 28 July, 1966.
2. WANL-TME-1389, "NRX-A5 Reactor Analysis Data", 15 April, 1966.
3. WANL-TNR-204, "NRX-A5 Test Specification", February, 1966.
4. WANL-TME-1108, "Modified Transient and/or Steady State (TOSS) Digital Heat Transfer Code", B. L. Pierce, February, 1965.
5. WANL-TME-1452, "Development of Drum Limit for NRX-A5 EP-IV Presentation to SNPO-C", 20 June, 1966.
6. NTO-R-0080, "NRX-A5, EP-IV Test Report, Second Power Test", 28 June, 1966.
7. RN-S-0317, "Data Analysis Report of NRX-A5 Tests".
8. WANL-TME-1478, "Para-Hydrogen Codes", B. L. Pierce, 15 August, 1966.
9. Letter from AGC to WANL, 7472:3041: EJF:vl, 4 March, 1966.
10. WANL-TME-1445, "Error Band Limits for WANL Measurements on NRX-A5", 23 June, 1966.
11. RN-TM-0353, REON Technical Memorandum, "Predicted Measurement Uncertainties, NRX-A5", 10 June, 1966.
12. WANL-TME-1210, "NRX/EST Reactor Analysis Data", 30 August, 1965.
13. WANL-TNR-216, "NRX/EST Reactor Test Analysis Report", December, 1966.
14. WANL-TME-773, "Review of NRX-A1 Thermal and Fluid Flow Performance and its Effect on NRX-A?", June, 1964.
15. WANL-TNR-199, "Analysis of NRX-A2 Reactor Test Results", April, 1965.
16. WANL-TNR-202, "NRX-A3 Reactor Final Test Report, December, 1965.
17. WANL-TME-1210, "NRX-A4/EST Reactor Analysis Data", 15 August, 1965.
18. WANL-TME-1388, "NRX-A5 Test Prediction Report", May, 1966.

CHAPTER 4

REFLECTOR SYSTEM, SHIELD, FILLER STRIPS, AND SUPPORT PLATE ANALYSIS*

4.1 SUMMARY

This section presents the results of the thermal and fluid flow analysis of the NRX-A5 reflector system, shield and the hot buffer region filler strips during the EP-III and EP-IV power tests. Measured and post test calculated state points are compared.

The average measured reflector pressure drop during the EP-III full power hold was 34 psi (2σ variance $\pm$ 2.2 psi) as compared to the calculated value of 35 psi, and during the EP-IV full power hold it was 31 psi (2σ variance $\pm$ 3.6 psi) as compared to the calculated value of 34 psi. The average reflector system pressure drop during the full power holds was 41 psi in NRX-A2, 41 psi in NRX-A3 and 43 psi in NRX/EST. The reduction in the reflector pressure drop in NRX-A5 is mainly due to the redesign of the reflector cooling channels, namely the addition of a longitudinal slot in the control drum cylinder and the enlargement of the cooling hole size in the inner reflector barrel.

The performance of the lateral support seal system in NRX-A5 was similar to NRX/EST. At the start of the first full power endurance test the seal chamber coolant axial pressure distribution was the same as predicted, but as the test continued the pressure at the core midband region decreased with test duration. The degradation of the seal chamber pressure is caused by core periphery corrosion which perturbs the coolant flow in the seal chambers.

The average power pickup from the reflector inlet plenum to core inlet plenum during NRX-A5 was about 2.2 percent of the total reactor thermal power. This is comparable to that of NRX-A3, but in NRX/EST the corresponding power pickup was about 2.4 percent which is about 10 percent higher than in NRX-A3 and NRX-A5. The higher power pickup in NRX/EST could be due to the presence of the external 135 degree privy shield for the

---

*Major contributors to this chapter were J. C. Guzek, L. Hamlin, A. Y. Lee, R. D. Taylor, M. D. Woods

NRX/EST test. The shield caused an increase in the radiation heating in the pressure vessel and the reflector system.

The measured sector and drum material temperatures at NRX-A5 full power conditions compared very well with post test calculations. Continuous temperature increases of the beryllium and the graphite materials during the full power holds were also observed in NRX-A5 as in NRX-A2, NRX-A3 and NRX/EST. The average rates of temperature rise at station 32 for these reactors are approximately as follows: for beryllium 1.2°R/min; and for the graphite barrel 7.2°R/min at R = 19.2 in., and 18.5°R/min at R = 18.2 in.

The measured maximum temperature differences across the diameter of the control drum at core stations 8 and 32 are less than 15°R during the EP-III and EP-IV startups. This temperature difference is very small as compared to the maximum value of 220°R observed in the NRX-A1 cold flow test, 120°R in NRX-A3, and 80°R in NRX/EST. This significant reduction in temperature difference is due to the cooling channel (a slot of 110 degree arc length and 0.10 in. depth) incorporated in the control drum cylinder. The coolant flow in the slot tends to equalize the chilldown effect on both sides of the cylinder, so that the resultant thermal bow is reduced. Control drum rubbing did not occur during the NRX-A5 startups.

Transient thermal analysis of the hot buffer filler strips was performed in some detail because 39 of the 54 strips in the hot buffer region were found to be broken in one or more places during the post test disassembly of the NRX-A5 reactor. All the strips in the nominal region remained intact, however. It was hypothesized that bridging of the hot buffer fillers occurred during reactor shutdown. The temperature difference between filler strips in the bridged condition resulted in severe tensile stresses in some strips. This temperature difference is due to the different strip thicknesses. The analysis of the EP-IV shutdown transient was performed for a 30 degree sector of the hot buffer filler strips. The maximum calculated temperature difference during this transient between the sector average and the coldest strip was 600°R at station 38 inches.

Steady-state maximum temperatures in filler strips were measured using thermal capsule placements in five hot buffer filler strips and one nominal filler strip. The indicated thermal capsule temperatures in the hot buffer filler strips were generally in agreement with predicted values except at the hot end where the measured temperatures were lower than predicted, i.e., about 1000°R lower than the 4400°R value predicted at station 50 inches. Thermal capsule temperatures measured in the nominal filler strip were within the range of predicted values. NRX-A5 nominal filler strip temperature data are compared with previous reactor test data.

Aside from the hot buffer filler strips, the reflector and lateral support system performed satisfactory during NRX-A5 power tests. All reactors performed consistently from NRX-A3 through NRX-A5, and all predictions and post-test calculations generally agree favorably with observations. With the previously mentioned exception of the hot buffer filler strip region in NRX-A5, the models and the analytical procedures for the reflector system of the NRX reactors are satisfactory and can provide design evaluation and predictions with a high degree of accuracy. For the filler strip region a more detailed analytical model is required.

4.2 DESCRIPTION OF THE REFLECTOR SYSTEM

The NRX-A5 reflector system is generally similar to the reflectors of all previous reactors with the exception of some fairly significant design changes. The major design changes are as follows:

1) The aluminum barrel outside the graphite inner reflector was eliminated. The impedance ring in the reflector annulus channel is now located at the inlet end of the channel in such a way that the inlet impedance is constant. In the previous reactors, the impedance ring was located at the exit end of the channel and the flow impedance depended on the annulus gap size which changed with reactor operating condition.
2) The inner reflector barrel cooling hole diameter was increased from 0.25 inches to 0.312 inches.
3) A longitudinal slot was added to the control drum cylinder opposite the control vane annulus to minimize the thermal bow of the drum cylinder during transient startup flow ramps.
4) There was a hot buffer filler strip zone of two sectors in the reactor for experiment purposes.

Details of the design changes are described in the NRX-A5 Data Book, WANL-TME-1389.

The reflector coolant flow paths and the major reflector components are shown in Figure 4-1. The state points at which the coolant temperature and pressures were measured and/or calculated are designated by location points from 1 to 13.

The following sections present the steady state reflector thermal and hydraulic conditions during the EP-III and EP-IV full power holds and the comparison of the predictions with the post test calculations. The beryllium sector and the graphite barrel material temperature rise and the lateral support seal chamber coolant pressure degradation during the full power hold is discussed. The temperature response of the redesigned control drum is also presented.

Since there were no measurements in the reflector located at the hot buffer region, the test analyses presented herein are confined to the region of the reflector system which is located at the nominal peripheral region. Pre-test design analyses were performed, however, for the two reflector regions. Results from analyses show that the thermal and hydraulic conditions in the outer reflector are not affected appreciably by the presence of the hot buffer filler strip arrangement. However, the conditions in the seal chamber and graphite barrel are affected by the hot buffer filler strip arrangement. For example, at the hot buffer region the seal chamber coolant exit temperature is 500°R lower and the maximum graphite barrel temperature at station 50 inches is 40°R lower than the nominal peripheral region of the reflector. The details of the results of these analyses are presented in the NRX-A5 Data Book, WANL-TME-1389.

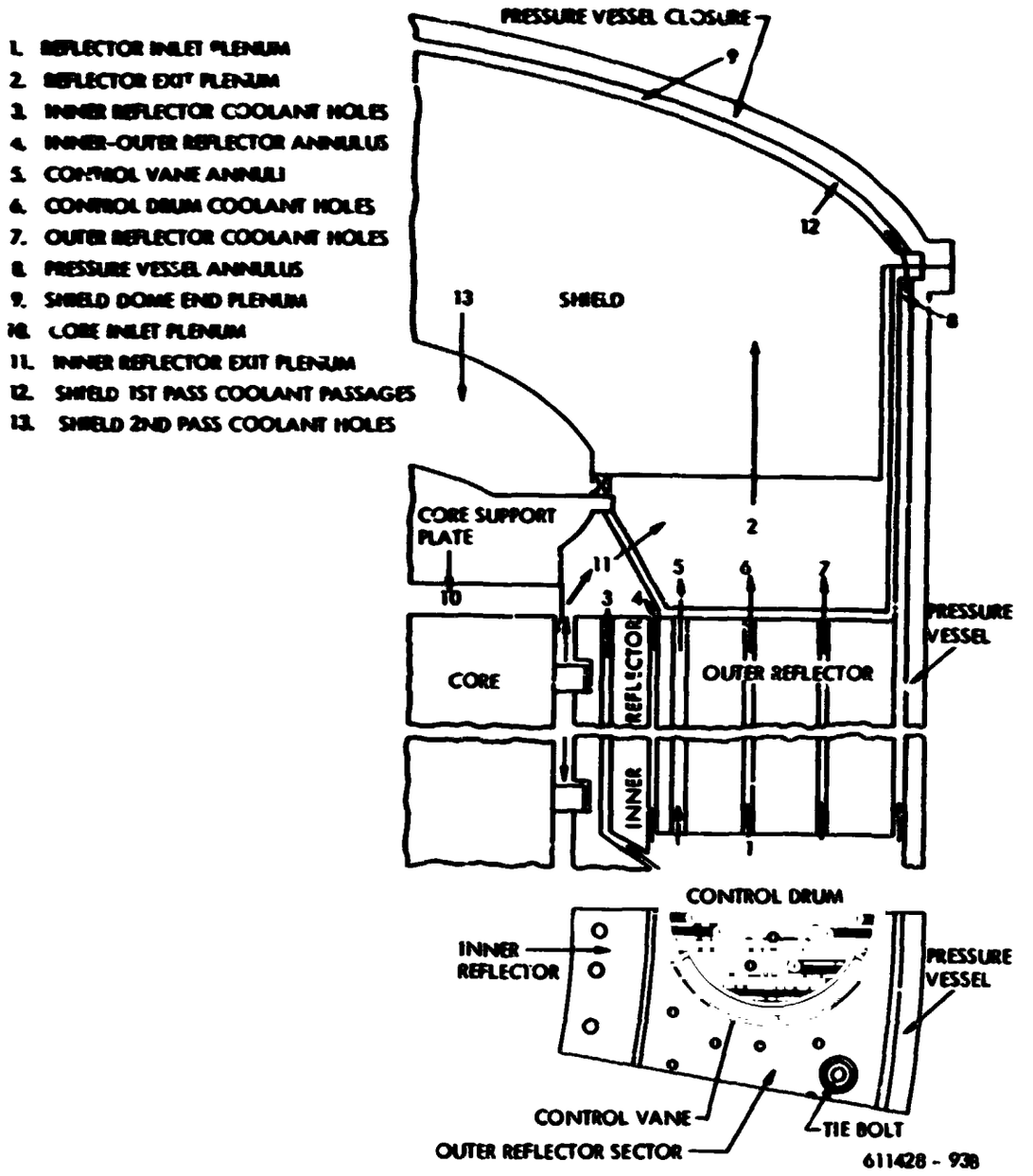

Figure 4-1. Reflector, Shield and Core Support Flow Schematic

4.3 STEADY STATE THERMAL AND HYDRAULIC CONDITIONS

4.3.1 Reflector System

Measured coolant temperatures and pressures at the various reflector locations described in Figure 4-1 are given in Table 4-1 for the EP-III and EP-IV full power holds. The predicted and post test calculated values are included for comparison. Calculations were performed by the MCAP-TOSS Computer Code.* Input boundary conditions are the measured flow rate, reflector inlet temperature and exit pressure.

The measured pressure drop across the outer reflector varies from 33 to 36 psi, and across the inner reflector from 31 to 32 psi during the EP-III full power hold, as compared to the calculated values of 35 and 33 psi respectively. The pressure drop across the core support cone is therefore, about 2 to 4 psi, as compared to the calculated value of 2 psi. During the EP-IV full power hold, however, the measured outer reflector pressure drop was about 1 psi lower than the inner reflector pressure drop. Since the pressure drop across the core support cone is very small, the amount of 1 to 2 psi is within the accuracy of the pressure measurements.

In NRX-A3 EP-V which had the comparable reactor flow rate of 71.3 lb/sec, the measured reflector system pressure drop was 42.5 $\pm$ 1.0 psi, as compared to the measured value of 34 psi in NRX-A5 EP-III. The decrease of about 8 psi is mainly due to the design changes in the reflector flow paths such as the addition of the slots in the control drums and the enlargement of the inner reflector barrel cooling holes for NRX-A5. Analysis shows that the difference in flow distributions between NRX-A3 and NRX-A5 is appreciable, but the coolant temperature rise and material temperatures do not differ appreciably. This decrease in pressure loss across the reflector reduces the pumping power requirement which gives a slight performance improvement.

---

* "A Program for Steady State Fluid Flow and Heat Conduction Coupled Calculations of Heat Generating Solids Cooled by Parallel Channels - Using the MCAP and TOSS Codes", WANL-TME-967, October, 1967.

The measured and the calculated coolant temperatures and pressures at the various reflector locations shown in Table 4.1 compare reasonably well. Similar fairly good agreement between measured and calculated temperatures and pressures was also obtained for the NRX-A3 and NRX/EST tests. This indicates that the analytical model and calculational procedures used to analyze the reflector system are satisfactory within the uncertainty limits of the internal heat generation rates and the impedance values used in the analysis.

The azimuthal temperature variation in the reflector inlet, dome end and core inlet plenums in NRX-A5, EP-III and EP-IV are presented in Figure 4.2. Within the 2σ variation of 6.6°R the reflector inlet plenum temperature did not show azimuthal assymmetry. However, the dome end and core inlet plenum temperatures were about 10°R lower in the hot buffer region than the respective average temperatures in the remainder of the plena. This indicates that the coolant temperature rise in the reflector in the hot buffer region is less than that in the remainder of the reflector system. Since there were no cooling channel exit gas and material temperature thermocouples in the hot buffer region, no azimuthal comparisons of these temperatures could be made. As mentioned previously the pretest analysis results show that in the hot buffer region the seal chamber coolant exit temperature is 500°R lower and the maximum graphite barrel radial average material temperature (at station 30 inches) is 40°R lower than that in the other region of the reflector. This could explain the lower dome end plenum and core inlet plenum temperatures in the hot buffer region.

Post test inspection of the NRX-A5 reactor* indicated that some of the filler strip ends in the hot buffer region were broken. It was theorized that at least some of the breakage occurred during the EP-III shutdown. In order to determine what effects this had on the reflector system pressure distribution, comparison was made in the pressure drop between the inner reflector dome end plenum and the core inlet plenum during the EP-III and EP-IV full power holds. Figure 4-3 shows the time history of the inner reflector dome end plenum and core inlet plenum pressures during the two full power holds. The pressure drop between these two

---

* "NRX-A5 Post-Operative Mechanical Evaluation", to be issued.

plena was the same for both full power holds. This indicates that the flow was not perturbed by the breakage of the filler strip in the hot buffer region.

The power pickup in the reflector and shield during the NRX-A5 power holds are also presented in Table 4-1. The average reflector and shield power was 23.3 MW, or 2.2 percent of the measured reactor thermal power. During the NRX-A3 full power hold the reflector and shield power was also about 2.2 percent. However, during the NRX/EST full power holds the average reflector and shield power pickup was about 2.4 percent. This indicates that the radiation heating deposited in the pressure vessel and reflector system in NRX/EST was about 10 percent higher than that in NRX-A3 and NRX-A5.

The increase in the heating in NRX/EST is due partially to the external shield which covered an angle of 135 degrees. A review of the azimuthal temperature distributions* in the NRX-EST reflector indicates that the measured material temperatures at the pressure vessel exterior wall and in the beryllium sector and the gas temperatures at the outer reflector exit plenum and the dome end plenum at the angular positions facing the external shield were higher than the corresponding temperatures away from the shield, although the differences were not sufficiently high to attribute all of the additional NRX/EST heating to this sector. The differences between the maximum measured temperature facing the shield and the average temperature away from the shield at the different locations are as follows: (1) for the pressure vessel external wall, at core station 32.8 inches, the maximum temperature difference was 25°R and at core station 45.2 inches, 37°R, (2) for the beryllium sector at core stations 8 and 32 inches, the temperature differences were 25°R, (3) for the outer reflector exit plenum the temperature difference was 30°R, and (4) for the dome end plenum the temperature difference was 20°R. A detailed discussion of the power pickup from reflector inlet to core inlet is presented in Section 3.5.2.

---

* WANL-TNR-216, "NRX/EST Reactor Test Analysis Report" and NRX/EST Calcomp Data.

4.3.2 Lateral Support System

The lateral support seal system for the NRX-A5 was slightly modified from previous reactors. The modification was in the seal segment and plunger arrangement. The details of this modification are described in the NRX-A5 Data Book. The purpose of this modification was to provide better seating for the seal segment against the inner reflector groove ledge and to assure free movement of the plungers in the plunger holes. The only measurements in the lateral support seal system were the seal chamber pressures at seals 7, 11, and 15 in the nominal core peripheral region. The comparison of the measured and predicted seal chamber axial pressure distribution in the nominal peripheral region is shown in Figure 4-4. The pressure distribution was normalized with the overall pressure drop from the lateral support inlet to outlet equal to unity. The pressure profile at the start of the EP-III full power hold agreed very well with the predicted profile. As the test progressed, a reduction in seal pressure was observed in the core midplane regions. Further reduction is noted during the EP-IV full power test. This is theorized to be caused by corrosion at the core periphery which resulted in radial inflow of the seal coolant to the core especially at the core midplane regions. The normalized pressure profile at the end of the NRX/EST EP-IVA test is included for comparison. The terminating drum angle in NRX/EST was 165 degrees as compared to 145 degrees for NRX-A5. The spread of the two profiles (at the end of NRX-A5 EP-IV versus at the end of NRX/EST EP-IVA) gives some indication of the relative extent of the seal chamber flow perturbation in the two reactors. The post operative examinations of the two reactors confirmed that the periphery of the NRX-A5 core was in better condition than the periphery of the NRX/EST core. These changes in the seal chamber pressure distribution are of no real concern from the standpoint of core instability. An order of magnitude of change would be required before there is any danger from this standpoint.

The variation of the seal chamber pressure with time for seals 7, 11, and 15 during EP-III and EP-IV is shown in Figure 4-5.

TABLE 4-1

NRX-A5 FULL POWER HOLD REFLECTOR HYDRAULIC CONDITIONS

EP	CONTROL ROOM TIME	LOCATION 1		W_T (1)	LOCATION 2		LOCATION 3	LOCATION 4	LOCATION 5	LOCATION 6	LOCATION 7	LOCATION 8		
		Temp. °R	P, Psia		Temp. °R	P. Psia	Temp. °R	Temp. °R	Temp. °R	Temp. °R	Temp. °R	Temp. °R	P. Psia	%, Lb/sec
	Predicted	145	745	71.3	242	712	273	264	273	202	253	200	744	10.9
III	Post Test Calc. at 26080	156	728	71.3	240	693	277	273	264	216	261	210	726	11.0
	25400	154	735	71.5		699	267	266		224	231			
	25700	150	716	70.9		683	259	278		216	227			
	25900	155	725	71.4		694	262	287		220	230			
	26080	156	726	71.3		693	262	288		218	232			
	26247.5	156	726	71.4		692	260	289		219	234			
IV	Post Test Calc at 13422.5	157	731	71.1	241	697	278	274	264	217	262	211	730	11.0
	12975	154	733	70.8		701	255	290		221	233			
	13182.5	154	731	71.1		699	257	291		216	229			
	13422.5	157	728	71.1		697	255	297		218	233			
	13602.5	158	724	71.0		697	256	301		221	233			
	13812.5	161	725	71.2		693	257	304		213	236			

EP	CONTROL ROOM TIME	LOCATION 9		LOCATION 10		Inner Refl. ΔP	Outer Refl. ΔP	SHIELD ΔP	I→III		I→10
		Temp. °R	P. Psia	Temp. °R	P. Psia	$P_1 - P_{11}$	$P_1 - P_2$	$P_2 - P_{10}$	Power MW	Preliminary Reactor Power	% Reactor Power
	Predicted	240	706	243	678	31	33	14	20.18	1120	2.35
III	Post Test Calc. at 26080	238	687	241	679	33	35	14	22.8	1090	2.17
	25400	221	694	242	690	32	36	9	24.4	1110	2.20
	25700	213	677	235	673	31	33	10	23.4	1050	2.22
	25900	218	688	239	684	32	34	10	23.4	1080	2.14
	26080	219	688	240	681	32	33	12	23.1	1050	2.19
	26247.5	219	687	241	680	31	34	7	23.7	1075	2.20
IV	Post Test Calc. at 13422.5	239	691	242	683	32	34	14	22.8	1100	2.07
	12975	218	694	238	689	33	32	12	23.12	1125	2.06
	13182.5	216	692	238	683	33	32	16	23.22	1105	2.10
	13422.5	217	690	239	683	33	31	14	22.42	1100	2.04
	13602.5	218	690	241	679	33	27	18	22.99	1090	2.11
	13812.5	222	686	243	676	34	32	17	22.83	1080	2.12

* Reactor Flow, W_T, lb/sec

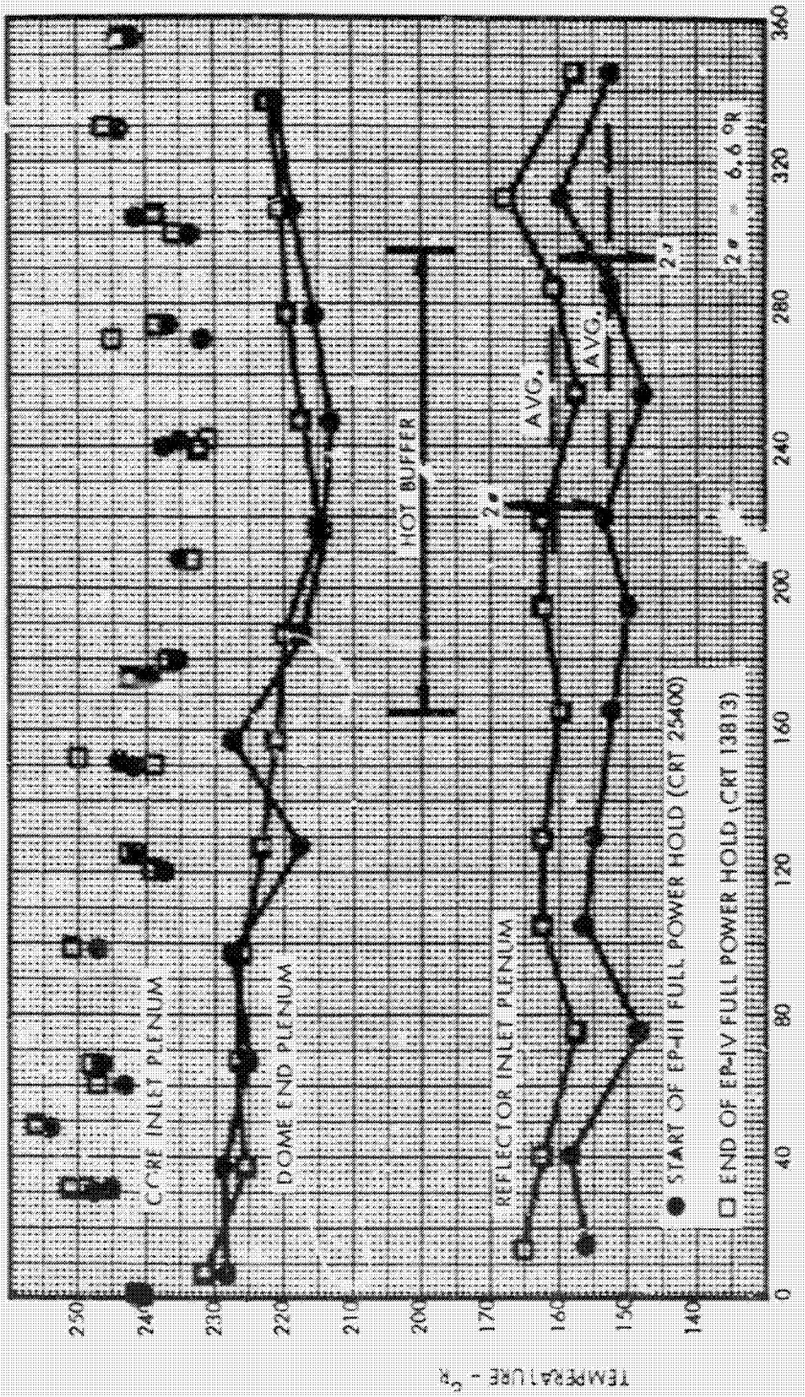

Figure 4-2. Azimuthal Reflector Inlet, Dome End and Core Inlet Plenum Temperatures, NRX-A5, EP-III, EP-IV

Figure 4-3. NRX-A5 Time History of the Inner Reflector Dome End Plenum and Core Inlet Plenum Pressures

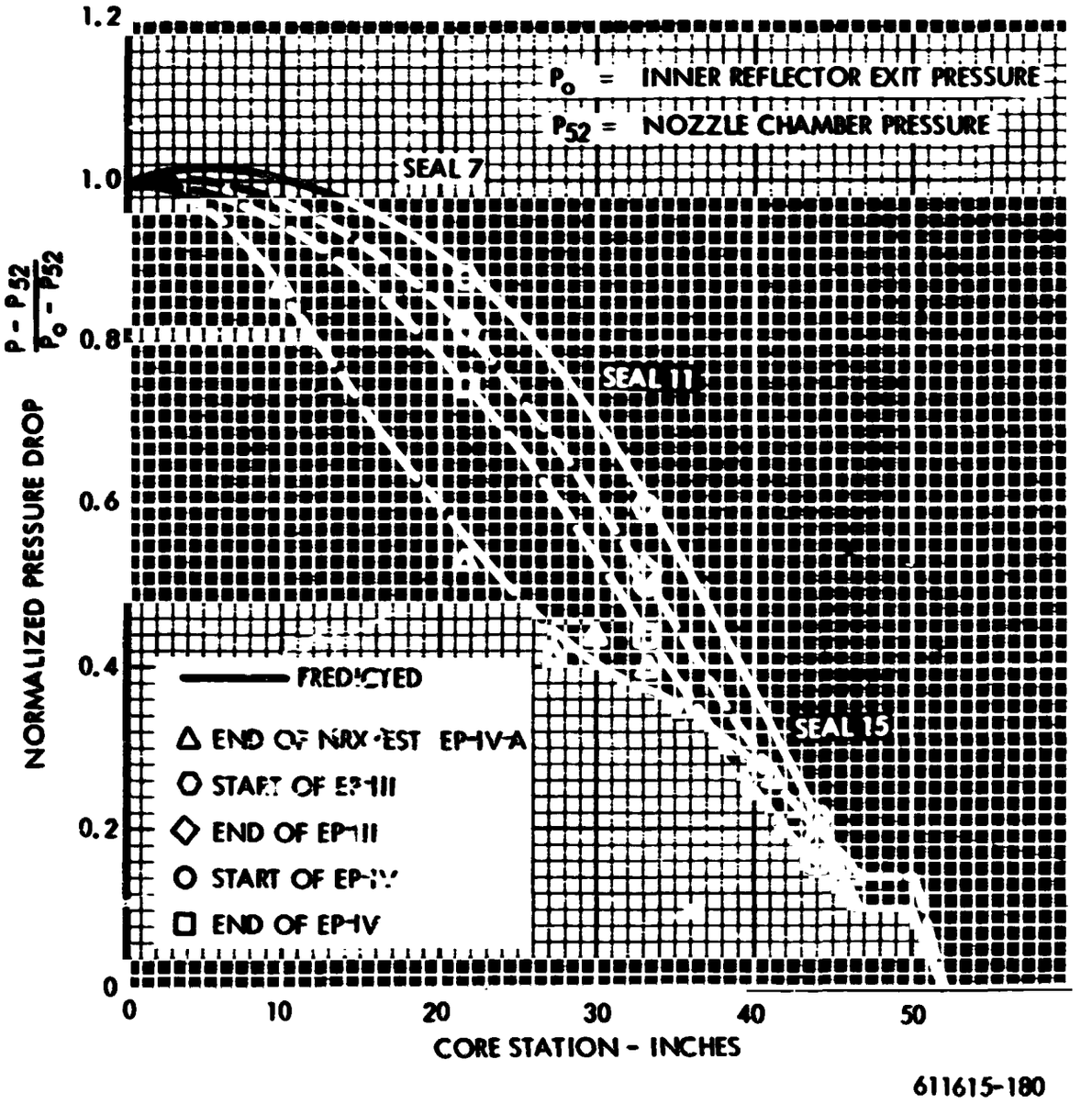

Figure 4-4. NRX-A5 Normalized Seal Chamber Pressure Profiles

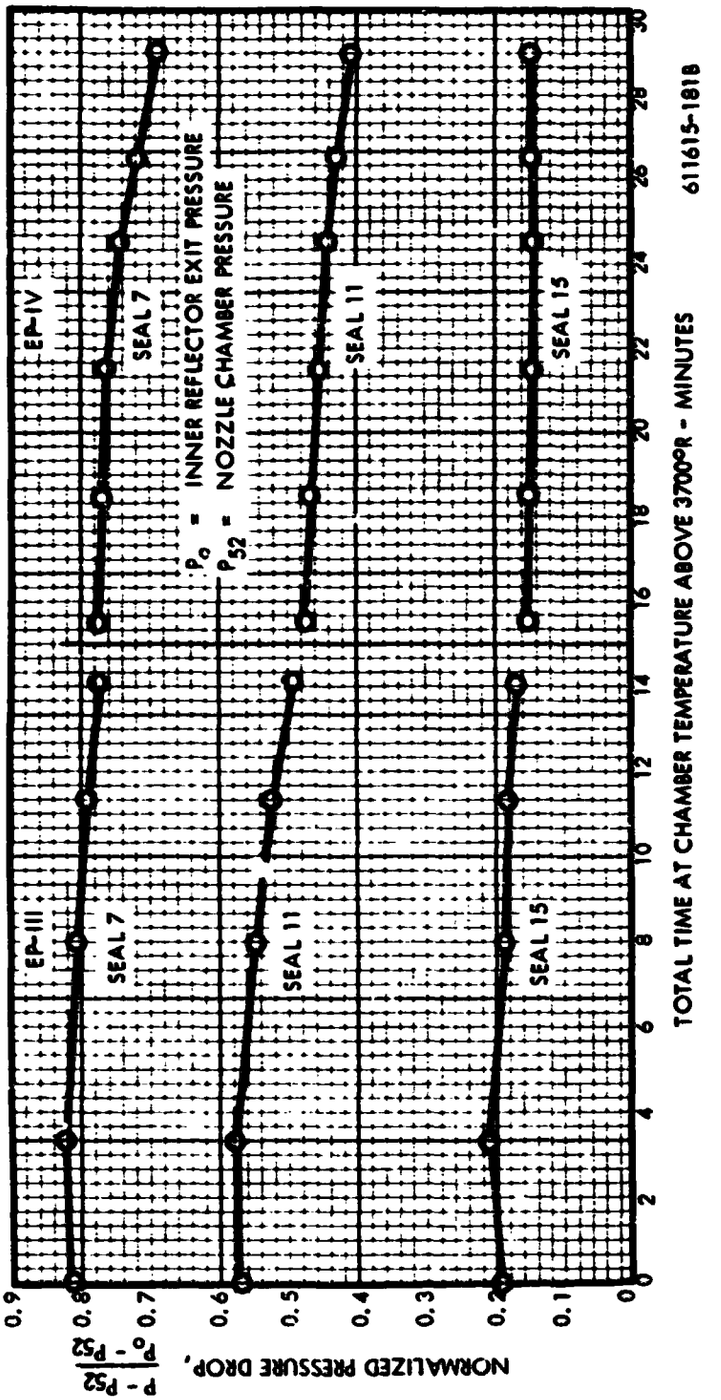

Figure 4-5. NRX-A5 Seal Chamber as a Function of Time

4.4 REFLECTOR AND LATERAL SUPPORT COMPONENT MATERIAL TEMPERATURE

Reflector and lateral support material temperatures are given in this section for full power and flow conditions at the start and end of the power holds of EP-III and EP-IV. Comparisons with previous reactor measurements are included. The performance improvement of the redesigned control drum in NRX-A5 will be discussed in detail.

4.4.1 Outer Reflector Sector Material Temperature

The outer reflector sector material temperatures recorded at the full power conditions of EP-III and EP-IV are shown as a function of axial station in Figure 4-6. The post test calculated temperatures are also shown for EP-III. The agreement between the measured and calculated values is satisfactory. Since there was only one thermocouple at each core station at which the temperature was measured, the range of uncertainty in the measured values cannot be determined. The maximum sector temperature in NRX-A5 EP-IV was about 365°R at station 20 inches. The calculated axial temperature profile also agrees well with the measured profile. Similarly good agreement was also observed in NRX/EST (at the angular position away from the external shield). The agreement in the axial temperature profiles in NRX-A2 and NRX-A3 was not as good as in NRX/EST and NRX-A5. The maximum difference between the measured and calculated temperatures was about 25°R for NRX-A3 and about 50°R for NRX-A2. The improvement is mainly due to improvements in the analytical model and the calculational method.

The temperature rise of the beryllium sector material as a function of time at full power is shown in Figure 4-7. The temperature variations at station 32 during NRX/EST EP-IVA and during NRX-A5 EP-V are also included. No appreciable temperature increase was observed in NRX-A2 mainly because of the short test. The temperature increase in NRX-A5 is comparable to that of NRX-A3 and is smaller than that during the NRX/EST EP-IVA full power hold. The higher temperature rise during the NRX/EST EP-IVA full power hold is attributed to the greater control drum roll-out than during NRX-A3 and NRX-A5.

4.4.2 Inner Reflector Graphite Barrel Material Temperatures

The temperature measurements obtained for the graphite barrel during NRX-A5 are presented in Figures 4-8 to 4-10. The axial temperature distributions at radial positions R = 18.2 inch and R = 19.2 inch during EP-III and EP-IV are shown in Figure 4-8. At the outer radial position, R = 19.2 inch, the calculated and the measured temperatures at the start of the EP-III full power hold agree within 80°R. Because of the considerable temperature rise in the graphite barrel material during a power hold, the comparison was made at the start of a power hold when the irradiation effect on the thermal conductivity of the graphite was minimal. At the inner radial position, R = 18.2 inch, the calculated temperature at station 32 inches is also within about 80°R of the measured value. The comparisons between the calculated and the measured temperatures are similar in NRX-A3 and NRX-EST. However, the agreement between the calculated and measured axial profiles in NRX-A5 is better than that in NRX-A3 and NRX/EST. Since the reflector annulus flow channel impedance in NRX-A5 (located at the inlet end) was constant and not dependent on the annulus gap clearance which changed with operating condition as for the previous reactors (impedance located at the exit end), the determination of flow distribution in the reflector system in NRX-A5 was more accurate.

The graphite barrel temperature variation during the NRX-A5 EP-III and EP-IV full power holds at station 20 in. and 32 in. is shown in Figure 4-9 for R = 19.2 in. and Figure 4-10 for R = 18.2 in. The temperature variations in NRX-A2, NRX-A3, and NRX/EST are included in the figure. A continuous graphite barrel temperature rise during a power hold has been observed in all reactor power tests. As explained in previous test analysis reports, the temperature increase during a power hold is primarily due to the decrease in thermal conductivity of the graphite as a result of the irradiation effect. However, this effect anneals out between power runs. This is shown on Figure 4-9 by the change in the graphite temperature between the end of the EP-III full power hold and the start of the EP-IV full power hold.

Comparisons of the rate of graphite barrel temperature increase during high power holds were made with previous test results. At the radial position R = 19.2 in., the rate of temperature increases are similar for NRX-A3 EP-V, and NRX-A5 EP-IV, but higher for NRX/EST EP-IVA. This is attributed to the greater drum roll-out during NRX/EST compared to NRX-A3 and NRX-A5. The NRX-A3 pretest calculated rate of temperature increase is about 7.6°R/min at station 32 in. for R = 19.2 in. The calculation considered a 7 percent reduction (linear with time in 15 minutes) in graphite thermal conductivity based on the total radiation dose received by the graphite in NRX-A2 during the 2 minutes at full power, then extrapolated to 15 minutes operation. This calculated rate of temperature increase agrees quite well with the NRX-A3 measured rate of temperature increase, but is higher than that measured in NRX-A5. In NRX-A2 the length of the full power hold was about 2 minutes and the measured temperature rise was about 25°R/min. This extremely high rate of temperature rise in NRX-A2 can be explained by (1) steady state conditions had not been attained in this short time and (2) the cooling efficiency was lower since 15 out of the 144 barrel cooling holes were plugged for instrumentation. In Figure 4-9 the temperature variations during the first minute of the power holds of NRX-A3, NRX/EST and NRX-A5 were omitted because during the first minute after the reactor reached full flow and full power, the material temperatures have not yet reached steady state conditions. Figure 4-9 shows a lower barrel temperature during NRX-A5 than during NRX-A3 and NRX/EST. The lower barrel temperatures during NRX-A5 are due to (1) an increase in the graphite barrel flow rate due to the enlargement of the diameter of the channels from 0.25 inches to 0.312 inches, and (2) an increase in the seal chamber coolant flow. Both of these reasons contribute to the lower temperatures as compared to the NRX-A3 and NRX/EST.

Figure 4-10 shows the temperature variations of the graphite barrel at the inner radial position, R = 18.2 in. The thermocouples in NRX-A2 and NRX-A3 were either erroneous or not operative; and therefore, only the NRX/EST and NRX-A5 data are presented. The rates of temperature rise for the various test runs are summarized in Table 4-2. The observed rate of temperature rise in the graphite barrel at R = 18.2 in. and station 32 is very low during NRX/EST, EP-IV. The measurements T-408.4A and T-409.4A appear to be questionable.

The data from the NRX-A2 through NRX-A5 power tests conclusively indicate that the temperature of the beryllium and graphite components increases continuously during steady state full power operation. The temperature rise is the result of the decrease in thermal conductivity of the material in an irradiation environment. Reliable analytical or experimental information on the effects of radiation damage to the thermal properties of these two NRX reactor materials are not yet available. Nevertheless, test data show that the increased material temperatures during high power operation did not affect the integrity and performance of these components.

4.4.3 Control Drum Assembly

The NRX-A5 control drum design is significantly different from all previous NRX reactors. The design was changed because the drum cylinder rubbed against the sector bore in the early stages of startup operation during previous reactor tests. The rubbing was caused by the bowing of the control drums due to transverse temperature differences across the drum. During the NRX-A1 cold flow tests, drum actuator torques above the design value were experienced during most of the transient flow ramps. In NRX-A2 the clearance between the drum cylinder and sector bore was increased from 0.045 in. to 0.078 in. (nominal dimensions), and the reflector was pre-cooled prior to start of run for the power tests. Consequently, no rubbing between the drum cylinder and the sector bore occurred. In NRX-A3, the reflector was not pre-cooled and high torques were again experienced during all power test startups with the exception of EP-V. In the NRX/EST reactor, the outer diameter of the aluminum housing cylinder of the drum assembly was reduced by machining off 0.024 in. at the mid-span of the assembly. Drum rubbing did not occur for any of the startups except during the second run of EP-III. The high torque during this startup was caused by an initial drum material temperature of 645°R which is considerably above the established limit of 540°R for this control drum design. This limit was established from analysis* and from previous reactor test experience which indicated that the amount of thermal bow of the drum cylinder

* "Transient Thermal Analysis of a Heat Generating Solid and Its Application to NERVA Reactor Control Drums", A. Y. Lee, M. D. Woods, and A. G. Eggers, AIAA paper No. 66-575, 1966.

depended on the flow ramp and the initial beryllium temperature. A flow ramp corresponding to a 150°R/sec startup would not cause rubbing of the NRX/EST drums provided that the initial temperature was below 540°R. The NRX-A5 control drum was modified with a 0.10 inch deep longitudinal slot of 110 degree arc length along the drum cylinder on the side opposite the control vane cooling annulus. The purpose of the slot was to provide symmetrical cooling on both sides of the cylinder to minimize the thermal bow. Transient thermal analyses were performed using the TRACK* computer code to determine the optimum slot size. The redesigned drum was then extensively tested in the laboratory using cold helium gas. The test results showed a maximum temperature difference across the drum at station 26 of about 95°R and a 0.014 inch bow in the drum cylinder with a 3.0 lb/sec^2 simulated reactor flow ramp (equivalent to approximately a 200°R/sec rate of chamber temperature startup). The nominal clearance between the drum cylinder and the sector bore is 0.078 in. This indicated that interference between the drum and the sector would not occur even during 200°R/second startups. In addition, the laboratory test results indicated that the thermal bow of the drum is insensitive to the startup flow ramp and initial material temperature. The test results were reported in WANL-TME-1408, "NRX-A5 Control Drum Bow Tests", March, 1966.

During the startups of the NRX-A5 EP-III and EP-IV power tests, the flow ramp was about 0.85 lb/sec^2 (corresponding to a nominal 50°R/sec chamber temperature ramp). The measured transient temperature differences across the drum at stations 8 and 32 for the EP-III startup are shown in Figure 4-11, and for the EP-IV startup in Figure 4-12. The maximum measured temperature difference at station 32 during the early stage of the chill-down was about 15°R in EP-IV. This temperature difference is much smaller than that during the NRX-A3 and NRX/EST tests. Table 4-3 shows the comparison of the flow ramps and maximum temperature differences during the NRX-A3, NRX/EST, and NRX-A5 startups. For comparable flow ramp rates, such as NRX/EST EP-IVA versus NRX-A5 EP-IV, the maximum temperature difference across the drum is reduced by a factor of 4 in NRX-A5. The results from the NRX-A5 power tests confirmed that the redesign reduced the drum bow and eliminated drum rubbing.

* Ibid.

The measured and calculated control drum temperature distributions at high power are shown in Figure 4-13. Considering the two sigma accuracy of 23°R for these thermocouples, the agreement between the measured and calculated temperature is very good.

4.4.4 Core Support Plate

Figure 4-14 shows core support plate material temperatures as a function of percent power divided by percent reactor flow rate for NRX-A5 EP-III and EP-IV. The predicted average material temperatures at full power conditions are also shown in the figure. The ratio of the core support plate material temperature to the core inlet temperature is as predicted and is similar to NRX/EST.

4.4.5 Shield and Reflector Tie Bolt Material Temperatures

In NRX-A5 the shield and the tie bolts were not instrumented with thermocouples. In the NRX-A3 and NRX/EST reactor tests, the agreement between the measured and predicted shield and tie bolt temperatures was very good. Using the beryllium sector cooling hole exit and dome end plena temperature measurements in NRX-A5, it can be concluded that the shield and tie rod performed as expected. The predicted shield and tie bolt material temperatures are shown in Table 4-4.

4.4.6 NRX-A6 Experimental Lateral Support Spring Temperature

One of the hydrogen conduction cooled lateral support springs to be used in NRX-A6* was installed in NRX-A5 as an experiment. The spring was located in the beryllium sector at station 26 in. Figure 4-15 shows the spring temperatures in NRX-A5, EP-IV at part power and full power conditions. The calculated temperature at full power is 830°R as compared to the measured value of 785°R at the start of EP-IV full power hold and 813°R at the end of the full power hold. The temperature rise of the spring is 28°R during

---

* "NRX-A6 Design Report, Vol. II, Thermal, Fluid Flow and Nuclear Analysis of the NRX-A6 Reactor", WANL-TME-1290, Oct. 1965.

the 15 minutes full power hold of EP-IV. This temperature increase is higher than the approximate 15°R increase of the beryllium sector at station 20 in. Although the reflector design of NRX-A6 is different from that in NRX-A5, the temperature rise of this magnitude would not affect the performance of the spring in NRX-A6.

Figure 4-6. NRX-A5 Axial Temperature Profile of Outer Reflector Sector at Full Power

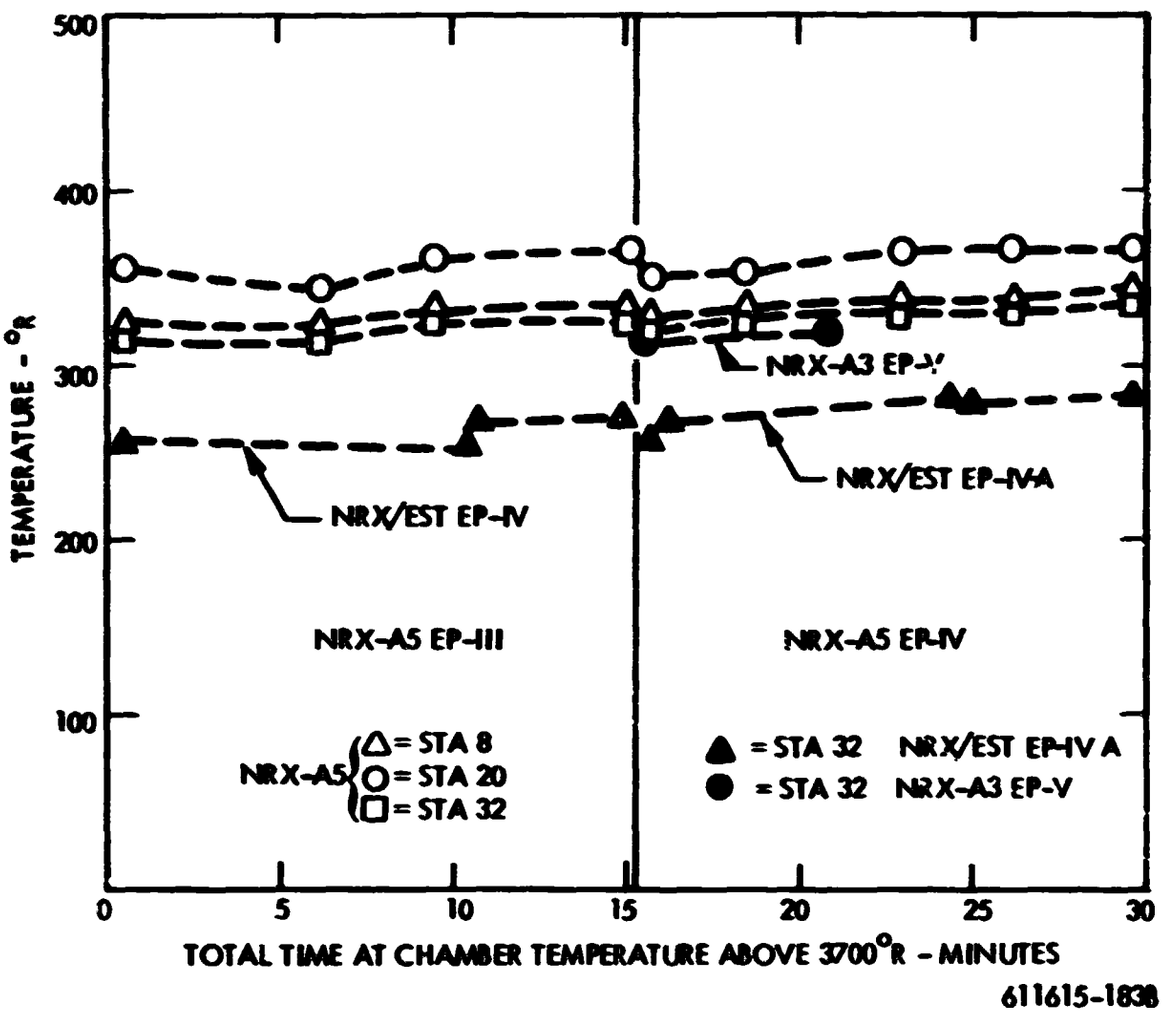

Figure 4-7. NRX-A5 Outer Reflector Sector Temperature Rise during Steady State Full Power Holds

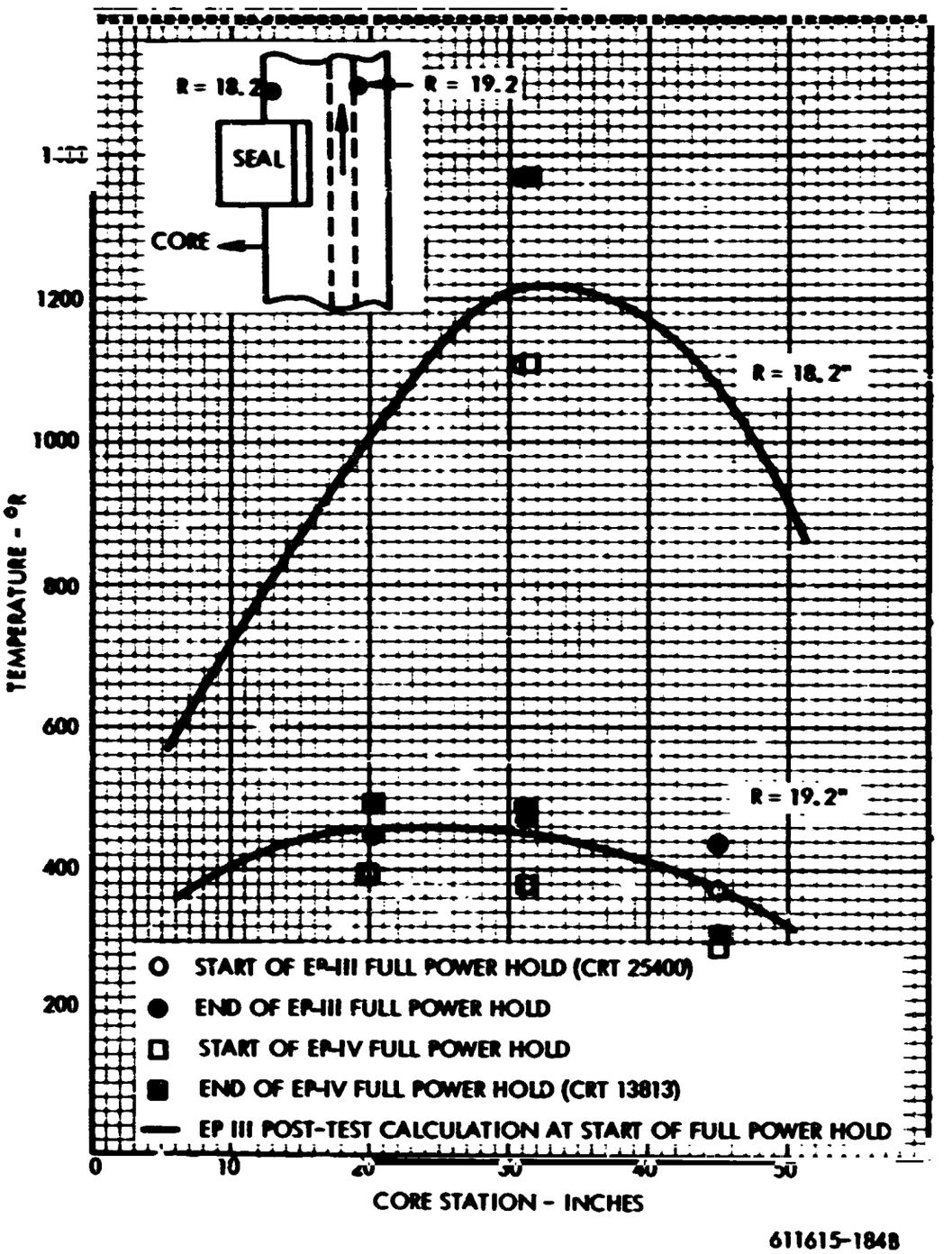

Figure 4-8. NRX-A5 Axial Temperature Profiles of Inner Reflector Graphite Barrel at Full Power

CONFIDENTIAL

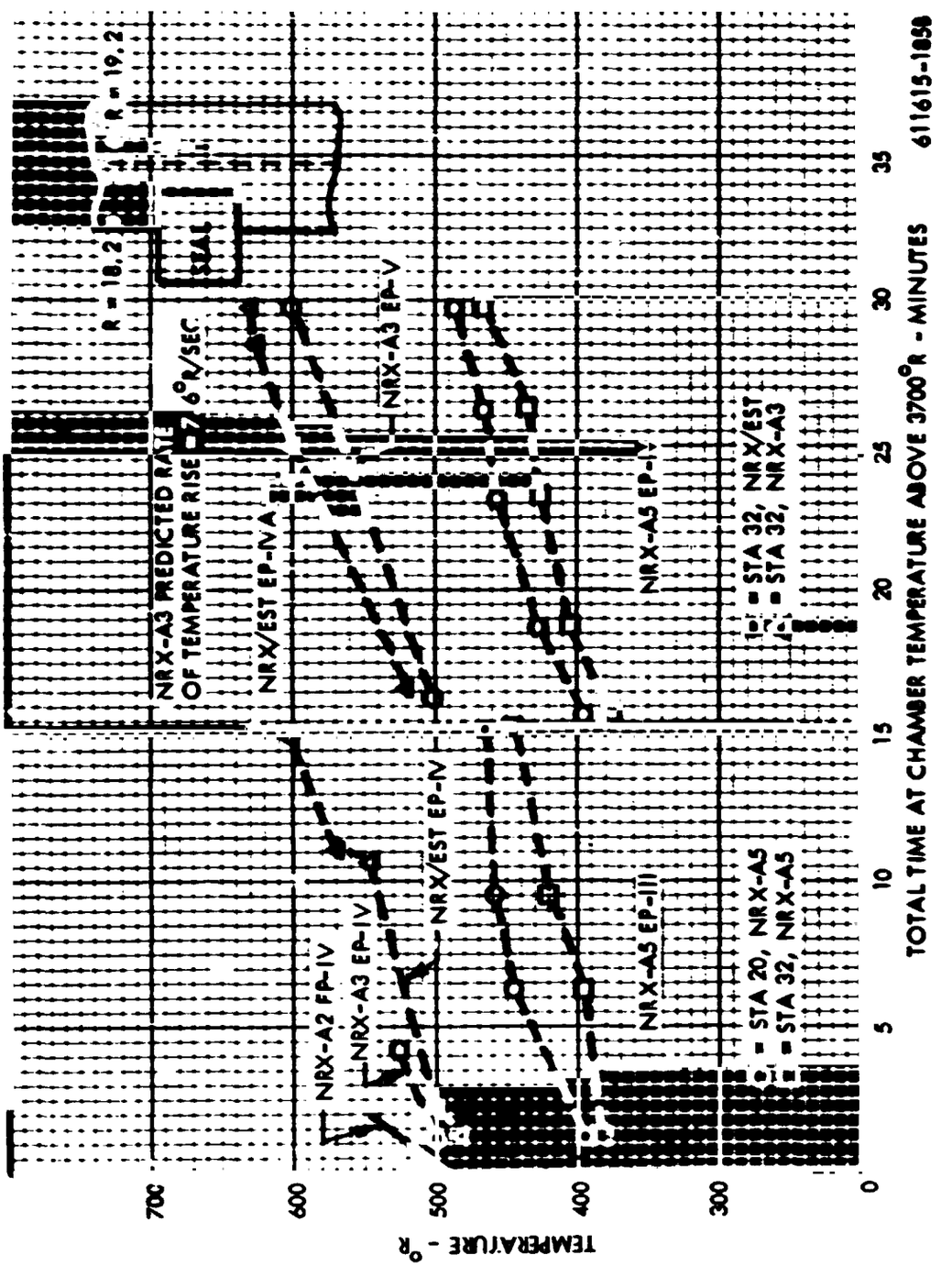

Figure 4-9. NRX-A5 Inner Reflector Graphite Barrel Temperature Rise during Full Power Holds at R = 19.2 Inches

CONFIDENTIAL

Figure 4-10. NRX-A5 Inner Reflector Graphite Barrel Temperature Rise during Full Power Holds at R = 18.2 Inches, STA = 32.5 Inches

TABLE 4-2

RATE OF TEMPERATURE INCREASE DURING FULL POWER HOLDS

Test Run	Rates*, °R/min Inner Reflector R = 19.2, C.S. 32	Inner Reflector R = 18.2, C.S. 32	Outer Reflector C.S. 32
NRX-A2 EP-IV	25.0***	---	---
NRX-A3 EP-IV	8.0	---	---
NRX-A3 EP-V	7.3	---	1.5
NRX-A3 Prediction	7.6	---	---
NRX/EST EP-IV	8.6	6.3**	0.9
NRX/EST EP-IVA	8.4	21.6	1.6
NRX-A5 EP-III	4.5	16.8	0.7
NRX-A5 EP-IV	6.4	17.0	1.1

* The rate is the arithmetic difference between the temperature at the end of the power hold and the temperature at the start of the power hold divided by the total run time.

** Measurements (T 408.4A, T 409.4A) are questionable.

*** NRX-A2 was not in temperature equilibrium since the total run time at full power was too short (110 seconds).

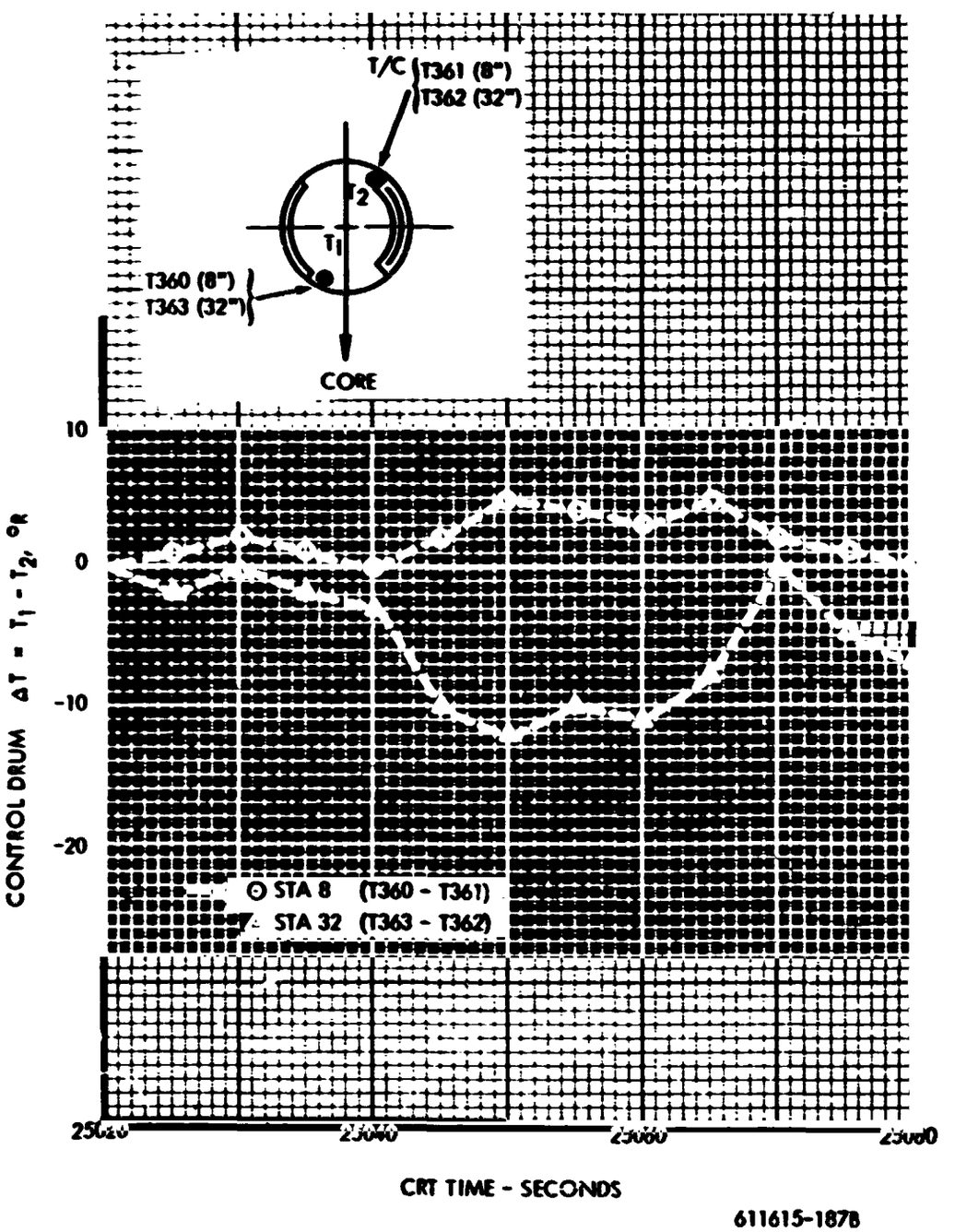

Figure 4-11. Control Drum Transient Temperature Difference during NRX-A5 EP-III Startup

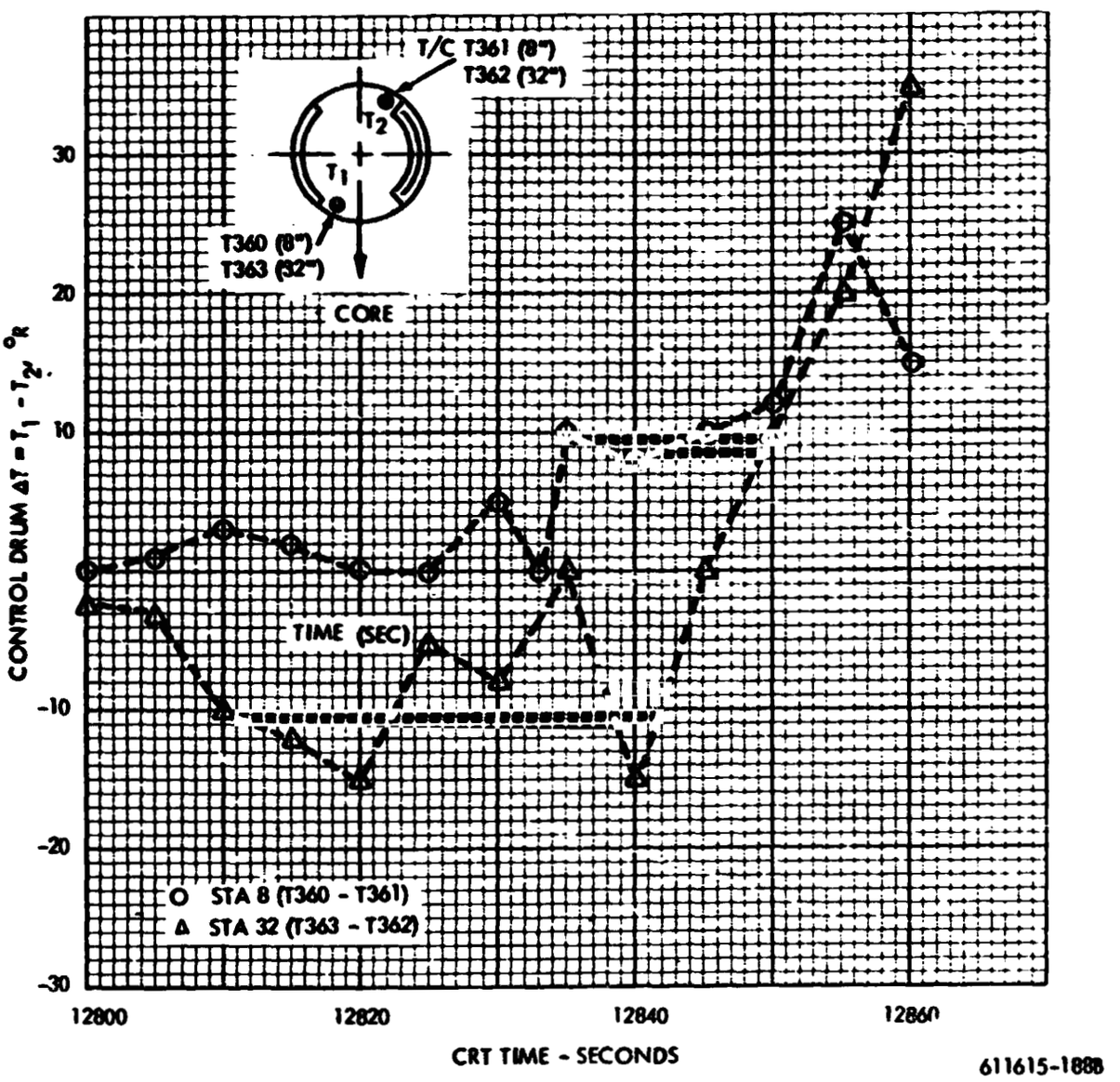

Figure 4-12. Control Drum Transient Temperature Difference during NRX-A5 EP-IV Startup

TABLE 4-3

COMPARISON OF NRX-A3, NRX/EST AND NRX-A5 CONTROL DRUM MATERIAL TEMPERATURE RESPONSES

Reactor Run	Approx. Ramp Rate, lb/sec^2	Initial Drum Material Temp. at CS32	Max. ΔT $^{\circ}R$	Rubbing Occurrence
NRX-A3 EP-I	1.38	518	100	yes
NRX-A3 EP-III	0.96	546	86	yes
NRX-A3 EP-IV	0.81	589	120	yes
NRX-A3 EP-IIIA	0.94	553	88	yes
NRX-A3 EP-V	0.82	409	55	no
NRX/EST EP-IIIrun 3	1.25**	645	80	yes*
NPX/EST EP-IVA	0.90**	435	55	no*
NRX-A5 EP-III	0.85	555	13	no
NRX-A5 EP-IV	0.85	525	15	no

* Drum and sector clearance was increased by 0.024 in.

** The ramp rate is the ramp before the first power hold during the startup.

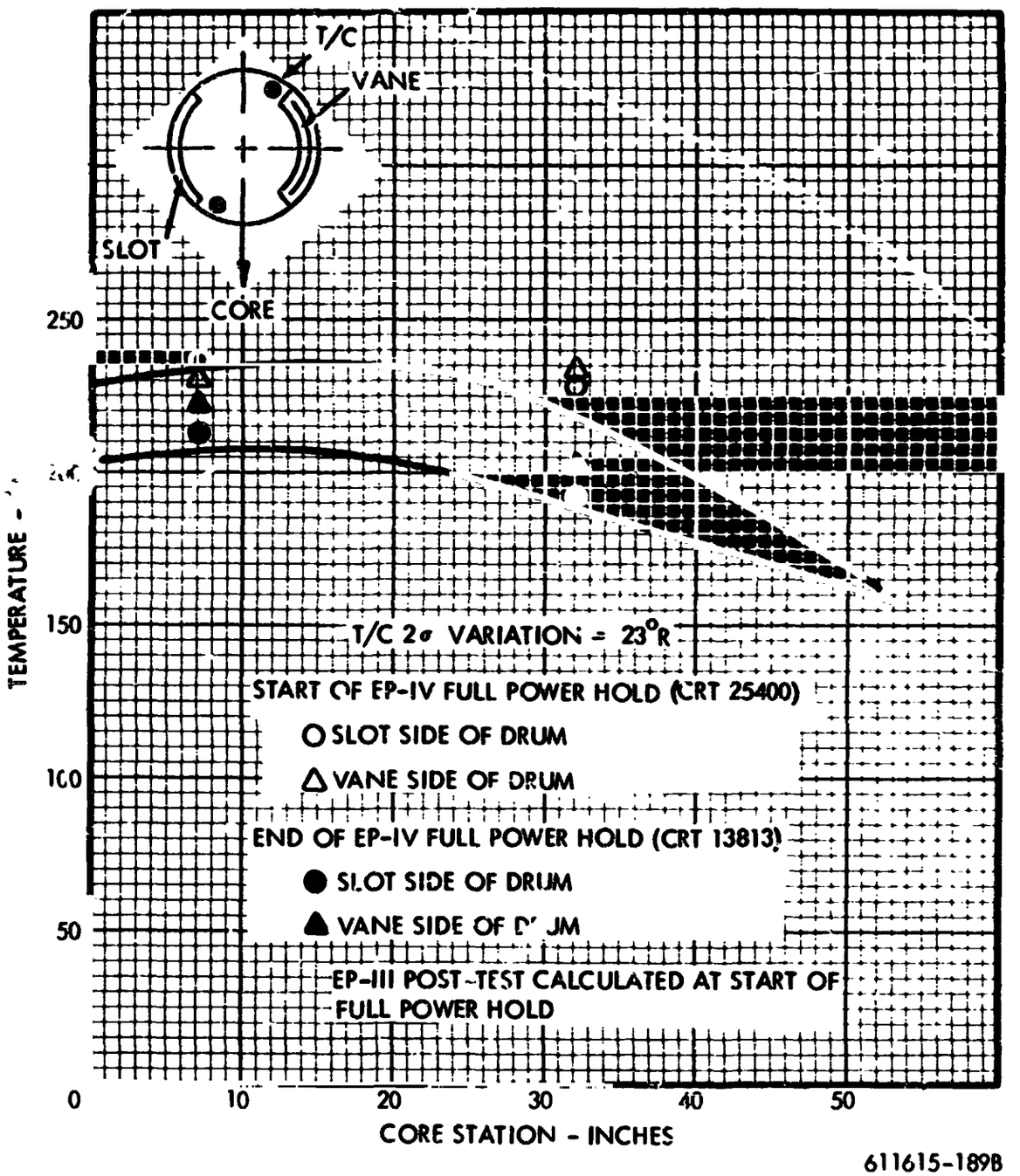

Figure 4-13. NRX-A5 Axial Temperature Profile of Control Drum at Full Power

TABLE 4-4

NRX-A5 CALCULATED SHIELD AND TIE BOLT MATERIAL TEMPERATURES

Shield Material		Tie Bolt Material	
Nozzle End Surface	Dome End Surface	Station 20	Station 32
334°R	245°R	240°R	235°R

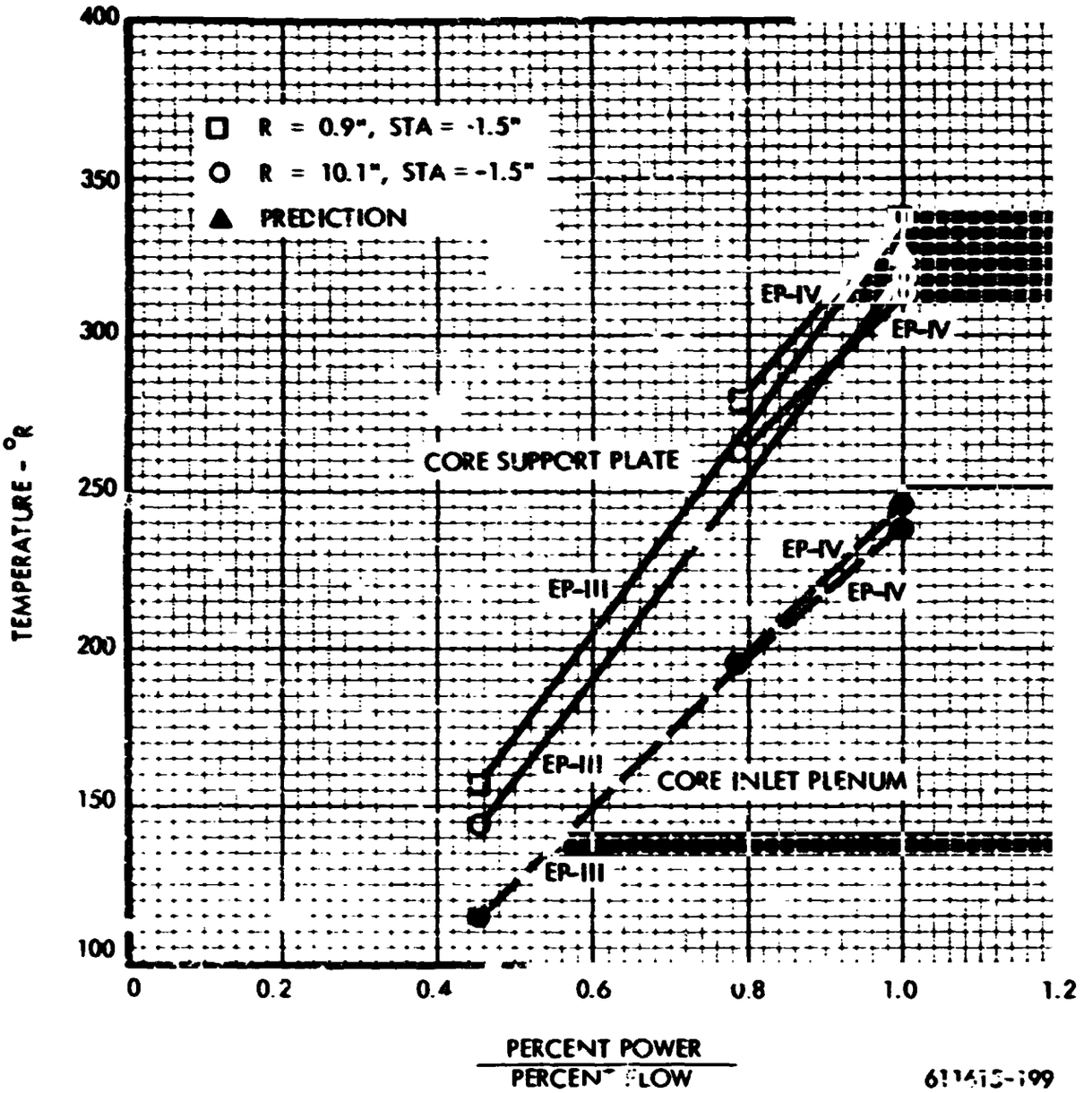

Figure 4-14. NRX-A5 Core Support Plate and Core Inlet Plenum Temperature

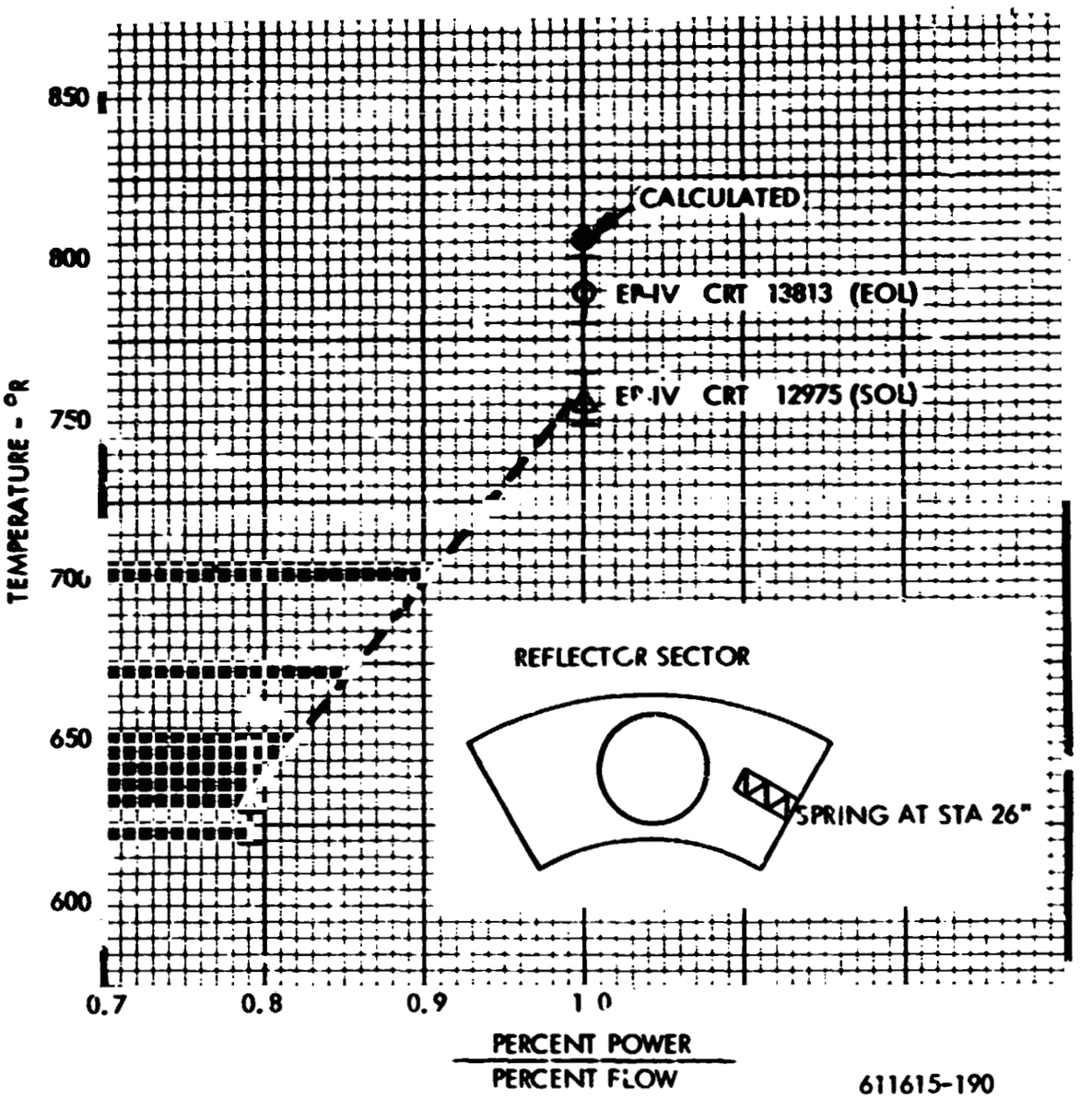

Figure 4-15. NRX-A6 Experimental Lateral Support Spring Temperature in NRX-A5 EP-IV Full Power Hold

4.5 NRX-A5 HOT BUFFER FILLER STRIP ANALYSIS

The NRX-A5 reactor periphery included two sectors of hot buffer filler strips. This design differs from the nominal filler strip design used in previous NRX-A reactors in the placement of the strips inside the pyrographite insulation. The intent of this relocation is to reduce the external surface corrosion of peripheral fuel elements by saturating the hydrogen flowing in from the seal system with graphite sacrificed by the hot buffer filler strips. The NRX-A5 hot buffer strips were not internally cooled and were expected to operate at temperatures above fuel element temperature at full power conditions.

During the NRX-A5 power tests, 39 of the 54 filler strips in the hot buffer region were broken in one or more places, but all the strips in the nominal design sectors remained intact. Table 4-5 gives a summary of the NRX-A5 filler strip breakage. The most probable cause of failure was concluded to be frictional lockup of the filler strips during shutdown. The filler strips bridge (lockup circumferentially) during shutdown because the temperature of the fuel elements decreases faster than the filler strips. Temperature variations between the bridged strips placed the relatively cooler strips in tension and caused them to break. Some of the filler strip damage apparently occurred during shutdown from the first full power test because there is evidence that a piece of broken filler strip plugged some fuel element orifices during EP-IV.

An analysis was made to obtain the transient temperature distributions in the hot buffer filler strips during the final shutdown of the NRX-A5 reactor test (EP-IV) for use in stress analysis. The model used in the analysis, a 30° sector of filler strips, pyrographite insulation and partial elements, is shown in Figure 4-16. Also included is a thin strip representing the fuel element. Boundary conditions are seal channel coolant temperatures and heat transfer coefficients and seal segment temperatures at the outer diameter and fuel element coolant temperatures and heat transfer coefficients at the inner diameter. A model of the J9 fuel cluster (see Figure 5-34 in Chapter 5) was used in the TRACK computer code to obtain fuel element boundary conditions. Coolant flow between adjacent filler strips was neglected because the gaps were expected to be very small (approximately 0.2 mils) in the hot buffer sectors.

Using these boundary conditions, TOSS transient analyses with the filler strip model were performed at 5 core stations. Figure 4-17 shows the temperature difference between the average of the filler strips and the minimum temperature strip as a function of time. The maximum difference is 600°R at core station 38 at 41 seconds after initiation of shutdown. Figure 4-18 gives the temperature difference between the maximum and minimum temperature strips. The maximum temperature difference is 1120°R at the same station and time. The azimuthal temperature variation is shown in Figures 4-19 and 4-20 at steady state and at the worst condition corresponding to 41 seconds after initiation of shutdown. Figure 4-21 shows a comparison between the average filler strip temperature.

It is interesting to note the effect of shutdown schedule on the temperature differences between filler strips. The NRX-A5, EP-IV shutdown chamber temperature ramp rate was approximately 60°R/sec. After 31 seconds, the average chamber temperature had reached 2500°R and the reactor was scrammed. Rapid cooling of the fuel elements following scram caused the temperature difference between filler strips to increase sharply above the peaks that occurred before scram. The worst condition occurs about 10 seconds after the scram.

Stress analysis of the 30° sector of the hot buffer filler strips using the detailed temperature distributions obtained from this thermal analysis resulted in a good correlation between computed stresses and observed breakage patterns.

4.5.1 NRX-A5 Test Temperature Data

Subsequent to the hot buffer filler strip shutdown analyses discussed above, thermal capsule data for the hot buffer filler strips were evaluated and indicate considerable deviation from the calculations near the hot end. Figure 4-22 gives thermal capsule temperatures for filler strip 4-8 and for a nearby central unfueled element. Also shown are the temperatures calculated for this filler strip and the adjacent fuel element. There is reasonable agreement between measured and calculated data except toward the hot end. At core station 50, the measured filler strip temperature is nearly 1000°R lower than calculated even though the measured and calculated fuel element temperatures agree reasonably well. It appears that

lateral support seal coolant flowing radially into the filler strip gaps and bypassing the seal segments could cause the lower than predicted filler strip temperatures at the hot end of the core. The gap between the hot buffer filler strips has been recalculated with thermal capsule temperature data and the axial gap distribution is shown in Figure 4-23. Also shown on this figure are the gap profile and the thermal bow for the pyrographite insulation strips. Core interelement gaps are shown for comparison.

The filler strip gap at the hot end of the core is 4 mils. For this gap and the pressure drop which exists across the aft end seals (20 psi), flow rates sufficient to remove all of the filler strip generated heat are possible. Exact calculation of the flow rates between filler strips is very difficult because of the indeterminate radial impedance around the pyrographite strips.

Although the seal coolant leakage between hot buffer filler strips has not been included in the thermal analysis of the strips, the conclusion that the filler strip breakage occurred during shutdown is still valid. While the strips were initially cooler at the nozzle end than had been calculated, core contraction would still cause bridging of the filler strips which would in turn cause a rapid decrease in flow between strips. With the convective cooling of the radial faces of the filler strips thus restricted, the cooldown of the strips would be controlled as before by conduction to the fuel elements.

TABLE 4-5

NRX-A5 HOT BUFFER FILLER STRIP BREAKAGE TABULATION

Number of	Forward End	Station 20 to 49	Aft End	Total
Filler Strips Broken	19	15	5	39
Filler Strip Breaks	19	46	5	70

Total number of filler strips in hot buffer region = 54

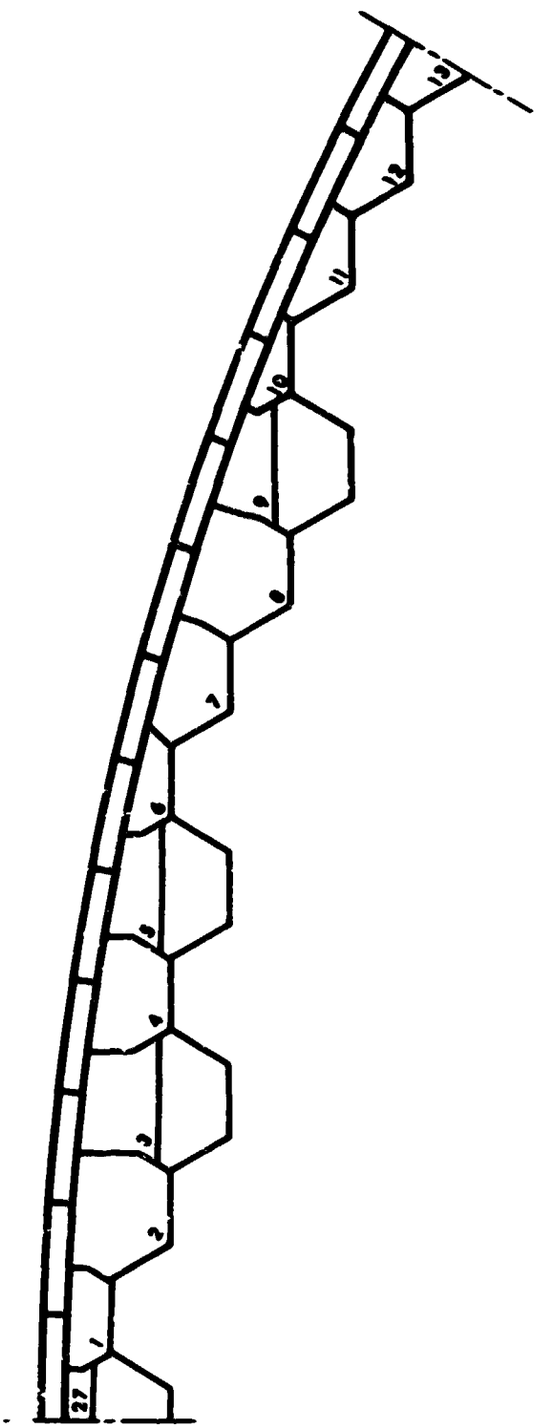

A5 Hot Buffer Filler Strip Model (30 Degree Sector)

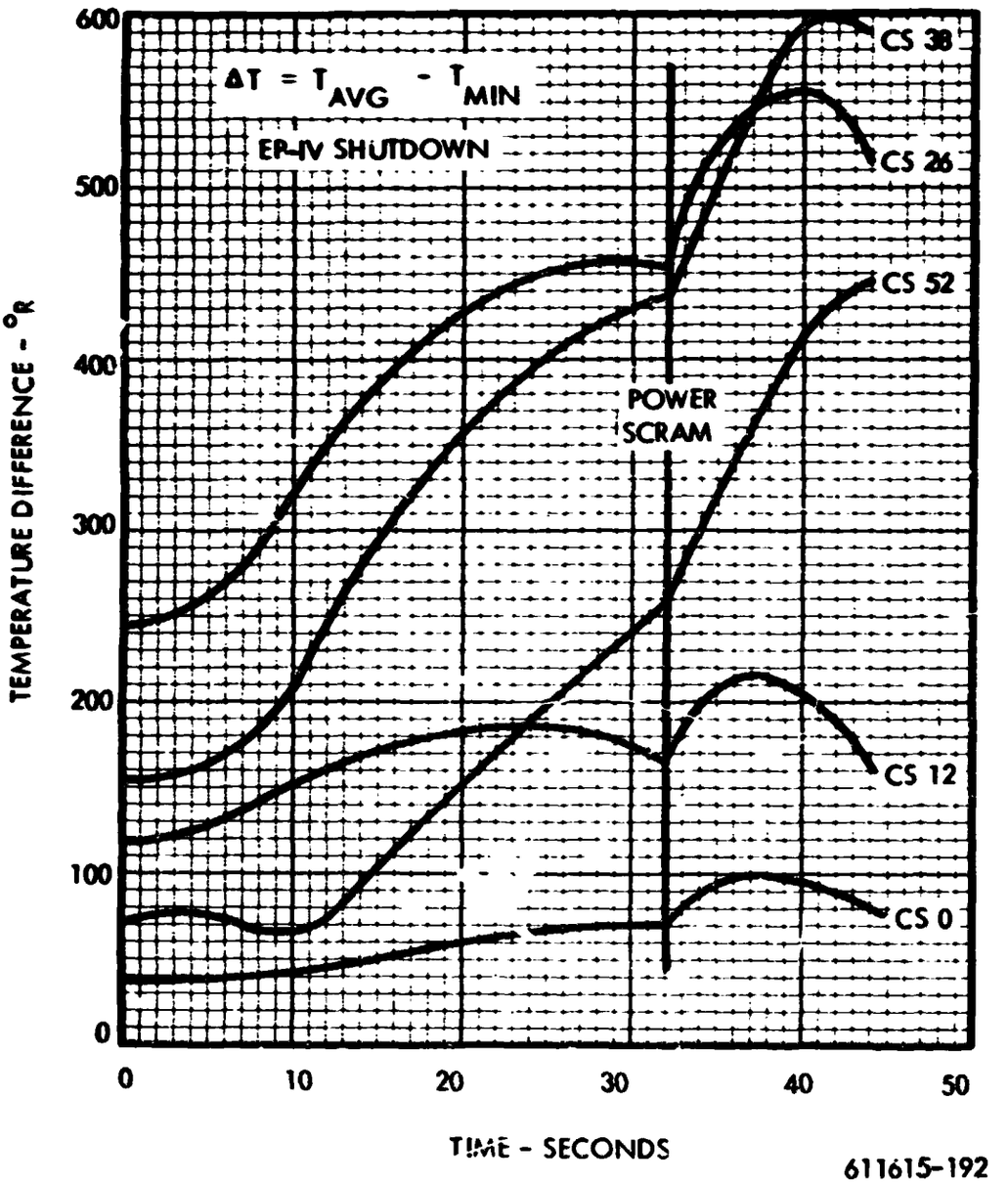

Figure 4-17. Temperature Difference between Average and Coldes Hot Buffer Filler Strip during NRX-A5 EP-IV Shutdown

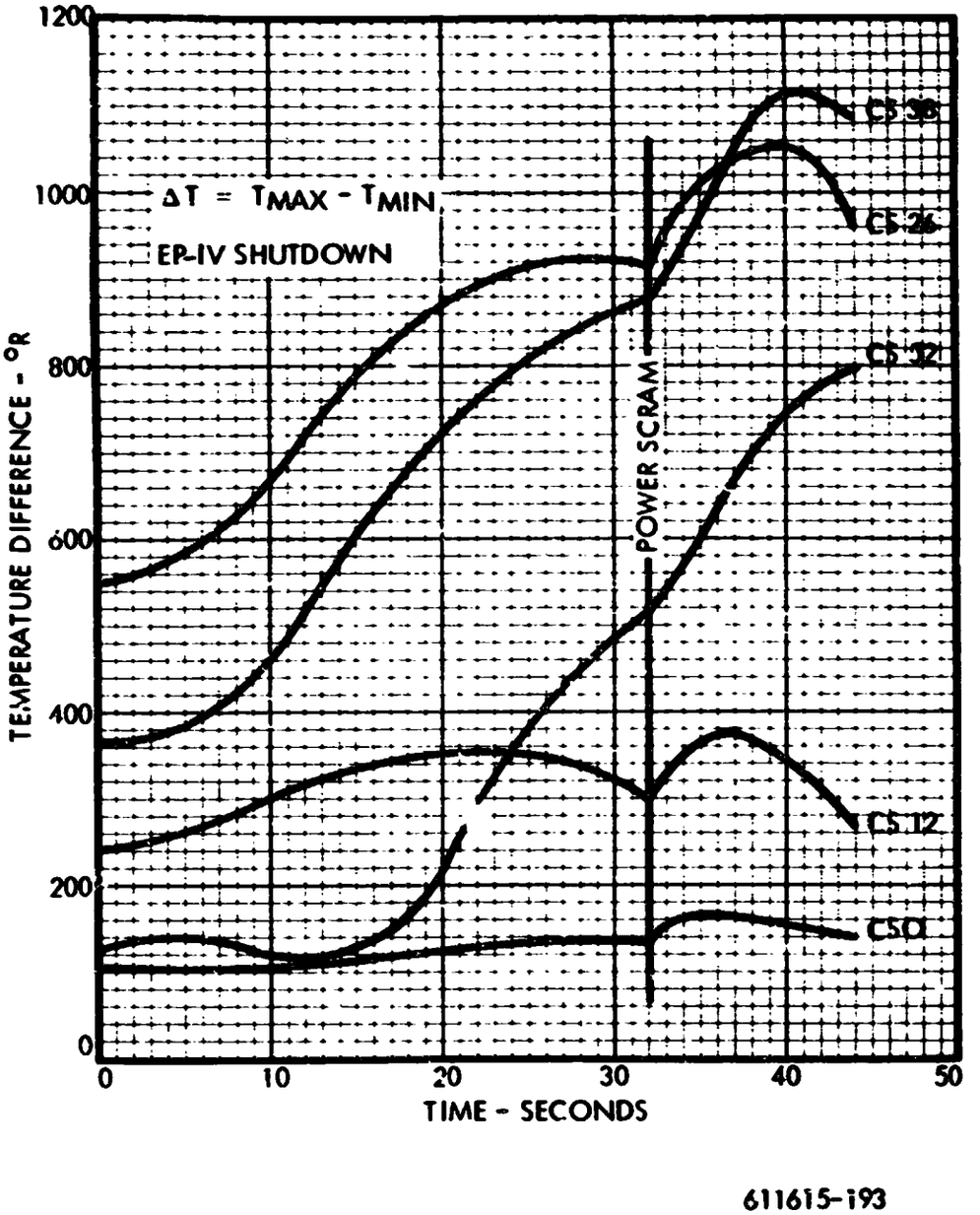

Figure 4-18. Temperature Difference between Hottest and Coldest Hot Buffer Filler Strip during NRX-A5 EP-IV Shutdown

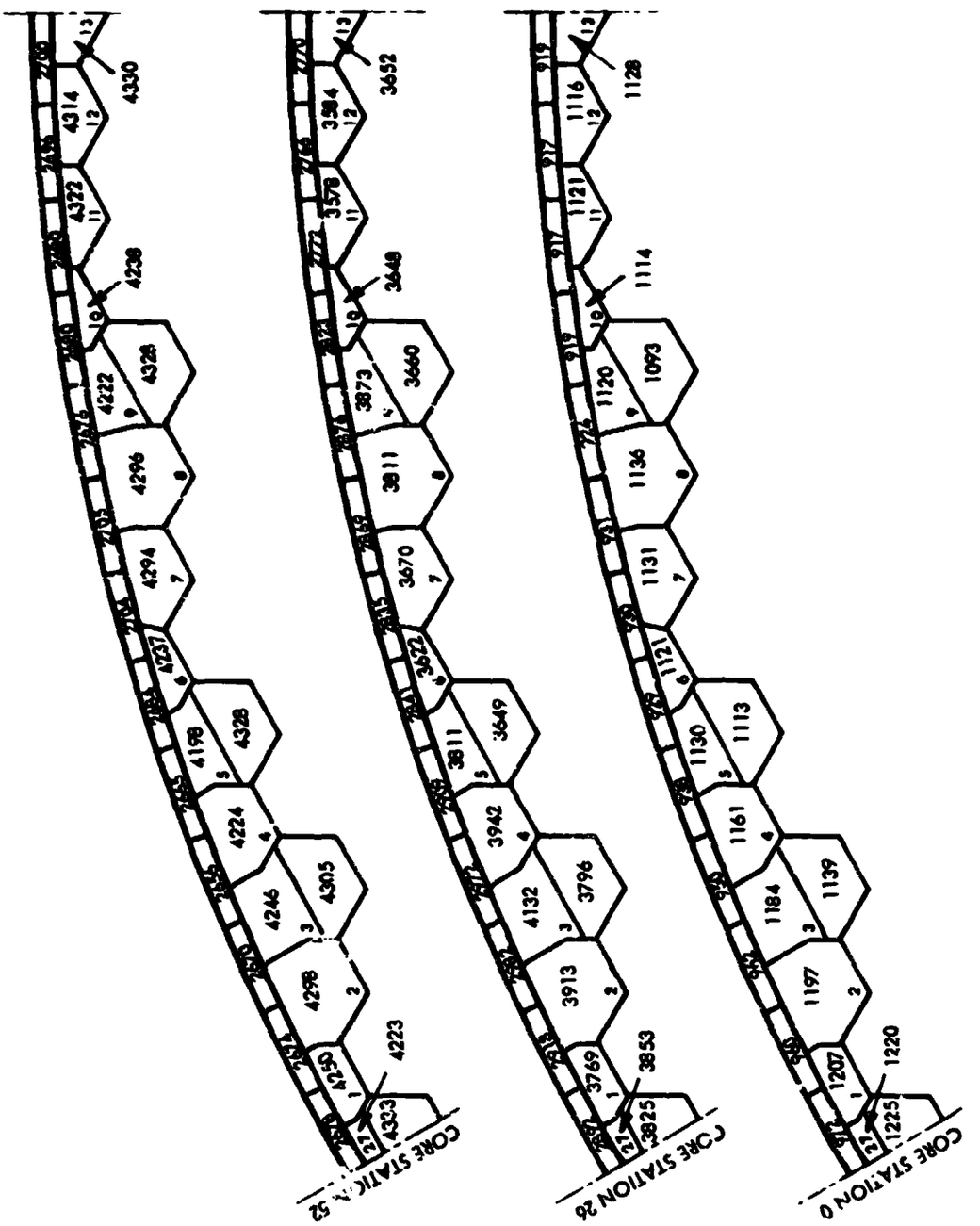

Figure 4-19. NRX-A5 Hot Buffer Filler Strip Temperatures at EOL - Steady State

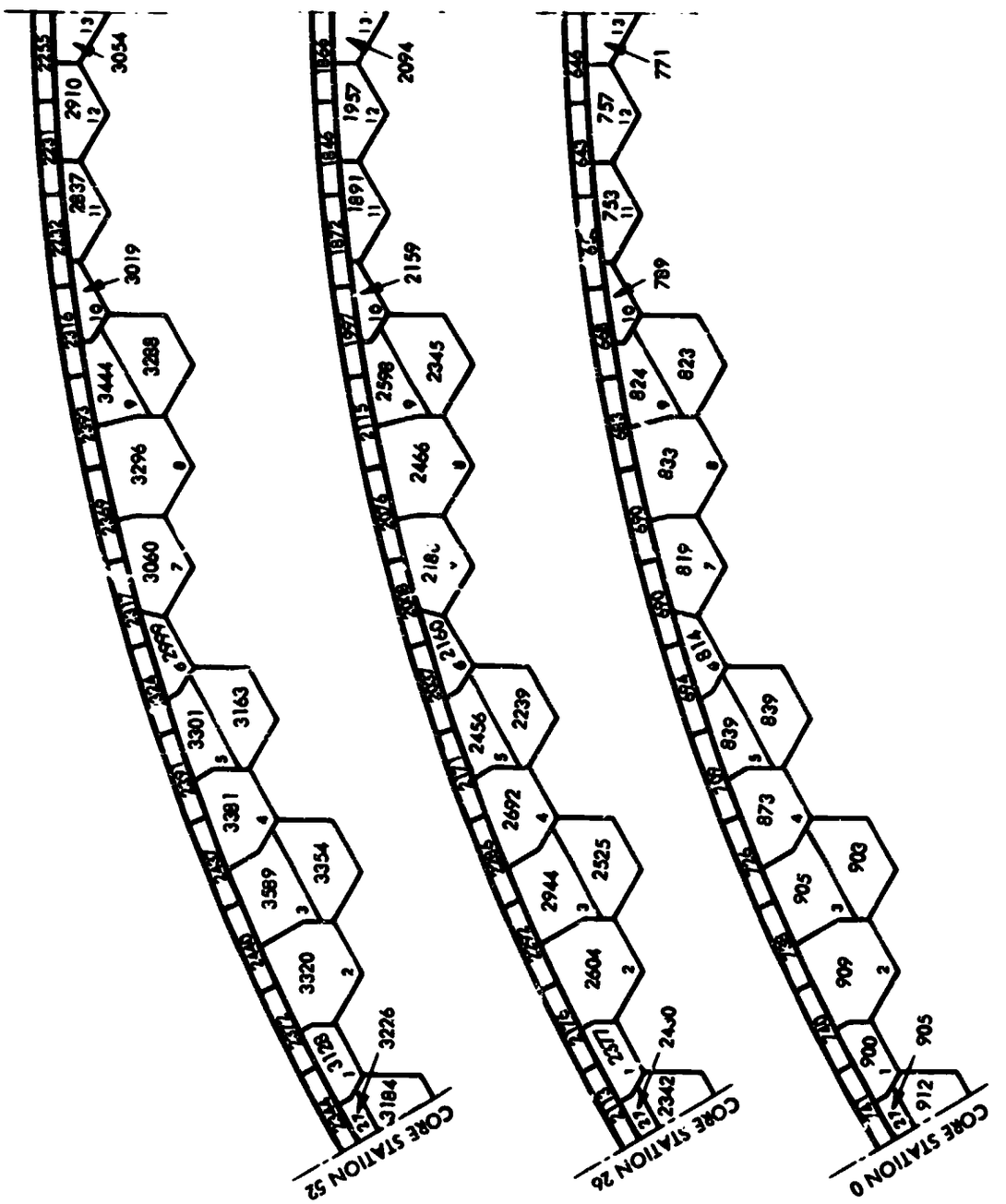

Figure 4-20. NRX-A5 Hot Buffer Filler Strip Temperatures 40 Seconds after Start of EP-IV Shutdown (Worst Condition)

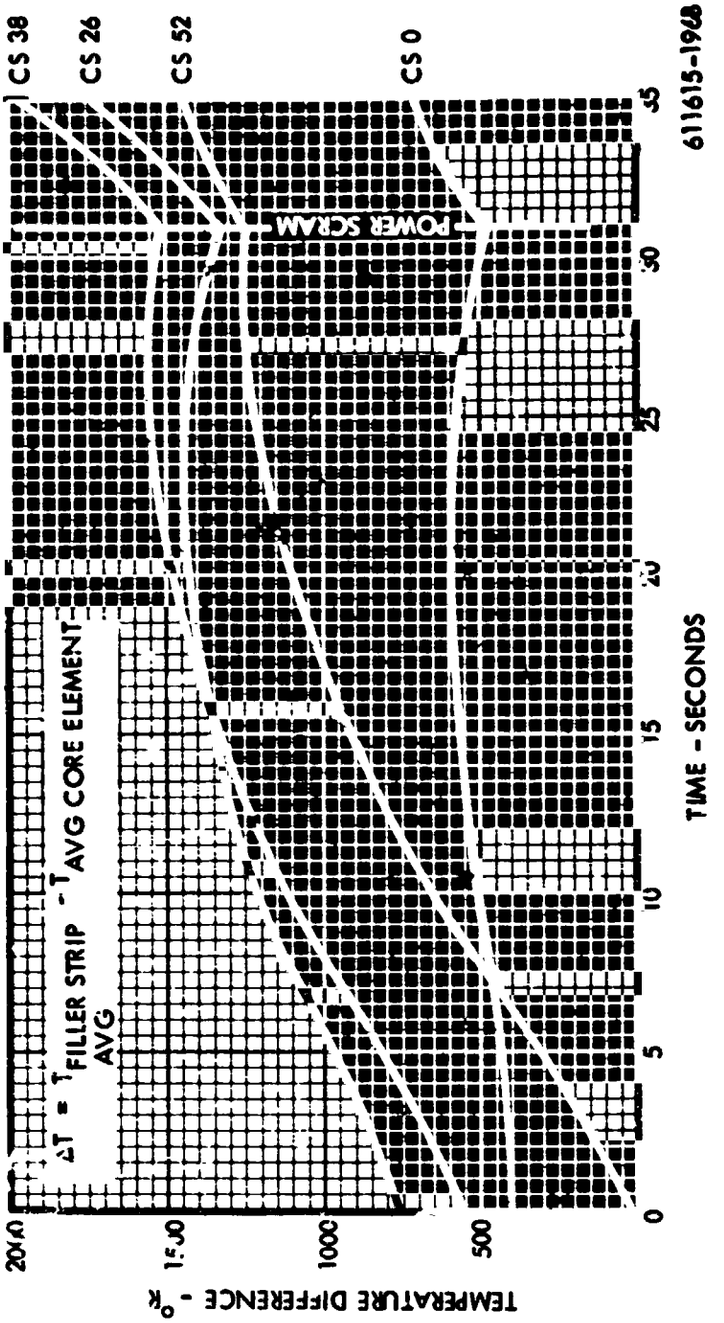

Figure 4-21. Temperature ference between Hot Burrer Filler Strip and Average Core during NRX-A5 EP-IV Shutdown

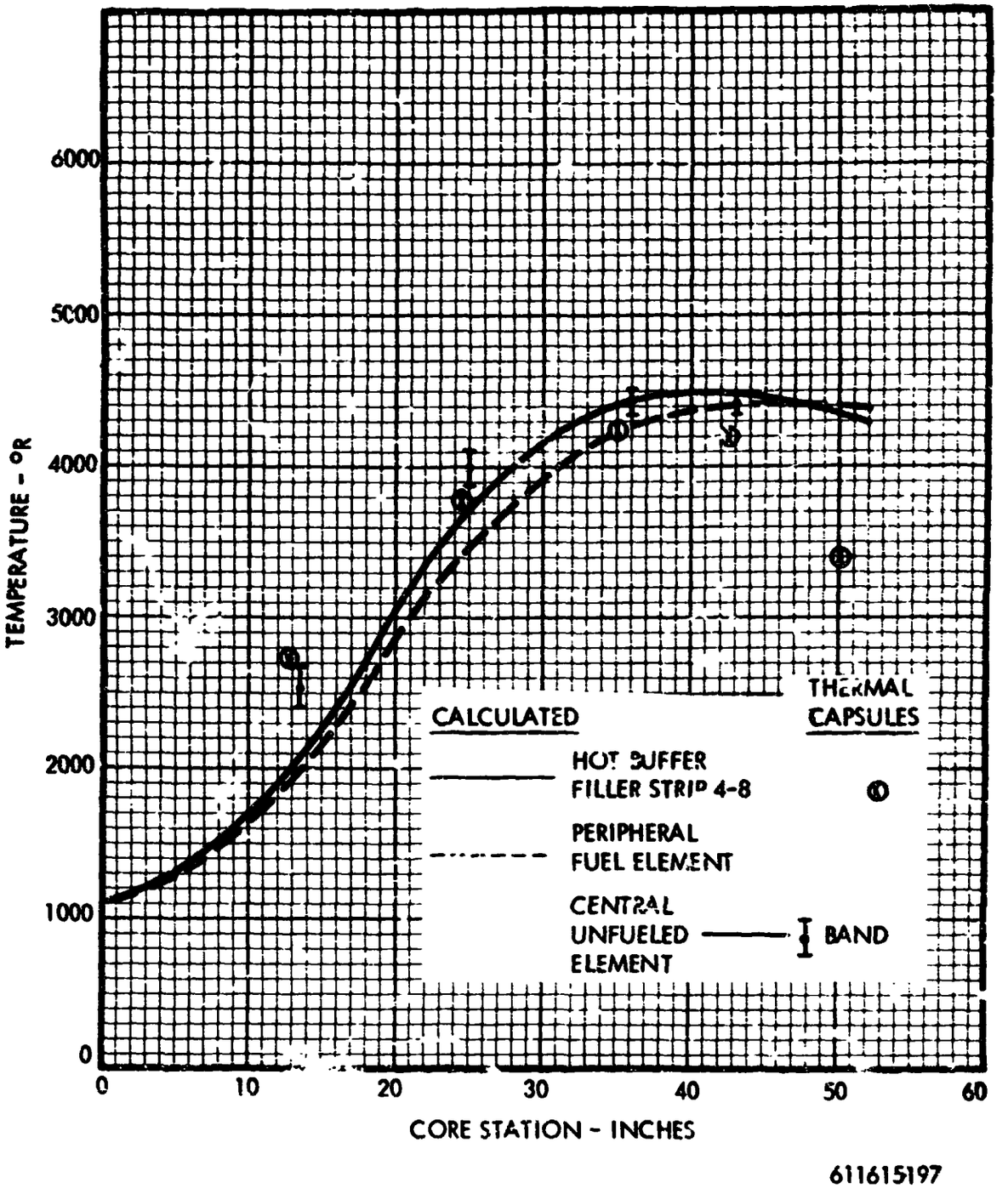

Figure 4-22. Axial Temperature Variation of NRX-A5 Hot Buffer Filler Strips - ECL

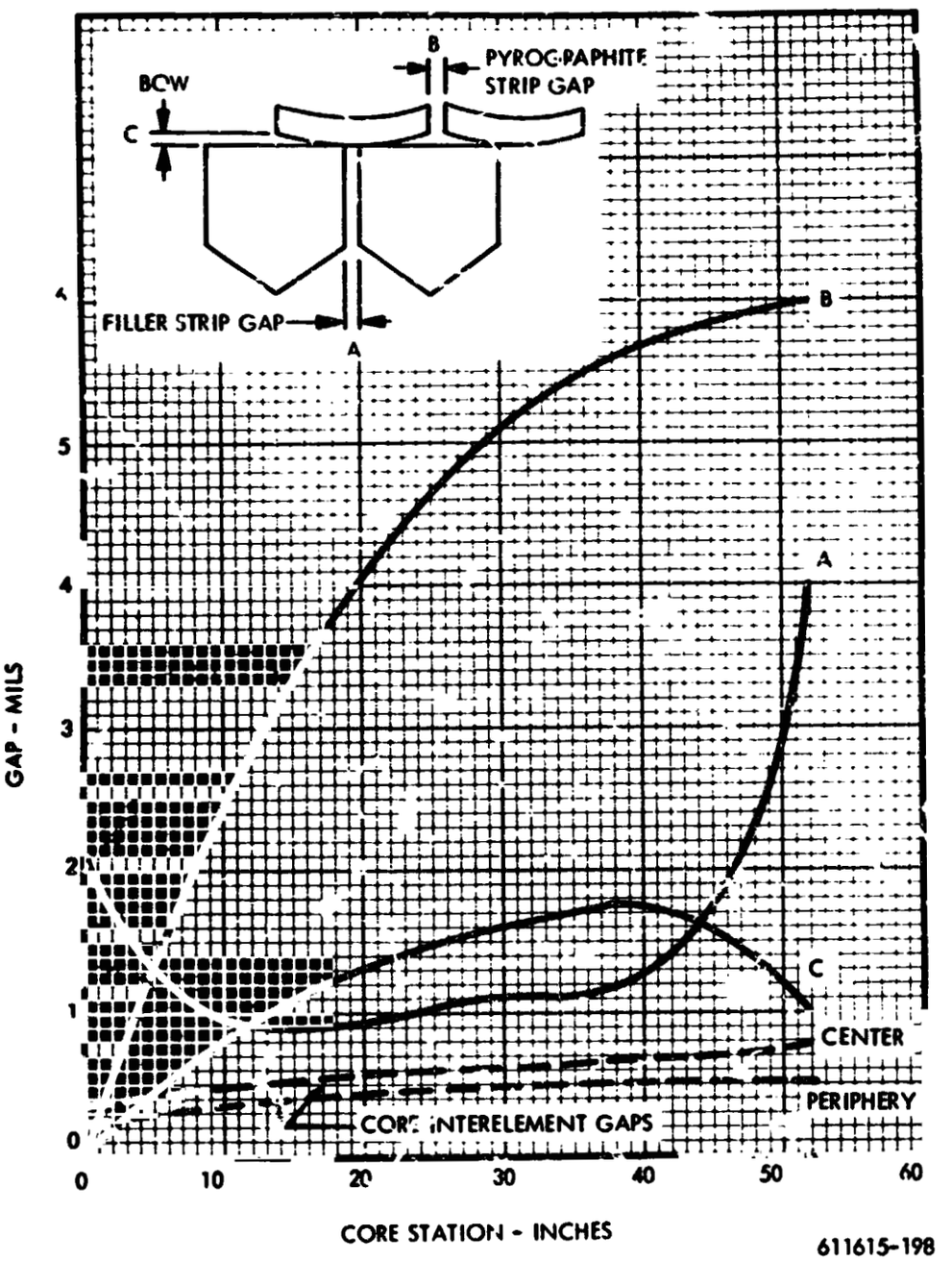

Figure 4-23. NRX-A5 End of Life Hot Buffer Periphery Gaps

4.6 FILLER STRIP THERMAL CAPSULE MEASUREMENTS

Thermal capsule temperature measurement in the core filler strips consisted of thermal capsule family distributions placed at six azimuthal positions.* Identical distributions were utilized in the five instrumented filler strips within the hot buffer region and were the same as the standard family distribution used in the unfueled elements within the core. The one instrumented filler strip outside the hot buffer region, i.e., filler strips "6-18" had a different thermal capsule wire distribution to accommodate the lower operating temperature levels of the normal filler strips. The filler strips in the hot buffer region which had thermal capsules were; "3-2", "4-8", "4-2", "4-5", and "4-18". Figure 4-24 is a schematic cross section of the core and identifies the filler strips which had the thermal capsules.

Evaluation of thermal capsule data makes use of post test radiographic examination in determining axial temperatures. This technique also makes possible the review of fracture patterns that were experienced. Fractures were observed only in the hot buffer filler strips. The one filler strip that had thermal capsules in the nominal filler strip design region, i.e., filler strip "6-18", had no noticeable evidence of fracture or corrosion. In addition to the evaluation of NRX-A5 filler strip thermal capsule data, a comparison has also been made of thermal capsule temperature measurements in the filler strip regions of previously tested reactors, i.e., NRX-A2, NRX-A3, and NRX/EST.

Figures 4-25 through 4-27 show NRX-A5 thermal capsule temperature data of the maximum temperatures measured in the hot buffer filler strips and also describe the thermal capsule wire distribution.

The axial distributions of measured data in the hot buffer region are in approximate agreement with the predicted values except at the hot end where the measured values are nearly 1000°R lower than predicted. The measured hot end (station 50) temperature of the hot buffer filler strips based on thermal capsules was between about 3400°R and 3600°R which corresponds to the calculated nominal value of 4400°R. A plausible explanation for these

---

* For identification of filler strip location, see NRX-A5 Reactor Analysis Data, WANL-TME-1389.

observed low hot-end temperatures can be attributed to higher than calculated radial in-leakage from the local lateral support seal system. The calculation of thermal and hydraulic conditions at the hot end of the filler strips does not fully consider leakage in the region of the last ineffective seal.

Axial temperature distributions obtained from thermal capsule data in the hot buffer filler strips were essentially identical in "4-8", "4-18", and "4-25" but lower in "3-2", and "4-2". Filler strips 4-8 and 4-18 each had a peak temperature of 4300°R which occurred between stations 36 and 40 inches. The peak value in filler strip 4-25 was slightly higher, i.e. 4400°R, and occurred further downstream at about station 43 inches. Peak thermal capsule temperatures in filler strips "3-2" and "4-2" (also in hot buffer region) were similarly measured near station 42 but were nearly 500°R lower. Peak temperatures in filler strips "3-2" and "4-2" were 3800°R and 4000°R respectively.

The fracture patterns which are also illustrated in Figures 4-25 through 4-27 reveal no striking similarity from a gross point-of-view except that all of the hot-buffer instrumented filler strips fractured in the axial region between station 32 and 40. Moreover, three of these filler strips which had fractures toward the cold end exhibit the tendency to fracture at station 24. Similar fracture patterns were observed at the hot end of filler strips "3-2" and "4-2" which are identical but located in adjacent sectors. Both of these filler strips had similar low axial temperature distributions relative to the other hot buffer filler strips. One of these filler strips, "3-2" which had a slightly lower temperature distribution did not fracture at station 24 (see Figure 4-26).

Figure 4-27 shows another comparison of thermal capsule data from two essentially identical filler strips (mirror image mates). These are strips "1-25" and "4-2" which were positioned near each other in the hot buffer region (see Figure 4-24). Both filler strips were fractured at station 24, but had different characteristics in other respects. Filler strip "4-25" had the highest temperature level (4400°R at station 43) and had a single fracture at station 38 whereas the maximum temperature in filler strip "4-2" was about 400°R lower

(4000°R at station 42) and it had multiple fractures at the hot end. The condition of filler strip 4-25 is notable in that there was considerable local corrosion around the single fracture at station 38. This degree of local corrosion was not evident in the radiographic evaluation of the other thermal capsule instrumented filler strips.

Figure 4-28 shows thermal capsule data of axial temperatures of filler strip "6-18" which was positioned outside the hot buffer region. The measured temperatures are in close agreement and within the range of predicted temperatures. Filler strip "6-18" had no noticeable fractures and the radiograph disclosed little or no detectable corrosion. Figure 4-28 also illustrates a comparison of filler strip thermal capsule data obtained from the NRX-A2, NRX-A3 and NRX/EST reactor tests. The lower temperatures shown for the NRX-A5 are associated with a different seal system design which had a lower flow impedance. Seal segments for the NRX-A5 reactor are 1 inch long compared to 1.5 inches for the previous NRX reactors. The resultant seal coolant flow is about 30 percent greater and the maximum seal coolant temperature was therefore 500°R lower for the NRX-A5 design as compared to the NRX/EST.

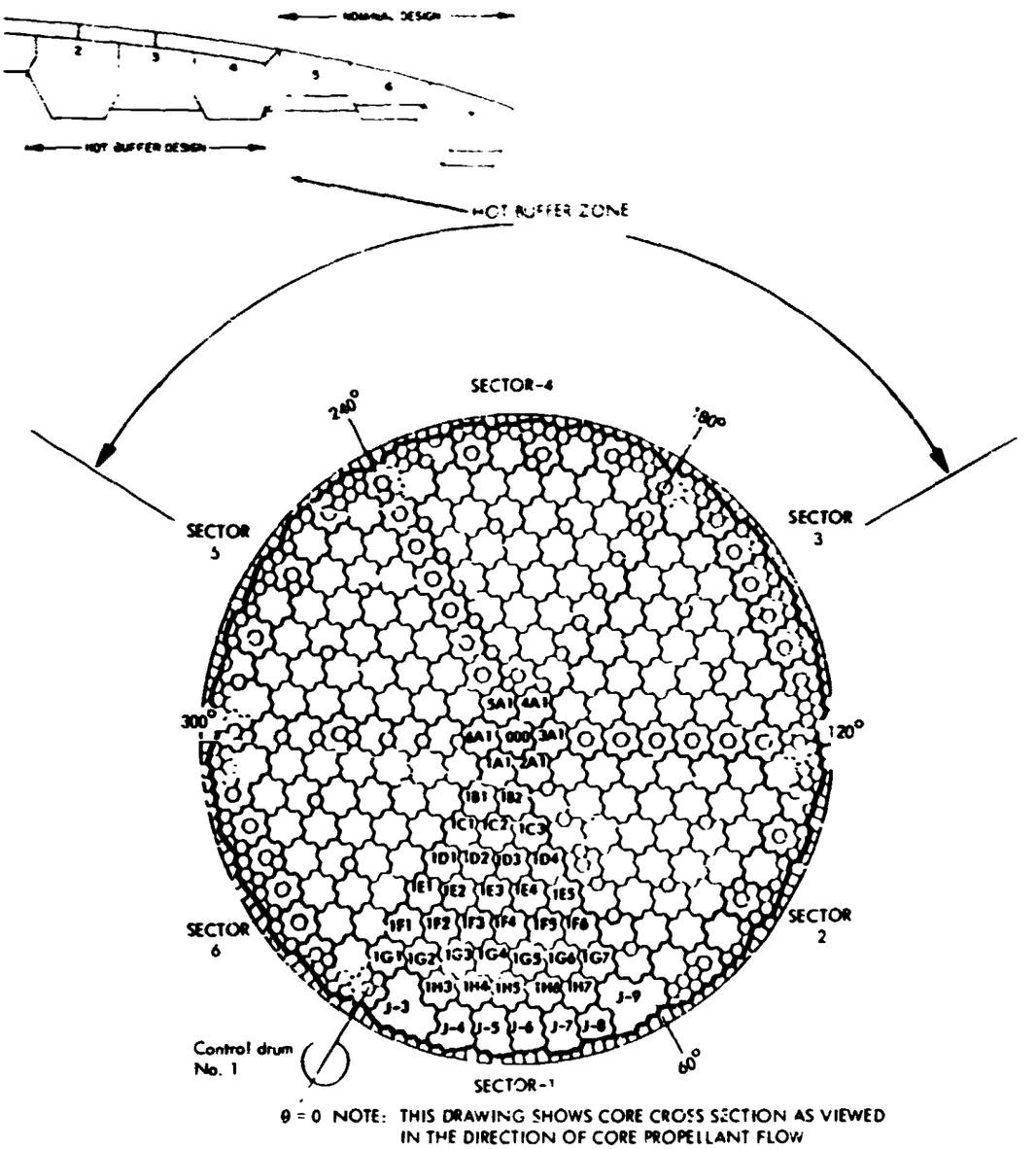

Figure 4-24. Core Orientation and Cluster Identification

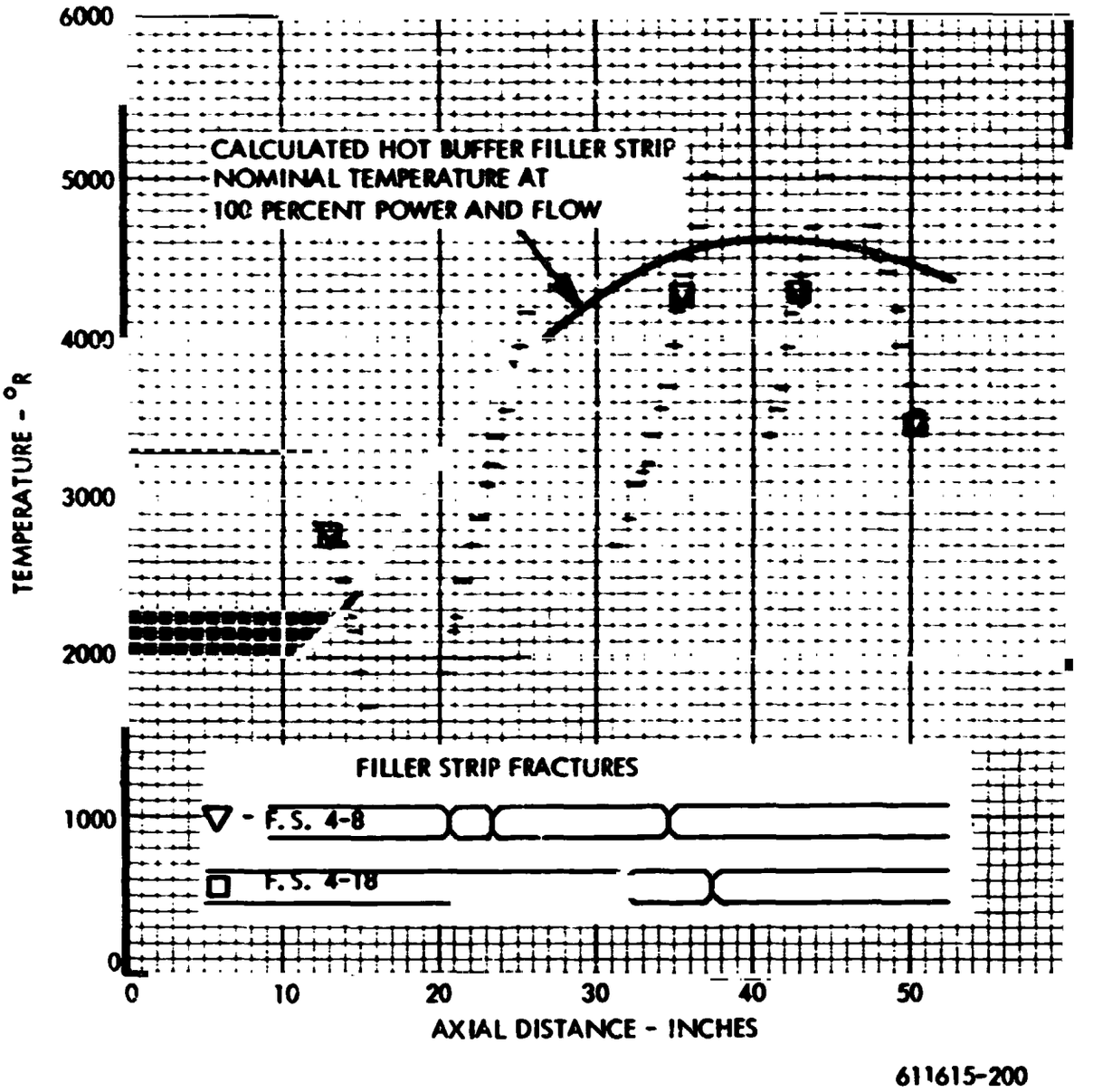

Figure 4-25. NRX-A5 Thermal Capsule Data in Hot Buffer Filler Strips - F.S. 4-8 and F.S. 4-18

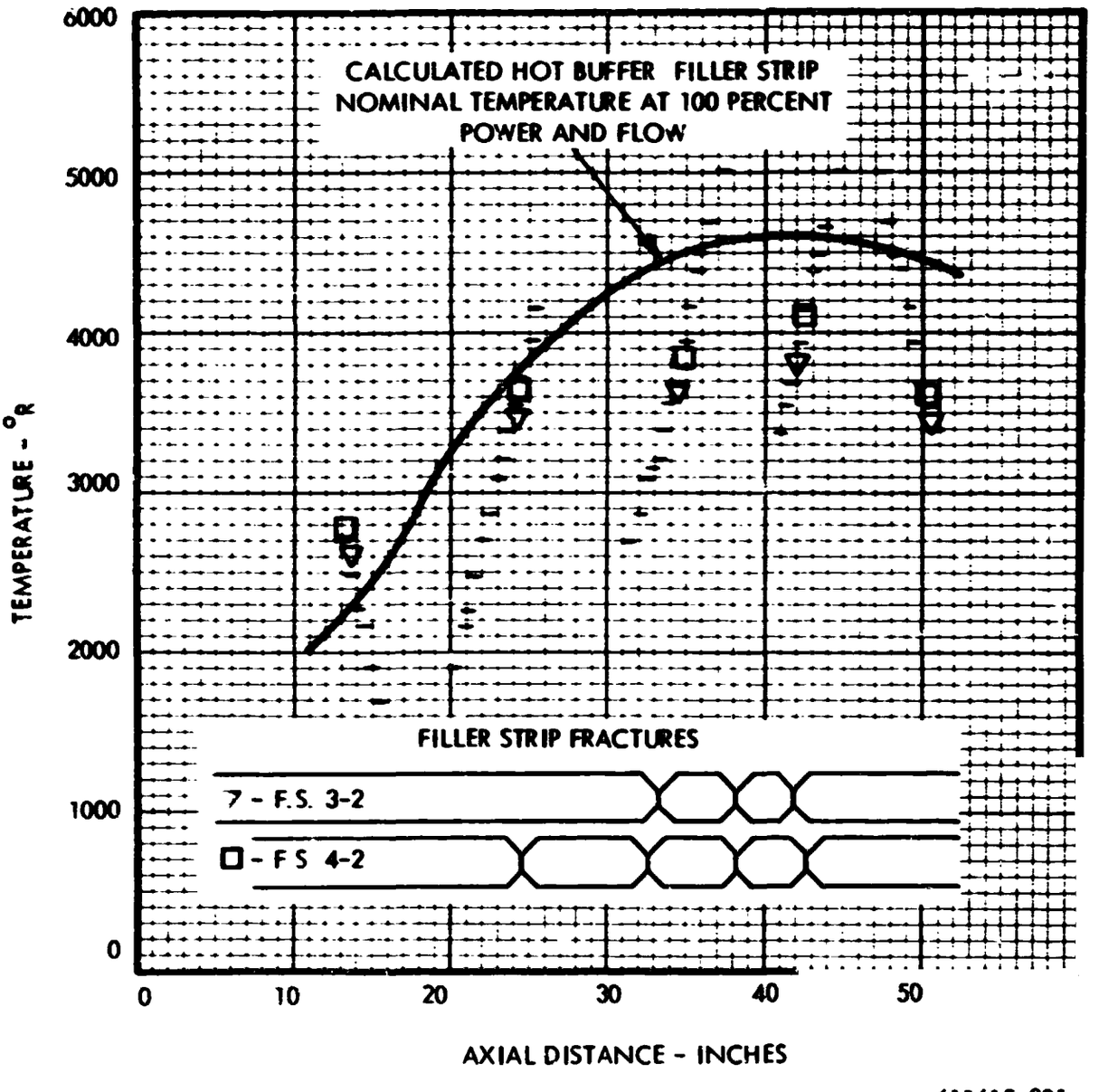

Figure 4-26. NRX-A5 Thermal Capsule Data in Hot Buffer Filler Strips - F.S. 3-2 and F.S. 4-2

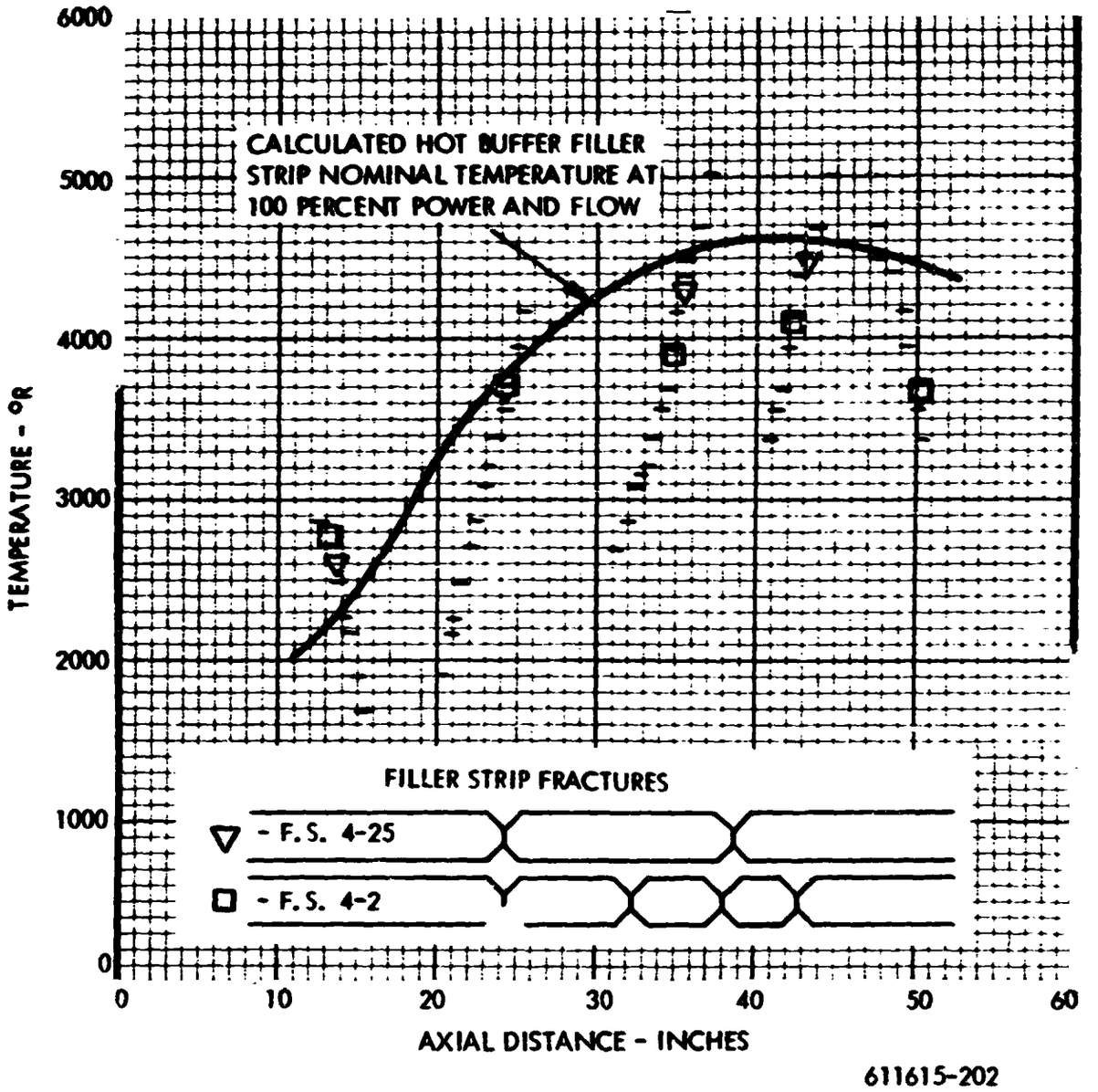

Figure 4-27. NRX-A5 Thermal Capsule Data in Hot Buffer Filler Strips - F.S. 4-25 and F.S. 4-2

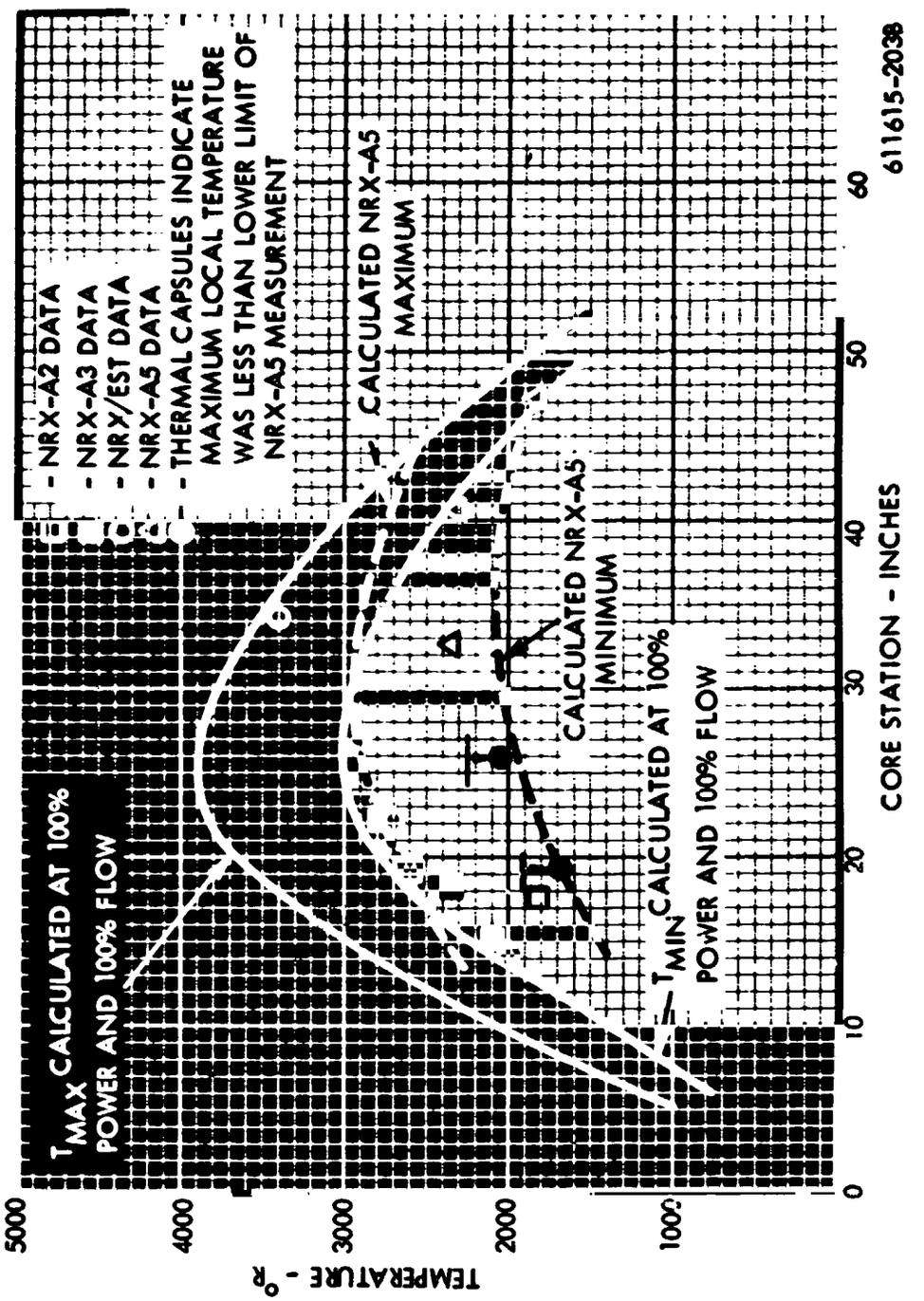

Figure 4-28. NRX-A5 Thermal Capsule Distribution in Nominal Filler Strip - F.S. 6-18

CHAPTER 5

CORE THERMAL ANALYSIS *

5.1 INTRODUCTION

The NRX-A5 core pressure drop and the results of the thermocouple and thermal capsule measurements are discussed. The change in core temperature distribution resulting from control drum movement, inlet temperature asymmetry, and the shim pattern are discussed. A transient analysis of a peripheral element during shutdown is included. Comparisons with previous reactor test data are made where applicable.

---

* Major contributors to this chapter were R. Agosti, G. Cort, W. Horton and M. Woods

5.2 SUMMARY

The NRX-A5 overall performance agreed reasonably well with pre- and post-test predictions using analytical models similar to those used for previous reactor analyses.

Temperature distributions within the core were obtained from the continuously recording thermocouples located in the unfueled elements at stations 8, 20, 26, and 32 and from thermal capsules which were also located in the unfueled elements and indicated maximum temperatures achieved during the test. There were also six thermocouples located in an 0.024 inch diameter hole drilled into the inlet end face of three fueled elements, IAIG, 5J9T, and 6J4H. Each of these elements had one thermocouple at core station 0.5 inches and one at the 1.0 inch location. Thirty-two of the thermocouple locations were pre-selected to provide data for a post test statistical analysis. The temperature distribution during steady state operation was essentially flat with minor variations caused by local differences in core inlet temperature and a major variation caused by corrosion and drum movement near the end of EP-IV. Thermocouples in the core central region experienced a sharp decrease in temperature at various times during EP-IV under otherwise steady state conditions. This behavior is believed due to severe local corrosion on the fuel elements.

The maximum temperature in the core central region, measured with a thermal capsule at station 44 in an unfueled element, was 4700°R $\pm$ 100. This temperature was believed to have occurred at the start of EP-III at a control drum position of 109 degrees. The maximum temperature measured at the core periphery was 4840°R which was probably reached at the end of EP-IV with the control drums at 145 degrees. The average fuel element exit gas temperatures that correspond to these maximum sensor temperatures were calculated to be 4277°R and 4275°R respectively.

Analysis of variance on the core thermocouples indicated that there was a slight radial and circumferential temperature variation throughout most of the full power life, but that a strong radial effect did not appear until the end of EP-IV. During the periods of full power operation in EP-III and EP-IV with control drum positions varying from 109 to 145

degrees, no azimuthal temperature variation could be detected related to the power scalloping caused by drum rotation. At the low power (229 MW) hold in EP-III with control drums at 97 degrees, the station 26 thermocouples indicated a slight azimuthal temperature variation which could be related to the power scalloping.

Measurements of core pressure drop were from 5 percent to 8 percent lower than post test calculations at the full power holds. Part of this difference is attributable to a change in flow impedance caused by significant bore corrosion and part must be attributed to lower friction factors than predicted.

The tie rod material temperatures at the core exit plane were measured in seven clusters and were nominally in agreement with calculated values at full power. At low power, the calculated temperatures were about 60°R cooler than measured. The latest thermal conductivity data on pyrographite sleeves were used for these calculations.

Cracking at the corners of the peripheral fuel elements was observed in the NRX-A5 and previous reactor tests. One contributing cause of these cracks is suspected to be temperature variations within elements and between elements during transients. A transient thermal analysis of a portion of the J9 fuel cluster was performed. Stress analysis indicated that the calculated temperature variations alone are insufficient to have caused failure of the element unless the cross section was considerably weakened by corrosion. The notching of the outermost corners of the peripheral fuel elements in the nominal (cold) filler strip sectors appears to be caused by the radial inflow of lateral support coolant.

5.3 CORE PRESSURE DROP

The post test calculations for the NRX-A5 core pressure drop were based on MCAP models for the as-built core similar to the ones described for previous reactors.* The model consisted of 28 parallel channels based on the power factors and orifice sizes for sixteen one-inch radial core increments with twelve additional channels at the core periphery. All of the power factors in the model were adjusted to account for drum angle effects at the various power holds.

Table 5-1 summarizes the calculated and measured core pressure drops at eight full power hold times in EP-III and EP-IV. The calculated values are consistently higher than measured by about the same amount as was observed in the NRX/EST, and the difference has a slight tendency to increase with running time. The increase in this pressure drop difference, coupled with the change in the measured value during the runs indicated that corrosion effects contribute to the observed differences, but do not explain the difference at start of life. Table 5-2 presents similar data for NRX/EST which also indicates that removal of graphite due to corrosion may increase the pressure drop difference at the end of life but that the 5 percent difference at start of life is real and unrelated to corrosion. The probable error is the friction factor correlation which is based on a channel roughness measurement made on NRX-A3 elements at ambient conditions. The combined effects of thicker coatings at operating temperatures in NRX/EST and NRX-A5 could account for approximately 4 psi of the observed pressure drop difference.

Table 5-3 presents the results obtained by using the measured pressure drop in the MCAP models to calculate the core flow. The inlet and exit plenum conditions are specified and the flow balances between tie rod and fueled channels are calculated for the specified pressure drop. In addition, the core and tie rod power are calculated by the enthalpy rise

---

* WANL-TNR-119, "Analysis of NRX-A2 Test Results"
WANL-TNR-202, "NRX-A3 Reactor Final Test Report"
WANL-TNR-216, "NRX/EST Reactor Test Analysis Report"

using the specified plenum conditions and the calculated flows. The calculated reactor flow is low by as much as 4 percent of the measurements and consequently the calculated reactor power is low by the same percentage. Since there is no evidence of additional flow bypassing the fuel element coolant channels, the calculated core pressure drop, power, and flow can be brought into agreement with measured values by adjusting the flow impedance (friction factor).

TABLE 5-1

NRX-A5 COMPARISON OF MEASURED AND CALCULATED CORE PRESSURE DROPS

	Control Room Time	Measured Psi	Calculated Psi	Percent Difference $100 \times \frac{\text{Calculated-measured}}{\text{Calculated}}$
EP-III				
	25400 (sol)	119	125.9	5.5
	25700	116	121.7	4.2
	25930	118	126.2	6.4
	26247.5	118	124.6	5.3
EP-IV				
	13002.5	118	125.3	5.8
	13242.5	118	124.4	5.1
	13482.5	118	125.5	6.0
	13812.5 (eol)	117	127.0	7.9

TABLE 5-2

CORE PRESSURE DROP COMPARISON BETWEEN
NRX-A5 AND NRX/EST

	NRX/EST	NRX-A5
Design Full Power	120	125
Start of Life		
Measured	109.0 (EP-III 22429)	119.0 (EP-III 25400)
Calculated	115.0	125.9
% Difference	5.2	5.5
Start of Second Full Power Hold		
Measured	112.1 (EP-IV A 9295)	118.0 (EP-IV 13002.5)
Calculated	122.5	125.3
% Difference	8.5	5.8
End of Life		
Measured	112.2 (EP-IV A 10045)	117 (EP-IV 13812.5)
Calculated	121.5	127.0
% Difference	7.7	7.9

TABLE 5-3

NRX-A5 COMPARISON OF MEASURED AND CALCULATED CORE FLOW AND POWER FOR MEASURED PRESSURE DROP AND CHAMBER CONDITIONS

	Control Room Time	Calc.	Meas.*	Calc.	Meas.*
EP-III					
	25400	69.6	71.5	1084.4	1119
	25700	69.3	70.9	1023.0	1051
	25930	69.1	71.4	1077.1	1089
	26247.5	69.7	71.4	1046.4	1081
EP-IV					
	13002.5	69.1	71.1	1086.7	1120
	13242.5	69.5	71.3	1066.8	1099
	13402.5	69.2	71.3	1069.3	1106
	13012.5	68.4	71.2	1063.9	1112

* Two Standard Deviation accuracy is ± 1 lb/sec in measured flow and approximately ± 22 MW in measured power

5.4 CORE TEMPERATURES

5.4.1 Placement of Sensors

The thermocouple locations in NRX-A5 differed from previous reactors chiefly in that some of the locations were planned to yield greater post test information. The locations were selected to achieve balance* between the effects of radius, axial position, and circumferential position and thus permit the statistical evaluation of these combined effects. Briefly, the thermocouples were installed in four axial stations - 8, 20, 26, and 32 inches; four radial positions - 2, 10, 14, and 16 inches; two circumferential regions - 120 degrees and 300 degrees; and either on-drums or between drums. In summary, the complete requirement of locations on this statistical basis represent 2^6 possible combinations of which one half were selected and utilized in the identification of thermocouple placements in the core. Additional thermocouples were placed in the NRX-A5 which exceeded the total number required by the statistical approach. These additional thermocouples were placed primarily for reactor control purposes. There were also three thermocouples at station 0.5 inches and three at station 1.0 inch in the NRX-A5. These six thermocouples were located in a 0.024 inch diameter hole drilled into the inlet end face of fuel elements, 1A1G, 5J9T, and 6J4H. Table 5-4 shows the core locations where thermocouples were positioned for the statistical analysis. Several of the thermocouple locations were duplicated in the central element by using more than one shim hole.

The analysis of the temperatures measured by the sensors shown in Table 5-4 takes the form of analysis of variance; a powerful tool which compares the observed variance attributed to planned or expected causes (such as core radius) with the residual, or random variance in the data.** The results of the statistical analysis of the thermocouples placed in the planned experiment is included in Section 5.4.9.

---

* An equal number of thermocouples at each different position.

** Parratt, Lyman G., Probability and Experimental Errors in Science, Wiley, New York, 1961. Davies, O. L., Design and Analysis of Industrial Experiments, Hafner, New York.

TABLE 5-4

INSTRUMENTATION FOR ANALYSIS OF VARIANCE IN NRX-A5

Cluster	Radial Distance (inches)	Station	Number of Thermocouples
1A1	2	8	1
		26	1
3A1	2	8	1
		26	1
4A1	2	20	1
		32	1
6A1	2	20	1
		32	1
3E1	10	20	1
		32	1
6E1	10	8	1
		26	2
3F3	10	8	1
		26	1
6F3	10	20	1
		32	1
3G1	14	8	1
		26	1
6G1	14	20	1
		32	1
3H3	14	20	1
		32	1
6H3	14	8	1
		26	1
2J9Q	16	20	1
		32	1
3J3Q	16	8	1
		26	1
5J9Q	16	8	2
		32	2
6J3Q	16	20	1
		32	1

5.4.2 Radial Core Temperature Distributions

5.4.2.1 Radial Temperature Profiles for EP-III and EP-IV

The measured thermocouple data is shown in Figures 5-1 through 5-4 as a function of radial position for two steady state hold times in EP-III and two in EP-IV. All of the data was utilized; not just the core thermocouples corresponding to the locations shown in Table 5-4. The multiple regression curve fit at each station and hold time is also shown with its three standard deviation error. This error represents the actual random temperature variation after subtracting the effects of instrument accuracy (error band).

The total random variation (3σ Total) includes the actual random temperature variation as well as the accuracy with which an individual temperature can be determined. The accuracy for each thermocouple reading (3σ Read) at full power is $46^{\circ}R$ at station 8, $100^{\circ}R$ at station 20, $117^{\circ}R$ at station 26, and $150^{\circ}R$ at station 32. The random temperature variation ($3\sigma_{Temp}$) is found by following equation:

$$3\sigma_{Temp} = \sqrt{(3\sigma_{Total})^2 - (3\sigma_{Read})^2}$$

The radial core temperature profiles for the first hold, the low power (229 MW) hold at the start of EP-III, are shown in Figure 5-1. The control drum position was 97 degrees. A slight radial dependence to the curve fit and small random errors in the data are evident. The total random error in the data is less than the instrument accuracy (thermocouple reading error) for stations 20, 26, and 32.

Figure 5-2 shows the radial core temperature profiles at the start of the first full power hold, CRT 25400 seconds in EP-III, at a control drum position of 109.2 degrees. The temperatures are flat with random variations from element to element. The random variations are larger than for the low power hold. Figure 5-3 shows similar data at the start of EP-IV at a control drum position of 114.8° (which corresponds to the core orificing angle). The random errors at stations 20 and 26 are slightly larger than at the start of EP-III due to the effect of mid-band corrosion, however, the temperature profiles are also flat.

At the end of life, the thermocouples in the core central region showed significant reductions in temperature due to pinholing and subsequent interstitial flow, see Section 5.4.4.2. Therefore, these thermocouple readings were excluded from the multiple regression analysis at the end of life. Figure 5-4 shows the temperatures and radial curve fits at the end of EP-IV, 13812.5 seconds (CRT). These curve fits indicate a strong radial dependence. Because of the lack of data at the core center, the curve fits were extrapolated in this region. Section 5.4.9 contains an additional discussion of the statistical analysis approach and comparisons with NRX/EST start of life (SOL) and end of life (EOL) core temperatures.

Figure 5-1. NRX-A5 EP-III CRT 25242.5 Drum Angle = 97 Degree Temperature versus Radius

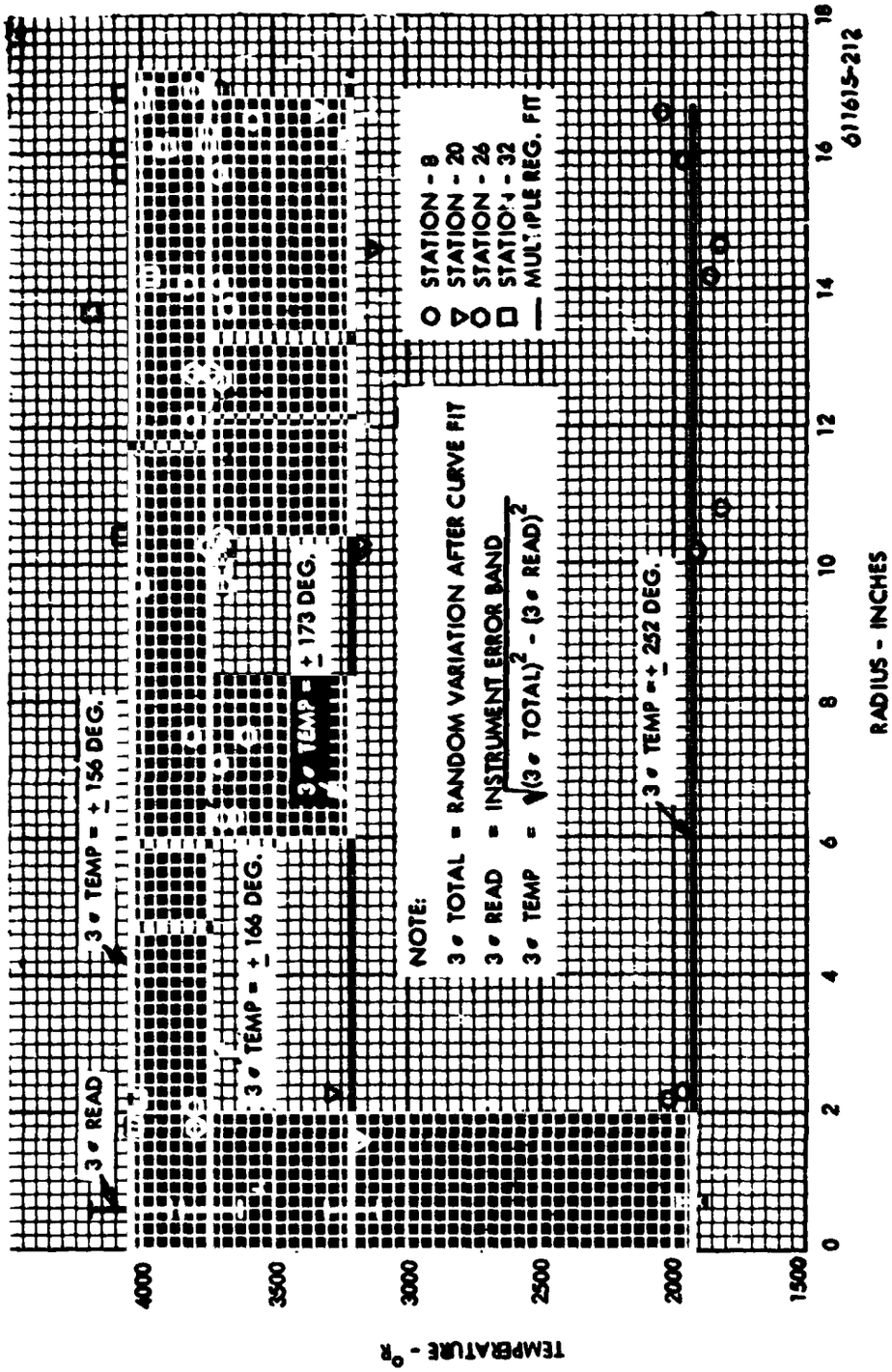

Figure 5-2. NRX-A5 EP-III SOL CRT 25400 Drum Angle = 109 Degree Temperature versus Radius

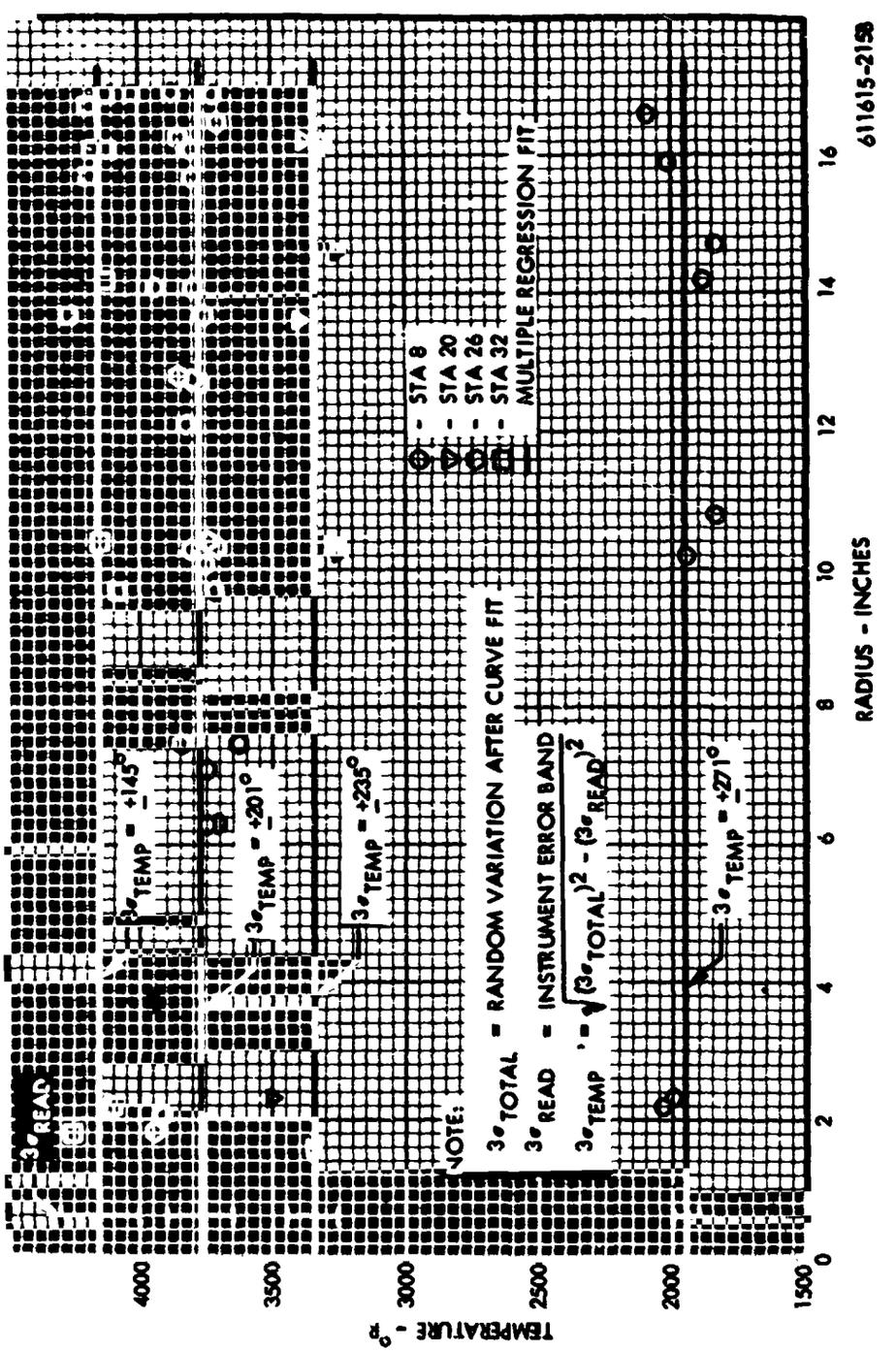

Figure 5-3. NRX-A5 SOL EP-IV CRT-13002. 5 Drum Angle = 114. 8 Degree Temperature versus Radius

CONFIDENTIAL

Figure 5-4. NRX-A5 EOL EP-IV CRT-13812, 5 Drum Angle = 145 Degree Temperature versus Radius

CONFIDENTIAL

5.4.2.2 TRACK Analysis

The NRX-A5 core was orificed to achieve a flat radial fuel temperature distribution at the design conditions* of 1120 MW power, 115 degree control drum position, 71.3 lb/sec flow rate, 242°R core inlet temperature, and 573 psia nozzle chamber pressure. Since the core operated very close to these design point conditions throughout most of the power runs, it is not surprising that the observed radial temperature distributions are relatively flat, except at the end of life.

Radial core temperature distributions were calculated by the TRACK** computer program using a model of a 30 degree symmetric segment of a fuel cluster which included the central unfueled element, associated hardware, and adjacent fueled elements. Radial conduction is considered at the core stations used in the model.

Figures 5-5 and 5-6 show the calculated radial sensor and fuel temperature distributions at stations 26, 32, and 44 at two full power holds in EP-IV. Also shown for comparison are the multiple regression curve fits of the measured sensor temperatures.

The core operating conditions at these two holds are shown in Table 5-5 and compared with the design values. Except for the control drum position at end of life, (CRT 13812.5) all of the parameters are close to the design values. The measured and calculated sensor temperatures are in agreement within the accuracy limits of the measurements.

---

* WANL-TME-1389 "NRX-A5 Reactor Analysis Data"

** A. Y. Lee, M. D. Woods, and A. G. Eggers, "Transient Analysis of a Heat Generating Solid and its Application to NERVA Reactor Control Drums", AIAA Paper No. 66-575.

TABLE 5-5

NRX-A5 CORE C ERATING CONDITIONS IN EP-IV AND COMPARISON WITH DESIGN VALUES

Condition	CRT-13002.5	CRT-13812.5	Design*
1. Reactor Power, MW	1120	1112	1120
2. Reactor Flow, lb/sec	71.1	71.2	71.3
3. Control Drum Position, Degrees	114.8	145	115
4. Core Inlet Temperature, °R	238	243	242
5. Nozzle Chamber Temperature, °R	4114	4089	4090
6. Nozzle Chamber Pressure, psia	566	558	573
7. Core Pressure Drop, psid	118	117	125
8. Average Fuel Exit** Gas Temperature, °R	4310	4275	4283

* WA[illegible]-TME-1389, "NRX-A5 Reactor Analysis Data."

** Calculated From Measured Data

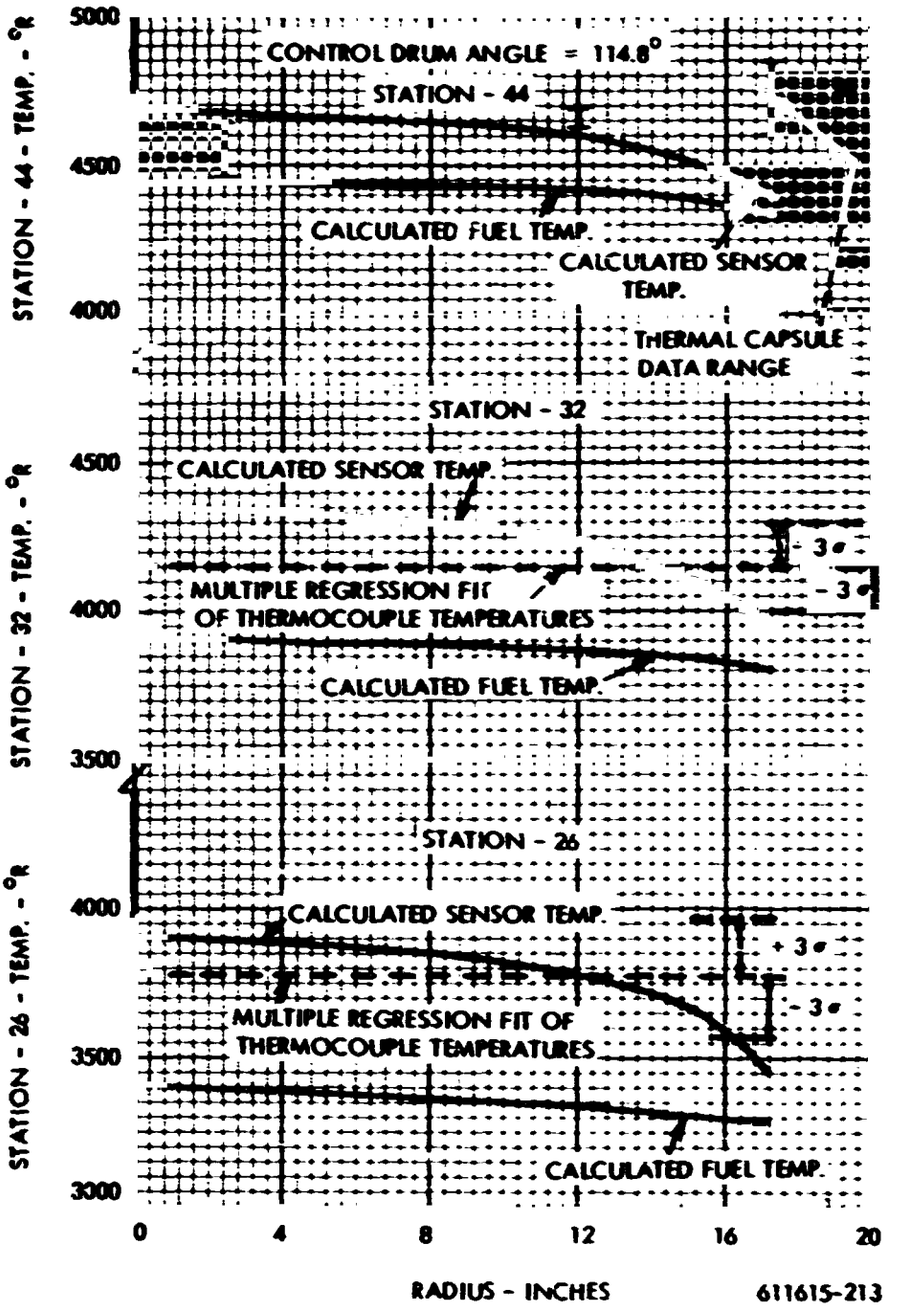

Figure 5-5. NRX-A5 EP-IV SOL CRT-13002.5 Comparison of Calculated and Measured Temperature

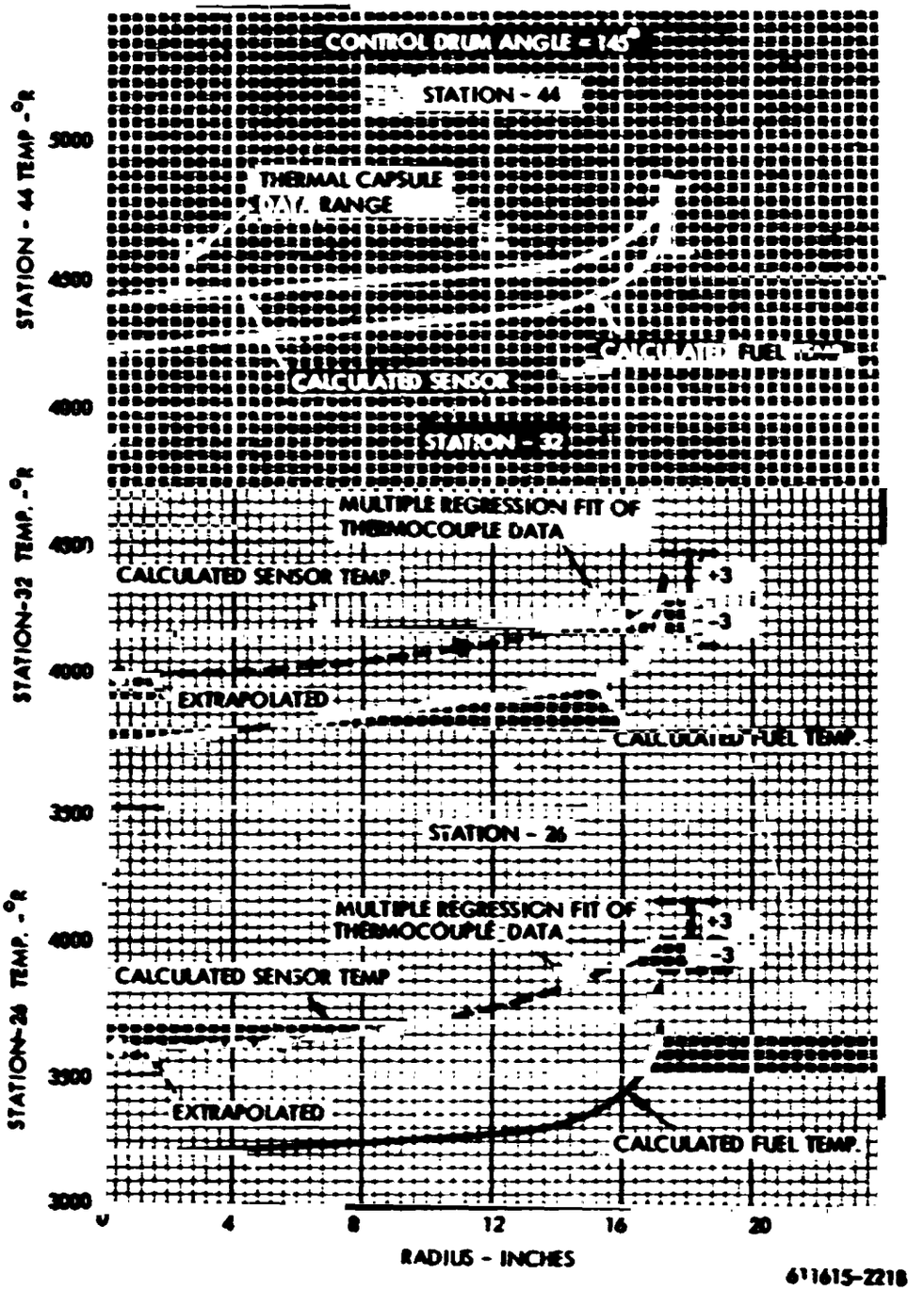

Figure 5-6. NRX-A5 EP-IV EOL CRT-13812.5 Comparison of Scale and Measured Temperature

5.4.3 Axial Temperature Profiles

Axial temperature profiles at the start and end of EP-IV are presented for the three radial regions (central, trough, and peripheral) which are described in Figure 5-7. These regions were selected on the basis of the observed corrosion behavior and the nominal radial power distribution which is also shown in Figure 5-7. The axial temperature profiles were calculated with the TRACK cluster model using the as-built orificing and the measured power and plenum conditions. The core design axial power distribution shown in the NRX-A5 data book,* Index E.5.g.12 was used for the calculation. Calculated temperatures between stations 0 and 8 inches are not presented because the presently available convective heat transfer correlations are in error in this region.

Figure 5-8 shows the calculated axial temperature profiles in the central region of the core at the start of EP-IV and Figure 5-9 shows the axial profiles at the end of EP-IV (EOL). The decrease in the central region temperatures due to corrosion and control drum roll-out is clearly evident by comparing the data on Figures 5-8 and 5-9. All of the curves include a tabulation of the pertinent core operating conditions. The thermal capsule data indicates the highest temperatures experienced during the lifetime of the core. For the central region the maximum temperatures probably occurred at the start of life. The sharp decrease in the stations 20, 26, and 32 measured temperatures which are shown in Figure 5-9 is caused by severe local corrosion. (See Section 5.4.5 for a detailed discussion.)

The measured and calculated temperatures in the trough radial region are shown in Figure 5-10 for start of EP-IV and in Figure 5-11 for end of EP-IV. The agreement between measured and calculated temperatures is quite good in the trough region, as may be expected since this region had smaller temperature variations as a result of gross corrosion, drum movement, and inlet temperature asymmetry than the central and peripheral regions.

---

* WANL-TME-1389, "NRX-A5 Reactor Analysis Data."

The temperatures in the peripheral region shown in Figures 5-12 and 5-13 increased significantly during the EP-IV high power hold. The thermal capsule data which corresponds to the end of life conditions only is shown on Figure 5-12 for comparison.

NRX-A5 had a considerable quantity of the instrumentation placed in corresponding element locations in six core sectors. Therefore, it is possible to obtain some well-defined axial temperature profiles using at least two sensors at every station. In addition, the thermal capsule data provided additional temperatures for these axial profiles. Figure 5-14 shows the measured axial temperature profile at the core center at the start of the EP-IV high power hold. The sensors are all in the A1A elements of the six sectors. The curve shows that the temperatures are in agreement. There is little difference between the thermocouple and thermal capsule readings.* Similar data and results are shown for the core periphery at end of life. Figure 5-15 shows all measurements in elements J9Q (six sectors), and Figure 5-16 shows all measurements in elements J3P and J3Q in the six sectors. It is to be noted that the elements 3J9Q (Figure 5-14) and 5J3P (Figure 5-16) were located in the hot buffer periphery zone. The data indicates that the temperatures in the hot buffer periphery may have been cooler than expected. The possible effect of the hot buffer periphery on the core temperatures is discussed in more detail in Section 5.4.4.3.

---

* The accuracy of an individual temperature reading is ± 100°R for the thermal capsules and ± 46°R, ± 100°R, ± 117°R, ± 150°R for each of the station 8, 20, 26, and 32 thermocouples respectively. These accuracies represent three standard deviation extremes.

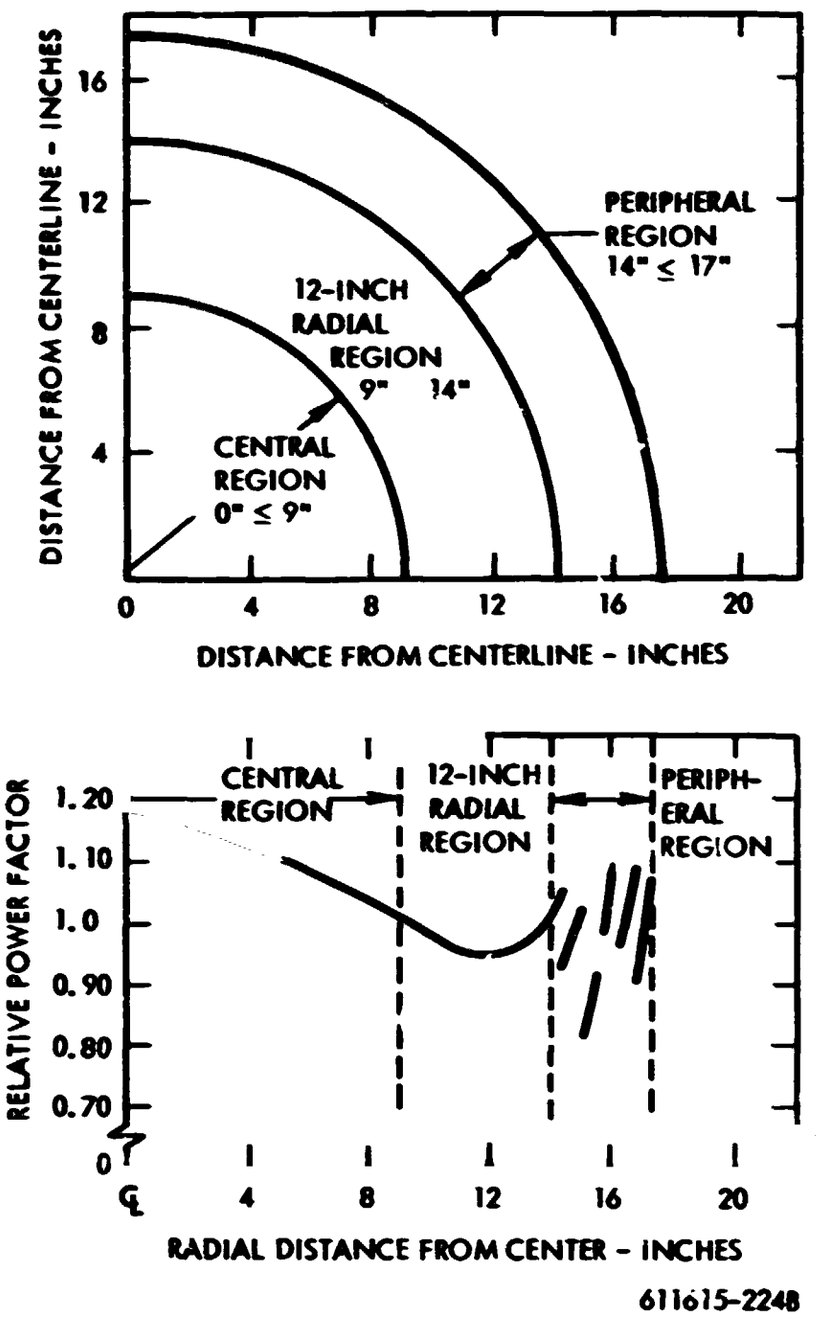

Figure 5-7. Quarter Cross Section of Core Regions of Discussion and NRX-A5 Nominal Radial Power Distribution

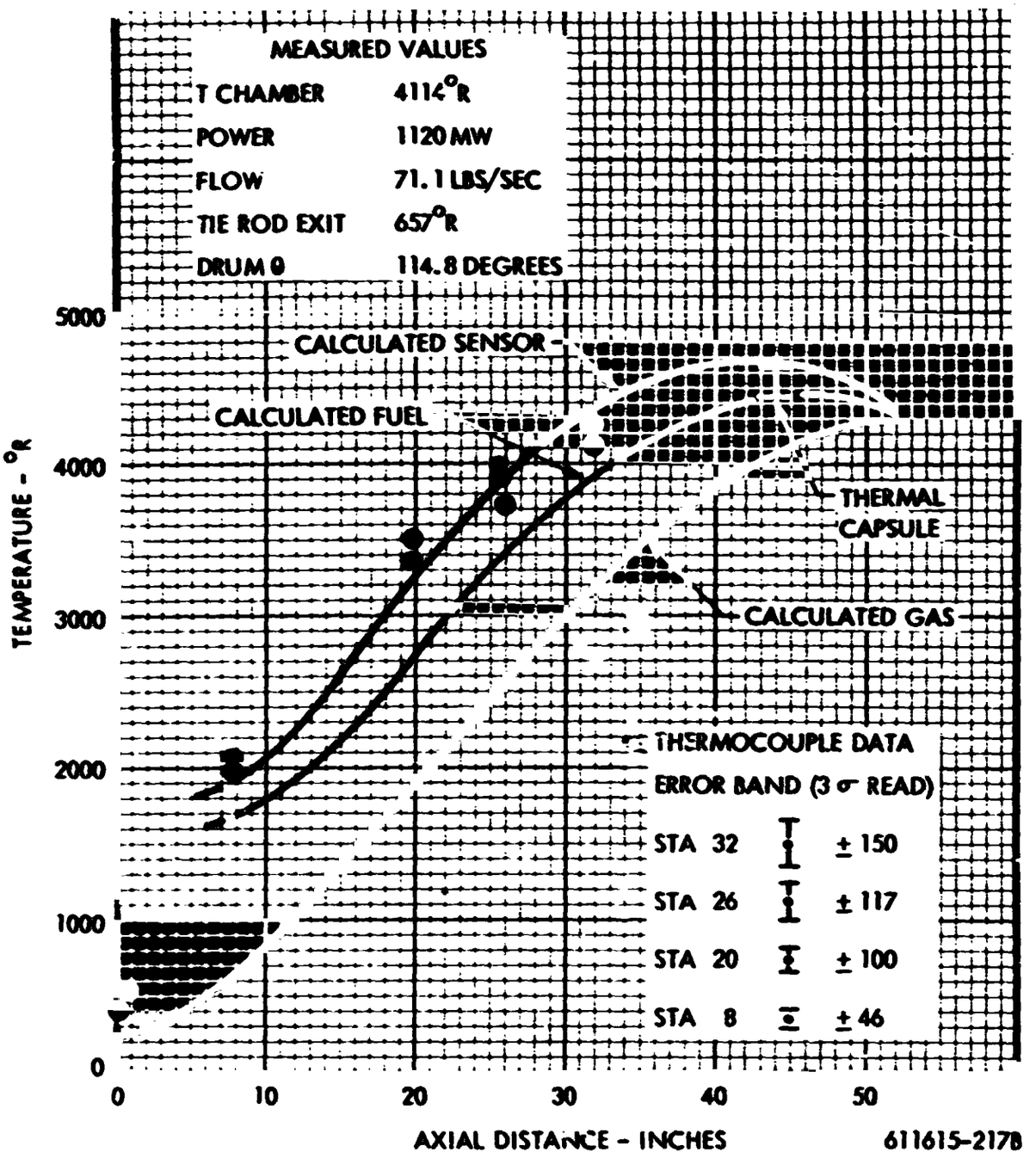

Figure 5-8. Axial Temperature Profile NRX-A5 EP-IV SOL CRT-13002.5 Central Region

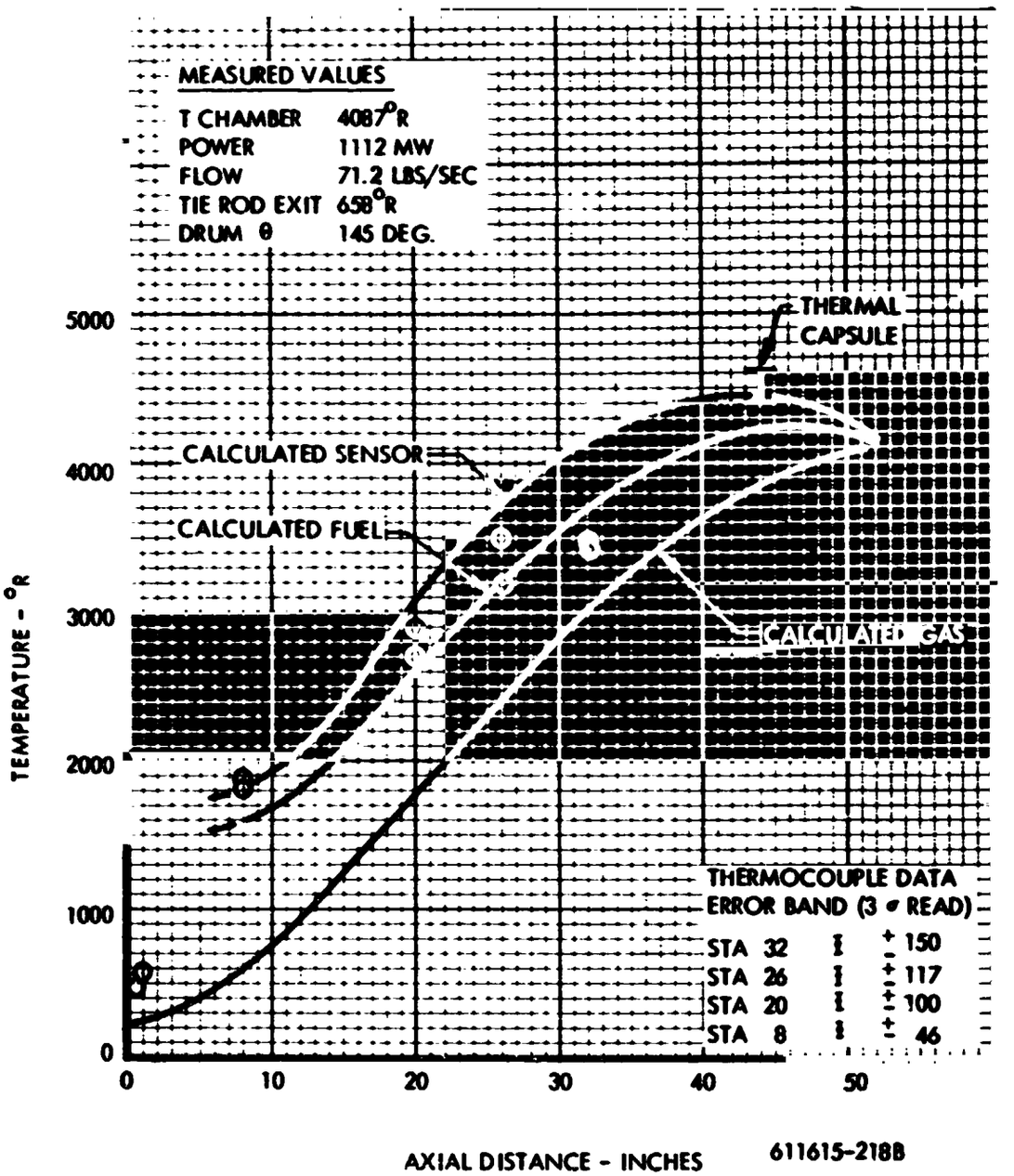

Figure 5-9. Axial Temperature Profile NRX-A5 EP-IV EOL CRT-13812.5 Central Region

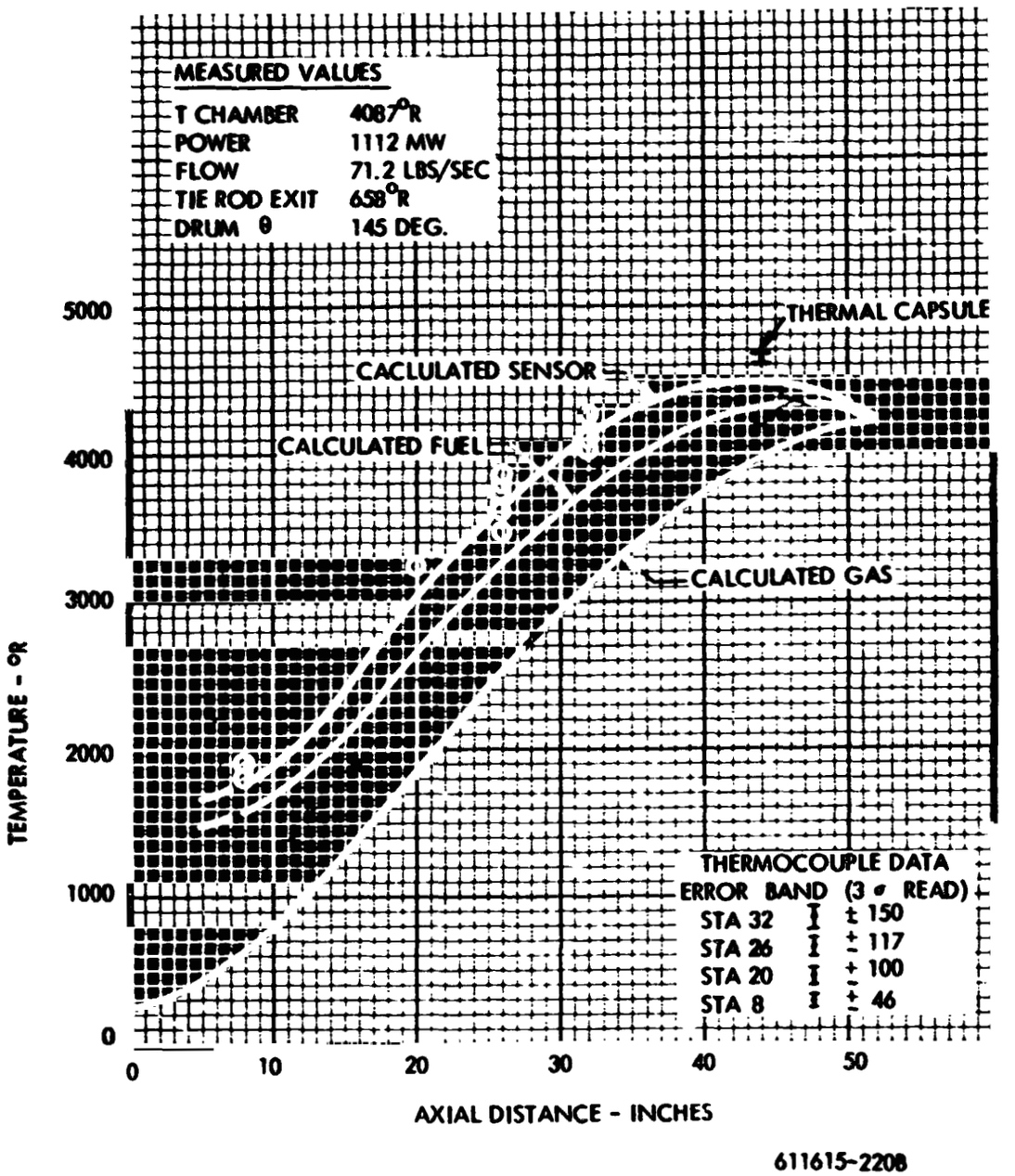

Figure 5-10. Axial Temperature Profile NRX-A5 EP-IV SOL CRT-13002.5 Trough Region

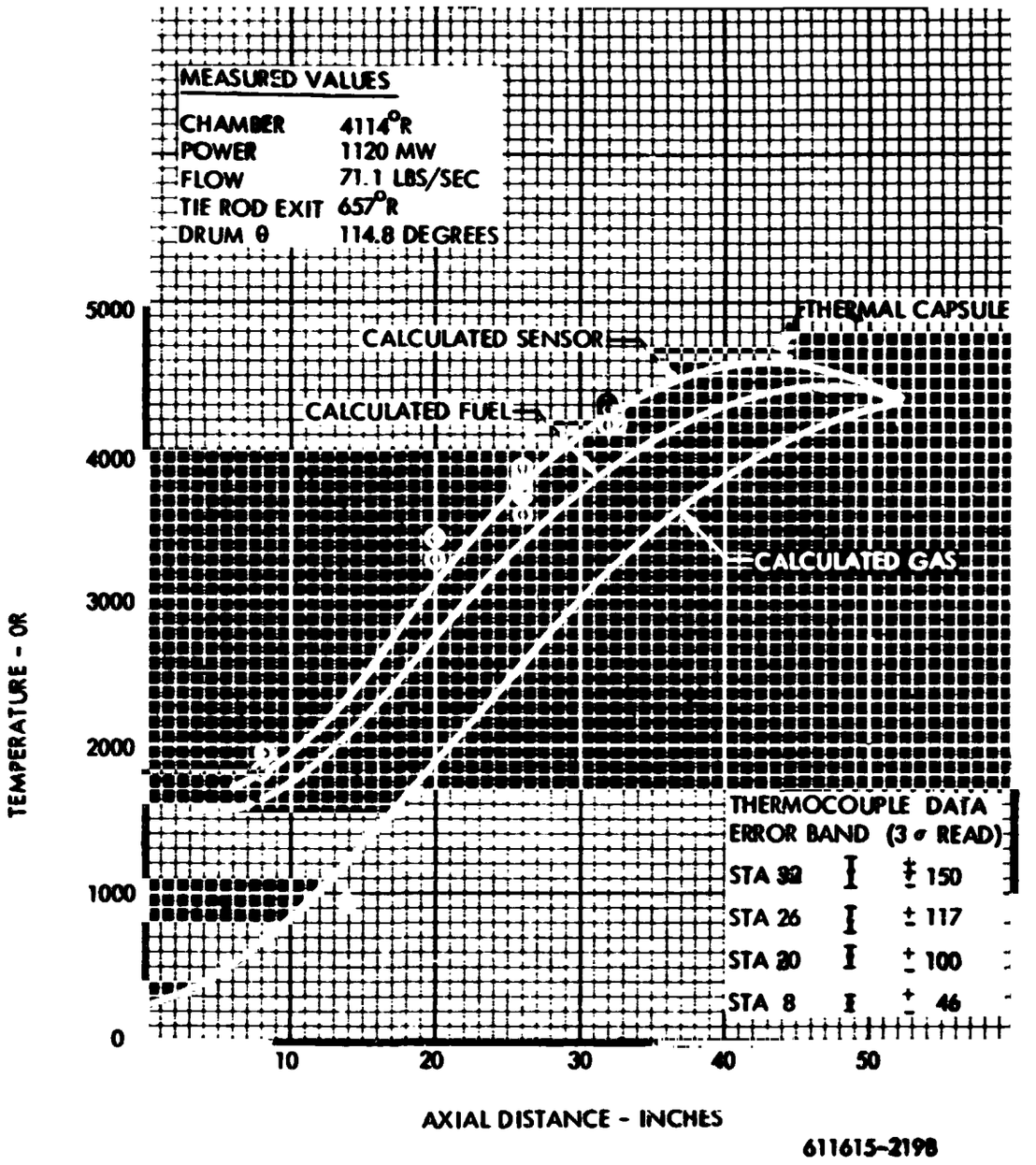

Figure 5-11. Axial Temperature Profile NRX-A5 EP-IV EOL CRT-13812.5 Trough Region

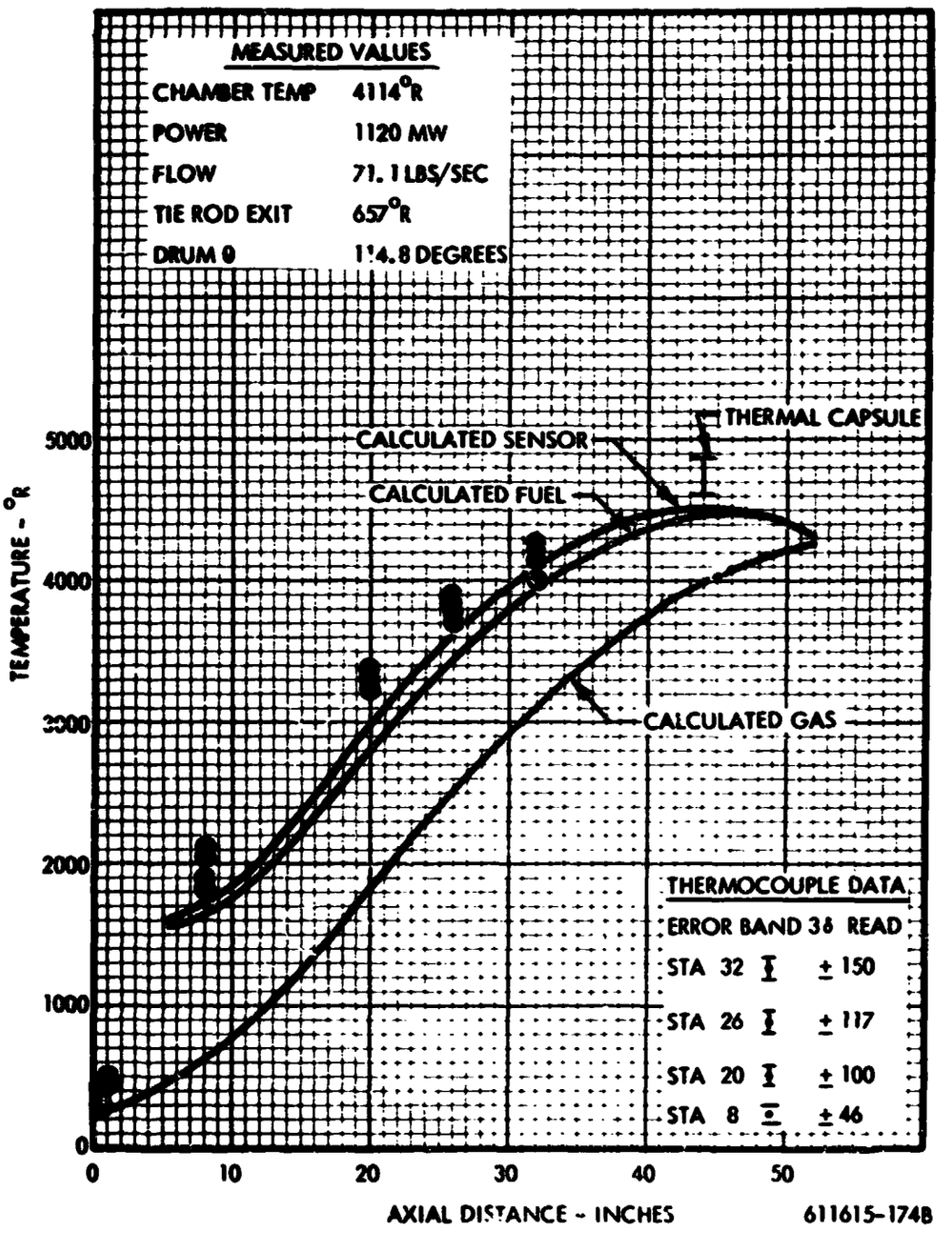

Figure 5-12. Axial Temperature Profile NRX-A5 EP-IV SOL CRT-13002.5 Peripheral Region

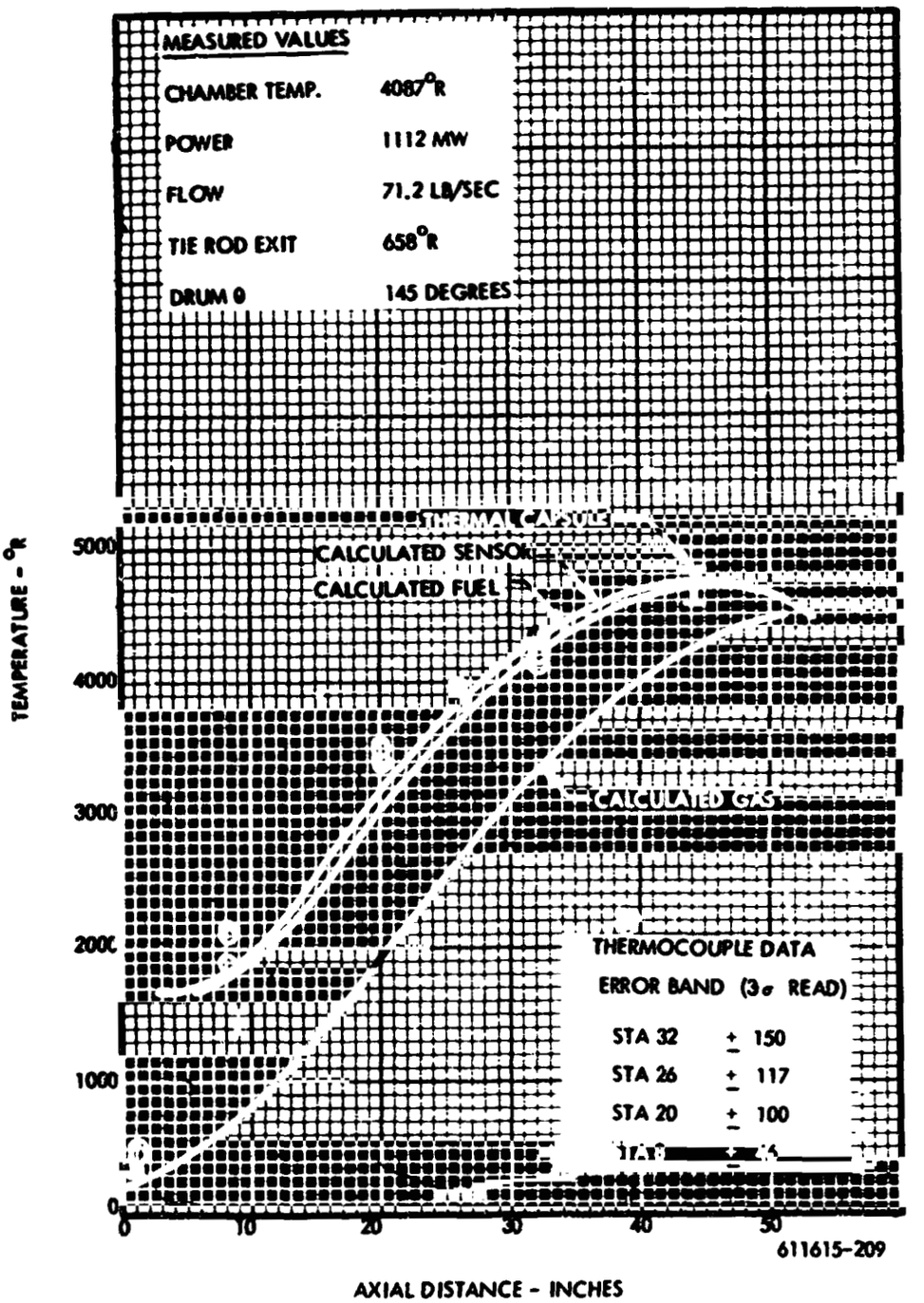

Figure 5-13. Axial Temperature Profile NRX-A5 EP-1V EOL CRT-13812.5 Peripheral Region

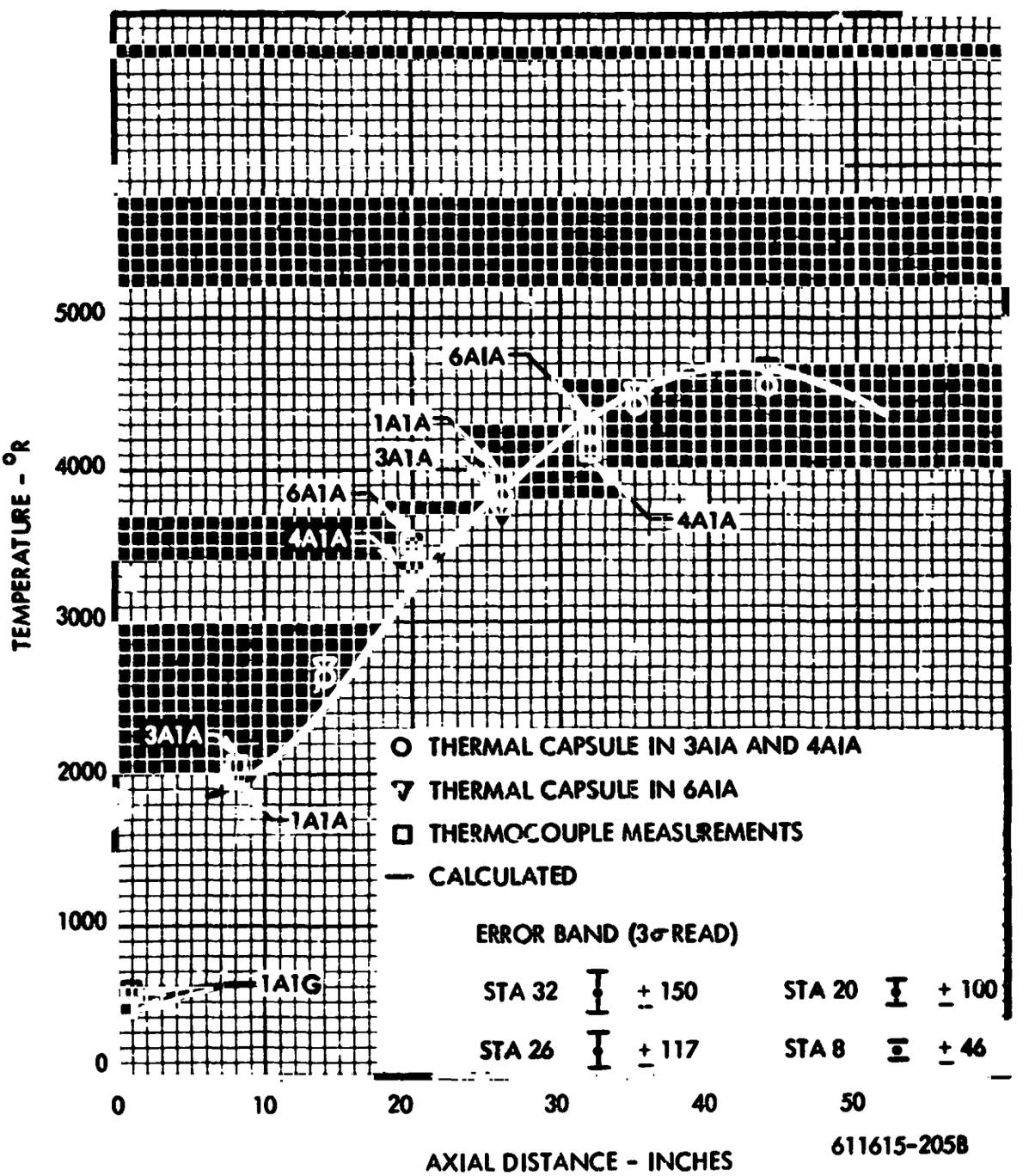

Figure 5-14. Axial Sensor Temperature Profile in the AIA Elements at SOL NRX-A5 EP-IV SOL CRT-13002.5

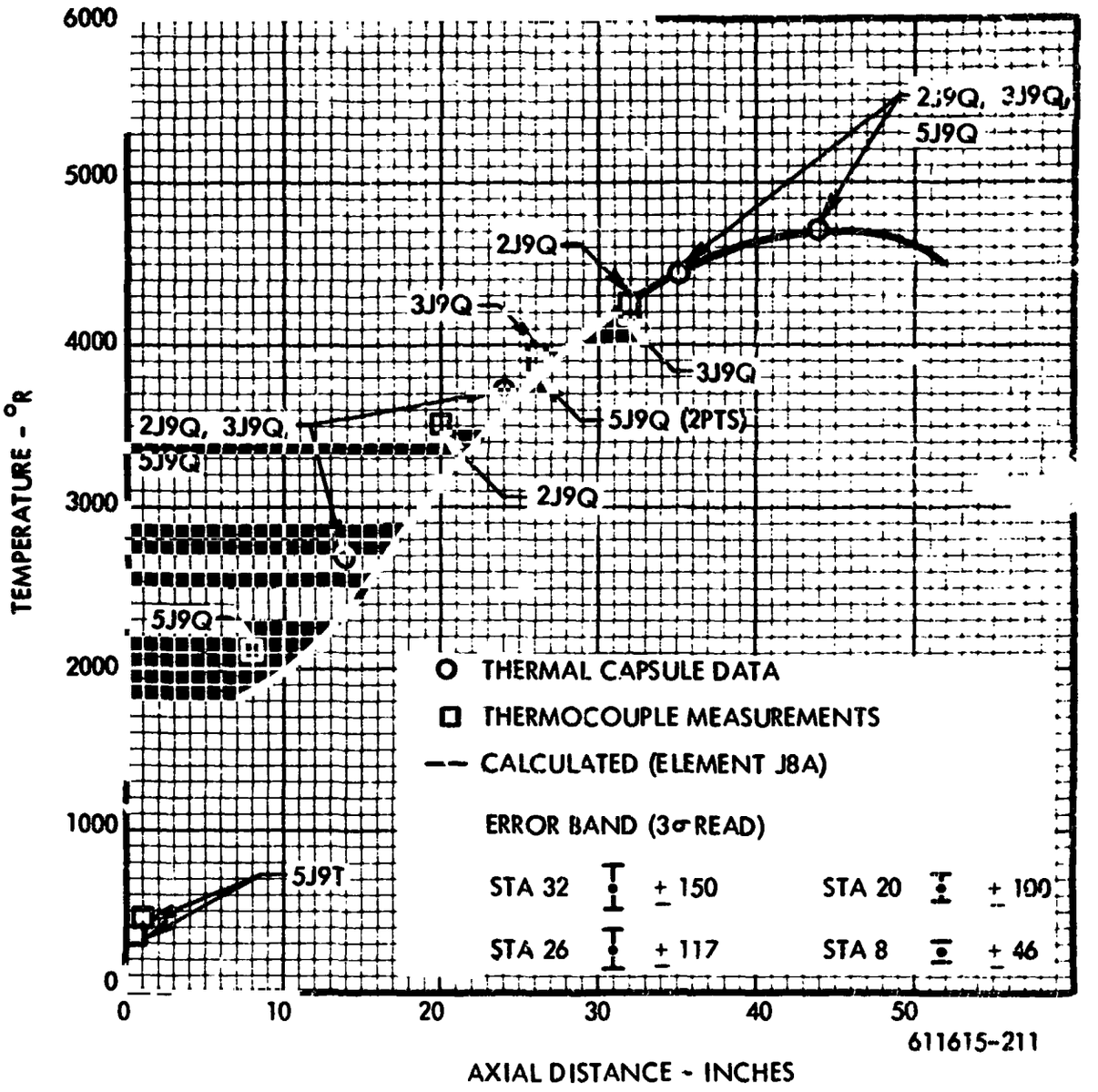

Figure 5-15. Axial Sensor Temperature Profile for J9Q Elements at EOL NRX-A5 EP-IV EOL CRT-13812.5

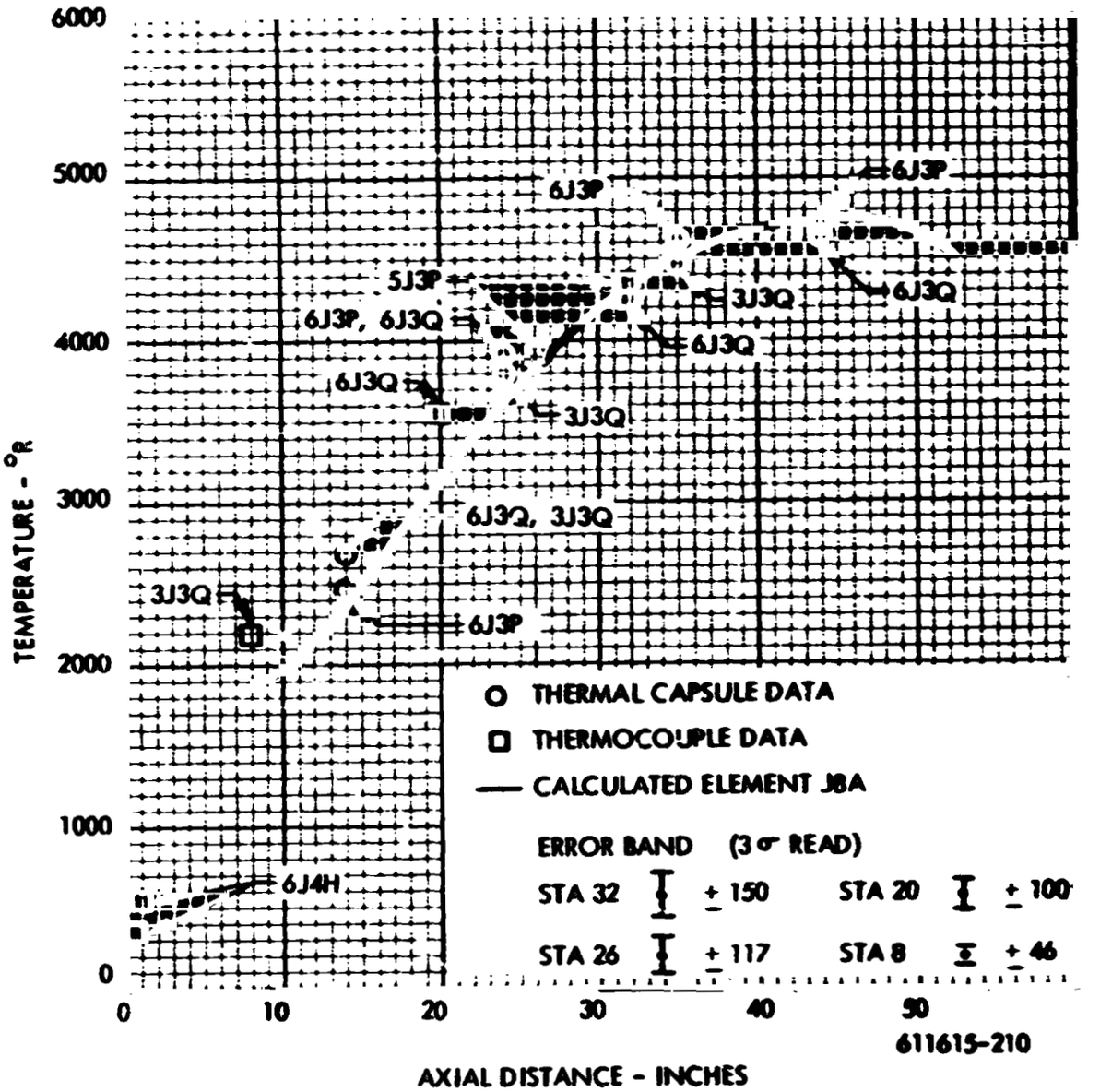

Figure 5-16. Axial Sensor Temperature Profile for J3 Cluster Elements at EOL NRX-A5 EP-IV EOL CRT-13812.5

5.4.4 Perturbations on Core Temperature Distributions

5.4.4.1 Control Drum Position

The large control drum roll-out strongly influenced the peripheral temperatures at the end of life in both NRX-A5 and NRX EST. The effect of control drum position on the radial temperature distribution is described in Section 5.4.2 and the effect on the thermal capsule measurements is described in Section 5.4.6. Table 5-6 shows the temperature increase due to control drum position increase from 114.8 degrees to 145 degrees during EP-IV at locations on drums (J9Q) and off-drums (J3Q and J3P). Also shown are the calculated temperature increases using the predicted power factor changes from PFENCE* in the MCAP* core model. As expected, the calculated temperature increases are larger for the on-drum core location than the off-drum location. However, the measured temperature increases do not show this characteristic. At core stations 1, 8, and 26, the measured temperature increase for the off-drum location is greater than calculated and is also greater than the measured increase for the on-drum location. At station 20, the measured temperature increase is greater than calculated at both locations and the measured increase for on-drums is greater than off-drums. The measured station 32 temperature increases average about the same at both core locations and both are less than calculated.

Probably the major reasons for these discrepancies are that the measured increases are calculated from small differences between large numbers, and that the magnitude of the temperature increases are within the range of the calculation and measurement uncertainties. In addition, a logical explanation for the larger than predicted increase of station 20 temperatures may be the observed effect of mid-band

---

*See WANL-TME-1091 A detailed nuclear code for calculating individual channel power factors.

**WANL-TME-944 A multiple channel analysis program (MCAP) for the temperature distribution in an internally cooled heat generating solid cooled by a compressible gas.

corrosion prior to pinholing while the smaller than predicted increases of the station 26 and 32 temperatures may be caused by thermocouple saturation and/or by the removal of fuel material and increased interstitial flow as a result of corrosion. The thermocouples may saturate at temperatures above 4000°R and all of the station 32 thermocouples in the J row are at temperatures between 4119°R through 4340°R at the end of the EP-IV high power hold. However, there is no clear evidence at this time that any of the NRX-A5 station 32 thermocouples actually did saturate.

Figure 5-17 shows the increase in station 32 temperature with increase in drum angle for NRX-A5 at full power. The measured and calculated temperature changes are referenced to a zero net change using measured temperatures and a control drum position (114.8 degrees) at 13002.5 seconds CRT time (start of the EP-IV hold). The drum angle during life varies from 109° at SOL in EP-III to 145° at EOL in EP-IV. The station 32 temperatures for the J Row are shown on the figure. The average core radius for these sensors is 16.4 inches. The MCAP calculation results correspond to a core radius of 16.3 inches. The calculated range for the on and off-drum positions is shown by the dotted lines in the figure. The measurements and calculations agree reasonably well except at the EOL. The temperatures for the second hold (control drums at 112°) are lower than expected because the average fuel exit gas temperature was only 4085°R compared to 4310°R at the reference hold (13002.5 CRT seconds).

TABLE 5-6

TEMPERATURE INCREASE DUE TO CONTROL DRUM ROTATION 114.8° to 145°
EP-IV (CRT-13002.5 to CRT-13812.5)

$T_{SENS\ 2}$ = Sensor Temperature at CRT-13812.5

$T_{SENS\ 1}$ = Sensor Temperature at CRT-13002.5

On-Drums:

Station	Element	Temperature Change $T_{SENS\ 2} - T_{SENS\ 1}$ Observed		Calculated
1"	5J9T	27		32
8"	5J9Q	80		107
20"	2J9Q	211		176
26"	3J9Q	137	Avg. 134	217
26"	5J9Q	116		
26"	5J9Q	148		
32"	2J9Q	99	Avg. 101	242
32"	3J9Q	103		
44"	----	---		259

Off-Drums:

1"	6J4H	36		27
8"	6J3Q	97		66
20"	6J3Q	146		112
26"	5J3P	191		139
32"	5J3P	136	Avg. 105	155
32"	6J3Q	74		
44"	----	---		167

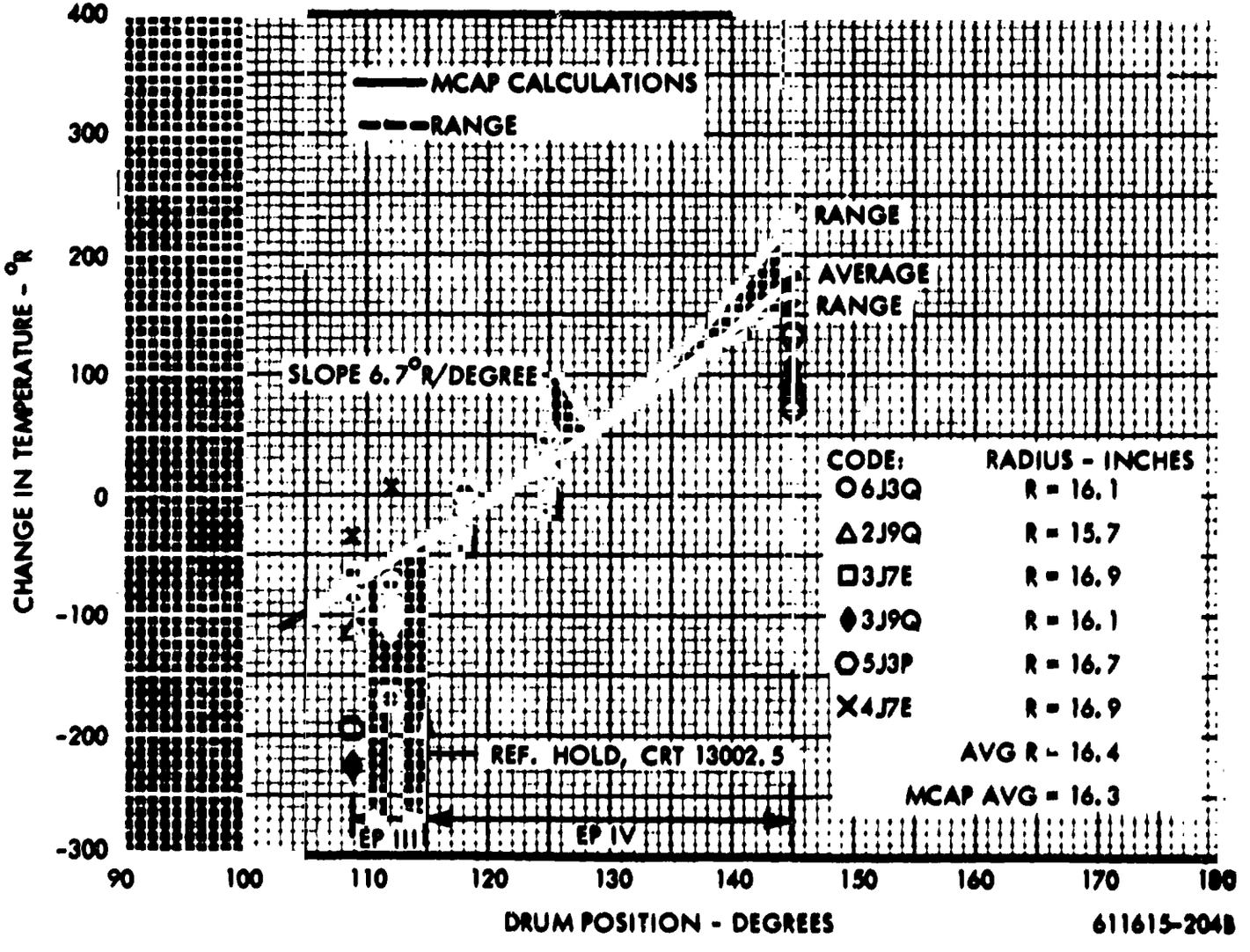

Figure 5-17. Comparison of the Measured and Predicted Fuel Temperature Change per Change of Drum Angle

5.4.4.2 Effects of Corrosion

The effect of mid-band corrosion on the thermocouple readings during EP-IV of NRX-A5 were similar to those observed during EP-IV A of NRX/EST. Figures 5-18 through 5-20 show the time traces for the station 20, 26, and 32 thermocouples near the end of the EP-IV high power hold. Note the series of sharp decreases in the T-668, T-625, T-680, T-621, T-678, T-664 and T-660 temperatures. These thermocouples are all located in the central region of the core. During this time period the other core thermocouples were showing either constant, or slightly increasing temperatures at the core edge due to drum rollout. The nozzle chamber temperature was also constant except for minor power trims. The sharp decreases in temperature of individual thermocouples are attributed to pinholes and channel exposure in adjacent fueled elements which result in increased interelement flow. Post test examination of these thermocouples revealed no damage which would prevent a true temperature reading.

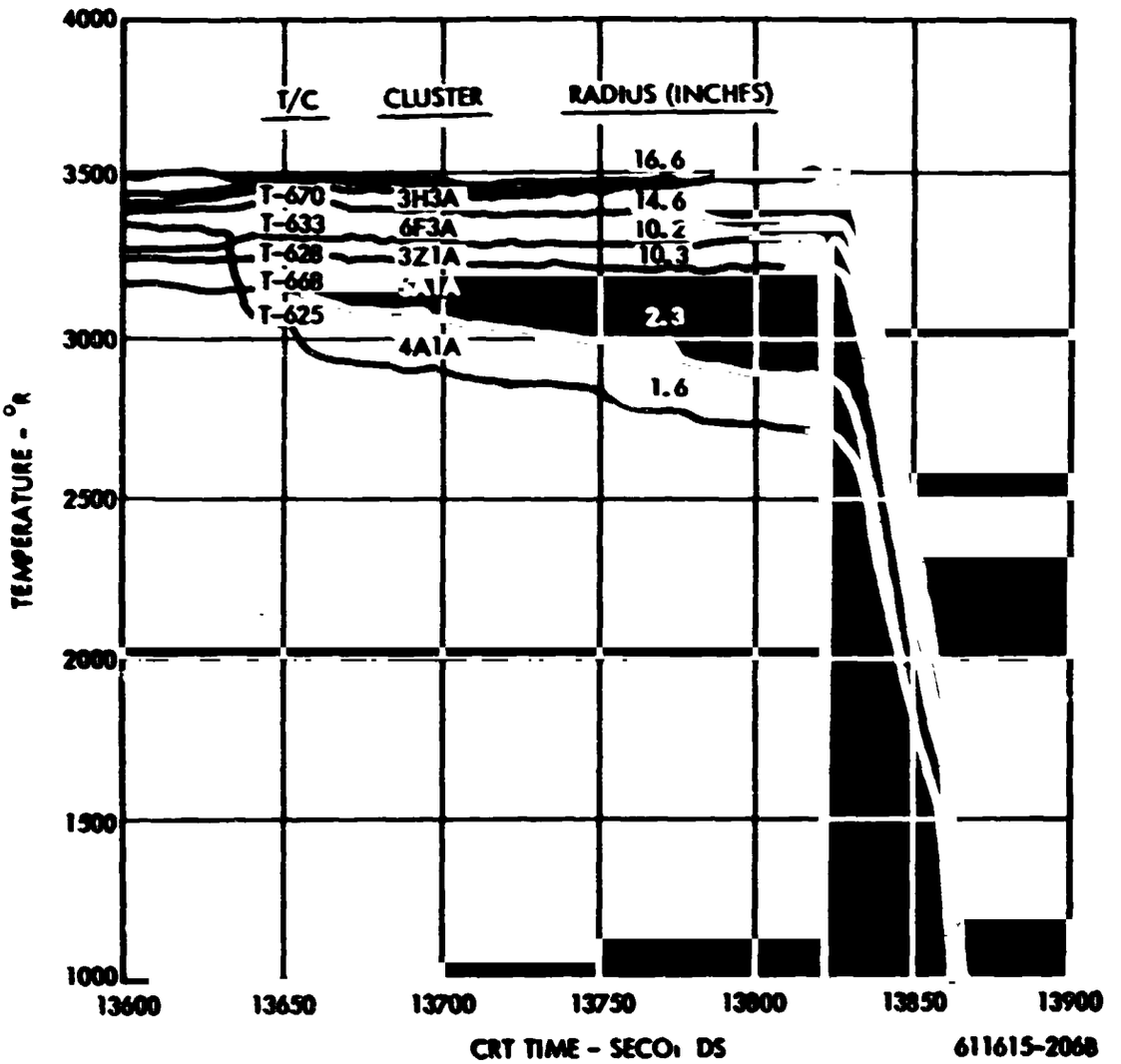

Figure 5-18. NRX-A5 EP-IV EOL Station 20 Core Material Temperatures

Figure 5-19. NRX-A5 EP-IV EOL Station 26 Core Material Temperatures - R 8 Inches

CONFIDENTIAL

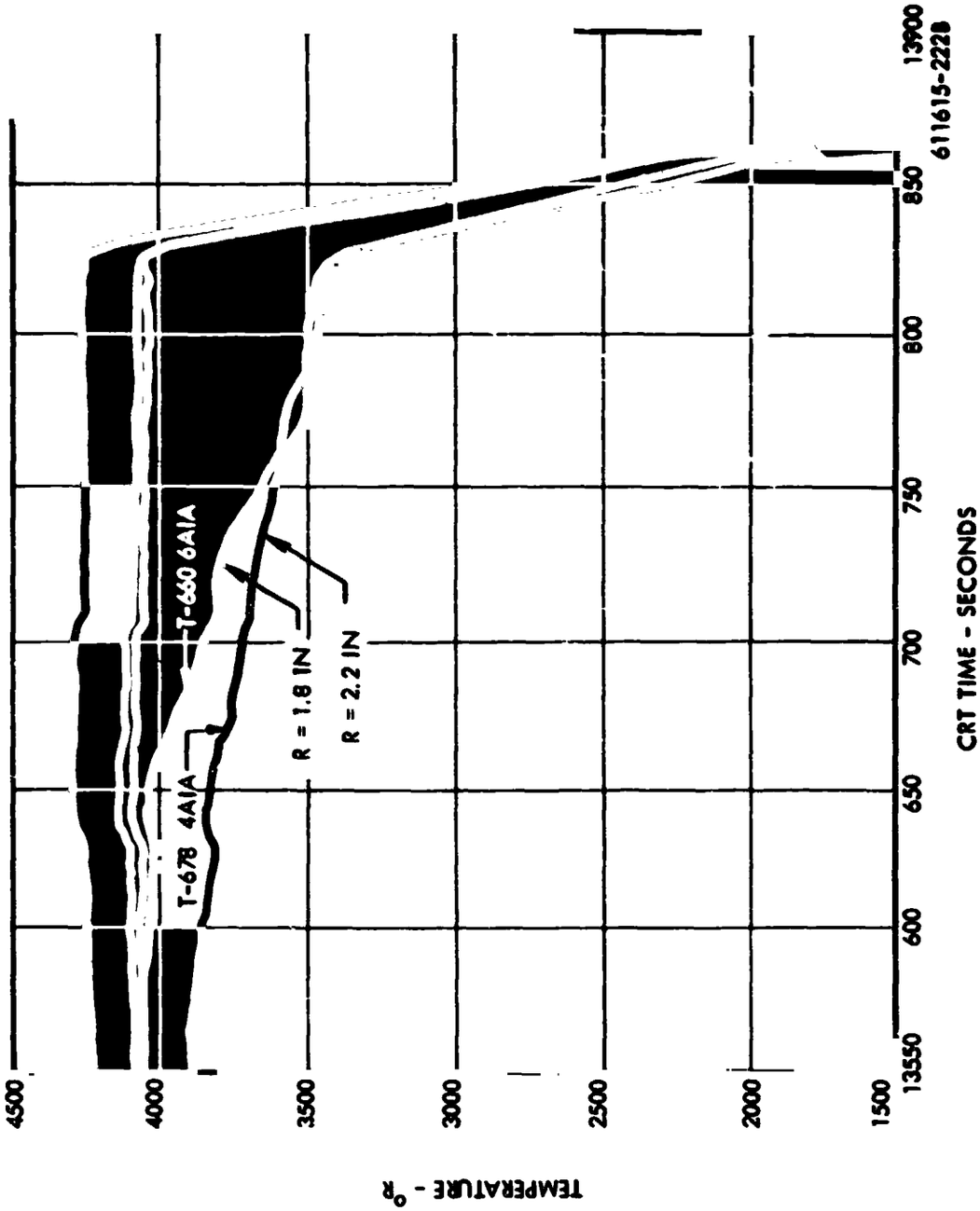

Figure 5-20. NRX-A5 EP-IV EOL Station 32 Core Material Temperatures - R 8 Inches

CONFIDENTIAL

5.4.4.3 Hot Buffer Periphery

A circumferential asymmetry was noted in the measured core material temperatures in the region of the hot buffer periphery (See Section 5.4.5). The measured core material temperatures were generally about 100°R cooler in the hot buffer region (1/2 of core sectors 3 and 5 and all of sector 4) than in the remainder of the core. This effect was noted at all steady state power holds except at the end of life. The reason for these cooler temperatures is attributed to a local reduction in the core inlet temperature in the hot buffer region (See Section 4.3.1 for additional discussion). A local decrease in the core inlet temperature of 10°R will cause a 50°R decrease in the channel exit temperature for a channel with a power factor of 0.9 relative to average (representative of the periphery). The local reduction of core inlet temperature is attributed to the fact that the filler strips in the hot buffer region are cooled by conduction to the adjacent fuel elements rather than by the flow in the lateral support region. The reduction in heat input to the lateral support flow could result in lower shield dome plenum and core inlet temperatures. The temperature asymmetry is not related to nozzle outlet temperature and/or the privy roof mounted shield as was the case in the NRX/EST, (NRX-A5 had no shield). Figures 5-21 and 5-22 show the azimuthal variation in the core inlet temperature, shield dome end temperature, and the reflector inlet temperature at the start and end of EP-IV. The reflector inlet temperatures are relatively constant within the 2σ accuracy of 6.6°R but the variation in the shield dome end temperature and core inlet temperature indicates that the source of the asymmetry is in the lateral support region. The additional heat conducted into the fuel elements from the uncooled filler strips does not significantly increase the core material temperatures at the edge because the amount of additional heat is relatively small compared with the fuel element power generation. The sensors are located in the first row of unfueled elements and the heat conducted from the filler strips does not cause a temperature increase beyond the second row of coolant channels in the outer row of fueled elements. Figure 5-23 shows the radial temperature distribution in element J9H in a direction perpendicular to the filler strip-element interface. The

temperature profile becomes nearly flat beyond the second row of channels, and hence the sensors are not influenced by heat conducted from the filler strips.

A minor contribution to the reduction in temperatures may be the reduced power generation at the hot buffer periphery because of the higher filler strip temperatures. This effect has been calculated to cause a 1 percent reduction in power although post test gross ionization measurements are inconclusive, (See Chapter 9).

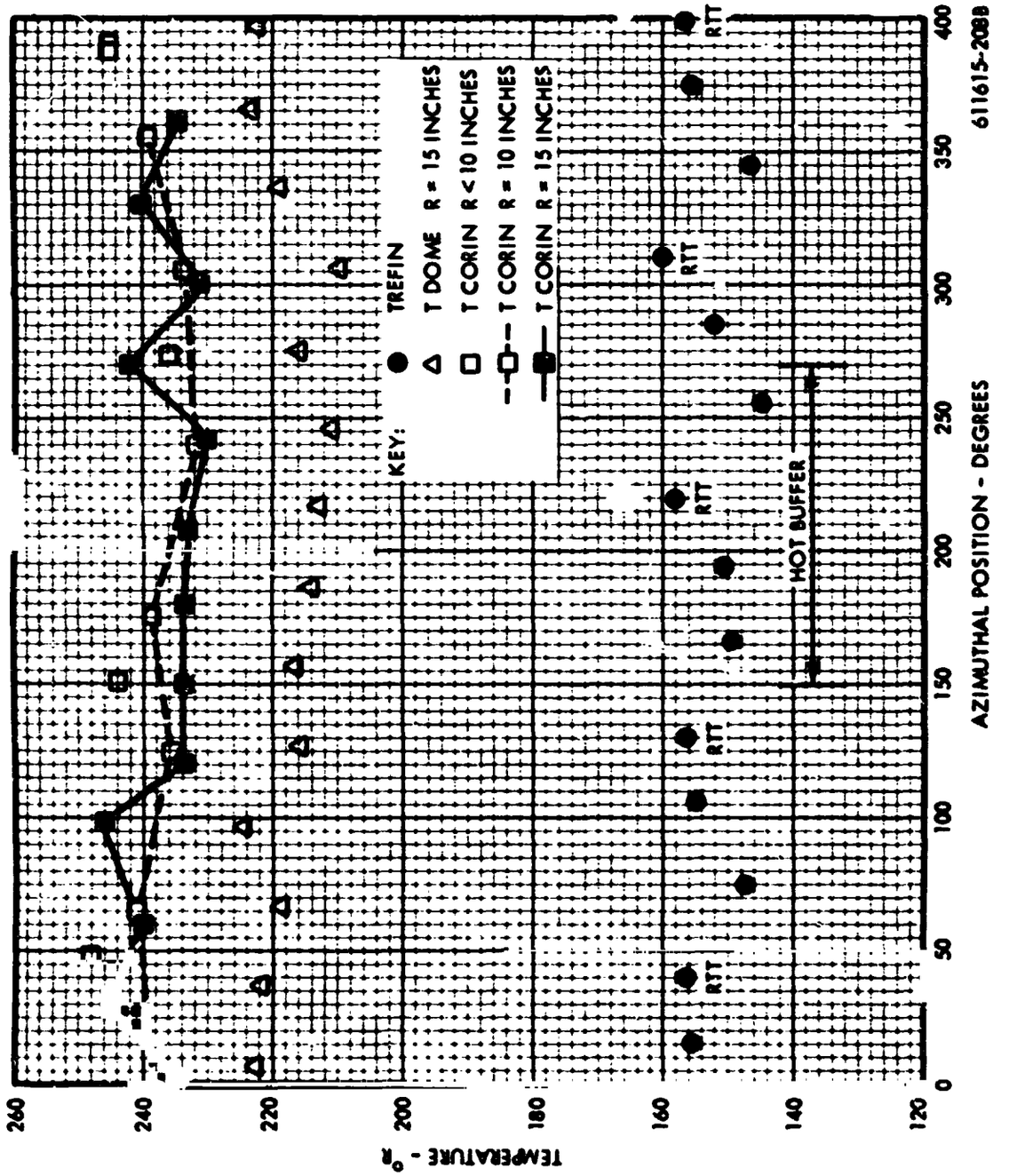

Figure 5-21. Azimuthal Temperature Variation in NRX-A5 Inlet EP-IV CRT-13002.5

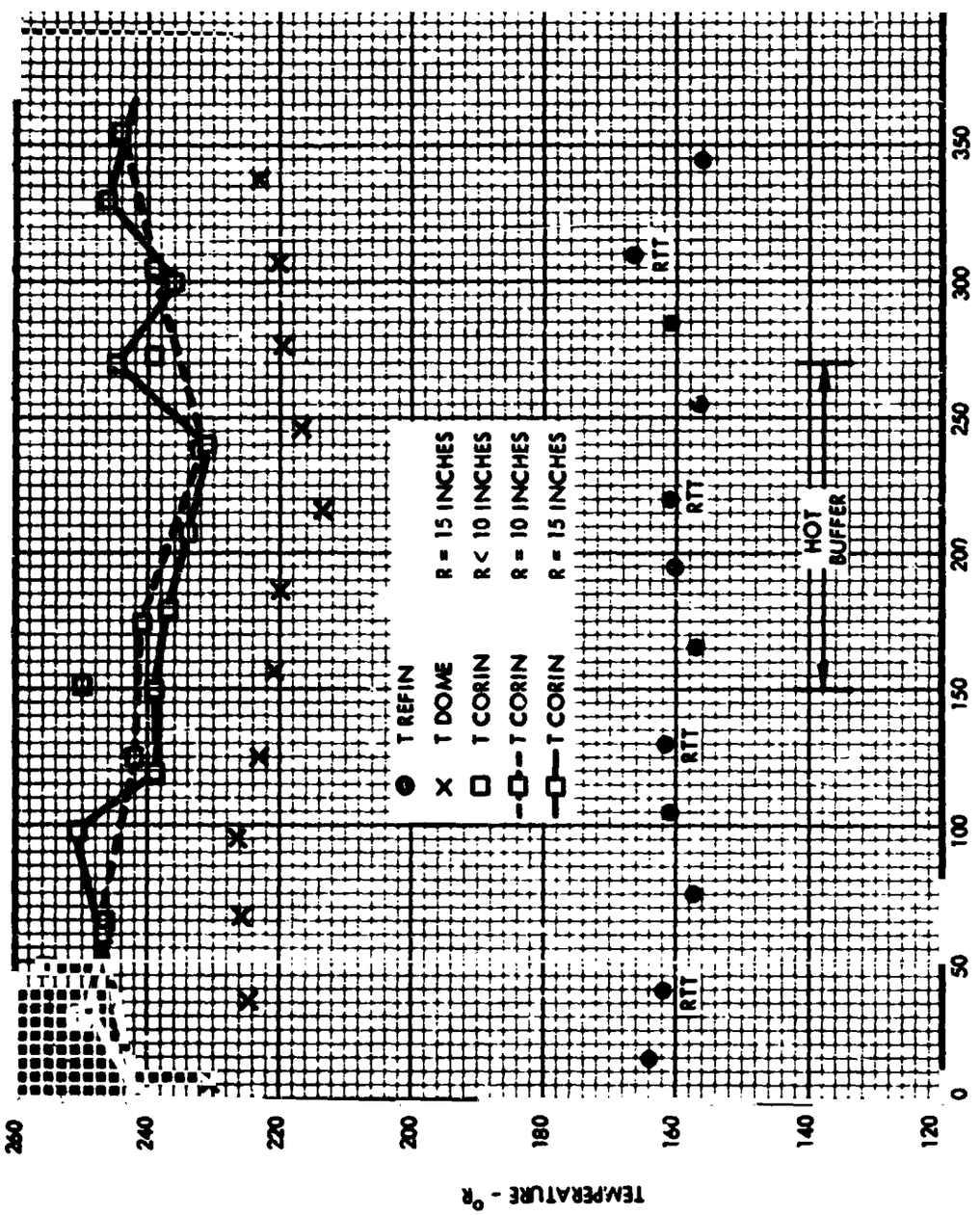

Figure 5-22. Azimuthal Temperature Variation in NRX-A5 Inlet EP-IV CRT-13812.5

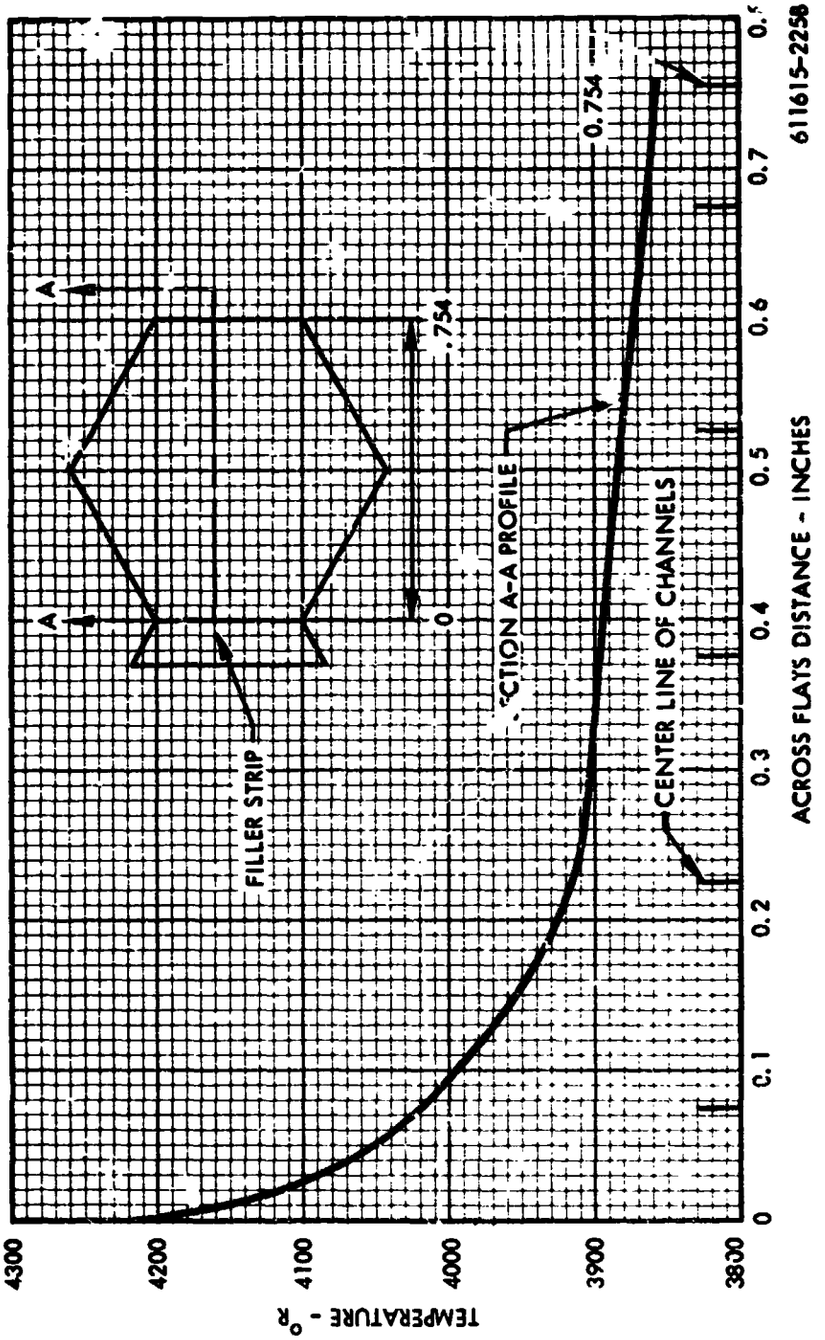

Figure 5-23. Radial Temperature Distribution Across J9H Adjacent to NRX-A5 Hot Buffered Peripheral - Steady State EP-IV EOL for Station 32

5.4.4.4 Effect of Shims

A slight azimuthal temperature effect caused by the shim pattern was reported in the NRX/EST Test Report, WANL TNR-216. No similar temperature asymmetry could be detected in NRX-A5, because both the shimming pattern and instrumentation were dispersed and very symmetrical. In the NRX/EST, 87 TAC (tantalum carbide dispersed in graphite) elements were concentrated near the core center while NRX-A5 had only 54 of these elements well-dispersed throughout the core as shown in Figure 5-24. However, the effect of the NRX-A5 shims was observed in the post test gross ionization measurements (See Chapter 9, Figures 9-6 and 9-10).

Although examination of individual thermocouple readings in NRX-A5 did not reveal a consistent asymmetrical effect due to the location of the TAC shimmed elements, the analysis of variance indicated a radial effect was present at all holds except the SOL in EP-III. Figure 5-24 reveals a relative concentration of shims in the "F" Row at core radius 11 inches. A relative shim density was defined as the number of shimmed elements per unit cross sectional area of the core in each of the radial bands containing shims. The number of TAC elements per square inch of core cross section was very close to a constant value of 0.06 at all core radii except near 11 and 14 inches. This distribution may be noted on Figure 5-25. The average core material temperatures also show a relative decrease at this approximate core radius. The local effect of the power depression caused by shims has been estimated to be from 1 to 3 percent which would result in from 50 to 150°R cooler exit temperatures in the fuel elements adjacent to the shims. This agrees with the observed temperature deviations shown in Figure 5-25, since the temperatures at radius 10 inches are approximately 100°R cooler than at other radial positions.

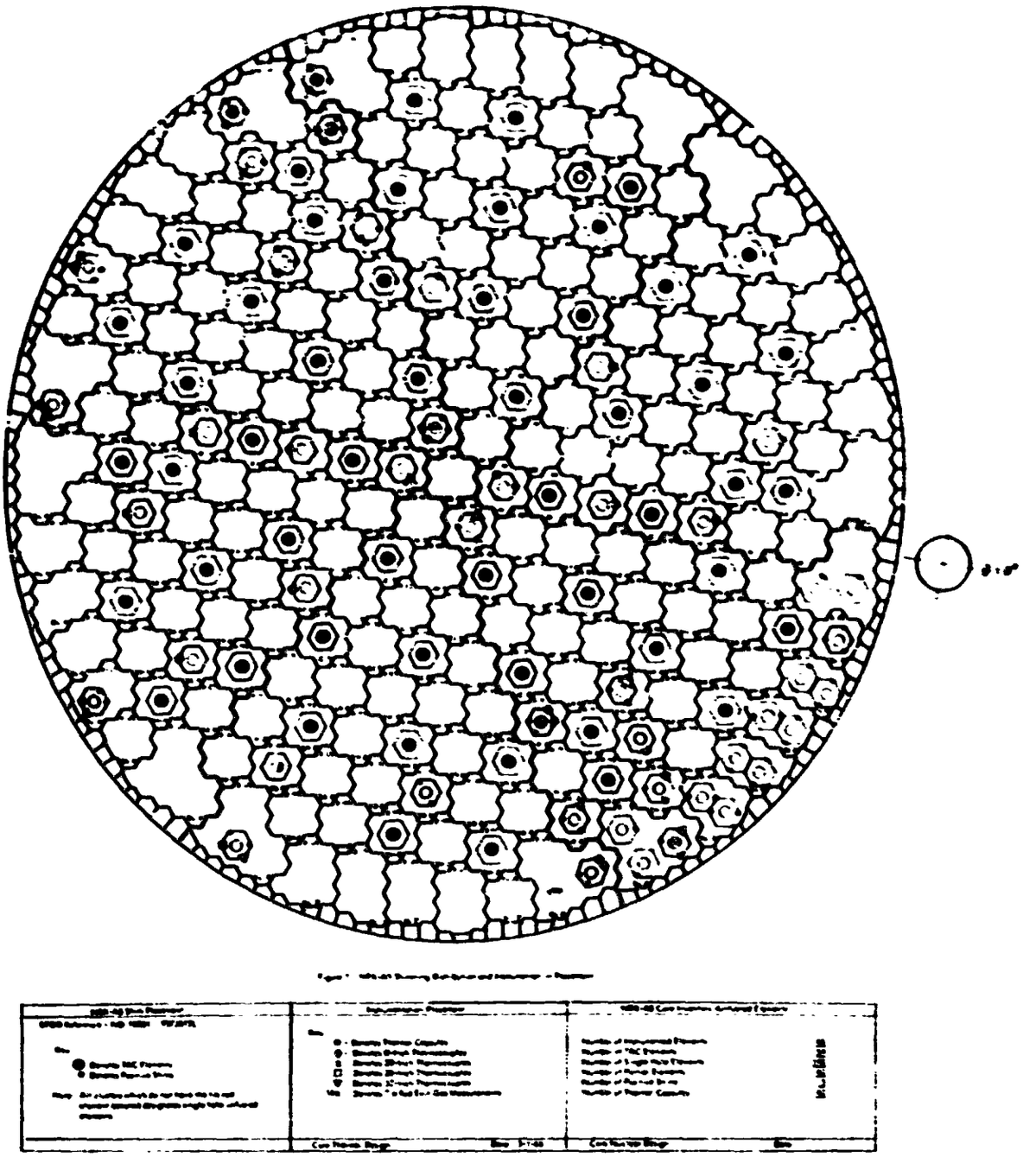

Figure 5-24. NRX-A5 Shimming Distribution and Instrumentation Placement

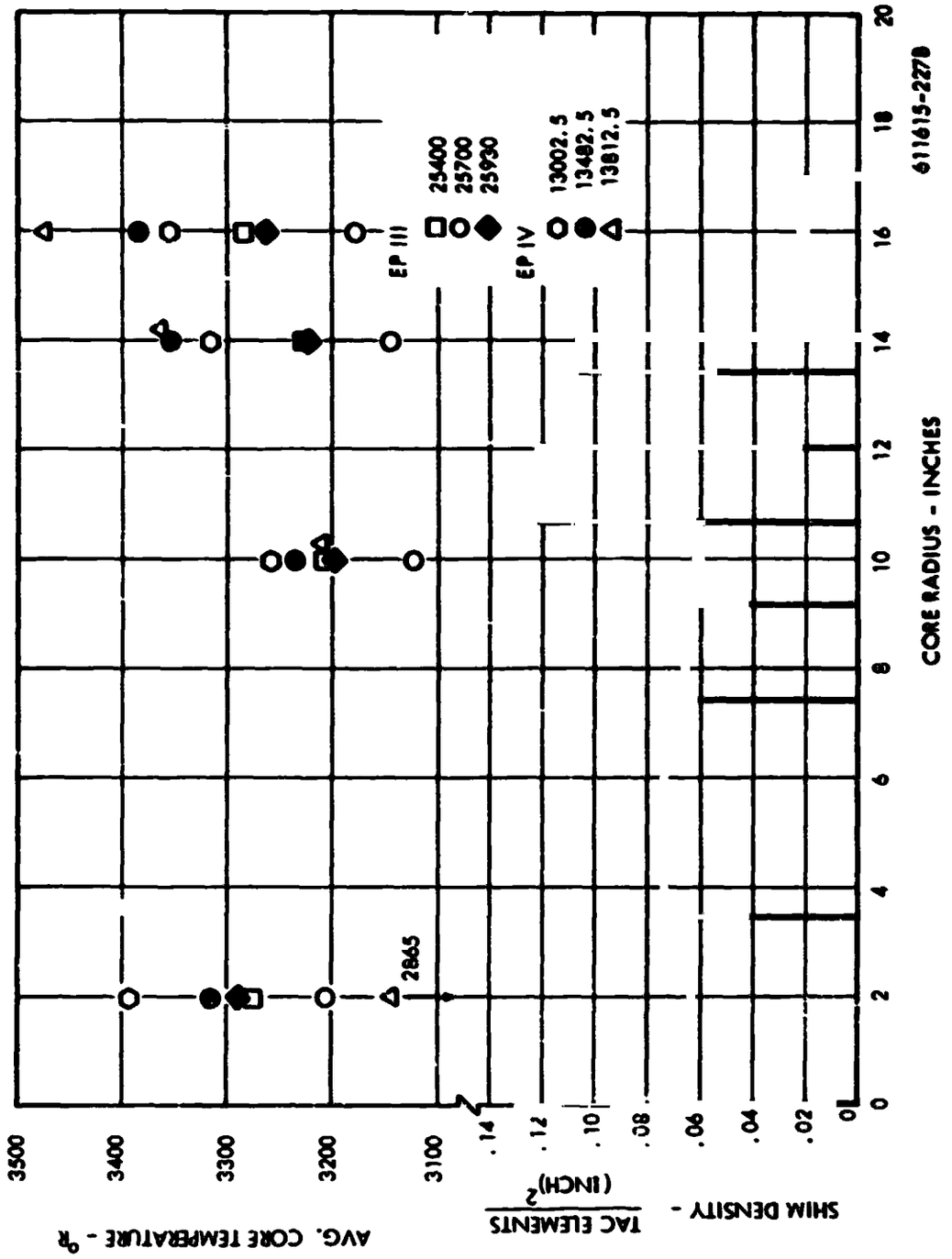

Figure 5-25. NRX-A5 Average Core Temperature and Shim Density versus Radius

5.4.5 Azimuthal Temperature Distribution

Azimuthal temperature variations were found in NRX-A5 relative to the hot buffer periphery. In addition, an analysis was made to determine the temperature variations between sensors located opposite the control drum centerlines and sensors located between control drums.

The gross azimuthal temperature variations at station 26 are shown in Figures 5-26 through 5-28 for three steady state holds. These figures show that the temperatures at comparable core radii are generally lower in the hot buffer region. Thermocouples in the 6.1 to 7.5 inch and the 9.7 to 12.8 inch radial regions indicate the asymmetry. These radial regions contained a sufficient number of sensors to make a good comparison. No sensors were located in the hot buffer region between radii of 13.7 and 15.7 inches and only two sensors were located outside the hot buffer region between radii of 16.1 and 16.9 inches. A negative slope in temperature exists in the hot buffer region from azimuth angles 150 through 270 degrees at the EP-III hold and at the start of the EP-IV hold. Referring to Figure 5-28 for the end of life, there is not as much evidence for the temperature reduction in the hot buffer region, probably because of the gross corrosion of the elements and the resulting control drum effects.

As explained in Section 5.4.4.3, the core inlet temperature is also lower in the hot buffer region and this contributes to the observed core material temperature reduction. Figures 5-21 and 5-22 show that the cooler core inlet temperature propagates radially from the core edge to approximately the 10 inch radius. In addition the core inlet temperatures display a negative slope from azimuth angles 150 through 270 degrees in the hot buffer region, similar to the core material temperatures.

Power factor scalloping in the core periphery is present at all control drum positions due to the design of the reflector system and the control drums. The degree of power factor scalloping is dependent on the control drum position. The power factor scalloping is greatest when the control drums are rotated "in" and the effect becomes

smaller as the drums rotate "out". Power factor scalloping is present at the orifice angle of 115 degrees, but the orificing compensates for this power distribution. Therefore, azimuthal temperature variations due to control drum positions were expected to occur at the start of life and end of life in NRX-A5 due to the scheme used in orificing and shimming the core.

A slight temperature variation associated with the control drum positions occurred during the low power hold (229 MW) at the start of EP III. The multiple regression analysis was used, as in NRX/EST, by normalizing all azimuthal positions of the data to a single symmetrical segment extending from on the drum centerline to midway between the drums. The normalized azimuthal position, θ', varied from 0 to 15 degrees. The assumed parameters to fit the data in the multiple regression analysis included θ' and $R^2\theta'$ terms. Figure 5-29 shows the data and the results of the correlation at station 26 for this low power hold. The resulting correlation equation is:

$$T = 1650 - 7.6163R + .01701R^2$$

where

T = sensor temperature, $^{\circ}R$

R = core radius, inches

θ' = normalized azimuthal position (0-15 degrees)

The total random error in the data was less than the thermocouple reading error. As expected, the temperatures are lower opposite the drums than between drums because of the "in" position (97°) relative to the orificed angle. No other correlation with azimuthal position was obtained for the power holds in EP-III and EP-IV.

A second attempt to determine the on-off drum variation at full power was the extensive thermal capsule data in the J Row of sector six. Additional data in the other five sectors were also utilized. As shown in Figure 5-30 no significant variation was apparent although the strong radial dependence at the end of life was evident. Thermal capsules in the J Row represent end of life conditions because the highest temperatures are experienced at the periphery with drums rolled out. The approximate size of the control drums is shown to give an indication of the scale. No temperature effects can be attributed to the proximity

to drums. This conclusion is in agreement with the results of the analysis of variance on core thermocouples which showed no measurable effect due to azimuthal sensor position relative to control drums.

No significant azimuthal (circumferential) core material temperature variations were found in NRX/EST except slightly lower temperatures were measured in the seal region, reflector and c ve periphery in line with the nozzle bleed port, and also in the region of the privy roof mounted shield.

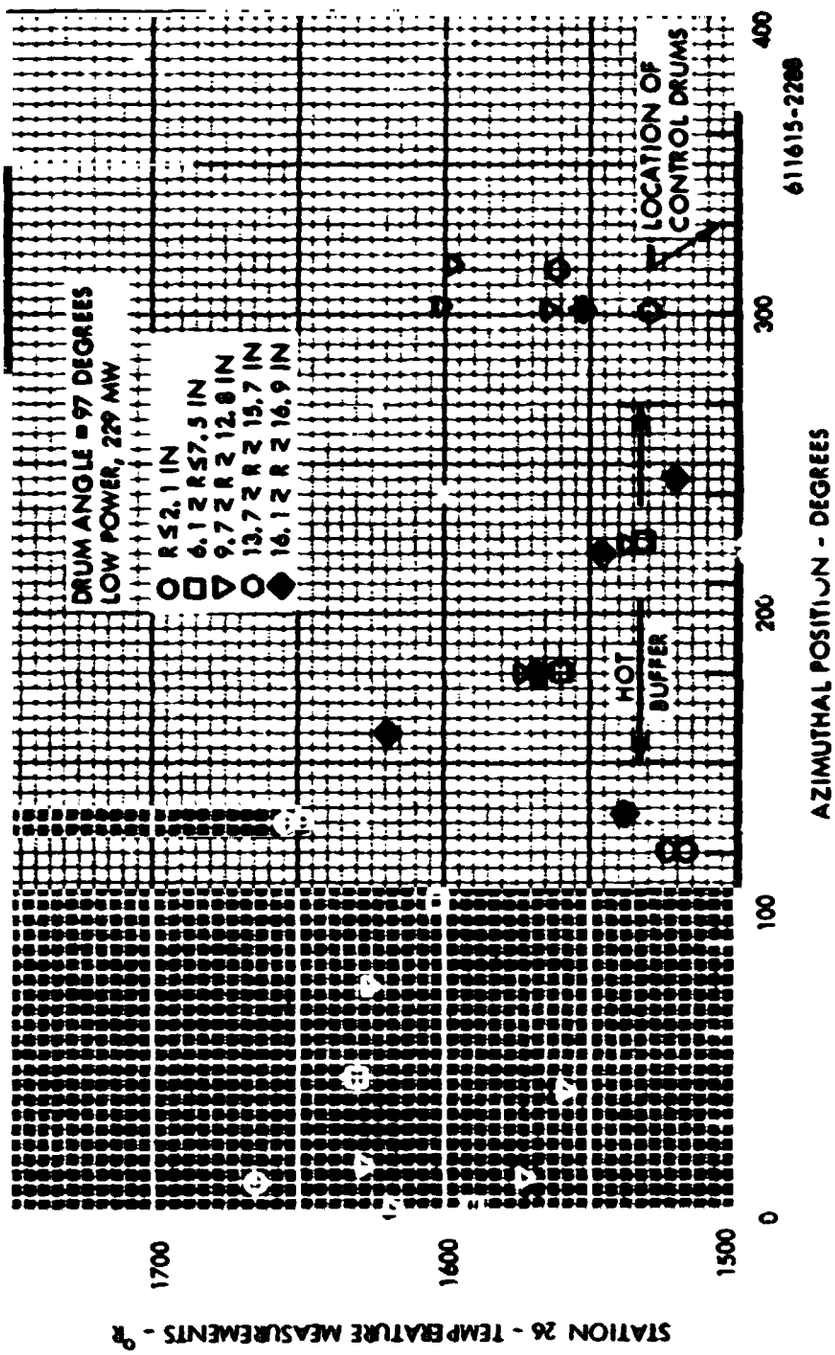

Figure 5-26. NRX-A5 EP-111 CRT 25247.5 Station 26 Temperature versus Azimuthal Position

Figure 5-27. NRX-A5 EP-IV SOL CRT-13002.5 Station 26 Temperature versus Axiumthal Position

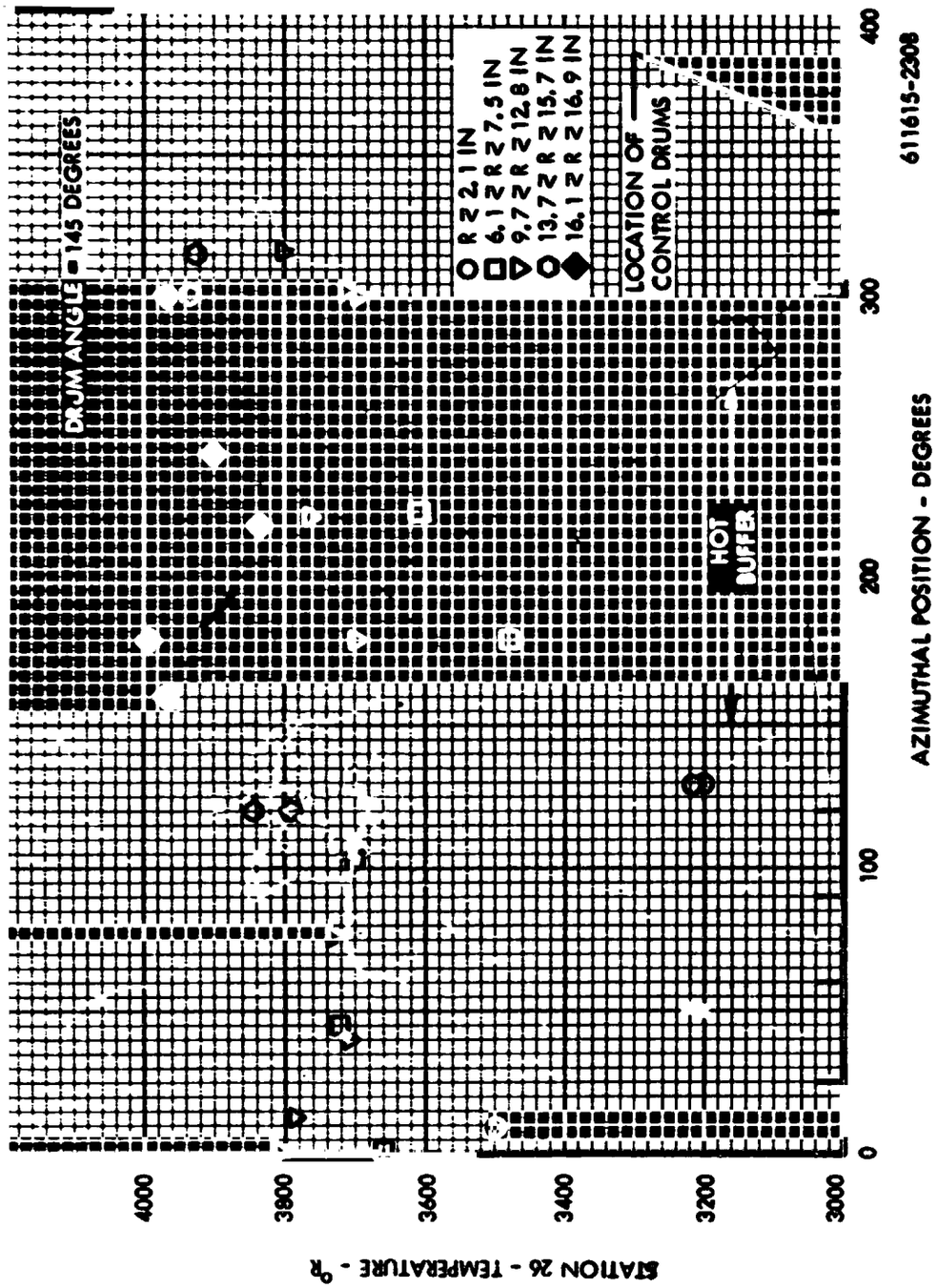

Figure 5-28. NRX-A5 EP-IV EOL CRT-13812.5 Station 26 Temperature versus Axiumuthal Position

Figure 5-29 NRX-A5 Core Material Temperatures versus Normalized Azimuthal Position

Figure 5-30. NRX-A5 Station 36 Thermal Capsule Temperatures versus Azimuthal Position

5.4.6 Thermal Capsule Measurements

The thermal capsule data cannot be related to any specific power hold because the data indicates only the highest temperatures experienced during operation. At the center of the core the highest temperatures occurred at the start of life and at the periphery the highest temperatures occurred at the end of EP-IV with the control drums at 145°. Table 5-7 presents the results of the multiple regression analysis and also includes the NRX/EST results for comparison. The random errors are considerably larger and the maximum temperatures are lower in NRX/EST chiefly because of additional central element cooling caused by the extensive hot end surface corrosion. The post-operative examinations of the two reactors and the lateral support pressure distributions* confirm that the periphery of the NRX-A5 core was in better condition (and hence had less radial inflow at EOL) than the periphery of the NRX/EST core. Figure 5-31 shows the radial fit to the NRX-A5 thermal capsule data at station 44 inches. Figure 5-32 shows similar data for NRX/EST. Fifteen data points were excluded from the NRX/EST regression fit shown in Figure 5-32.

The thermal capsule reading error of $\pm$ 100°R was subtracted from the total random error in the data in both cases similar to past practice, i.e.,

$$3\sigma_{\text{Temp}} = \sqrt{(3\sigma_{\text{total}})^2 - (100)^2}.$$

The maximum thermal capsule temperature of 4840°R, occurred in elements 6J5E and 6J9J. The maximum temperatures in NRX/EST were 4800°R. Using the multiple regression equations for all thermal capsule data, the maximum temperatures were 4860°R at core radius 17.0 inches in NRX-A5 and 4850°R in NRX/EST. The 2σ variation was applied in each case.

---

* See Section 4.3.2 for further discussion

The station 44 thermal capsule temperatures at the center of the core in NRX-A5 were nearly 200°R hotter than in NRX/EST. In the radial band between 0 and 10 inches, NRX-A5 had only 3 readings compared to 10 readings for NRX/EST. The highest central region temperatures were generally expected at the start of life for both reactors. The comparison in Section 5.4.7 confirms that material temperatures, power and nozzle chamber temperatures were higher at SOL in NRX-A5 than in NRX/EST. However, the difference is not great enough to account for all of the 200°R temperature difference between reactors. An additional difference between NRX/EST and NRX-A5 is that NRX/EST had considerably more shims in the central region which reduce the local power generation. Comparison of gross ionization measurements in the two reactors confirm that the average power factor deviations could account for lower central temperatures of NRX/EST than NRX-A5. Again, the difference is not great enough to account for all of the 200°R difference.

TABLE 5-7

EQUATIONS OF MULTIPLE REGRESSION FIT TO THERMAL CAPSULE TEMPERATURES, CORE STATION 44 INCHES

T = Temperature, ^{o}R

r = core radius, inches

		NRX-A5		NRX/EST*
All Data				
T (r)	=	$4613 + 0.03\ r^3$	=	$4412 + 1.0\ r^2$
3σ Temp	=	$\pm$ 141		$\pm$ 271
No. of Points		38		40
T (r = 17)	=	4760	=	4701
T (r = 0)	=	4613	=	4412
Central Only (r from 0 to 15)				
T (r)	=	$4607 + 0.48\ r^2$	=	$4411 + 0.95\ r^2$
3σ Temp	=	$\pm$ 66		$\pm$ 283
No. of Points		11		23
T (r = 0)	=	4607	=	4411
J Row Only (r from 15 to 17)				
T (r)	=	3521 + 74.56r	=	4688
3σ Temp	=	$\pm$ 149		$\pm$ 230
No. of Points		27		17
T (r = 17)	=	4788	=	4688

*Excluding data points in J row reading less than 4450^{o}R

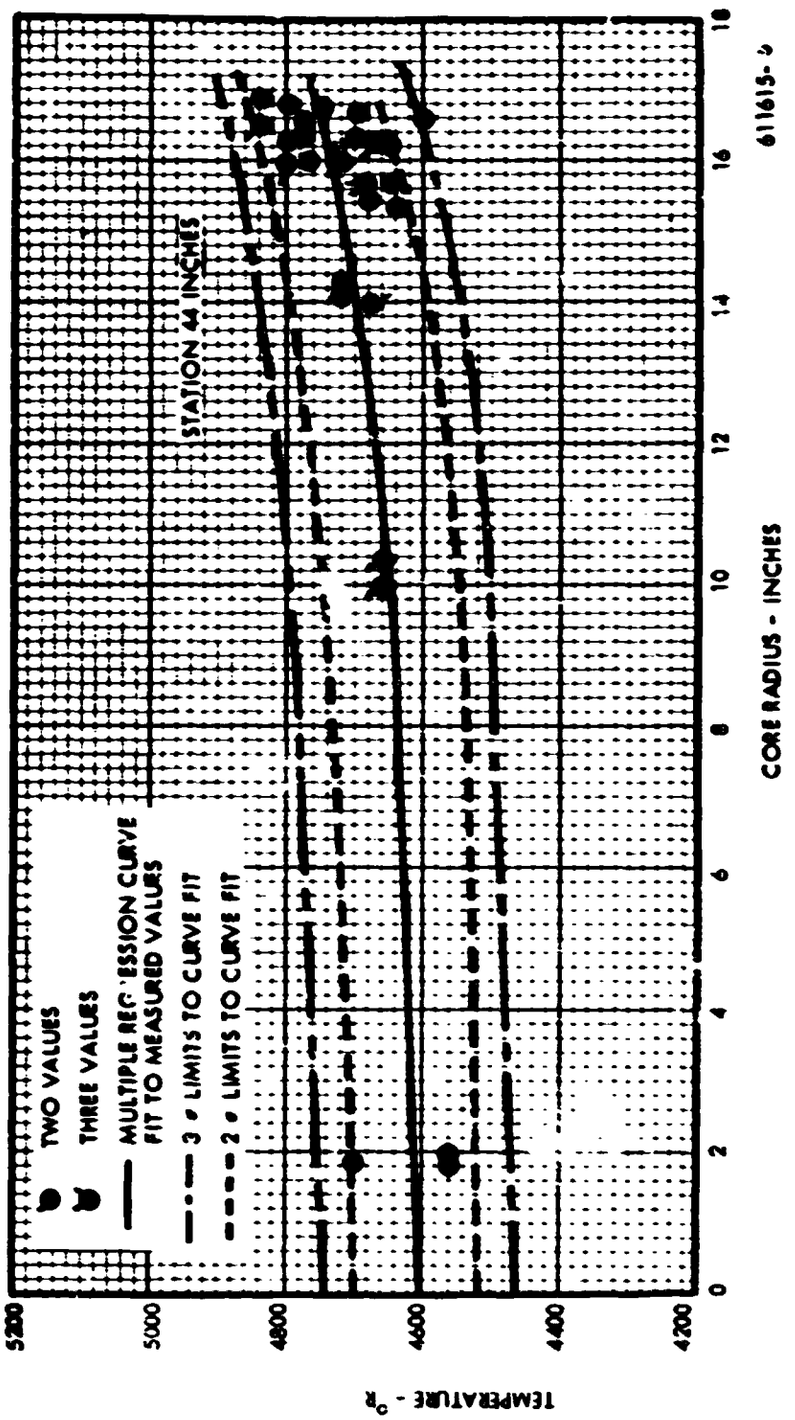

Figure 5-31. NRX-A5 Thermal Capsule Data versus Core Radius

Figure 5-32. NRX/EST Thermal Capsule Data versus Core Radius

5.4.7 Tie Rod Temperatures

Post test calculations of the tie rod material temperatures at full power are within 50°R of measurements. The thermocouples were installed at core station 53.5 inches in the centers of the hollow 0.122 inch diameter tie rods. To compensate for the reduction in channel flow area of the annulus between the tie rod and the stainless steel liner, the tie rod orifice diameter was increased from 32.5 mils to 37.0 mils for the seven instrumented tie rods. In addition, minor changes were made in the support cone to accomodate the larger tie rod diameter. No tie rod exit gas thermocouples were used in NRX-A5. The seven tie rod material temperatures show a flat radial distribution within limits of ± 100°R at all holds. Figure 5-33 shows the temperatures during the low power (229 MW) hold at the start of EP-III (CRT 25247.5 seconds) and two full power holds in EP-IV (CRT 13002.5 and CRT 13812.5, EOL). A least-squares curve fit to the test data gives a flat radial temperature profile for the low power hold and the EOL hold. The calculated tie rod material temperatures are shown by dotted lines in the figure and are slightly cooler than the measured values at low power. The slight temperature increase (approximately 30°R) at the core edge during EP-IV is attributed to higher peripheral power as a result of increased control drum angle. This temperature increase is also verified by the calculations. At the center of the core, the measured tie rod temperature shows a large drop during EP-IV. This is probably caused by the additional cooling due to interstitial flow adjacent to the tie rod element. The large temperature drop cannot be verified analytically since it is impossible to calculate the local interstitial flow. It has been estimated that a drop in tie rod exit temperature of 90°R could result from an adjacent interelement flow of only 0.00029 lb/sec (less than 1/10 the nominal flow in a fuel channel in the core central region), assuming that the interelement flow only cools the unfueled element. Since the fuel material temperatures of radius 2 inches dropped sharply near the end-of-life due to gross corrosion and interelement flow (See the figures in Section 5.4.4.2), it is reasonable to assume that the additional flow also reduced the tie rod exit temperatures. A tie rod program calculation was made using the lower measured fuel material temperatures at EOL as a boundary condition, however, the tie rod temperature

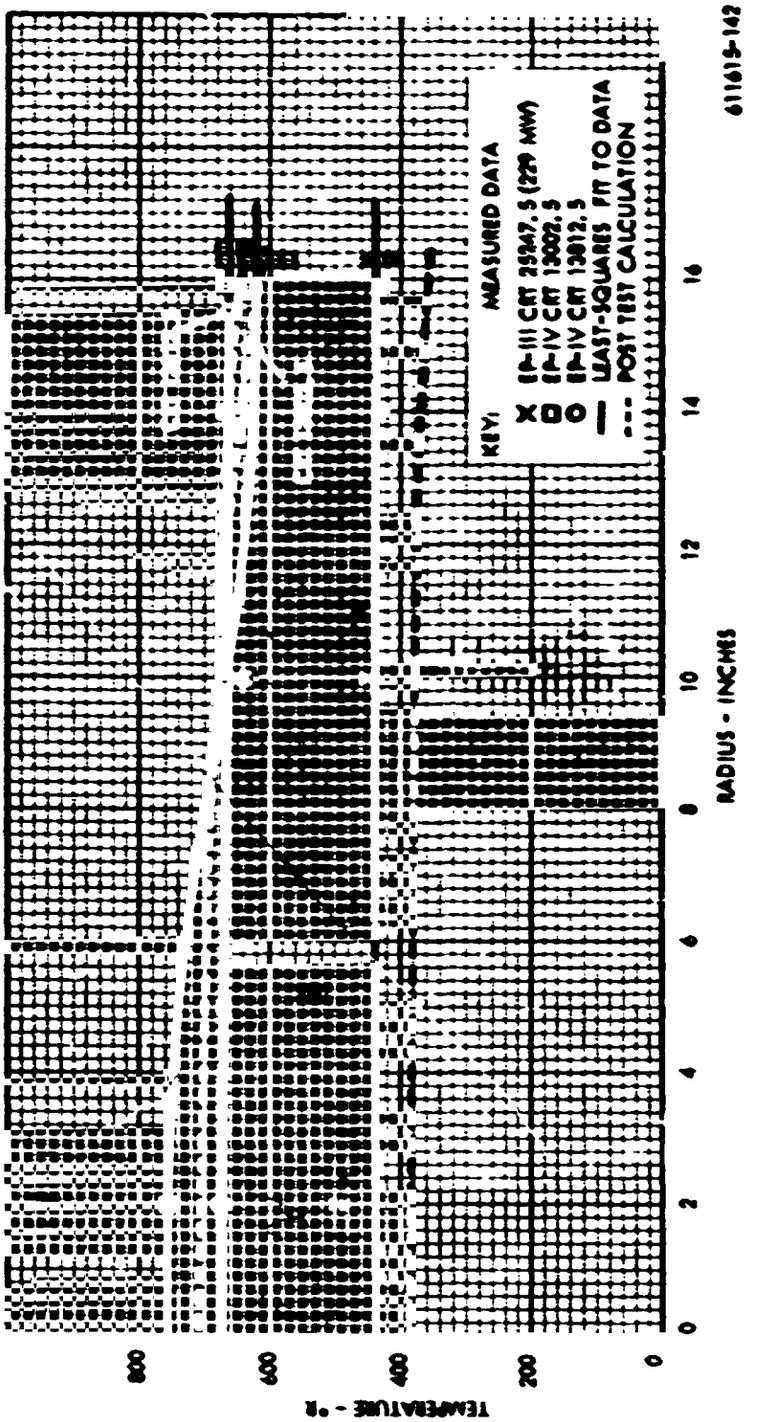

Figure 5-33. NRX-A6 Tie Rod Material Temperatures versus Radius for EP-III and EP-IV

decreased by only 2°R. The tie rod calculation model does not account for cooling by interstitial flow; however, these results illustrate the relative insensitivity of tie rod exit material temperature to fuel material temperatures.

In conclusion, the tie rod calculation model accurately predicts the relative behavior of the tie rod temperatures at design conditions as a function of radius but the calculated temperatures are approximately 60°R lower than measured at low power conditions. The agreement with measurements is better than was observed for NRX/EST, as can be seen by referring to Figure 5-25 in WANL-TNR-215, "NRX/EST Reactor Test Analysis Report".

The largest uncertainty in the tie rod model is the thermal conductivity of the pyrographite sleeves. A discussion of this uncertainty was presented in WANL-TNR-202 "NRX-A3 Reactor Final Test Report". The recent thermal conductivity measurements performed by the Southern Research Institute give generally higher thermal conductivities than previous data, especially at temperatures above 2400°F. The previous data used for NRX-A2 predictions and adjusted analytically for the NRX-A3 and NRX/EST predictions were obtained from tests conducted with helium at one atmosphere pressure and without purging the test chamber. The recent data, used for the NRX-A5 calculations in this report, was taken after purging the chamber with helium at 200 psia. A further adjustment to the pyro sleeve conductivity was made at WANL to account for the difference in conductivity between helium and hydrogen. However, the recent data, because of wide scatter and lack of data at low temperatures, does not appear to yield results at low power that are as close to measured values as the previous data.

5.4.8 Peripheral Fuel Element During EP-IV Shutdown

Cracking at the corners of peripheral fuel elements was observed in the NRX-A5 and previous reactors. For NRX-A5, this cracking was observed for both the hot buffer and nominal filler strip sectors. The axial distribution of cracks in the hot buffer region was random compared to a symmetric pattern in the nominal filler strip region. Temperature variations within elements and between elements during transient operation are suspected of contributing to this failure. Radial inflow of coolant from the lateral support system into the core is also

a possible cause of failure as is evident by the correlation of crack axial location with position of the lateral support seals in the nominal filler strip sectors.

A portion of a J9 fuel cluster in the hot buffer region was analyzed to obtain the temperature variations between peripheral fuel elements and the gradients across elements during the EP-IV shutdown. An analysis of an average fuel element for the same transient was made for comparison. Plenum conditions and power and flow schedules were obtained from a TNT calculation. A CAT calculation provided lateral support seal coolant conditions. A model of a portion of the J9 fuel cluster shown in Figure 5-34 was used with the TRACK computer code to obtain fuel element boundary conditions. A single orifice size and power factor was associated with individual fuel elements in this model. The external boundaries of this model were assumed adiabatic.

Figures 5-35 through 5-37 show the temperature profiles for each element including the unfueled partial and the unfueled central elements at core stations 8, 26, and 52. In Figures 5-38 to 5-40 the temperature differences between these elements and in the average fuel element are compared. The unfueled partial element lags considerably behind an average fuel element at core station 26 (1440°R at 35 seconds after shutdown). Fuel element J9H lags the average element by 650°R at this time, and the temperature lag is still increasing.

The temperature variations (maximum to minimum and average to minimum) in fuel elements J9H and J9K during the EP-IV shutdown are shown in Figures 5-41 and 5-42 for core station 26 and 52, respectively. The maximum to minimum temperature variation across element J9H is nearly 500°R and still increasing at 35 seconds after initiation of the shutdown.

Stress analyses of the peripheral fuel elements were made with the temperature distributions obtained from the thermal analyses discussed above. It was concluded that the computed temperature variations across an element are insufficient to cause failure of the element unless the cross section has been considerably weakened by substantial corrosion. It is felt that the majority of the peripheral fuel element breaks occurred during disassembly. This is indicated by the clean, uncorroded appearance of the break areas. However, notching of the outermost corners of peripheral fuel elements in the nominal (cold) filler strip sectors

appears to be caused by radial inflow of lateral support seal coolant. The notches are formed by corrosion which follows the formation of cracks at the corner. The notches are generally alighne with the forward edge of the lateral support seal rows.

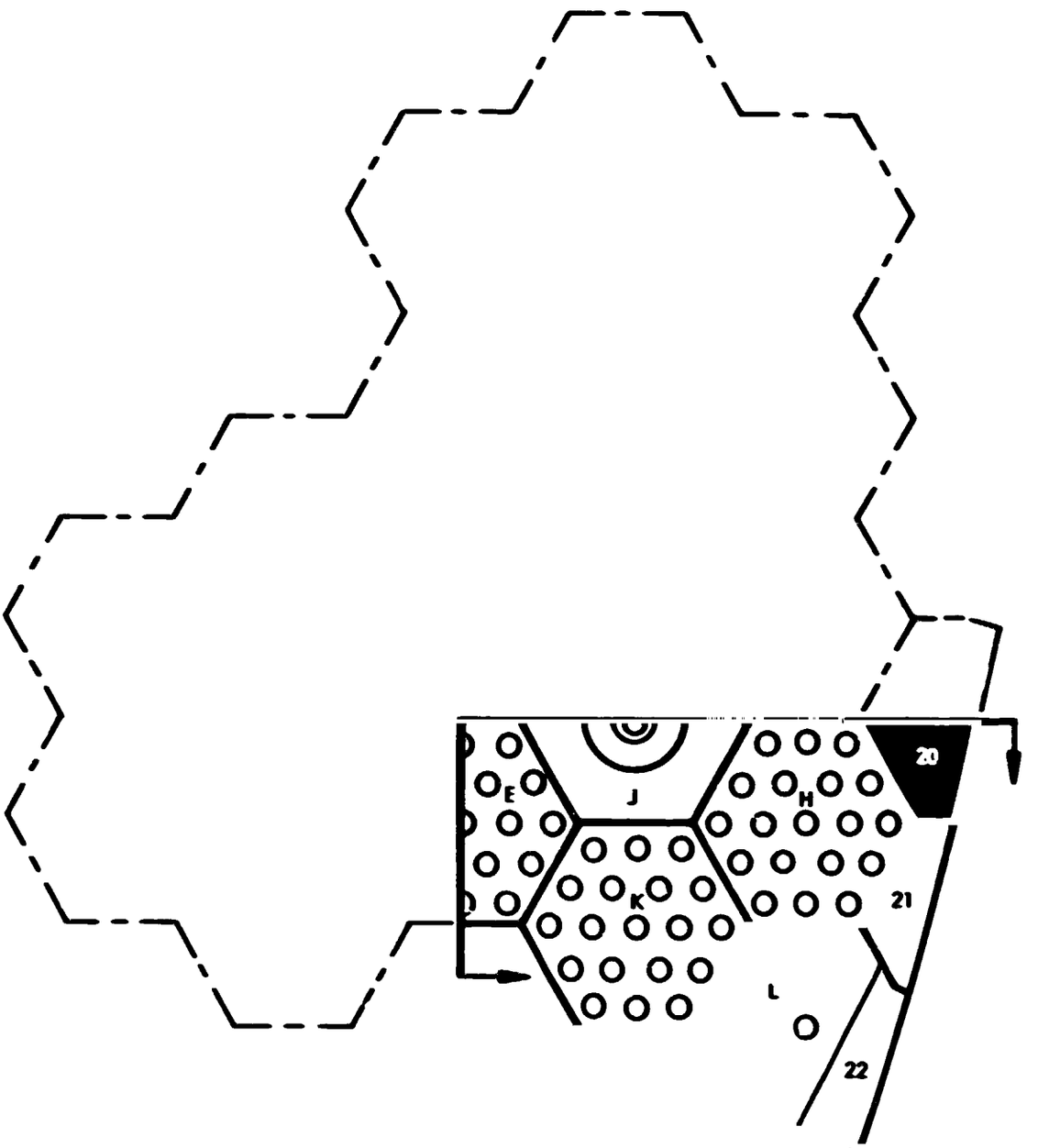

Figure 5-34. J9 Cluster Model

Figure 5-35. J9 Cluster Element Temperatures during NRX-A5 EP-IV Shutdown

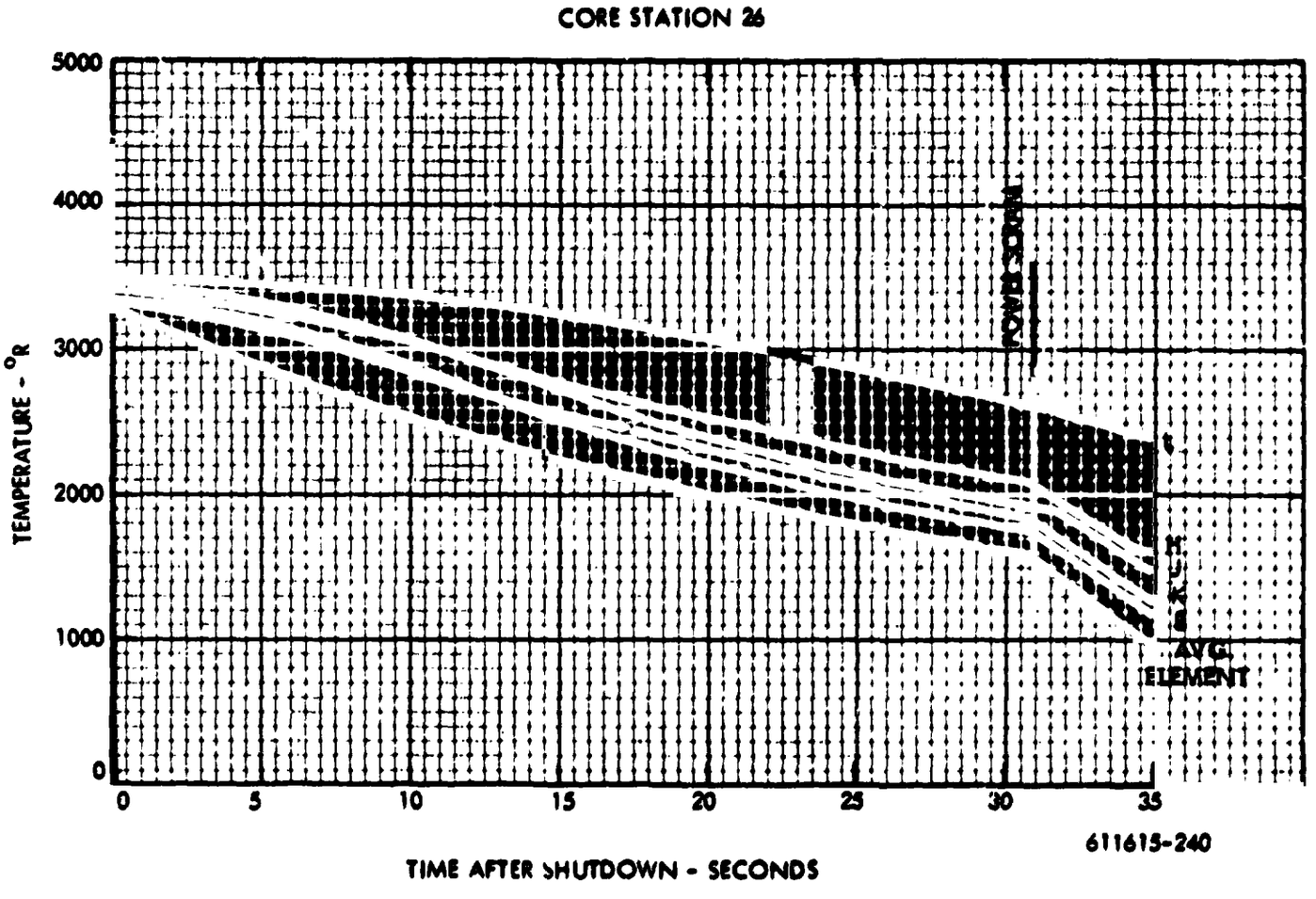

Figure 5-36. J9 Cluster Element Temperatures during NRX-A5 EP-IV Shutdown

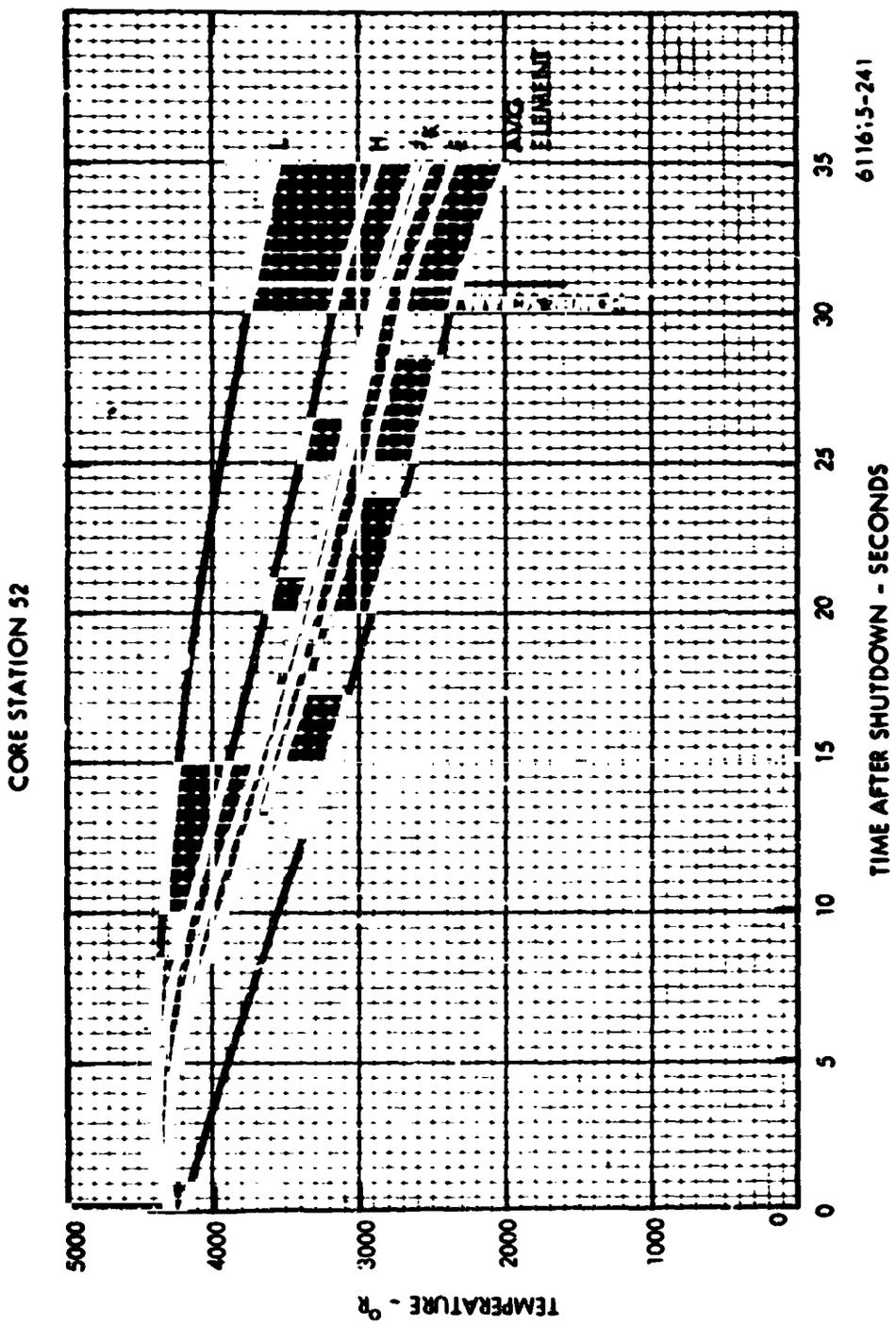

Figure 5-37. J9 Cluster Element Temperatures during NRX-A5 EP-IV Shutdown

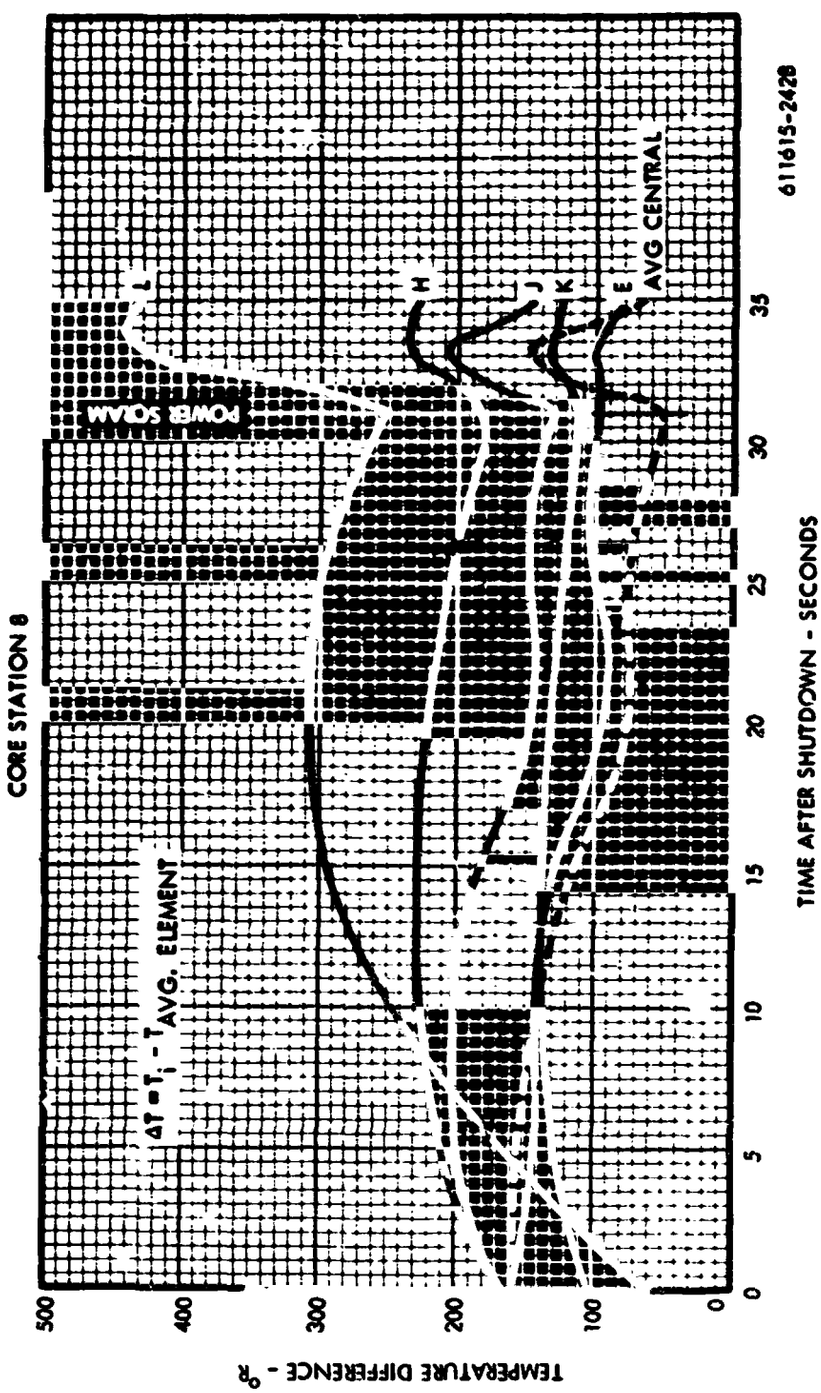

Figure 5-38. J9 Cluster Element Temperatures Variations NRX-A5 EP-IV Shutdown

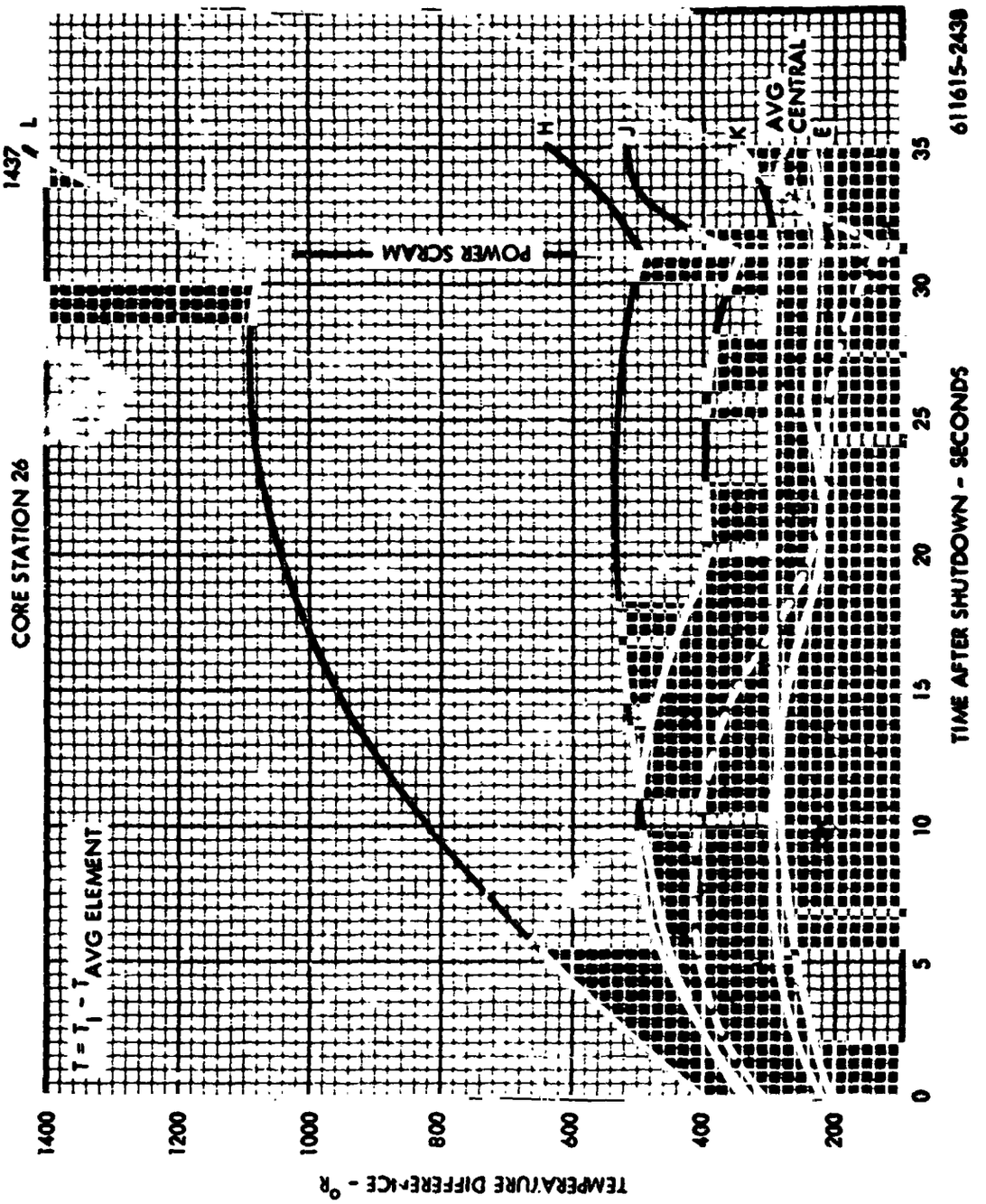

Figure 5-39. J9 Cluster Element Temperatures Variations NRX-A5 EP-IV Shutdown

Figure 5-40. J9 Cluster Element Temperatures Variations during NRX-A5 EP-IV Shutdown

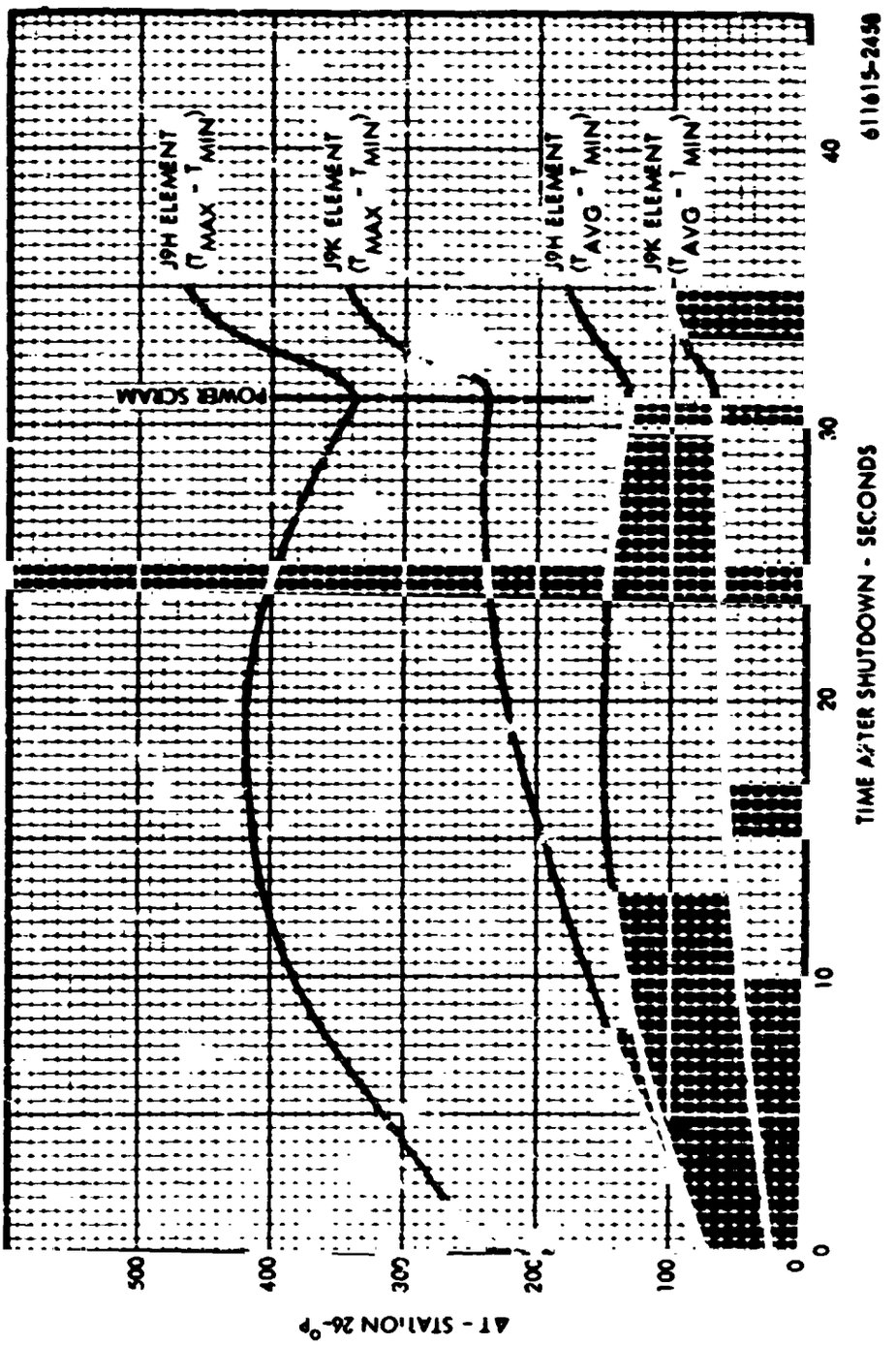

Figure 5-41. Peripheral Element Temperature Difference NRX-A5 EP-IV Shutdown Station 20

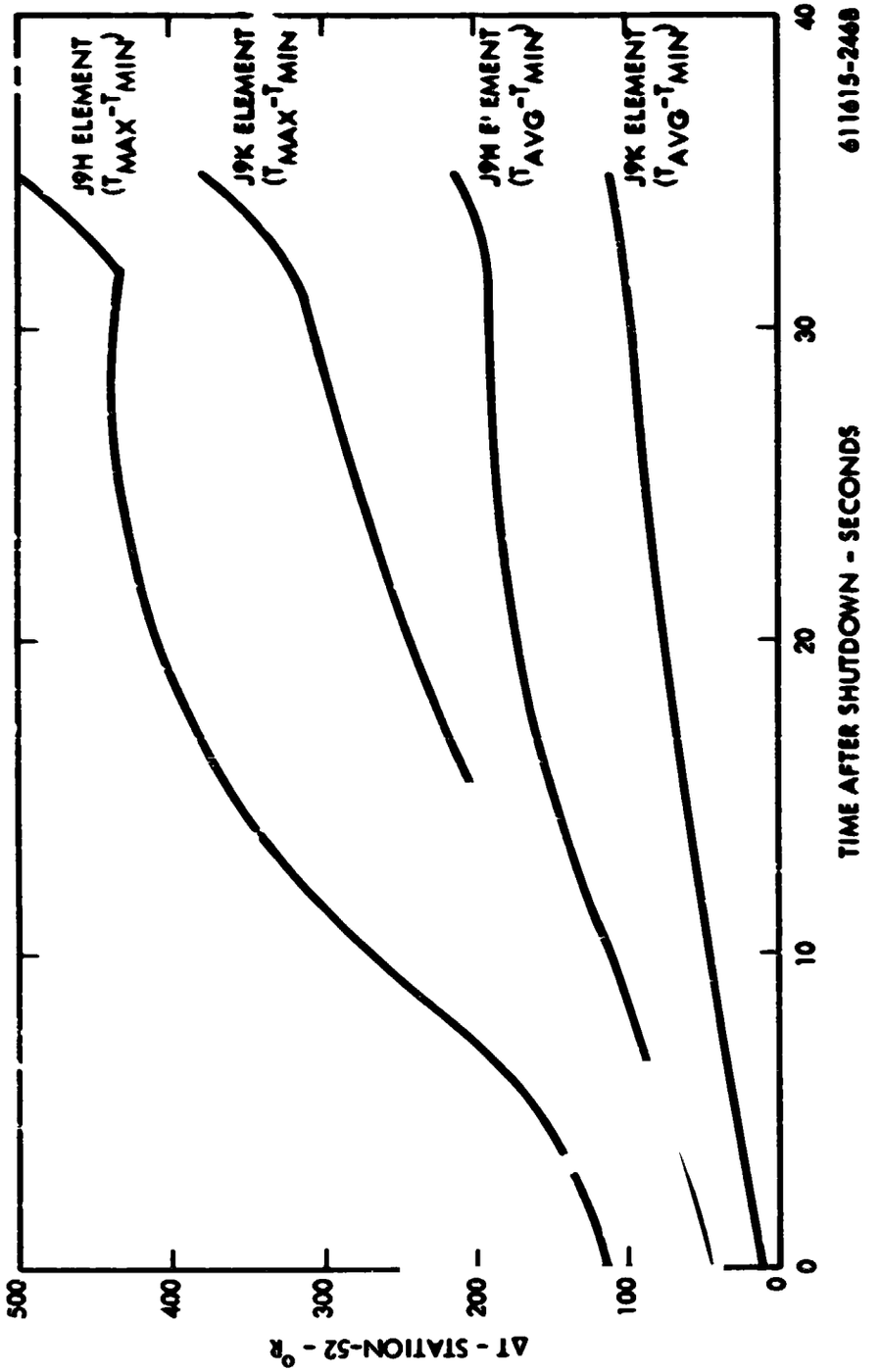

Figure 5-42. Peripheral Element Temperature Difference for Station 52 NRX-A5 EP-IV Shutdown

5.4.9 Statistical Analysis of Core Temperatures

In previous reactors, the radial and azimuthal variations in measured core temperatures were analyzed by a multiple regression technique.* While this method is adequate for determining the extent to which initially random temperature variations can be reduced by fitting a curve to the data, the statistical plan for the thermocouple placement in NRX-A5 permitted a more comprehensive analysis of the data and insures the proper evaluation of otherwise undetectable systematic variations. As described in Section 5.4.1, 32 thermocouples were placed in one-half of the possible 64 combinations (4 radial positions, 4 axial positions, 2 circumferential positions, and 2 ON-OFF control drum positions). The placement and the resulting analysis of variance permits an evaluation of these independent position variables and their interactions. This analysis also minimizes the possibility of overlooking any independent variables in the multiple regression analysis. Finally, a confidence level related to the significance of the independent variables and their interactions was assigned.

Table 5-1 presents the thermocouple placement plan for the NRX-A5. More than 36 thermocouples were installed in the core; most of these were installed at station 26 for control purposes. In the analysis of variance these "extra" sensors were not included because they would alter the planned balance between core locations. In the multiple regression analysis, all available data was utilized except thermocouples which were influenced by pinholing and subsequent interstitial flow.

5.4.9.1 Analysis of Variance of Core Temperatures

The analysis of variance for the NRX-A5 core temperatures was performed with the 32 sensors listed in Table 5-1. Details of this method and sample calculations are contained in Section 5.5. Major conclusions are:

1) No statistically significant temperature variation with respect to control drums (ON or OFF-drums) existed. The interaction of the location near drums with the other variables are also not significant.

*SHARE Program ERMPR2, "Stepwise Multiple Linear Regression", Esso Research and Engineering Co., July 1958

2) The axial temperature variations are statistically significant at the 99 percent confidence level.

3) The temperature variations with respect to full power operation time were statistically significant during EP-III and EP-IV. Also, the changes which occurred in the radial, circumferential and axial temperature distributions with operating time are statistically significant.

4) All two-factor and higher order interactions between the core radius, azimuth, and axial position are not significant during EP-III and EP-IV except at the end of life. At control room time 13812.5 seconds in EP-IV, the axial and radial temperature variations interact at the 99 percent confidence level, i.e. the axial temperature profile depends on the core radius and the radial temperature profile is a function of the axial station.

5) The temperatures at an azimuth angle of 120 degrees are 51°R lower on the average than the temperatures at an azimuth angle of 300 degrees. This characteristic is statistically significant at the 95 percent confidence level.

6) Temperatures in the 10-inch radial region average approximately 70°R lower than the average temperature of all radii at full power holds when the control drum position was close to the orifice angle. This effect is statistically significant at the 95 percent confidence level.

7) The random variation in the thirty-two temperatures at the eight holds analyzed for EP-III and EP-IV ranged from $\pm$ 51.4°R to $\pm$ 68.3°R (1σ), after accounting for the significant temperature variations with position.

5.4.9.2 Multiple Regression Analysis

The comparison of multiple regression results between NRX-A5 and NRX/EST at SOL and EOL is shown in Table 5-8. This table confirms that the NRX-A5 operated hotter at the start of life than NRX/EST. The random errors are reasonably consistent except at the end of life where NRX/EST shows considerably greater errors. The plotted results of the multiple regression analysis are shown in Sections 5.4.2 and 5.4.6. It is interesting to note that the total (before subtracting thermocouple reading errors) standard

deviation in the data after curve fitting by multiple regression is in agreement with the standard deviation from the analysis of variance. This value varied from 50 to 80°R depending on core station and operating time. Although the two techniques are not strictly comparable they give assurance that:

1) The multiple regression analysis of all core thermocouples gives an adequate representation of the actual core temperature distribution.

2) No interactions between independent variables are being overlooked.

3) Although the analysis of variance disclosed additional significant radial and circumferential effects which were not brought out in the multiple regression curve fits, the effects are small enough so as not to invalidate conclusions based on the multiple regression results.

5.4.9.3 Maximum Measured and Calculated Temperatures and Element-to Element Variations

Calculated random element-to-element variations were obtained by combining the effects which may occur in adjacent elements. The method used is described in WANL-TME-202, "NRX-A3 Reactor Final Test Report", and the factors considered are listed in Table 5-9. This list excludes factors which are systematic in their effects such as drum motion or average core inlet temperature. The 3σ deviation in power factor was calculated from the NRX-A5 gross ionization measurements in the J Row. It represents a random element-to-element variation in the J Row and not a systematic or absolute error which occurs in the core periphery. The post test gross ionization data was used to estimate the random variation in power factor for the NRX/EST test analysis; however in the NRX-A3 and NRX-A2, a pre-test prediction of the power variation was used, which was lower than the post test data. Since the gross ionization data includes experimental errors in measurement and analysis (corrections for corrosion weight loss etc.), it represents an over-estimate of the random variability in power factor. Since this effect is the largest single contributor to the calculated element-to-element temperature variations, the results are higher for NRX/EST and NRX-A5 than the calculated results for NRX-A3 and NRX-A2. The calculated 3σ element-to-element random temperature variation was 320°R for NRX-A5. It would have been 205°R if the power factor variation had been zero.

The maximum nominal thermal capsule temperatures, fuel temperatures, random variations, and maximum statistical temperatures at station 44 inches are listed in Table 5-10 for the four reactors. The maximum temperature occurred at the core edge for all reactors except for NRX-A3 which had an EOL drum angle less than the orificed drum angle.

The maximum nominal thermal capsule temperature for NRX-A5 was 4760°R using the multiple regression curve fit compared to the highest data point of 4840°R. The calculated temperature for the thermal capsule location from the TRACK results was 4740°R. The 3σ standard deviation value for measured thermal capsule data was 141°R while the hot channel analysis predicts an element-to-element random variation of $\pm$ 320°R. The maximum statistical thermal capsule temperatures were found by adding the 3σ random variations to the nominal maximums. The fuel temperatures were computed by subtracting the sensor-to-fuel temperature difference from the thermal capsule temperatures.

TABLE 5-8

COMPARISON OF RADIAL TEMPERATURES IN NRX/EST AND NRX-A5

T = Temperature, °R r = radius, inches

	NRX/EST	NRX-A5
START-OF-LIFE		
Experimental Plan	EP-IV	EP-III
Control Room Time	CRT-1192.5	CRT-25400
Drum Angle	110°	109°
STATION 20		
Curve Fit	T = 3118	T = 3221
3σ meas.	± 139	± 173
STATION 26		
Curve Fit*	T = 3645	T = 3745
3σ meas.	± 73	± 166
STATION 32		
Curve Fit*	$T = 4007 - 0.02r^2$	T = 4045
3σ meas.	± 220	± 156
REACTOR POWER, MW	1086	1113
CORE FLOW, (lb/sec.)	70.5	71.5
NOZZLE CHAMBER TEMPERATURE, °R	4012	4088
POWER/CORE FLOW	15.404	15.550
END-OF-LIFE		
Experimental Plan	EP-IV	EP-IV
Control Room Time	CRT-10042.5	CRT-13812.5
Drum Angle	161.5°	145°
STATION 20		
Curve Fit*	$T = 3134 + 0.01r^3$	$T = 3068 + 1.75r^2$
3σ meas.	± 135	± 185
STATION 26		
Curve Fit*	T = 3862	$T = 3581 + 1.35r^2$
3σ meas.	± 385	± 135
STATION 32		
Curve Fit*	$T = 3800 + 24.97r$	$T = 3999 + 0.9r^2$
3σ meas.	± 323	± 172
STATION 44 (Thermal Capsule, all data)		
No. of Data Points	40	38
Curve Fit*	$T = 4412 + 1.00r^2$	$T = 4613 + 0.03r^3$
3σ meas.	± 271	± 141
[illegible]	4701	4760
[illegible]	1118	1112
[illegible]	71.7	71.2
[illegible] URE, °R	4061	4089
[illegible]	15.593	15.618

* A constant value indicates no radial variation.

TABLE 5-9

FACTORS CONSIDERED IN ANALYSIS OF ELEMENT-TO-ELEMENT TEMPERATURE VARIATIONS

	3σ Deviations	
Element Effects	Cause	Effect
1. Power Factor* (At Core Periphery)	± 5.37	245
2. Upper Plenum Flow Distribution	± 4.5%	155
3. Upper Plenum Temperature Distribution	± 18.9**	95
Channel Effects		
1. Channel Diameter Change	± 0.0005 in.	62
2. Fuel Mass	± 17.3%	340
3. Orifice Coefficient	± 50°R	50
4. Orifice Mismatch	± 200°R	200
5. Orifice Leakage	± 100°R	100
6. Air Impedance	± 0.0009	110
7. Friction Factor	± 4%	26

*Excluding Drum Angle Effects, based on Test Data, NRX/EST was ± 5.2%

**From Test Data

TABLE 5-10

TABULATION OF MAXIMUM TEMPERATURES IN NRX-A2, NRX-A3, NRX/EST AND NRX-A5

	A2 Core Edge	A3 Core ℄	NRX/EST Core Edge	NRX-A5 Core Edge
I. Thermal Capsule Temperatures at Station 44 Inches Radial Position				
A. Maximum Nominal Thermal Capsule Temperature				
1. Predicted by multiple regression curve fit to test data	4359	4461	4701*	4760
2. Maximum thermal capsule data point	4400	4550	4800	4840
3. Calculated by TRACK**	4331	4530	4812	4740
B. Statistical Variation from Maximum (3σ)				
1. Measured data analyzed by multiple regression	268 (34 points J row only)	259 (44 points center and periphery)	271* (40 points center and periphery)	141 (38 points center and periphery)
2. Calculated by hot channel analysis	268	235	326	320
C. Maximum Statistical Thermal Capsule Temperature (I.A. + I.B., above)				
1. Measured from multiple regression fit	4627	4720	4972	4901
2. Calculated	4599	4765	5138	5060
II. Fuel Temperature (Average of nodal points at station 44 in. - Found by subtracting calculated temperature difference from thermal capsule temperatures)				
A. T sensor - T $fuel_{avg}$ from TRACK results at Station 44 Inches	4	149	27	40
B. Maximum Nominal Fuel Temperature (I.A. - II.A., above)				
1. Measured from multiple regression fit	4356	4312	4674	4720
2. Calculated	4327	4381	4785	4700
C. Maximum Statistical Fuel Temperature (I.C. - II.A., above)				
1. Measured multiple regression	4623	4571	4945	4861
2. Calculated	4595	4616	5111	

* Thermal capsules in J row which read abnormally low (4450°R and lower) are excluded from the data.

** Continual improvements in the TRACK program and the cluster model as well as actual differences in core operating conditions account for variability among the four reactors in the calculations. Additionally, the data for the various cores are not necessarily in the same cluster locations, because of changes in instrumentation placement.

5.5 APPENDIX

5.5.1 Analysis of Variance Method

The analysis of variance technique is a statistical method whereby the total variation in a set of data from a properly designed experiment can be partitioned into the variations assignable to the controlled experimental factors, their joint effects, and a residual due to extraneous or inherent effects. The ratio of the variance due to controlled factors and the variance due to extraneous effects provides a measure of the confidence level to which the controlled variance represents a real difference. For example, for 40 temperature data points with 20 of these at each of two different core radii, the total sum of squares is

$\sum_{i=1}^{40} (x_i - \bar{X})^2$, where $\bar{X}$ is the grand mean of the 40 data points. This total sum of squares is mathematically equal to the sum of squares between radii plus the sum of squares within radii:

$$\sum_{i=1}^{40} (x_i - \bar{X})^2 = \sum_{p=1}^{2} (\bar{X}_p - \bar{X})^2 + \sum_{p=1}^{2} \sum_{j=1}^{20} (x_j - \bar{X}_p)^2$$

where:

$\sum_{p=1}^{2} (\bar{X}_p - \bar{X})^2$ = sum of squares between radii

$\sum_{p=1}^{2} \sum_{j=1}^{20} (x_j - \bar{X}_p)^2$ = sum of squares within radii

$\bar{X}_p$ = the mean of the 20 data points at radius p

x_j = the 20 data points at one radius

The variance estimates for each of the sums of squares (called mean squares) is the sum of squares divided by the number of possible comparisons (degrees of freedom). Since there are 19 possible comparisons within each radius, and one comparison between radii, the variances are respectively,

$$\frac{\sum_{p=1}^{2} (\bar{X}_p - \bar{X})^2}{1}$$

and

$$\frac{\sum_{p=1}^{2} \sum_{i=1}^{20} (x_i - \bar{X}_p)^2}{19 + 19}$$

If a true difference between the average temperatures at the two core radii exists, then the variance between radii would be noticeably larger than the variance within radii. The ratio of the two variances:

$$F = \frac{\sum_{p=1}^{2} (\bar{X}_p - \bar{X})^2}{1} \Bigg/ \frac{\sum_{p=1}^{2} \sum_{i=1}^{20} (x_i - \bar{X}_p)^2}{38}$$

is termed the "F" ratio. Probabilities for such F-ratios have been computed and tabulated to judge whether or not the ratio of variances is great enough to be significant. Referring to a standard table, for 1 and 38 degrees of freedom, F is 4.10 at the 0.05 significance level. This means that if the F ratio is greater than or equal to 4.10 then the probability is 95 percent that the difference in the mean temperatures for the two radii is real (not random) and the corresponding probability is 5 percent that it is due to random variability alone. This technique can be extended by comparing the effects of two or more independent

variables and their interactions. The precision of the analysis is determined by the degrees of freedom (comparisons) available for estimating the variance for each source of variation.

5.5.2 Results of NRX-A5 Analysis of Variance

A preliminary analysis of the NRX-A5 temperature data showed the effects of locations with respect to control drums (on or off-drums). Interactions with other independent variable were not significant. This indicates no variation due to scalloping in the temperature data at the core edge and confirms the conclusion of Sections 5.4.5 and 5.4.4 that the drums did not cause an azimuthal temperature variation. The next step was to combine the data at several steady state holds to determine if the run times interact with the other variables. A summary of this analysis for EP-III is presented in Table 5-11. This table is divided into two parts, the first uses the four selected hold times in EP-III without considering run time effects to be a source of variation. In other words, the run time effects, if any, were averaged out by combining the data for the four selected holds in EP-III. The analysis of variance for EP-IV parallels the development presented for EP-III and therefore, the details for EP-IV will be omitted. Using the data for thirty-two thermocouples averaged over the four holds in EP-III, part 1 of the table shows the circumferential and radial positions to be significant at the 95 percent confidence level and the axial position to be significant at the 99 percent confidence level. The significance is determined by the "F" level test as described in the example, but does not necessarily imply that a temperature effect is large relative to the absolute temperature. For example, an effect may have only a 10°R difference in temperature between two core positions with zero scatter in the data and be significant at the 99 percent level, while another effect has a 100°R difference in temperature but a considerable amount of scatter which would make it less significant. Briefly, the significance of an effect refers to the probability that it is a real (not random) effect. The significance does not directly apply to the absolute magnitude of the effect. The intermediate steps shown in Table 5-11 represent the steps shown in the example problem. The mean squares (column 4) are the quotients of the sums of squares (column 3) over the respective degrees of freedom (column 2). The "F" levels (which are not in the table) were

found by dividing each respective mean square by the residual mean square. The significance of each effect is found by comparing the computed "F" level with the tabulated values for the degrees of freedom indicated. For example; for the radial (R) effect in Part 1 of Table 5-11, the sum of squares is 153999.02. Dividing this by the 3 degrees of freedom (since there are four different core radii represented), one obtains 51333.01 for the mean square. Dividing this by the thermocouple residual mean square which is 9990.01, one obtains the "F" level, which is 5.130. Referring to the tables of "F" levels, for 3 and 9 degrees of freedom the "F" level at the 95 percent confidence level is 3.86 and at the 99 percent confidence level it is 6.99. Since the computed "F" level is greater than 3.86 but not greater than 6.99, one can say that the observed differences in average temperature as a function of radius for the 4 run times in EP-III are real with a 95 percent probability of being correct. The two factor interactions (C x A, C x R, and A x R) are not significant, i.e., the circumferential effect, (C), appears independently of the core axial position, (A), and radius, (R).

In part 2 of Table 5-11, the run time (T) effects are included and are significant at the 99 percent confidence level. The two factor interactions (T x C, T x A, and T x R), are also significant at the 99 percent confidence level. Therefore, the analysis of variance ought to be carried out for each of the four run times separately. However, the three factor interactions with the run time are not significant. The thermocouple residual within run time is computed in two ways. The 26 degrees of freedom applies when the non-significant three-factor interactions are included in the analysis and result in a residual mean square of 173.60. If the three factor interactions are ignored (because they have been found non-significant) the additional degrees of freedom can be pooled to obtain a better estimate of the thermocouple residual within run time. This improved value of 275.24 was then used to re-calculate the "F" levels for the significant variables. The composite random variance (computed from the residual within run time and the thermocouple variance) is 2703.93. The square root of the variance is the standard deviation and is equal to 52.0 degrees. This represents the random variation in the thermocouple data after accounting for all significant position effects. Based on the results from part 2 of Table 5-11 which

show that run time effects are easily distinguishable from the random variations, the analysis of variance was then carried out for each of the four run times in EP-III. Because similar results were obtained for EP-IV, this was also done for four run times in that hold. The details of the calculation for the start-of-life in EP-III are shown in Table 5-12. The only significant effect at this run time is the axial position and the non-significant two factor interactions are again pooled to obtain a better estimate of the random variance.

Similar calculations were carried out for each of the seven other run times and the results are summarized in Table 5-13. Note that the circumferential effect is merely a comparison between sensors at 120° and 300° azimuthal position which are both outside the hot buffer region. The circumferential effect increases in significance during EP-III and then becomes insignificant during EP-IV. The average difference between the temperatures at 120° and 300° azimuthal position is 51°R in EP-III. It is also 51°R in EP-IV, however, the random variability in the data in EP-IV is greater which causes the circumferential effect to be non-significant. As expected, the radial effect increases in significance with increase in run time. The existence of this effect near the start-of-life is due to the lower temperatures near core radius 10 - 14 inches which are discussed in Section 5.4.4.1. The average difference in EP-III is 46.1°R cooler at the 10-inch radius and 19.3°R cooler at the 14-inch radius. In EP-IV the increase of the peripheral temperature at the end-of-life is the principal cause of the radial effect. Although the analysis of variance indicates a radial effect at all but one of the run times, the curve fit by multiple regression did not indicate this significance. This is primarily due to the non-uniform radial spacing of thermocouples at 2, 10, 14, and 16-inch radii.

TABLE 5-11

NRX-A5 TEMPERATURE - EP-III (4 HOLDS)

ANALYSIS OF VARIANCE
(DRUM ANGLE FOUND NON-SIGNIFICANT)

	1. Source of Variation	2. Degrees of Freedom	3. Sums of Squares	4. Mean Squares (Variances)	5. Significance (From "F" Level)
1.	Ignore run time effects (average 4 holds)				
	Circumference (C)	1	83079.07	83079.07	*
	Axial Position (A)	3	87032182.62	29010727.54	**
	Radial Distance (R)	3	153999.02	51333.01	*
	C x A	3	53822.02	17940.67	---
	C x R	3	38020.71	12673.57	---
	A x R	9	148262.63	16473.63	---
	Thermocouple Residual	9	89910.07	9990.01	**
2.	Run Time Effects (4 Holds)				
	Run Time (T)	3	187856.90	62618.97	**
	T x C	3	2996.09	998.70	**
	T x A	9	26014.09	2890.53	**
	T x R	9	6471.32	719.04	**
	T x C x A	9	2942.69	326.97	(Pooled)
	T x C x R	9	1332.76	148.08	(Pooled)
	T x A x R	27	10752.65	398.25	(Pooled)
	Residual Within Run Time	26	4513.69	173.60	
	Residual Within Run Time (Pooled)	71	19541.79	275.24	
	TOTAL	126[1]	5 342157.00		

[1] One degree of freedom lost for missing value.

---Not significant
*Significant at 95 percent confidence level
**Significant at 99 percent confidence level

TABLE 5-12

NRX-A5 TEMPERATURES - EP-111 (25400)

ANALYSIS OF VARIANCE
(DRUM ANGLE FOUND NON-SIGNIFICANT)

1. Source of Variation	2. Degrees of Freedom	3. Sums of Squares	4. Mean Squares (Variances)	5. Significance (From "F" Level)
Circumference (C)	1	13041.12	13041.12	---
Axial Position (A)	3	21318222.62	7106074.21	**
Radial Distance (R)	3	31909.38	10636.46	---
C x A	3	11632.12	3877.37	(Pooled)
C x R	3	10579.38	3526.46	(Pooled)
A x R	9	43590.88	4843.43	(Pooled)
Residual	8	24838.00	3104.75	
Residual (Pooled)	23		90640.38	3940.89
TOTAL	30(1)	21453813.50		

(1) One degree of freedom lost for missing value

---Not significant

**Significant at 99 percent confidence level

Astronuclear Laboratory

TABLE 5-13

SUMMARY OF RESULTS OF ANALYSIS OF VARIANCE
ON NRX-A5 THERMOCOUPLES

Effect	EP-III Run Time 25400	25700	25930	26248	Average
C Circumference	--	*	*	**	*
A Axial	**	**	**	**	**
R Radial	--	*	*	*	*
All 2 factor interactions	--	--	--	--	--
σ	62.8	57.1	59.7	63.0	52.0

Effect	EP-IV Run Time 13003	13243	13483	13813	Average
C Circumference	*	--	--	--	*
A Axial	**	**	**	**	**
R Radial	**	*	*	**	**
A x R	--	--	--	**	--
All other 2 factor interactions	--	--	--	--	--
σ	52.5	51.4	51.6	68.3	59.7

--Not significant
*Significant at 95 percent confidence level
**Significant at 99 percent confidence level

C Circumference = thermocouples at 120° versus 300° azimuth.

A Axial = thermocouples at 8, 20, 26, and 32 inch station.

R Radial = thermocouples at 2, 10, 14, and 16 inch radius.

σ = one standard deviation value of random thermocouple variation

CHAPTER 6

CORROSION*

6.1 SUMMARY

This chapter presents a detailed review of the corrosion data obtained from the NRX-A5 test. These data include: fuel element, filler strip, and support block corrosion. The fuel element was assessed with regard to overall weight losses, incremental weight losses, external surface weight losses, pinholes, channel exposure, and hot end condition. External surface regression data was obtained and evaluated for filler strips adjacent to both the normal and hot buffer regions. A detailed analysis was performed on both the mechanical and corrosion performance of the support blocks. In an attempt to isolate the significant environmental and property parameters which affect element weight, multiple regression analyses were performed on the fuel element data. The analytical techniques used to predict bore corrosion, surface corrosion, and pinholing are presented. At the conclusion of this chapter a tabulation is given concerning the conclusions resulting from the evaluation of the NRX-A5 corrosion data.

---

* Major contributors to this chapter were R.A. Agosti, L. Boman, K. Cooper, G.E. Cort S.L. Davidson, F. Ebert, S. Goldberg, C. Goodin, A.Y. Lee, A.F. Maguire and J.C. Reese

6.2 INTRODUCTION

The NRX-A5 reactor operated for 30.1 minutes above 3700°R chamber temperature. Based on the NRX/EST operating experience and available analytical information, the limiting drum angle was set at 145°* at which time it was expected that the loss of carbon would not affect the structural integrity of the fuel elements. It was concluded that a drum angle of 145° would be adequate to demonstrate that the NRX-A5 fuel is behaving significantly better than the NRX/EST. In addition to fuel element corrosion, local corrosion damage was observed in the filler strips and support blocks. This did not present an imminent threat to the ability of the core to continue functioning.

This chapter has been arranged to discuss both qualitatively and quantitatively the corrosion damage associated with the NRX-A5 fuel elements and core support components. The corrosion damage has been categorized and appears in the following order in this chapter: (1) fuel element weight losses, overall, incremental, and external surface, (2) pinholing, (3) channel exposure, (4) hot end corrosion and (5) support block corrosion. The state of the art is not completely satisfactory for predicting in detail the bore or surface weight losses. Therefore, as in the case of the NRX/EST, the analytical tools proved inadequate and are presently being refined. In all cases where applicable the corrosion damage has been compared to the NRX-A3 and NRX/EST reactors.

---

* "Development of Drum Limit for NRX-A5 EP-IV Presentation to SNPO-C, 20 June 1966", WANL-TME-1452.

6.3 FUEL ELEMENT CORROSION

6.3.1 Fuel Element Overall Weight Losses

Based on the 1551 fuel elements out of the 1584 fuel elements in the NRX-A5 core which were weighed, the total core weight loss was calculated to be approximately 43 kilograms. Table 6-1 is a summary of the weight loss data as measured which includes the unweighed elements. It was assumed that the unweighed elements were broken and equal in weight to the average of the weighed broken elements at the same radial location. The implied average overall weight loss per element was thus estimated to be 27.0 grams/element of which the average WAFF element weight loss was 36.9 grams and the average Y-12 element weight loss was 16.0 grams. The radial weight loss distribution for each broken and unbroken element is shown in Figure 6-1. There are three important results shown in this figure. First, the greatest losses occurred at the core center and core periphery with a region of relatively low weight loss from approximately core radius 8.0 in. to 13.0 in.. Second, there is a significant difference in weight loss suffered by the Y-12 and WAFF elements in the region from core radius 10.4 in. to 14.4 in. where they overlap. The WAFF elements at core radius 14.4 in. show approximately two times the Y-12 weight losses. Third, in general, there is a wide scatter and variance in element performance for both the WAFF and Y-12 fuel elements.

A comparison of the overall average weight loss for previous reactor tests indicated for the NRX-A3, 10.6 grams/element and for the NRX/EST 32.4 grams/element. Figure 6-2 presents a comparison of the average weight loss distributions for all three reactors. The trends of Figure 6-2 exhibit on all three plots a noticeable region of low weight loss from core radius 8 in. to 12 in.. This is more evident on the NRX/EST and NRX-A5 where the greatest weight losses occurred at the core center and core periphery. It should be noted that in the periphery (14 in. to 17 in.), the NRX/EST contained no Y-12 elements and in the NRX-A5, 48 Y-12 elements. In both the NRX/EST and NRX-A5 there is a significant difference in weight loss suffered by the Y-12 and WAFF fuel elements in the region where they overlap.

TABLE 6-1

NRX-A5 TOTAL FUEL ELEMENT WEIGHT LOSS

	WAFF	Y-12	ALL
Total No. of Fuel Elements	839	745	1584
Total No. Intact (Weighed)	252	673	925
Total No. Broken (Weighed)	562	64	626
Fraction Broken	0.700	0.097	0.416
No. of Unweighed Elements	25	8	33
Average Weight Loss - Intact Elements (gms)	20.8	14.4	16.2
Average Weight Loss - Broken Elements (gms)	43.8	30.5	42.4
*Implied Average Weight Loss - All Elements (gms)	36.9	16.0	27.0

* Assuming that unweighed elements are broken and equal in weight to the average for weighed broken elements.

The NRX-A5 average fuel element weight losses were reduced into the six core sectors to investigate the azimuthal variation of weight loss which may be attributed to operational characteristics or fuel element quality. Figures 6-3 and 6-4 provide the sector radial weight loss distributions for both the Y-12 and WAFF fuel elements in the NRX-A5 core. When the core average weight loss is compared to the sector average weight losses, a merit factor of the individual sector performance can be obtained. Similar data was extracted from the NRX-EST overall weight losses. The results from this analysis showed that the average element weight loss as a function of core radius was approximately equivalent in all sectors of the NRX/EST and NRX-A5 reactor cores.

The broken elements found in the NRX-A5 may be attributed to regions of high localized weight loss and the handling of elements during post test disassembly. The elements which experienced high weight losses were characteristic of the elements which were broken. The total number of broken elements in the NRX-A5 was 626. This compares to 189 observed in the NRX/EST. The fraction of broken elements in the NRX-A5 was 0.42 and the fraction of broken elements in the NRX/EST was 0.37. These fractions include the unweighed elements which were assumed to be broken. An examination of the break patterns indicated that in general the breaks occurred at the position of the peak incremental weight loss. The NRX/EST showed more multiple breaks than the NRX-A5. This is obvious, if one examines the peak incremental weight losses for the NRX/EST which indicate both a mid band peak and hot end peak. The difference in axial weight loss distribution between the NRX/EST and NRX-A5 is due to the difference in operating profiles. The distribution of the fraction of broken elements for NRX-A5 is given on Figure 6-5. The comparison of break patterns for both reactors is given on Figure 6-6. The greater number of broken elements in the NRX-A5 is evident on this figure and is attributed to the high local mid-band weight loss.

In order to summarize the overall weight loss performance of both the NRX-A5 and NRX/EST which experienced approximately the same time at full power, Table 6-2 was devised. Table 6-2 groups the average overall weight loss data in pertinent core radial regions i.e.,

the core central region 0 in. to 9.0 in., the core mid-radial region 9 in. to 14 in. and the core peripheral region 14 in. to 17 in. These radial core regions will be used consistently throughout the text to exhibit areas of corrosion damage.

TABLE 6-2

COMPARISON OF THE NRX/EST AND NRX-A5 FUEL ELEMENT WEIGHT LOSS

	Central Region 0 - 9"						Mid-Radial Region 9" - 14"						Peripheral Region 14" - 17"					
	NRX/EST			NRX-A5			NRX/EST			NRX-A5			NRX/EST			NRX-A5		
	WAFF	Y-12	Total	WAFF	Y-12	Total	WAFF	Y-12	Total	WAFF	Y-12	Total	WAFF	Y-12	Total	WAFF	Y-12	Total
Total No. Fuel Elements	0	426	426	324	102	426	357	267	624	29	595	624	534	0	534	486	48	534
Total No. Intact (Weighed)	0	369	369	70	89	159	210	255	465	11	550	561	267	0	267	171	34	205
Total No. Broken (Weighed)	0	39	39	250	13	263	53	7	60	18	38	56	40	0	90	294	13	307
Fraction Broken	0	0.134	0.134	0.784	0.127	0.627	0.412	0.045	0.235	0.621	0.076	0.101	0.50	0	0.50	0.648	0.292	0.614
No. Unweighed	0	18	18	4	0	4	94	5	99	0	7	7	177	0	177	21	1	22
(Weighed only) Avg. Wt. Loss - Broken Elements	0	47.3	47.3	56.0	41.0	54.4	71.0	17.8	64.8	32.3	26.4	28.3	58.1	0	58.1	34.1	32.2	34.0
Avg. Wt. Loss - Intact Elements	0	14.5	14.5	30.8	17.5	23.4	30.1	11.6	20.0	16.8	13.7	13.8	29.2	0	29.2	17.0	17.6	17.1
Implied Wt. Loss - All Elements (Includes Unweighed Elements)			18.9			43.3			31.9			15.1			43.7			27.3

Astronuclear Laboratory

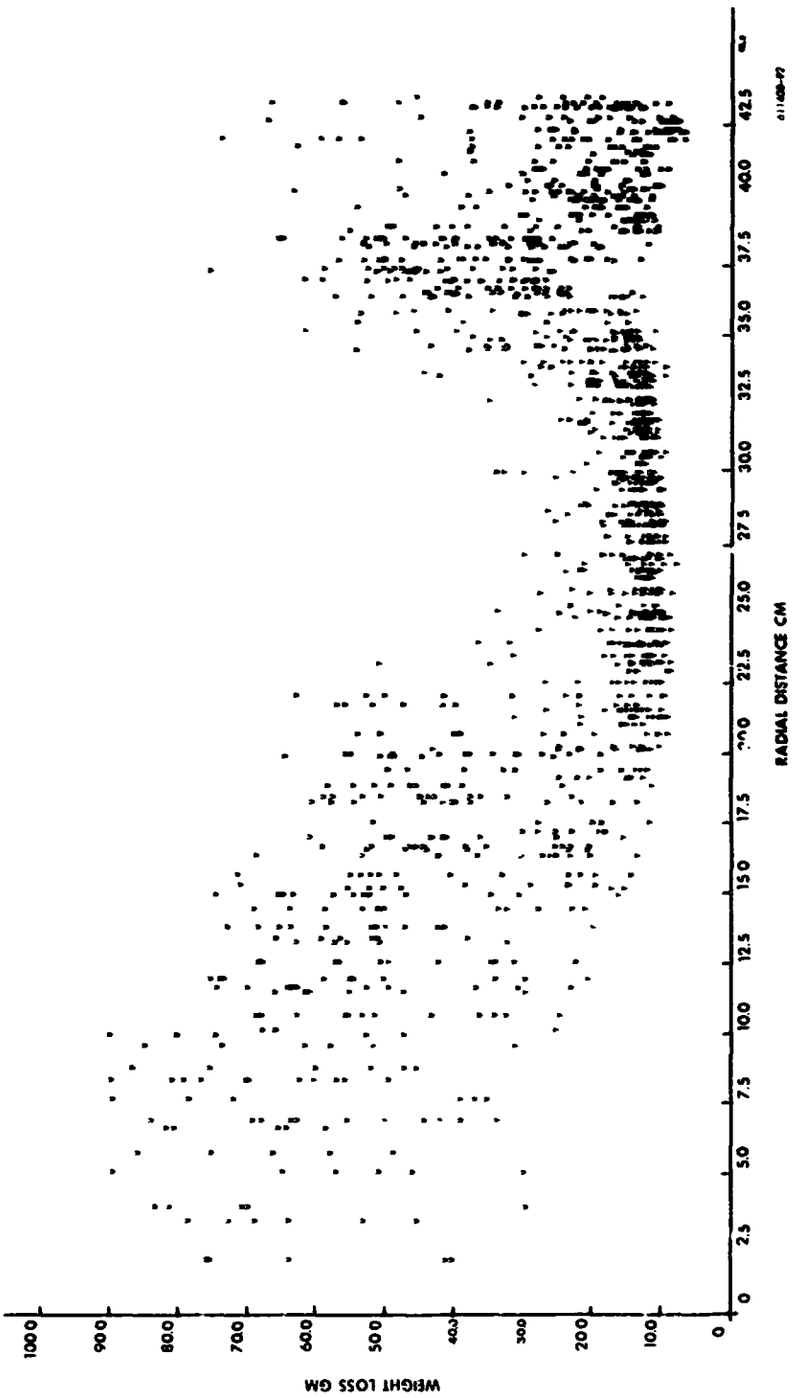

Figure 6-1. Radial Distribution of NRX-A5 Overall Fuel Element Weight Loss

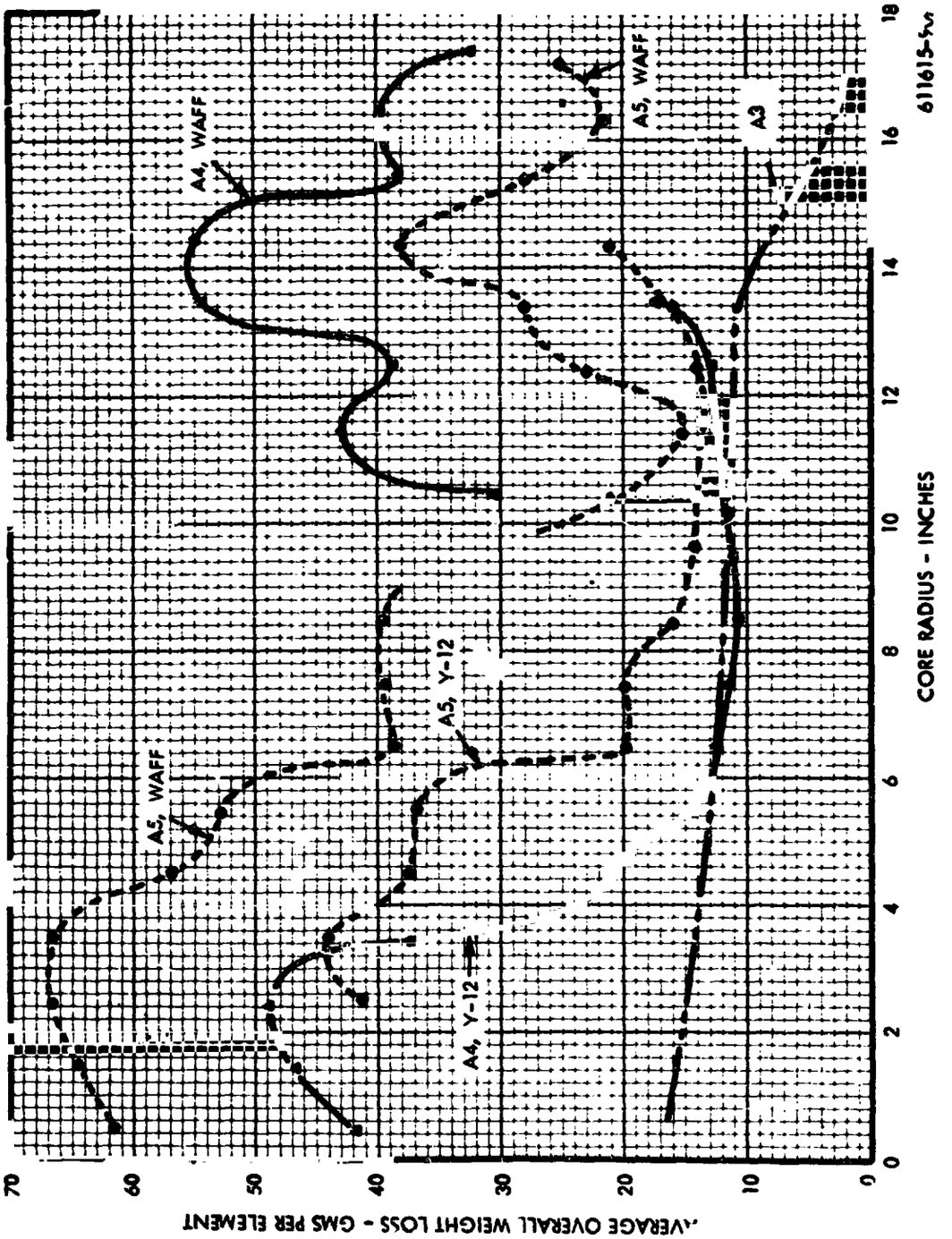

Figure 6-2. Radial Distribution of Overall Weight Losses in the NRX-A3 NRX/EST, and NRX-A5

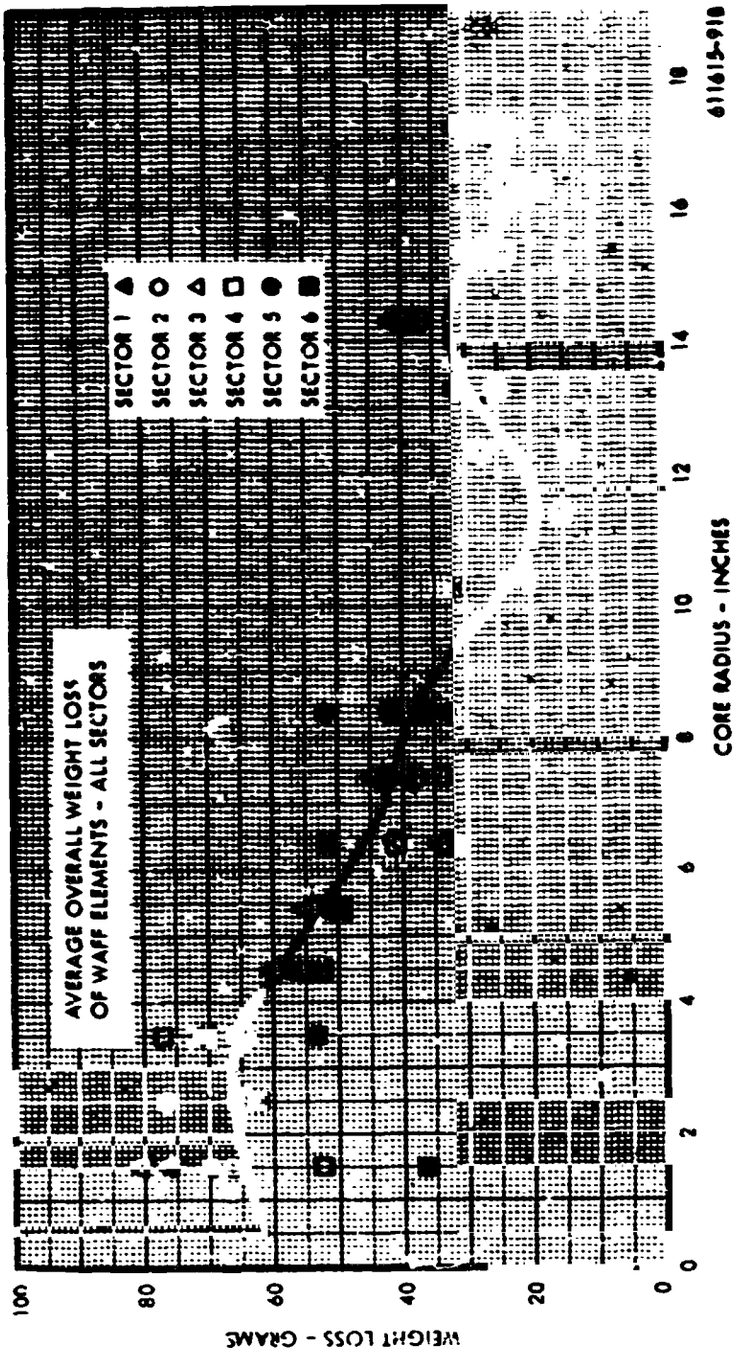

Figure 6-3. Azimuthal Variation of NRX-A5 Overall Weight Loss for WAFF Fuel Elements

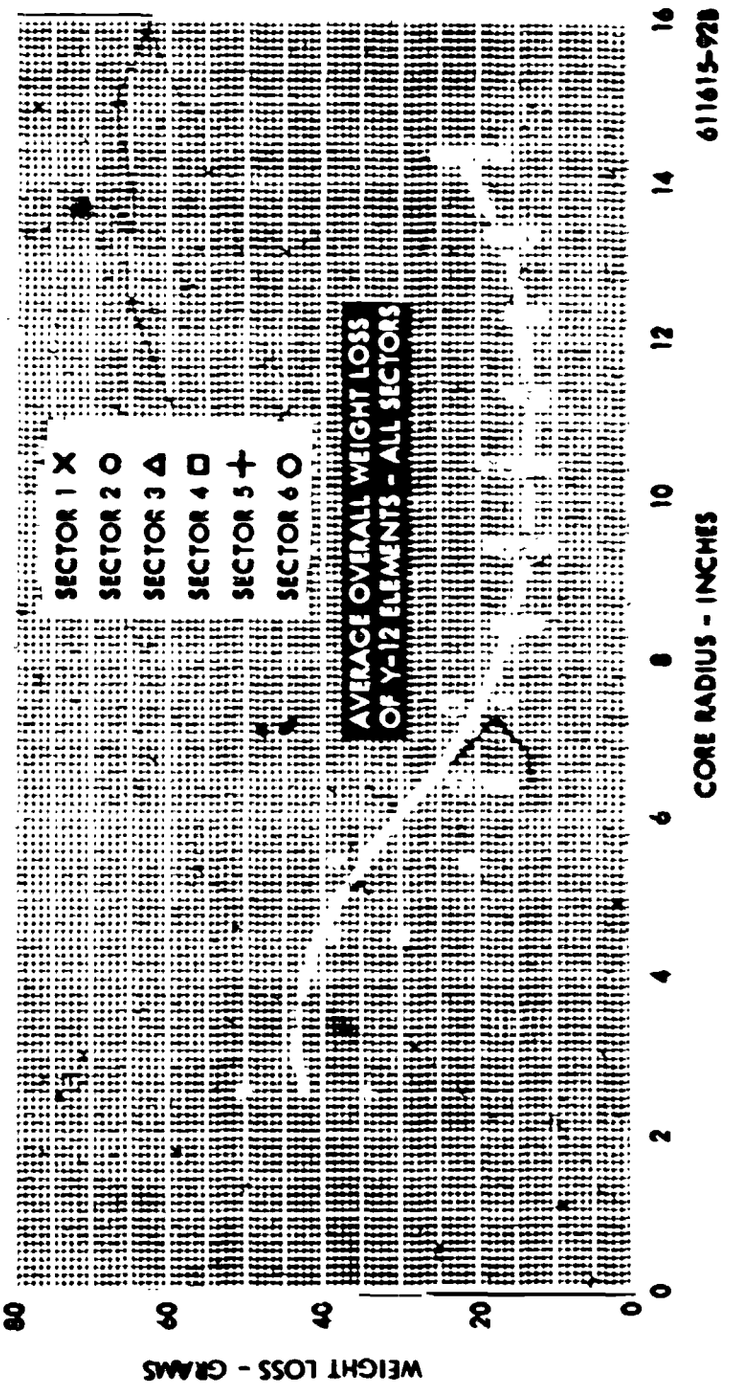

Figure 6-4. Azimuthal Variation of NRX-A5 Overall Weight Loss for a-12 Fuel Elements

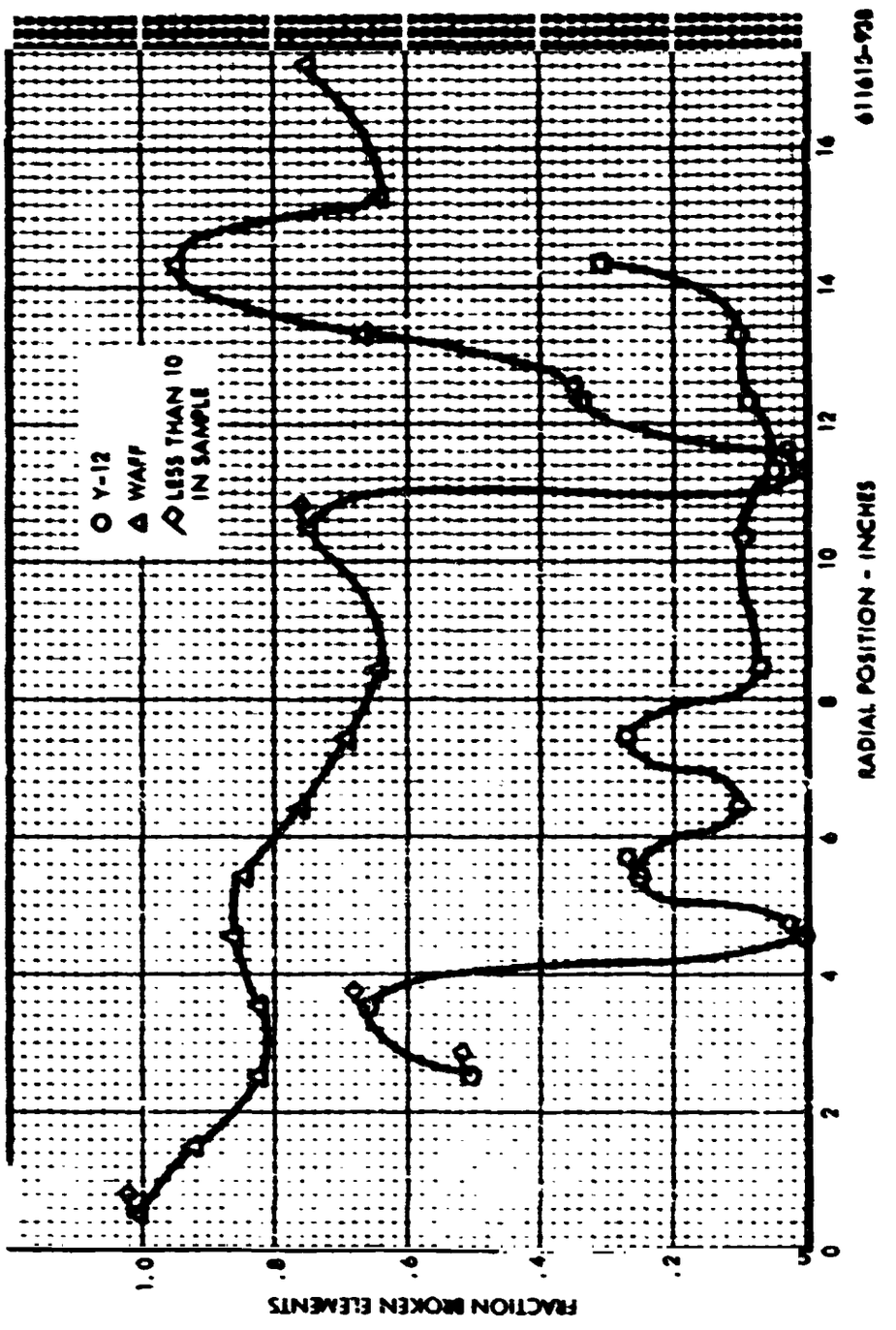

Figure 6-5. Distribution of the Fraction of Broken Elements in the NRX-A5 Reactor

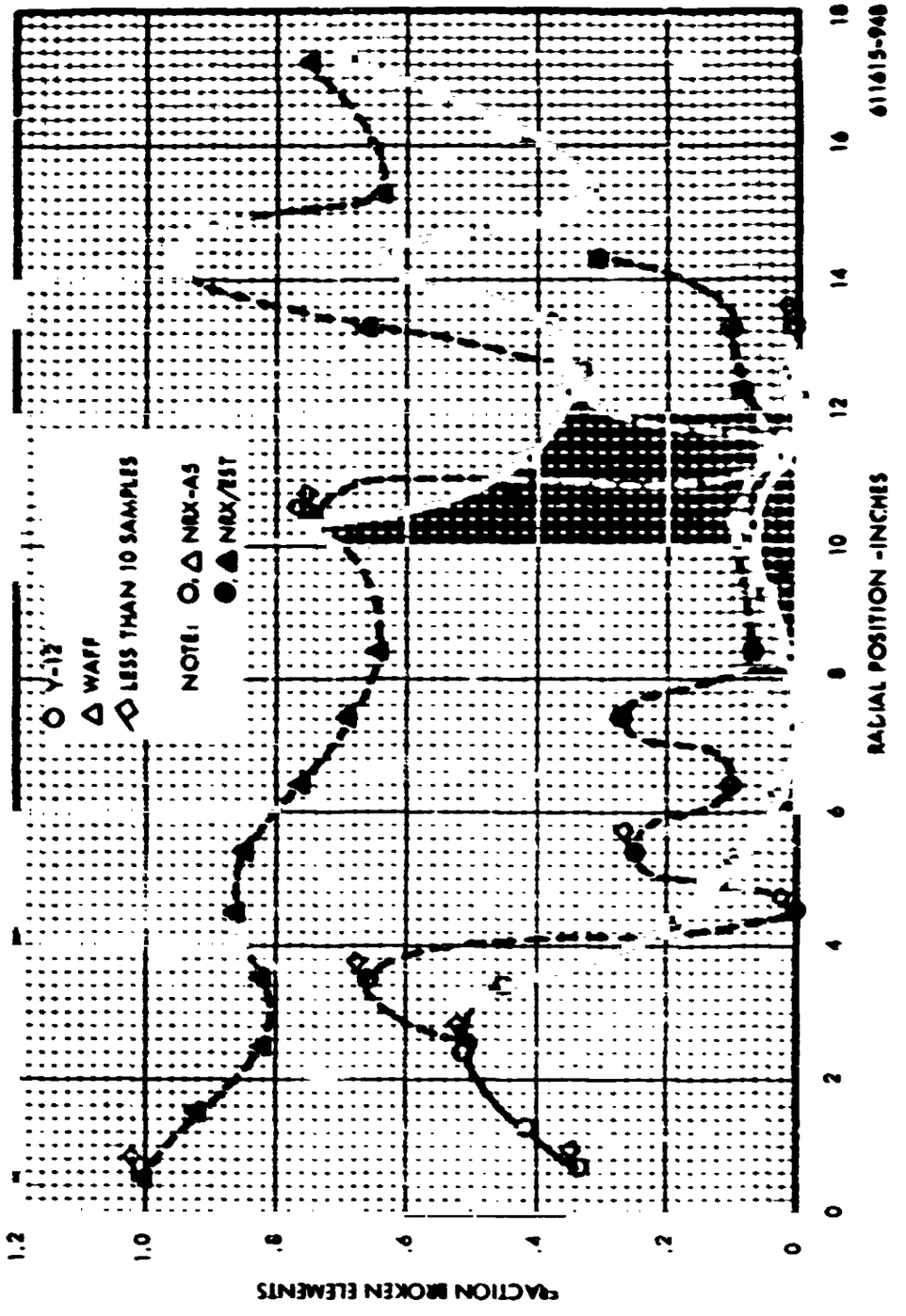

Figure 6-6. Comparison of the Fraction of Broken Elements in the NRX/EST and NRX-A5 Reactors

6.3.2 Fuel Element Incremental Weight Losses

The incremental weight loss data provided for 66 NRX-A5 fuel elements* were studied in an attempt to define the corrosion influencing parameters. The incremental axial weight loss distributions were divided into the three groups judged to be appropriate for the NRX-A5, core central region 0 in. to 9 in., core mid-radial region 9.0 in. to 14.0 in., and core peripheral region 14.0 in. to 17.0 in. The average incremental weight losses for these radial regions are given in Figure 6-7. This Figure indicates that the integrated weight loss is highest in the central region and lowest in the mid-radial region. In addition, a well defined peak mid-band weight loss is exhibited at approximately core station 20.0 in. for all regions. A low hot end weight loss from core stations 30 in. to 52 in. was noted in the NRX-A5 in contrast to the NRX/EST illustrated in Figure 6-8. A comparison of the peak midband losses yielded 4.25 grams/in. in the NRX-A5 and 7.6 grams/in. in the NRX/EST. An additional correlation of interest was performed with the incremental weight losses. The combined data on all the Y-12 and WAFF elements were averaged and then compared to the average of all the Y-12 elements. Figure 6-9 shows the result of this correlation. The shape of the two distributions are similar, however, the higher level of fuelea material weight loss suffered by the WAFF elements is clearly demonstrated.

The maximum incremental weight loss occurring in the midband region between stations 20 in. to 30 in. was plotted for the NRX/EST and NRX-A5 incrementals. Figure 6-10 presents the radial distribution of this peak weight loss and clearly illustrates, in general, for all core regions that the NRX-A5 peak incremental weight losses are higher than the NRX/EST. The peak weight losses, as expected, follow the overall weight loss distributions.

---

*"Post Operational Examination Results For The NRX-A5 Fuel Elements" (To be Issued).

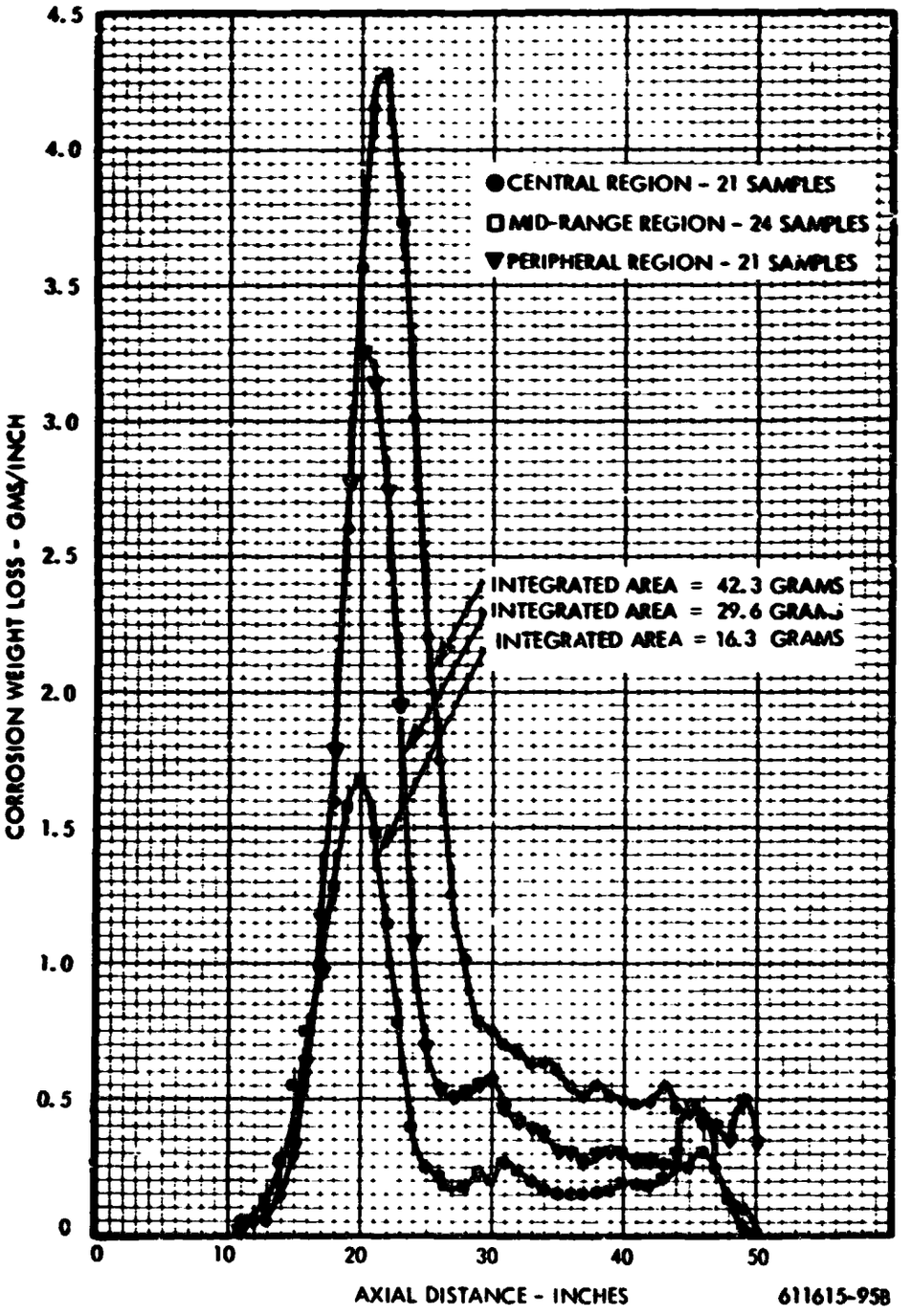

Figure 6-7. NRX-A5 Incremental Weight Losses in Three Radial Regions

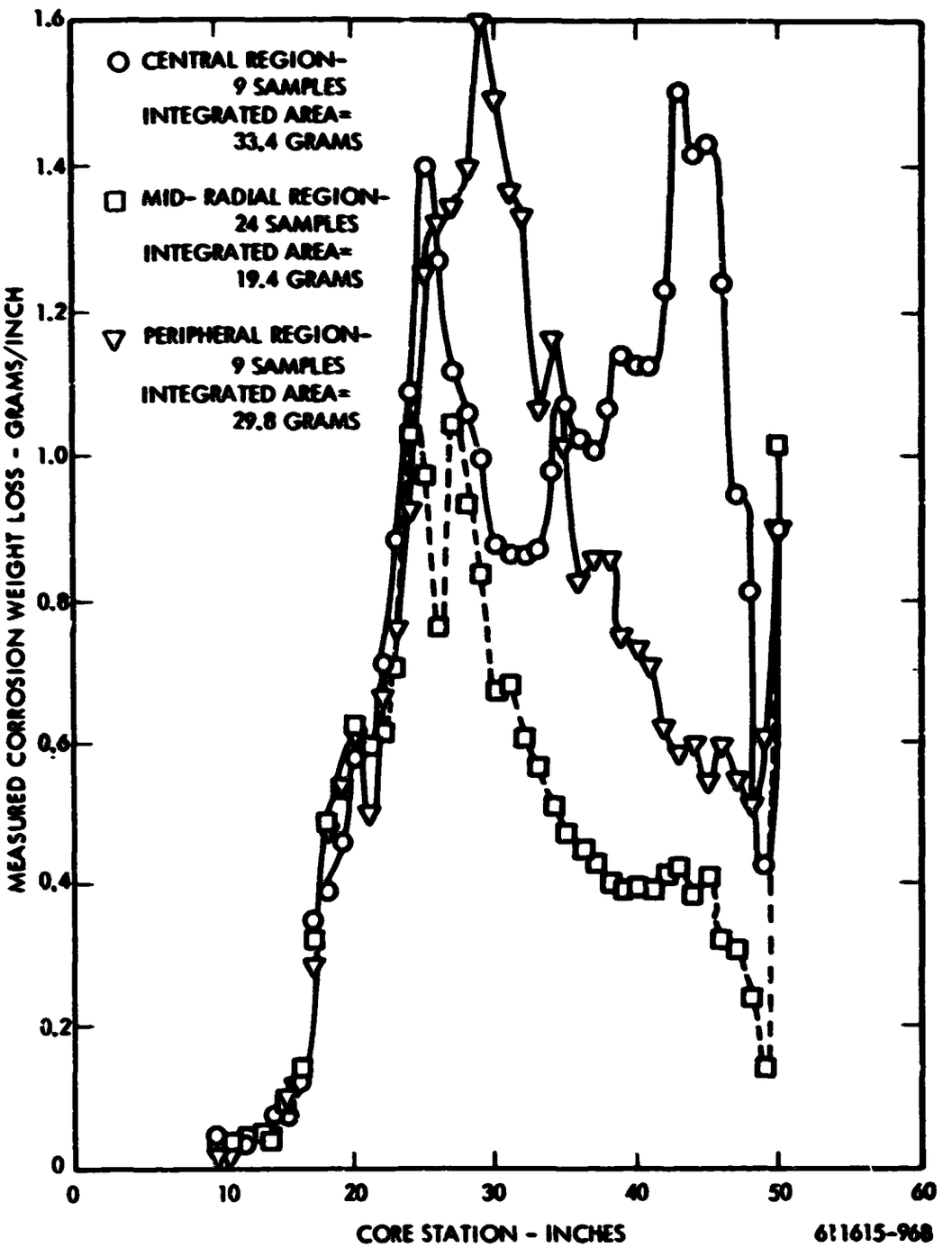

Figure 6-8. NRX/EST Incremental Weight Losses in Three Radial Regions

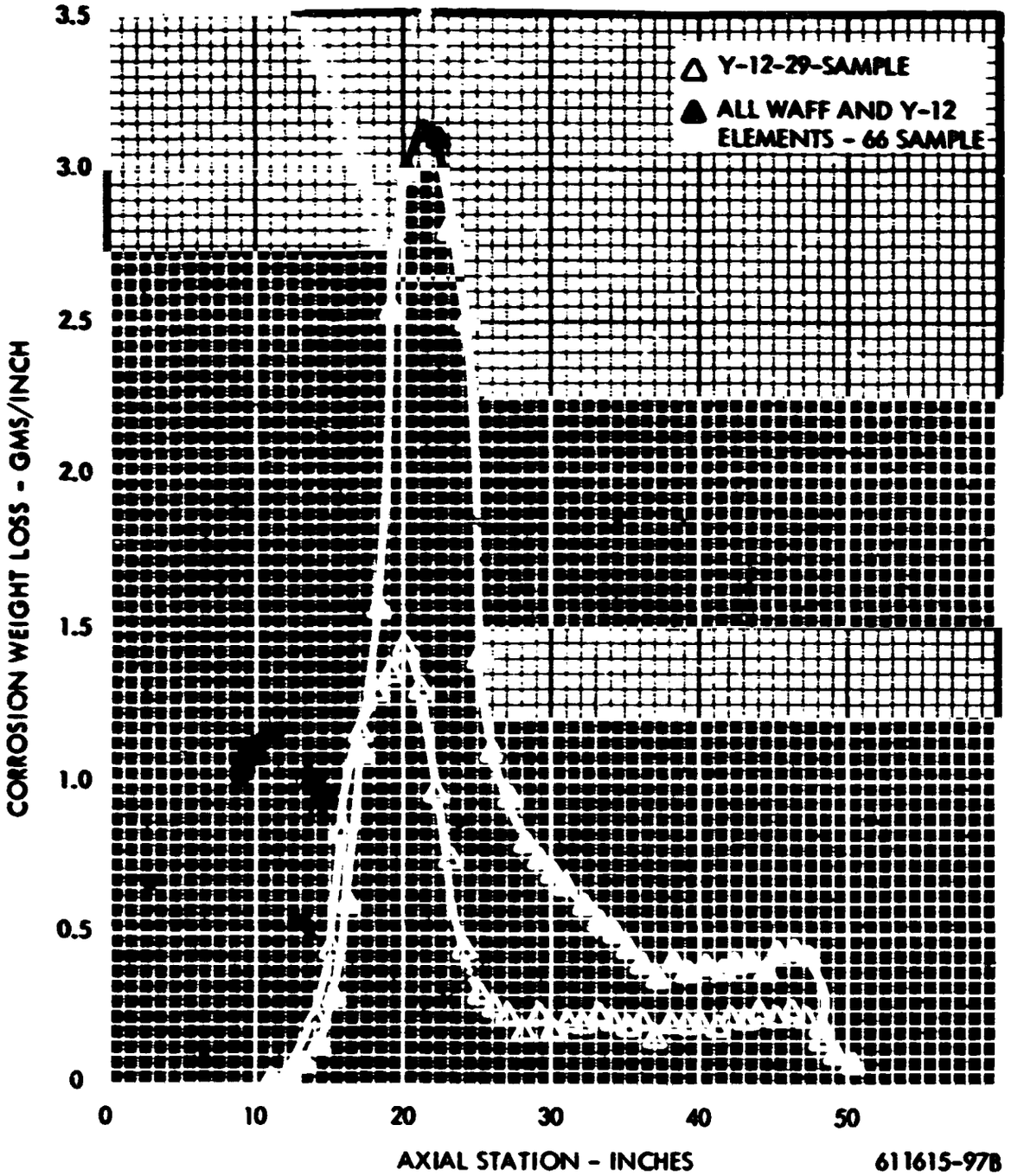

Figure 6-9. NRX-A5 Average Incremental Weight Losses for all WAFF and Y-12 Fuel Elements

CONFIDENTIAL

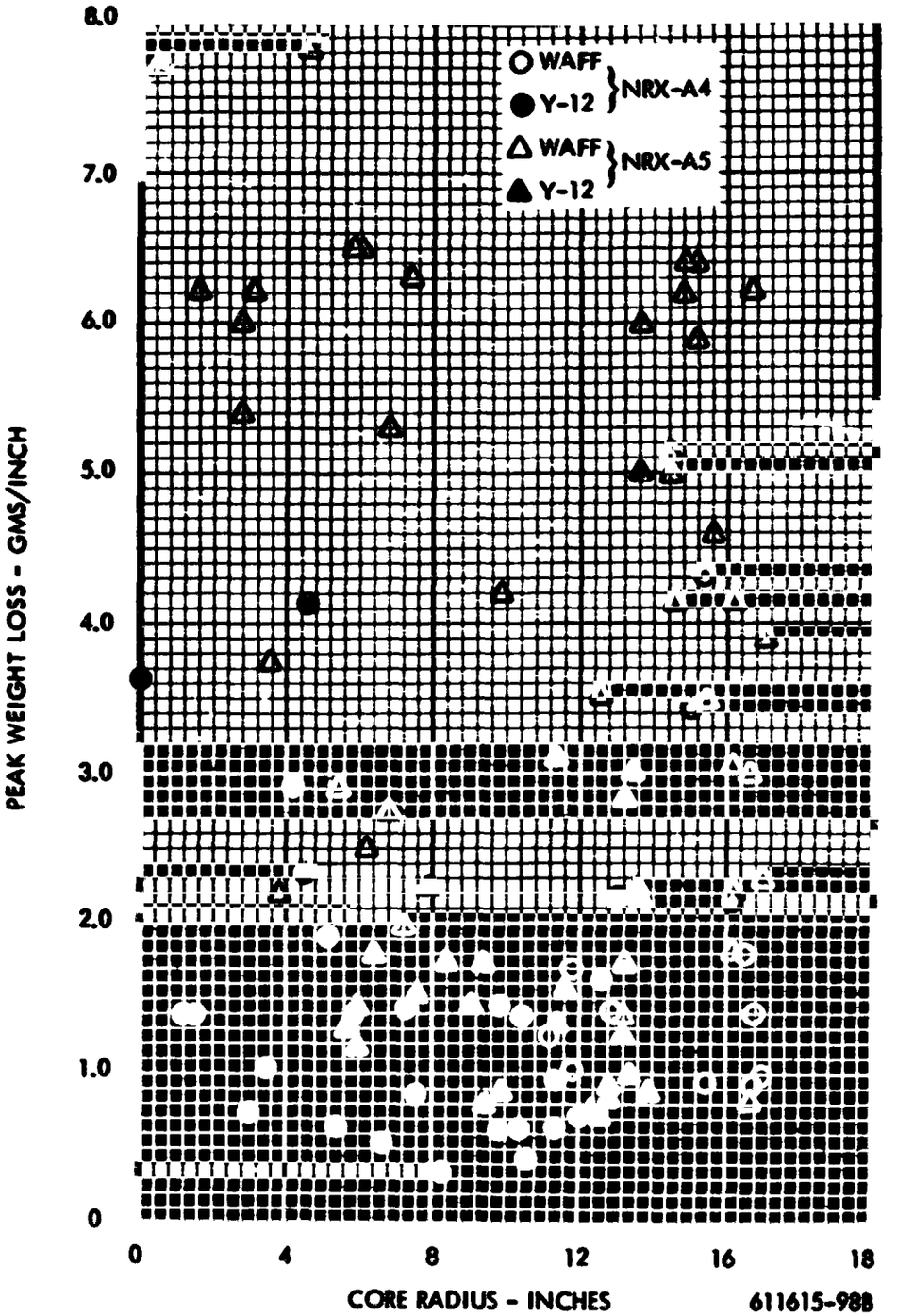

Figure 6-10. Radial Distribution of Peak NRX/EST and NRX-A5 Weight Losses

CONFIDENTIAL

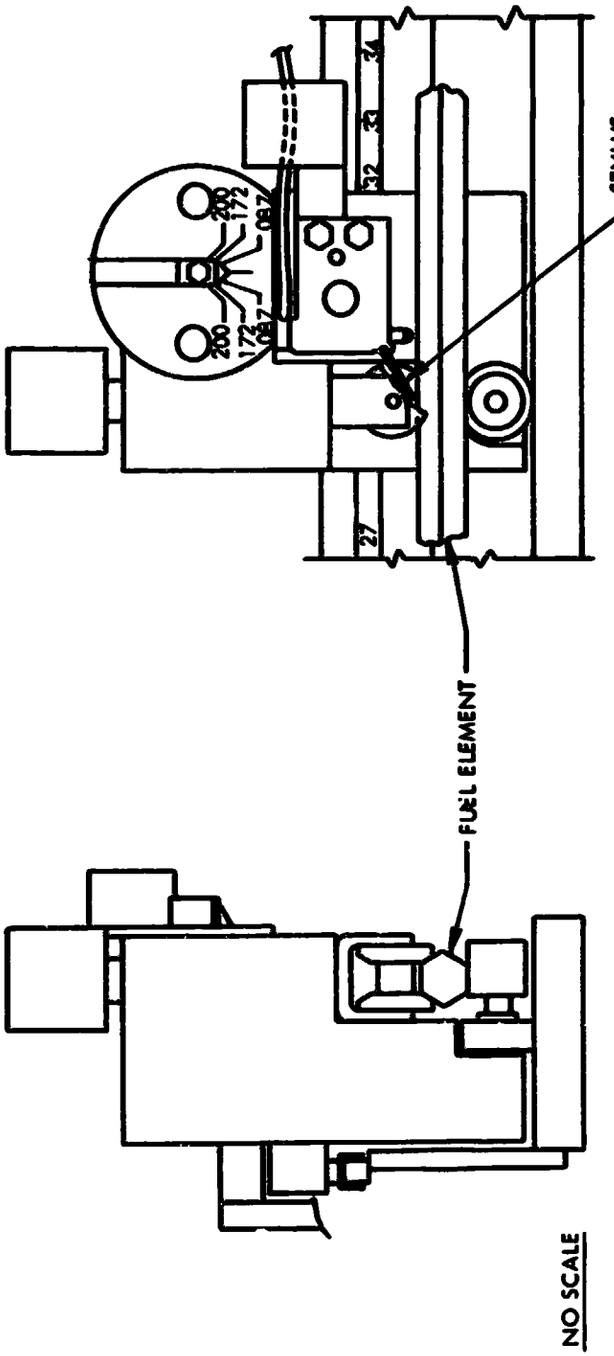

Figure 6-11. External Surface Corrosion Measuring Apparatus

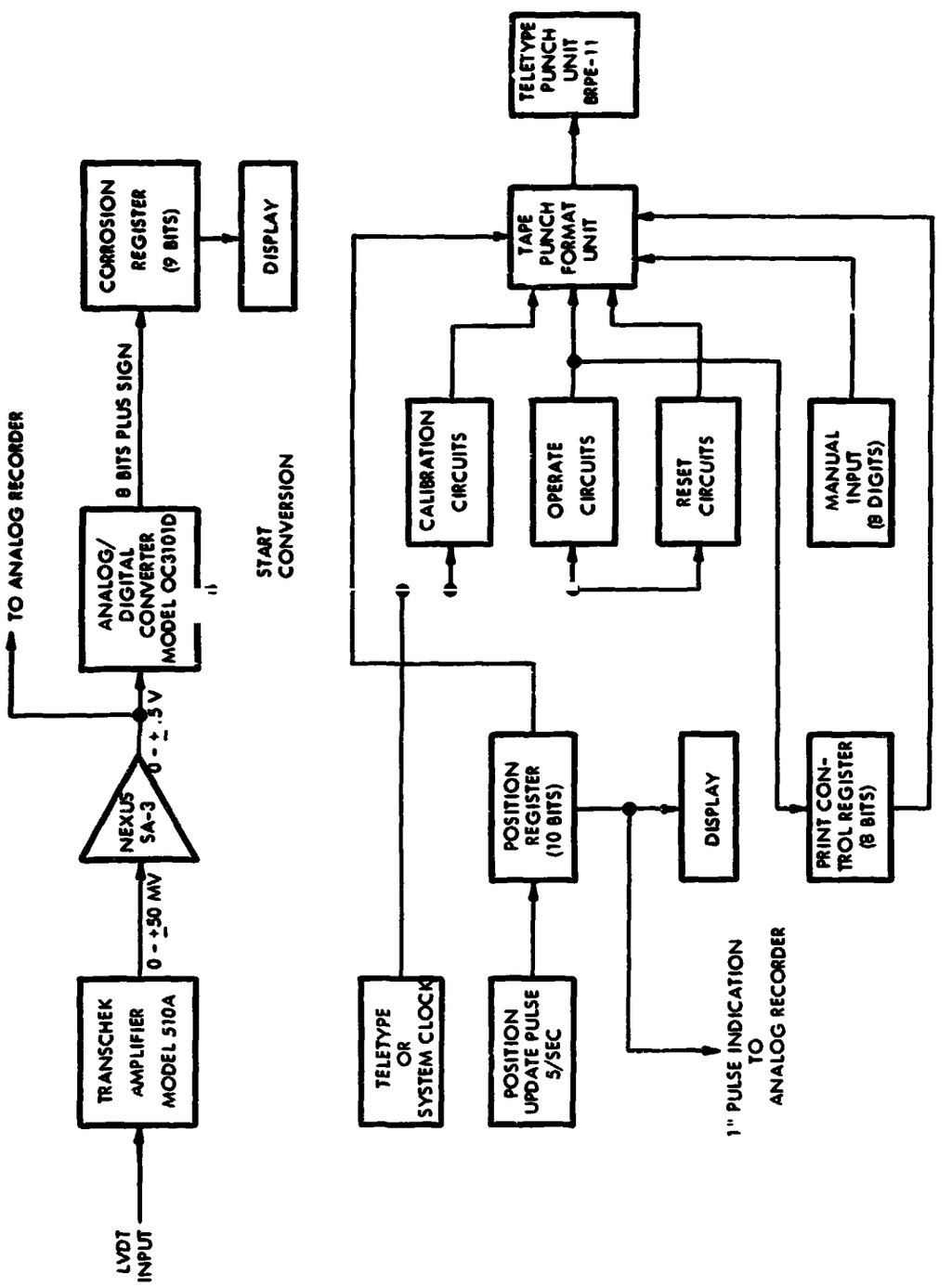

Figure 6-12. Block Diagram of Digitized Surface Corrosion Measuring System

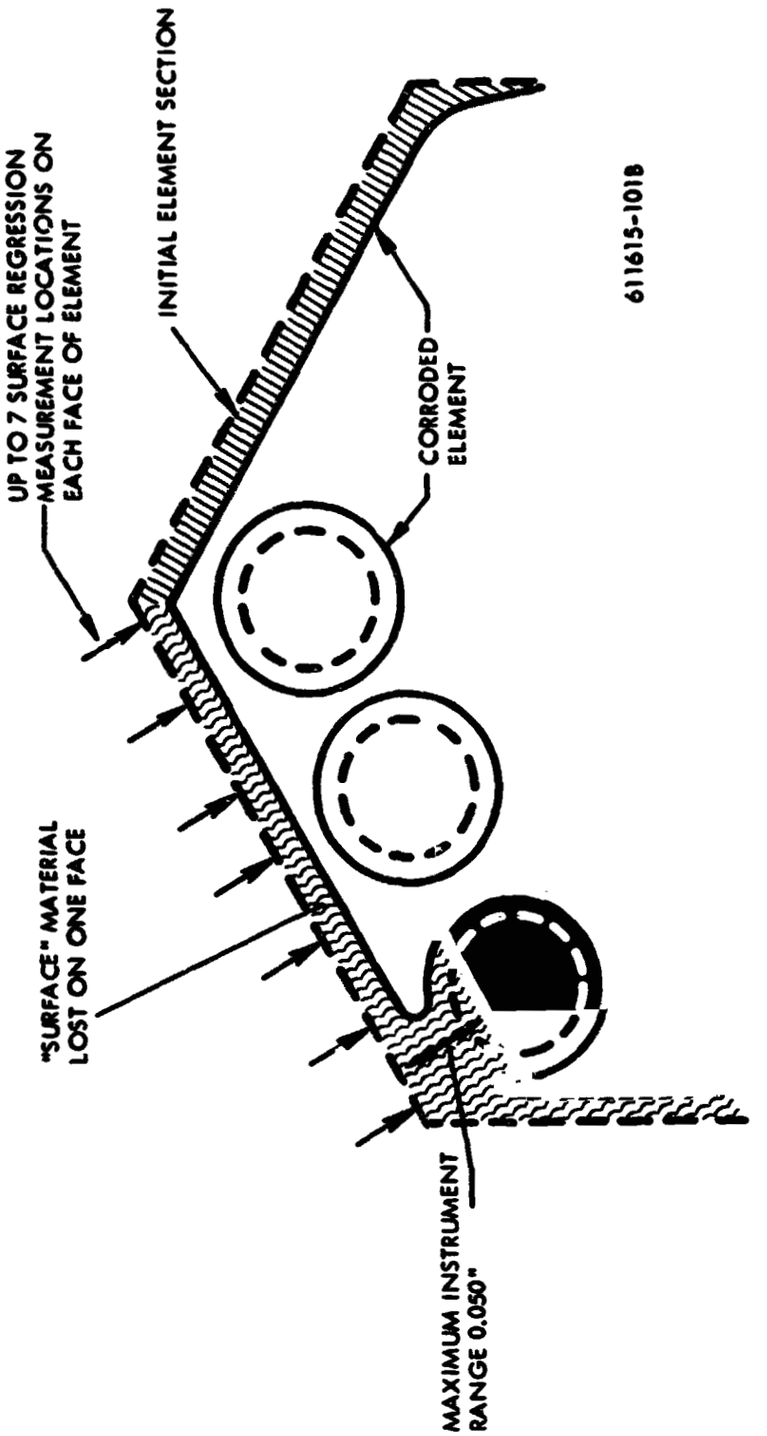

Figure 6-13. Location of Trace Data

6.3.3 Fuel Element External Surface Weight Losses

Post test external trace data were taken on selected NRX-A5 fuel elements. Similar data were obtained on selected NRX-A3 and NRX/EST fuel elements and are included in this section for comparison. Figure 6-11 shows a sketch of the trace apparatus. The purpose of these surface regression measurements was to provide data which would allow an estimate to be made of the extent of the external fuel element corrosion. An extensive effort was required both to obtain these traces and to reduce the data into a usable form. The following tabulation gives the number of axial traces, the number of element faces examined, and the total number of fuel elements examined for the NRX/EST and NRX-A5.

	NRX/EST	NRX-A5
No. of Elements	122	127
No. of Faces	343	317
No. of Traces	1334	1381

In this section the measurement of surface regression and the conversion of this data into a usable form are described. The results of the NRX-A3, NRX/EST, and NRX-A5 surface measurements are also given.

6.3.3.1 Data Acquisition

The method of acquiring element surface corrosion data has progressed a long way since the use of a dial indicator on the NRX-A2 fuel elements. In the acquisition of the surface corrosion data for the NRX-A3, NRX/EST, and the NRX-A5 the differences appeared in the recording of the raw data. Strip charts were used to record the data for the NRX-A3, and the NRX/EST. For the NRX-A5 a digitized corrosion measuring system was used employing a paper tape to record the surface regression. The block diagram for this system is illustrated in Figure 6-12.

The corrosion depth measuring instrument consisted of a LVDT connected to a stylus which is mechanically driven along the element. Measurements are obtained of the changes in the distance between the stylus and a reference roller on which the element rests. The stylus makes a complete 52 in. axial trace at a given location on the element periphery. Instrument accuracy is plus or minus one mil with a measurement range of 60 mils. The axial trace could be made at seven locations on any face. The seven locations are shown in Figure 6-13.

6.3.3.2 Data Reduction

The data for the NRX-A5 was reduced into a usable form by converting the paper tape into a deck of coded IBM cards which were read on magnetic tape in preparation for use as computer input. A series of computer programs were required (1) to convert the coded data to uncoded data, (2) to realign the data by averaging the data from 1 to 10 inches and using this average as a zero base, (3) to separate the broken elements from the whole elements, (4) to add core locations and sort the data into element serial number sequence and (5) to prepare the data format for insertion into the data compilation and plotting program. Item (5) compiles the data by face and trace, summarizes the data for each element and then summarizes the elements into 10 regions. These 10 regions are identified by row and provide the input for plotting the averages for these 10 regions. The program is capable of giving plots of individual elements or faces of elements.

6.3.3.3 Results of Surface Regression Measurements

Surface regression measurements and the associated weight loss calculation (integration of the surface corrosion depth measurements) as performed in the data reduction code were expected to give high results. A "double amplitude" problem existed because the trace measurements reflected "across flat measurements" due to the nature of the measuring fixture. Consequently, what is reported for one face may include the corrosion which has occurred on the reported face plus what has occurred on the opposite face.

For this reason, the weight losses calculated from the depth measurements must be interpreted cautiously. The "double amplitude" effect cannot be easily corrected, therefore, the data is published showing a plus zero, minus 50 percent band of uncertainty.

The axial variation of the average surface regression in each core radial region has been determined for the NRX-A5. Figures 6-14, 6-15, and 6-16 show this distribution for the central, mid-radial, and peripheral regions, respectively. In addition, the NRX-A3 and NRX/EST are included for comparison.

These figures also contain the calculated NRX-A5 surface regression for the central and the mid-radial regions. No calculation is shown for the peripheral region because of its two rows of externally coated elements. In the corrosion predictions code it is assumed that there is no surface corrosion on externally coated elements.

The calculated corrosion that is presented was obtained by using an average between the corrosion rate at the start of life and the corrosion rate at the end of life for the core. The end of life calculations were made using the as measured surface regression for the interelement gaps. This was done because the TDC-2 calculations of surface corrosion do not change the interelement gaps as the corrosion progresses.

When the calculations are compared to the measured NRX-A5 surface corrosion it is seen that the peak corrosion of both occurs near the same axial station. However, there is quite a difference in the amplitude. The calculations are too high for the midband corrosion and too low for the hot end corrosion. A comparison of the NRX-A5 results to the NRX/EST results, Figures 6-17 and 6-18, shows that the NRX-A5 calculation is much closer to its measurements than the results for NRX/EST. This reflects the improvement to the model, as discussed in Section 6.8, and the use of the end of life conditions in the NRX-A5 calculations. In addition, the calculation resolves the major differences of run profiles between the NRX/EST and NRX-A5 tests.

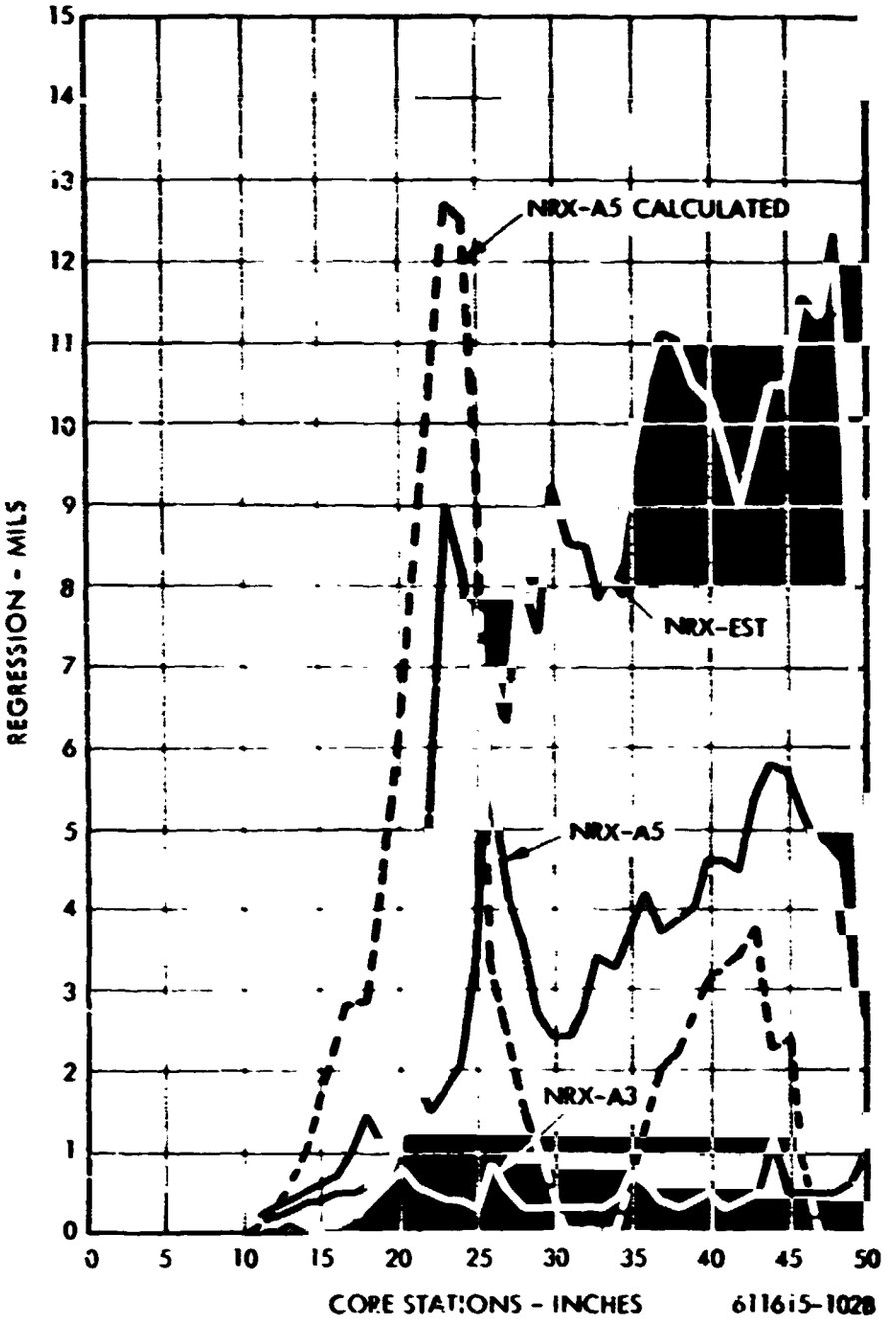

Figure 6-14. Central Region Surface Corrosion in the NRX-A3, NRX/EST, and NRX-A5

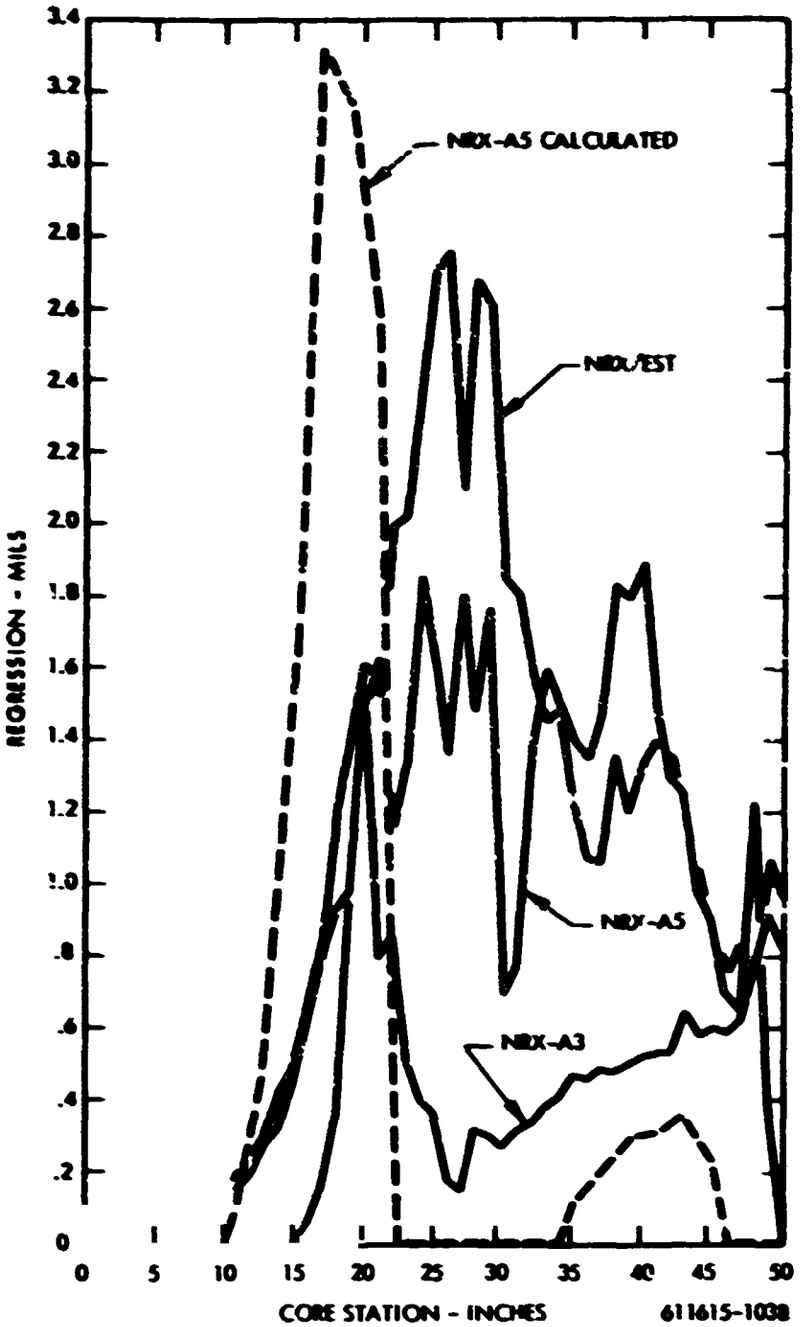

Figure 6-15. Mid-Radial Region Surface Corrosion in the NRX-A3, NRX/EST, and NRX-A5

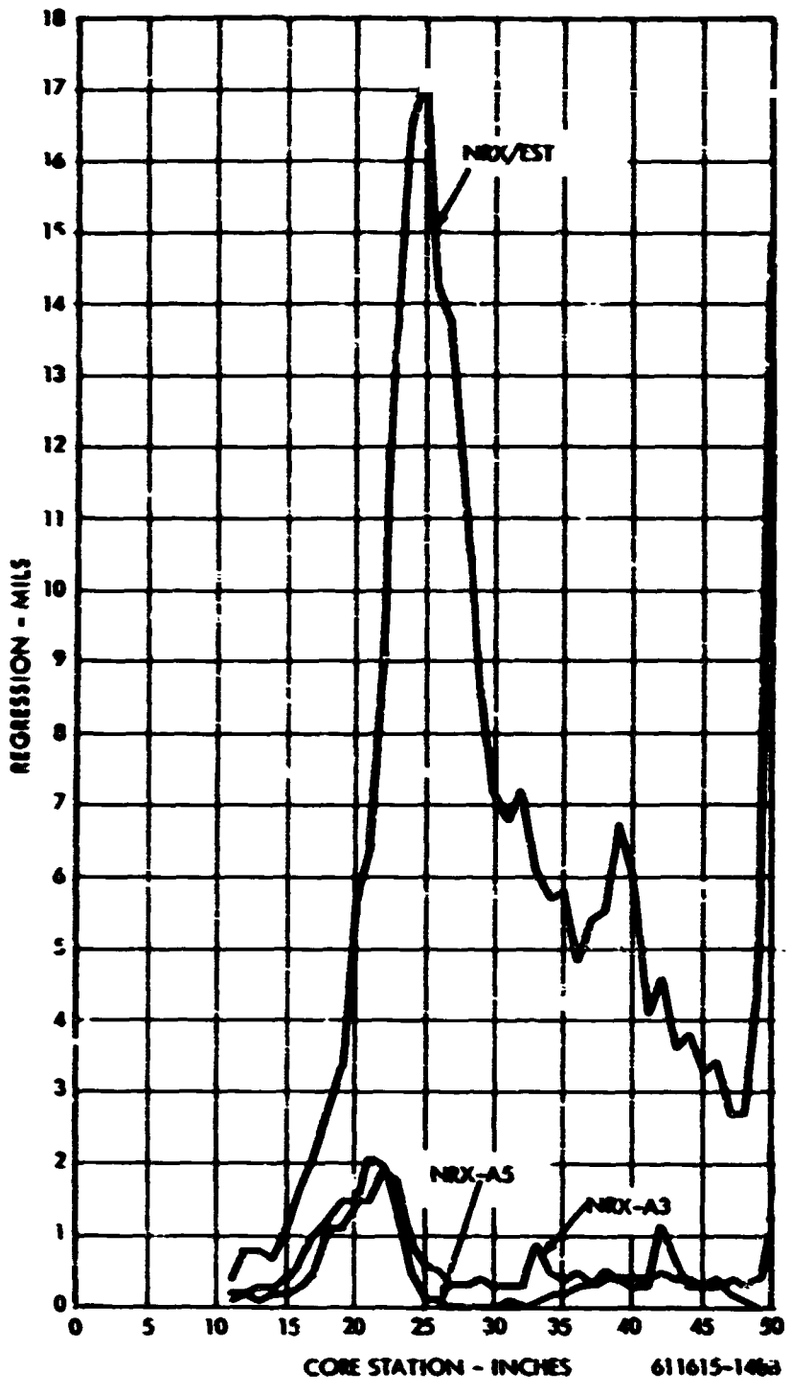

Figure 6-16. Peripheral Region Surface Corrosion in the NRX-A3, NRX/EST, and NRX-A5

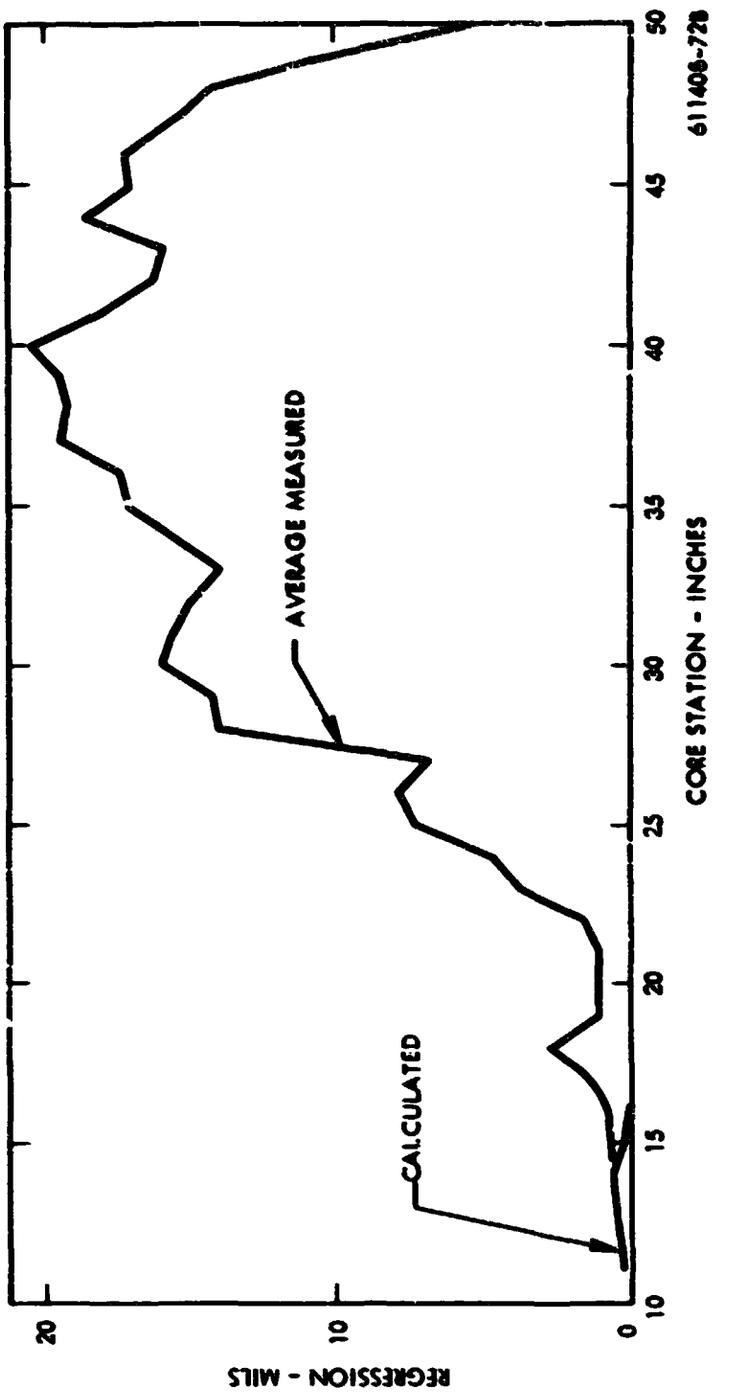

Figure 6-17. Calculated and Measured Surface Regression for NRX/EST, A Cluster

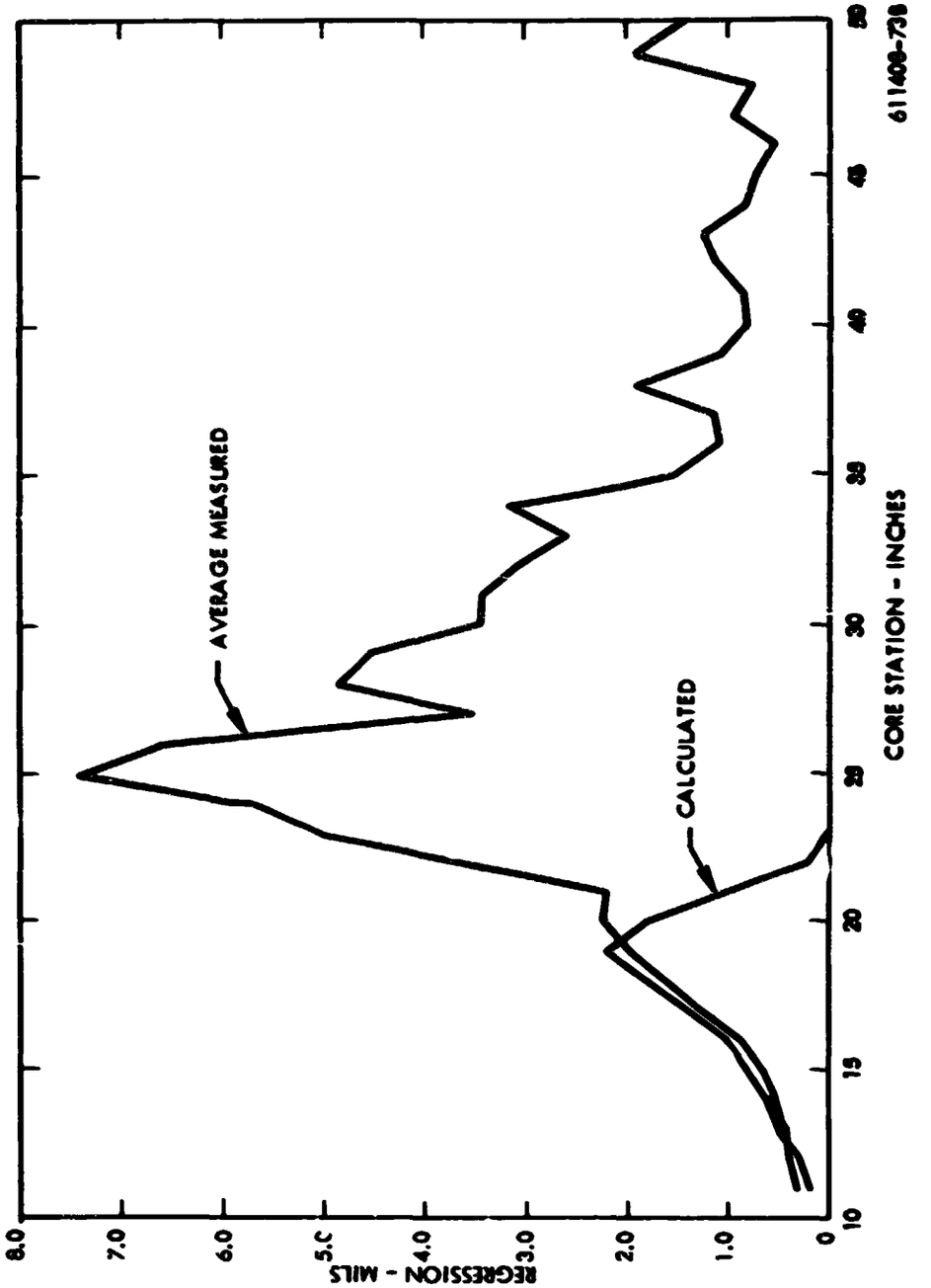

Figure 6-18. Calculated and Measured Surface Regression, for NRX/EST, G Cluster

6.3.3.4 Fuel Element Bore Weight Loss Deduced From Incremental and Surface Corrosion Measurements

Detailed correlations of incremental weight loss data and surface corrosion data have been made for selected NRX-A5 elements. The NRX-A5 fuel element bore weight losses were obtained by subtracting the surface weight losses from the element overall weight loss.

Figure 6-19 shows the estimated external surface weight loss axial distribution for central region fuel element 3A1D compared with the measured incremental weight loss. The area between the solid curves defines the plus zero, minus 50 percent band of uncertainty due to the "double amplitude" measurement problem. The comparison for this element shows the weight loss due to external surface corrosion is 19 to 37 percent of the total measured loss. Figure 6-20 shows the axial distribution of bore weight loss for 3A1D. These losses are based on the difference between the low limit of the estimated weight loss due to surface corrosion and the incremental weight loss values. A comparison with the LOWERE Code * bore loss calculations based on the "as run" profile also appears on Figure 6-20. Within the limitations of the data correlation, the calculated and measured results are quite different.

Figure 6-20 and 6-21 present for mid-radial fuel element 2H6G the same information as was presented for 3A1D. Figure 6-21 indicates an estimated 6.8 to 13.7 percent of the total weight loss is due to external surface corrosion.

Figure 6-22 shows for peripheral fuel element 2J7F the axial distribution of measured total and external surface corrosion. Both the bore corrosion as deduced from the total and also the surface corrosion with its appropriate range of uncertainty are shown. The fraction of total weight loss attributable to surface corrosion was estimated to be 7.9 to 16.8 percent of the total weight loss of element 2J7F.

---

* "Fuel Element Bore Weight Loss Code and its Application to the NERVA Core Design", WANL-TME-1344, January 1966.

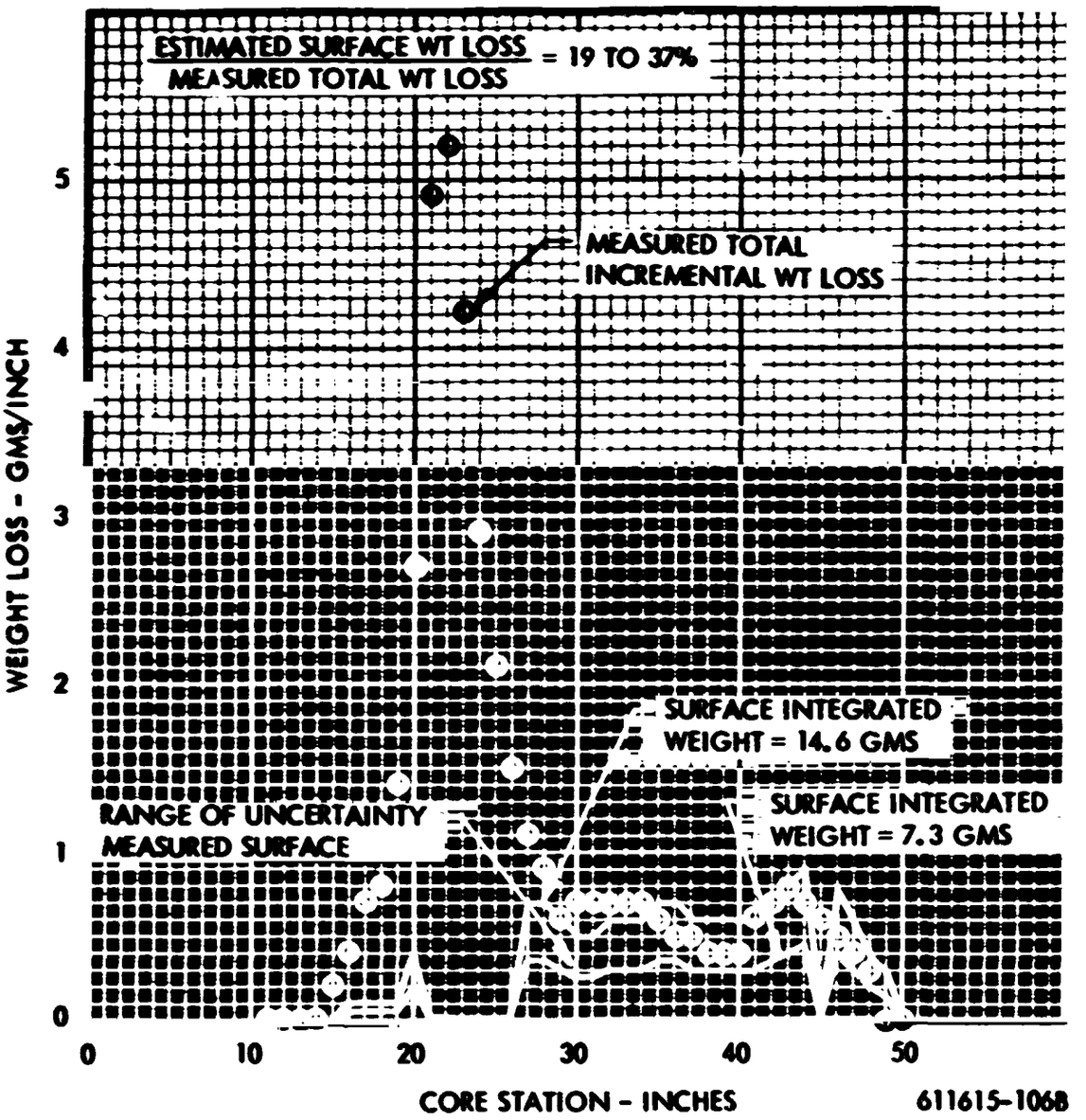

Figure 6-19. External Surface Weight Loss Distribution for NRX-A5 Fuel Element 3A1D

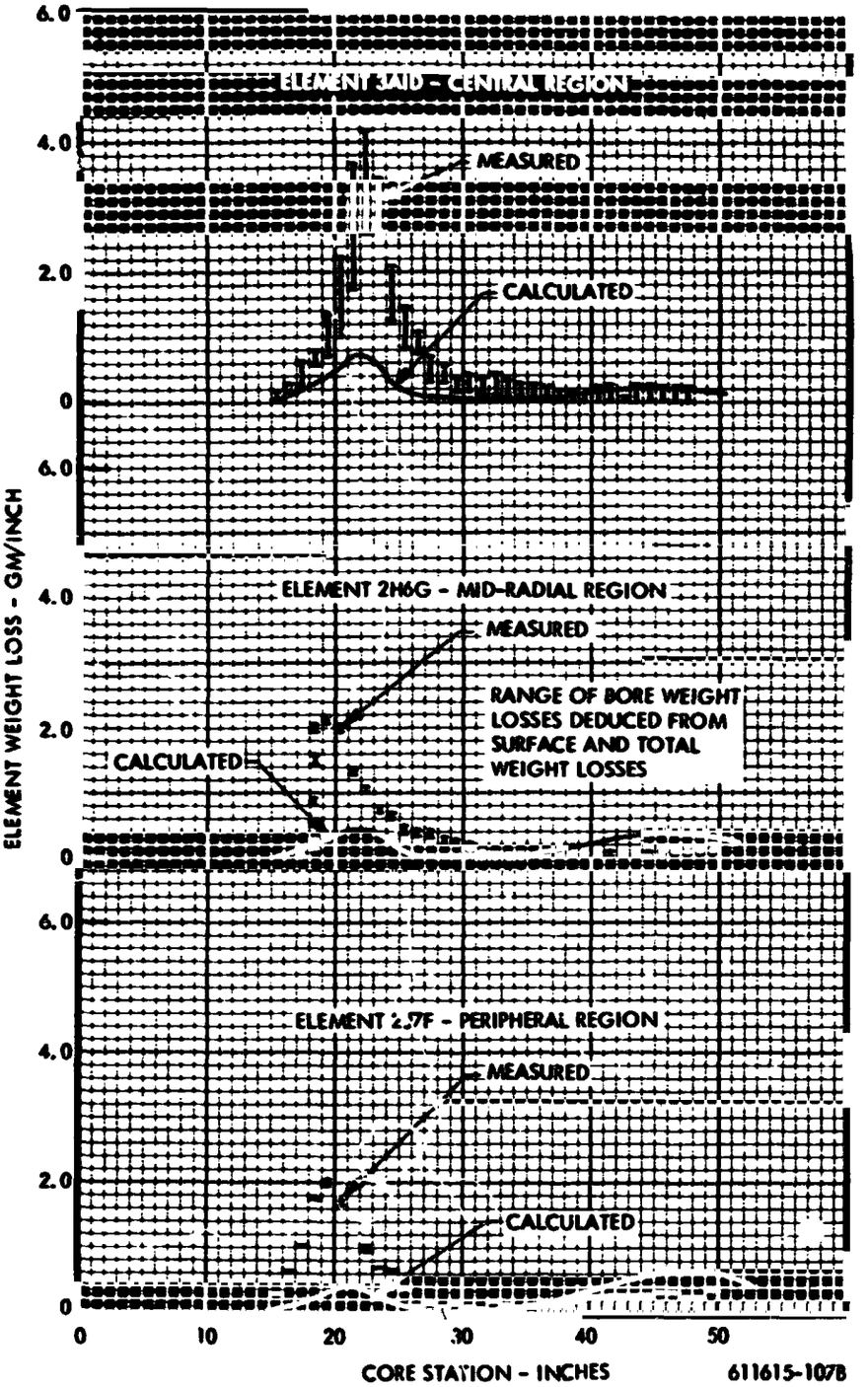

Figure 6-20. Axial Distribution of NRX-A5 Incremental Weight Loss

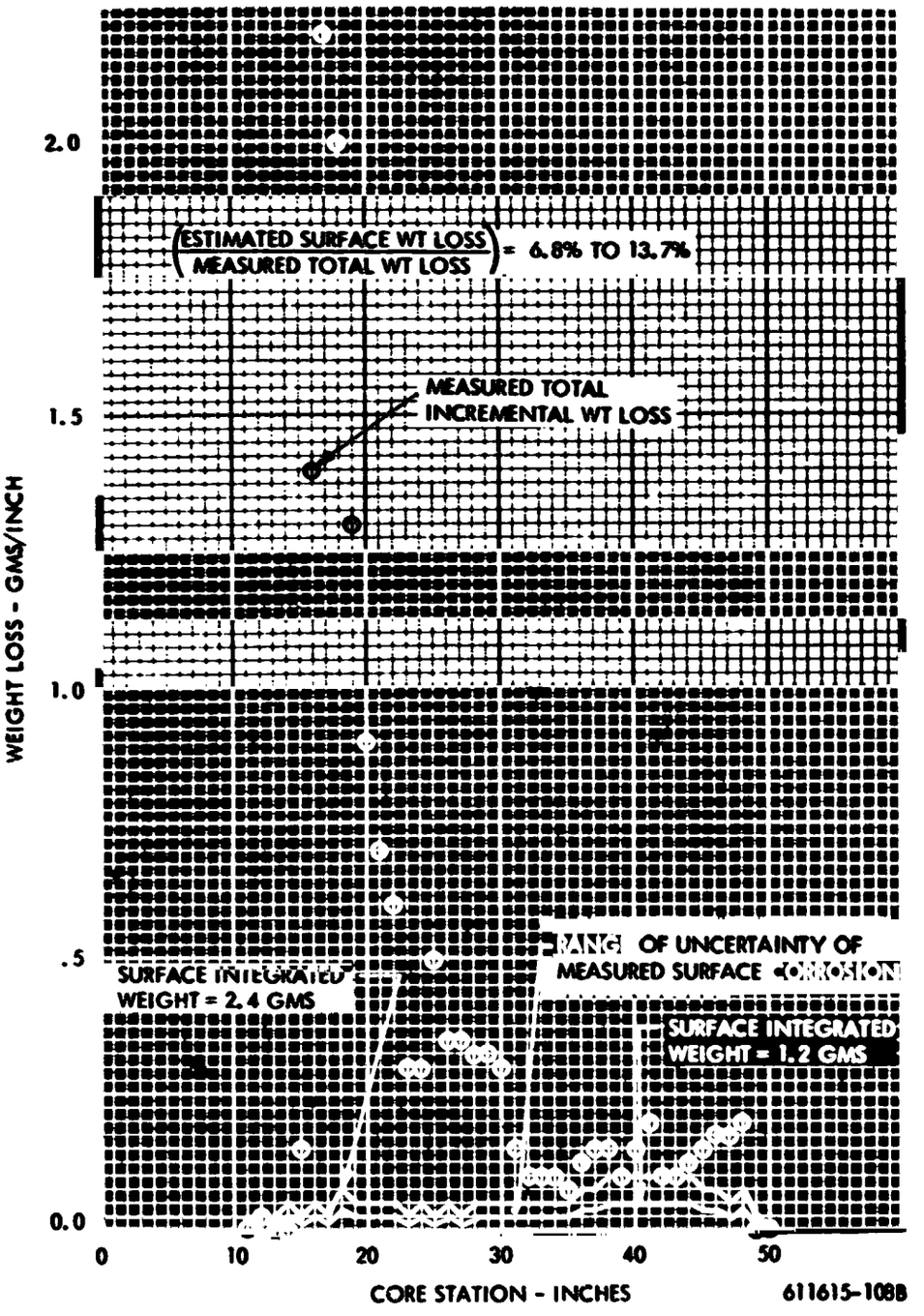

Figure 6-21. External Surface Weight Loss Distribution for NRX-A5 Fuel Element 2H6G

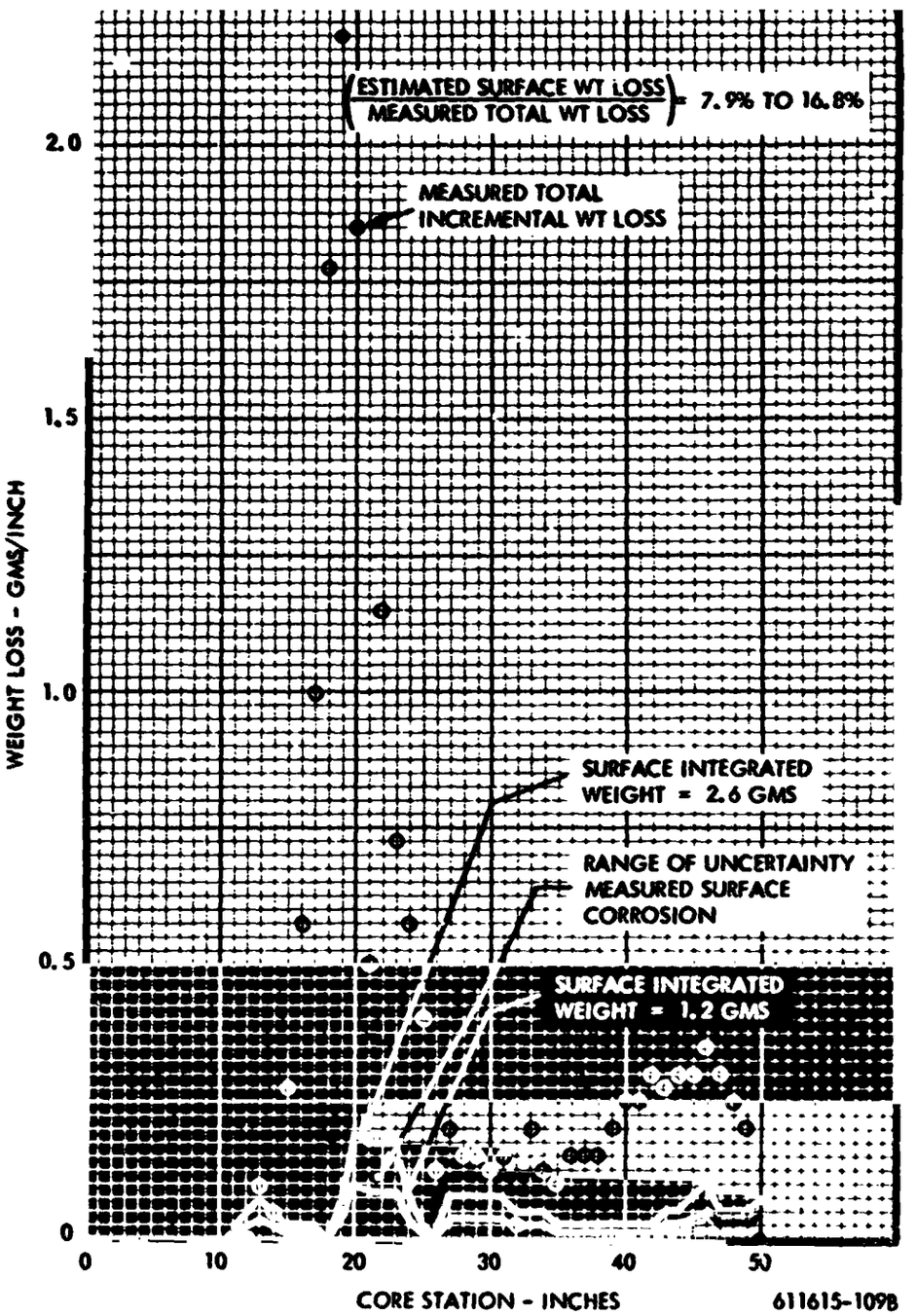

Figure 6-22. External Surface Weight Loss Distribution for NRX-A5 Fuel Element 2J7F

In all three cases, the calculated bore losses are not entirely consistent with the measured data. These elements are not necessarily representative of the three regions of the core. In fact, the large differences between individual element performance make it difficult to choose typical elements.

The axial distribution of bore weight loss for three elements in both the NRX-A3 and NRX/EST, are shown in Figures 6-23 and 6-24. These bore weight loss distributions may be compared to those presented for the NRX-A5.

Using similar data for all reactors, the surface and bore weight losses are given as a function of radius for the NRX-A3, NRX/EST and NRX-A5 in Figures 6-25, 6-26 and 6-27, respectively. From these figures, it may be concluded that:

1) The material loss from the surface of the elements was considerably higher in the center of the core than in the other regions.

2) The high WAFF element weight loss in the core edge region (radius greater than 11 inches) is principally due to bore corrosion.

3) 15 to 30 percent of the total NRX/EST and NRX-A5 core weight loss is due to surface corrosion.

The surface regression traces show that the axial distribution of surface weight loss is considerably different than bore weight loss; much of the surface loss is downstream of core station 27 inches.

6.3.3.5 Surface Regression Maximum Point Frequency

An analysis was performed to establish the relationship between the average surface regression in a region and the maximum regression to verify the frequency with which the points on the maximum curve appear in the data.

To determine the maximum curves, the averages for the faces of the elements in each of the 9 radial regions were examined. The maximum readings for the stations occurring at the first peak of the average curve were selected. In most cases the peaks were between core stations 16 and 35. The maximum and average readings were then plotted as a function of core station.

Figure 6-28 is an example of the average and maximum curves for region 4 which corresponds to the "D" cluster row in the core.

To obtain the frequency at which the points on the maximum curve appear in the data, the maximum regression for a region was divided into 10 bands. The individual traces for elements in a particular region were reviewed and divided into these bands. The number of points in each band was then plotted against the axial station. This resulted in 10 plots for each region. Figure 6-29 shows for region 4 the 10 bands into which the maximum regression was divided and the frequency for each station that a reading within that band appeared in the data. The following data shows the percent of the total for each region that appeared in the tenth band (36 mils and up):

Region	Percent
1	1.5
2	9.8
3	0.4
4	0.4
5	0.9
6	0.1
7	0.4
8	0.4
9	1.6

A review of the frequency data indicated that there were few points in the tenth band demonstrating that there were relatively few occurrences of maximum regression in this band for the regional areas examined. Therefore, the average curves used in the evaluations would tend to give high regressions.

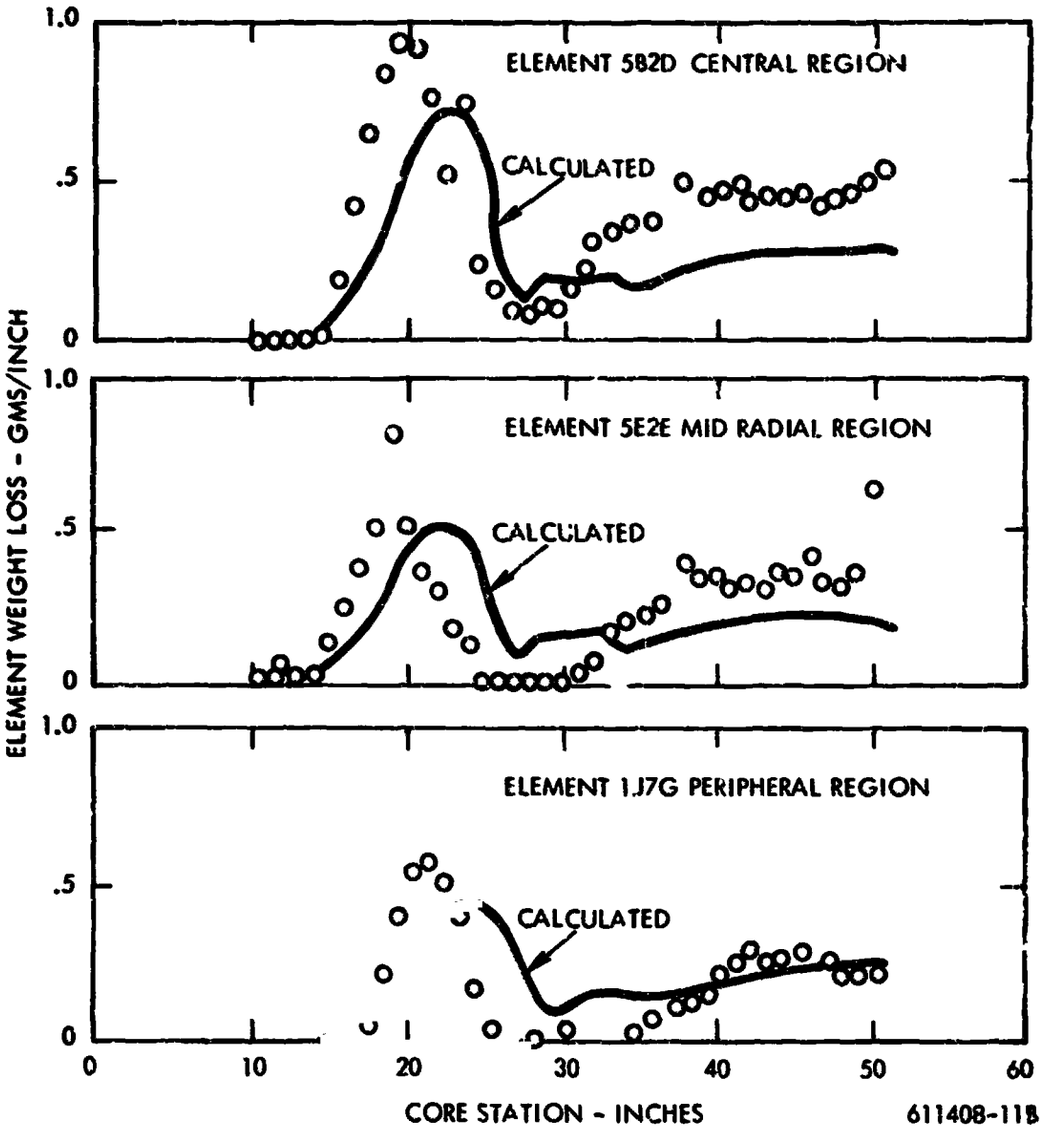

Figure 6-23. Axial Distribution of NRX-A3 Incremental Weight Loss

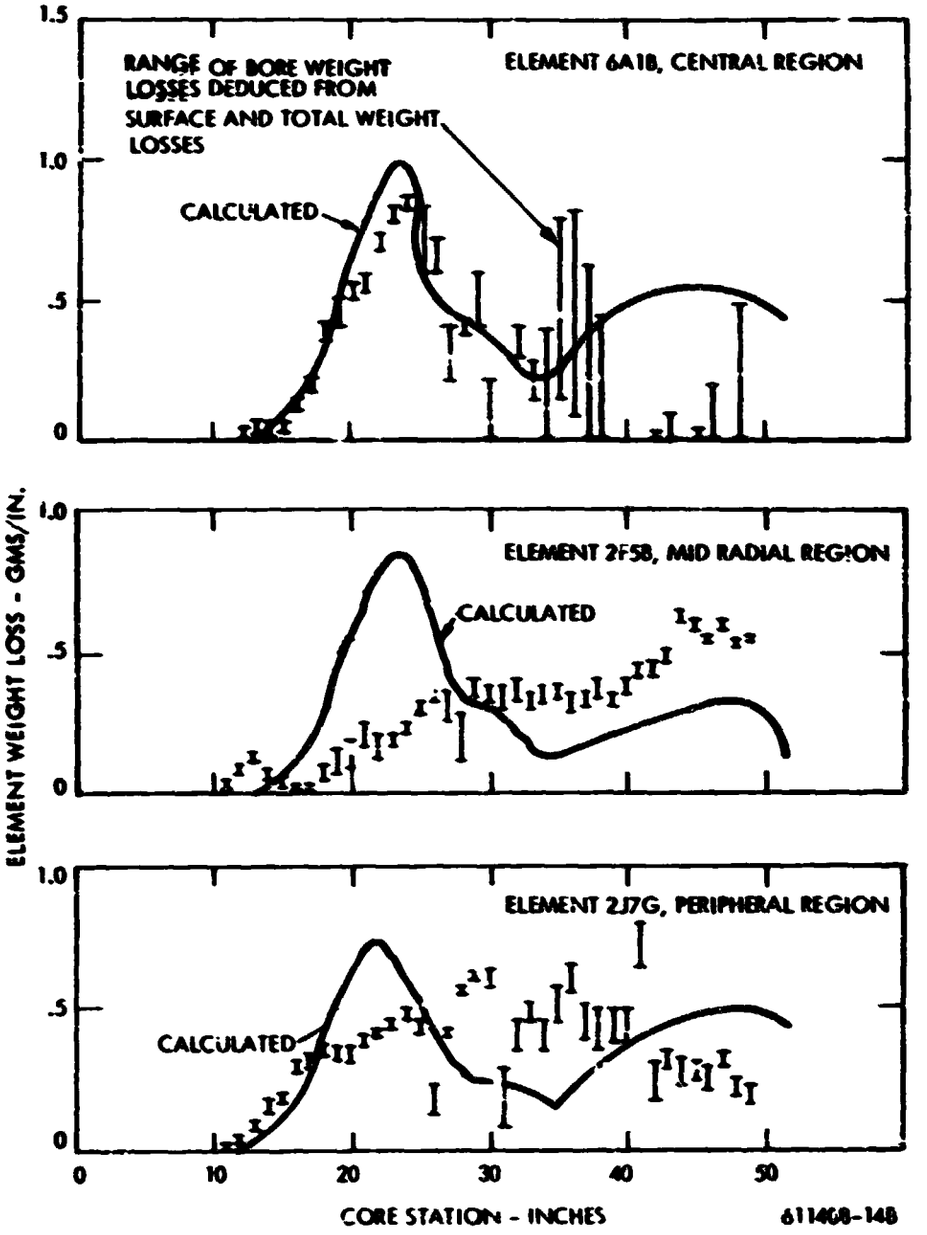

Figure 6-24. Axial Distribution of NRX/EST Incremental Weight Loss

Figure 6-25. NRX-A3 Estimated Division of Fuel Element Bore and Surface Weight Losses

Figure 6-26. NRX/EST Estimated Division of Fuel Element Bore and Surface Weight Losses

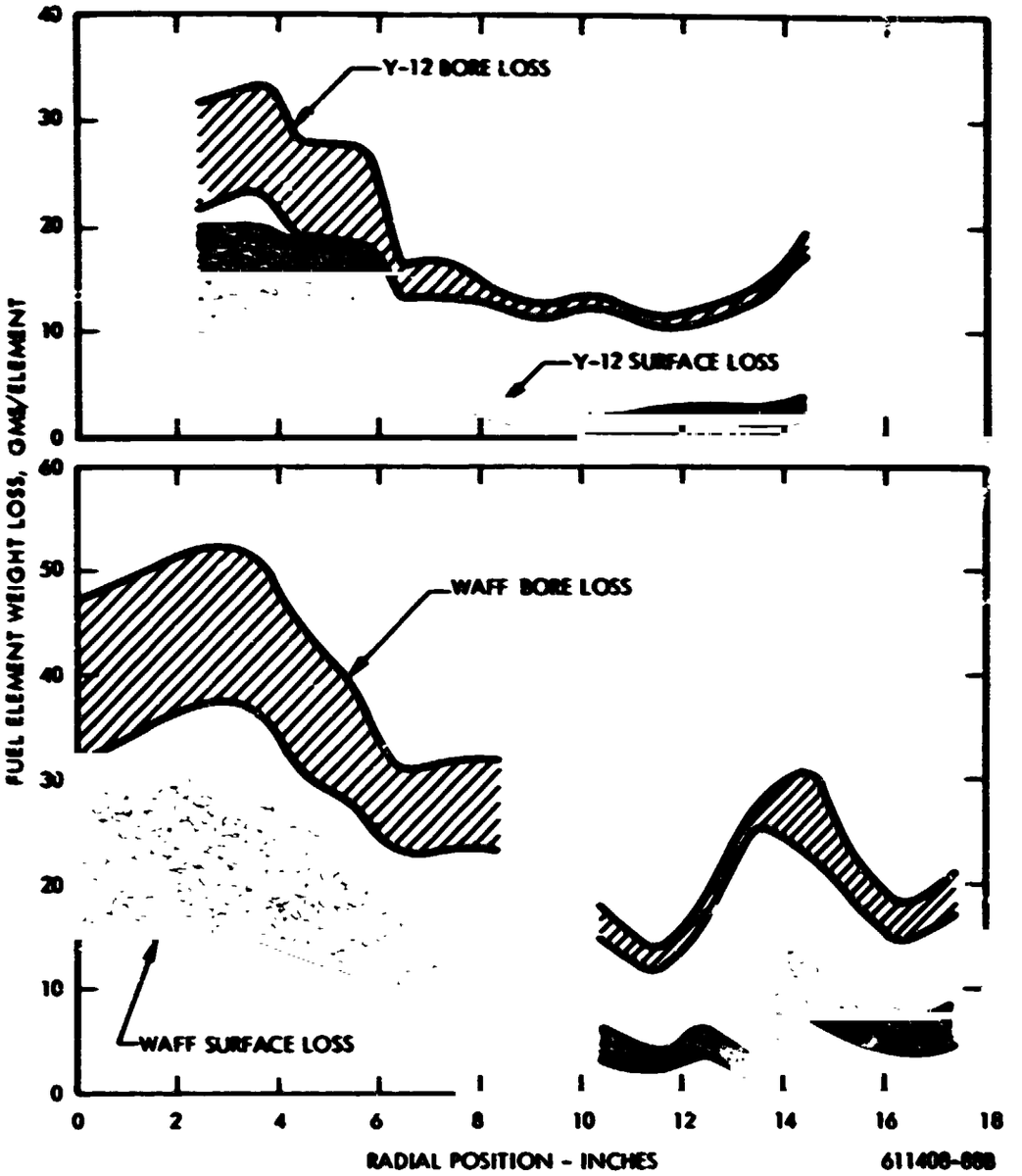

Figure 6-27. NRX-A5 Estimated Division of Fuel Element Bore and Surface Weight Losses

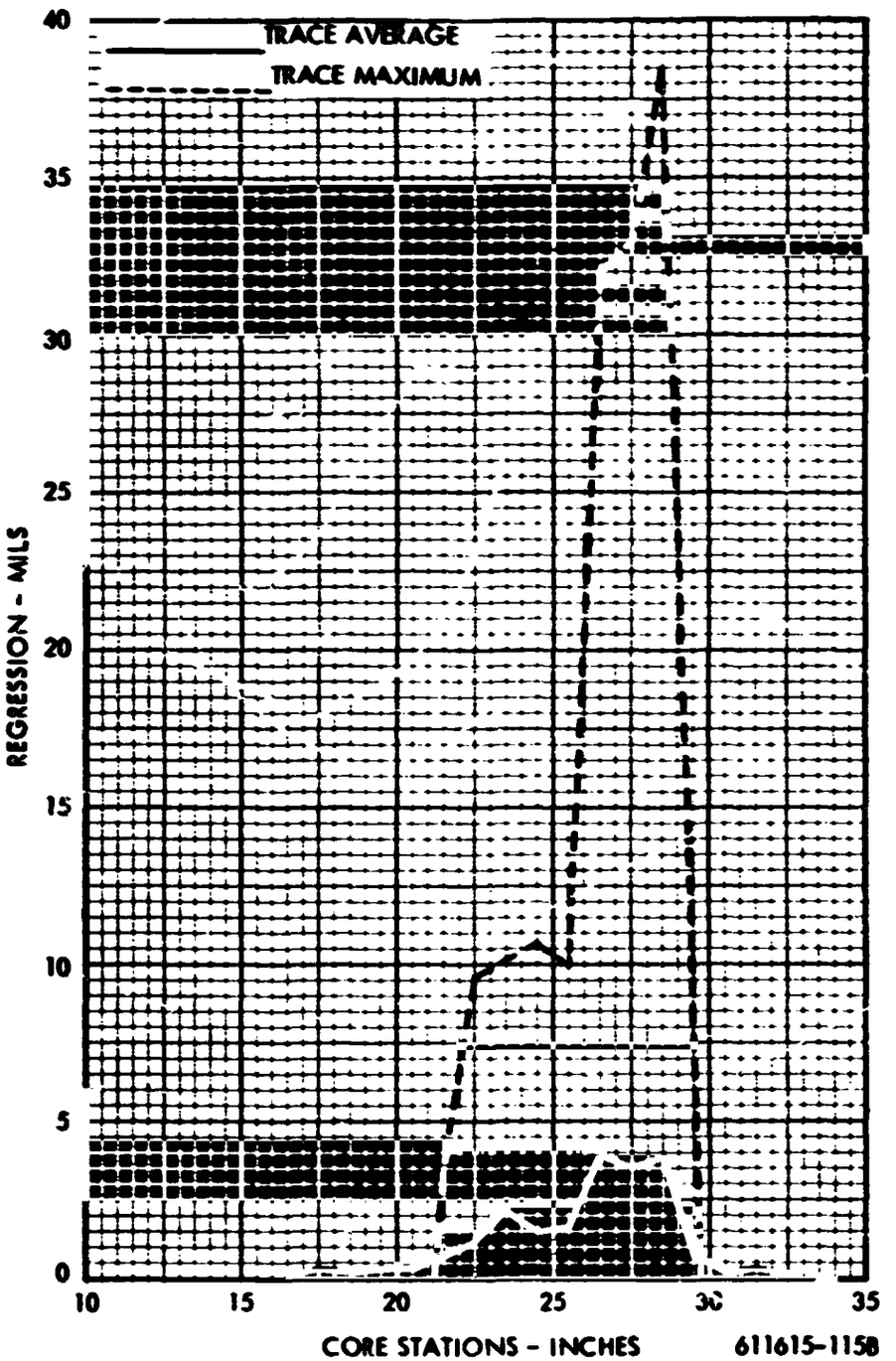

Figure 6-28. NRX-A5 Average Surface Regression Region 4-D

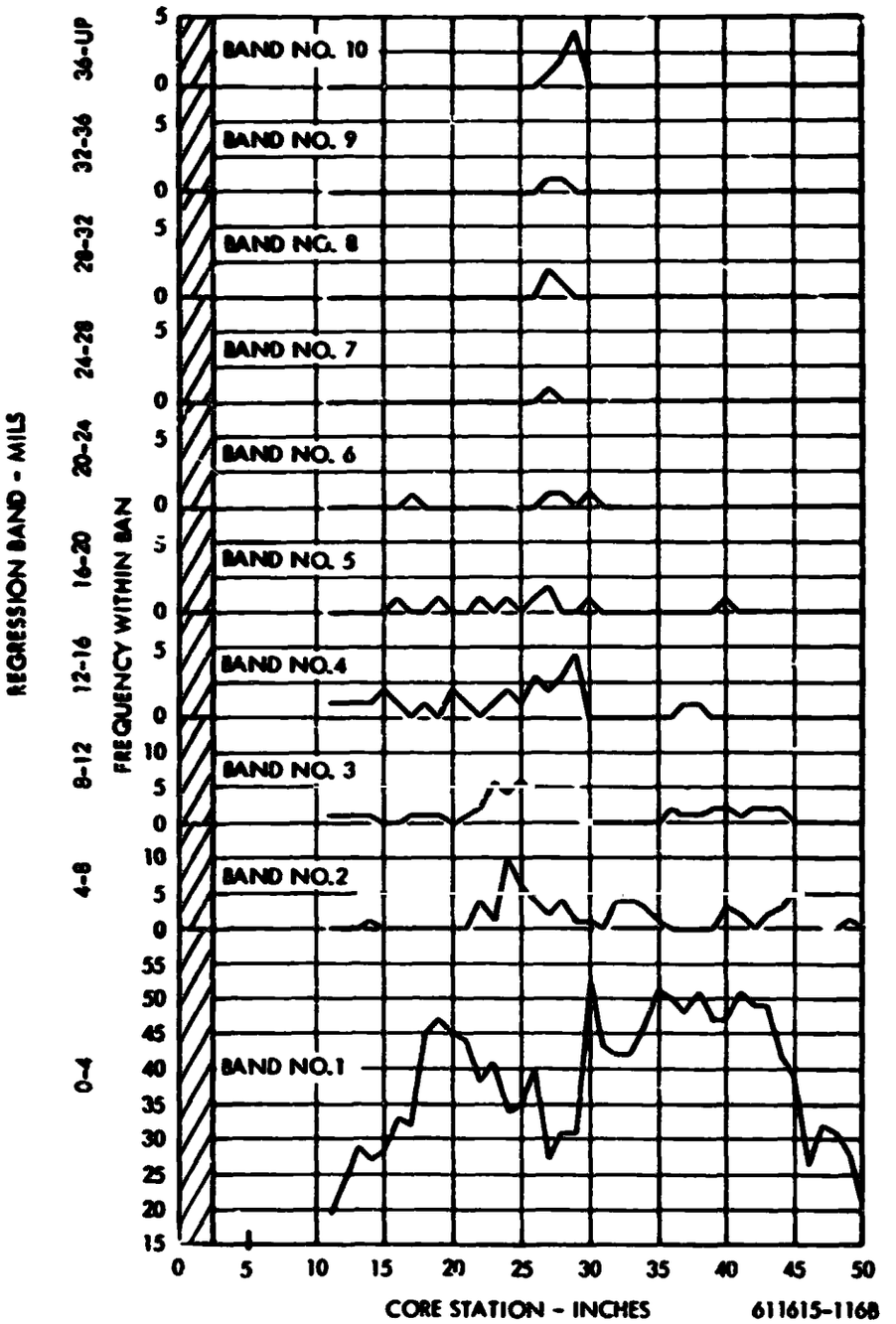

Figure 6-29. Frequency of Points in the Maximum NRX-A5 Surface Regression Curves for Region 4-D

6.3.4 Peripheral Fuel Element Evaluations

An investigation was made of the NRX-A5 periphery using the overall element weight loss values and the overall appearance of the element in an attempt to evaluate the effects of the hot buffer, fuel element loading, and fuel element location. Figure 6-30 is a sketch of the NRX-A5 hot buffer area. It appeared that the hot buffer was beneficial for the first row of peripheral coated elements, but that its effect had substantially diminished in the second coated row. The effects of loading and element location were less clearly defined, but it appeared that high loading, location behind either partial elements or thin filler strips, and high power factor were all detrimental conditions.

6.3.4.1 Hot Buffer Region

The values of the overall weight loss and element conditions for the first and second rows in the hot buffer region were correlated. A tabulation of these results appears in Tables 6-3 and 6-4. A judgement was made for (+) or against (-) the hot buffer, based on the average weight loss and element condition of each element location (usually two elements in the hot buffered region and four in the normal periphery). The first row of elements showed 12+, 6- and 1 even in favor of the hot buffer, and the second row showed 6+, 3- and 7 even. Thus in the second row, there appears little or no difference between the nominal and hot buffer peripheral regions. In addition, a comparison was made of the percent of elements broken, which were believed to be broken as a result of disassembly, and the percent of elements with less than 10 grams total weight loss. Table 6-5 summarizes these results.

The average weight losses for the first row of elements behind the hot buffer and behind the normal periphery were 18.7 grams and 24.9 grams, respectively, and for the second row elements were 22.6 grams and 22.1 grams, respectively. It was concluded therefore, that the hot buffer was beneficial for the first row of elements but that no significant advantage for the second row was demonstrated.

TABLE 6-3

NRX-A5 FIRST ROW ELEMENTS (WAFF) (CODE 39) OVERALL WEIGHT LOSS - GRAMS

Location Rating Factor	Element Location	Sector 1	2	3	4	5	6	Average HB	Average NP	Judgment for HB	Number Broken	Average Location	Average Power Factor
--	J3H	35.1	0	112.7	16.4	19.4	48.1	17.9	65.3	+	5	46.2	0.95
+	J3N	16.1	25.1	28.4	0	12.7	17.5	12.7	21.8	+	4	19.9	0.95
+	J3T	20.1	0	22.2	0	14.4	16.2	14.4	19.5	+	3	18.2	0.911
+	J3U	16.5	19.0	14.8	35.2	27.1	15.8	31.2	16.5	-	4	18.5	0.910
+	J4M	10.8	16	15.2	66.3	8.9	14.9	37.6	14.2	-	4	19.6	0.94
--	J4H	92.1	45.4	27.7	24.2	20.6	18.5	22.4	45.9	+	6	38.0	1.015
++	J4K	9.3	10.9	27.9	25.3	9.0	9.3	17.2	14.4	-	1	15.2	0.835
-	J5H	26.3	44.8	14.6	-0	8.3	30.2	8.3	29	+	4	24.8	0.901
+	J5J	21.3	0	33.5	22.7	13.5	16	18.1	23.6	+	5	21.4	0.989
++	J6H	9.9	7.4	23.2	13.9	19.8	8.1	18.6	11.3	-	3	13.7	0.914
+	J7H	37.4	14.5	0	12.4	16.9	23.9	12.4	23.2	+	5	21.0	1.01
-	J7K	37	29.8	16.5	14.7	12.8	33.8	15.6	28.4	+	6	24.1	1.006
++	J8D	14.1	10.6	11.9	6.5	7.0	10.0	9.2	10.4	draw	0	10.0	0.853
++	J8F	12.8	9.2	66.8	8.4	9.4	20.3	37.6	12.9	-	2	21.1	0.906
--	J9H	113.1	23.8	73.8	55.9	0	56.2	34.8	64.4	+	6	52.5	0.982
++	J9P	0	17.5	10.3	8.3	19.1	24.1	9.3	20.2	+	4	15.8	0.886
++	J9T	0	26.1	8.4	7.6	22.6	15.9	8.0	21.5	+	1	16.1	0.837
++	J9U	8.6	17.6	8.1	6.5	13.2	21.3	7.3	15.2	+	1	12.5	0.803
	Avg.	29.1	20.8	27.4	20.8	15.4	21.6	18.7	24.9	+12 - 6	867414 58.8%		0.919

Hot Buffer

— broken once
= broken more than once

TABLE 6-4

NRX-A5 SECOND ROW ELEMENTS (WAFF) OVERALL WEIGHT LOSS - GRAMS

Judgment for HB	Element Location	Number Broken	Sector 1	2	3	4	5	6	Average HB	Average NHB
draw	J3J	3	37.4	0	24.8	62.6	17.3	23.4	40	28.5
draw	J3V	2	13.1	13.5	37.7	0	12.7	14.8	12.7	19.8
+	J3S	1	14	12.2	14.1	12.5	11.6	19.8	12	15
+	J4D	0	16.7	27.8	12.2	11.7	15.6	10.7	13.6	16.8
+	J4F	3	14.7	15.1	29.4	14.7	19.6	25.5	17.2	21.2
draw	J5D	2	13.3	19.3	18.3	19.2	12.2	10.0	15.7	15.2
-	J5K	3	13.6	22.9	53.4	59.1	25.7	20.4	42.4	27.6
-	J6D	2	30.3	12.6	21.7	21.1	41.4	12.2	28.1	18.4
+	J6F	3	19.3	15.7	19.7	10.6	32.1	11.2	15.2	19.6
draw	J7D	3	12.5	16.5	15.3	28.3	16.9	48	21.8	23.5
-	J7F	3	16.5	15.3	25.7	20.5	12.4	37.2	23.1	20.4
draw	J8C	4	10.8	24.4	10.5	26.1	9.9	26.5	18.3	17.9
draw	J8G	5	21.1	18.7	12.6	20.8	30.0	12.0	16.7	20.4
+	J9S	0	27.3	17.7	27.1	8.9	20.8	28.3	18.0	23.5
+	J9V	4	47.9	13.9	19.3	12.6	14.6	12.2	16	22.2
draw	J9K	5	23.9	37.4	56.6	23.9	13.8	73.4	40.2	37.1
6+ 3- 7 draw		B43/96	21.2 (Avg. J3S excluded)	19.3	25.6	24.3	19.7	24.4	22.6	22.1
			46.7%		Hot Buffer					

— = broken once

═ = broken more than once

TABLE 6-5

COMPARISON OF PERCENT ELEMENTS BROKEN IN NORMAL AND HOT BUFFER PERIPHERY

	Less Than 10 grams Total Weight Loss	Broken
Hot Buffer, First Row	11/34 = 0.324	21/38 = 0.553
Normal Periphery, First Row	11/70 = 0.157	46/76 = 0.605
Hot Buffer, Second Row	1/32 = 0.0312	18/33 = 0.546
Normal Periphery, Second Row	2/62 = 0.0323	25/63 = 0.402

Evaluation of the filler strips showed that 72 percent were broken in the hot buffer region as compared to no breaks in the normal periphery. A detailed analysis of a possible cause for these broken filler strips is given in Section 4.5.

The surface corrosion analyses in the NRX-A5 hot buffer region were limited to the first row of uncoated elements in from the periphery. It was necessary to combine the surface regression traces in the same location on the faces with respect to the corner being analyzed. Figure 6-31 shows the location on the face of an element where the traces were taken. Due to the limited amount of data available seven traces were averaged together to make a trace of one element face. Figure 6-32 shows the plot of these averages. Trace B closest to the corner, shows a maximum regression of approximately 17.2 mils at station 23. Traces C and D show a maximum regression of approximately 7.4 to 7.7 mils at station 22. Traces C and D are 10 mils less than trace B. In dividing the available data into the hot buffer region, Figure 6-33 and normal regions, Figures 6-34, 6-35, and 6-36, it was found that in the normal regions all three traces, B, C, and D approach the average maximum of 17.2 mils regression in the area of station 20 to 25.

In the hot buffer regions there were 14 corner surface traces available and in the normal region there were 9 corner surface traces available. The maximum corner surface regression observed in the hot buffer and normal regions were 4.5 mils and 50 mils, respectively. It appears from the limited sample of corner surface regression measurements that the hot buffer region tends to reduce the amount of corner corrosion in the first row of uncoated fuel elements.

On the figures of the normal buffer region, calculated corrosion is also presented. The peak of the calculated midband corrosion is quite close relative to axial location but unlike the measurements, the calculated corrosion becomes greater towards the periphery. The calculated corrosion is 4 mils high at location D (as shown on Figure 6-31) and 16 mils high at location B. The calculation does not, however, show the high measured hot end corrosion.

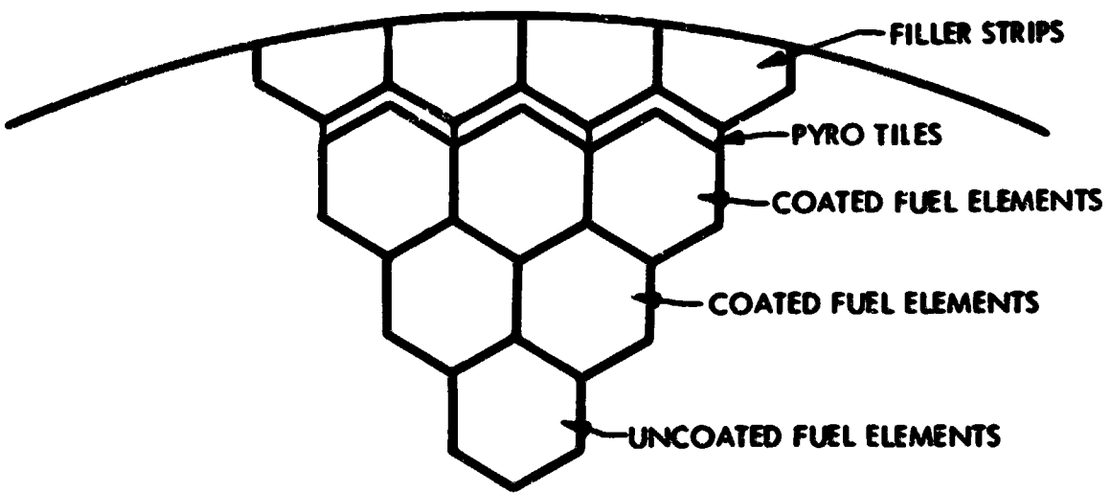

NOTE: HOT BUFFER REGION LOCATED IN CORE SECTOR 4, AND PART OF SECTORS 3 AND 5

611615-117B

Figure 6-30. Sketch of NRX-A5 Hot Buffer Region

LOCATION OF SURFACE REGRESSION MEASUREMENTS

D to C = .087
D to B = .172
D to A = .200

NOTE: TRACES C, B, A REFERS TO NRX/EST CORE
TRACES D, C, B, A REFERS TO NRX-A3 AND NRX-A5 CORES

611615-1188

Figure 6-31. Location of Surface Regression Measurements

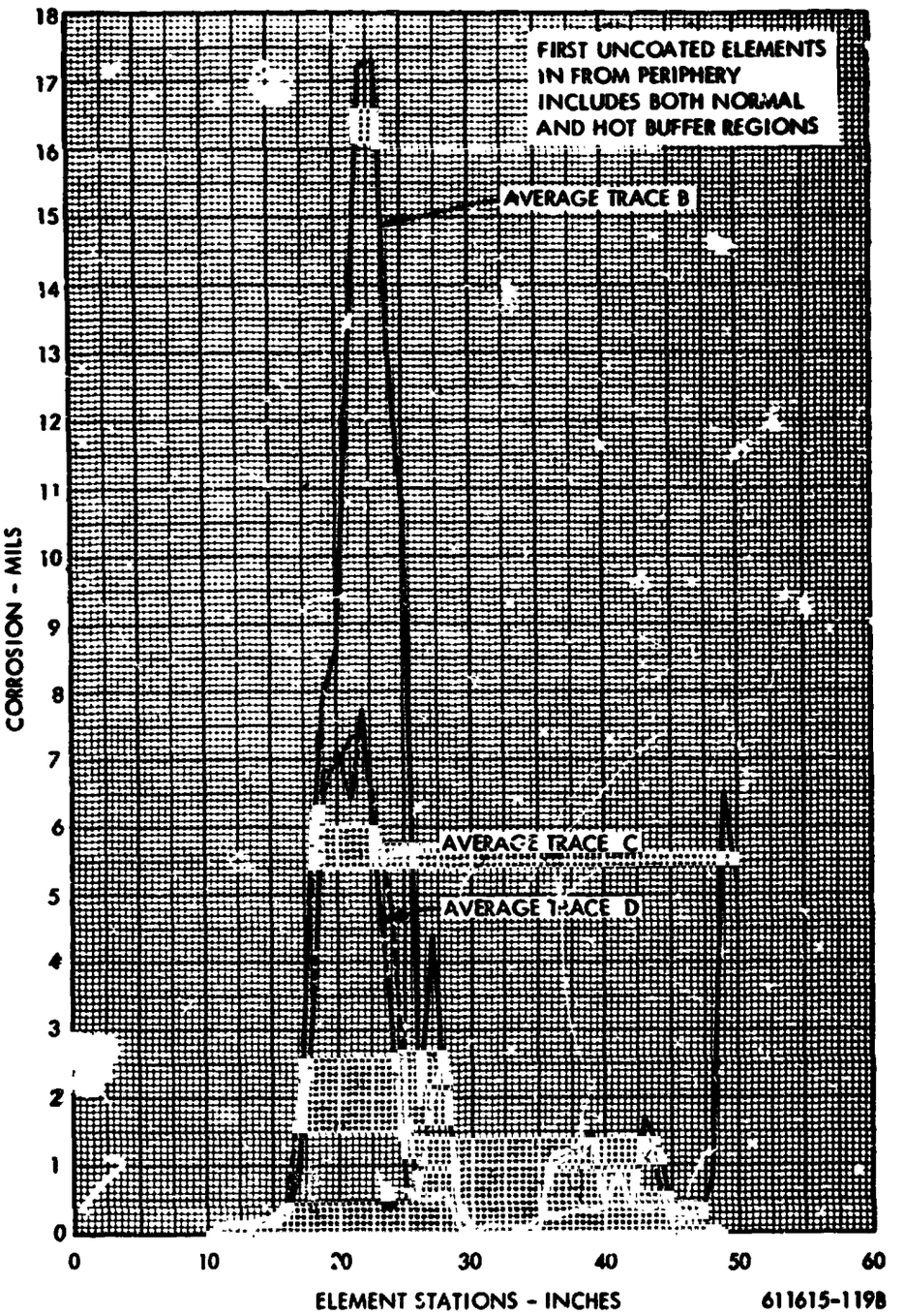

Figure 6-32. NRX-A5 Average Corner Surface Corrosion

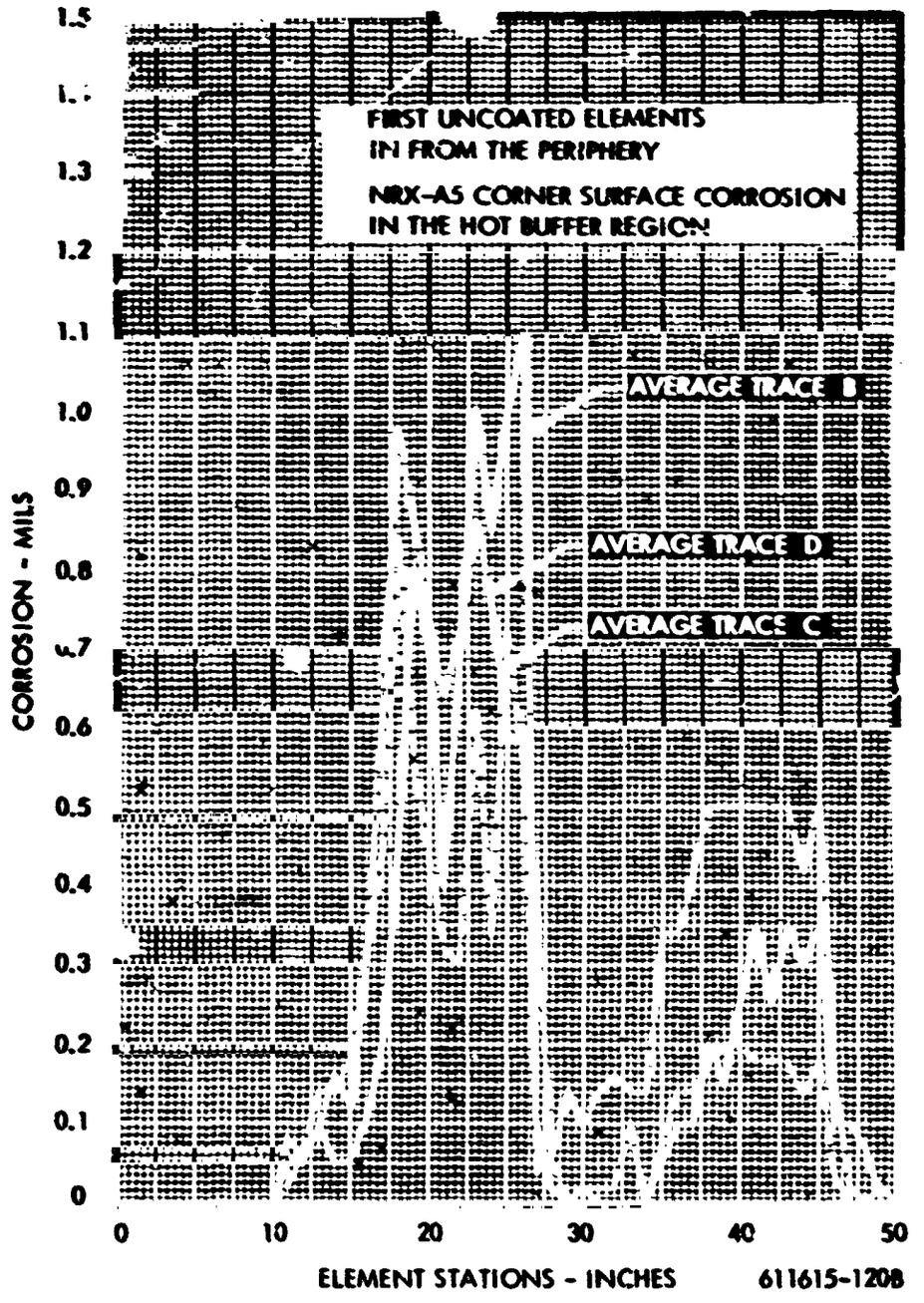

Figure 6-33. NRX-A5 Corner Surface Corrosion in the Hot Buffer Region

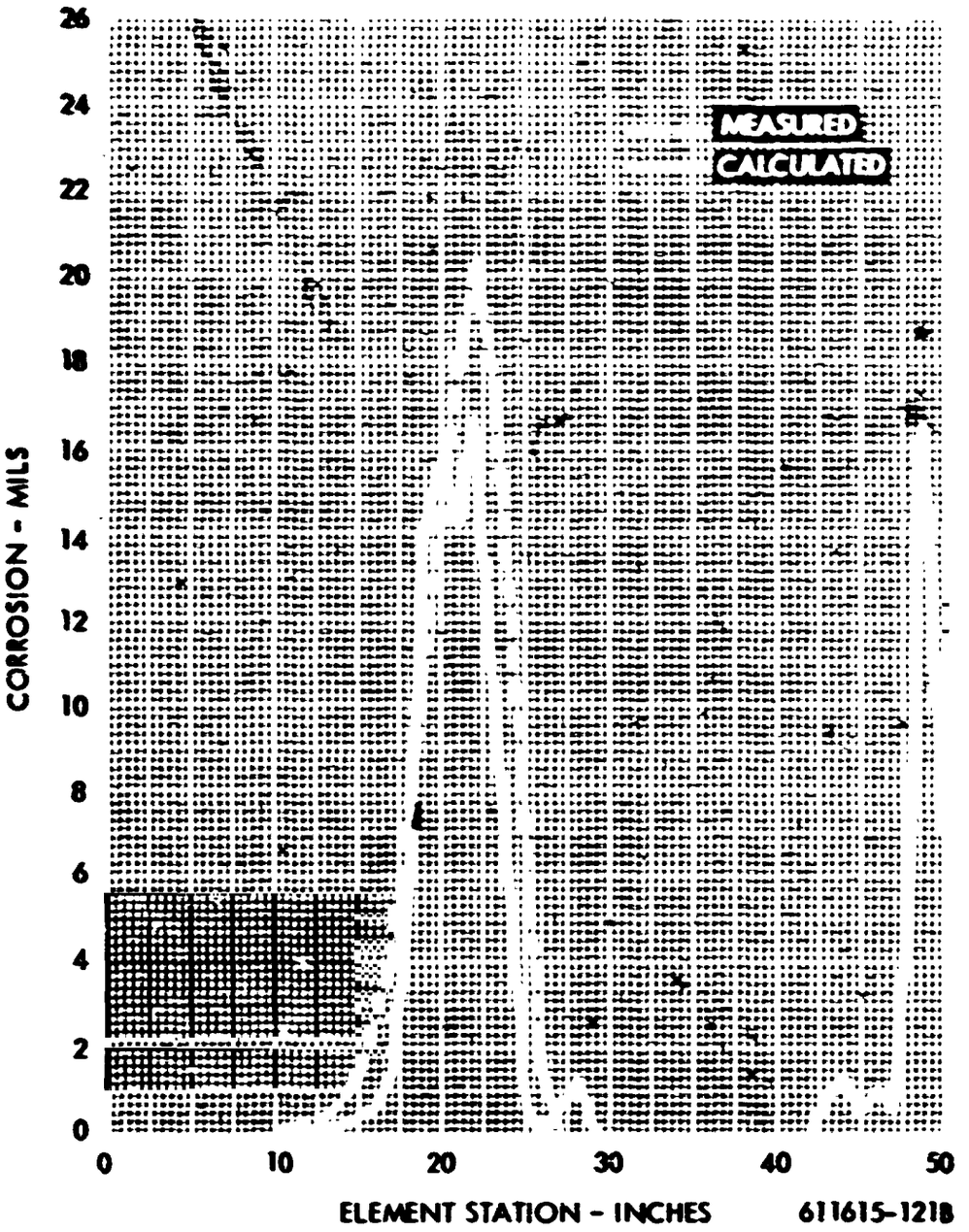

Figure 6-34. NRX-A5 Surface Corrosion, Outermost Uncoated Row, Location D, Normal Buffer Region

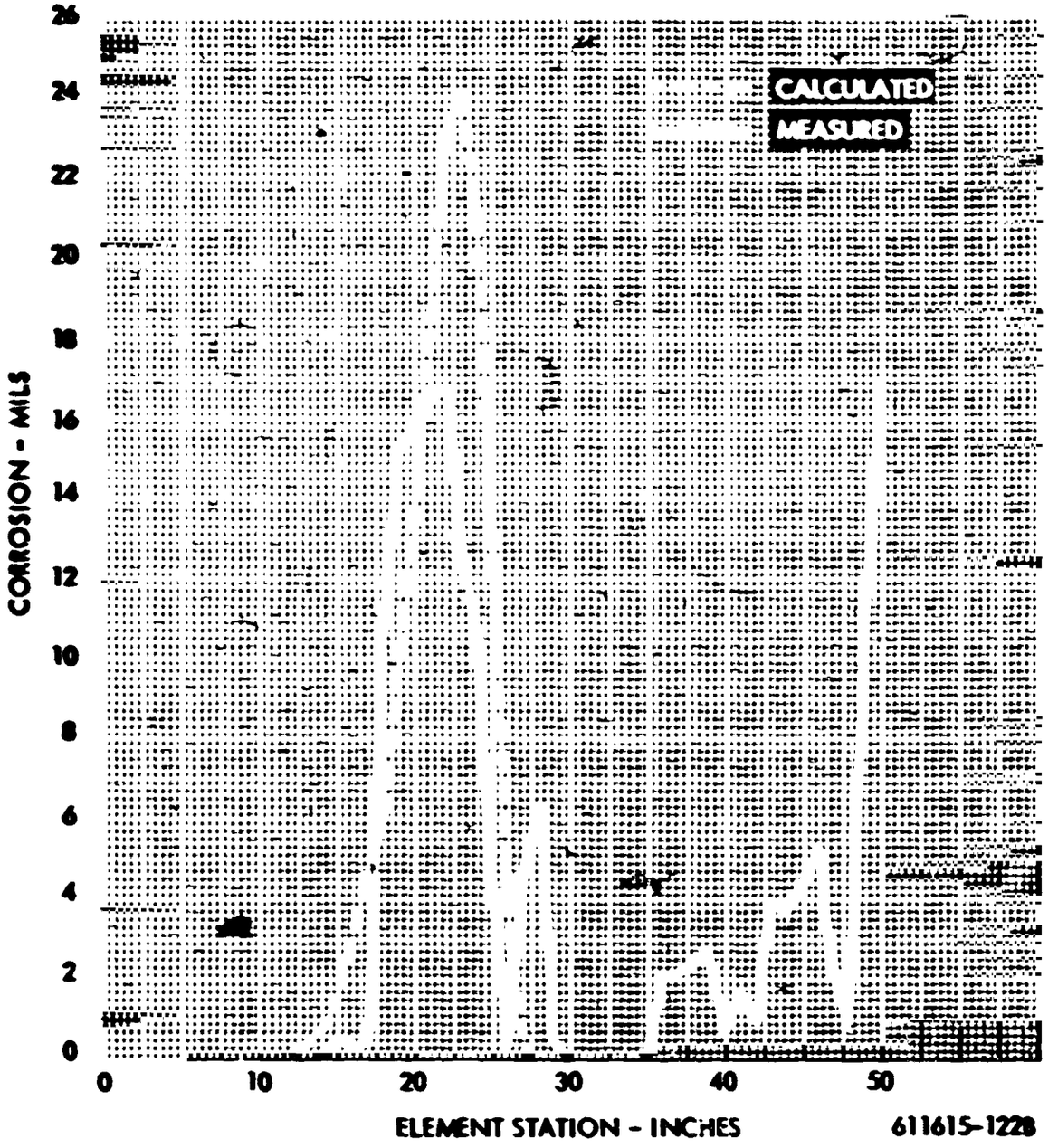

Figure 6-35. NRX-A5 Surface Corrosion Outermost Uncoated Row, Location C, Normal Buffer Region

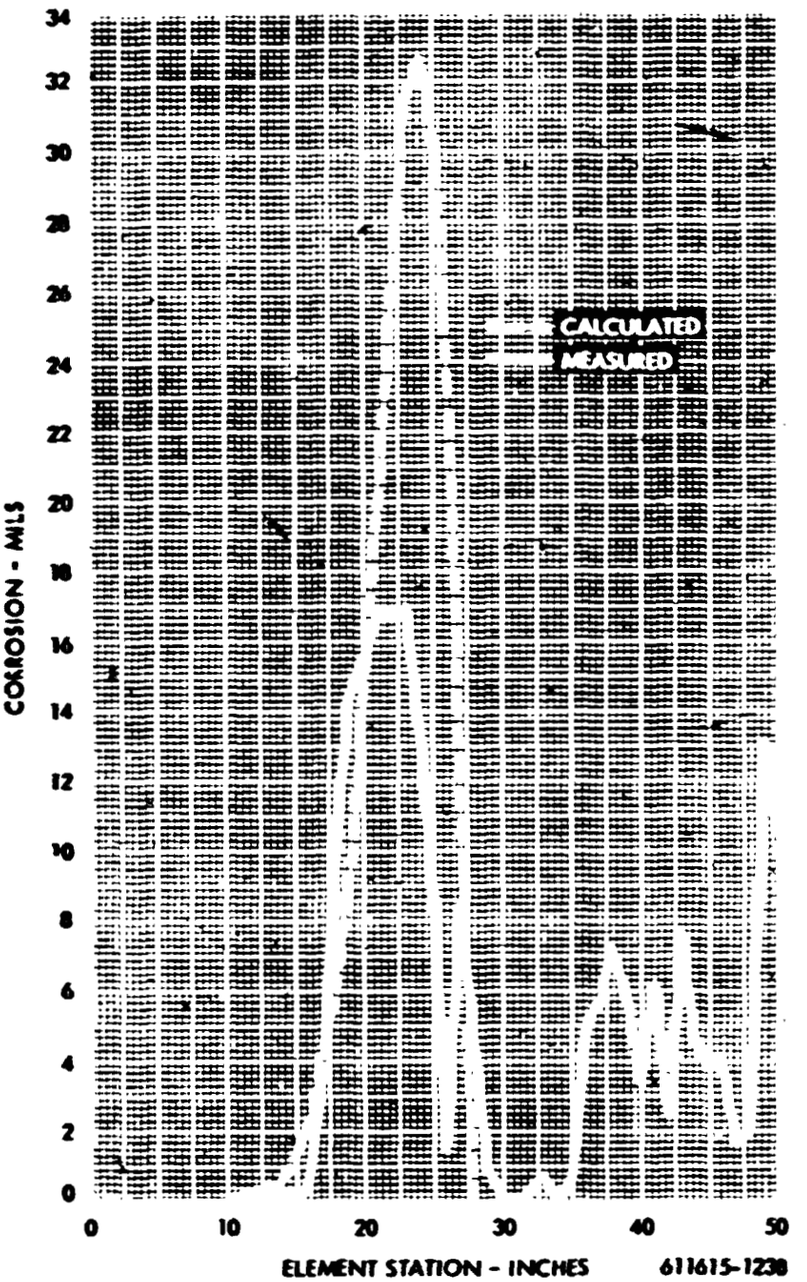

Figure 6-36. NRX-A5 Surface Corrosion Outermost Uncoated Row, Location B, Normal Buffer Region

CONFIDENTIAL

6.3.4.2 Fuel Loading Effect

Figure 6-37 presents the average weight loss for each loading for both the NRX/EST and NRX-A5. The NRX-A5 general trend is an increase in weight loss with increased loading. It is possible that the peripheral effects are production process effects and cause the code 39 to 49 average weight losses to be higher and the code 59 element weight losses to be lower. This latter possibility appears to be confirmed by the percent of broken elements shown in Figure 6-38. Despite the relatively high percentage of broken elements and relatively higher average power factor of the code 59 elements, the overall weight loss is relatively low. The reasons for this apparent difference may be attributed to lower permeability which the lower loaded elements tend to exhibit.

6.3.4.3 Element Location Effect

The overall element weight losses were averaged by location (sum of element weight loss in the same location of each sector divided by 6). A rating factor for each location was then determined based on the location average weight loss relative to the overall average for the row. The grouping of rating factors is given in Table 6-6

TABLE 6-6

LOCATION RATING FACTORS

Location Rating Factor	Description of Weight Loss	Amount of Weight Loss Relative to Row Averaging
++	Much less than average	5-15gm less
+	Less than average	0-5gm less
0	Average	Average
-	More than average	0-5gm more
--	Much more than average	5-15gm more

The results of this location rating are shown in Figure 6-39.

CONFIDENTIAL

The peripheral elements with the minimum average weight loss are as follows: J8D - 10.0gms, J9U-12.5gms, J9R-13.4gms and J3S-14.0gms. Except for location J9R, the minimum weight loss locations are first row elements behind relatively thick filler strips and adjacent to unfueled central elements and partial elements. The other element locations with much-less-than-average weight loss are behind relatively thin filler strips and directly behind partial elements. The only apparent deviation from this pattern is found in locations J5H and J5J; however, the range of weight loss values at each of these locations is large and the location averages are only 2 grams from the overall row average.

Figure 6-40 shows the number of broken elements at each location. The element location with zero breaks were the following: J8D. J9S, and J4D. Location J8D also had minimum average weight loss and, in general, the number of breaks at each location is consistent with the average weight loss.

An attempt was made to correlate element location rating with average power factor for the six elements at that location and the results are presented in Figure 6-41. Although the spread is considerable, there is a slight trend toward less weight loss at lower power factors.

6.3.4.4 Comparison of NRX-A3, NRX/EST, and NRX-A5 Peripheral Fuel Element Performance

A comparative study was made of the surface regression on peripheral elements (1st row of uncoated elements) on NRX-A3 and NRX/EST, to determine possible effects of radial inflow. Figure 6-31 shows the location of the surface regression measurements on the elements which were averaged according to letter group as shown in Figure 6-42 for the NRX-A3 and Figure 6-43 for the NRX/EST. The NRX-A3 elements showed high material loss between flow channels (Trace C) Figure 6-31, over the forward part of the elements, and high loss close to the periphery over the aft portion. NRX/EST elements showed decreased surface regression farther away from the periphery.

In comparing the surface corrosion on the outermost row of fuel elements in the NRX-A3, NRX/EST, and NRX-A5, it appears from the trace average data that the hot buffer region in the NRX-A5, Figure 6-33, shows a definite reduction in the amount of surface corrosion for the limited sample of surface data available.

Figure 6-37. NRX/EST and NRX-A5 Weight Loss versus Loading Code

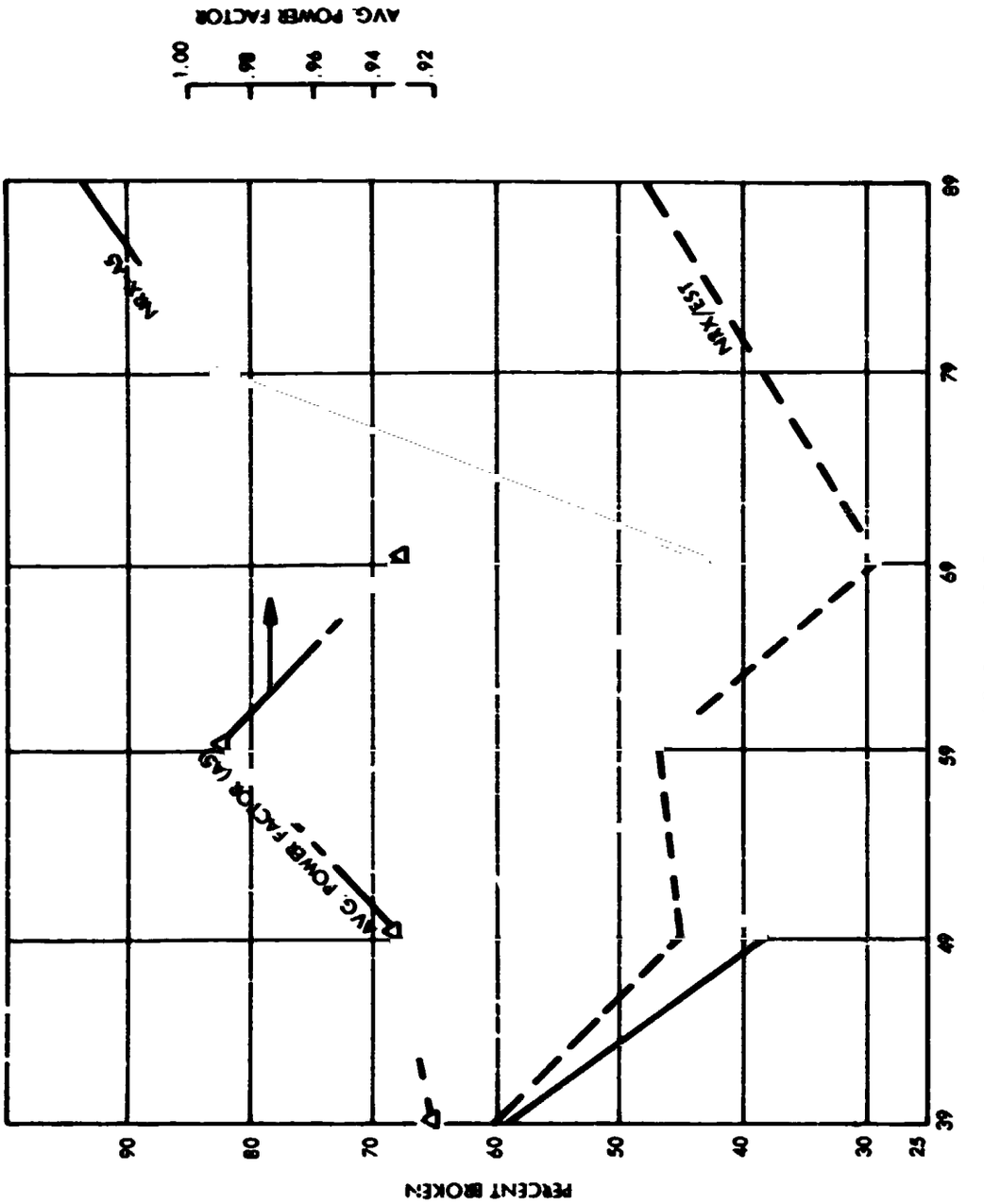

611615-125

Figure 6-38. NRX/EST and NRX-A5 Percent Broken Elements versus Loading Code

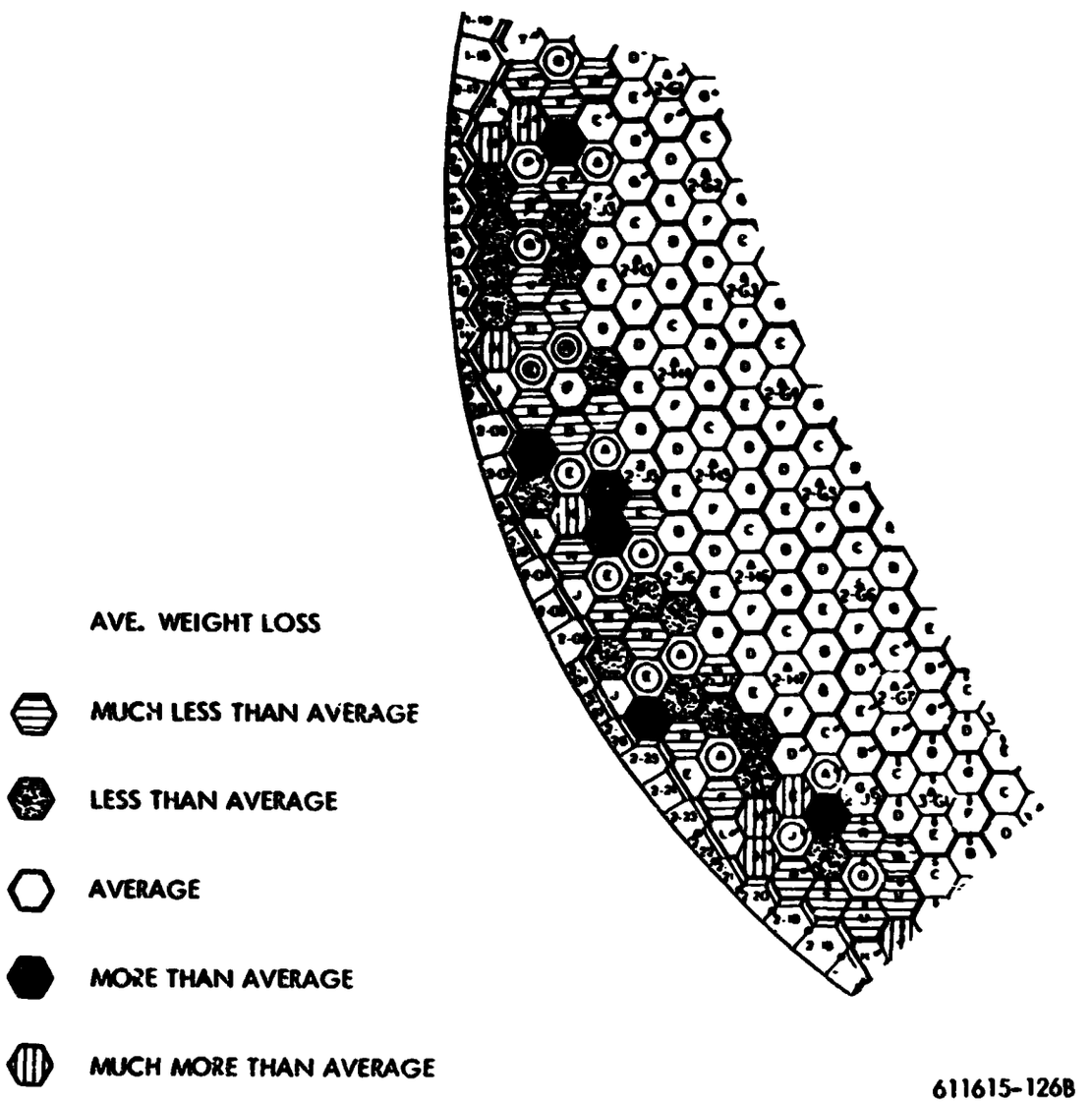

Figure 6-39. Location Rating Factor for the NRX-A5 Core

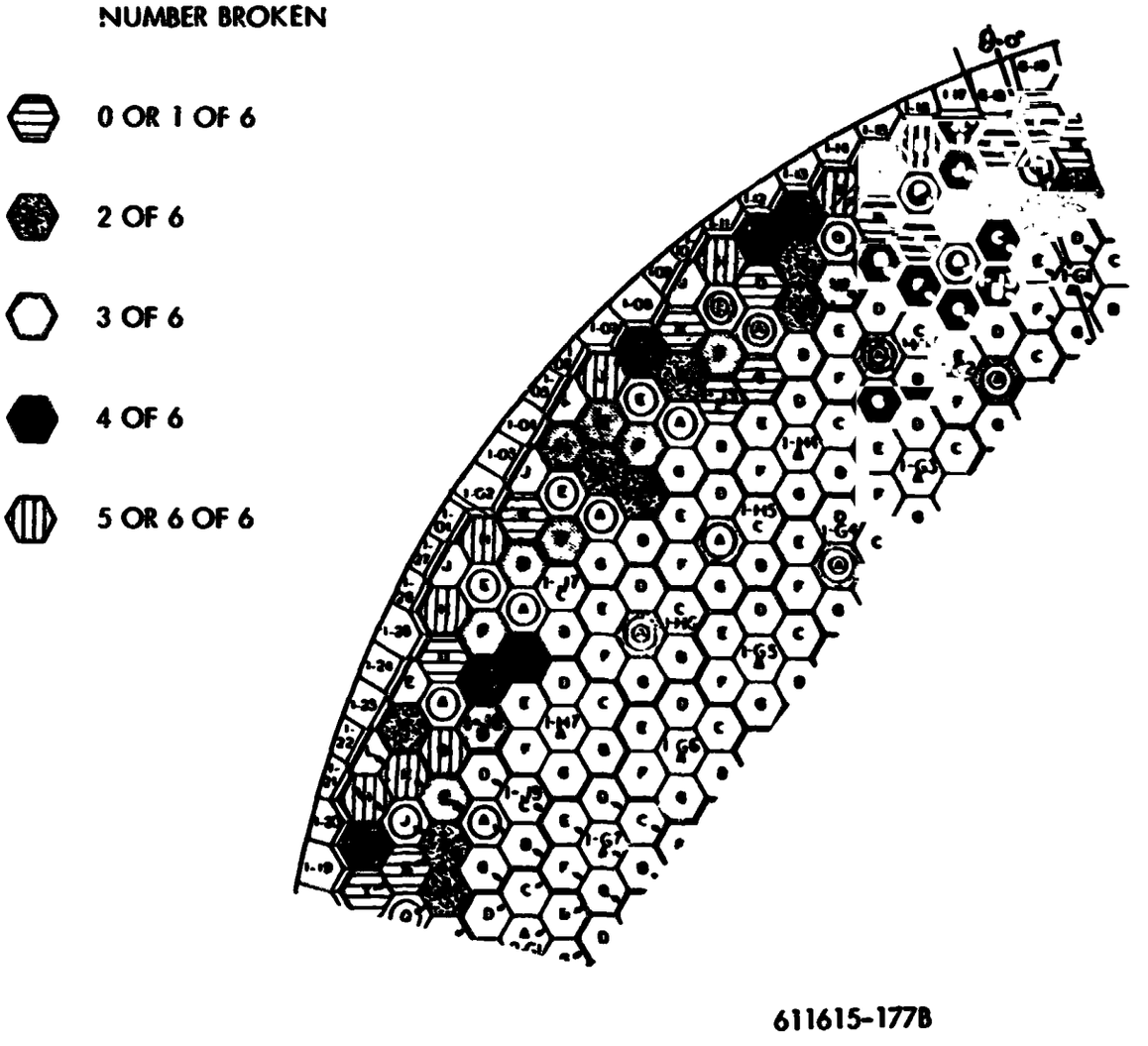

Figure 6-40. Peripheral Element Breakage Pattern for the NRX-A5 Core

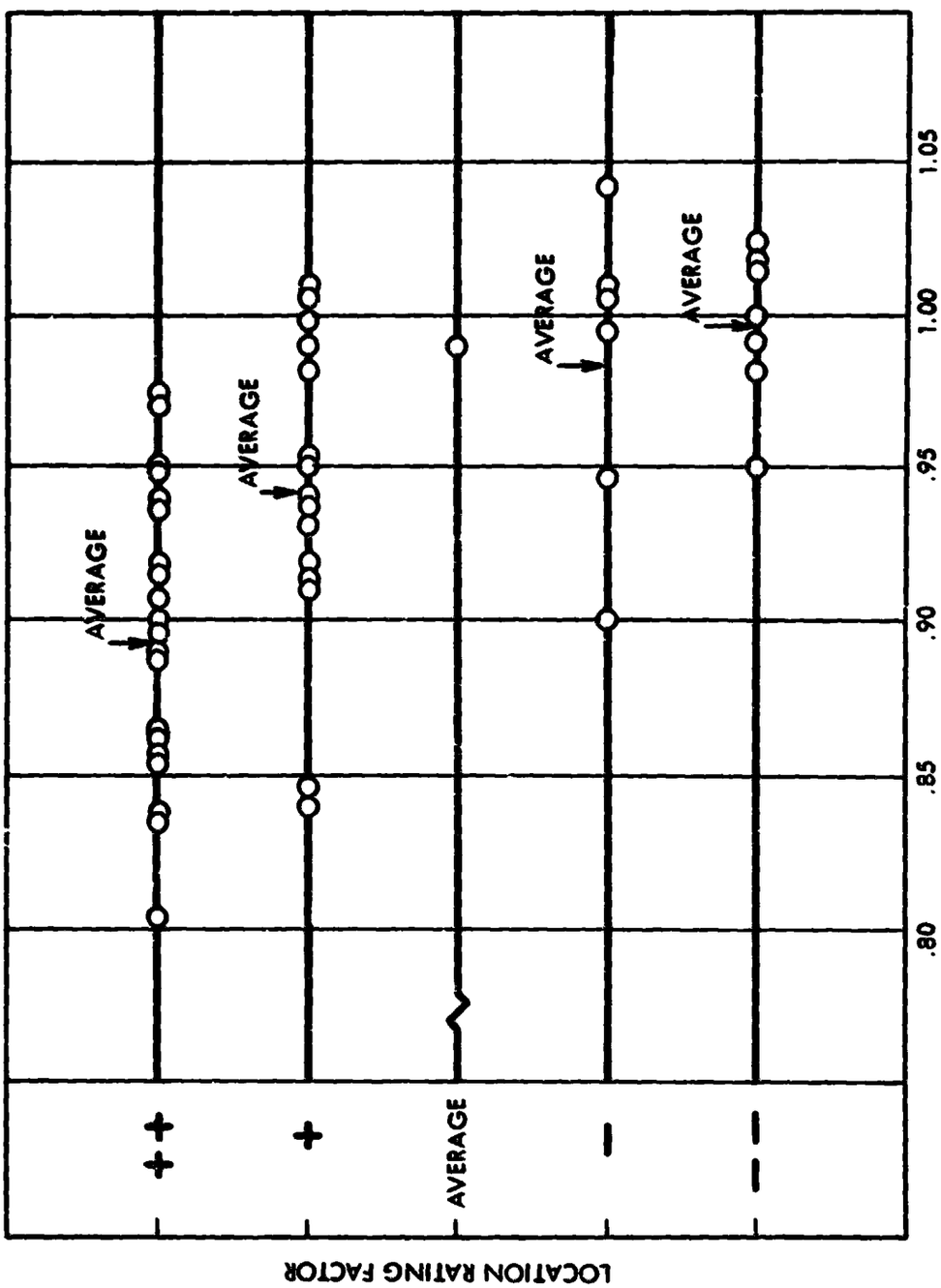

Figure 6-41. Location Rating Factors versus Average Power Factor for the NRX-A5 Core

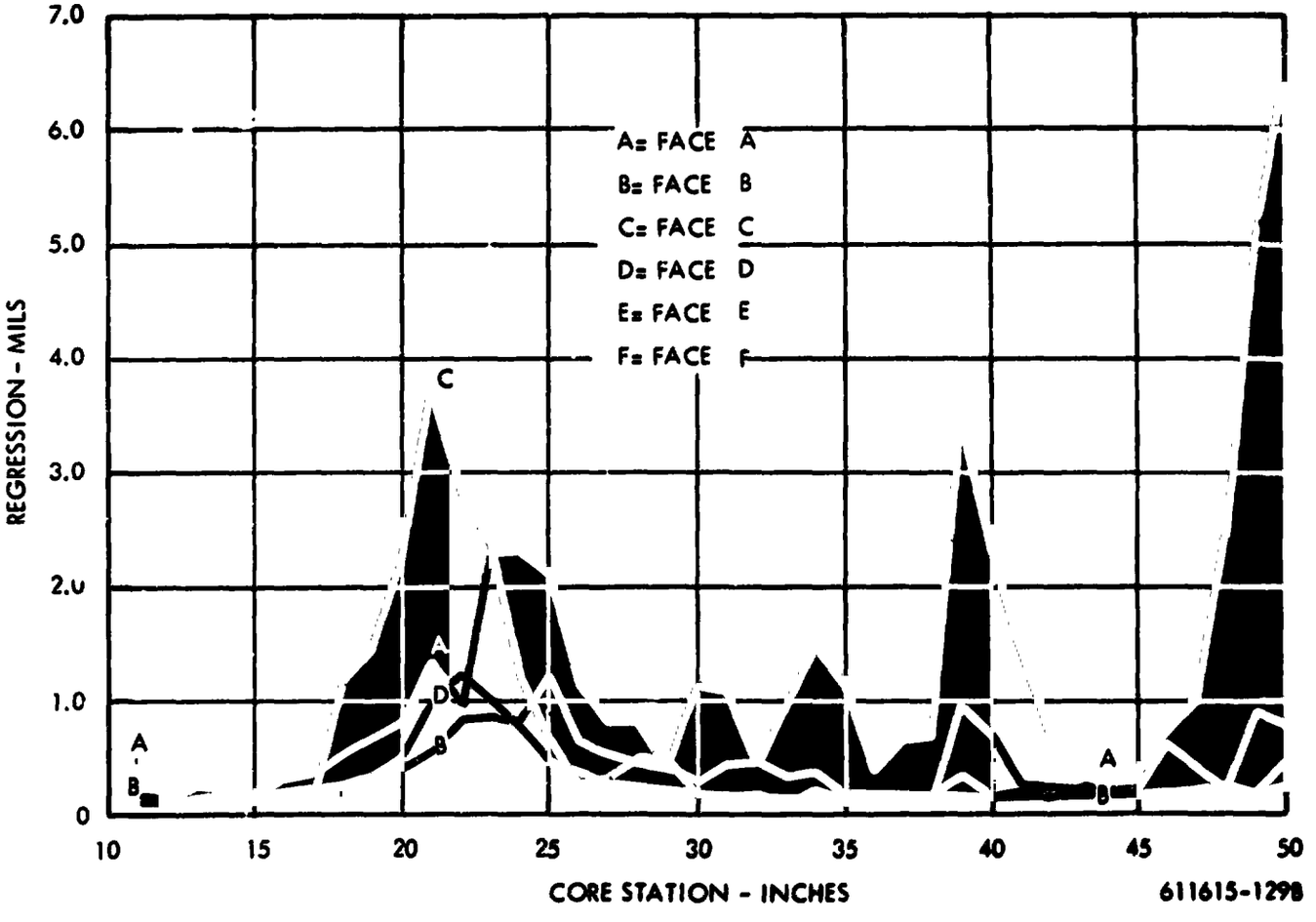

Figure 6-42. Average Surface Regression all NRX-A3 Elements, First Row Uncoated

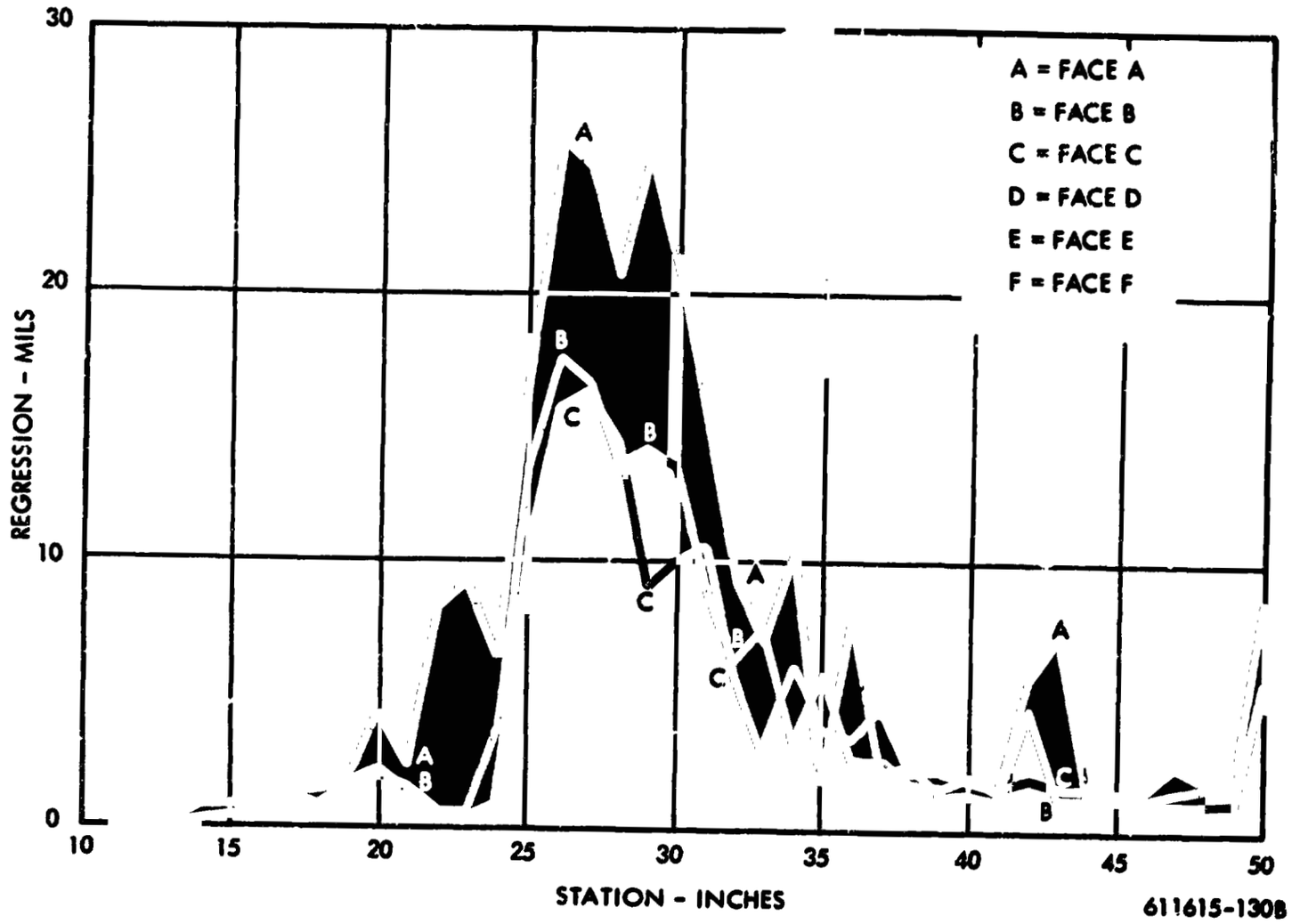

Figure 6-43. Average Surface Regression all NRX/EST Elements, First Row Uncoated

6.3.5 Pinholes and Channel Exposure

6.3.5.1 Background

Examination of the NRX-A5 fuel elements for pinholing and channel exposure was accomplished by converting each element face data to appropriate IBM data cards. The element data was originally compiled from photographic examination of all six faces of each element. A computer program designated HEC 1 (holes or exposed channels) was used as a sorting program to reduce the data. Axial data started from the 10-inch axial station and consisted of three-inch increments, thereby making 14 axial stations for each face of each element. In addition to the results presented herein, the code output also presents the data on an element basis. The main output summarizes the data by sector. In each sector the data is broken down by row (a radial band option also exists) and axial increment. Each row is summarized with a radial calculation. The sector is then summed by axial increments. The code distinguishes between pinholes (>1/16 in. diameter) and holes (< 1/16 in. diameter); however, the results presented herein are based on the total count within each increment.

Table 6-7presents a summary of the pinhole and channel exposure data for NRX-A5, and comparative NRX-A3 and NRX/EST data. For comparable reactor operating times the data indicate that the total number of pinholes for NRX-A5 is about half that for NRX/EST, even though the "A" row channel exposure for NRX-A5 is twice that of NRX/EST. For a single fuel element the maximum number of channels that could be exposed is 18 and therefore, the maximum value of channel exposure is 936 inches of channel exposure per element.

The following three sub-sections contain data on (a) NRX-A5 pinholes and channel exposure, (b) comparison of NRX-A3, NRX/EST and NRX-A5 pinholes and channel exposure and (c) "zero defect" pinhole and channel exposure elements. This data was reduced primarily for correlating pinholing and channel exposure with weight loss and fuel element performance.

TABLE 6-7

PINHOLING AND CHANNEL EXPOSURE

Reactor Core	Total Number of Elements Examined	Total Number of Pinholes	Row A Pinholes/ Elements	Total Number of Elements Examined	Total Inches of Channel Exposed	Row A Inches Channel Exposed/ Element
NRX/EST (A4)	1216	25091	15.5	1091	23937	39.8
NRX-A5	1305	12619	33.0	1300	24287	87.0
NRX-A3	1504	3354	6.5	---	---	---

6.3.5.2 NRX-A5 Pinholes and Channel Exposure

Table 6-8 is a summary of NRX-A5 pinholes and channel exposure calculations on a sector basis. The number of pinholes per element for the Y-12 elements are relatively constant for all sectors, with the exception of sector 5. Since all of the Y-12 elements were of Code 99 it appears that the number of pinholes per element may be a function of temperature and loading. The exception in sector 5 appears to be a consequence of the blockage of some coolant flow channels in element 5F5C and 5F4F. The Y-12 channel exposure characteristic given by inches of channel exposure per element increases azimuthally from sector 1 through 5, and then decreases abruptly for sector 6. The Y-12 average number of pinholes per element is about equal to the inches of channel exposure per element.

The WAFF sector tabulation exhibits no distinguishing characteristic in pinholing or channel exposure other than that the average channel exposure is about three times the average pinholing. This indicates a faster rate of channel exposure from pinholes for the WAFF elements than for the Y-12 elements. The core averages of both WAFF and Y-12 elements indicate a channel exposure characteristic twice that of the pinholing characteristic.

The axial and radial distributions of the average number of pinholes per element are given in Figure 6-44 for both the WAFF and the Y-12 elements. The radial distribution indicates that the Y-12 elements exhibit a smaller number of pinholes per element from about core radius 6 in. to 10 in.. Both element types indicate trends with peaks near the core centerline and the core periphery. There appears to be a lower slope for the WAFF than the Y-12 element data. The Y-12 elements also exhibit lower trough values for the average number of pinholes per element for a greater radial increment than do the WAFF elements. The axial distribution indicates that the Y-12 elements have a lower average number of pinholes per element examined for all core stations except between 31 and 34 inches where the WAFF elements are lower valued. The principal peak is at about

23 inches and the second main peak is at about 38 inches. A smaller peak occurs at about station 32.5 inches and is in the region where the WAFF average values of data are lower than the Y-12 data. The principal WAFF peak at 23 inches is a consequence of the large number of pinholes at this axial station principally in cluster rows B, C, and D of sectors 1, 5, and 6. The characteristic shape of this curve is the same as that exhibited by the weight loss curve. The axial and radial distribution of inches of channel exposed per element are shown on Figure 6-45. The axial distribution of the WAFF element generally matches that of the Y-12 elements and is relatively constant except for the axial increment from 21 inches to 32 inches. In this region there is a sharp increase in the average channel exposure which coincides with the pinhole characteristic. The characteristic of maximum channel exposure is about three times that of the maximum pinholing. The radial distribution of the channel exposure shows two peak values, the maximum is at about the 2 in. radius and the other one of about one-sixth of this maximum is at the 13 in. radius. The Y-12 element characteristic at the 4 in. and 5.6 in. radius, are in juxtaposition. This occurred because the elements examined were in the "C" rows in sectors 4 and 5 only, while the remaining plot includes elements in all sectors and the element characteristic has a distinct azimuthal asymmetry. The radial distribution characteristic of channel exposure agrees generally with that of pinholing and both of these indicate a trough region at the 10 in. to 11 in. core radius. Both of these distributions are remarkably characteristic of the weight losses shown in Figure 6-1.

The axial distributions of the pinhole and the channel exposure characteristic for the "A" row, which contained only WAFF elements, are shown on Figure 6-46. The peak pinhole characteristic values consistently alternate for about a 6 in. and 9 in. axial incremental distance between peak values. This alternating constant slope characteristic of NRX-A5 is predominantly due to the pinhole distribution in sectors 3, 4, and 5, implying that some radial effect of the hot buffer regions extend to the "A" row elements. The channel exposure characteristic does not appear to follow that of the pinholing but exhibits a relatively smooth relationship from both sides of the peak value

at 23.5 inches. The ratio of the characteristics at the 23.5 inch axial station is about 4/1 (channel exposures to pinholes). In a comparison of this figure with the axial distribution of corrosion depth it was observed that the pinholes exhibit a somewhat similar characteristic but the channel exposure does not, except for the peak at about 24 inches.

The axial distribution characteristic of pinholing and channel exposure for the J row, which contained only WAFF elements, is shown on Figure 6-47. The peak values of both characteristics in this row do not occur at the same core station and the peaks and valleys of the pinholing are not as distinct as for the "A" row. These are probably a consequence of the asymmetry of the J row clusters.

An attempt was made to duplicate the pinholing effects analytically. A computer code discussed in Section 6.8 designated CAFING, was developed to reflect the bore-induced surface regression due to pinholes. Figures 6-48 and 6-49 illustrate the magnitude of surface regression assuming a pinhole size and pinhole pattern for full power conditions at the core central and mid radial regions. In both cases a characteristic "sawtooth" pattern was observed along the core axis. The peak surface regression occurred at core station 45 in. for both pinhole patterns.

The calculated surface regression at the end of a 15 minute operation at full power is much smaller than the measured values obtained from the surface trace data. The difficulties in the calculation of bore induced surface corrosion are three fold: (1) The calculated flow in the interelement gap channel strongly depends on the gap size assumed at SOL for the calculation. In turn, the surface corrosion rate is strongly dependent on the flow rate in the gap channel. (2) The pinhole size and pinhole pattern at SOL are not known from post test inspection data. No acceptable correlation to predict the formation of pinholes is available. The only available data are from the electrical furnace tests. The first attempt to use these test data to predict pinhole formation was not completel, successful. (3) The analytical model considers isolated flow in the gap channel. Lateral flow between adjacent gap channels was not considered. Thus, the model may not

represent the actual flow pattern in the reactor. A three dimensional flow network may be required. With these difficulties in mind, further development of the analytical technique to analyze bore induced corrosion is continuing.

TABLE 6-8

NRX-A5 SUMMARY DATA FOR PINHOLING AND CHANNEL EXPOSURE OF FUEL ELEMENTS EXAMINED

Pinholing:

Sector	WAFF ELEMENTS: Number of Pinholes + Holes	WAFF ELEMENTS: Number of Elements	WAFF ELEMENTS: Pinholes Per Element, Sector	Y-12 ELEMENTS: Number of Pinholes + Holes	Y-12 ELEMENTS: Number of Elements	Y-12 ELEMENTS: Pinholes Per Element, Sector	WAFF Plus Y-12 Pinholes/element, sector
0	58	5	11.6	---	---	---	11.6
1	2171	114	19.06	685	117	5.85	12.36
2	761	102	7.46	609	117	5.20	6.25
3	937	104	9.0	818	120	6.83	7.84
4	995	115	8.65	775	117	6.63	7.64
5	1199	75	16.	1571	120	13.1	14.2
6	1416	88	16.1	624	111	5.62	10.25
TOTALS	7537	603	Avg. 12.5	5082	702	Avg. 7.25	9.67 Avg. of Core

CHANNEL EXPOSURE

	WAFF ELEMENTS: Inches of Channels Exposed	WAFF ELEMENTS: Number of Elements	WAFF ELEMENTS: Inches of CE/ Element, Sector	Y-12 ELEMENTS: Inches of Channels Exposed	Y-12 ELEMENTS: Number of Elements	Y-12 ELEMENTS: Inches of CE/ Element, Sector	WAFF Plus Y-12 Inches of CE/Element Sector
0	294	4	73.5	---	---		73.5
1	2988	114	26.2	183	114	1.61	13.9
2	3670	97	37.85	608	128	4.75	19.
3	4774	103	46.2	642	118	5.44	24.47
4	3540	113	31.35	1138	118	9.64	20.25
5	2225	73	30.5	1429	123	11.6	18.66
6	2463	86	28.7	333	109	3.06	14.32
TOTALS	19954	590	Avg. 33.85	4333	710	Avg. 6.1	16.7 Avg. of Core

CONFIDENTIAL

CONFIDENTIAL

Aerojet Nuclear Laboratory

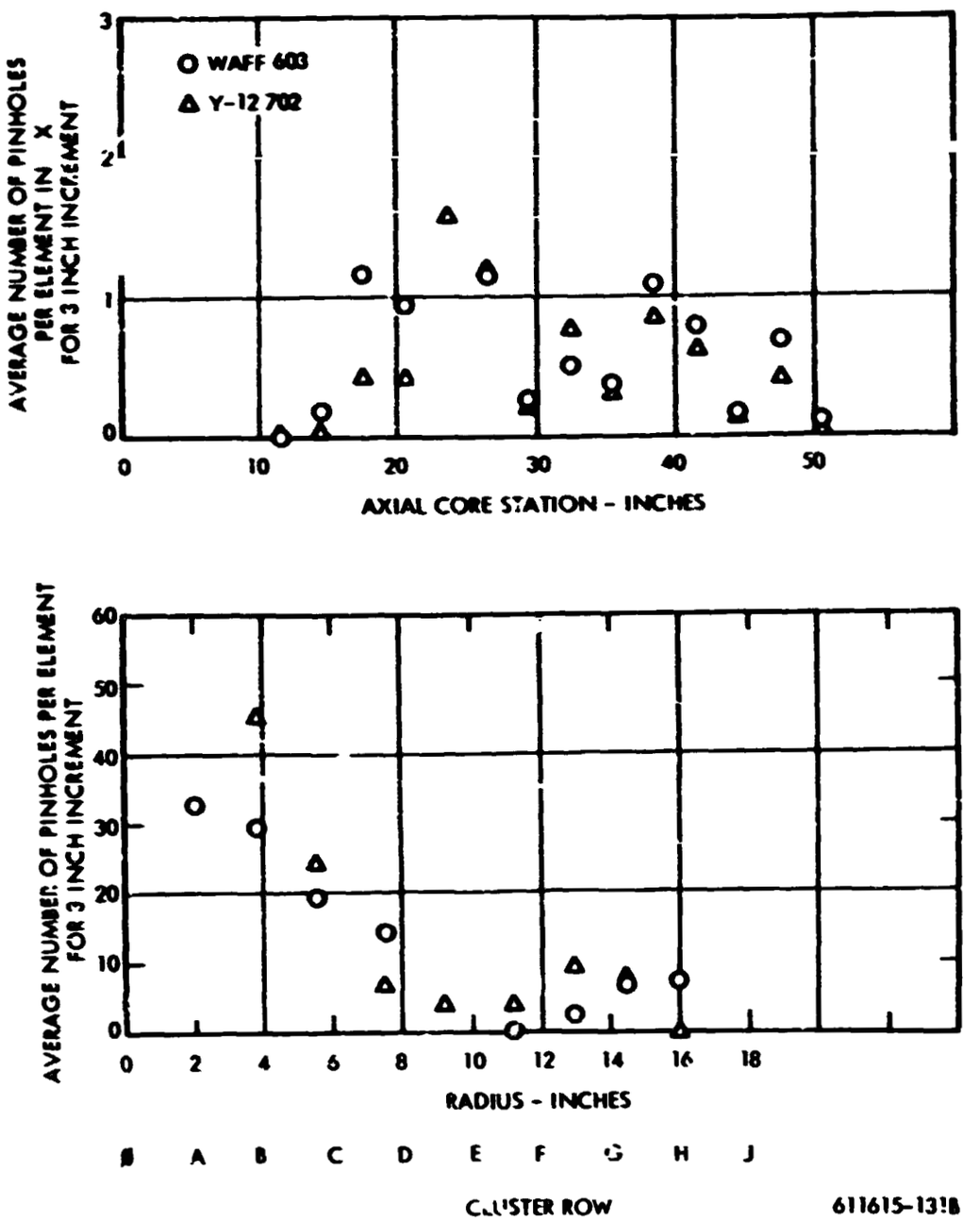

Figure 6-44. NRX-A5 Axial and Radial Distribution of Number of Pinholes per Element

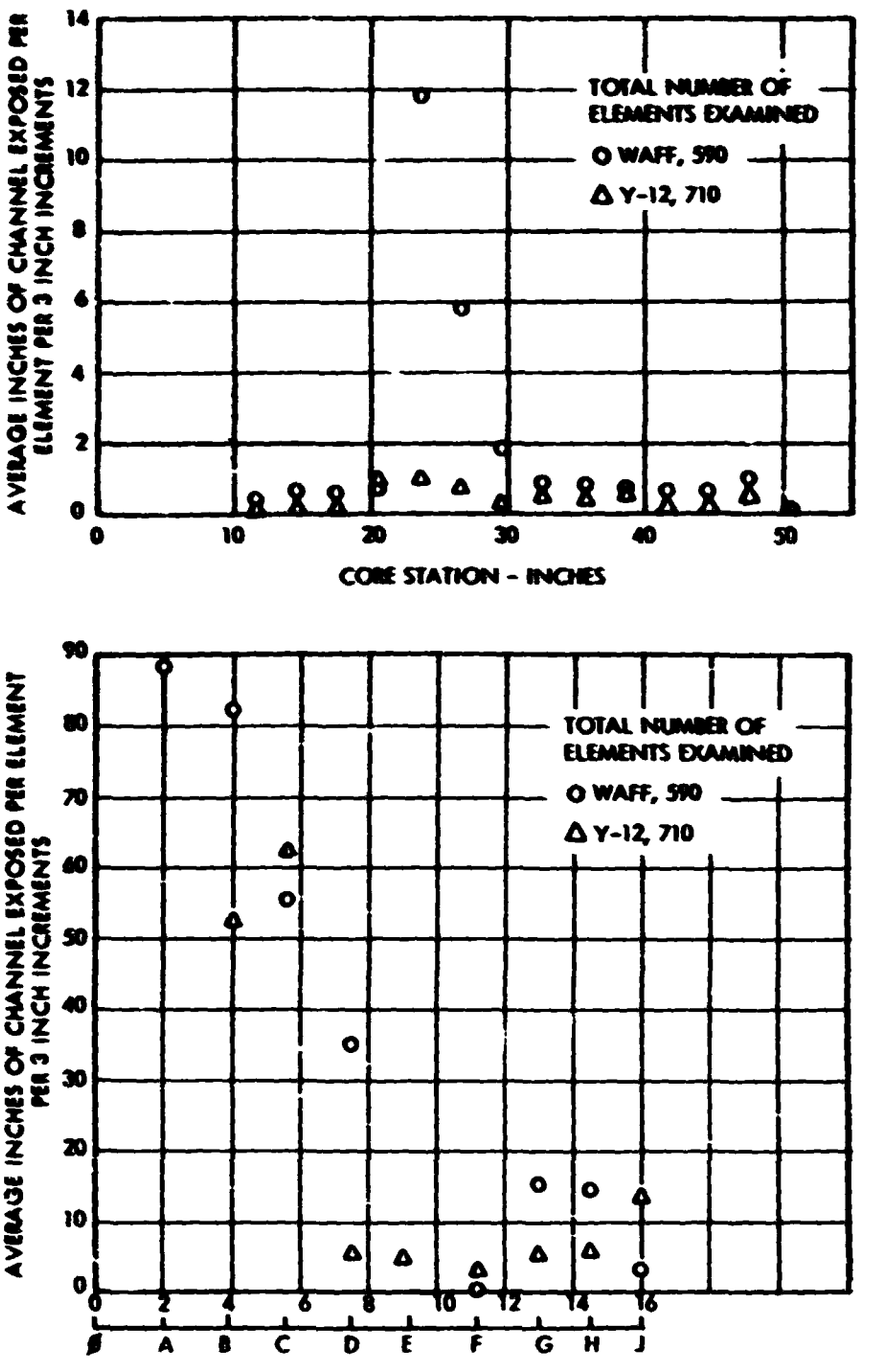

Figure 6-45. NRX-A5 Axial and Radial Distribution of Inches of Channel Exposed Per Element

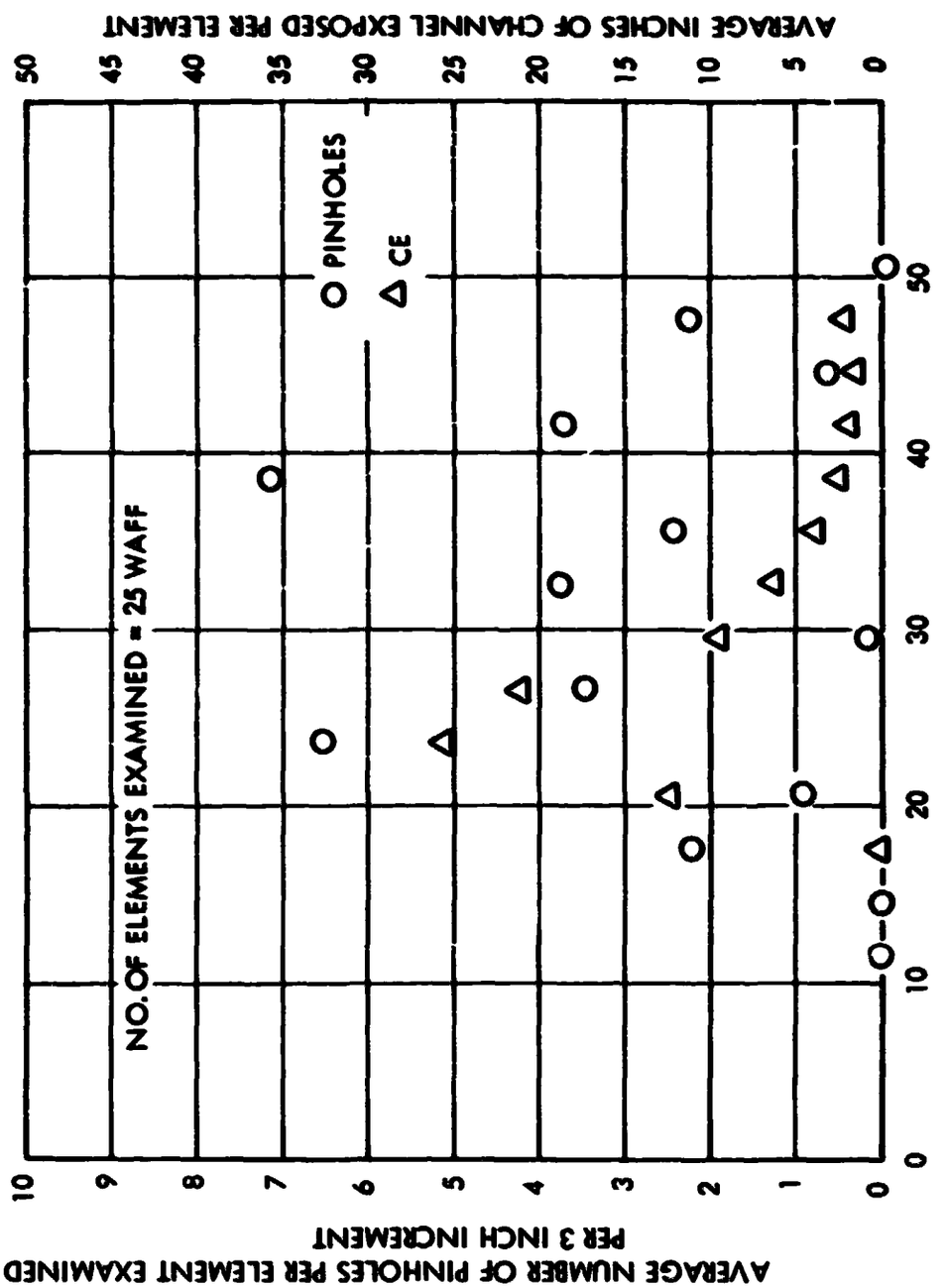

Figure 6-46. NRX-A5 Axial Distribution of the Pinhole and Channel Exposure Characteristics of Row A

Figure 6-47. NRX-A5 Axial Distribution of the Pinhole and Channel Exposure Characteristics of Row J

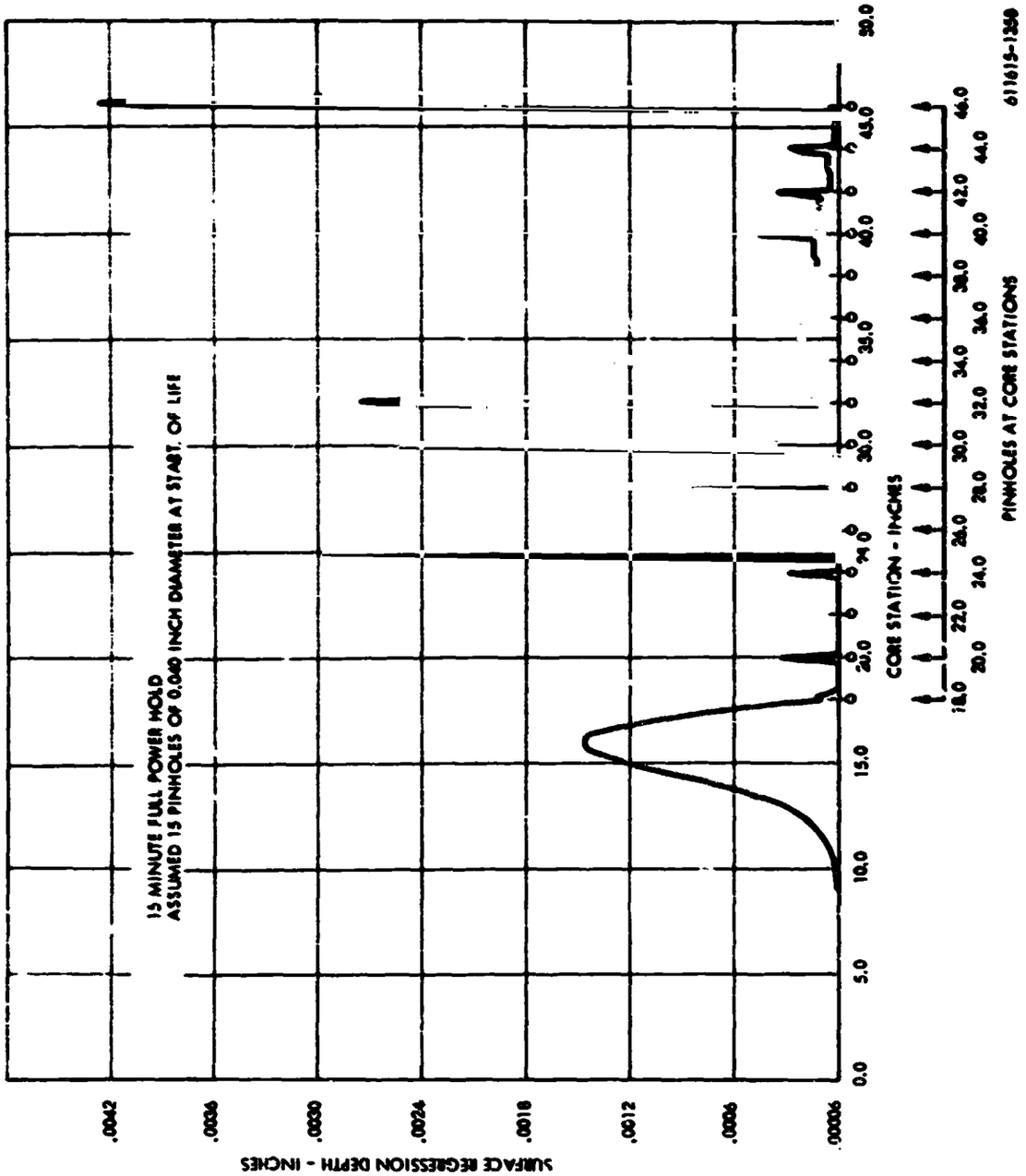

Figure 6-48. NRX-A5 EP-IV EOL Surface Corrosion Depth due to Pinholes, Core Center Region

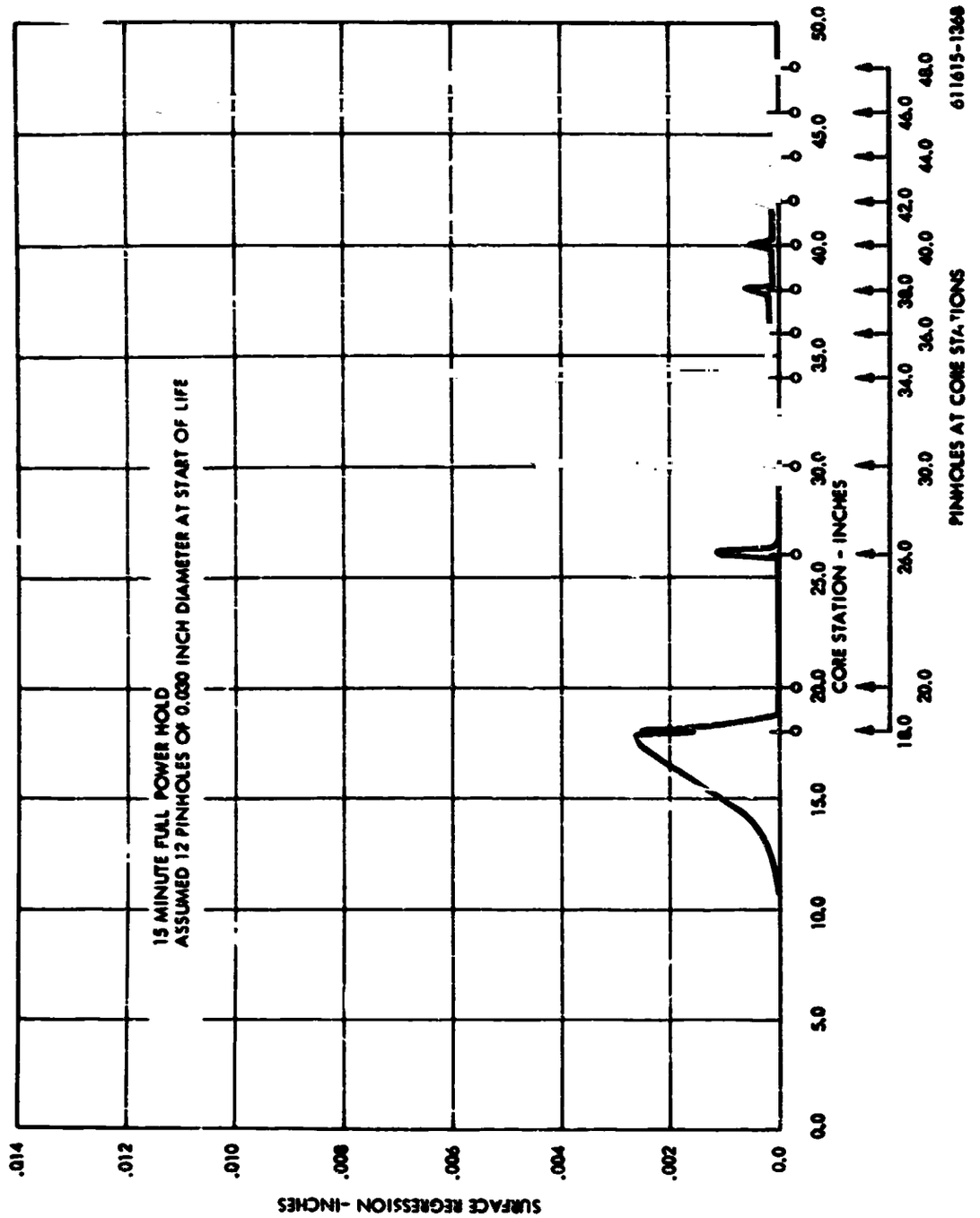

Figure 6-49. NRX-A5 EP-IV EOL Surface Corrosion Depth due to Pinholes, Core Mid-Radial Region

6.3.5.3 Comparison of NRX-A3, NRX/EST, and NRX-A5 Pinholes and Channel Exposure

The radial distribution of the number of pinholes per element for the three reactor cores are compared on Figure 6-50. The trough region appears to be located at about core radius 9 in. for all three reactors. The maximum average for the NRX/EST is greater than at the center, however, the center of the core had fewer elements examined. The improvement in peripheral performance of the NRX-A5 may be due to the external surface coating of NbC on these elements and the two hot buffer sections. The lower values of the NRX/EST up to the trough may reflect the fact that the NRX/EST had all Y-12 elements in this region. The NRX-A3 characteristic shape is remarkably similar to the radial weight loss shown in Figure 6-25, with the pinholes following the bore weight loss to about the 6 in. radius. For greater core radii the pinholes appear to follow the surface weight loss.

The radial distribution of the average channel exposure per element is compared on Figure 6-51 for the NRX/EST and NRX-A5.

The axial distribution of the average number of pinholes per element is compared on Figure 6-52 for the three reactors. These indicate an axial shifting to a lower station of the peak values with subsequent reactor designs. The NRX/EST and NRX-A3 did not exhibit the alternating peak and valley characteristic as did the NRX-A5 data.

The axial distribution of the average inches of channel exposure per element are compared on Figure 6-52 for the NRX/EST and NRX-A5. The axial peak characteristic value is also shifted to a lower station for the NRX-A5 than for the NRX/EST. This indicates that the inches of channel exposure per element for the NRX/EST was greater than the NRX-A5 after core station 25, while the reverse was true from station 15 to 25 inches.

Figure 6-50. Comparison of NRX-A3, NRX/EST and NRX-A5 Radial Distribution of Pinholes per Element

Figure 6-51. Comparison of NRX/EST and NRX-A5 Radial Distribution of Channel Exposure per Element

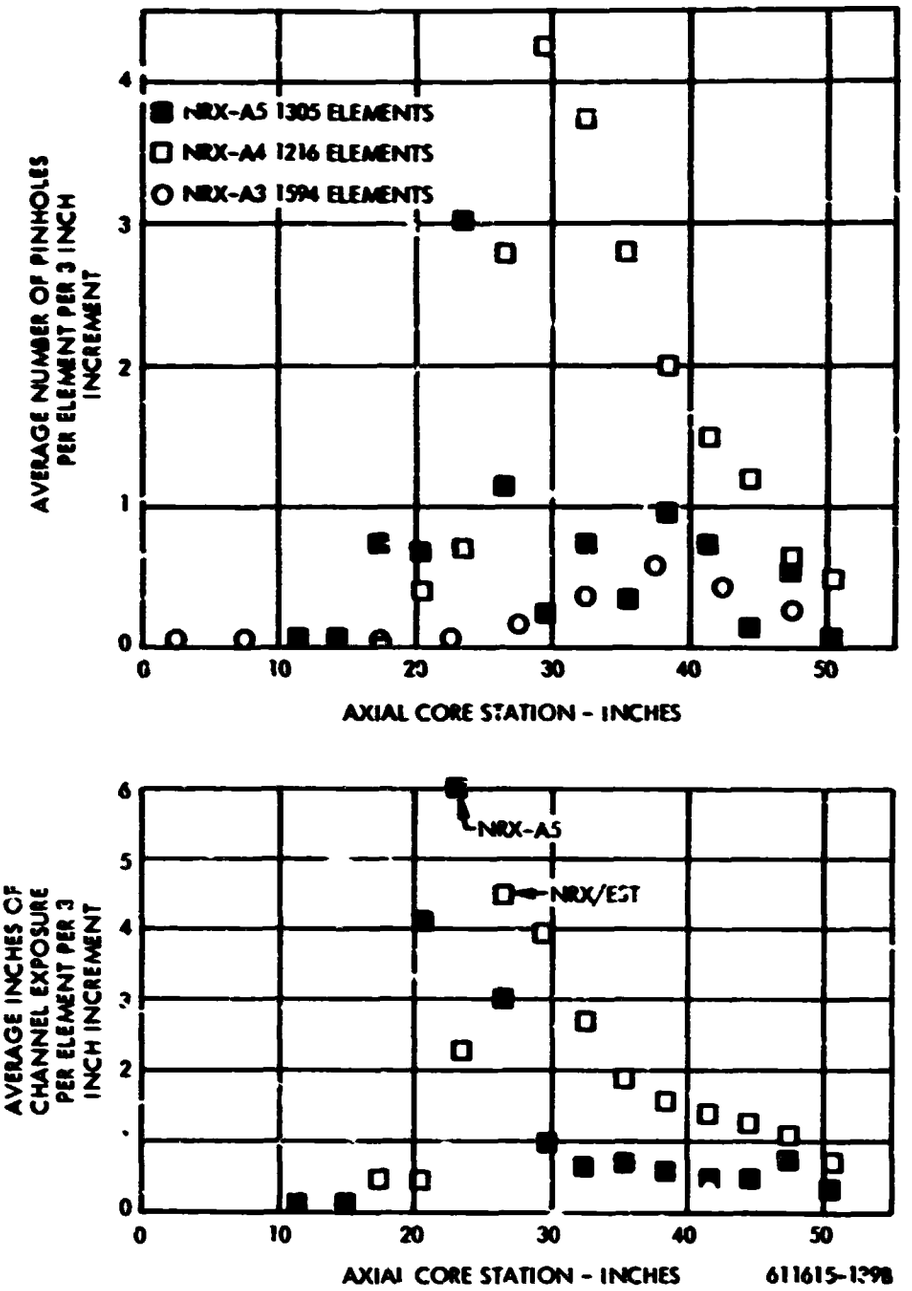

Figure 6-52. Comparisons of the Axial Distribution of the Average Number of Pinholes per Element and the Inches of Channel Exposure for the NRX-A3, NRX/EST, and NRX-A5

6.3.5.4 "Zero Defect" Pinhole and Channel Exposure Elements

All of the NRX-A5 fuel elements which were examined for pinholing and channel exposure were reviewed in order to determine which of the elements had neither pinholes nor channels exposed. Table 6-9 contains a tabulation of all such "zero defect" elements found. If the single "break" elements are eliminated from this list then approximately 1.8 percent of the core fuel elements examined were "zero defect" elements and 56 percent of these "zero defect" elements were in the hot buffer region and 77 percent were in the J row. Of these J row "zero defect" elements, 60 percent were externally coated with NbC.

Examination of the regions that contained both Y-12 and WAFF elements indicated that the three WAFF elements 1F3C, 4H3E, and 6H5G showed no pinholes or channel exposure. Of the total number of elements examined in the F and H rows, the percentage of WAFF elements for each row was 1.9 percent and 33 percent respectively.

TABLE 6-9

NRX-A5 FUEL ELEMENTS WITH ZERO PINHOLES AND ZERO CHANNEL EXPOSURE

Serial No.	Position	Average Loading Gms/Inch x 100	Radius - Inches	Weight Loss Grams
99-25891	1D4E (1)	239	7.9	12.4
99-25966	1F3C	244	10.5	12.7
89-29628	1H3C (1)	203	14.4	24.5
89-29631	1H6D (1)	202	14.4	28
89-29751	1H6E (1)	202	14.7	28.2
39-27214	1J6H (3)	75	16.8	---
69-29173	2J3E	144	15.7	13.7
69-29067	2J9W (1)	144	15.2	55
39-26943	3J9U (?) (3)	75	16.5	8.1
79-29405	4H3E	178	15.1	11.8
69-29060	4J3R (1)	144	15.7	13.2
69-29079	4I4C	145	15.7	11.3
49-27706	4J4D (3)	103	16.4	11.7
69-29241	4J4G	144	15.2	10.7
39-27044	4J4K (4) (3) (1)	75	16.7	25.3
49-27725	4J7D (3)	103	16.2	20.3
49-27582	4J7F (1) (3)	103	16.2	22.5
39-27190	4J8D (2) (3)	75	16.6	6.5
69-29086	4J9R (1)	145	15.4	11.0
49-27761	4J9S (3)	103	16.1	8.9
39-27110	4J9T (2) (3)	75	16.7	7.6
59-27846	4J9V (3) (1)	124	15.8	12.6
39-27077	4J9U (2) (	75	16.5	21.3
49-27696	5J3S (3)	103	16.3	11.6
49-27599	5J3V (3)	103	16.4	12.7
69-29176	5J5C	144	15.4	15.1
89-29603	6G1E (1)	202	14.5	30
99-25892	6H5G	240	13.3	14
69-29113	6J5C	146	15.3	13.3

(1) Broken element (one place)
(2) In hot buffer zone periphery - all sector 4 in hot buffer region
(3) Externally NbC coating 40 inches from nozzle end

6.4 FILLER STRIP CORROSION

External surface regression data was available for 14 filler strips. Three of the filler strips were outside the hot buffer regions and the other 11 were in the hot buffer region. The hot buffer filler strip design was intended to both reduce radial inflow of seal coolant and also to saturate the inflow from the filler strips.

The reference for the location of the surface regression data was the serial number of the filler strip. The serial number area on the filler strip is approximately 1.6 inches long, therefore,filler strip measurement stations may be as much as 1.6 inches off in either direction. Figures 6-53 and 6-54 show the average of the data available for filler strip surface regression in and outside of the hot buffer region, respectively. The filler strips in the hot buffer region showed substantially more surface corrosion than those outside the hot buffer area. The deepest corrosion occurred on the lateral faces at the outside diameter. The corrosion was more extensive at the aft end than expected and some corrosion was observed on the faces opposite the fuel elements and on the inner corners.

On the radial surfaces the corrosion exhibited intermittent swirling patterns to core station 30 in. From core station 30 - 51, corrosion cuts across the entire radial face in axial corkscrew fashion and deepens towards the hot end. Between core stations 49 and 51, there is severe undercutting of up to 0.125 inches in depth. The coated surfaces which start at core station 51 are generally intact. The fuel side face corrosion was lighter than the radial surface corrosion, it started at core station 13 and progressed to core station 51 in. in intermittent traverse paths which become wider and deeper toward the hot end.

These flow patterns indicate a considerable amount of axial flow in the filler strip region, particularly at the hot end of the core. The question on the filler strip performance is whether this flow was from the exposed and pinholed fuel element channels, or from the lateral support region. There is evidence which points toward radial inflow from the seal region. This evidence consists of corrosion patterns on the filler strips, the decrease in seal pressure with operating time and the thermal capsule data. Figure 6-53 shows an increasing cyclic pattern of increase and decrease of surface corrosion at about every 3 inches.

The cycle pattern implies that the corrosion may be connected with seal system flow configurations, however, the data is insufficient to fully identify this as the primary cause.

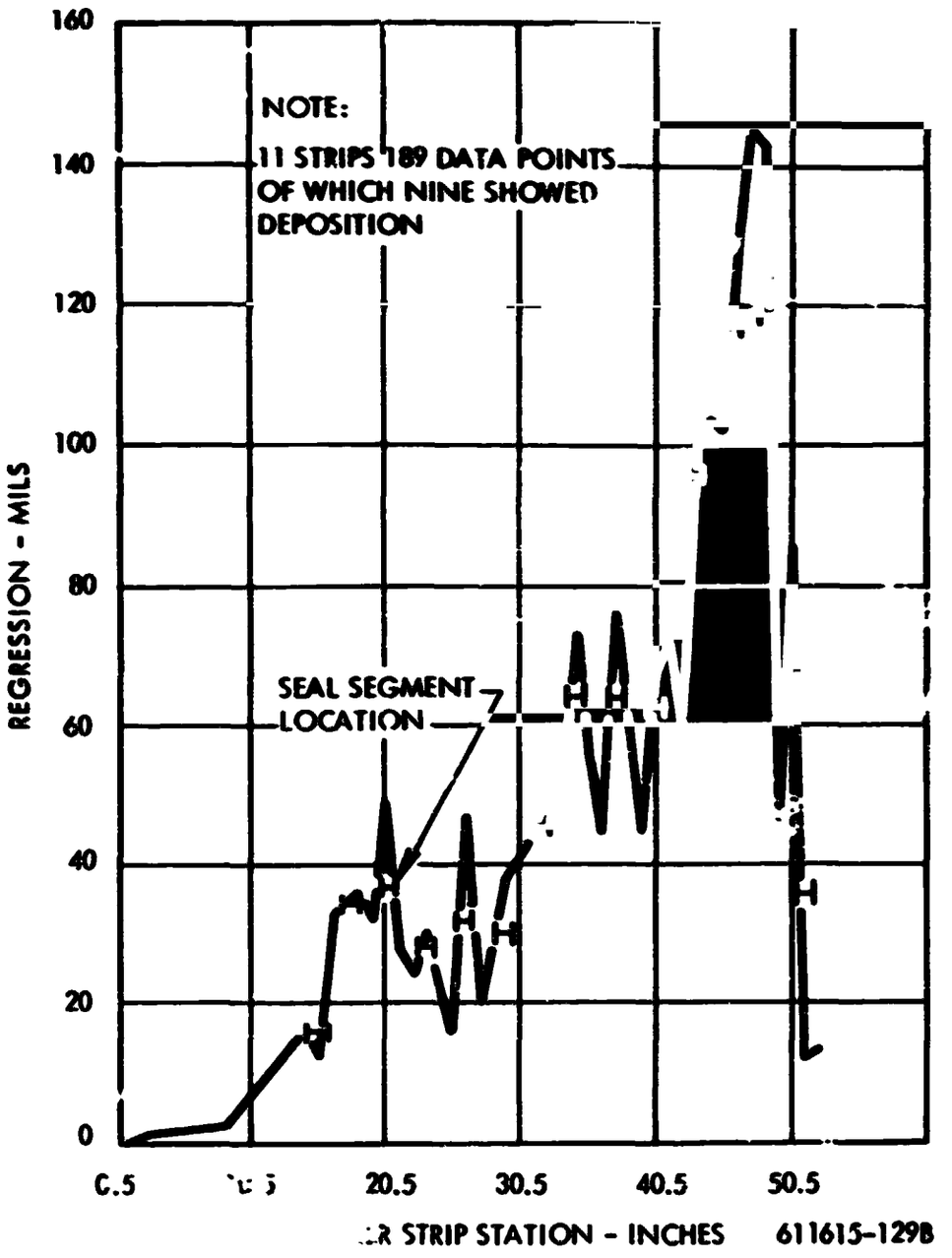

Figure A · · · · · Regression in Hot Buffer Region

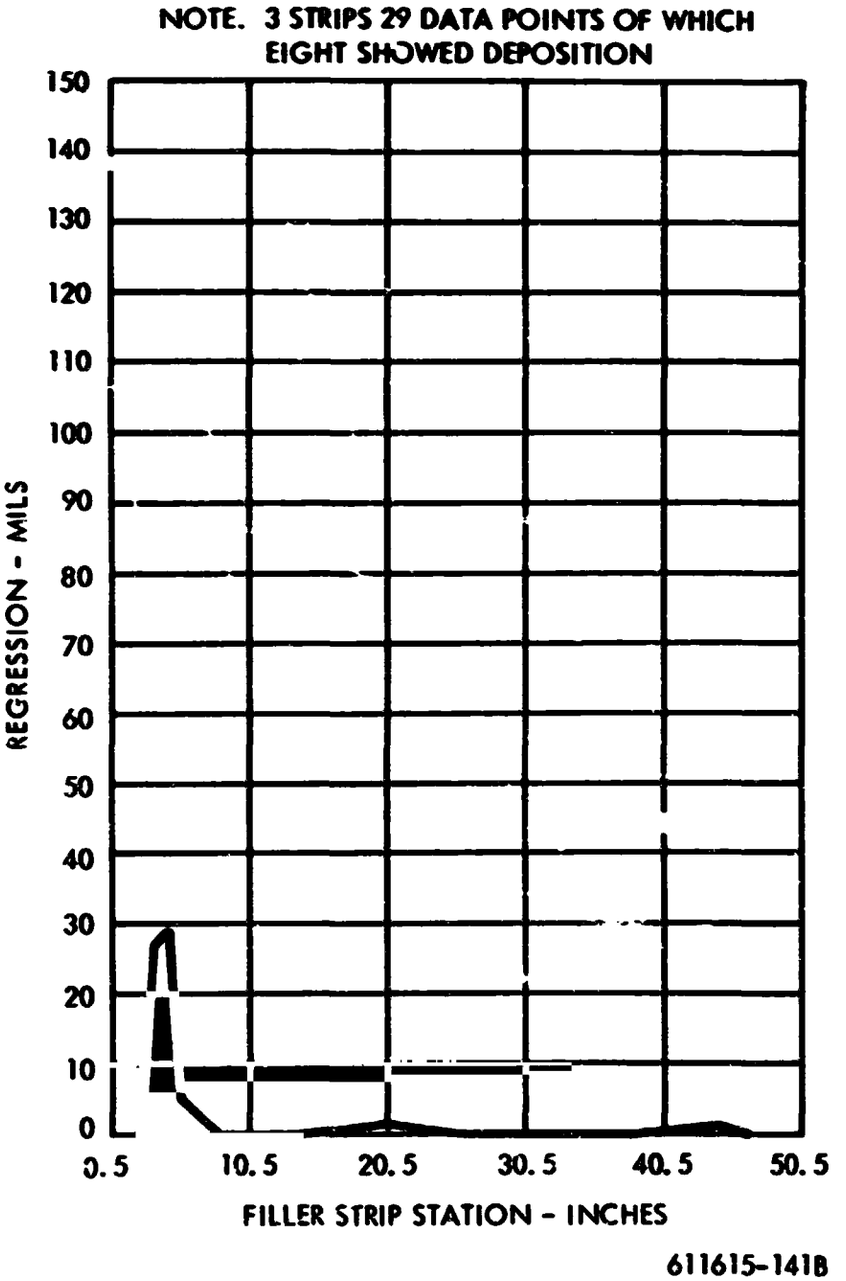

Figure 6-54. NRX-A5 Filler Strip Surface Regression Outside Hot Buffer Region

6.5 FUEL ELEMENT HOT END CONDITION

A review was made of the visual observations of the NRX-A5 hot end condition. A representation of the NRX-A5 hot end is sketched on Figure 6-55. For comparison both the NRX/EST and the NRX-A3 hot end designs are also shown. The major differences between the NRX-A5 and NRX/EST designs are in the coating length and depth of undercut after coating. Two experimental clusters of elements in the NRX/EST had a hot end design with a 1/4 inch tapered tip and no additional undercut. These hot ends showed little sign of corrosion. All of the NRX-A5 hot ends had a reduced undercut depth and length similar to the experimental elements in the NRX/EST. As a result of this modification, the NRX-A5 fuel element hot end condition was found to be excellent.

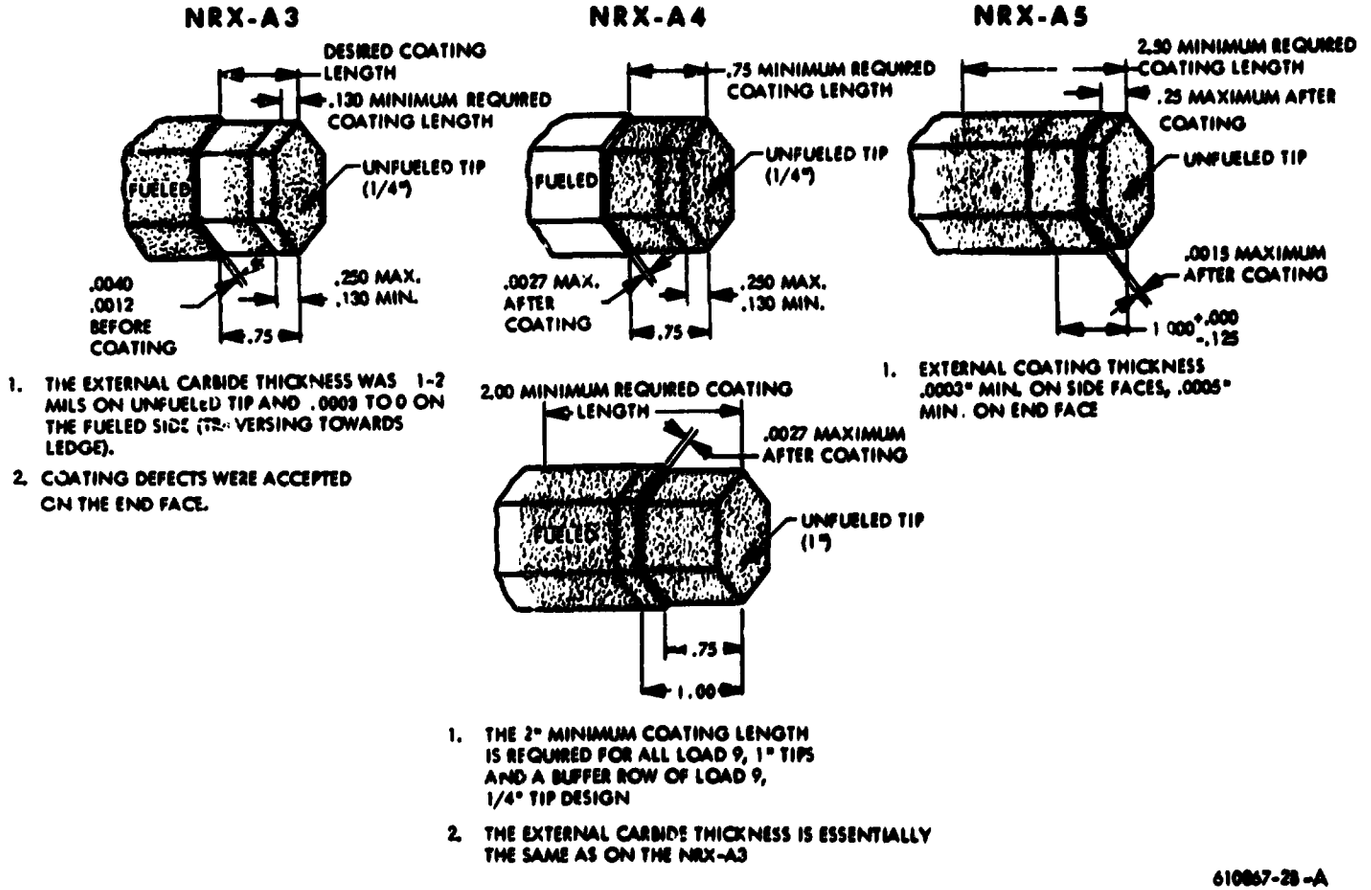

Figure 6-55. Fueled Element Hot End Design

CONFIDENTIAL

CONFIDENTIAL

Astronuclear Laboratory

6.6 SUPPORT BLOCK MECHANICAL AND CORROSION PERFORMANCE

A detailed analysis was performed by the Materials Department on both the mechanical and corrosion performance of the NRX-A5 support blocks. Some of the pertinent observations are reviewed in this section. Calculations performed on the J-9 support block to determine the temperature patterns for stress analysis are presented to support the mechanical performance.

6.6.1 Mechanical Performance

Macro-observations on the support blocks in the NRX-A5 reactor revealed an absence of cracks and corrosion pockets at the cup counter-bore radius. This type of cracking was evident in the NRX/EST. Measures were taken in the NRX-A5 to reduce the possibility of such cracking by increasing the cup counter bore radius and by using ATJ washers with grafoil inserts. The increase in the cup counter bore radius, the use of the ATJ washers with grafoil inserts and lower ramp rates relieved the stress concentrations at this location which were identified as the incipient cause of this damage.

Observations revealed both transverse and axial cracks in the NRX-A5 irregular blocks. The axial cracks appeared to be more severe and were probably due to the in-plane stress distribution in the block. To reduce this problem in the NRX-A6, and XE-1, the partial lobes of the J-3, J-5, and J-9 support blocks were removed.

The support blocks prior to the NRX-A5 had uncoated areas which resulted from support fixture contact during coating. In the NRX-A5 the use of NbC pins to provide support during the block coating operation proved successful in that no pins were missing and no block damage was attributed to the presence of the NbC pins.

6.6.2 Corrosion Performance

The support blocks were rated according to the appearance of the coating after disassembly. On this basis approximately two-thirds of the NRX-A5 support blocks showed performance rating between good and excellent.

The weight loss data for the blocks was correlated with surface coating appearance. The blocks with good to excellent performance showed an average weight loss of 1.43 percent. The blocks which exhibited severe crazed and/or flaked coatings had an average weight loss of 2.13 percent. In all cases the higher weight losses were associated with specific areas of damage and were not the result of uniform weight loss.

The poor performance of the blocks was, in general, associated with specific coating furnace runs. Similar to fuel element performance, it was difficult, due to the random scatter, to correlate the good and bad furnace runs with the test performance.

The correlation band of the support block position in the reactor versus its performance showed the following trends: (1) regular blocks giving good performance (based on coating appearance) were located in the center of the reactor, poor performing blocks were generally located in the E, F, and G rows; (2) blocks showing a high percent weight loss were randomly distributed with some slight preference to locations in the center of the core, rows A through C; (3) some correlation existed between high fuel element weight loss (greater than 51 grams) and the location of high weight loss blocks in the center of the core. Massive element damage resulted in exceptionally poor block performance. The NRX/EST also showed a correlation between badly corroded fuel elements and support blocks with badly corroded forward faces.

In general, the overall performance of the NRX-A5 blocks including both mechanical and corrosion properties was slightly better than the NRX/EST blocks. It is believed that this conclusion is attributed to the absence of the low power mapping runs and fewer cycles in the NRX-A5.

6.6.3 J9 Peripheral Support Block Temperature Responses During NRX-A5 EP-IV Startup

The detailed transient temperature distribution of the J9 peripheral support block (in the nominal peripheral region) during the NRX-A5, EP-IV startup was calculated using the TRACK computer code. Boundary conditions input for the calculation were the measured core inlet temperature and pressure, core pressure drop and power schedule, as a function of

startup time. Figure 6-56 presents the calculated maximum temperature difference ($T_a - T_b$) in the block. The measured average chamber temperature, T_c, is also included in the figure for reference. This temperature difference increased during the rise in power to the first hold and then decreased with hold time. The rate of chamber temperature rise in the ramp from the 3200°R hold to full power was approximately 60°R/sec. The calculated maximum temperature difference was 716°R as compared to the maximum temperature difference of 1260°R in NRX/EST EP-IVA startup. In the NRX/EST EP-IVA startup the actual average ramp rate attained was about 140°R/sec.

ure 6-55. Temperature Difference in J-9 NRX-A5 Support Block Cluster EP-IV Startup

6.7 CORRELATION OF WEIGHT LOSS IN THE NRX-A5 AND NRX/EST

In an attempt to isolate the significant environmental and property parameters which affect element weight loss, multiple regression analyses were performed on the NRX-A5 and NRX/EST fuel elements to correlate the data. Four separate samples of elements were examined, 113 NRX-A5 WAFF with a as-leached or total body permeability measurements, all weighed NRX/EST elements, the elements in the NRX-A5 with hole location deviations, and the loading code 69, 79, 89 NRX/EST elements chosen because of variation in fission product content as measured with an ionization chamber in the hot cell. The average orifice diameter, which is indicative of power factor, mass flow, and orifice pressure drop, was compared with the total fuel element weight loss for the NRX/EST coating batches. The NRX-A5 elements were reviewed for hole location and a comparison was made between weight losses in comparable core locations. The observation that there was a pronounced peak in the NRX/EST total weight loss and in the power factor deviations as determined from gross ionization measurements led to an attempt at correlating these two parameters.

6.7.1 Correlation of Total Weight Loss Data for NRX-A5 Elements Having As-Leached Body Porosity Data

Because of the expectation based on Y-12 versus WAFF comparisons* that the as-leached permeability would influence the corrosion rate, the 113 WAFF elements for which as-leached permeability data was available were exter. ely evcluated. The total weight loss of these 113 elements was correlated against the batch average weight loss, core radius, pressure differences (bore to bore and bore to interstitial), and other variables. The multiple linear regression analysis ve: used which includes a least-squares curve fit of up to 59 independent variables.

---

* Y-12 elements had significantly lower as-leached (before coating) body permeability than WAFF fuel elements.

There were 113 elements in NRX-A5 for which the as-leached total body permeability measurements were available. All of these were WAFF elements with GA beads from 11 different bore coating batches. Forty four were code 99 loading and were placed in rows A through D. Sixty-nine were loading code 39, 49 and 59 and were peripheral coated. The NRX-A5 multiple regression analysis was concentrated on these 113 elements because they represented a good sample of the core center and J row, although they were not selected as a truly random sample. The batches are listed in Table 6-10. Loading code 89, 79, and 69 elements were not chosen to be included in this analysis because of the belief that their corrosion rates may be unduly influenced by the following two factors: (1) in the NRX-A5 the code 89, 79, and 69 elements had 3M fuel beads and were treated independently from the elements with GA beads which had loadings of 39, 49, 59, and 99. (2) Post-test gross ionization measurements on NRX/EST indicate power factor deviations in this region of up to 5 percent too high. As a matter of interest, the NRX/EST code 69, 79 and 89 elements have been analyzed for a possible relationship between weight loss and power factor error the results are discussed in the following sections.

Since the WAFF elements exhibit the highest matrix permeability measurements, it may be expected that this sample will show up greater effects of pressure differences and coatings than a sample of Y-12 elements. If bore to interelement pressure difference affects corrosion, it may be expected that this sample will show this effect. The range of measured weight losses for the 113 elements is from 18.7 to 73.5 grams/element with an average of 48.4 grams for the 44 elements in Rows A through D, and from 8.7 to 73.4 grams/element with an average of 21.8 grams for the 69 elements in the J row.

The total element weight losses were correlated against the list of independent variables shown in Table 6-11 singly and in combinations, by a least-squares curve fit technique.* The 44 elements in rows A through D and 69 J row elements were considered separately.

---

* This technique has been previously described in WANL-TNR-202.

TABLE 6-10

SUMMARY OF COATING BATCHES IN ELEMENTS USED FOR NRX-A5

MULTIPLE REGRESSION ON TOTAL WEIGHT LOSS

Off Loaded (Code 39, 49 and 59) Elements in J Row (69 Elements)

Coating Batch		No. In	Avg W	No. In
Bore	Back	Core	gm	Sample
C257	C260	8	17.3	8
C257	F225	5	11.5	5
L142	C263	7	42.9	7
L142	C264	6	28.8	6
F224	C265	6	13.8	6
F224	L147	9	12.6	9
C258	L144	8	14.5	8
C259	L145	5	16.1	5
C259	L146	9	23.7	9
C226	L149	8	44.9	5
C226	L150	3	18.3	1

Code 99 Elements in Rows A through D (44 Elements)

Coating Batch		No. In	Avg. W	No. In
Bore	Back	Core	gm	Sample
C256	L143	18	54.3	12
C261	L148	11	31.9	10
C267	L153	13	58.2	10
C268	L154	24	60.0	8
F229	F233	21	53.1	4

TABLE 6-11

CORRELATION PARAMETERS

DEPENDENT VARIABLE

ELEMENT TOTAL WEIGHT LOSS, OR

ELEMENT INCREMENTAL WEIGHT LOSS

INDEPENDENT VARIABLES

ENVIRONMENTAL FACTORS

1) Bore-to-bore pressure difference
2) Bore-to-interstitial pressure difference
3) Channel Reynolds number*
4) Channel wall temperature*
5) Temperature difference in fuel from hot spot to wall*
6) Element average power factor
7) Element average orifice size

PHYSICAL PROPERTIES OF ELEMENT

8) As-leached (before bore coating) body permeability**
9) Coating thickness
10) After bore coating body permeability
11) Fuel loading

OTHER FACTORS

12) Radius from core centerline
13) Average weight loss for coating batch

---

* Used for incrementals only

** Used for NRX-A5 total weight losses only

The single most important measure of how well the correlation fits the data is the reduction in random error between the raw data with the correlation and the raw data without the correlation. The best correlation for a single coating batch was able to predict an element's weight loss to a ±7 gram (1σ) accuracy. The conclusions from this analysis are as follows:

1) The coating batch is the most important independent variable, not as a correlation against the electrical test but simply the average weight loss of the coating batch in the reactor.

2) For the 67 peripheral elements (loading code 39, 49 and 59), the second most important variable is the bore-to-bore pressure difference. However, the improvement in the correlation is almost negligible when this variable is added (standard error reduced from ±7.34 to ±7.01 grams/element).

3) For the 44 loading code 99 elements, the results of the correlation attempt are shown in Table 6-12.

6.7.2 Correlation of Average Orifice Diameter Versus Total Weight Loss

The average orifice diameter and the total fuel element weight loss show a trend of increasing weight loss with average orifice size. The coating batches with six or more elements were analyzed for both the Y-12 and WAFF fuel elements. Figure 6-57 shows representative results of the influence of the average orifice size on the fuel element weight loss. The sensitivity of the weight loss to orifice size is demonstrated by the large increase in weight loss with a relatively small increase in orifice diameter. The average orifice size is indicative of the fuel element power factor, channel mass flow rate, and the orifice pressure drop. A large orifice is associated with a high power factor and high flow rate channel and the small orifice with a low power, low flow rate channel. A large orifice channel experiences a low orifice pressure drop and a high pressure level in the channel, whereas a small orifice channel experiences a high orifice pressure drop and a lower pressure level in the channel.

• This technique has been described previously in WANL-TNR-202.

TABLE 6-12

RESULTS OF CORRELATION ON NRX-A5 TOTAL WEIGHT LOSS MEASUREMENTS

I. Elements in Sample

A) WAFF Elements in Rows A through D

B) Core Radius from 0 to 8.7 Inches

C) All GA Beads

D) 5 Coating Batches, 44 Elements in Sample

II. Table of Partial F2 Factors Correlation Coefficients. If the absolute value of the correlation coefficient is greater than 0.4000, the probability is less than 1 percent that the correlation is due to chance alone, if greater than 0.312, the probability is less than 5 percent.

Independent Variable	Symbol	Units	Correlation Coefficient	Max. Value	Avg. Value	Min. Value
1) Interstitial – Bore Pressure at Station 20	ΔP	Psi	-0.334	28.0	19.6	7.0
2) Average Weight Loss for Coating Batch	$\overline{\Delta W}$	Gm/Ele	0.564	50.0	51.0	31.9
3) Core Radius	R	Inch	-0.375	0.0	6.61	8.7
4) Average Element Power Factor	PF	--	0.368	1.1557	1.0795	1.029
5) Average Element Orifice Diameter	$\overline{DOR}$	Mils	0.417	45.26	39.2	36.0
6) As Loaded Body Permeability	PL	Divisions	-0.425	27.0	13.1	5.5
7) After Bore Coat Body Permeability	PB	Divisions	0.315	9.5	3.4	1.0
8) Coating Thickness	CT	Mils	0.433	2.20	1.71	1.45

III. Correlation

$$\Delta W = 4.440 + 0.878\ \overline{\Delta W} + 432.1\left[\frac{CT \times PB}{PL \times \Delta P}\right] - 153.9\left[\frac{PB}{\overline{DOR}}\right]$$

IV. Standard Deviations and Comparison of Correlation with Measured ΔW

A) Raw Data; σ = 14.3 Gm/Element

B) With Correlation; σ = 8.1 Gm/Element

C) Comparison	1B1F (Highest ΔW in Sample)	1D2E (Lowest ΔW in Sample)
ΔW (Measure)	80.1	18.7
ΔW (Correlation)	68.7	25.8

V. Effect of Adding Terms to Correlation

A) Raw Data; σ = 14.3 Gm/Element

B) (CT PB / PL ΔP) Term Only; σ = 10.9

C) ($\overline{\Delta W}$) Term Included Also; σ = 9.9

D) (PB / $\overline{DOR}$) Term Included Also; σ = 8.1

VI. Significant Variables

Term in Correlation	Symbol	Influenced by	Effect on $\overline{W}$	Effect on W
1st	$\overline{\Delta W}$	Process	$\overline{\Delta W}$ ↑	ΔW ↑
2nd	CT	Process	CT ↑	ΔW ↑
	PB*	Process	PB ↑	ΔW ↑
	PL	Process	PL ↑	ΔW ↑
	ΔP	Environment	ΔP ↑	ΔW ↑
3rd	PB*	Process	PB ↓	ΔW ↓
	$\overline{DOR}$	Environment	$\overline{DOR}$ ↑	ΔW ↓

*Overall effect of PB depends on values of other parameters

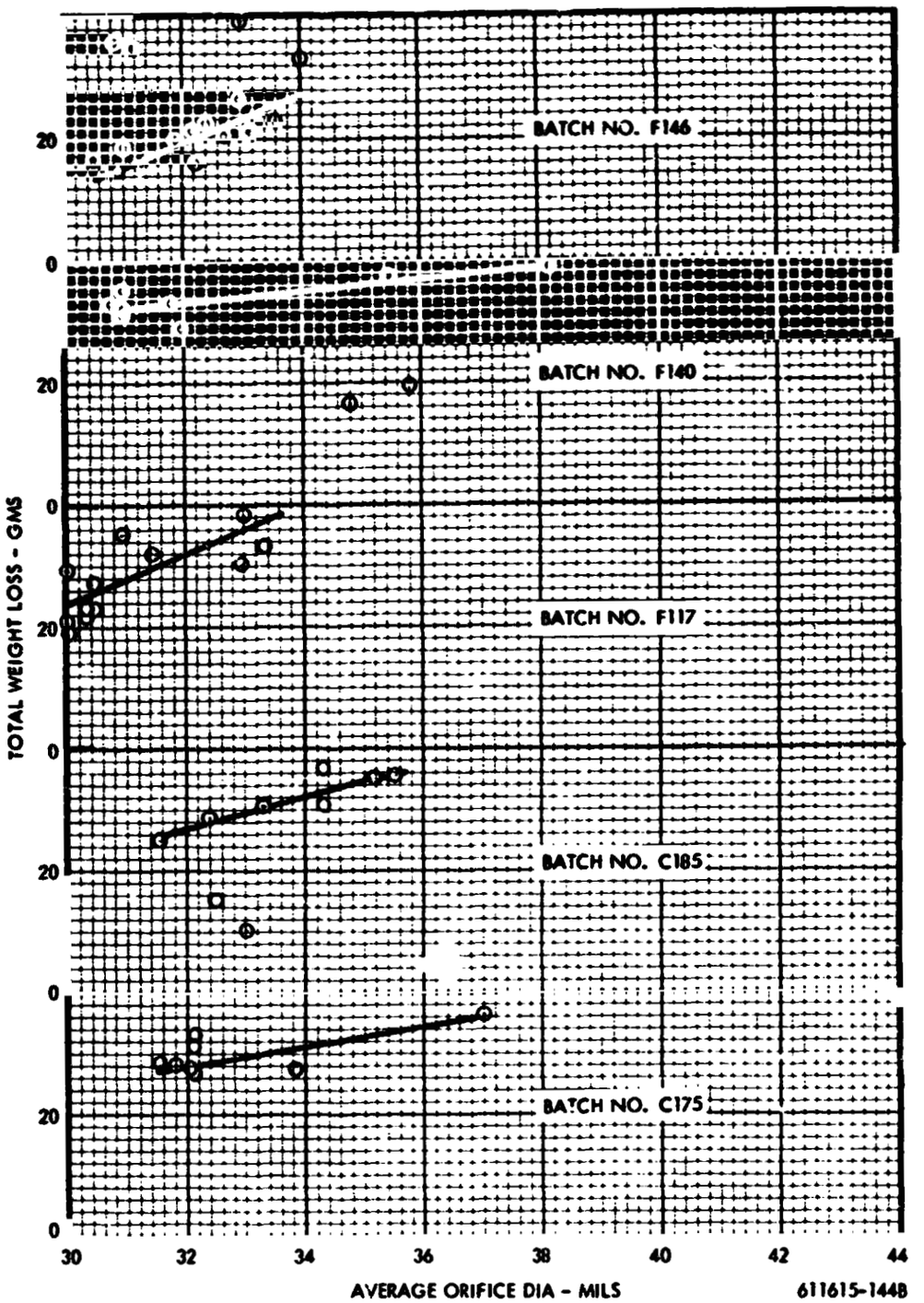

Figure 6-57. NRX/EST WAFF Fuel Elements Total Weight Loss versus Average Orifice Size

6.7.3 Effect of Hole Location

NRX-A5 elements which had hole location deviations* were compared against the weight losses in comparable core locations (six sectors with same cluster, row and element). None of the Y-12 elements had hole location VR's and the comparison is between WAFF elements only. The results are summarized for 17 element locations in Table 6-13. In eight cases the hole location VR element had the highest weight loss of those compared (assuming broken elements have the highest weight loss). In one of these cases, location J4H, the two elements with highest weight loss both have hole location VR's and both are in the same coating batch. This was a "poor" coating batch in comparison to others. The weight losses are 92.1 grams and 45.4 grams. The other four elements in the other sectors have weight losses of less than 27.7 grams.

In seven cases, the hole location VR element had the second highest weight loss of the six sectors. However, in seven cases, the lowest weight loss elements also had hole location VR's. It cannot be concluded from this data alone that hole location had a significant effect on total weight loss for the WAFF elements.

6.7.4 Correlation of NRX/EST Total Weight Loss With Gross Ionization Measurements

The pronounced radial peak in the NRX/EST total weight losses at the same approximate location as the largest deviations in element power factor** led to an attempt at correlating these two parameters. A difference of 1 percent in power factor from the design value causes a 50°R change in gas exit temperature at full power, and this may possibly affect total element weight loss. The elements showing the deviation in power factor were mostly loading code 69, 79, and 89 elements. The correlation of deviation in

---

* Hole locations were held by drawing to within 0.012 in. radius of true position except the displacement of outer holes toward the outer envelope was limited to 0.006 in. maximum. VR's (Variation Requests) were accepted up to 0.014 in. and 0.008 in., respectively.

** As measured by the post-test gross ionization technique described in WANL-TNR-216, "NRX/EST Final Test Report".

power factor versus weight loss was done for 179 elements with these loadings. Sixty-seven broken elements without weight loss data were not included in the correlation, however, the average power factor deviation was only 0.66 percent higher than predicted for these elements. The average power factor deviation for the 179 unbroken elements in the sample was 1.01 percent higher than predicted, which by comparison with the broken elements indicate no gross effect of power factor deviation on element breakage. The correlation, using the multiple regression technique, was tried for all 179 unbroken elements as a group, all loading code 89 elements as a group, and finally, three different coating batches were run separately. None of the correlations showed a significant dependence of weight loss on power factor deviations. All of the NRX/EST elements in this sample had GA fuel beads and the comparable elements in NRX-A5 had 3M beads.

In summary, the results of these correlations are:

1) The correlation of total weight loss data for the NRX-A5 elements having as-leached body porosity data indicated:

a) The coating batch is the most important independent variable considered. This was not a correlation against the electrical test but simply the average weight loss of coating batch in the reactor.

b) For the 67 peripheral elements (loading code 39, 49 and 59), the second most important variable is the bore-to-bore pressure difference. However, the improvement in the correlation is almost negligible when this variable is added (standard error reduced from ± 7.34 to ± 7.01 grams/element).

2) The correlation of average orifice diameter versus total weight loss showed a trend of increasing weight loss with average orifice size.

3) It could not be concluded from the correlated data that hole location had a significant effect on total weight loss for the WAFF elements.

4) Correlating the NRX/EST total weight loss with gross ionization measurements did not show a significant dependence of weight loss on power factor deviations.

TABLE 6-13

COMPARISON OF WEIGHT LOSSES IN ELEMENTS WITH HOLE LOCATION VR'S

Located in Different Sectors, Same Cluster and Element Location

Location	W (gm)	Hole Location VR
H6B	42.1	yes
	28.9	no
	Y-12 elements	↓
67D	48.0	yes
	28.3	no
	16.9	↓
	16.5	
	15.3	
	12.5	
J3T	Broken*	yes
	Broken	no
	22.2	↓
	20.1	
	16.2	
	14.4*	
J8D		
	14.1	no
	11.9	↓
	10.6	
	10.0	
	7.0	
	6.5	yes

*Indicates elements in the same coating batch

TABLE 6-13 (CONTINUED)

J6H	23.2	yes
	19.8	no
	13.9	↓
	9.9	↓
	8.1	↓
	7.4	↓
C3D	58.5	no
	50.9	↓
	50.7	↓
	47.2	yes
	Y-12 elements	↓
J4H	92.1*	yes
	45.4*	yes
	27.7	no
	24.2	↓
	20.6	↓
	18.5	↓
J95	28.3	no
	27.5	no
	27.1*	yes
	20.8*	no
	17.7*	yes
	8.9	yes
J7F	37.2	no
	25.7	yes
	20.5	no
	16.5	no
	15.3	no
	12.4	no

TABLE 6-13 (CONTINUED)

J3J	Broken	no
	62.6*	yes
	37.4	no
	24.8*	no
	23.4	no
	17.3	no
J9P	Broken	no
	24.1	no
	19.1	yes
	17.5	no
	10.3	no
	8.3	yes
J5J	Broken	yes
	3.5	no
	22.7	yes
	16.0	yes
	13.5	yes
J3T	Broken*	yes
	Broken	yes
	22.2	no
	20.1	no
	16.2	yes
	14.4*	yes

*Indicates elements in the same coating batch.

TABLE 6-13 (CONTINUED)

J5D	19.3	no
	19.2	yes
	18.3	no
	13.3	
	12.2	
	10.0	
6J3V	Broken	no
	37.7	no
	14.8*	yes
	13.5	no
	13.[illegible]	yes
	12.7	no
J3S	19.8*	no
	14.1*	yes
	14.0*	no
	12.5	yes
	12.2	no
	11.6	no
D2F	58.7	yes
	57.1	yes
	53.1	no
	50.5	yes
	44.8	no
	37.5	no

*Indicates elements in the same coating batch.

6.8 ANALYTICAL TECHNIQUES

6.8.1 Bore Corrosion

The analytic method, LOWERE Code*, formulated up to this time to predict the NRX reactor corrosion behavior has proved inadequate. Several attempts have been made to improve the midband and hot end relationships used in the LOWERE computer code. In an attempt to duplicate the bore midband weight loss behavior in the NRX-A5 core, an analysis of bore corrosion using the observed characteristic ring geometry was undertaken. The developed ring equation calculated the regression of a ring aligned with an average observed crack in the NbC coating. Both the forward reaction and backward reaction rates were incorporated. Of significance in the expression was the time dependency of this model which led to an accelerating corrosion rate. The reaction rate which was developed by the Fluid Flow Laboratory based on the electrical furnace observations included a pressure differential term (difference in pressure between the bore and external surface). This pressure differential term was applied only where the bore pressure was greater than the external pressure. Calculations using this relationship to predict the NRX-A5 reactor weight losses proved inadequate.

As a result of the "Fuel Element Assessment Program", the electrical furnace tests provided overall weight loss data as a function of operating time. These data were separated into both midband and hot end weight losses for WAFF and Y-12 elements. Relationships were developed for the three core radial regions of interest, namely, central, mid-radial, and peripheral. Figure 6-58 shows the characteristics of these midband relationship derived from electrical test data.

---

* "Fuel Element Bore Weight Loss Code and Its Application to the NERVA Core Design" WANL-TME-1344, January 1966.

The calculated weight losses using the mid-band relationships given in Figure 6-58 was normalized to the measured NRX-A5 incremental weight loss to obtain the as-measured bore weight loss distributions given in Figures 6-59, 6-60, and 6-61. The calculated data includes only the effects of bore mid-band and bore hot end corrosion losses and assumed only graphite weight loss. The niobium and uranium weight losses have been neglected.

6.8.2 Surface Corrosion

Two computer programs, THT-B and TDC-2 were used to predict surface corrosion in the NRX cores. The purpose of these computer programs is to analytically determine the pressure distribution, flow distribution, and corrosion distribution in the core interelement gaps and on the external surfaces of the elements. Previous calculations of external surface corrosion proved inadequate and an attempt was made to improve the predicted values. To accomplish this, the program models were revised: (1) to account for the radial variation of gap size by including 8 distinct zones for specifying this variable versus radius and (2) to account for the radial variation of element porosity and bore pressure by including 9 distinct zones for specifying these variables versus radius. Thirty axial zones within each of the radial zones were included for specifying these variables versus core station. The TDC-2 program was also modified to include the effect of porous flow on the interelement corrosion.

Since significant changes in the interelement flow patterns occur as corrosion damage progresses, an accurate calculation of core performance requires a stepwise solution in time with gap sizes, element porosity, number of pinholes, temperature, etc. varying as a function of the accumulated corrosion.

6.8.3 Pinholing Effects

A computer program designated CAPING, (Corrosion Analysis of Pinhole and Gap) was developed to calculate the fuel element surface corrosion weight loss due to pinholing. The program calculates the weight losses in the pinholes and on the external surface resulting from pinhole and interelement flow.

The program considers an element at an isolated region of the core. A coupled fluid flow, heat conduction, and corrosion calculation is performed. The fluid flow and heat conduction model used for the analysis is shown in Figure 6-62, it consists of a portion of a fuel element and 1/2 of a central element. There are six flow channels, namely, the tie rod, the interelement gap and four fuel channels. Each pinhole must be located at the end of an axial interval. This means that the pinhole can form at every 2.0 in. interval along the fuel element. This restriction is due to the present computer memory capacity.

The pinhole flow can be from bore to gap or vice versa depending on the pressure differential. The pinhole flow was evaluated from a correlation derived from pinhole flow test data*. The correlation is of the form:

$$\Delta P = K \frac{W^2_c}{2\varsigma (D_p D_g)}$$

where

ΔP = pressure differential between bore and gap before a pinhole is formed, psi

W = flow lb/sec

---

* "Core Effective Gap Test Results", WANL-TME-1570, February 1967.

v = specific volume, $in.^3/lb.$

D_p = pinhole diameter, in.

D_s = interelement gap, in.

g = gravitation constant

K = flow impedance constant

The value of this constant was obtained by fitting the flow test data.

The gap size was included in the equation in order to reflect the gap impedance on the pinhole flow. The above correlation assumed that the bore coating crack is of the same diameter as the pinhole. The fluid flow and heat conduction calculation was performed by the TAP code and the surface corrosion calculation by a modified ICAP code. The flow in the interelement gap was assumed to be one dimensional which implies that no radial and circumferential communications with other interelement channels was considered.

Calculations using the CAPING Code to predict the pinholing effects in the NRX-A5 are given in Section 6.3.5.2

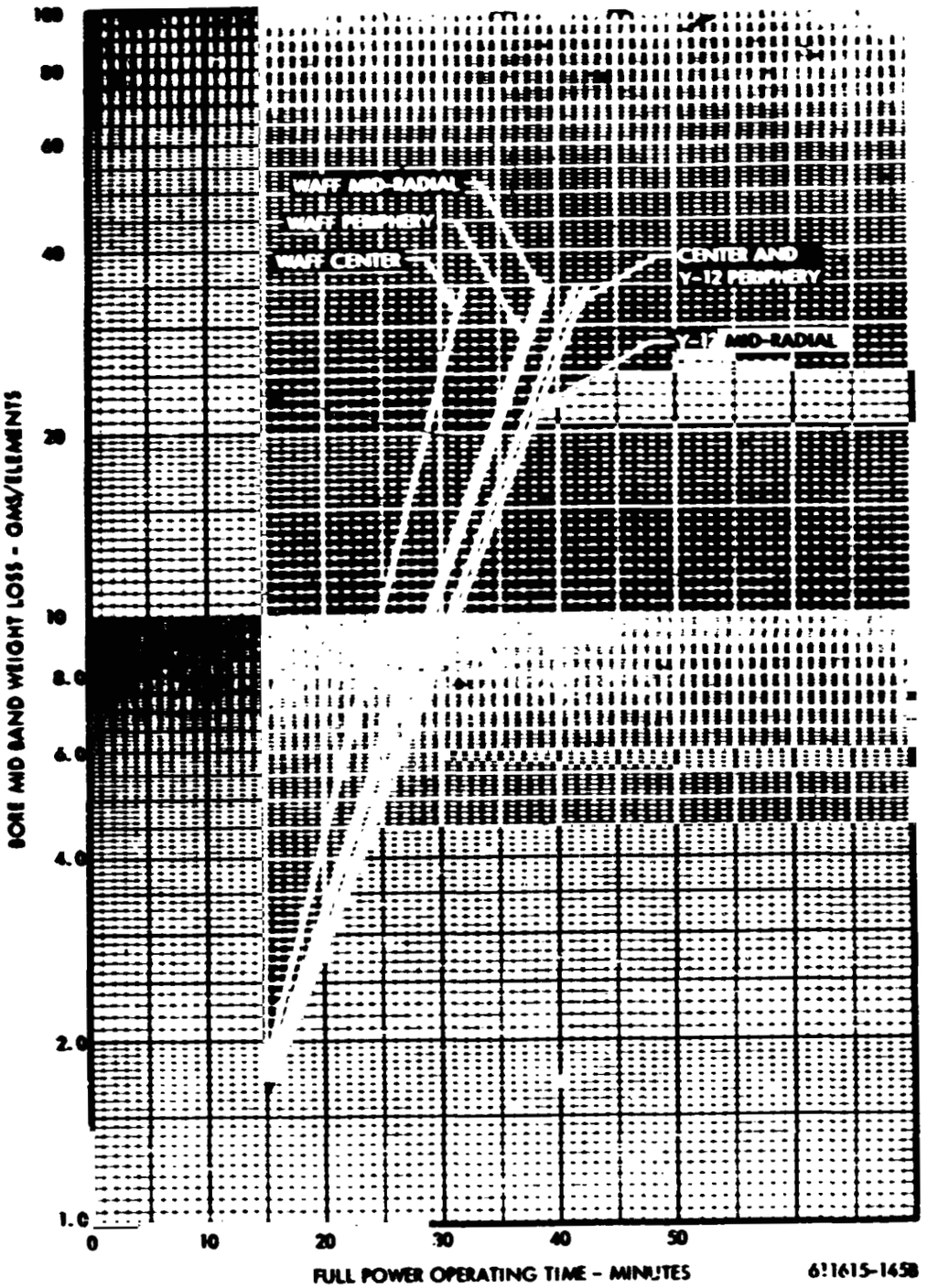

Figure 6-58. NRX-A5 Midband Core Characterization

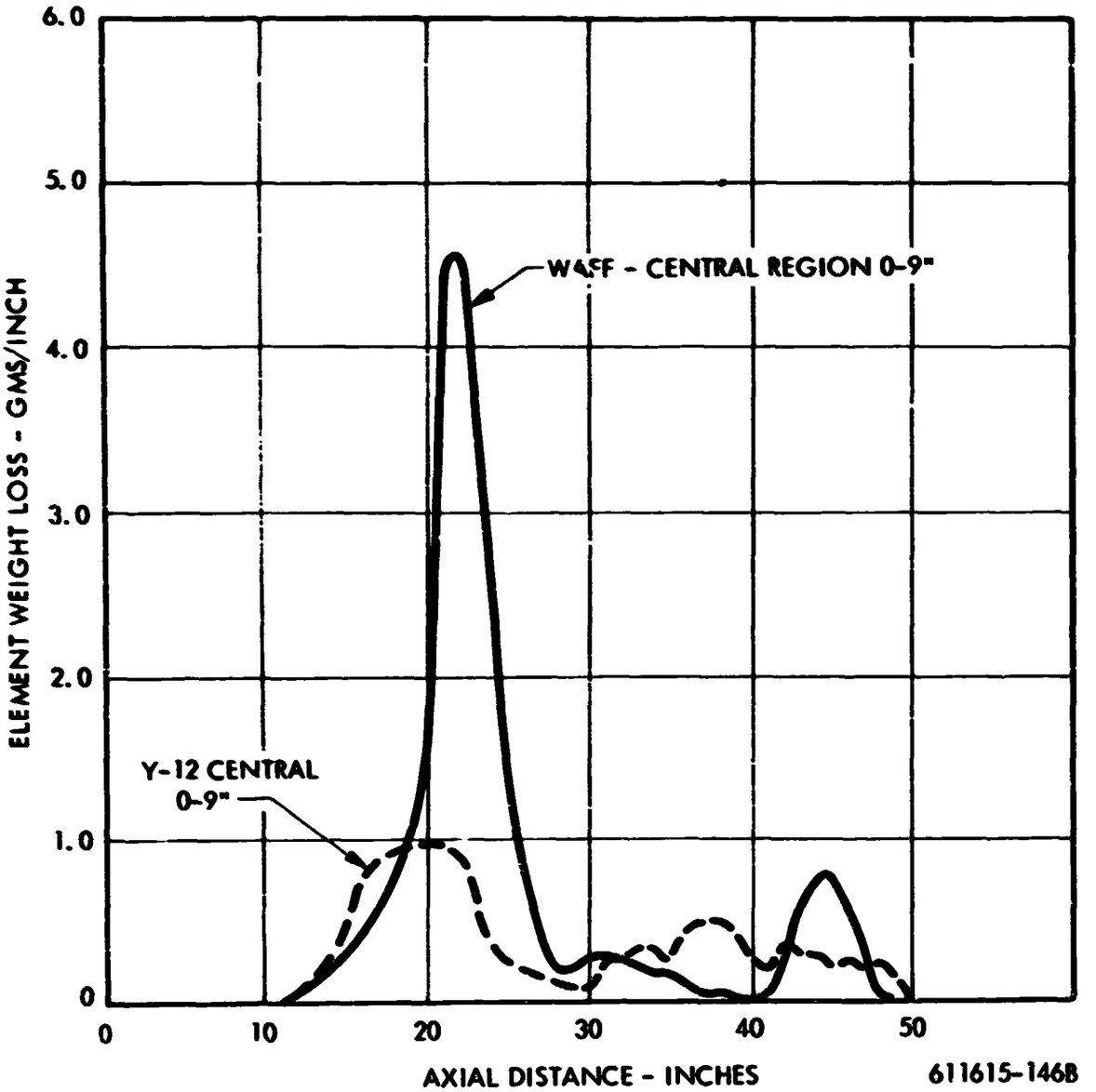

Figure 6-59. Calculated NRX-A5 Bore Weight Loss Distributions Normalized to Measured Data - Core Central Region

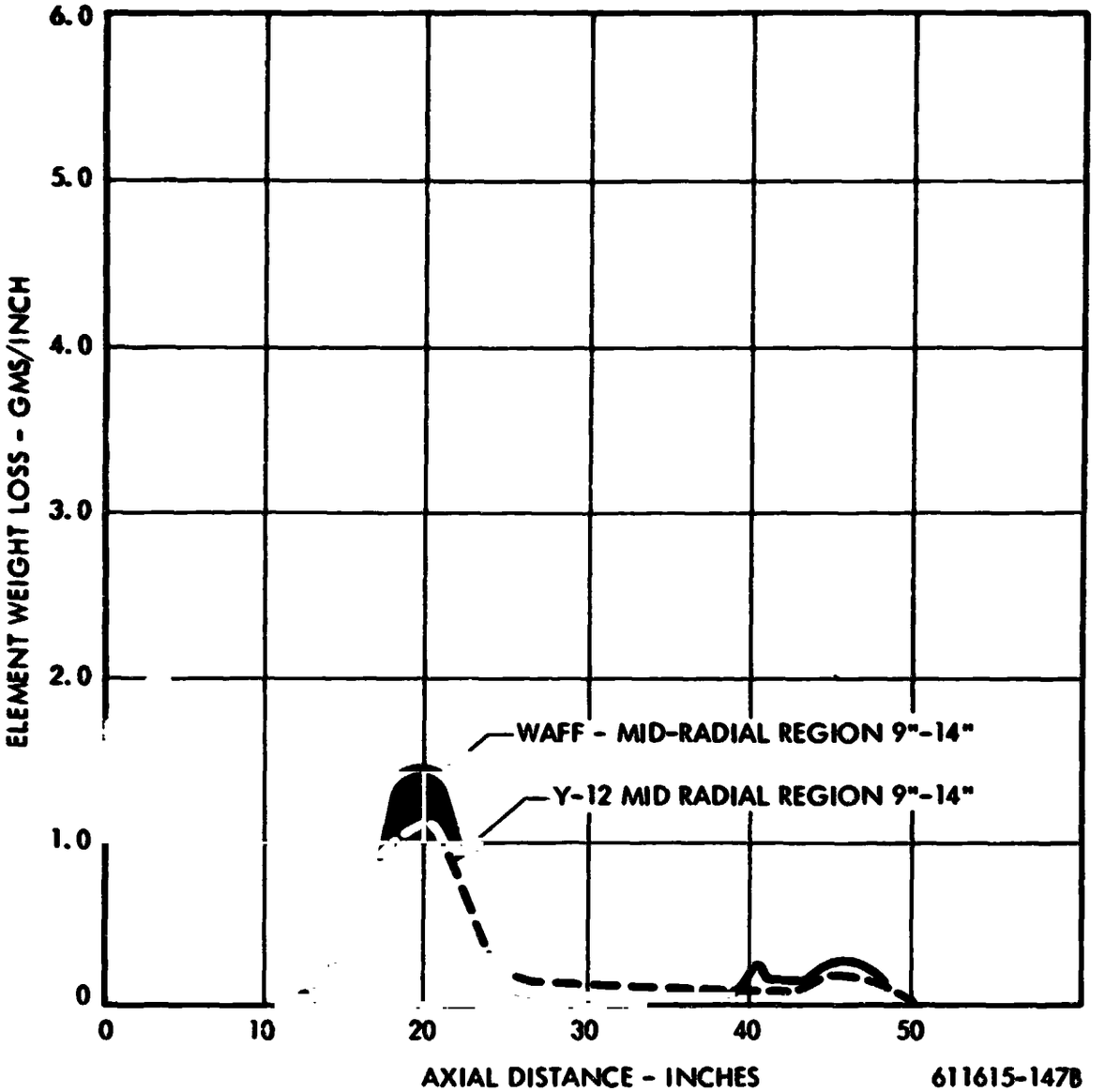

Figure 6-60. Calculated NRX-A5 Bore Weight Loss Distributions Normalized to Measured Data - Core Mid-Radial Region

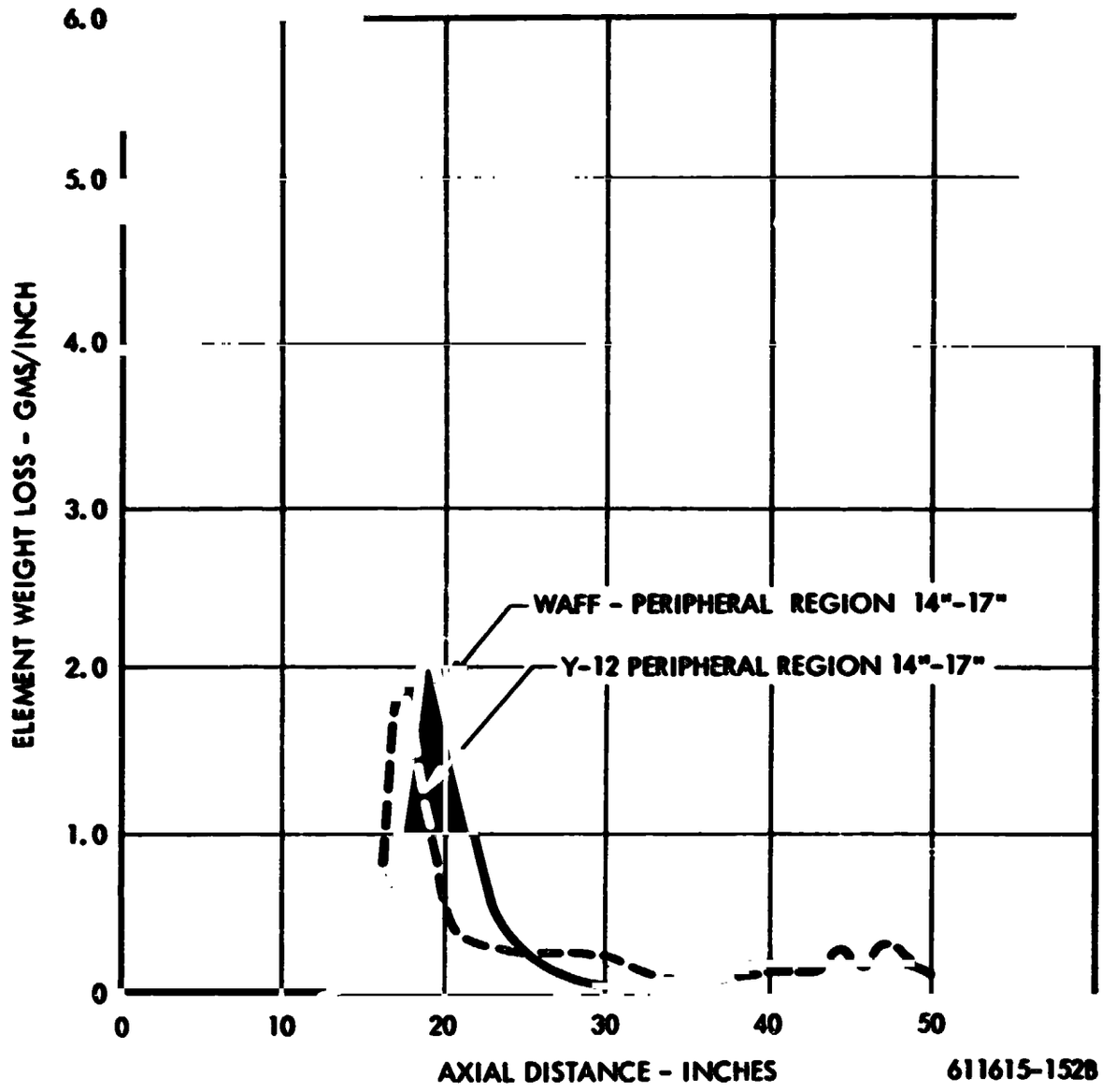

Figure 6-61. Calculated NRX-A5 Bore Weight Loss Distributions Normalized to Measured Data - Core Peripheral Region

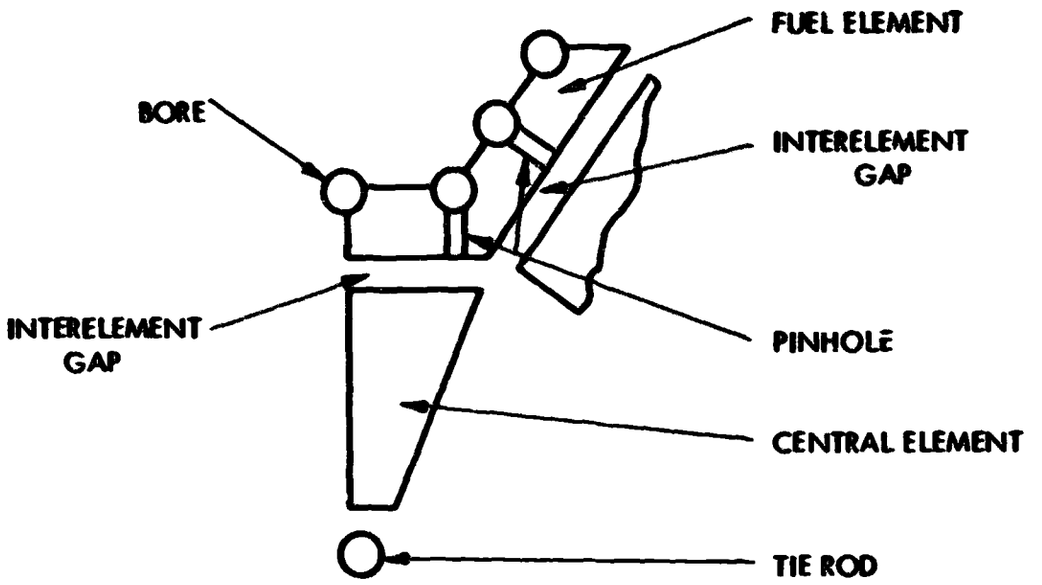

Figure 6-62. Equations Used in CAPING Code

6.9 CONCLUSIONS

The major conclusions based on a review of the corrosion performance data from the NRX-A3, NRX/EST and NRX-A5 reactor cores are summarized in this section.

1) The overall weight loss performance of the Y-12 fuel elements was better than the WAFF fuel elements in both the NRX/EST and NRX-A5. The average Y-12 element weight loss was approximately 16.0 grams/element in both reactors. The WAFF weight losses were significantly greater; 45.0 grams/element in the NRX/EST and 36.9 grams/element in the NRX-A5.

2) The implied average weight loss for all the elements in the NRX/EST was 32.4 grams/element, in the NRX-A5, 27.0 grams/element and in the NRX-A3 10.7 grams/element.

3) The fraction of broken elements in the NRX-A5 was 13 percent higher than in the NRX/EST. The maximum loss at the midband region was also greater in the NRX-A5 than the NRX/EST which resulted in weaker elements and thus more breaks during disassembly.

4) The largest fraction of broken elements for both the NRX/EST and the NRX-A5 are in the core peripheral region 14 in. to 17 in.

5) The NRX-A5 WAFF fuel elements in the core peripheral region indicated significantly less weight loss than the WAFF fuel element in the NRX/EST.

6) The average overall element weight losses for the NRX/EST and NRX-A5 appears to be independent of core sector.

7) An evaluation of the overall incremental weight loss data indicated that (a) the integrated weight loss was highest in the central region and lowest in the mid-radial region for both the NRX/EST and NRX-A5, (b) in the NRX/EST the central region elements were characterized by an aft end peak, (c) the NRX-A5 exhibited a well defined peak midband weight loss at core station 20.0 in., (d) a lower hot end weight loss from core stations 30.0 in. to 52 in. was observed in the NRX-A5 than in the NRX/EST due to the absence of extended low power testing.

8) Measured surface corrosion in the NRX-A3, NRX/EST and NRX-A5 bores for clusters A, D, & H, which are representative of the central, mid-radial, and peripheral regions, was the greatest over the aft portion of the core. It was more pronounced in the NRX/EST.

9) On the basis of similar data for all reactor cores, the surface and bore weight loss given as a function of radius indicated (a) the high weight loss in the center of the core was principally due to material loss from the surface of the elements, (b) the high WAFF element weight loss in the core edge region (r = 11.0 in.) was principally due to bore corrosion, (c) 15 to 30 percent of the total NRX/EST and NRX-A5 core weight loss was attributed to surface corrosion, (d) the surface regression traces showed that the axial distribution of surface weight loss was considerably different than the bore weight loss with the majority of the surface loss downstream of core station 27.0 in.

10) The hot buffer region in the NRX-A5 appeared to be beneficial for the first row of peripheral coated elements, however, its effect had substantially diminished in the second coated row.

11) In the assessment of the peripheral fuel elements the effects of loading and element location were not clearly evident. It appeared that high loading, location behind either partial elements or thin filler strips, and high power factor all contributed to increased weight loss.

12) In comparing the surface corrosion on the outermost row of fuel elements in the NRX-A3, NRX/EST, and NRX-A5, the trace average data for the NRX-A5 hot buffer region showed a reduction in the amount of surface corrosion for the limited sample of surface data available.

13) The evaluation of pinholes and channel exposure in the NRX-A5 showed: (a) the number of pinholes per element for the Y-12 fuel elements were relatively constant for all sectors, the average number was 7.25, (b) the Y-12 average number of pinholes/element was about equal to the inches of channel exposure per element, 6.1 inches/element, (c) the WAFF elements exhibited no distinguishing characteristic in pinholes

or channel exposure other than the average channel exposure, ~ 85 inches/element, was about three times the average pinholing, 12.5 inches/element, (d) the core average channel exposure characteristic for both WAFF and Y-12 elements, 33.85 inches/element, and 18.7 inches/element respectively, were twice that of the pinholing characteristic.

14) Comparisons of the NRX-A3, NRX/EST and NRX-A5 pinhole and channel exposure data showed: (a) a region of a relatively low number of pinholes existed in all three reactors at about core radius 9.0 in. similar to the overall weight loss distributions, (b) an improvement in the peripheral performance of pinhole damage in the NRX-A5 compared to the NRX/EST, possibly due to the surface coating with NbC and the two hot buffer sections, (c) the maximum number of pinholes shifted to a lower station for all three reactors starting with the NRX-A3, (d) the maximum axial channel exposure value also shifted to a lower station in the NRX-A5 compared to the NRX/EST

15) In the NRX-A5 approximately 1.8 percent of the core fuel elements examined were "zero defect" elements, i.e., exhibited neither pinholes nor channel exposure. Fifty-six percent of these "zero defects" elements were in the hot buffer region and some 77 percent were in the J row. Of these J row zero defect elements, 60 percent were externally coated with NbC.

16) The NRX-A5 filler strips in the hot buffer region sustained more surface corrosion than those outside the hot buffer region. The deepest corrosion occurred on the lateral faces at the outer diameter of the strips.

17) As a result of the reduced undercut depth on the NRX-A5 hot ends, the condition of the fuel element hot ends was found to be excellent.

18) A statistical treatment of the NRX-A5 weight losses indicated (a) for the elements where as-leached body porosity data was available, the coating batch was the most important independent variable considered and the second variable of importance was the bore-to-bore pressure difference, (b) the correlation of average orifice diameter versus total weight loss showed a trend of increasing weight loss with increasing average orifice size.

(c) it was not possible to conclude from the correlated data that hole location had a significant effect on total weight loss for the WAFF fuel elements, (d) none of the correlations of the NRX/EST total weight loss with gross ionization measurements showed a significant dependence of weight loss on power factor deviations.

19) The overall performance of the NRX-A5 support blocks including both mechanical and corrosion performance was slightly better than the NRX/EST support blocks. In the NRX-A5 this was thought to be related to the absence of the extended low power operation and the use of low startup ramps, of 60°R/sec maximum.

20) The analytic methods used to predict bore and surface corrosion proved as in the case of the NRX/EST, inadaquate to predict the NRX-A5 reactor corrosion behavior. Improvements to the THT and TDC codes resulted in better corroboration of calculated surface regression data and measured data. A new code, CAPING, was developed for the specific purpose of predicting pinhole formation and the effect of pinholes.

CHAPTER 7

NUCLEAR ANALYSIS*

7.1 SUMMARY

Analysis of NRX-A5 and NRX/EST data indicates that detector placement has proved to be of high importance in deriving quantitative sub-criticality by the inverse multiplication method. Although the estimated shutdown is relatively insensitive to axial displacement of the detector from the source plane for the source-detector-reactor geometries tested, it is a function of the radial distance of the detector from the reactor vessel surface. A "close-in" detector at a 4 inch distance can be expected to give a conservative estimate of shutdown, while extrapolations from a "far-out" detector at a 36 inch distance should be suspected as nonconservative.

An understanding of the inherent reactivity of the NRX-A5 reactor was demonstrated by the relatively close prediction of initial criticality. The actual critical drum position of 99.3 degrees compared well with the final prediction of 95.0 degrees and reasonably well with the 93 $\pm$ 7 degree angle originally sought at the time of reactivity shimming during assembly.

It has been shown that if the inverse multiplication technique is calibrated by rotating one drum to 180 degrees, it may be used to quantitatively estimate shutdown in dollars. In the deeply shutdown condition (about 10$) conservatism is good and as the wire-free condition is approached, precision becomes very good.

The analysis of drum worth data (1) confirmed the uniformity of the individual drum worths, (2) showed that single drum insertion and single drum withdrawal techniques are essentially equivalent, and (3) indicated that the NRX-A5 control drum span was 8.2$ compared with the predicted 8.5$ $\pm$ 0.3. The power control technique used for uniformity measurements in this test series is evaluated as excellent and is recommended for further use.

---

*The major contributor to this chapter was L. I. Ortenberg.

The low power core station 8 temperature coefficient of reactivity inferred from test data is -0.182 ¢/°R, in excellent agreement with the NRX/EST value of -0.19 ¢/°R. The power range over which this coefficient is clearly applicable is approximately 50 to 100 KW. Use of the analytical core coefficient, -0.11 ¢/°R, should be continued at conditions of very low power (100 watts, for example) and where core temperatures are fairly uniform.

The beryllium reflector temperature coefficient of reactivity has been found to be in the range +0.069 to +0.092 ¢/°R near ambient temperature. The agreement with the calculated coefficient, +0.0943 ¢/°R, is reasonably good. Thus, the calculated reflector coefficient can remain in use for correction of near-ambient reactor conditions.

The total reactivity loss in the NRX-A5 test series was 2.36$ based on the change in ambient critical positions. The variation of the loss with time was again found to be exponential, taking the form:

$$\Delta\rho\ (¢) = 5.7\ (\exp\ (t/8.23) - 1.0)$$

This loss function has been supported by statistical analysis.

The 50¢ discrepancy in EP-IV between reactivity loss during operation and that inferred from the pretest and post-test criticals as indicated by early analysis has been explained essentially by hyarogen accumulation in the corroded areas and hydrogen diffusion into the natural pores of the fuel in the early stages of the test.

The NRX-A5 reactivity swings to full power are well represented by the NRX/EST empirical reactivity feedback model. The one sigma uncertainty in the model has been found to be 7.25¢ with a 98 percent confidence range from 5 22¢ to 11.63¢.

7.2 APPROACH TO CRITICALITY

7.2.1 Peripheral Poison Wire Removal

The peripheral poison wires were removed in the R-MAD Building prior to nozzle installation in accordance with operating procedure NRX-A5-P5[1]. Out of a total inventory of 6990 wires, distributed as shown in Figure 7-1, 6207 wires were extracted from the core

1 NRX-A5-P5, "NTO Operating Procedure for Test Assembly, Mechanical Assembly", 3/66

NOTE: BECAUSE OF THE INTENDED USE OF EXIT GAS TEMPERATURE THERMOCOUPLES, THE POISON WIRE LOADING PATTERN IS NOT PRECISELY SYMMETRICAL IN ALL SECTORS. CLUSTER DRAWINGS 936J638 AND 936J39 DESCRIBE THE EXACT ARRAY OF WIRES IN EACH CORE SECTOR.

Figure 7-1. Typical Poison Wire Loading Pattern for NRX-A5 Core Sectors

during this operation in the R-MAD Building. This number represents a slight departure from past procedure. In NRX-A2, NRX-A3, and NRX/EST, there were 6192 peripheral poison wires. The anticipated presence of exit gas thermocouples which would have shadowed 15 coolant channels in cluster rows A and B and prevented insertion of poison wires resulted in a shift of 15 wires from the "central" region (rows A, B, and central cluster) to the peripheral region (rows C to J). Thus 6207 wires were involved in the NRX-A5 peripheral poison wire removal instead of 6192.

During the wire removal[1], changes in neutron multiplication were monitored with four BF_3 detectors, located as shown in Figure 7-2. Only one detector, C-2*, was located relative to the source such that its geometry approximated that of the prediction[2]. The NRX-A5 inverse multiplication prediction, which was based on analysis of NRX/EST measurements[3], was developed by averaging the response of two detectors; one (C-4) located on the source plane, 6 inches from the pressure vessel, and the other (C-5) positioned 11 inches above the source plane, and 4 inches from the pressure vessel. Both detectors were displaced azimuthally from the source by 180 degrees. Detector C-2* in the NRX-A5 experiment was displaced axially 22 inches from the source plane and was effectively 4 inches from the pressure vessel. In this location its response was actually better approximated by that of the C-5 detector in NRX/EST, since the NRX/EST analysis showed that detector response is more sensitive to distance from the pressure vessel than to axial displacement from the source plane.

Tables 7-1 and 7-2, reproduced here from the "NRX-A5 Pre-Test Report",[1] summarize the poison wire removal sequence and the count rate data collected during this operation. For each of the four detectors the inverse multiplication values, give in the second table have been normalized to 1.0 at the full wire inventory. This normalized data is plotted in Figure 7-3 which shows a comparison of the measurements with the prediction and with the results of NRX/EST detector C-5 alone.

---

1 NTO-R-0075, "NRX-A5 Pre-Test Report", 5/66
2 WANL-TME-1388, "NRX-A5 Test Prediction Report", 3/66
3 WANL-TNR-216, "NRX/EST Reactor Test Analysis Report", 12/66

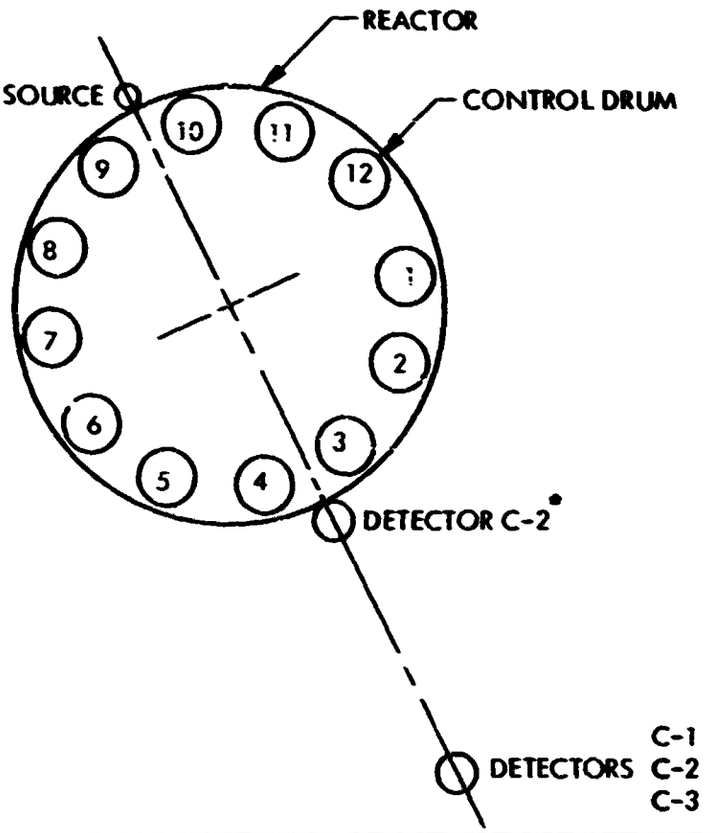

DETECTOR	AXIAL STATION, INCHES	DISTANCE FROM PRESSURE VESSEL, INCHES
C-1	26	36
C-2	22	36
C-3	19	36
C-2*	35	~0
Source	17	~0

611615-68B

Figure 7-2. Source and Detector Locations for NRX-A5 Peripheral Poison Wire Removal

TABLE 7-1

PERIPHERAL POISON WIRE REMOVAL INCREMENTS

Poison Wire Removal Increment Number	Number of Wires Removed this Increment	Total Removed	Clusters Removed This Increment Sector - Row - Cluster
1	651	651	1J3, 1J5, 1J7, 1J9, 3J3, 3J5, 3J7 3J9, 5J3, 5J5, 5J7, 4J5, and 1F1
2	627	1278	2J3, 2J5, 2J7, 2J9, 4J3, 4J5, 4J7, 4J9, 6J3, 6J5, 6J7, and 6J9
3	531	1809	1J4, 1J6, 1J8, 2J4, 2J6, 2J8, 3J4, 3J6, 3J8, 4J4, 4J6, 4J8, 5J4, 5J6, 5J8, 6J4, 6J6, 6J8, and 1H3
4	687	2496	1H4, 1H5, 1H6, 1H7, 2H3, 2H4, 2H5, 2H6, 2H7, 3H3, 3H4, 3H5, 3H6, 3H7, 4H3, 4H4, 4H5, 4H6, 4H7, 5H3, 5H4, 5H5, 5H6, 5H7, 6H3, 6H4, 6H5, 6H6, and 6H7
5	498	2994	1G1, 1G3, 1G5, 1G7, 2G2, 2G4, 2G6, 3G1, 3G3, 3G5, 3G7, 4G2, 4G4, 4G6, 5G1, 5G3, 5G5, 5G7, 6G2, 6G4, and 6G6
6	501	3495	1 2, 1G4, 1G6, 2G1, 2G3, 2G5, 2G7, 3G2, 3G4, 3G6, 4G1, 4G3, 4G5, 4G7, 5G2, 5G4, 5G6, 6G1, 6G3, 6G5, and 6G7
7	402	3897	1F3, 1F5, 2F1, 2F3, 2F5, 3F1, 3F3, 3F5, 4F1, 4F3, 4F5, 5F1, 5F3, 5F5, 6F1, 6F3, and 6F5
8	432	4329	1F2, 1F4, 1F6, 2F2, 2F4, 2F6, 3F2, 3F4, 3F6, 4F2, 4F4, 4F6, 5F2, 5F4, 5F6, 6F2, 6F4, and 6F6
9	372	4701	1E1, 1E3, 1E5, 2E2, 2E4, 3E1, 3E3, 3E5, 4E2, 4E4, 5E1, 5E3, 5E5, 6E2, and 6E4
10	378	5079	1C2, 1E4, 2E1, 2E3, 2E5, 3E2, 3E4, 4E1, 4E3, 4E5, 5E2, 5E4, 6E1, 6E3, and 6E5
11	402	5481	1D1, 1D2, D3, 2D2, 2D4, 3D1, 3D2, 3D3, 4D2, 4D4, 5D1, 5D2, 5D3, 6D2, and 6D4
12	243	5724	1D4, 2D1, 2D3, 3D4, 4D1, 4D3, 5D4, 6D1, and 6D3
13	240	5964	1C1, 1C3, 2C2, 3C1, 3C3, 4C2, 5C1, 5C3, and 6C2
14	162	6126	2C1, 2C3, 4C1, 4C3, 6C1 and 6C3
15	81	6207	1C2, 3C2, and 5C2

TABLE 7-2

NRX-A5 PERIPHERAL POISON WIRE REMOVAL DATA

Removal Increment	Total Counts Channel Number				Counts Per Minute Channel Numbers				Inverse Multiplication (1/M) Channel Numbers				
	C-1	C-2	C-3	C-2*	C-1	C-2	C-3	C-2*	C-1	C-2	C-3	C-2*	Average (1, 2, 3)
0	33418	33553	20782	3505	6684	6711	4156	351	1.0	1.0	1.0	1.0	1.0
1	36611	36521	22671	4059	7322	7304	4534	406	0.913	0.913	0.919	0.864	0.916
2	39469	40428	24597	2373	7894	8086	4919	475	0.847	0.830	0.845	0.739	0.841
3	44329	45351	27746	3101	8866	9070	5549	620	0.754	0.740	0.749	0.565	0.748
4	51024	53325	31870	3944	10205	10665	6374	789	0.655	0.629	0.652	0.444	0.645
5	55848	58463	35417	4566	11170	11692	7083	913	0.598	0.573	0.587	0.384	0.586
6	62511	65753	39776	5680	12502	13151	7955	1136	0.535	0.510	0.522	0.309	0.522
7	27595	28937	17609	6699	13798	14469	8805	1340	0.484	0.464	0.472	0.262	0.473
8	31202	32712	19563	7863	15601	16356	9782	1573	0.428	0.410	0.425	0.223	0.421
9	33953	36710	21744	9427	16977	18355	10872	1885	0.394	0.366	0.382	0.186	0.381
10	39365	42086	25201	11355	19683	21043	12601	2271	0.340	0.319	0.330	0.154	0.330
11	45479	48550	28669	14406	22740	24275	14335	2881	0.294	0.276	0.290	0.122	0.287
12	51565	55289	32459	6817	25783	27645	16229	3409	0.259	0.243	0.256	0.103	0.253
13	59104	63760	37400	7893	29552	31880	18700	3947	0.226	0.211	0.222	0.089	0.220
14	64180	69576	40448	8976	32090	34788	20224	4488	0.208	0.193	0.205	0.078	0.202
15	69042	74554	43496	9416	34521	37277	21748	4708	0.194	0.180	0.191	0.074	0.188

Counting interval was five minutes for first six wire removal increments and two minutes for remaining removal increments.

CONFIDENTIAL

Astronuclear Laboratory

The good agreement in curve shape between NRX/EST detectors C-5 and C-2* has been noted previously. Both of these detectors were at the same radial distances (the sensitive volumes of the detectors were in both cases about 4 inches from the pressure vessel surface), but were located at different axial positions (11 inches from the source plane for detector C-5 and 22 inches for detector C-2*). An intercomparison of NRX-A5 data further indicates that the effect of axial displacement from the source plane is also seen to be relatively unimportant. NRX-A5 detectors C-1, C-2, and C-3 were each located 3 feet from the pressure vessel and 180 degrees azimuthally from the source, but were in different axial locations separated by 9, 5, and 2 inches, respectively, from the source plane. The inverse multiplication values obtained with these three detectors essentially coincide (as shown in Figure 7-3). In order to obtain a quantitative measure of the effect of the small differences which do exist between the detector responses, a least squares linear fit was made to the last five data points for each detector. Figure 7-4, an enlarged portion of Figure 7-3, shows the suitability of the assumed linear form since the data is seen to be well represented by a straight line. To avoid the error involved in graphical extrapolation, the least squares equations were then used to calculate the zero (1/M) intercept for each detector, permitting a simple comparison between detectors. Summarized in Table 7-3 is this comparison as well as the equation for each line and the respective correlation coefficient. The magnitude of the correlation coefficients further substantiates the assumed linear form of the fit, thus indicating the strong - and linear - relation between the two variables, (1/M) and number of wires, for this particular geometry and shutdown range.

The comparison between detectors C-1, C-2, and C-3 is shown graphically in the inset in Figure 7-4, where the axial displacement of the three detectors is plotted against the zero (1/M) intercept of the three least squares lines. Although there is little or no statistically significant difference between the three intercepts, for consistency alone a least squares fit to the three data points was made to provide a way to meaningfully combine the values. The zero intercept in this case, 7606 wires, would have been the result expected if a detector has been located with zero displacement from the source plane, which is believed to be the theoretically ideal location axially in this general source-detector configuration. The conclusion to be drawn from the foregoing, similar to that reached in the NRX/EST

Figure 7-3. Inverse Multiplication during Peripheral Poison Wire Removal

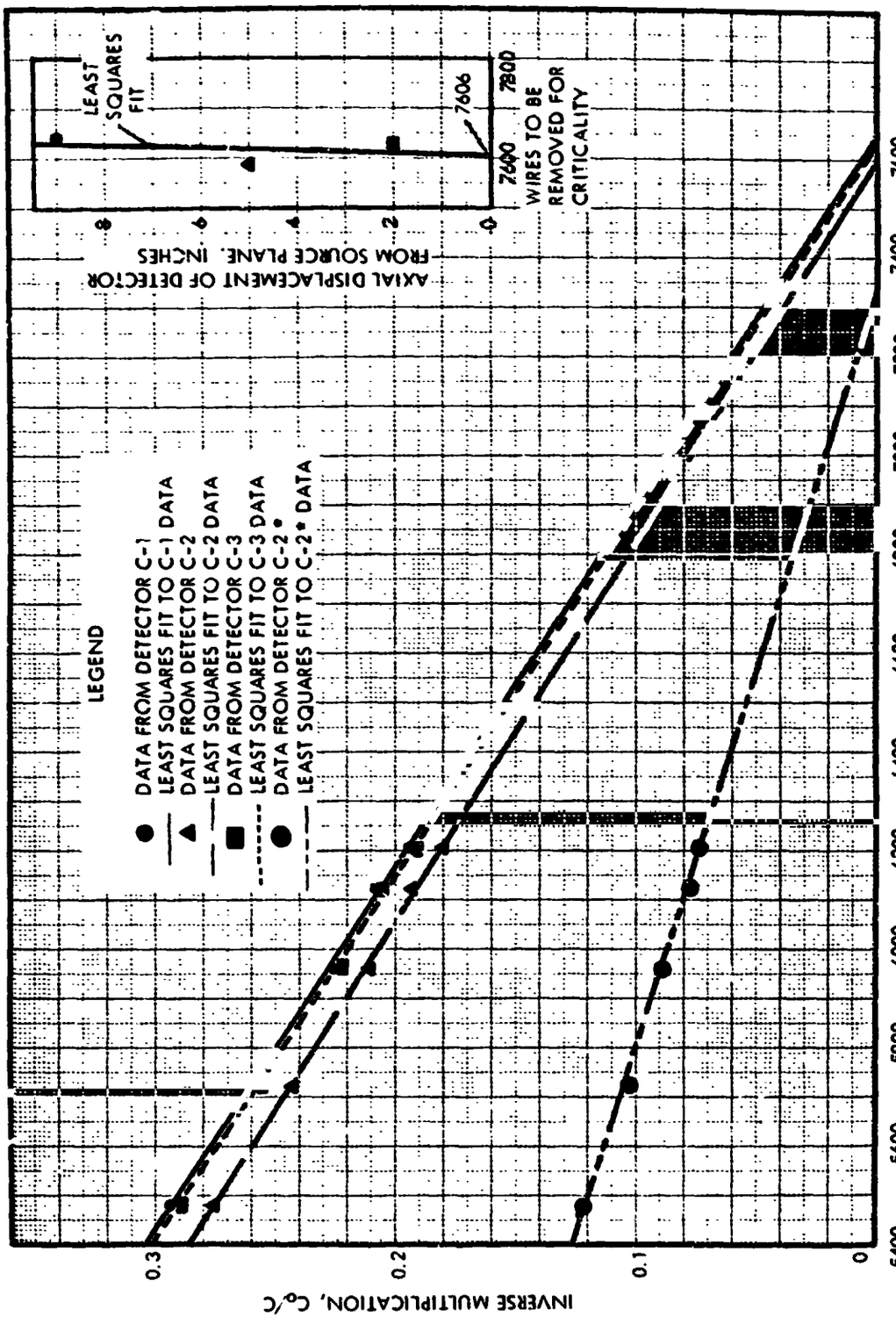

Figure 7-4. Inverse Multiplication during Last Five Steps of NRX-A5 Peripheral Poison Wire Removal

TABLE 7-3

EFFECT OF AXIAL POSITIONING ON DETECTOR RESPONSE DURING NRX-A5 PERIPHERAL WIRE REMOVAL

Detector	Axial Position Relative to Source Plane, Inches	Distance From Pressure Vessel, Inches	Least Squares Fit to Last Five Data Points, (1/M) = a + b W*		Correlation Coefficient	(1/M) = 0 Intercept, Wires
			a	b		
C-1	9	36	1.0352	-1.3542×10^{-4}	-0.9985	7641
C-2	5	36	0.9908	-1.3054×10^{-4}	-0.9989	7588
C-3	2	36	1.0277	-1.3444×10^{-4}	-0.9982	7628
C-2*	22	4	0.4809	-0.6570×10^{-4}	-0.9974	7313

* W = total number of wires to be removed for criticality.

Astronuclear Laboratory

analysis, is that the estimate of shutdown is relatively insensitive to axial displacement of the detector from the source plane. It must be emphasized that this statement applies only to the source-detector geometries typified by Figure 7-2 where (1) the azimuthal displacement of the detector from the source is 180 degrees and (2) both source and detector are positioned between drums near the midplane and are not shielded by the B^{10}-Al control vane.

A consistent comparison of the effect on detector response of distance from the reactor is shown also in Table 7-3 by the zero (1/M) intercept values. As above, the last 5 data points during the peripheral wire removal for detector C-2* were also fit with a least squares straight line and that line extrapolated to apparent criticality (1/M = 0). The resultant shutdown, expressed in number of wires, is (7313 - 6990 =) 323 wires in contrast with that from detectors C-1, C-2, and C-3 which is (7606 - 6990 =) 616 wires. The actual shutdown, as measured by the "rod drop" method in EP-1 after criticality was achieved, was about 5$ which is equivalent to about 464 wires[1]. Thus, in the deeply poisoned condition (central 783 wires remaining) a detector about 4 inches from the reactor can be expected to give a conservative estimate of shutdown while a detector at 36 inches should be suspected as giving a non-conservative estimate.

---

1 WANL-TNR-216, "NRX/EST Reactor Test Analysis Report", 12/66

7.2.2 Central Poison Wire Removal

Prior to NRX-A5, the procedure used for attaining initial criticality of the NRX reactors was to remove the central[1] poison wires by increments at the Test Cell. The central poison wires were removed in increments during control room operations and the multiplication determined after each increment until the reactor went critical with the drums near 180 degrees. The remaining wires were then removed in several additional increments with the successive critical angles gradually approaching an angle near 90 degrees when all wires were removed. This method of attaining criticality involved considerable time and many entries to the Test Cell restricted area.

A different method was used for NRX-A5. All of the poison wires were removed at the R-MAD Building without taking the reactor critical. The initial criticality of the reactor was then accomplished at Test Cell A during EP-1 by determining neutron multiplication as a function of drum position.

The NRX-A5 poison wire removal operation was thus concluded in the R-MAD Building with the removal of 783 poison wires from the central portion of the core. The removal was in accordance with procedure NRX-A5-P9[2] and was carried out under the following restrictions:

1) No more than two clusters of wires could be pulled during one removal increment.
2) No more than 15 percent of the extrapolated number of wires to criticality could be pulled at one interval except that in the final step a whole cluster of wires could be pulled.
3) Central poison wire removal at the R-MAD Building was to be terminated if the difference between the point of extrapolated criticality (in terms of number of wires removed) and the actual number of wires removed, was 325 wires or less with all drums at zero degrees.

---

1 "Central" refers to those wires in the 0-00, A and B clusters, typically 19 clusters of 42 wires each.

2 NRX-A5-P9, "NTO Operating Procedure for Central Poison Wire Removal at R-MAD for NRX-A5", 4/66.

The general method used to remove the central wires was to pull a group of wires, take a multiplication count, rotate drum number one to 180 degrees and take another multiplication count. This process was repeated for each wire removal increment. Prior to making the first removal, base counts were obtained with all drums at zero and then with drum number one at 180 degrees and the remaining drums at zero.

The source-detector geometry used in this operation was as shown in Figure 7-5. A Pu-Be source of 2.4×10^6 n/sec strength was located against the pressure vessel surface at approximately station 26. The source was positioned within a one-foot cube of paraffin with a cadmium shield on the side away from the reactor. Three detectors, C-1*, C-2*, and C-3*, were placed in contact with the pressure vessel at the same axial location. The source and these detectors were suspended from the nozzle-vessel flange. Two additional detectors, C-1 and C-3, were place at approximately three feet from the pressure vessel in the geometry used for the peripheral poison wire removal operation (See Figure 7-2). All of the detectors mentioned are covered with 1.25 inches of polyethylene. Except for their axial location, detectors C-1 and C-3 and the source were in the same relationship as they had been during the peripheral wire removal. A further minor difference was the absence of a cadmium sheet on the back of the paraffin block. Since neither of these factors is presumed important, it is expected that the response of C-1 and C-3 will permit a consistent analysis of the entire poison wire removal sequence.

A rather thorough treatment of the data collected during these wire removal operations and a discussion of the shutdown values calculated has been completed by NTO personnel and is reported in the NRX-A5 Pre-Test Report[1]. The discussion that follows here relies heavily on this work. Tables 7-4 to 7-6 have been reproduced from that report for the convenience of the reader.

Several methods were used to calculate an apparent shutdown margin and to insure that the shutdown limit of 325 wires or the equivalent was maintained. In the first two methods, the shutdown is determined by subtracting the actual number of wires removed from the extrapolated point at which $1/M = 0$. The only difference between the methods is the manner of extrapolation.

---

1 N.. 2-0075, "NRX-A5 Pre-Test Report", 5/66

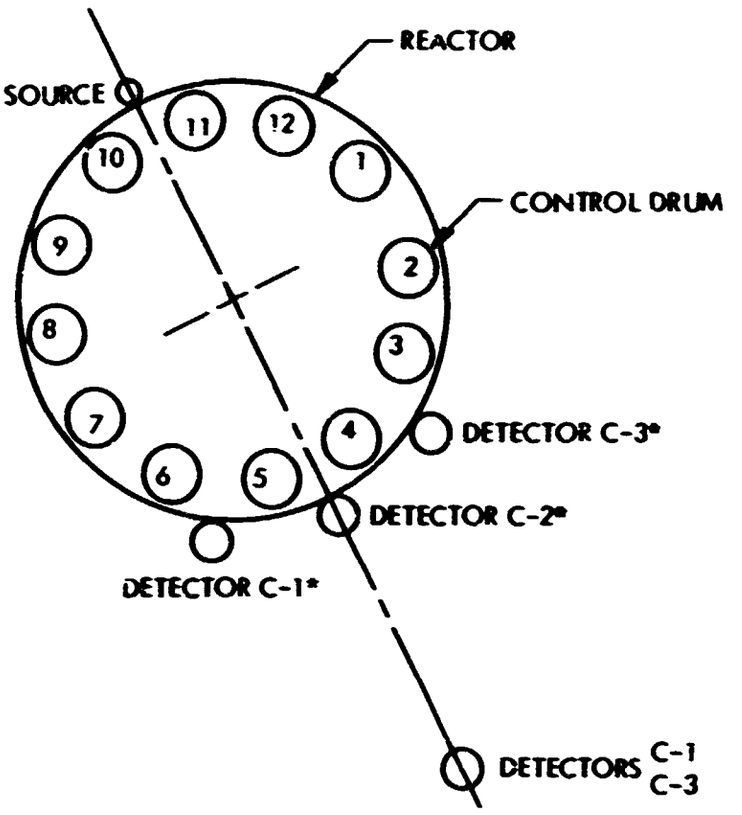

DETECTOR	AXIAL STATION, INCHES	DISTANCE FROM PRESSURE VESSEL, INCHES
C-1*	26	~ 0
C-2*	26	~0
C-3*	26	~0
C-1	~ 26	36
C-3	~ 26	36
Source	26	~0

611615-71B

Figure 7-5. Source and Detector Location for NRX-A5 Central Poison Wire Removal

TABLE 7-4

CENTRAL POISON WIRE REMOVAL DATA
(ALL DRUMS AT ZERO)

Position of Wire Removed (Increment Number)	Wires Removed this Increment	Total Wires Removed	Total Wires Remaining	Configuration Removed this Increment	Counts per Minute C-1°	Counts per Minute C-2°	Counts per Minute C-3°	Counts per Minute (less background) C-1°	Counts per Minute (less background) C-2°	Counts per Minute (less background) C-3°	Inverse Multiplication C-1°	Inverse Multiplication C-2°	Inverse Multiplication C-3°	Inverse Multiplication $C_{Avg.}$	Shutdown Margin (expressed in pcm/in of rod) C-1°	Shutdown Margin (expressed in pcm/in of rod) C-2°	Shutdown Margin (expressed in pcm/in of rod) C-3°	Shutdown Margin (expressed in pcm/in of rod) $C_{Avg.}$
C_0	0	0	783	0	21674[1]	21588[1]	13221[1]	21311	21164	12103	1.0	1.0	1.0	1.0				
1	79	79	704	181 481	23540[1]	23397[1]	14160[1]	23177	23043	13942	0.919	0.918	0.960	0.926	896	884	1218	999
2	84	163	620	282 582	25679	25529	15564	25316	25175	15346	0.842	0.841	0.856	0.846	849	862	953	891
3	84	247	536	182 482	28344	27971	16851	27981	27617	16633	0.762	0.766	0.788	0.772	791	809	918	836
4	84	331	452	381 681	30692	30778	18636	30329	30424	18418	0.702	0.696	0.711	0.703	783	758	814	783
5	84	415	368	281 581	34120	34670	20808	33757	34316	20590	0.631	0.617	0.643	0.630	710	669	747	707
6	84	499	284	382 682	38638	38612	23080	38275	38258	22862	0.557	0.553	0.573	0.561	627	617	670	638
7	79	578	205	1A1 4A1	43596	44156	26286	43233	43807	26068	0.493	0.483	0.503	0.493	562	560	585	562
8	84	662	121	2A1 5A1	50813	51242	30756	50250	50888	30538	0.424	0.416	0.429	0.423	487	472	497	485
9	42	704	79	3A1	56315	56720	33857	55952	56566	33639	0.381	0.374	0.390	0.382	433	421	450	435
10	37	741	42	6A1	61719	62681	36839	61356	62327	36621	0.347	0.340	0.358	0.348	394	382	413	396
11	42	783	0	000	70560	70882	41795	70197	70528	41577	0.304	0.300	0.315	0.306	342	336	360	345

Background C-1° 363 County/Minute
C-2° 354 County/Minute
C-3° 218 County/Minute

[1] Five minute counts, all other counting intervals were for one minute.

TABLE 7-5

CENTRAL POISON WIRE REMOVAL DATA (ONE DRUM AT 180°)

Poison Wire Removal Increment Number	Wires removed this increment	Total Wires Removed	Total Wires Remaining	Counts per Minute C-1°	Counts per Minute C-2°	Counts per Minute C-3°	Counts per Minute (less background) C-1°	Counts per Minute (less background) C-2°	Counts per Minute (less background) C-3°	Inverse Multiplication C-1°	Inverse Multiplication C-2°	Inverse Multiplication C-3°	C° Avg.	Shutdown Margin (expressed in poison wires) C-1°	Shutdown Margin (expressed in poison wires) C-2°	Shutdown Margin (expressed in poison wires) C-3°	C° Avg.
C_o	0	0	783	23,123[1]	23,089[1]	14,353[1]	22750	22734	14120	1.0	1.0	1.0	1.0				
1	79	79	704	25,187[1]	25,186[1]	15,431[1]	24814	24833	15197	0.917	0.915	0.929	0.920	873	850	1034	909
2	84	163	620	27,447	27,722	16,669	27074	27367	16456	0.840	0.831	0.858	0.843	836	801	985	875
3	84	247	536	30,528	30,108	18,362	30155	29713	18129	0.754	0.764	0.779	0.766	757	800	871	809
4	84	331	452	33,333	33,506	20,520	32960	33151	20287	0.690	0.686	0.696	0.691	727	723	758	740
5	84	415	368	37,175	37,838	22,696	36802	37483	22463	0.618	0.607	0.629	0.618	671	641	704	671
6	84	499	284	42,417	42,750	25,865	42044	42395	25632	0.541	0.538	0.551	0.543	588	576	612	593
7	79	578	205	47,604	49,190	29,346	47231	48835	29113	0.482	0.466	0.485	0.478	538	504	544	529
8	84	662	121	54,884	58,197	34,687	54511	57842	34454	0.403	0.393	0.407	0.401	447	429	454	443
9	42	704	79	63,344	65,039	39,020	62971	64684	38787	0.361	0.351	0.364	0.359	398	381	403	394
10	37	741	42	70,764	71,831	42,003	70391	71476	42770	0.323	0.318	0.330	0.324	354	346	365	355
11	42	783	0	82,032	84,202	50,090	81659	83847	49857	0.279	0.271	0.283	0.278	303	291	309	301

Background: C-1° 373 Counts/Minute
C-2° 355 Counts/Minute
C-3° 233 Counts/Minute

(1) Five minute counts, for other counting intervals were for one minute.

TABLE 7-6

CENTRAL POISON WIRE REMOVAL DATA
(EXTRAPOLATION USING RECENT AND NEXT MOST RECENT DATA POINTS)

Poison Wire Removal Increment Number	Total Wires Removed	Wires Removed This Increment	Counts per Minute N_d						Shutdown Margin (expressed in poison wires)			
			C-1*	C-2*	C-3*	C-1*	C-2*	C-3*	Avg.	C-1*	C-2*	C-3*	Avg.
C_o 0	0	0	21311	21164	13103								
1	79	79	23177	23043	13942	979	970	600	850				
2	163	84	25316	25175	15346	1073	1076	996	1048	910	913	833	885
3	247	84	27981	27817	16833	1037	1114	1250	1134	790	867	1003	887
4	331	84	30329	30424	18418	1332	1156	1114	1201	1001	825	783	870
5	415	84	33757	34316	20390	1157	1071	1197	1142	742	656	782	727
6	499	84	38275	38258	22862	1127	1231	1192	1150	628	732	693	649
7	578	79	43233	43802	26068	1187	1135	1141	1154	609	557	663	576
8	662	84	50250	50888	30538	1180	1181	1151	1171	518	519	489	509
9	704	[illegible]	55952	56566	33639	1074	1080	1118	1091	370	376	414	387
10	741	37	61356	62327	36621	1124	1104	1157	1128	383	363	416	387
11	783	42	70197	70528	41577	1074	1102	1094	1090	291	319	311	307

[redacted]

The first technique of extrapolation uses the base point (1/M = 1) and the most recent data point (value of inverse multiplication, C_o/C_i). Rather than relying on the conventional inverse multiplication plot, this extrapolation is made by use of the simple formula

$$N_{xi} = \frac{N_i}{1 - \frac{C_o}{C_i}} \qquad (7\text{-}1)$$

(symbols defined below) which is derived from the equation of a straight line passing through the two points noted above. The calculations were performed both for the "all drums at zero degrees" condition and for the "one drum at 180 degrees" conditions. The data taken, the resulting inverse multiplication, and the apparent shutdown margins (expressed in wires) are tabulated in Tables 7-4 and 7-5. Inverse multiplication plots for each of the three detectors and the average of the three detectors are given on Figures 7-6, 7-7, 7-8, and 7-9. In each case these are compared with the predicted inverse multiplication curves[1]. Differences are the result of several factors. First, for simplicity the prediction was based on a single wire worth of 1¢ per wire. Past experience indicated that the actual wire worth varied from below 0.67¢ to about 1.4¢ per wire. Secondly, the prediction was based on an expected ambient critical drum position of 93.0 (± 7.0) degrees. The actual critical position measured in EP-I was 99.3 degrees. Finally, the prediction assumed a drum worth of 8.5$ (±0.3). The best interpretation of drum worth as discussed in Section 7.3 was 8.2$. While these last two factors were within the uncertainty band of the prediction, they nevertheless contributed to the total error seen in Figures 7-6 to 7-9. The second and third factors tend to offset one another and in fact would result in slightly poorer agreement between measurement and a new "prediction" if it were made on the basis of the measured drum worth and ambient critical position. The error seen in Figures 7-6 to 7-9 thus results predominantly from deviation of the true wire worth from the assumed 1¢ per wire.

---

1 WANL-TME-1388, "NRX-A5 Test Prediction Report", 3/66

Figure 7-6. Inverse Multiplication Plot for Detector C-1* during Central Poison Wire Removal

Figure 7-7. Inverse Multiplication Plot for Detector C-2* during Central Poison Wire Removal

Figure 7-8. Inverse Multiplication Plot for Detector C-3° during Central Poison Wire Removal

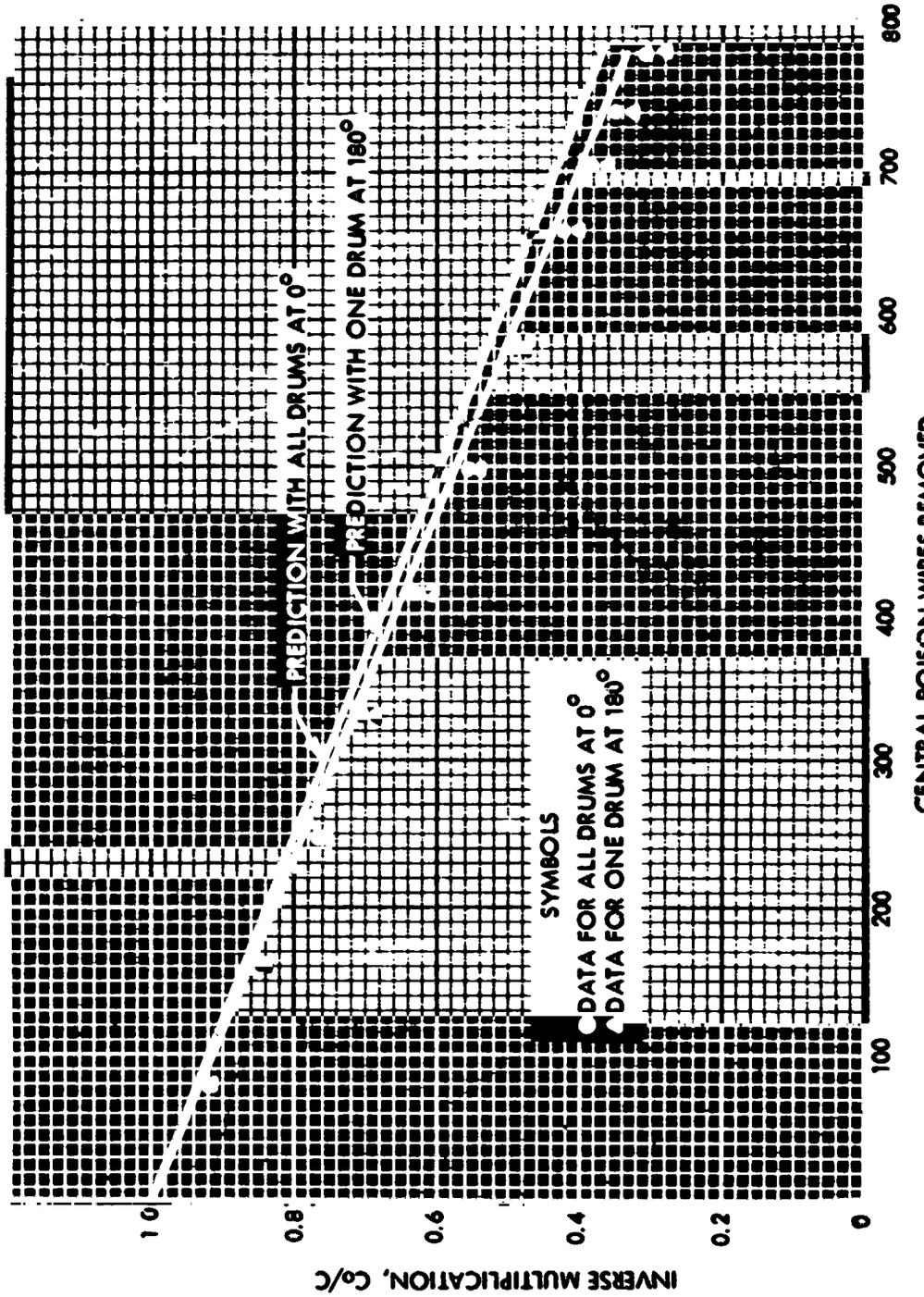

Figure 7-9. Average Inverse Multiplication Plot during Central Poison Wire Removal

In the second extrapolation technique, use is made of the most recent and the next-most-recent data points. The analysis in this case has only been done for the "all drums at zero" condition. The extrapolation was made using the formula as follows:

$$N_{xi} = N_{i-1} + \frac{C_i}{C_i - C_{i-1}} \left(N_i - N_{i-1}\right) \qquad (7\text{-}2)$$

where N_{xi} = number of poison wires at criticality, as extrapolated at i-th step.

N_i = number of poison wires removed for most recent data point,

N_{i-1} = number of poison wires removed for next-most-recent data point,

C_i = count rate for most recent data point, and

C_{i-1} = count rate for next-most-recent data point.

The results of this extrapolation and the resulting apparent shutdown margin (expressed in wires) for each wire removal increment are shown in Table 7-6. Although this method is preferable to Method I if the 1/M curve is nonlinear, it is sensitive to variability in the count rate date. Note, for example, the inflection in the neighborhood of 42 to 79 wires remaining.

The apparent shurdown margin (expressed in dollars) for each wire removal increment was also evaluated by a third technique, Method 3, based on the ratio between the count rate with all drums at zero and the count rate with one drum at 180 degrees. The formula used was as follows:

$$K_{SD}\,(\$) = \frac{\Delta\rho}{\bar{\beta}\left[1 - 2\,\Delta\rho - R\,(1 - \Delta\rho)\right]} \qquad (7\text{-}3)$$

where K_{SD} = Shutdown margin expressed in dollars,

$\frac{\Delta\rho}{\bar{\beta}}$ = Worth of a single control drum = 0.708$,

$\Delta\rho$ = 0.00503,

$\bar{\beta}$ = 0.0071, and

$R = \frac{C_0}{C_{180}} = \frac{\text{Count rate with all drums at zero}}{\text{Count rate with one drum fully withdrawn}}$.

The results of these calculations are shown in Table 7-7. The calculated shutdown values are seen by the above equation to be essentially directly proportional to the single drum worth, $\frac{\Delta\rho}{\beta}$. While this worth is shown in Section 7.3 to be about 4.5 percent less than the predicted value (70.8¢), the shutdown calculations have nevertheless been based on the predicted single drum worth. Differences, however, would not be large. For example, the 4.75$ average value calculated for the zero wire case is reduced to 4.58$.

A comparison of the three techniques is shown in Figure 7-10. These have been placed on a consistent basis by converting the shutdown margins expressed in number of wires to reactivity by use of the cumulative wire worth curve shown in WANL-TNR-216[1]. This same wire worth curve was used in conjunction with the 4.76$ shutdown measured in EP-1 to provide the best estimate of the true shutdown at each wire content. This is represented in Figure 7-10 by a solid line. Examination of the figure shows that the values obtained with Method 3 are in very good agreement with the best estimate over the entire range. As will be shown in Section 7.3, the 8.5$ drum span used in the prediction was high; the agreement is further improved if the measured drum span is used. The plotted data is summarized in Table 7-8.

The analysis of the other two detectors present during the central poison wire removal (as mentioned above) will not be repeated here. The analysis has been performed by NTO personnel and is reported in the NRX-A5 Pre-Test Report"[2]. This work yielded a shutdown similar to that obtained with detectors C-1*, C-2*, and C-3*. From Figure D-8 of the "NRX-A5 Pre-Test Report"[2] and Figure 5.1.2 of the "NRX-A5 Site Test Report"[3], the shutdown inferred from the average of these detectors is from 310 to 360 wires, essentially in agreement with the other detectors.

It might also be noted in passing that the shutdown inferred during the peripheral poison wire removal from a detector in similar geometry to C-2* here was (7313-6990=) 323 wires[4]. This is in good agreement with the 336 wire extrapolation from equation

1 WANL-TNR-216, "NRX/EST Reactor Test Analysis Report", 12/66
2 NTO-R-0075, "NRX-A5 Pre-Test Report", 5/66
3 NTO-R-0084, "NRX-A5 Site Test Report", 7/66
4 See Table 7-3

TABLE 7-7

CALCULATED SHUTDOWN MARGIN DATA

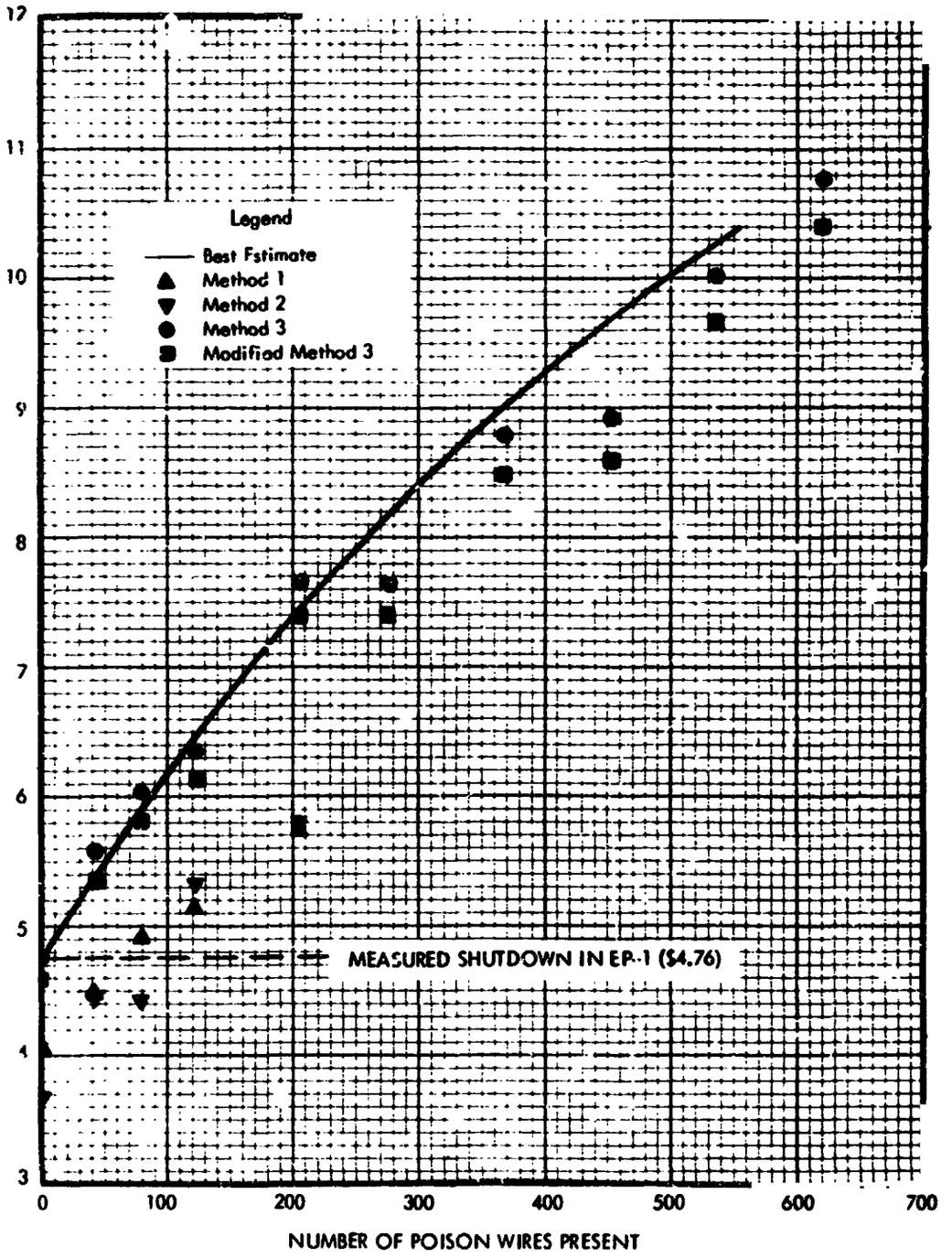

Figure 7-10. Comparison of Various Techniques of Computing Shutdown

TABLE 7-8

SUMMARY OF SHUTDOWN DATA

Poison Wires Present	Best Estimate of Shutdown[1], S	Indicated Shutdown, S			
		Method 1[2]	Method 2[3]	Method 3[4]	Modified Method 3[5]
783	---	---	---	11.30	10.90
704	---	---	---	10.32	9.96
620	---	---	---	10.79	10.41
536	10.28	---	---	10.03	9.68
452	9.67	---	---	8.90	8.59
368	9.00	---	---	8.79	8.48
284	8.21	---	---	7.66	7.39
200	7.66	5.73	5.80	7.66	7.39
121	6.45	5.16	5.33	6.36	6.14
79	5.89	4.90	4.41	6.03	5.82
42	5.36	4.47	4.41	5.56	5.36
0	4.76	4.05	3.67	4.75	4.58

1. Based on FP-1 shutdown indication of 4.76$ and the cumulative poison wire worth curve.
2. Based on equation 7-1 of Section 7.2.2 and the cumulative poison wire worth curve.
3. Based on equation 7-2 of Section 7.2.2 and the cumulative poison wire worth curve.
4. Based on equation 7-3 with the prediction value of drum worth (8.5$).
5. Based on equation 7-3 with the best estimate of the drum worth (8.2$).

that appears in Table 7-4 for detector C-2*.

7.2.3 Conclusion

The results shown in Figure 7-10 indicate that Method 3 based on the single drum rollout is conservative when the reactor is deeply shutdown, and provides a good quantitative shutdown estimate as the wire free condition is approached. Methods 1 and 2 provide very conservative shutdown estimates when the wire worth is evaluated from a "wires present" cumulative wire worth curve while the methods themselves provide shutdown in terms of "wires not present".

In a reactor which has been shimmed to an ambient critical position near to that required to provide an adequate safety margin, Method 3 appears to be the best technique to evaluate shutdown because of its very good precision. Although the method requires an estimate of the drum bank worth, it is not unduly sensitive to error in the assumed worth.

7.3 CONTROL DRUM WORTH

The NRX-A5 control span was predicted to be 0.3$ less than NRX/EST or 8.5$ because of a design change. A slot 0.116 inches deep and extending over 110 degrees of arc was milled opposite the control vane plate to reduce thermal distortion during transients.

Since some of the initial analysis of the test results were even lower and also showed some internal inconsistencies, a broad variety of drum worth indicators were evaluated in hope that they would improve an understanding of the problem. The methods that were used are as follows:

1) Single Drum Withdrawal Measurements
2) Single Drum Insertion Measurements
3) Drum Bank Differential Measurements
4) Drum Bank Integral Measurements
5) Feedback Reactivity in GH_2 Flow Test
6) Cold-to-hot Swing to Full Power

These are discussed in detail in the sections that follow.

7.3.1 Single Drum Withdrawal and Insertion Measurements

Early analysis by the DRAGON Team at NRDS of the NRX-A5 drum No. 2 calibration data indicated the drum worth to be less than predicted; however, it remained for a detailed kinetic analysis to show that this indeed was the case. The program used for this purpose, R-102, solves the space-independent neutron kinetics equations in an inverse fashion, taking as input the reactor physical constants and the complete measured power-time history and calculating the reactivity changes that must have occurred to produce the measured power variations. The results of the R-102 analysis are shown in Table 7-9. It is interesting to note that there is little difference between the average values obtained by the early somewhat crude approach and that resulting from R-102 analysis. The differences in each case are qualitatively explainable by the sign of the correction term ΔK_o which is a measure of the system non-equilibrium immediately prior to the measurement (either withdrawal or insertion). ΔK_{Bump} is essentially the asymptotic value of the system reactivity after the drum rotation has been made. The difference between the initial excess reactivity

TABLE 7-9

ANALYSIS OF DRUM NO. 2 CALIBRATION DATA

BY R-102

Withdrawals ($0^{\circ} \rightarrow 180^{\circ}$)

EP-1 CRT Interval, sec.	ΔK_{Bump}, %	ΔK_o, %	Indicated Drum Worth[1], ¢	Value From Period Analysis,[2] ¢
19356 - 376	0.00500	+0.000122	68.7	69.0
19848 - 868	0.00477	-0.000110	68.7	65.5
20670 - 700	0.00488	-0.000195	66.0	67.2
21195 - 225	0.00471	-0.000121	68.0	65.3
	Average Values		67.9	66.8

Insertions ($180^{\circ} \rightarrow 0^{\circ}$)

EP-1 CRT Interval, sec.	ΔK_{Bump}, %	ΔK_o, %	Indicated Drum Worth[1], ¢	Value From Power Ratio Method,[2] ¢
19918 - 948	Note 3	Note 3	Note 3	65.0
20725 - 790	-0.00473	+0.000210	69.6	78.3 (90.2-69.1)[4]
21286 - 326	-0.00455	+0.000245	67.5	67.5
	Average Values		68.6	70.3

1 Calculated from $(\Delta K_{Bump} - \Delta K_o) / 0.0071$.

2 See NRX-A5 DRAGON Memo No. 4.

3 Calcomp data channel saturated and unreadable.

4 Range of measured value.

(ΔK_o) and the asymptotic value following the rotation is the indicated drum worth, which appears in the fourth column of Table 7-9. The drum bank span inferred from each type of measurement is:

Withdrawals (67.9¢/drum) ..... 8.15$

Insertions (68.6¢/drum) ..... 8.23$

7.3.2 Drum Bank Differential Worth Measurements

Using the same R-102 technique briefly discussed above, the two drum bank "bumps" in EP-1 were analyzed. The results are summarized in Table 7-10. Again the difference between the values of reactivity change here (column 4) and the early work[1] is explainable qualitatively from the correction term ΔK_o. The ratio that appears in the last column of Table 7-10 is that of the measured differential drum bank worth to the predicted worth which was based on a drum span of 8.5$. The average value of this ratio was 0.977, implying that the actual drum span is (0.977 x 8.5$=) 8.30$. Use of the ratio in this manner assumes that the predicted differential drum worth has the proper shape but is 2.3 percent too large in magnitude. Since the predicted shape reflects experimental data from many WANFF measurements this assumption is reasonable.

7.3.3 Drum Bank Integral Worth Measurements

Table 7-11 reproduces the analysis of NRX-A5 drum worth by the "rod drop" method. The negative reactivity insertion from 99.4 degrees to the scrammed position was inferred from the neutron flux decay[2]. The resulting 5.0$ average shutdown worth can be compared to a prediction of 4.94$ for this angular interval. The observed value is 1.2 percent higher than predicted, implying that the actual drum span is (8.50$ x 1.012=) 8.60$, again assuming that the predicted differential worth has the same percentage error at all angles.

7.3.4 Feedback Reactivity in GH_2 Flow Test

In the high flow rate portion of the NRX-A5 GH_2 test ($P_c = 65 \pm 4$ PSIA), the change in drum bank position from cold critical (corrected to 540°R core, reflector and gas

---

1 Values of reactivity change for the two measurements of about 83¢ and 60¢ were published in NRX-A5 EP-1 DRAGON Memo No. 4.

2 This data is reported in EP-1 DRAGON reports.

TABLE 7-10

ANALYSIS OF DRUM BANK BUMPS BY R-102

EP-1 CRT Interval, sec.	ΔK_{Bump}, %	ΔK_o, %	Reactivity Change, *¢	$\Delta\theta$, Degrees	A $\frac{\Delta\rho}{\Delta\theta}$, ¢/Degree	B Predicted Value of ¢/Degree	Ratio A/B
22766 - 762	0.00590	-0.000135	85.0	111.5-99.3 = 12.2	6.97	7.12	0.979
23147 - 152	0.00438	-0.000400	67.3	108.4-98.8 = 9.6	7.01	7.19	0.975
					Average Ratio =		0.977

* Caiculated from $(\Delta K_{Bump} - \Delta K_o) / 0.0071$

TABLE 7-11

SUMMARY OF SELECTED EP-1 SHUTDOWN REACTIVITY MEASUREMENTS

Control Room Time, Seconds	P_o	P_{15}	P_{15/P_o}	Shutdown Reactivity, $	Drum Position Prior to Scram, Degrees	Shutdown Corrected to 99.4°, $ *
11998	0.29	0.012	0.414	5.08	99.3	5.09
14871	0.59	0.025	0.424	4.86	99.4	4.86
26472	0.59	0.025	0.424	4.86	97.4	5.01
30297	0.495	0.021	0.424	4.86	97.4	5.01
31211	0.45	0.019	0.422	4.88	97.5	5.02
					Average	$5.00

* Corrected for differences in drum position by the formula: $R_x - R_{99.4}$ $4.25\ (1 - \cos\theta_x) - 4.25$

$(1 - \cos 99.4^\circ)$, where R is the reactivity in dollars and θ is the dru position prior to scram.

temperatures) was -11.5°. Applying a temperature correction to a similar NRX/EST test, the change in drum position at the same chamber pressure and temperatures would be -10.7°. The ratio of these two motions is $\frac{10.7}{11.5} = 0.93$. Assuming that the difference between these two tests is a measure of the relative drum spans of the two reactors, the apparent drum bank worth of NRX-A5 is 0.93 times the NRX/EST drum worth, or (0.93 x 8.8$ =) 8.18$.

A comparison of NRX-A5 data with NRX/EST data at the low flow hold would be misleading since the flow profiles were reversed, resulting in differences in core "compaction" or core "pressurization".

7.3.5 Cold-to-Hot Swing to Full Power

Summarized in Table 7-19 of Section 7.6 are the NRX-A5 cold-to-hot swing data. The change in reactivity to the two start-of-life conditions has been calculated on two bases, an 8.2$ drum span and an 8.5$ drum span. These values are shown in the lower portion of the table. The upper part gives the chamber conditions and the expected reactivity change, based on a least squares fit to NRX/EST data.[1] In order to compare the formula value with the A5 experimental data, two corrections would normally be required. One, a delayed neutron non-equilibrium correction, has been calculated by the R-102 program and is given in the table. The second correction to account for an actual difference in cold-to-hot swing between the NRX/EST and the NRX-A5 reactor was found to be unnecessary, since calculations have indicated that it is negligible.

Comparing, then, the final column of the upper part of the table with the last two columns of the lower part, it can be seen that in Case 1 there is better agreement between experiment and calculation when the 8.5$ drum span is used, while in Case 2 the agreement is better when the 8.2$ span is used. Therefore, cold-to-hot considerations cannot be used here to aid in a choice of the true drum span.

7.3.6 Individual Drum Uniformity Measurements

In the past an effort has been made to obtain absolute drum worth data along with a measurement of the uniformity of the individual drums. However, in the NRX-A5 test

---

1 WANL-TNR-216, "NRX/EST Reactor Test Analysis Report", 12/66.

program a departure was made from this philosophy. The experiment was designed to yield only uniformity information, thereby both shortening the test and analysis time required, and reducing the uncertainties that have plagued these measurements in the past.[1] The sequence of experimental steps taken was briefly:

1) Establish criticality with twelve drums.
2) Place system in twelve drum "Power Control".
3) Switch the selected drum to "Individual Control".
4) Make the following rotations of the selected drum:
   a) From twelve drum critical position to 0°
   b) From 0° to 180°
   c) From 180° to the twelve drum critical position.
5) Return selected drum to "Gang Control".
6) Repeat Steps 3 to 5 for each drum.

To compensate for the reactivity removed or inserted in each of the rotations of Step 4 the power controller rotated the eleven drums remaining under its control in a direction to maintain constant reactivity. The relative worth of the drum being rotated is then indicated by the change in the steady state critical position after rotations a and b in Step 4. The data accumulated in this procedure is shown in Table 7-12 and a comparison with prediction is shown in Figure 7-11. As is evident from this comparison, the drums are of approximately equal worth within experimental uncertainty. Since this type of measurement results only in a relative measure of the drum worths, it is not significant (from a worth standpoint) that all of the measured 11 drum rotations are greater than predicted. This may have been caused simply by the method of measurement, i.e., use of 11 drums in power control to "shadow" one drum in position control.

7.3.7 Conclusion

A value of 8.2$ has been selected as the best estimate of the NRX-A5 drum span; for comparison the predicted span was 8.5$ ± 0.3. The results upon which the 8.2$ value is based are summarized below:

---

1 See, for example, the analysis of drum uniformity measurements in WANL-TNR-216, "NRX/EST Reactor Test Analysis Report", 12/66.

Method	Best Value of Span, $
Single Drum Withdrawal Measurements	8.15
Single Drum Insertion Measurements	8.23
Drum Bank Differential Measurements	8.30
Drum Bank Integral Measurements	8.60
Feedback Reactivity in GH_2 Flow Test	8.18

The worth of the individual drums in NRX-A5 has been shown to be uniform. The technique used is evaluated as excellent.

TABLE 7-12

DRUM PRINTOUT DATA FOR RELATIVE INTEGRAL DRUM WORTH MEASUREMENTS

CRT	Drum Printout Event Number	No. 1	No. 2	No. 3	No. 4	No. 5	No. 6	No. 7	No. 8	No. 9	No. 10	No. 11	No. 12	Eleven Drum Average
21995	(2) 925	1.2	105.6	106.4	106.0	106.4	107.0	105.4	105.6	105.2	105.4	105.8	105.4	105.9
22125	(3) 055	181.0	94.6	95.4	95.2	95.6	95.8	94.6	94.8	94.2	94.6	94.8	94.6	94.9
22185	(3) 115	105.2	1.4	105.2	105.6	106.2	106.8	105.2	105.4	105.0	105.2	105.4	105.2	105.5
22220	(3) 150	94.4	181.2	95.6	95.2	95.6	96.0	94.6	94.8	94.2	94.4	94.8	94.6	94.9
22260	(3) 190	105.6	105.8	1.2	106.2	106.6	107.2	105.6	105.8	103.4	105.6	105.8	105.8	105.9
22280	(3) 210	94.4	94.8	181.0	95.2	95.4	96.0	94.6	94.8	94.2	94.4	94.6	94.6	94.8
22312	(3) 242	105.4	105.8	106.6	1.4	106.4	107.0	105.4	105.6	105.2	105.4	105.8	105.6	105.9
22328	(3) 258	94.2	94.6	95.6	180.8	95.4	95.8	94.4	94.6	94.2	94.2	94.6	94.4	94.7
22335	(3) 286	105.2	105.6	106.6	106.2	1.4	107.0	105.4	105.6	105.2	105.4	105.6	105.6	105.8
22365	(3) 295	94.2	94.6	95.6	95.4	181.2	95.8	94.4	94.6	94.2	94.4	94.6	94.6	94.8
22390	(3) 320	105.4	105.8	106.6	106.2	106.8	1.6	105.4	105.8	105.2	105.4	105.6	105.6	105.8
22405	(3) 335	94.4	94.8	95.6	95.4	95.6	181.4	94.6	94.8	94.2	94.6	94.8	94.6	94.9
22433	(3) 363	105.4	105.6	106.6	106.0	106.6	107.0	1.6	105.6	105.0	105.2	105.6	105.4	105.7
22455	(3) 385	94.2	94.8	95.6	95.2	95.6	96.0	181.2	94.8	94.2	94.4	94.6	94.6	94.8
22485	(3) 415	105.2	105.6	106.4	106.0	106.6	107.0	105.4	1.4	105.0	105.2	105.4	105.4	105.7
22500	(3) 430	94.4	94.8	(1)	(1)	95.6	96.2	94.8	181.0	94.2	94.4	94.8	94.6	94.9
22523	(3) 453	105.2	105.4	(1)	(1)	106.4	107.0	105.4	105.6	1.4	105.2	105.4	105.2	105.6
22540	(3) 470	94.2	94.6	(1)	(1)	95.6	96.0	94.6	94.6	181.0	94.2	94.6	94.4	94.8
22570	(3) 500	105.2	105.6	(1)	(1)	106.6	107.0	105.4	105.6	105.2	1.4	105.4	105.4	105.7
22582	(3) 512	94.2	94.6	(1)	(1)	95.4	96.0	94.6	94.6	94.2	181.0	94.6	94.4	94.8
22608	(3) 538	105.2	105.6	(1)	(1)	106.4	107.0	105.4	105.6	105.2	105.6	1.4	105.4	105.7
22618	(3) 548	94.0	94.6	(1)	(1)	95.4	96.0	94.6	94.6	94.2	94.6	181.0[2]	94.4	94.7
22645	(3) 575	105.2	105.4	(1)	(1)	106.4	107.0	105.4	105.4	105.2	105.4	105.6	1.4	105.7
22660	(3) 590	94.0	94.6	(1)	(1)	95.4	96.0	94.6	94.6	94.2	94.6	94.6	181.2	94.7

(1) Printer not working.

(2) Printer did not indicate the position, but it is felt that drum was at 181°.

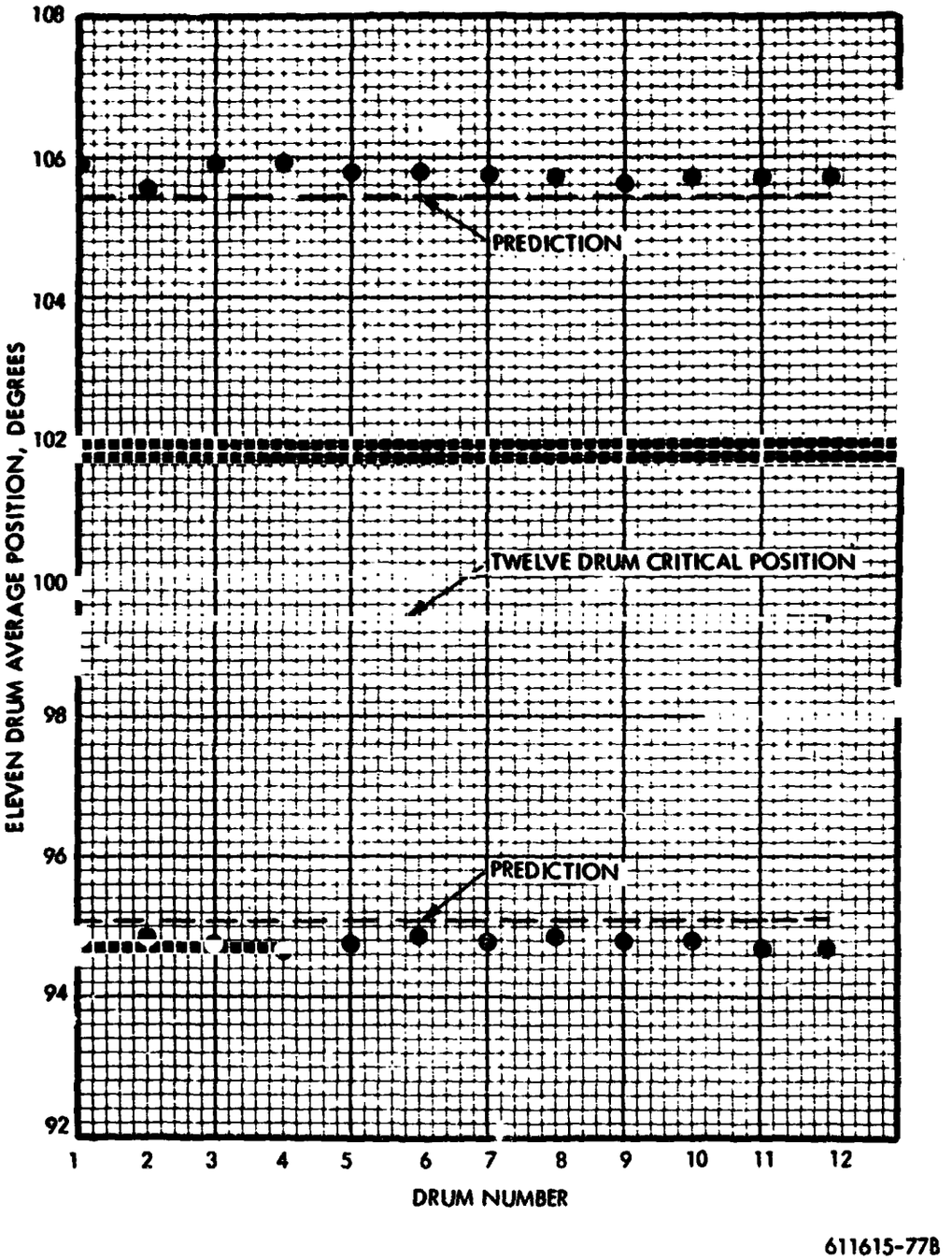

Figure 7-11. Relative Drum Worth Uniformity Comparison

7.4 TEMPERATURE COEFFICIENTS FROM NEAR AMBIENT TESTING

Following the techniques first introduced in the NRX/EST analysis,[1] additional near ambient, low power temperature coefficient data has been analyzed. The resulting values have provided an additional indication of the core station 8 temperature coefficient of reactivity and the beryllium reflector average temperature coefficient of reactivity.

7.4.1 Station 8 Temperature Coefficient of Reactivity

During the Neutronics Calibration Phase of EP-II the reactor was operated for a period of about 17 minutes in the power range 50 to 60 KW. In this time the reactor heated up about 100°R at station 8 while the reflector temperature changed by only several degrees R. The control drums rotated outward about 1°. Figure 3-6 shows the typical variation of temperatures throughout the core during this period. An average rate of change of temperature at station 8 was established from that experienced in the later portions of the calibration period. A time interval for analysis, again near the end of calibration, was then selected and this rate of change applied to it to determine the temperature change. Selecting, then, the time interval 6860 to 7340 seconds (control room time) the quantities appropriate to this analysis are:

1) $\Delta\theta = 100.8^{\circ} - 99.9^{\circ}$

   $\Delta\rho = -6.34¢$

2) $\Delta T_8 = 480 \text{ sec.} \times 0.0763^{\circ}\text{R/sec} = 36.6^{\circ}\text{R}$

3) $\Delta T_{Be} = 3.6^{\circ}\text{R}$

4) $\dfrac{\Delta\rho}{\Delta T_8} = -0.173 ¢/^{\circ}\text{R}$

In this calculation the effect of the 3.6°R increase in beryllium temperature was neglected. If the COHOT[2] beryllium temperature coefficient of +0.094¢/°R is used to account for this

---

1 WANL-TNR-216, "NRX/EST Reactor Test Analysis Report", 12/66, pp 6-73 - 6-88.
2 See Appendix A

temperature difference, the calculated station 8 coefficient changes to -0.182¢/°R, in excellent agreement with the -0.[illegible]¢/°R and -0.19¢/°R values found in the NRX/EST analysis[1].

7.4.2 Beryllium Reflector Temperature Coefficient of Reactivity

After the EP-III and EP-IV power runs, criticality measurements were conducted at two temperature levels, one in the range 700°R to 800°R and the other near ambient temperature. In each of the four conditions the critical position was established at several power levels. Only the measurements made in the 50 to 60 KW range are used here.

A summary of the pertinent data appears in Table 7-13. The analytical model to which these data will be fit is as follows:

$$\Delta\rho = C_8 (\Delta T_8) + C_r (\Delta T_{Be}) \qquad (7\text{-}4)$$

where

$\Delta\rho$	=	reactivity change,
C_8	=	core station 8 temperature coefficient,
ΔT_8	=	temperature change at core station 8,
C_r	=	reflector temperature coefficient, and
ΔT_{Be}	=	change in the average reflector temperature.

Note that the station 8 temperature has been used since it has been established that at a power level of 50 KW the core is heating rapidly enough after 100 to 200 seconds to be considered in the linear portion of the heating curve[1]. The 50-60 KW power level was maintained in these tests for about 200 seconds. Although a longer time would have been desirable, examination or Figure 3-6 indicates that the temperature rise was close to linear.

---

1 WANL-TNR-216, "NRX/EST Reactor Test Analysis Report", 12/66, figures 6-25, 6-26.

TABLE 7-13

SUMMARY OF SELECTED NRX-A5 POST-TEST CRITICALITY DATA

EP	Approximate Control Room Time, Seconds	Average Control Drum Position, Degrees	Unnormalized Reactivity*, Cents	Average Station 8 Core Temperature, °R	Average Beryllium Reflector Temperature, °R
III	17140	109.2	544.8	882	740
	21307	103.5	505.7	585	523
IV	15180	142.5	735.3	743	681
	19025	137.8	713.7	539	513

* Calculated from the equation $R = 4.1 (1 - \cos \theta)$ \$ where θ is drum position. It has been shown that this equation provides an excellent fit to the measured integral drum worth data.

Substituting the tabulated post-test data into (7-4), the following equations result

$$505.7 - 544.8 = C_8 (882 - 585) + C_r (740 - 523)$$

$$713.7 - 735.3 = C_8 (743 - 539) + C_r (681 - 513)$$

These may be rearranged to give the following

$$C_8 + 0.7306\ C_r = -0.1316 \qquad (7\text{-}5)$$

$$C_8 + 0.8235\ C_r = -0.1059 \qquad (7\text{-}6)$$

Solving (7-5) and (7-6) simultaneously gives values for the coefficients of

$$C_8 = -0.334\not{\epsilon}/^{\circ}R$$

$$C_r = +0.277\not{\epsilon}/^{\circ}R$$

As in the comparable NRX/EST analysis, the derived values disagree substantially with those in the COHOT analytical model[1], with those derived from NRX/EST data, and with the coefficient derived for core station 8 in the previous section.

Again as in NRX/EST, the reason for this disagreement is clear from examination of the solution to equations (7-5) and (7-6). The determinant of the coefficients of C_8 and C_r which forms the denominator of the ratio used to solve[2] for each of these factors is the difference between 0.7306 and 0.8235 or -0.0929, a very small difference relative to the two values. Thus, the solution is overly sensitive to small errors in the coefficients of C_8 and C_r in the equations. For example, an uncertainty of $\pm$ 10°R in the coefficient of C_r in equation (7-5) results in a solution for C_8 which varies from $-0.463\not{\epsilon}/^{\circ}R$ to $-0.273\not{\epsilon}/^{\circ}R$. Thus, the results of a straightforward solution to equations (7-5) and (7-6) are clearly suspect.

---

1 See Appendix A.

2 Done by the well-known "Cramer's Rule" technique.

In order to extract useful information from equations (7-5) and (7-6), one can assign to the station 8 temperature coefficient the value of -0.182 derived in section 7.41. The reflector coefficient, C_r, may then be found from either equation, giving values of +0.069¢ /°R and +0.092¢ /°R. The average is +0.081¢ /°R, in a fair agreement with the +0.0943¢ /°R coefficient used in the COHOT analytical model[1]. The corresponding average from NRX/EST was 0.10¢ /°R.

7.4.3 Conclusions

The low power core station 8 temperature coefficient of reactivity inferred from test data is -0.182¢ /°R in excellent agreement with the NRX/EST value of -0.19¢ /°R. The power range over which this coefficient is clearly applicable is approximately 50 to 100 KW. The COHOT temperature coefficient, -0.11¢ /°R, is recommended for use at very low power (100 watts, for example) and where core temperatures are spatially uniform.

The values for the beryllium reflector temperature coefficient of reactivity that have been derived are +0.069¢ /°R and +0.092¢ /°R. The same method yielded values of 0.081¢ /°R and 0.120¢ /°R in NRX/EST analysis. The average of all these determinations is 0.091¢ /°R in good agreement with the calculated coefficient +0.0943¢ /°R. The COHOT reflector coefficient has thus been verified, specifically for near-ambient reactor conditions.

---

1 See Appendix A.

7.5 OPERATING REACTIVITY CHANGES DUE TO CORROSION

7.5.1 Summary of Pre-Test and Post-Test Criticality Measurements

The various delayed critical drum bank positions at ambient temperature throughout the NRX-A5 test series are listed in Table 7-14. The initial critical position in EP-I was 99.5 degrees. Correcting to 540°R, the initial critical position becomes 99.3 degrees. For comparison, the design critical position, as utilized in calculating the appropriate number of TaC-loaded reactivity shim elements, was 93 degrees. The measurement just fell within the predicted ± 7 degree uncertainty band. For perspective it should be noted that this uncertainty is not a statistically derived quantity, but was derived by an error analysis in which a number of incompletely verified constituent uncertainties were included out of necessity.

Relative to the final pre-criticality prediction of 95.0 degrees, reflecting knowledge of the final material inventory of the reactor, the error in the predicted reactivity of the NRX-A5 reactor was only about 32¢. This small error is typical of that experienced in the past as is shown by the summary in Table 7-15 of criticality predictions and measurements to date.

An anomaly frequently seen in prior testing is that the critical position appears to change slightly between runs, as shown in Table 7-14. As in previous analyses this anomalous behavior must be attributed to such factors as changing core moisture content or temperature, data system drift, and slight changes in core geometry.

7.5.2 Observed Reactivity Loss

There are two independent methods for calculating the total reactivity change in a test. The first, and simplest method, is based on the difference in ambient critical positions before and after the test. The second technique utilizes the measured control drum motion during a test. The results obtained by these two approaches are generally slightly different. The differences that have been seen in the past, as viewed from a slightly different standpoint are summarized in Table 6-22 of the "NRX/EST Reactor Test Analysis Report". The differences were about 5¢ for NRX-A3, 20 to 30¢ for NRX/EST and

TABLE 7-14

SUMMARY OF CRITICAL CONTROL DRUM POSITIONS

EP	Date Performed	Measured Ambient Critical Position, Degrees	Core Station 8 Temperature, °R	Average Beryllium Reflector Temperature, °R	Critical Position Corrected to 540°R, Degrees
I	5/26/66	99.5	562	550	99.3
II/III Pre	6/8/66	99.7	605	554	98.9
Post	6/10/66	103.5	585	523	102.1
IV Pre	6 23/66	102.9	604	573	102.4
Post	6/27/66	137.8	539	513	137.3

TABLE 7-15

PREDICTED VERSUS EXPERIMENTAL COLD CRITICAL
DRUM POSITION OF NERVA REACTORS

Reactor	Aim Drum Position, Degrees	Final Prediction of the Drum Position, Degrees	Actual Drum Position, Degrees	Reactivity Discrepancy Relative to the Final Prediction, $
NRX-A2	90	91.6	97.8	-0.47
NRX-A3	90	92.4	89.1	0.25
NRX/EST	94	100.1	99.1	0.08
NRX-A5	93	95.0	99.3	-0.32

50¢ for NRX-A5 (preliminary value for EP-IV alone). In the sections that follow the two methods of reactivity loss calculation are discussed further and compared.

7.5.2.1 Reactivity Loss from Ambient Criticality Data

Using the drum positions summarized in Table 7-14 the reactivity loss due to corrosion is calculated to be:

EP-III	22.5¢
EP-IV	213.3¢
Total	235.8¢

A drum span of 8.2S as developed in Section 7.3 has been used here. This method of computing the total loss differs slightly from that used in the past, wherein the total was based on the shift in drum position from first to last criticality. There is indeed little justification for choosing between these two methods. Differences are fortunately small. The method used here appears to be more theoretically consistent in that it eliminates the small anomalous shifts in drum position between tests.

7.5.2.2 Reactivity Loss During Operation

During operation at power, fuel material is lost from the core by corrosion. Since carbon is the predominant constituent of this lost material, a net reactivity loss occurs. The power controller (or temperature controller) accordingly must signal the drum controller to rotate the drums outward, inserting additional reactivity into the system to compensate for the reactivity worth of the material lost. The drum motion experienced during the two power tests in the NRX-A5 test series is shown in Figures 7-12 and 7-13. A comparison with NRX/EST is shown in Figure 7-14. Although corrosion is the main cause of reactivity change, other processes are known to influence reactivity, for example: redistribution of flow, hydrogen accumulation in fuel element pores, loss of NbC coating, and, of course, changes in fluid flow and temperature. All of the effects except the temperature and flow parameters have relatively small effect, however. Thus, if the drum motion is corrected to constant thermal conditions, the reactivity change inferred from it can, with reasonable

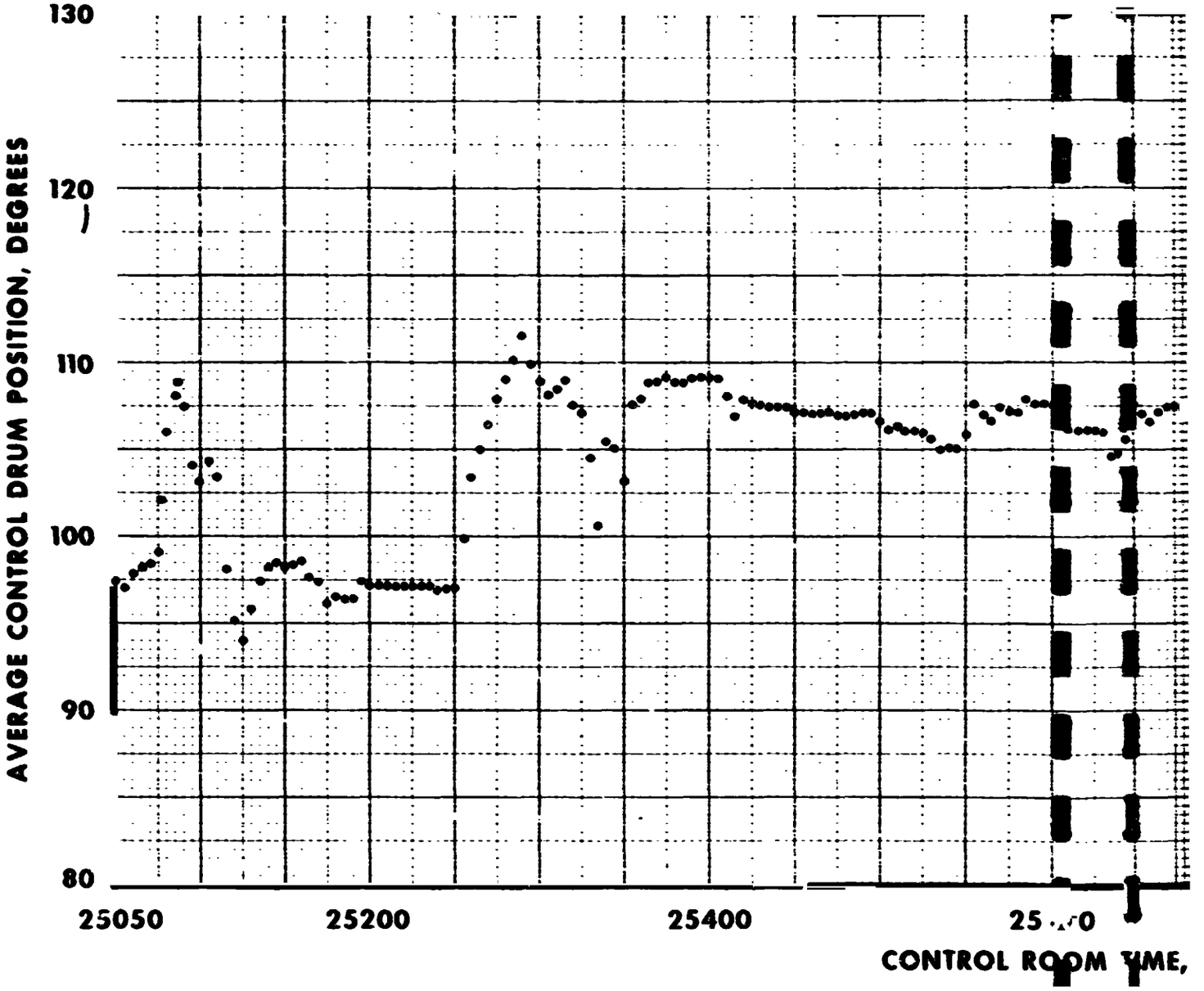
130
120
110
100
90
80
AVERAGE CONTROL DRUM POSITION, DEGREES
25050
25200
25400
CONTROL ROOM TIME,

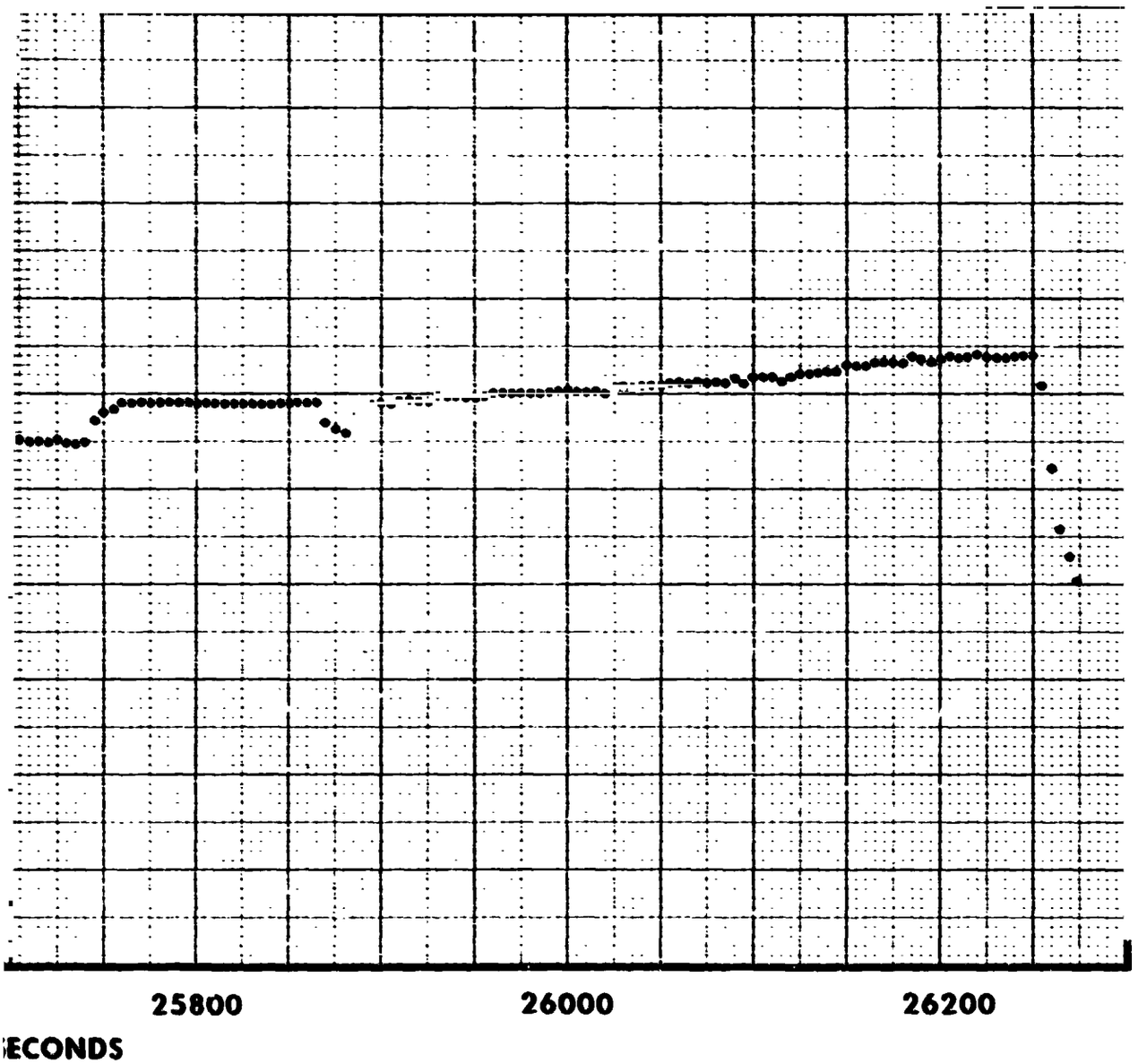

Figure 7-12. Variation of Control Drum Position during EP-III

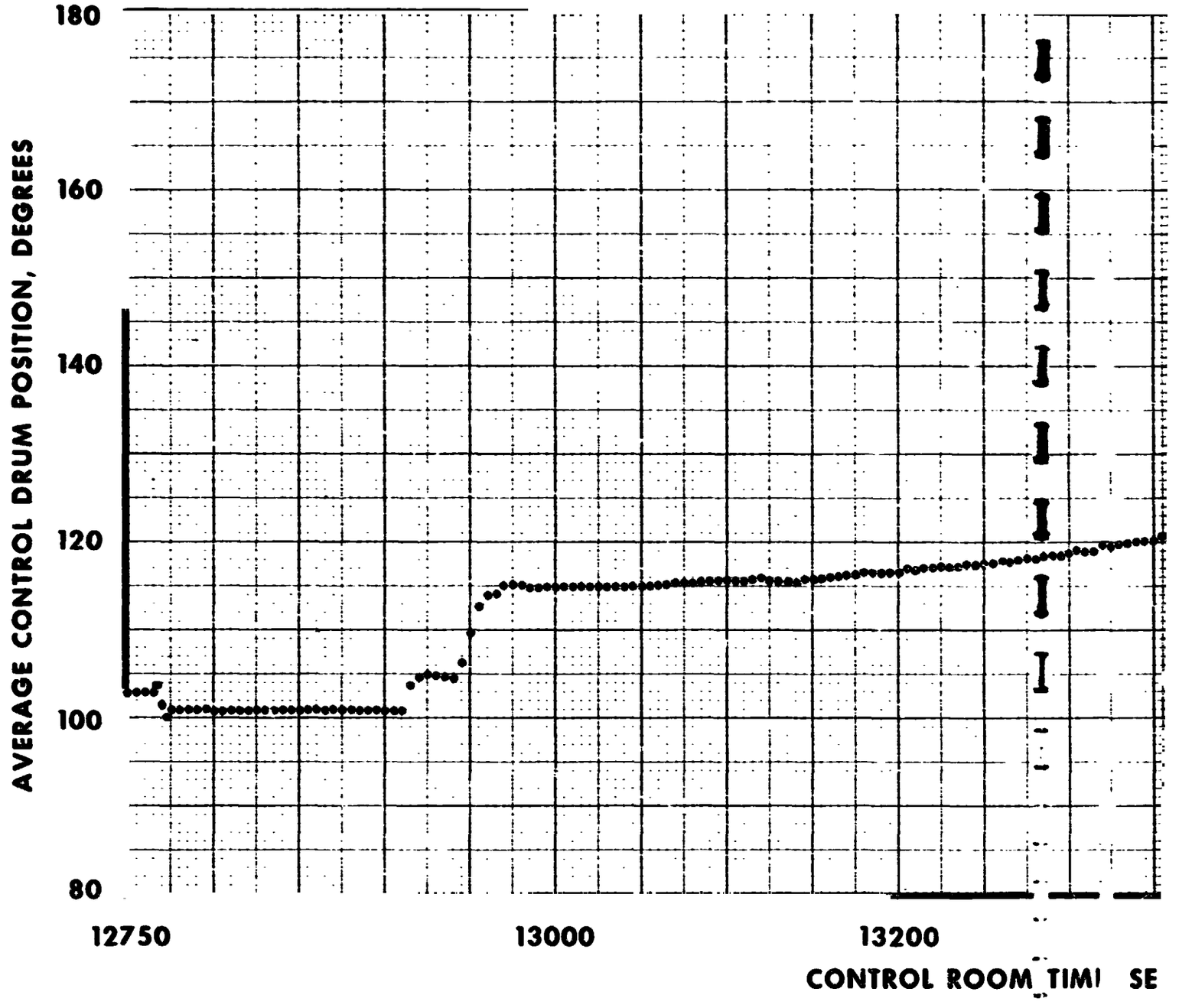

Figure 7-13. Variation of Control Drum Position during EP-IV

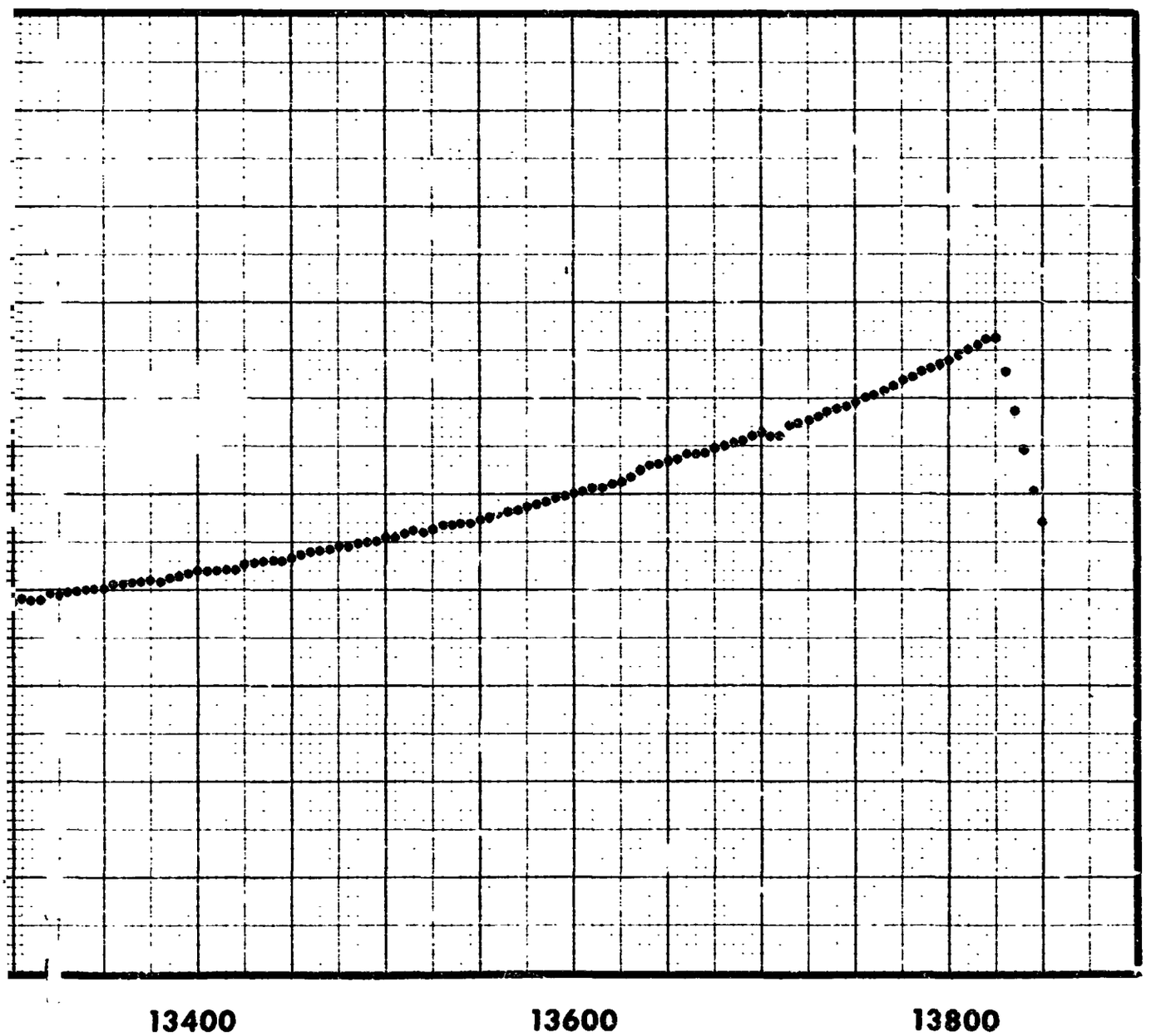
13400
13600
13800
IMI SECONDS

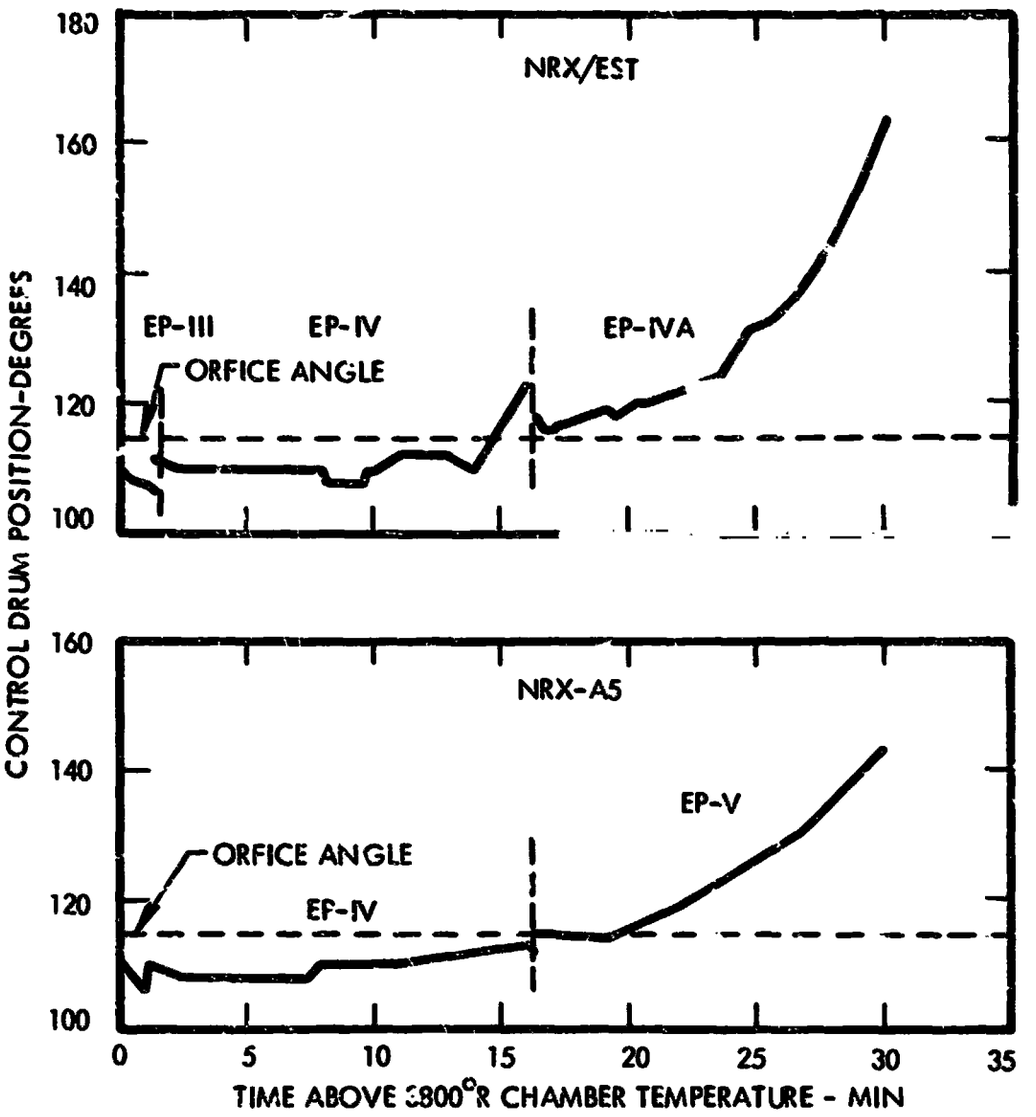

Figure 7-14. NRX/EST and NRX-A5 Control Drum Position during Operation above 3800°R Chamber Temperature

accuracy, be attributed only to corrosion and can be used to provide an understanding of the time behavior of the corrosion process, supplementing the post-operative weight loss measurements.

The method by which the reactivity effect of varying thermal conditions was analytically removed from the observed reactivity change is explained in the following paragraphs.

The change in critical angle from an[illegible]onditions to a wide range of operating conditions is given by the following formula:[1]

$$\Delta\theta = -6.9 - 0.009\ T_c - 133.(P_c/T_c) \qquad (7\text{-}7)$$

where

$\Delta\theta$ = the change in drum position, degrees,

T_c = the measured chamber temperature at operating conditions, °R, and

P_c = the measured chamber pressure at operating conditions, psia.

This equation was determined from an empirical fit of the observed reactivity changes at various flow and temperature conditions in the NRX/EST test. At design full power conditions (T_c = 4090°R, P_c = 563 psia), the cold-to-hot drum angle change predicted by this equation is 11.8 degrees.

Equation (7-7) allows us to correct the measured control drum position at any time, t, to what it would have been at that time, but at design full power flow and temperature conditions. The corrected angle is given by the equation

$$\theta_c(t) = \theta_m(t) + (11.8^\circ \quad \Delta\theta(t)) \qquad (7\text{-}8)$$

---

1 This formula was originally based on preliminary data but does not differ significantly from the least squares fit given in WANL-TNR-216.

where

θ_c = the corrected control drum position, degrees,

θ_m = the measured control drum position, degrees,

$\Delta\theta$ = change in drum position given by equation (7-7), degrees, and

t = time.

The corrected control drum position, θ_c, is related to the excess reactivity, ρ, over that at zero degrees drum angle by the equation

$$\rho(t) = 4.1\,(1 - \cos\theta_c(t)) \qquad (7\text{-}9)$$

The units of ρ in this equation are dollars. This equation has been shown to fit the measured differential worth curve very well.

To determine the reactivity loss $\Delta\rho$ due to corrosion at any time t, $\rho(t)$ as defined by equation (7-9) is subtracted from the initial value at time zero.

The drum motion shown in Figure 7-12 and 7-13 was converted to reactivity loss by the above method. The reactivity loss as a function of time is shown in Figure 7-15 for EP III and in Figure 7-16 for EF IV.

From the corrected reactivity loss behavior with time, the reactivity loss rate at any time t could then be calculated from the incremental reactivity loss associated with each time increment. The reactivity loss rate so determined is shown in Figures 7-17 and 7-18 for EP-III and EP-IV, respectively. A comparison of NRX/EST and NRX-A5 reactivity loss rate data is shown in Figure 7-19.

Analysis was first conducted on the reactivity loss data for EP-IV because this information appeared to be the most consistent. Examination of Figure 7-16 shows that the cumulative reactivity loss for EP-IV is not a linear function of time on a semi-log plot. If, however, the quantity (ρ + 40) cents is plotted against time, an excellent fit is obtained, as shown in the figure. The same straight line also fits the EP-III data well, as shown in Figure 7-15.

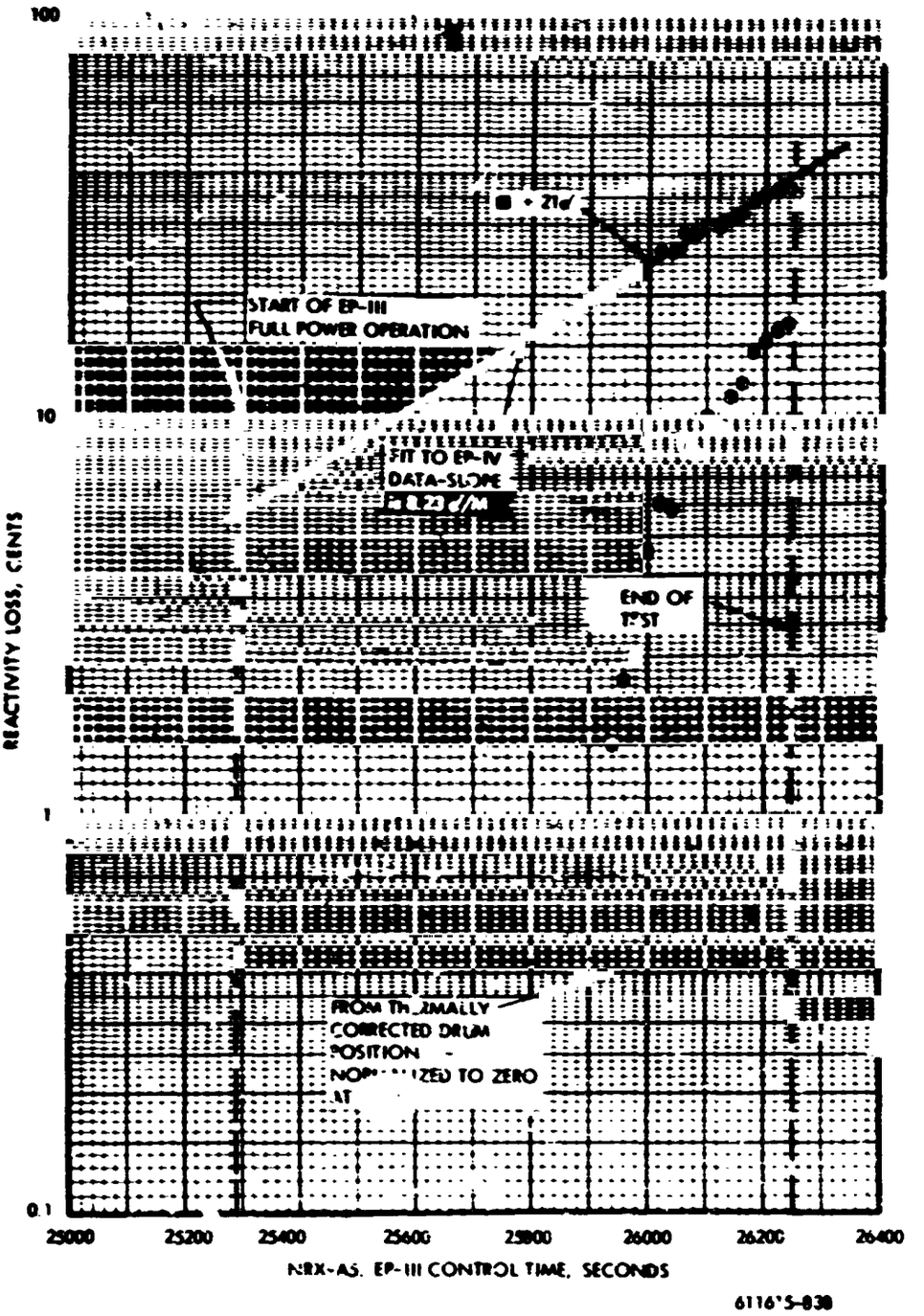

Figure 7-15. NRX-A5 Reactivity Loss in EP-III

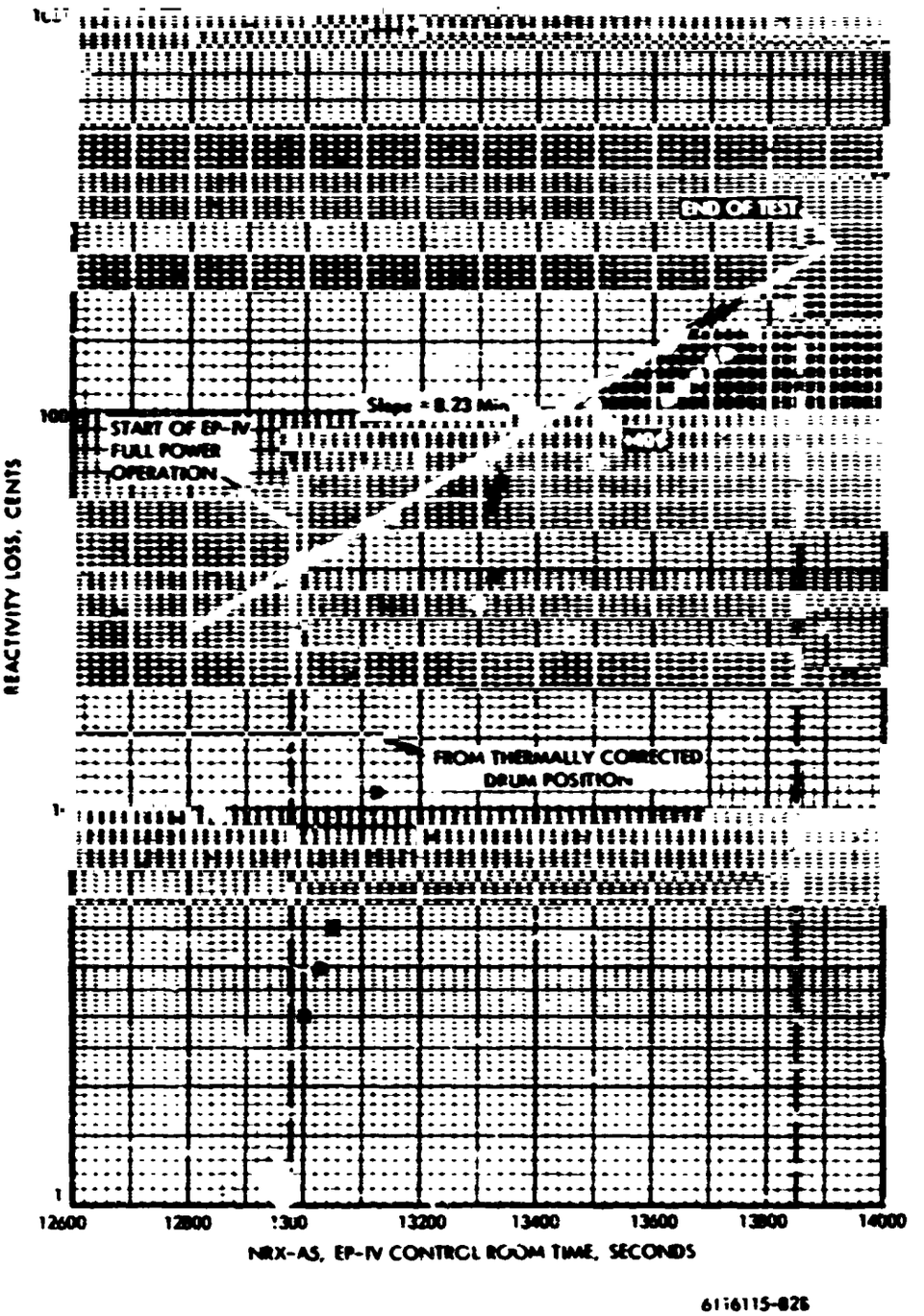

Figure 7-16. NRX-A5 Reactivity Loss in EP-IV

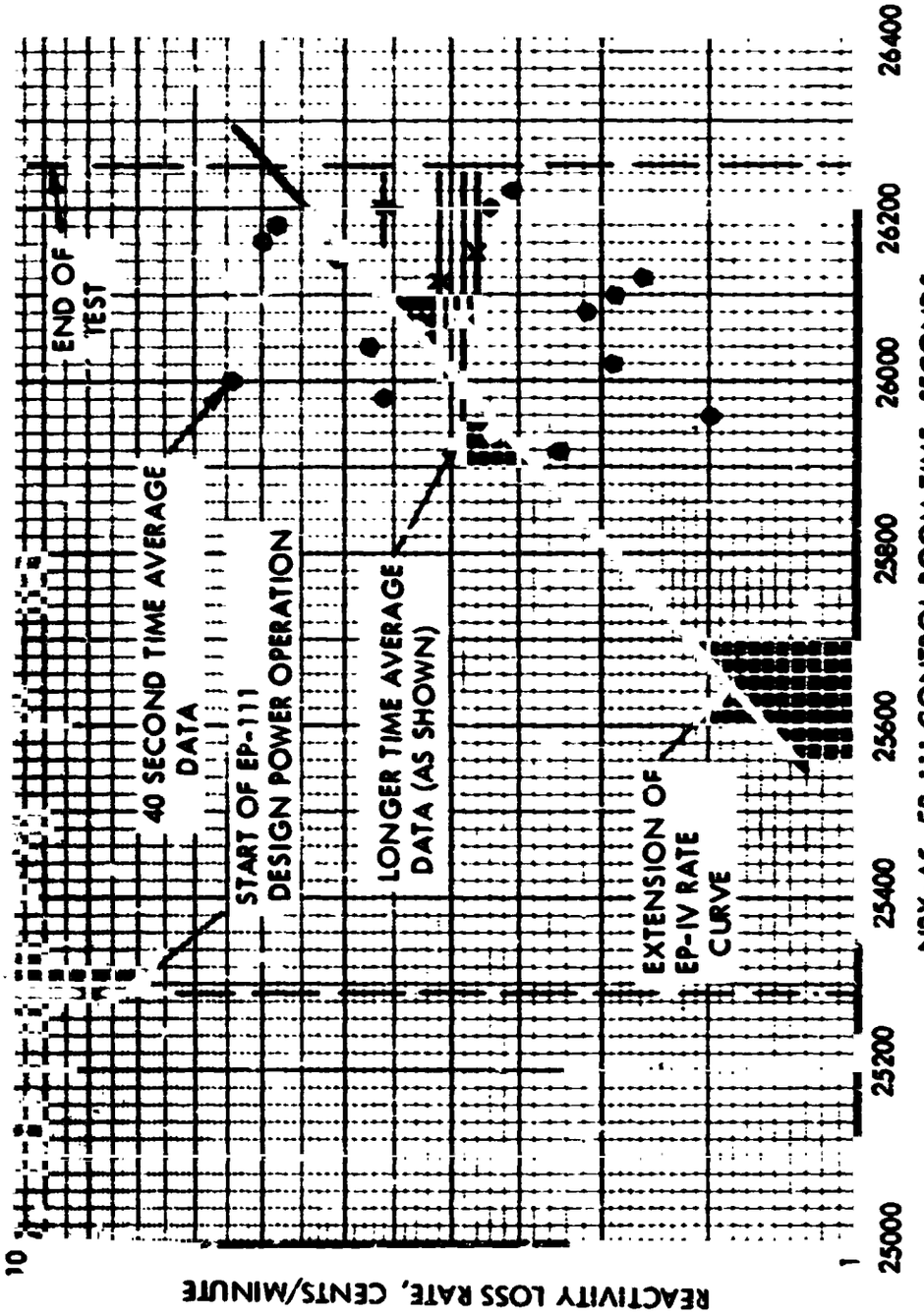

611615-848

Figure 7-17. NRX-A5 Reactivity Loss Rate in EP-III

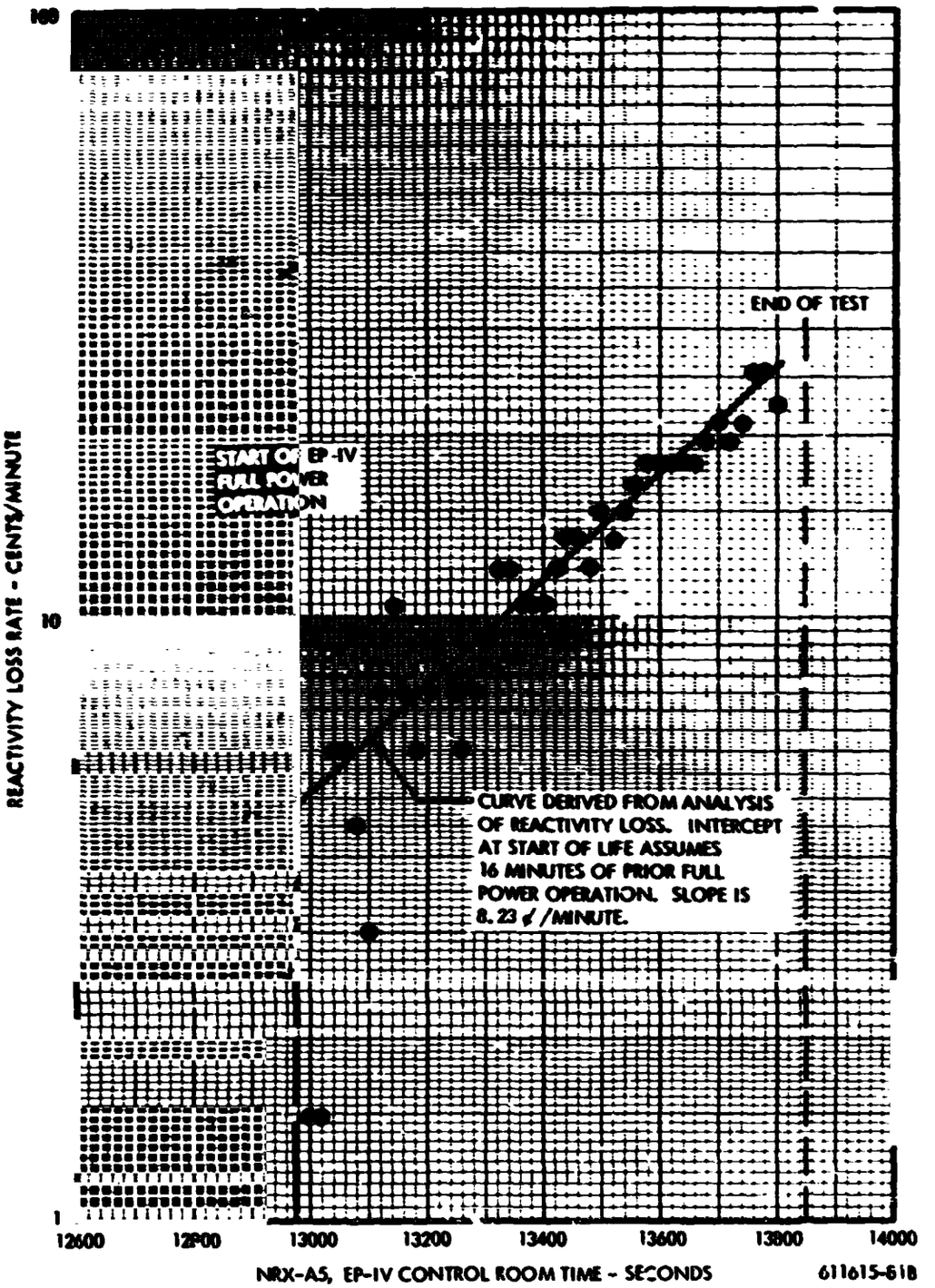

Figure 7-18. NRX-A5 Reactivity Loss Rate in EP-IV

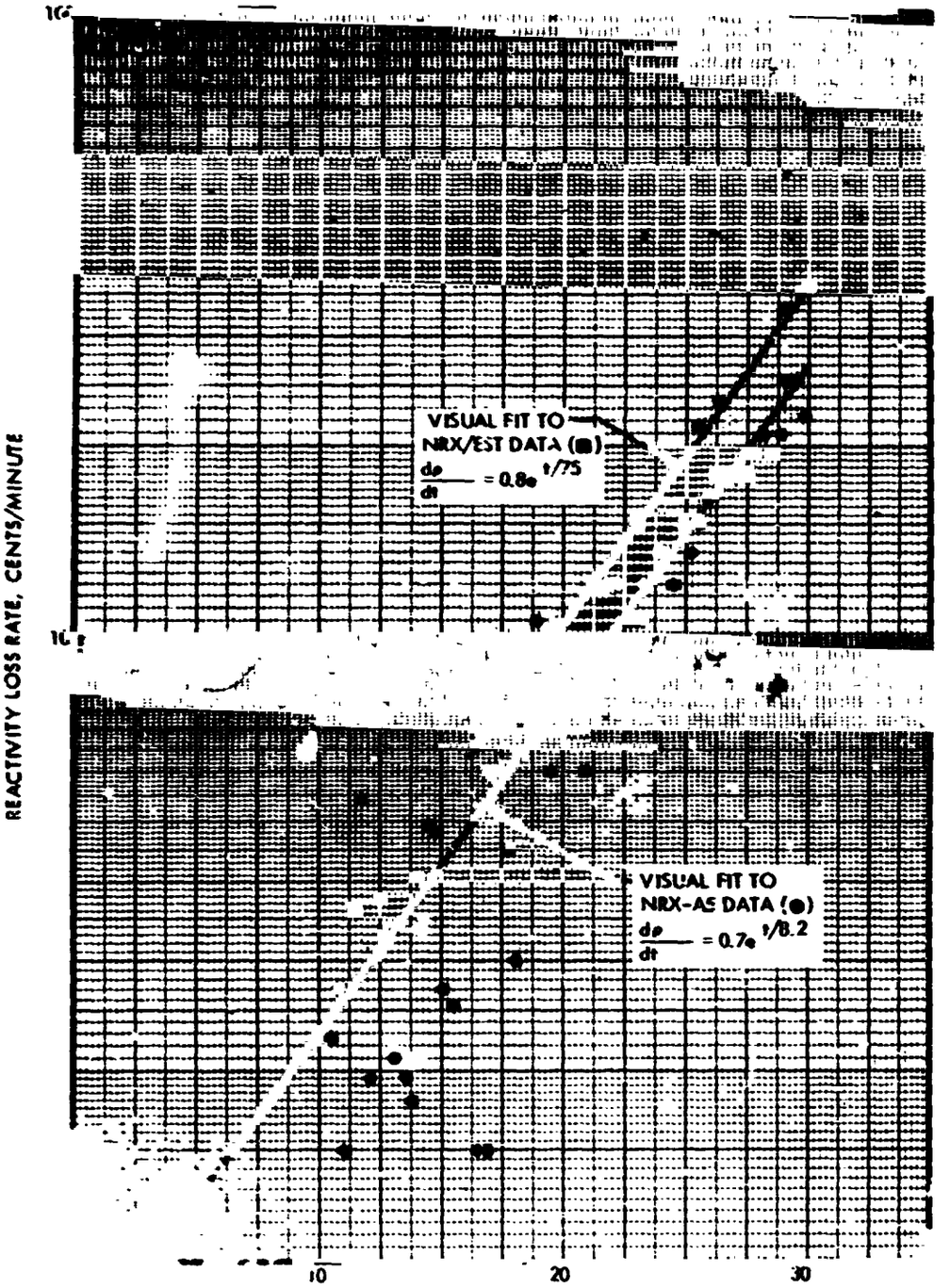

Time Behavior of Reactivity Loss Rate

The following equations for reactivity and reactivity loss were obtained from the visual fits to the NRX/EST and NRX-A5 data.

NRX/EST:

$$\rho = 6.0 (\exp (t/7.5) - 1.0) \quad (7-10)$$

$$d\rho/dt = 0.8 \exp (t/7.5) \quad (7-11)$$

NRX-A5:

$$\rho = 5.7 (\exp (t/8.23) - 1.0) \quad (7-12)$$

$$d\rho/dt = 0.7 \exp (t/8.23)$$

where:

ρ = reactivity loss, cents,

$d\rho/dt$ = reactivity loss rate, cents/minute, and

t = time, minutes.

As noted above, a single line was used to fit the reactivity loss rate data for the entire NRX-A5 test. It was not possible to determine whether the reactivity loss rate in the first power test differed from the rate in the second power test because of the large scatter in the reactivity loss rate data for the first power test. Figure 7-17 shows this reactivity loss rate data for the first power test.

In order to provide a firmer basis for the choice of the above functions, a statistical analysis of reactivity loss and reactivity loss rate data for NRX-A5 EP-III and IV was performed with a multiple regression computer code. In simple terms the purpose of the analysis was to determine whether the corrosion rate was truly exponential with time, or whether it could be fit equally well with other simple functions.

Table 7-16 gives the results of this analysis along with the correlation[1] coefficient and the expression for the best polynomial or exponential fit to the NRX-A5 reactivity loss and loss rate data. It should be noted that the equations in Table 7-16 have not been corrected for initial reactivity losses. That is, the equations are those which are obtained when the reactivity loss is equal to zero at the beginning of the test. Therefore, the multiplicative constant in the exponential fit of the data will not agree with the constant obtained graphically. However, the time constant, T, in these equations is comparable.

The most reliable data, which is the reactivity loss data for EP-IV, indicated that an exponential fit of the data is a significantl, better fit than a polynomial function. The reactivity loss data for EP-III and the reactivity loss rate data for EP-III and EP-IV did not indicate any significant difference in the correlation of an exponential or polynomial function.

As an additional test, the expressions fitting the cumulative reactivity were differentiated and compared with independently derived expressions fitted to the reactivity loss rate data. (The comparable numbers are 2.28 and 2.01 for EP-III and 4.97 and 5.4 for EP-IV.) This close agreement is not true of the best polynomial fits to the reactivity loss data. Therefore, considering the foregoing discussions, it is concluded that an exponential function is the best fit of the experimental data.

The total reactivity loss by this technique for the NRX-A5 was obtained by evaluating equation (7-12) above for 30.23 minutes of full power operation. The value obtained is 218.7¢ in reasonable agreement with the 235.8¢ obtained from the shift in ambient critical positions. A similar comparison with the reactivity loss from the drum motion at full power is more instructive if only EP-IV data are used, because of the varying thermal conditions in EP-III noted previously. In EP-IV the drum motion at full power indicates a reactivity loss of 170¢, in contrast with the 184.7¢ value derived from equation (7-12). Although the agreement is reasonably good, it appears that the operating reactivity is influenced by factors other than corrosion, e.g., the propellant diffusion effect believed to occur in the early stages of a

1 The correlation coefficient is a measure of how well the experimental data is explained by the analytical function which is fit to it.

TABLE 7-16

REGRESSION ANALYSIS OF NRX-A5 REACTIVITY LOSS AND LOSS RATE DATA

Case	Regression Fits to Total Loss and Loss Rate	Time Devivative of Regression Fits of Total Loss	Correlation Coefficient
Reactivity Loss EP-III	$\rho = 21.0\ (e^{t/9.2} - 1.0)$	$d\rho/dt = 2.28\ e^{t/9.2}$	0.94
	$\rho = 0.70468 + 0.05176t$	$d\rho/dt = 0.05176$	0.94
Reactivity Loss Rate EP-III	$d\rho/dt = 2.01\ e^{t/9.2}$		0.23
	$d\rho/dt = 2.06471 + 0.00524t$		0.21
Reactivity Loss EP-IV	$\rho = 40.0\ (e^{t/8.05} - 1.0)$	$d\rho/dt = 4.97\ e^{t/8.05}$	0.99
	$\rho = 0.67394 + 0.06585t + 0.00001t^2$	$d\rho/dt = 0.06585 + 0.00002t$	0.74
Reactivity Loss Rate EP-IV	$d\rho/dt = 5.4\ e^{t/8.5}$		0.87
	$d\rho/dt = 6.449 + 0.00003t^2$		0.84
Visual Fit to Cumulative Reactivity Loss	$\rho = 5.7\ (e^{t/8.23} - 1.0)$		

Astronuclear Laboratory

test. This process has been found previously to cancel the apparent reactivity loss in the early part of a power run.

The early analysis based on preliminary data that resulted in the anomalous 50¢ difference mentioned in Section 7.5.2 is now changed as follows. While the net reactivity loss in EP-IV was 170¢, the analysis described above shows that the permanent reactivity loss due to corrosion is in reality about 185¢. The reactivity loss from the pre- and post-test criticals as shown in Section 7.5.2.1 is 213¢ for EP-IV alone. Thus, the unexplained difference has been reduced from 50¢ to (213.3 - 184.7 =) 28.6¢.

Two factors have been investigated in an attempt to explain this discrepancy, namely (1) redistribution of flow and (2) hydrogen accumulation in the void space created in the fuel by the action of corrosion in removing fuel material.

A radial redistribution in propellant flow occurs during operation as the control drum angle steadily increases. As the control drums rotate outward to maintain criticality, temperatures in the peripheral fuel elements rise causing an increased flow impedance in the peripheral coolant channels. At constant total flow this results in an increased coolant flow to the central channels where the hydrogen worth is increased. Thus a net reactivity gain is produced, which would tend to mask the reactivity loss due to corrosion. The effect was evaluated by examination of two MCAP calculations which approximated[1] start-of-life and end-of-life conditions in EP-IV. A comparison of the coolant density distributions from these two runs is shown in Figure 7-20. These two profiles were then weighted by the

(1) number of channels each calculation point represented,

(2) the area of the coolant channels for each of the points, and

(3) the radial variation in the hydrogen worth (from WANL-TME-936).

The results are summarized in Table 7-17. Note that due to small differences in the two MCAP runs a minor correction is required (Step c) to put the calculations on the same basis (equal average density). The resulting increase in core hydrogen worth is only 1¢, well within the convergence of the MCAP runs, and is considered negligible.

---

1 MCAP runs for 115 degrees and 140 degrees were used. Actual drum motion in EP-IV ranged from about 115 degrees to about 146 degrees.

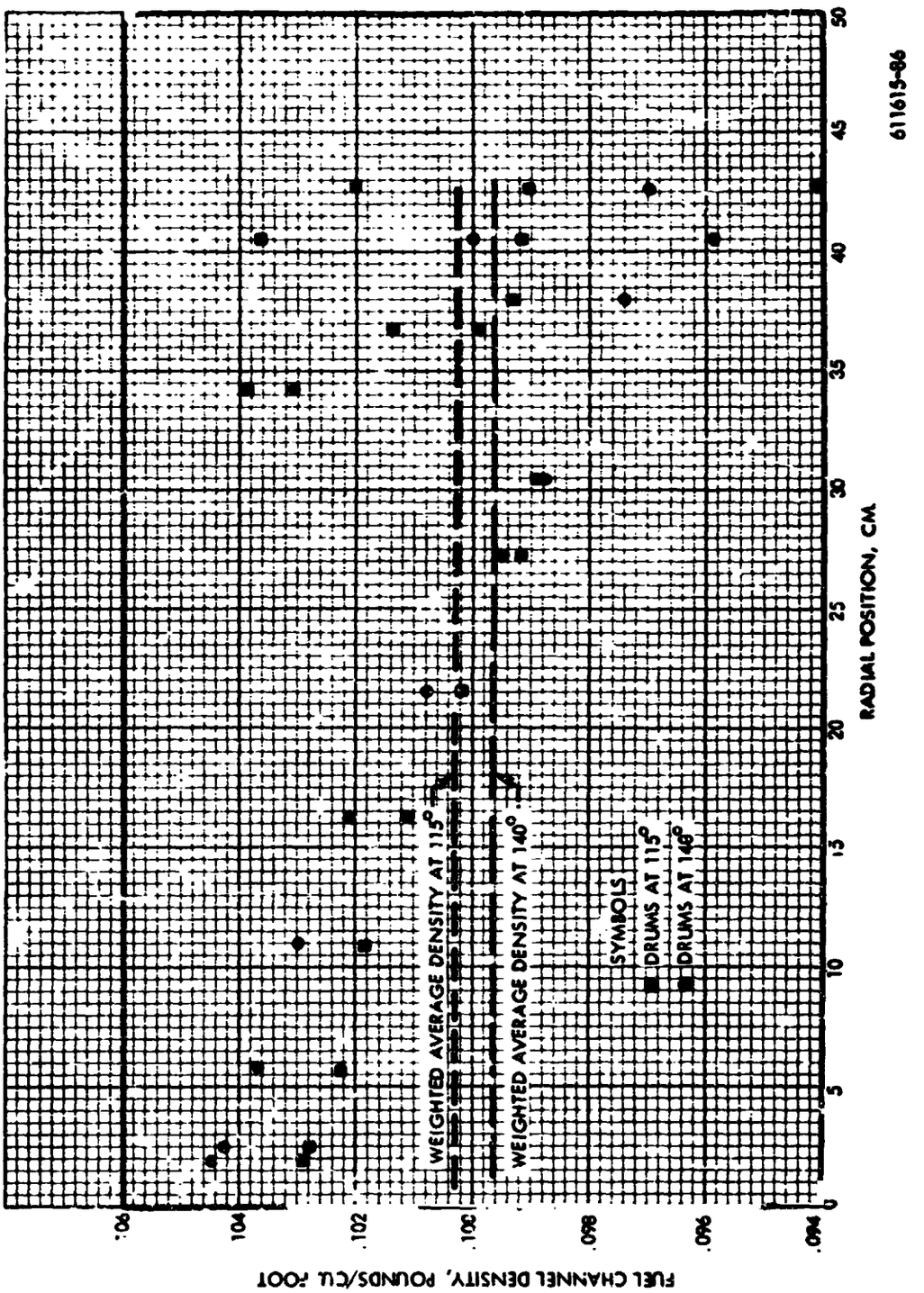

Figure 7-20. Variation with Azimuthal Position of Radial Fuel Channel Coolant Density-MCAP Calculation

TABLE 7-17

SUMMARY OF REACTIVITY EFFECTS RESULTING FROM PROPELLANT FLOW REDISTRIBUTION

A. Total Relative Reactivity Worth of H_2 at 140° = 0.6115

Average density at 140° = 0.09966 lb/ft^3

B. Total Relative Reactivity Worth of H_2 at 115° = 0.6125

Average density at 115° = 0.10033 lb/ft^3

C. At the same density as 115° the relative reactivity worth at 140° is

$$0.6115 \frac{0.10033}{0.09966} = 0.6156$$

D. Ratio of Reactivity Worths

$$\frac{\text{at } 140^\circ}{\text{at } 115^\circ} = \frac{0.6156}{0.6125} = 1.005$$

E. Change in Worth of Core Hydrogen

$$= (1.005 - 1.0) \ \$1.75^{1} \cong 1¢$$

---

[1] Approximate worth of core hydrogen.

The second factor investigated, accumulation of propellant in the corroded areas, proved to be more important. Based on the measured weight loss distributions[1], the total volume available to hydrogen was calculated assuming that the material lost was graphite with density 1.86 gm/cc. The reactivity worth of this hydrogen was found to be 23¢ assuming axially uniform hydrogen at a density of 0.1 lb/ft^3. In this analysis two simplifications were made. First, the void volume is created preferably near the core midplane, due to midband corrosion, which acts to increase the worth of the accumulated hydrogen by about 27 percent. Second, the local hydrogen density at this station is considerably less than the axial average density. At station 22 and downstream the corrosion is highest. The combined effect of these factors is to reduce the worth of the accumulated hydrogen. Thus 23¢ probably represents an upper limit. The calculation is summarized in Table 7-18.

In summary, the discrepant 28.6¢ seems to be reasonably well explained by the accumulation of propellant in the corroded areas.

7.5.2.3 Comparison of KIWI B-4E, PHOEBUS 1A, NRX-A3 and NRX/EST Reactivity Loss Rate Information

Analysis of the reactivity loss rates experienced by KIWI B-4E, PHOEBUS 1A, NRX-A3 and NRX/EST was performed to determine whether any significant differences in the corrosion rates existed. Data for this analysis was determined in a manner similar to that discussed above. The results of this analysis are shown in Figure 7-21, reproduced here from WANL-TNR-216.[2]

It was found that no significant difference in reactivity loss rate could be distinguished in the PHOEBUS 1A, NRX-A3 and NRX/EST power tests. Although the KIWI B-4E appeared to have a different rate of loss, this particular analysis is not considered to have great validity, as substantial analytical adjustments were made in the interpretation (the uncorrected trend of reactivity change in KIWI B-4E actually showed an anomalous increase in the early part of the power run).

---

1 See Chapter 6.

2 WANL-TNR-216, "NRX/EST Reactor Test Analysis Report", 12/66.

TABLE 7-18

HYDROGEN WORTH CALCULATIONS

Region Radial Position, Inches	Number Of Elements In Region	Measured Average Weight Loss Per Element,[1] gms	Total Volume,[2] cc	A Mass H_2,[3] gms	B H_2[4] Worth, ¢/gm
0-9	426	43.3	9917	15.9	0.85
9-14	624	15.1	5066	8.1	0.59
14-17	534	27.3	7838	12.6	0.38
				$\sum A \times B$	23¢

[1] Data taken from Table 5-2.

[2] Calculated assuming a density for material lost of 1.86 gm/cc (for graphite).

[3] Assumed density of H_2 is 0.1 lb/ft^3.

[4] Worths taken from WANL-TME-936, "Development of a Method for Computing the Cold-to-Hot Reactivity Change in the NRX-A Assemblies", 9/64.

CONFIDENTIAL

Astronuclear Laboratory

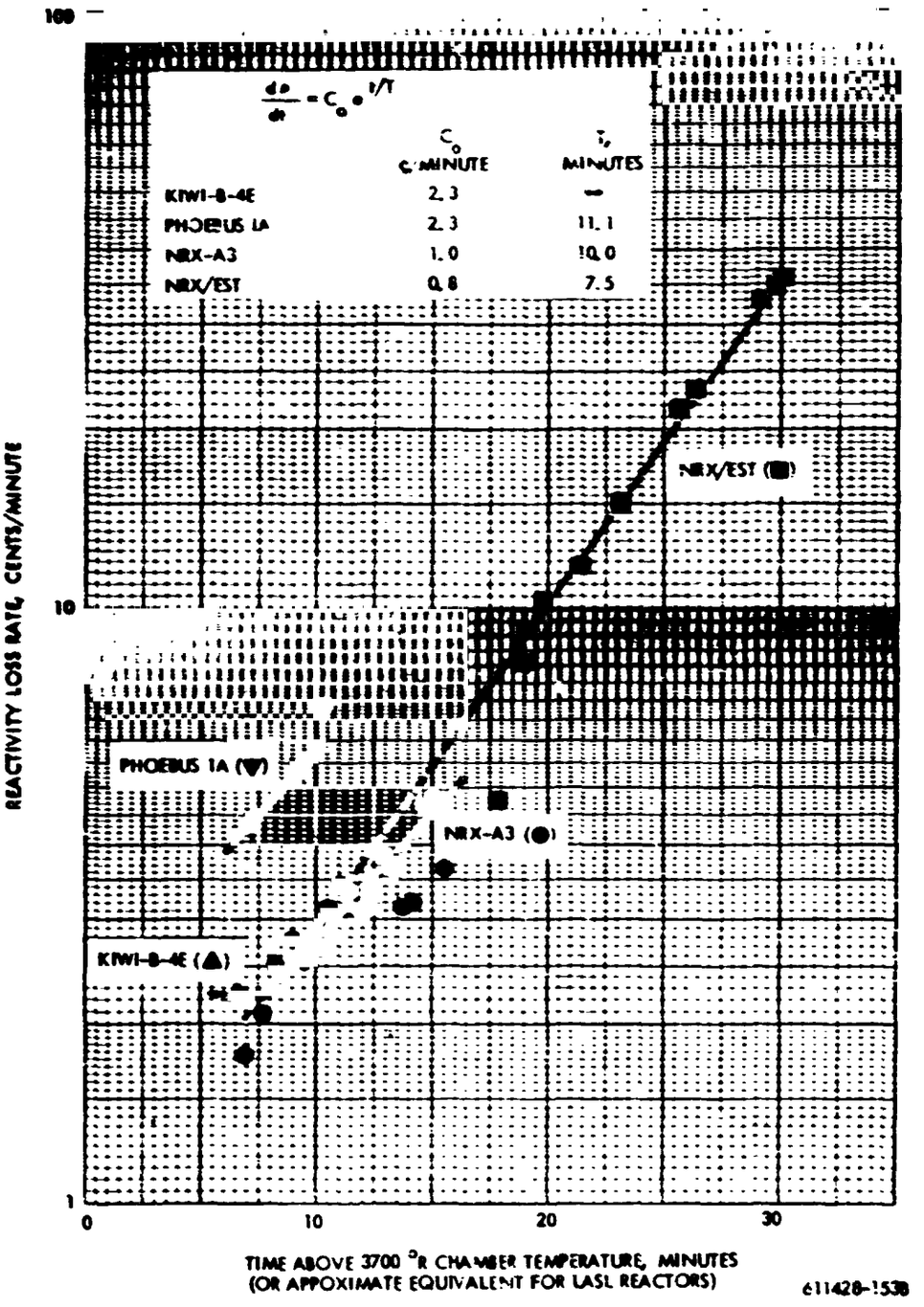

Figure 7-21. Summary of Reactivity Loss Rate Experience to Date

7.5.2.4 Conclusions

The total reactivity loss in the NRX-A5 test series was 2.36$, as calculated from the difference in ambient critical positions at the start and end of the series.

The variation of the loss with time was found to be an increasing exponential, as in the NRX/EST test:

$$\Delta\rho\ (\$) = 5.7\ (\exp\ (t/8.23) - 1.0)$$

where t is in minutes.

The 50¢ discrepancy in EP-IV between the apparent reactivity loss from the critical positions at power and that inferred from the pre- and post-test criticals is tentatively explained as the result of hydrogen accumulation in the corroded areas and hydrogen diffusion into the natural pores of the fuel in the early stages of the test.

7.6 NUCLEAR ANALYSIS OF POWER RUNS

The two power tests performed during the NRX-A5 test series provided little new opportunity to evaluate the analytical feedback reactivity model.[1] This opportunity had been provided in abundance by the NRX/EST test program, in which reactivity was measured over a broad span of reactor operating power and flow conditions. This permitted an empirical reactivity equation to be derived by a least squares linear fit to the NRX/EST data in terms of two parameters, chamber temperature T_c and (P_c/T_c), the ratio of chamber pressure to chamber temperature, which is approximately proportional to propellant density. For convenience, this map has been reproduced in Figure 7-22. The equation derived for the net reactivity change from ambient to any operating point is as follows:

$$\Delta\rho\,(¢) = 34.2 - 0.0601\,T_c + 978.\,P_c/T_c \qquad (7\text{-}13)$$

The analyses of the two cold-to-hot swings in EP-III and EP-IV have been mentioned briefly above in Section 7.3.5. A summary of these calculations is shown in Table 7-19. The upper part of the table shows the reactivity swing as calculated by the empirical equation. A correction for delayed neutron precursor non-equilibrium has been included in the "Total Calculated Reactivity Change" shown in the last column. In the lower half of the table, the measured change in drum position is shown and is converted to reactivity on the basis of two different drum spans. Using the reactivity based on the 8.2S drum span, the difference between the measurement and the calculation ranges from 2.7¢ to -3.8¢. The significance of this difference can be determined by considering (1) the uncertainties in the empirical fit and (2) the unknown but probably substantial uncertainties inherent in the non-equilibrium correction and in our understanding of the fluid flow differences between the NRX-A5 and NRX/EST reactors with regard to feedback reactivity.

One of these factors may be readily calculated. The best estimate of the one sigma uncertainty in the empirical fit is + 7.25¢, with a 98 percent confidence range from 5.22¢ to

1 Appendix A

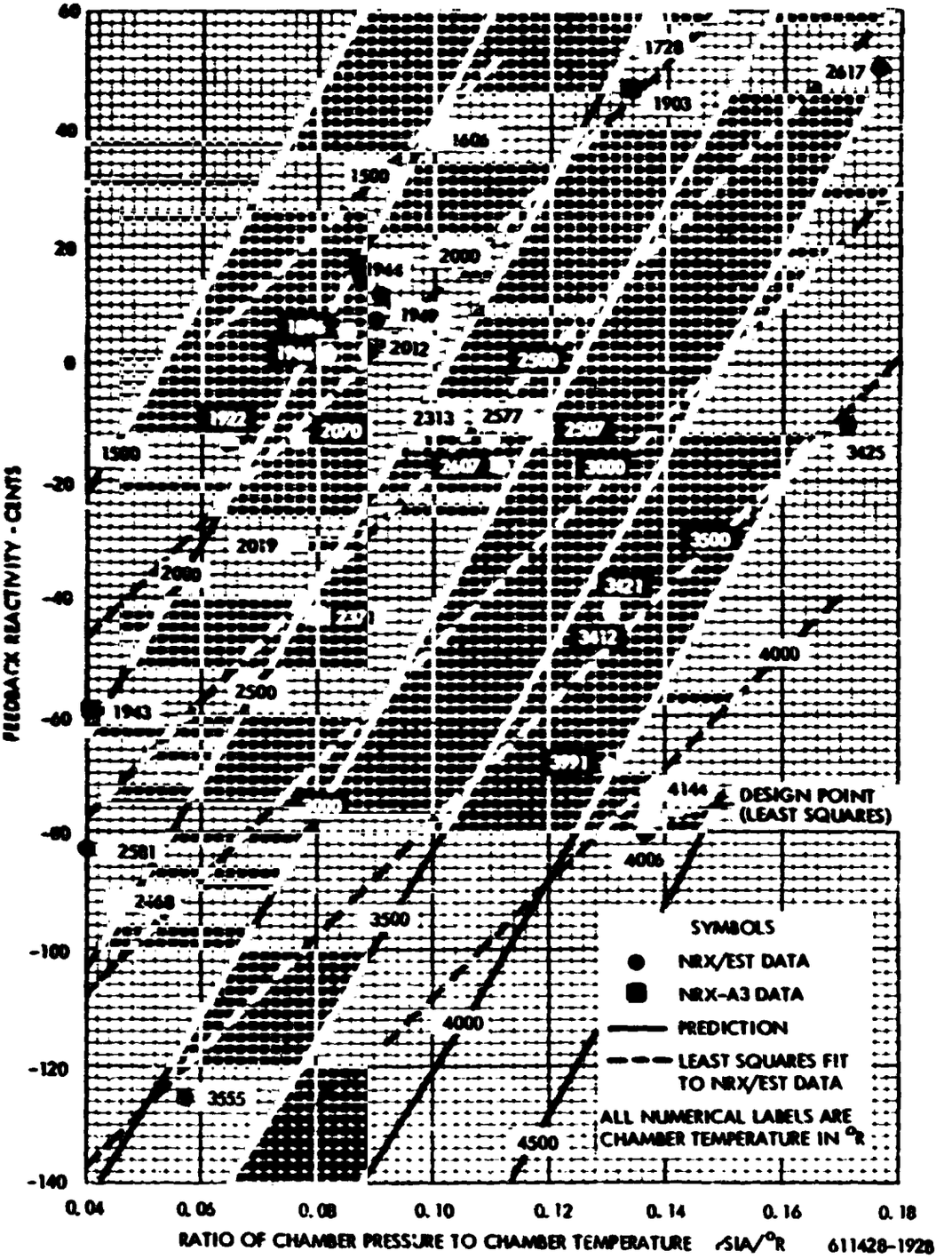

Figure 7-22. NRX/EST Performance Map

TABLE 7-19

SELECTED NRX-A5 COLD-TO-HOT SWING CALCULATIONS

Case	Test	CRT, sec.	$P_{c'}$ Psia	$T_{c'}$ °R	Δρ from Formula, [1] ¢	R-102 Correction for Non-equilibrium, ¢	Total Calculated Reactivity Change at This CRT, [2] ¢
1	EP-III	25300	555.165	3854.258	-56.6	+12.0	-68.6
2	EP-IV	12975	569.599	4169.391	-75.5	+ 5.9	-81.4

Case	Cold Critical Position (at 540°R), Degrees	Hot Critical, Degrees	(¢) Cold-to-Hot Swing to this CRT Based on Drum Span of: 8.2$	8.5$ (prediction)
1	99.3	108.8	-65.9	-68.3
2	102.4	115.0	-85.2	-88.4

[1] Least squares fit to NRX/EST data: $\Delta\rho = (34.2 - 0.0601\ T_c + 978.\ P_c/T_c)$ ¢

[2] (Δρ) - (R102 correction) = Total reactivity change

[3] Calculated from formula $\Delta\rho = W\ (1-\cos\theta_{hot}) - W\ (1-\cos\theta_{cold})$ where W is half worth (4.1 and 4.25 here).

Astronuclear Laboratory

11.63¢. Thus, from this viewpoint alone the differences quoted above are insignificant and the NRX-A5 reactivity feedback is well represented by the NRX/EST empirical model.

CHAPTER 8

DOSIMETRY *

8.1 SUMMARY

During the testing of the NRX-A5 reactor, a dosimetry program was carried out which resulted in the measurement of gamma ray dose rates, fast neutron fluxes (E>2.9 Mev) and thermal neutron fluxes (E<0.4 ev) at 57 locations around the facility.
Since the NRX-A5 reactor test configuration was very similar to the NRX-A3 reactor the philosophy of the A5 dosimetry program was to obtain data which would fill in the gaps and areas of uncertainty in gamma and neutron data measured during the NRX-A2, NRX-A3, and NRX/EST reactor tests in an effort to understand more thoroughly the radiation patterns around the NRX test facility.

The NRX/EST reactor was operated in a different facility environment than either the NRX-A2, NRX-A3, or NRX-A5. The main differences were in the privy roof mounted shield and direct component shield which were used to protect engine components mounted on the test car during the NRX-A4 tests. However, there are areas around the NRX-A4 which should have the same radiation environment as the NRX-A5; where this is the case, the NRX/EST data are included in comparisons.

Based on the NRX-A2 through NRX-A5 dosimetry test data, along with calculations where needed, typical radiation patterns around an NRX reactor in Test Cell "A" were determined. The data are presented in forms of iso-flux contours for fast neutrons, iso-dose rate contours for gamma rays, and iso-heating rate contours for radiation heating in aluminum.

Measurements obtained during the NRX-A5 reactor test included: fast neutron fluxes (E>2.9 Mev), thermal neutron fluxes (E<0.4 ev), gamma ray dose rates, and calorimetric heating rates.

---

*Major contributors to this chapter were M. A. Capo and R. N. Nassano
**Superscripted numbers in this chapter are keyed to References listed in paragraph 8.10.

Fast neutron fluxes (E>2.9 Mev) were obtained using sulfur pellets. These data were in good agreement with similar data obtained during the previous reactor tests.

Thermal neutron fluxes (E<0.4 ev) were also measured using bare and cadmium covered gold foils. These data were generally in good agreement with previous test data where comparisons are valid.

Gamma ray dose rates were measured using thermoluminescent detectors and silver metaphosphate glass detectors. At locations close to the reactor, i.e. up to five feet from the center of the core, the NRX-A5 measurements were in reasonable agreement with previously measured gamma ray dose rates. In general, the gamma ray data obtained at greater distances were found to be less reliable than that obtained from the earlier reactor tests. This can be attributed to the uncertainties in the high gamma ray background at the test facility from the testing of previous reactors.

Six calorimeters (four aluminum, one beryllium and one steel) were tested during the NRX-A5 high power runs. These calorimeters were of a slightly different design than calorimeters used in the previous NRX reactor tests. Essentially, the design changes improved the calorimeters from a mechanical standpoint but slightly degraded the calorimeters from a thermal standpoint. The deficiencies in the NRX-A5 calorimeter design are being corrected for those calorimeters to be used during the NRX-A6 reactor test.

8.2 EXPERIMENTAL PROGRAM

An experimental radiation measurement program was carried out in conjunction with the NRX-A5 reactor test. The objectives of the NRX-A5 radiation measurements program were: (1) to resolve discrepancies observed in the experimental data obtained during the NRX-A2, NRX-A3, and NRX/EST reactor tests, (2) to determine the radiation environment at locations that were not covered during previous reactor tests, and (3) to gain a better understanding between calculated and measured data.

Radiation measurements were made during the low power reactor runs, EP-I and EP-II. Independent determination of the total power generated during these runs was necessary to normalize the dosimetry data to a one watt power level. The integrated power levels for EP-I and EP-II as reported by the test site (Reference 1) are 5.3×10^6 and 6.1×10^7 watt-seconds, respectively.

The dosimetry program employed in the NRX-A5 test was of the passive or integral type. Two types of gamma ray dosimeters were used: silver metaphosphate glass plates and Li-7 fluoride thermoluminescent detectors. Cold foils were exposed with and without cadmium covers to obtain thermal neutron fluxes. Sulfur pellets provided neutron fluxes for an energy threshold of 2.9 Mev.

Table 8-1 presents the following data for each NRX-A5 dosimeter placement: identification number, station (inches), radius (inches), and reactor azimuth angle (cylindrical coordinate system). Reactor stations specify the axial distances in inches from the inlet end of the reactor core. Positive numbered stations are located toward the nozzle end of the core. Reactor θ is the core azimuth angle defined such that $\theta = 0^\circ$. It is located 120° from the normal to the test cell wall (measured counterclockwise, looking down).

Figure 8-1 is a sketch of the reactor assembly and associated facility shielding showing the location of some 35 detector points. All of the data points shown in Figure 8-1 are considered to be in a plane containing the reactor axis and normal to the reactor wall. In addition, fourteen dosimeter packets were positioned on the dosimeter pole which was mounted on top of the privy roof shield.

Figure 8-2 shows a view of the test cell wall and the locations of the 6 points at which dosimetry data were obtained during the NRX-A5 power runs. Figure 8-3 shows the location of dosimeters on the test cell pad.

TABLE 8-1

LOCATION OF NRX-A5 DOSIMETRY

General Description	Identification	θ (degrees)	Radius (inches)	Elevation (inches)
Nozzle Manifold	N 1	120	16	106.5
(See Figure 8-1)	N 2	300	16	106.5
Nozzle Flange	NF 1	120	23	63.2
(See Figure 8-1)	NF 2	300	23	63.2
Transducer Box	TB 1	300	63.4	-113.2
(See Figure 8-1)	TB 2	300	63.4	-124
	TB 3	300	63.4	-140.4
	TB 4	300	84	-113.2
	TB 5	300	84	-124
	TB 6	300	84	-140.4
Privy Roof Top	P 1	190	30	- 51
(See Figure 8-1)	P 2	190	15	- 51
Test Car	CA 1	120	66	-108
(See Figure 8-1)	CA 2	120	83	-106
	CA 3	120	108	-106
	CA 4	120	136	-106
	CA 5	120	84	-125.5
	CA 6	120	84	-112
	CA 7	120	84	- 89
	CA 8	120	84	- 65
Calorimeter Locations	C 1	345	300	26
(See Figure 8-1)	C 2	155	34	- 17.8
	C 4	32	0	- 55
	C 5	126	52.4	- 51
Inside Privy	IP 1	0	0	-104
(See Figure 8-1)	IP 2	0	0	-146
	IP 3	0	0	- 74.5
Dosimeter Pole	DP 1	323	47	- 40
(Shown In Figure 8-1)	DP 2	323	47	- 30
	DP 3	323	47	- 20
	DP 4	323	47	- 15
	DP 5	323	47	- 10
	DP 6	323	47	0
	DP 7	323	47	10
	DP 8	323	47	40
	DP 9	323	47	50
	DP 10	323	47	60
	DP 11	323	47	70
	DP 12	323	47	80
	DP 13	323	47	90
	DP 14	323	47	100
Trolley Line	TL 1	355	750	26
	TL 3	355	3600	26
Test Cell Wall	TCW 1	197	680	26
(See Figure 8-2)	TCW 2	190	450	26
	TCW 3	120	156	26
	TCW 4	120	156	- 10
	TCW 5	120	156	- 70
	TCW 6	120	156	-130
Test Cell Pad	TP 1	194	437	-182.3
(See Figure 8-3)	TP 2	200	673	-182.3
	TP 3	300	350	-182.3
	TP 4	300	600	-182.3
Pressure Vessel Surface	SP 1	240	25	50
	SP 2	240	25	26
	SP 3	240	25	2
Near Shield Flange	SD 1	240	21.5	- 15

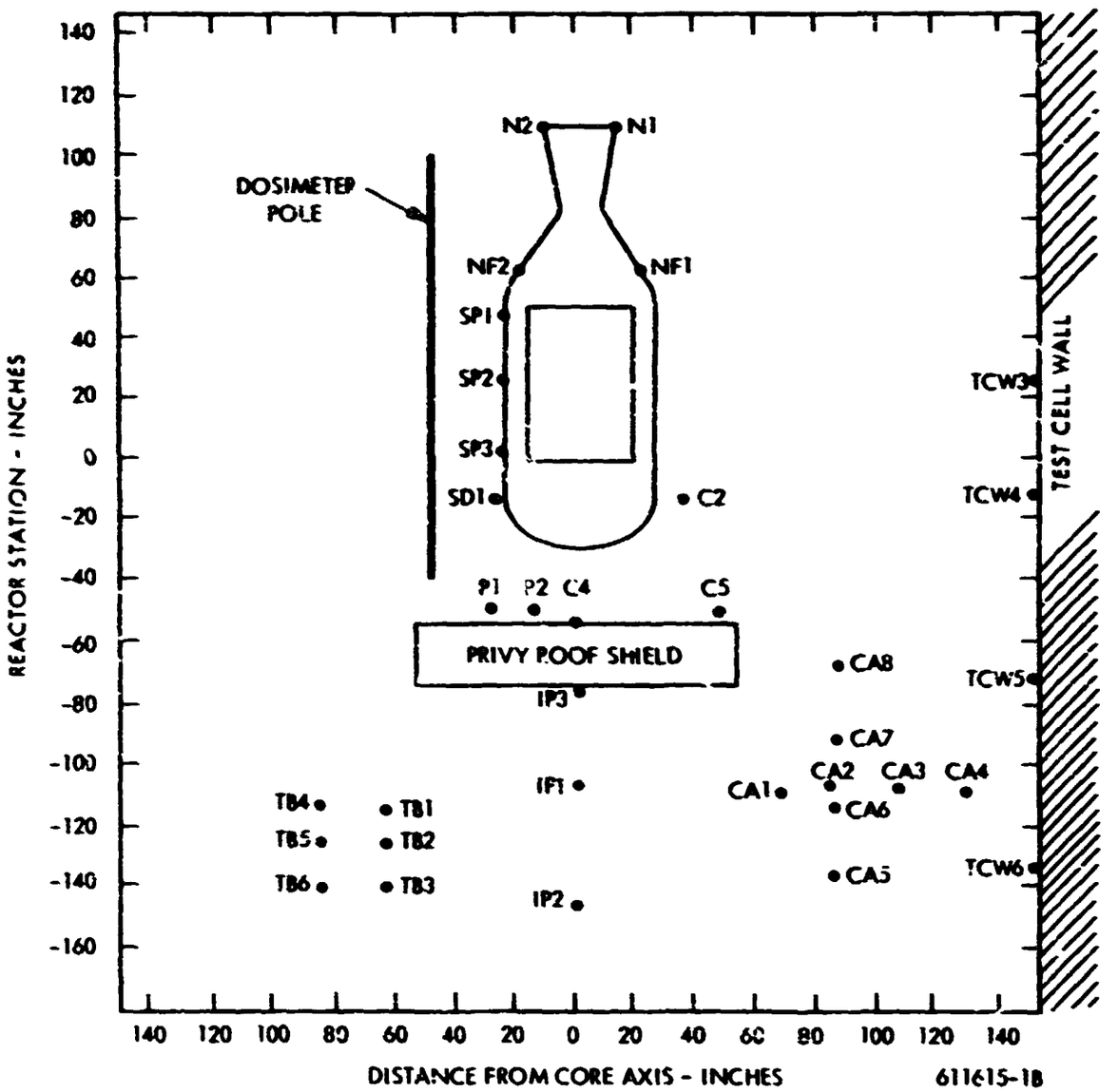

Figure 8-1. Cross Sectional View of NRX-A5 Showing Dosimeter Locations

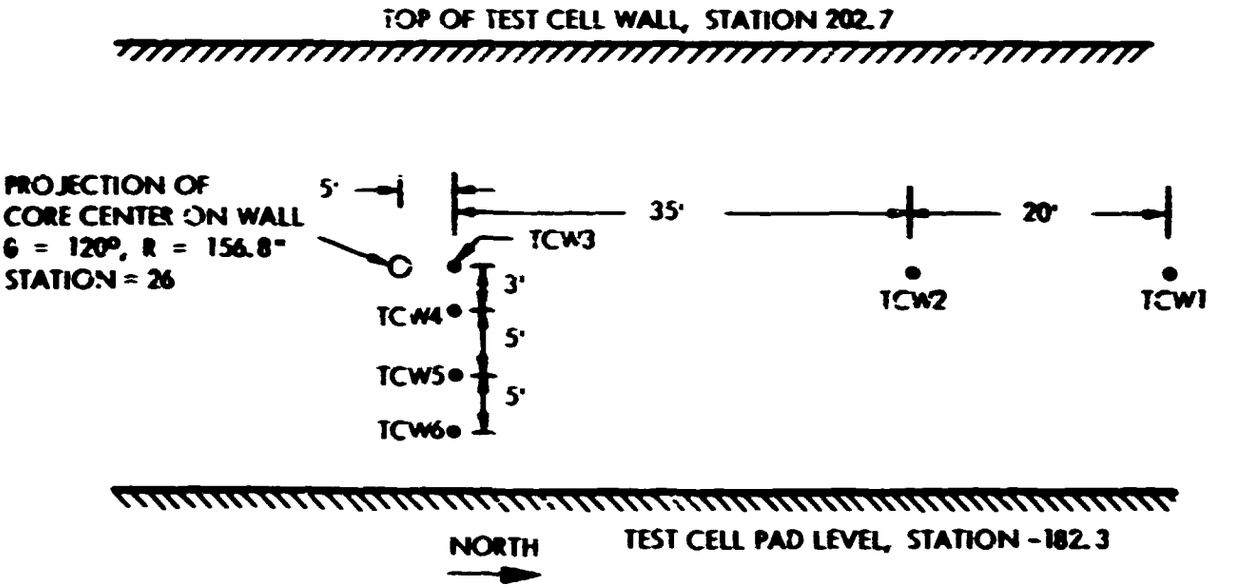

Figure 8-2. Elevation View of Test Cell Wall Showing NRX-A5 Dosimeter Locations

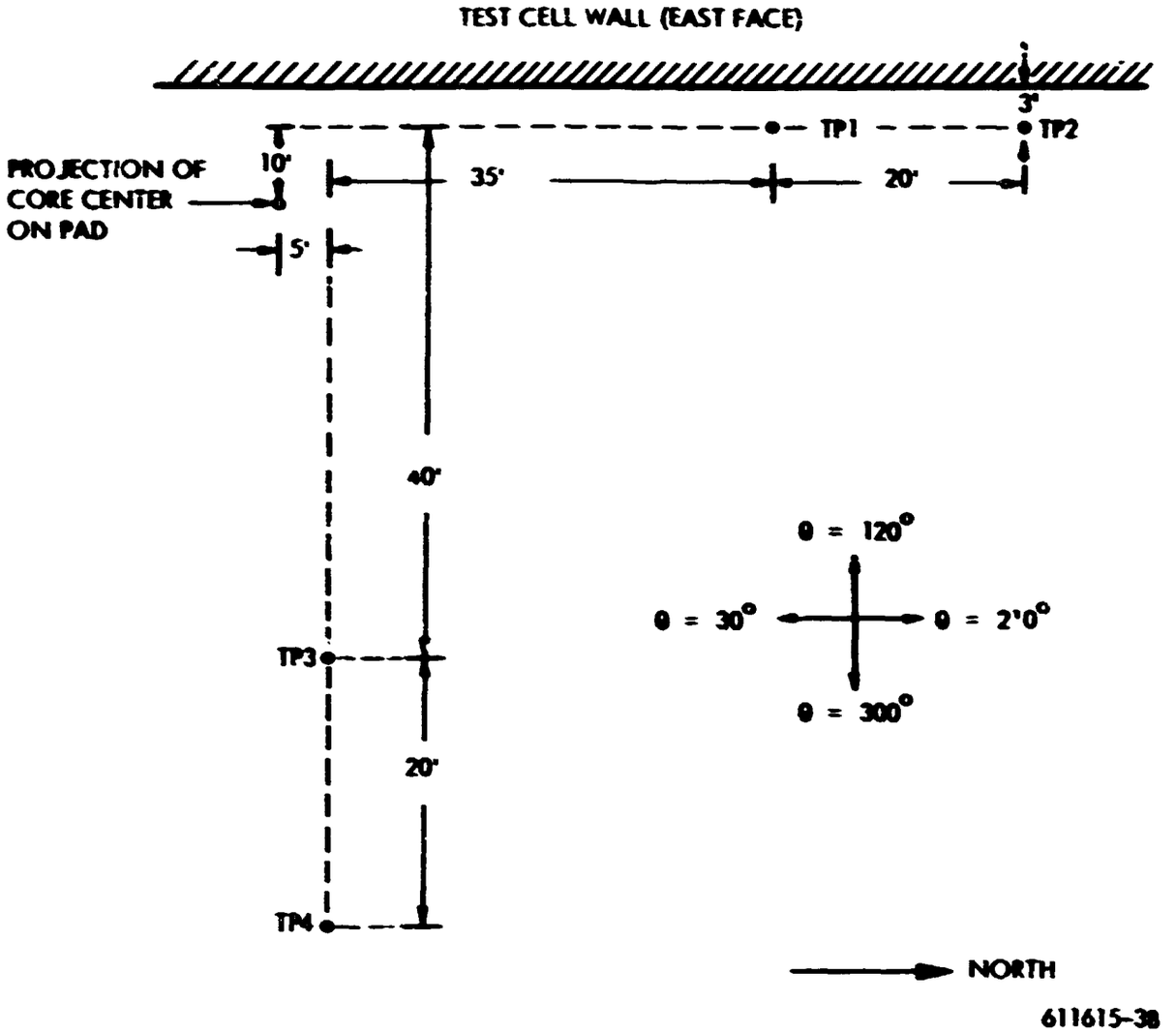

Figure 8-3. Plan View of Test Cell Pad Showing NRX-A5 Dosimeter Locations

8.3 ANALYTICAL METHODS

The NRX-A2, NRX-A3, NRX/EST and NRX-A5 reactors were all very similar in design. Hence the radiation environment surrounding these reactors (with one exception) are also very similar. The one exception is the NRX/EST which employed a shadow shield mounted vertically on the privy roof to protect the test cell wall and a horizontal shield connecting the privy roof with the test cell wall to protect the engine components. The analytical techniques used to analyze the test data are basically the same as those used in the analysis of the NRX-A3 reactor. The techniques are described in detail in Reference 4 and hence will not be repeated here except for the brief discussion given below.

Calculations of gamma ray dose rates must be placed in two categories: (1) data points which "see" the reactor directly and (2) data points which lie in the shadow of the privy roof shield.

Program 14-0 (Reference 5) which applies the point kernel technique, is used exclusively for computing gamma ray dose rates above the level of the privy roof shield. Gamma ray sources in the active core, the reactor components, the privy roof shield and the test cell wall and pad are included in the program 14-0 calculations. The gamma ray source terms are obtained using reaction response functions which incorporate cross-sections for neutron interactions that produce gamma rays, in conjunction with neutron fluxes calculated using neutron transport codes. Transport codes used were DTK (Reference 6) for one dimensional studies and TDC (Reference 7) for two dimensional studies. The application of these neutron codes is explained in more detail in Reference 4.

Under the privy roof shield, calculations of gamma ray dose rate are more complex and in fact are semi-empirical in that measured thermal neutron fluxes are required to compute gamma ray source terms for the test car and other components. The calculation of these secondary sources and the method of determining dose rates from said sources is described in detail in Reference 4. Another important contributor to the gamma ray dose rate in the shadow of the privy roof are the gamma rays which scatter off the pad or the

test cell wall into the shadow of the roof. Program SAP, (Reference 8) which incorporates multiple scatter albedoes, was used to compute the scattered gamma ray levels under the privy roof.

The calculational techniques for determining fast neutron fluxes with energy E>2.9 Mev apply the point kernel method (Program 14-0) using carbon moments data for all data points not in the shadow of the privy roof. In the shadow of the roof where scattered neutrons contribute the greater portion of the flux level, the SAP code which incorporates a concrete dose albedo is used to calculate the scattered component of the fast neutron flux. The method is described fully in Reference 4.

8.4 GAMMA RAY DOSE RATE DATA

Gamma ray dose rate measurements were obtained at 53 locations outside the NRX-A5 reactor. The measured data are compared with calculated data for each detector point in Table 8-2. The total gamma ray dose given in column two of Table 8-2 in units of roentgens include the background radiation from the test cell wall and pad. (This background radiation is the residual activity resulting from previous reactor tests.) Most of the dosimeter packets were exposed for a period of three weeks prior to EP-I and were not removed from the test cell until two weeks following the EP-II run. Five background packets were also exposed for the three-week period prior to EP-I. These background packets were located very close to dosimeter locations CA-5, CA-6, IP-1, TB-6, and SP-2 (See Figure 8-1). Most of the background data given in Column 3 of Table 8-2 are based on the data measured with these five background packets. Health Physics gamma activity surveys (Reference 12) were made on the test pad during the time interval between the NRX/EST and NRX-A5 tests. Data from these surveys were used to estimate the background for several of the detector locations given in Table 8-2. Included in Column 3 of Table 8-2 is the source of information on which the background is estimated. The gamma ray dose rates given in Table 8-2 were obtained by subtracting the background from the measured dose and then dividing the result by 18,370 watt-hours.

As noted in Table 8-2, both silver metaphosphate glass (SG) and thermoluminescent detectors (TLD) were employed. In general, the TLD data are lower than the SG data, and the calculated data are in closer agreement with the TLD data than with the SG data.

Data given in Table 8-2 are presented graphically in Figures 8-5 through 8-13 for most detector points. Experimental data from other reactor tests (References 9, 10, 11) are included (where applicable) on these figures. Each figure is discussed in the sections below.

TABLE 8-2

COMPARISON OF EXPERIMENTAL WITH CALCULATED NRX-A5 GAMMA RAY DOSE RATE DATA

Dosimeter Identification		Measured Dose, R (for 183°D operation)		Background Dose, R	Adjusted Dose, R (Measured-Background)		Dose Rate (R/hr)		Calculated Dose Rate (R/hr)	Ratio of Measured/Calculated	
		SG	TLD	(see footnote)	SG	TLD	SG	TLD		SG	TLD
N	1	[illegible]	---	120 (SP2)	[illegible]	---	[illegible]	---	[illegible]	[illegible]	---
N	2	[illegible]	---	120 (SP2)	[illegible]	---	[illegible]	---	[illegible]	[illegible]	---
NE	1	[illegible]	---	120 (SP2)	[illegible]	---	[illegible]	---	[illegible]	[illegible]	---
NE	2	[illegible]	---	120 (SP2)	[illegible]	---	[illegible]	---	[illegible]	[illegible]	---
E	1	490	---	112 (TBe	88	---	[illegible]	---	[illegible]	[illegible]	---
E	2	132	---	112 (TBe	20	---	[illegible]	---	[illegible]	[illegible]	---
E	3	92.6	---	112 (TBe	---	---	---	---	---	---	---
E	4	456	---	112 (TBe	344	---	[illegible]	---	[illegible]	[illegible]	---
E	5	165	---	112 (TBe	53	---	[illegible]	---	[illegible]	[illegible]	---
P	1	---	1251	120 (SP2)	---	1131	---	[illegible]	[illegible]	---	[illegible]
P	2	---	1455	120 (SP2)	---	1335	---	[illegible]	[illegible]	---	1.62
CA	1	331	364	161 (CAs	344	197	[illegible]	[illegible]	[illegible]	[illegible]	0.92
CA	2	---	397	161 (CAs	---	230	---	[illegible]	[illegible]	---	[illegible]
CA	3	---	456	161 (CAs	---	293	---	[illegible]	[illegible]	---	0.63
CA	4	---	362	161 (CAs	---	195	---	[illegible]	[illegible]	---	0.85
CA	5	126	245	133 (CAs	---	112	---	[illegible]	[illegible]	---	0.51
CA	6	---	297	161 (CAs	---	230	---	[illegible]	[illegible]	---	0.93
CA	7	---	476	161 (CAs	---	309	---	[illegible]	[illegible]	---	0.65
CA	8	---	727	161 (CAs	---	565	---	[illegible]	[illegible]	---	0.78
C	1	---	309	74 P19 *	---	435	---	[illegible]	[illegible]	---	1.05
C	2	2187	1521	126 (SP2)	2062	1401	[illegible]	[illegible]	[illegible]	1.88	[illegible]
C	4	---	1257	126 (SP2)	---	1131	---	[illegible]	[illegible]	---	1.48
C	5	---	1257	126 (SP2)	---	1131	---	[illegible]	[illegible]	---	1.35
B	1	---	1190	120 (SP2)	---	1070	---	[illegible]	[illegible]	---	1.41
B	2	---	1219	120 (SP2)	---	1099	---	[illegible]	[illegible]	---	1.14
B	3	---	2930	120 (SP2)	---	2780	---	[illegible]	[illegible]	---	1.07
B	4	---	3703	120 (SP2)	---	3583	---	[illegible]	[illegible]	---	1.14
B	5	---	5826	120 (SP2)	---	4906	---	[illegible]	[illegible]	---	1.23
B	6	---	7876	120 (SP2)	---	6956	---	[illegible]	[illegible]	---	1.12
B	7	---	9589	120 (SP2)	---	8469	---	[illegible]	[illegible]	---	1.06
B	8	---	9986	120 (SP2)	---	9866	---	[illegible]	[illegible]	---	1.17
B	9	---	7288	120 (SP2)	---	7088	---	[illegible]	[illegible]	---	1.22
B	10	---	4895	120 (SP2)	---	4575	---	[illegible]	[illegible]	---	1.19
B	11	---	3540	120 (SP2)	---	3126	---	[illegible]	[illegible]	---	1.21
B	12	---	2315	120 (SP2)	---	2195	---	[illegible]	[illegible]	---	1.23
B	13	---	1706	120 (SP2)	---	1666	---	[illegible]	[illegible]	---	1.23
B	14	---	1389	120 (SP2)	---	1269	---	[illegible]	[illegible]	---	1.11
TE	1	---	86	32 P19 *	---	74	---	[illegible]	[illegible]	---	1.20
TE	3	---	6.6	3.4 P19 *	---	3.2	---	[illegible]	[illegible]	---	1.29
TCW	1	---	198	67 (CA61*	---	131	---	[illegible]	[illegible]	---	2.04
TCW	2	---	436	67 (CA61*	---	369	---	[illegible]	[illegible]	---	3.85
TCW	3	---	3445	67 (CA61*	---	3378	---	[illegible]	[illegible]	---	4.89
TCW	4	---	2804	67 (CA61*	---	2737	---	[illegible]	[illegible]	---	3.64
TCW	5	---	2004	67 (CA61*	---	1937	---	[illegible]	[illegible]	---	4.08
TCW	6	---	1078	67 (CA61*	---	1011	---	[illegible]	[illegible]	---	4.38
TP	1	---	119	13 P19 *	---	106	---	[illegible]	[illegible]	---	1.33
TP	2	---	46	13 P19 *	---	33	---	[illegible]	[illegible]	---	0.82
TP	3	---	165	13 P19 *	---	152	---	[illegible]	[illegible]	---	1.72
TP	4	---	126	13 P19 *	---	113	---	[illegible]	[illegible]	---	2.3
SP	1	10980	10912	120 (SP2)	10860	10792	[illegible]	[illegible]	[illegible]	[illegible]	[illegible]
SP	2	44110	35909	120 (SP2)	43990	35789	[illegible]	[illegible]	[illegible]	[illegible]	[illegible]
SP	3	6369	13894	120 (SP2)	6279	12974	[illegible]	[illegible]	[illegible]	[illegible]	[illegible]
SD	1	3042	2778	120 (SP2)	2922	2658	[illegible]	[illegible]	[illegible]	[illegible]	[illegible]

Note: Data in parentheses refer to the dosimeter location where the background measurement was made. The data indicated by an * refer to a background exposure of 2 weeks. All other data have a background exposure of 5 weeks. Data in brackets indicate data were obtained from the P19 survey (Reference 12).

8.4.1 Pressure Vessel Surface

Experimental gamma ray dose rates obtained during low power tests of NRX-A2, NRX-A3, and NRX-A5 reactors on an axial traverse at the surface of the pressure vessel are presented in Figure 8-5 as a function of reactor station. Also included in Figure 8-5 are some experimental data obtained from the PAX-C reactor (a critical mockup similar to the NRX-A3 reactor). The solid curve shown in Figure 8-5 was calculated using point kernel program 14-0.

Figure 8-5 shows a significant spread in the experimental data. Of the six A5 measurements shown in the figure, three are in good agreement with the A3 and PAX measurements. On the midplane, however, the A5 measured data appear to be too high. There are two reasons why the A5 data are high, both concerned with the mounting of the detectors. The earlier detectors (i.e., NRX-A2 and NRX-A3) were mounted on the vessel on aluminum bands in such a fashion that the A2 and A3 detectors "saw" about 1/4 inch more aluminum than did the A5 detectors which were mounted directly on the vessel. Also, the mounting bands for the A2 and A3 detector were not in direct contact with the vessel but were positioned so that the A2 and A3 detectors were actually at a distance of about one and a half inches from the vessel. Calculations indicate that the attenuation factor for the additional 1/4 inch aluminum is about 0.92 and the attenuation factor due to the additional 1.5 inch distance from the reactor is 0.91. The combination of these factors indicates that the NRX-A5 data on the vessel at the midplane should be about 20 percent higher than the A2 or A3 data.

If the A2 and A3 data shown in Figure 8-5 would be adjusted by this amount, then there would be better agreement with the NRX-A5 results. The A2 data are observed to be consistently lower than any other set of measured data on the pressure vessel surface.

The calculated gamma ray dose rates are in good agreement with the PAX and A3 data. However, because of the spread in the various experimental data, the gamma ray dose rate along the surface of the pressure vessel cannot be defined more accurately than by a factor of two.

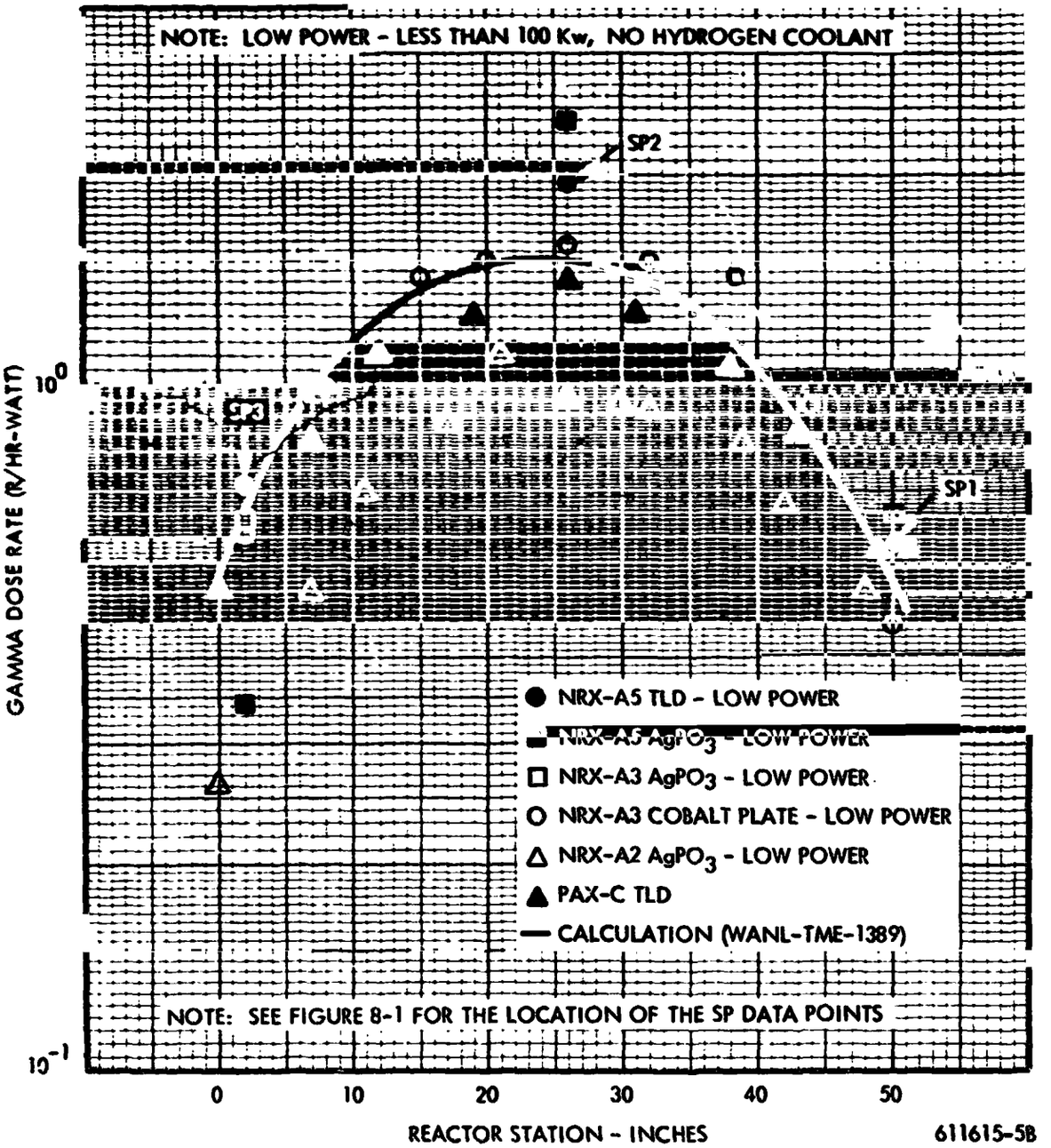

Figure 8-5. Axial Distribution of the Gamma Ray Dose Rate on the Surface of the Pressure Vessel

8.4.2 Dosimeter Pole

NRX-A5 measured and calculated gamma ray dose rates at locations on the dosimeter pole are shown in Figure 8-6 as a function of reactor station. The dosimeter pole is a vertical pole mounted on the privy roof at a distance of 47 inches from the core axis and at a reactor angle (θ) of 323 degrees. A dosimeter pole was not employed during previous reactor tests. However, data from interpolations of measurements on the meridian ring, employed in previous reactor tests, are included for comparison in Figure 8-6. Again, it is noted that the A2 data are generally lower than the other measured data. The A5 data are in reasonable agreement with the meridian ring data. The point kernel calculations range from 6 to 40 percent lower than the A5 measurements.

8.4.3 Radial Midplane

Comparison of experimental and calculated gamma ray dose rates as a function of radial distance from the reactor in the core midplane (Station 26) is shown in Figure 8-7. The A5 measurements were made at 25, 62.5, and 300 feet from the center of the core on the midplane in order to extend the radial traverse to distances further from the reactor than previously measured with the other NRX reactors. At the 25 and 62.5 feet locations, where data are available from other reactor tests, the A-5 data are slightly higher, but are within the accuracy of the measurements. The calculated curve, which was obtained using the point kernel code 14-0, is in good agreement with the measurements. One data point obtained during high power (approximately 1100 MW) is included in Figure 8-7. No measurable difference is apparent, within the accuracy of the present data, between normalized power data measured at high power from that measured at low power.

8.4.4 Top of the Privy Roof Shield

Measured and calculated gamma ray dose rates are plotted in Figure 8-8 as a function of radial distance on the top surface of the privy roof. The measured gamma ray dose rate ranges from 0.02 to 0.07 R/hr watt on the surface of the roof. The A5 data are

higher than, and the A2 data lower than, the A3 measured data, as was observed on the surface of the pressure vessel and on the radial traverse. Within each specific reactor test, the data are generally flat as a function of radial location, i. e., there is less than a 50 percent increase from the center to the edge of the roof. The point kernel calculations are in good agreement with the A3 measurements. The area between the privy roof and the reactor is very congested with hardware. The NRX-A5 also has the INIS neutronic detector system located in this area. It is not unusual then, considering the local effects on radiation produced by hardware on the roof, that there is a considerable spread in the data. Calculations include effects of the privy roof, but do not include effects due to all the hardware between the roof and reactor.

8.4.5 Test Car

Gamma ray dose rates were measured at various locations on the test car (see Figure 8-1 for detector locations). A horizontal traverse, shown in Figure 8-9 extended approximately the length of the test car at an elevation of about 11 feet below the center of the core (station - 108). With the exception of location TB-4 (Figure 8-9), the NRX-A5 data fall within the range of previously measured data. The measurement at TB-4 is about a factor of two higher than measurements taken at the same location for the earlier NRX tests. This discrepancy is not understood at this time.

With the exception of location TB-4, measured data at specific locations are self-consistent to within a factor of two. This reproducibility of experimental data is better than might be expected in view of the complexity of the geometry of the test car and associated hardware. The calculations (which are explained in detail in Reference 10) are in reasonable agreement with the bulk of the data.

Included in Figure 8-9 are several data points which were obtained during high power (approximately 1100 MW) operation. No significant differences between normalized (on a per watt basis) high power and low power data can be observed.

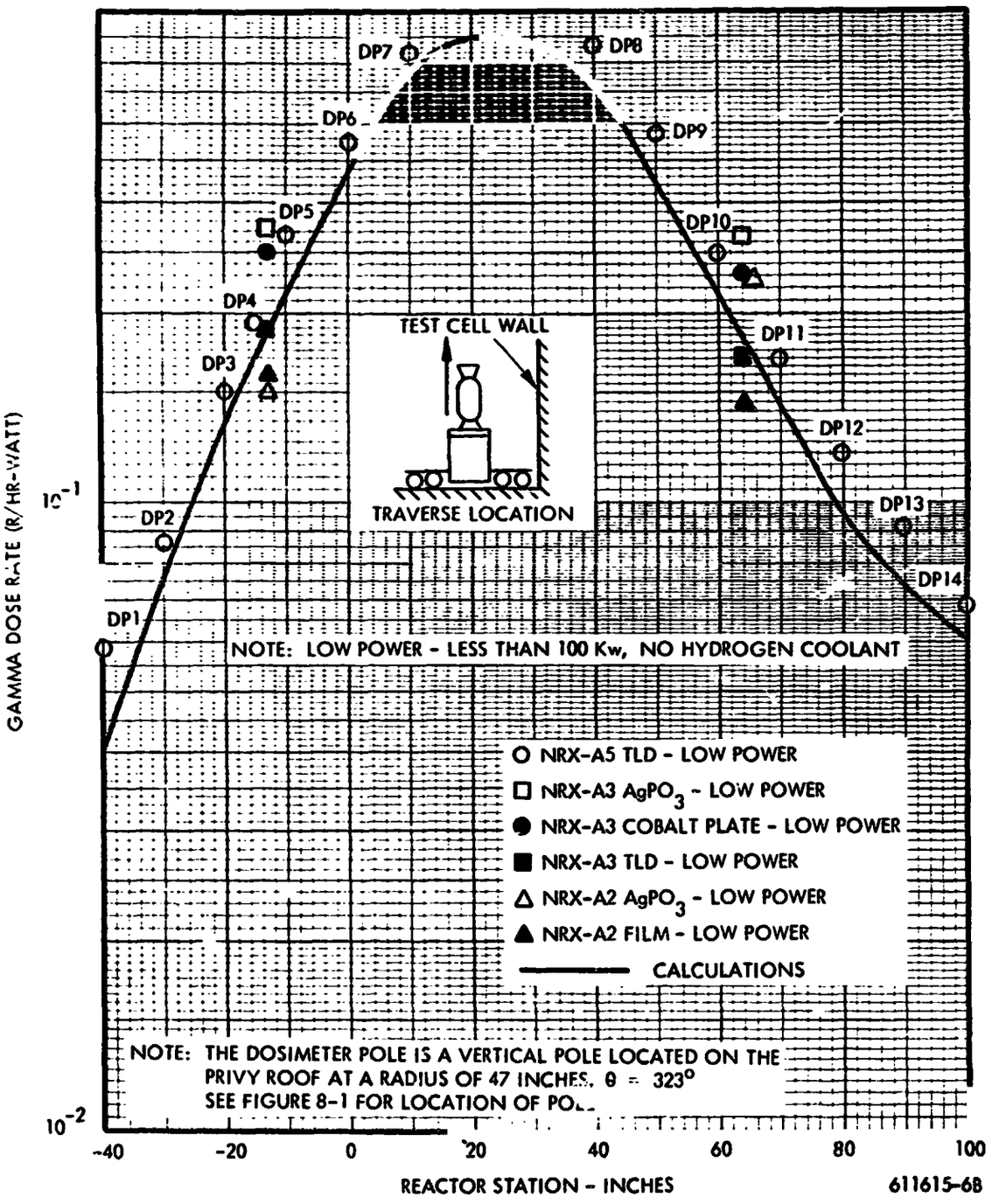

Figure 8-6. Gamma Ray Dose Rate Distribution on the Dosimeter Pole

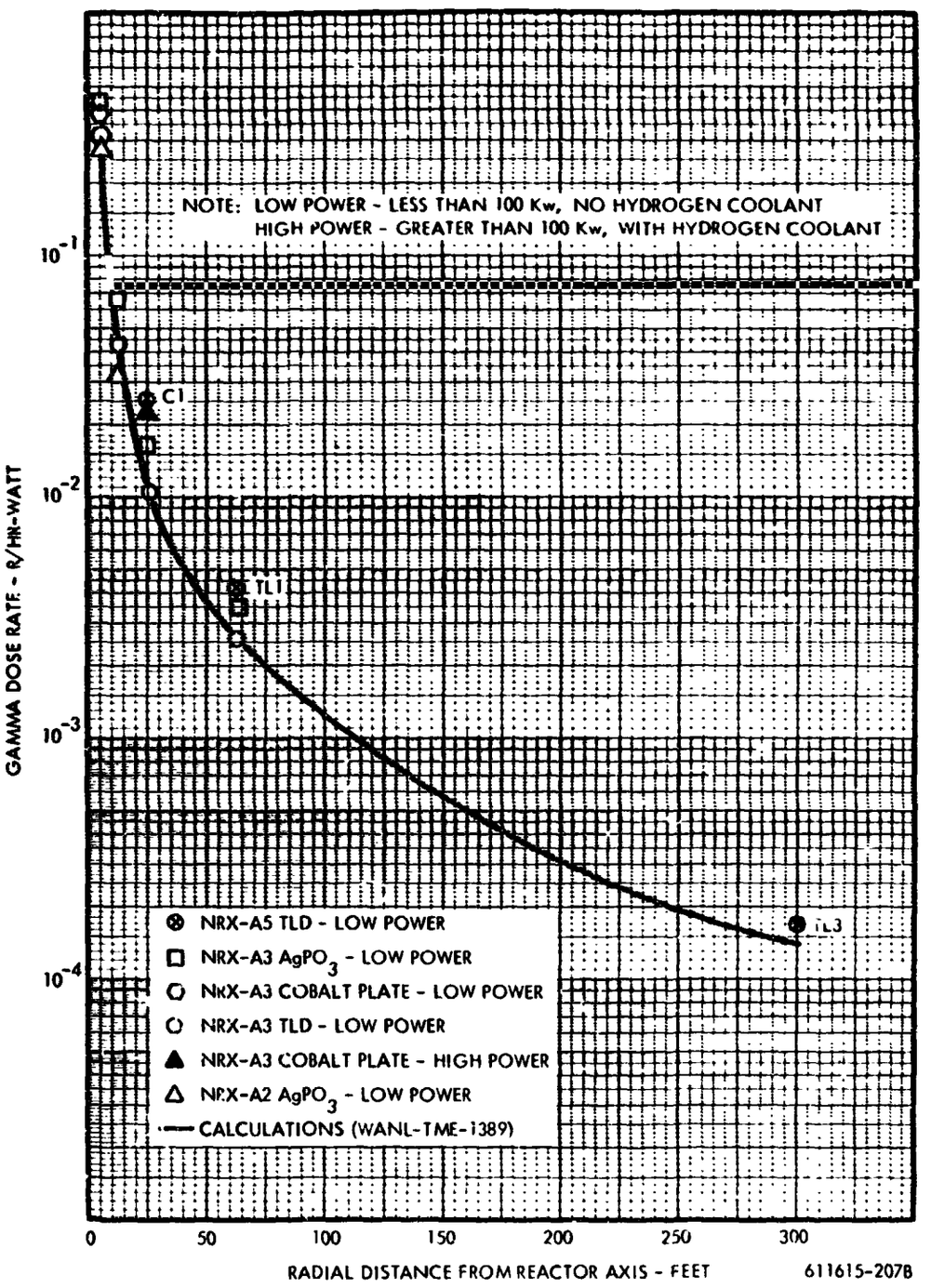

Figure 8-7. Gamma Ray Dose Rate on the Reactor Midplane versus Distance from Reactor Axis

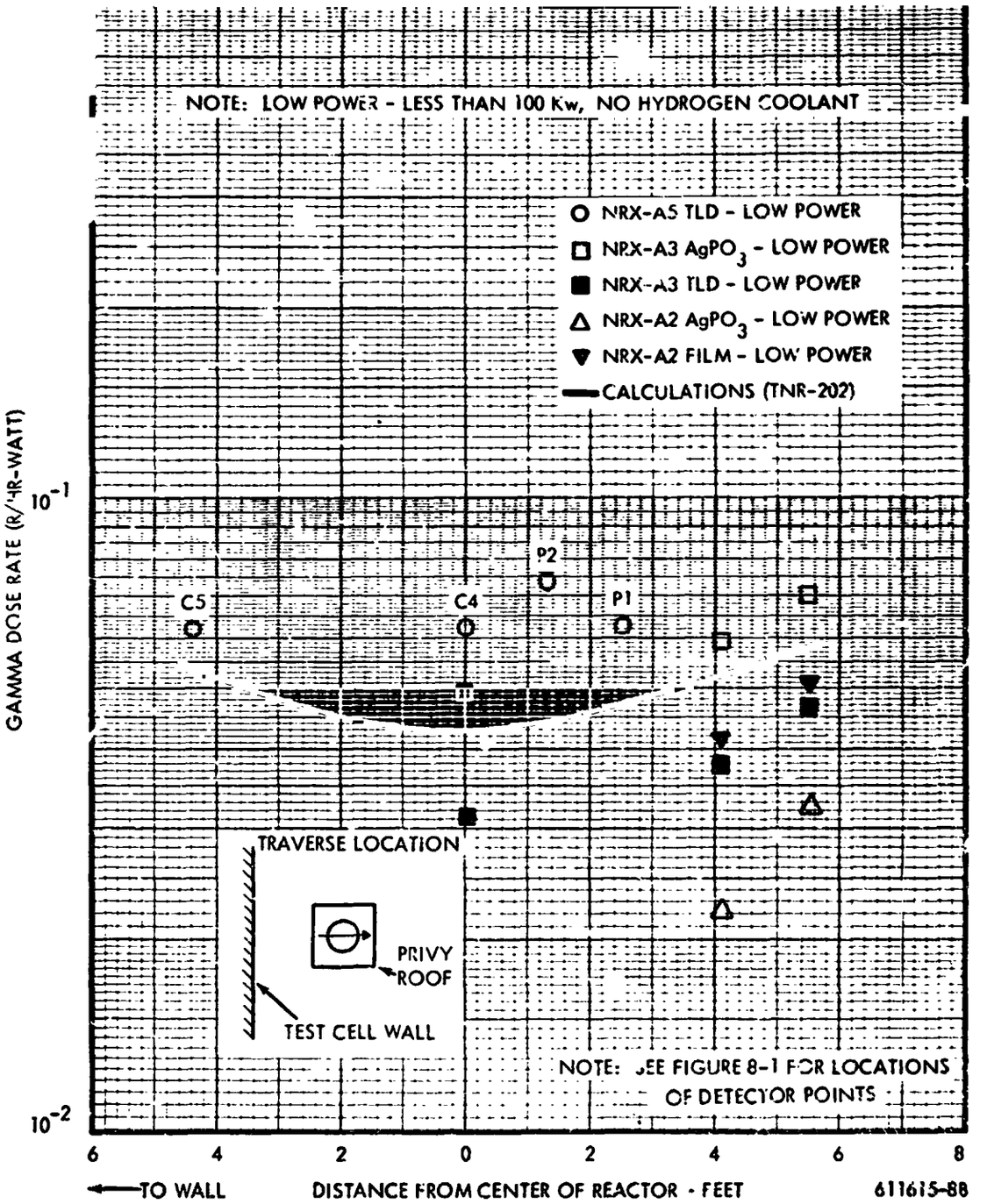

Figure 8-8. Gamma Ray Dose Rate Distribution on the Top Surface of the Privy Roof Shield

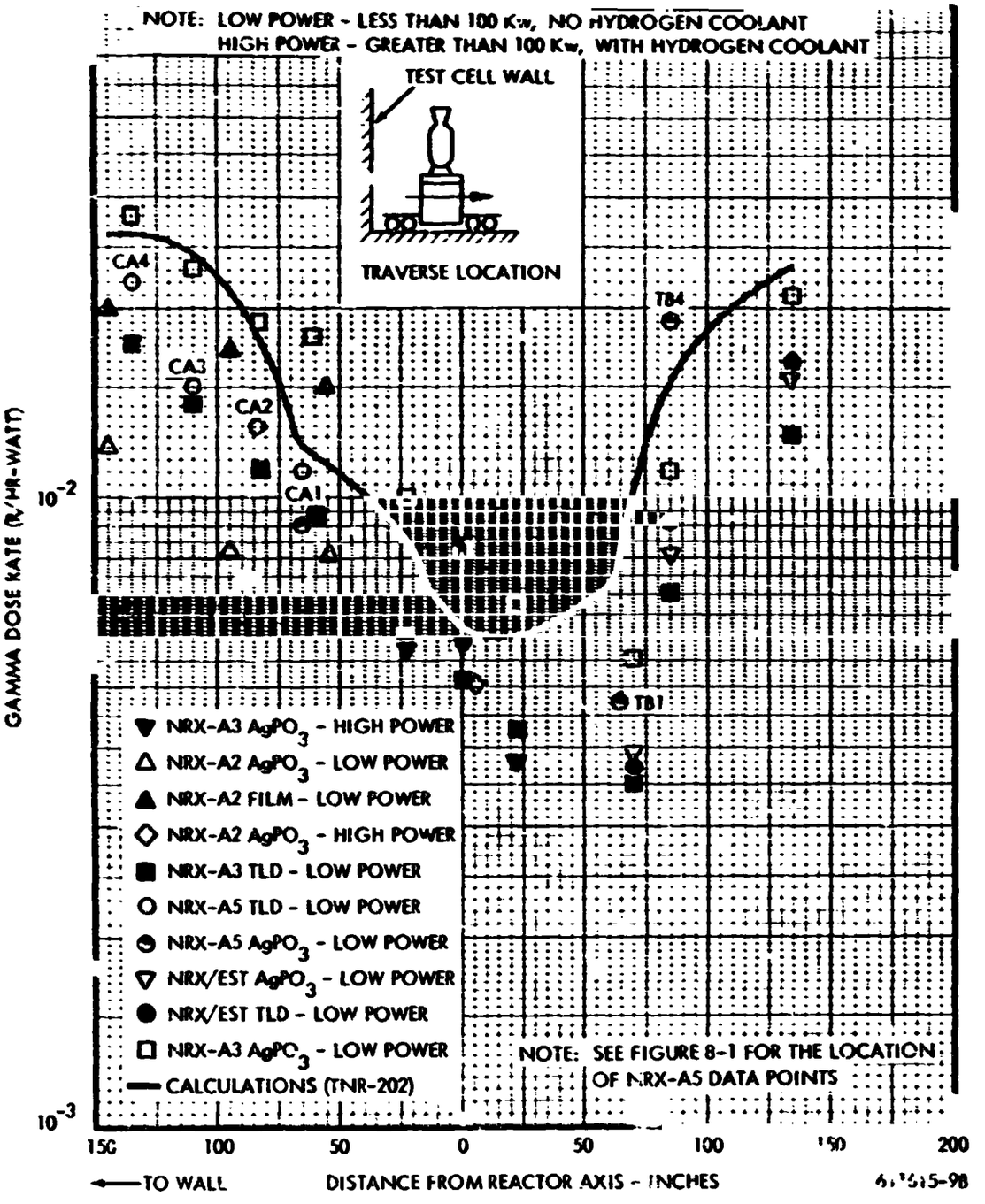

Figure 8-9. Gamma Ray Dose Rate Distribution unde[illegible]
(Horizontal Traverse at Approximately Station -108)

8.4.6 Test Cell Wall

Figure 8-10 presents a horizontal traverse in the core midplane on the test cell wall. Figure 8-11 presents a vertical traverse on the wall 5 feet north of the normal projection of the core center. (See Figure 8-2 for detector locations.) From Figures 8-10 and 8-11, it is immediately obvious that the A5 measured gamma ray dose rates are significantly higher than any previous measurements. There are two reasons why the A5 data are considerably (about a factor of three) higher than the A3 data: (1) due to the addition of a test cell wall heat shield, the detectors were positioned 1 to 2 feet closer to the reactor than for the A3 test; (2) the background radiation levels given in Table 8-2 for detectors TCW 1 through TCW 6 were based on measured background levels at location CA-6 because no background levels were measured on the wall. Location CA-6 is about 6 feet from the wall. Although there were some measurements of the test cell activity made prior to the A-5 tests (Reference 12) these data could not be incorporated in the analysis since the surveys did not include data point locations on the wall any nearer than location CA-6. If the wall itself is the important background radiation source, it is obvious that using the background level at CA-6 is an underestimate of the background level in the wall. Hence, the radiation levels for the TCW detectors given in Table 8-2 and Figures 8-10 and 8-11 are too high.

Calculations of the effect of detector location change from A3 to A5 (item 1 above) indicate that the A5 data should be about 30 percent higher than the A3 data. Consequently, it is believed that the discrepency between the A5 and the A3 gamma ray dose rate data on the test cell wall is due to an underestimate of the background radiation level on the wall for NRX-A5.

8.4.7 Test Cell Pad

Four detectors were exposed on the test cell pad during the A5 test. The detectors were located at positions not instrumented during previous reactor tests. The gamma ray dose

rate levels are presented in Figures 8-12 and 8-13 along with previous reactor test data. Figure 8-12 shows a traverse on the pad 3 feet from the wall and parallel to the wall, extending to 60 feet north of the core. Figure 8-13 presents a traverse on the pad normal to the wall, 5 feet north of the reactor, extending to a distance of about 50 feet from the wall. The A5 measured data appear to be reasonable with respect to the other measured data. However, it should be pointed out that the background radiation levels (see Table 3-2) for those locations are a significant portion of the total measured radiation dose. The background estimates for these data were based on the Health Physics activity surveys taken after the NRX/EST tests and prior to the NRX-A5 tests. The locations of the survey data points were about 1 meter above the pad whereas the A5 detectors were exposed directly on this pad. Since the background levels applied to these locations were not actually measured at each location, an uncertainty exists in the data presented in Figures 8-12 and 8-13.

The calculated gamma ray dose rates (Reference 10) are in good agreement (within a factor of 2) with all the measured data on the pad.

8.4.8 Summary

At locations close to the reactor, the NRX-A5 gamma ray dose rates were in reasonable agreement with previously measured data. However, at distances further than 5 feet from the reactor, the gamma ray measurements obtained during the NRX-A5 were not as reliable as similar type of data obtained during previous reactor tests and were higher than previous measurements. This discrepancy is probably due to the high residual activity in the test cell "A" area from previous reactor tests. Although five dosimeters were exposed for three weeks prior to the test in an effort to obtained background correction data, apparently these data were not sufficient to define the variation of the background radiation throughout the facility. Nor were the data obtained from the Health Physics activity surveys made on the pad prior to the A5 tests adequate to determine the background. Also, the power integral (18,370 watt-hours) was nor high enough to provide doses at various

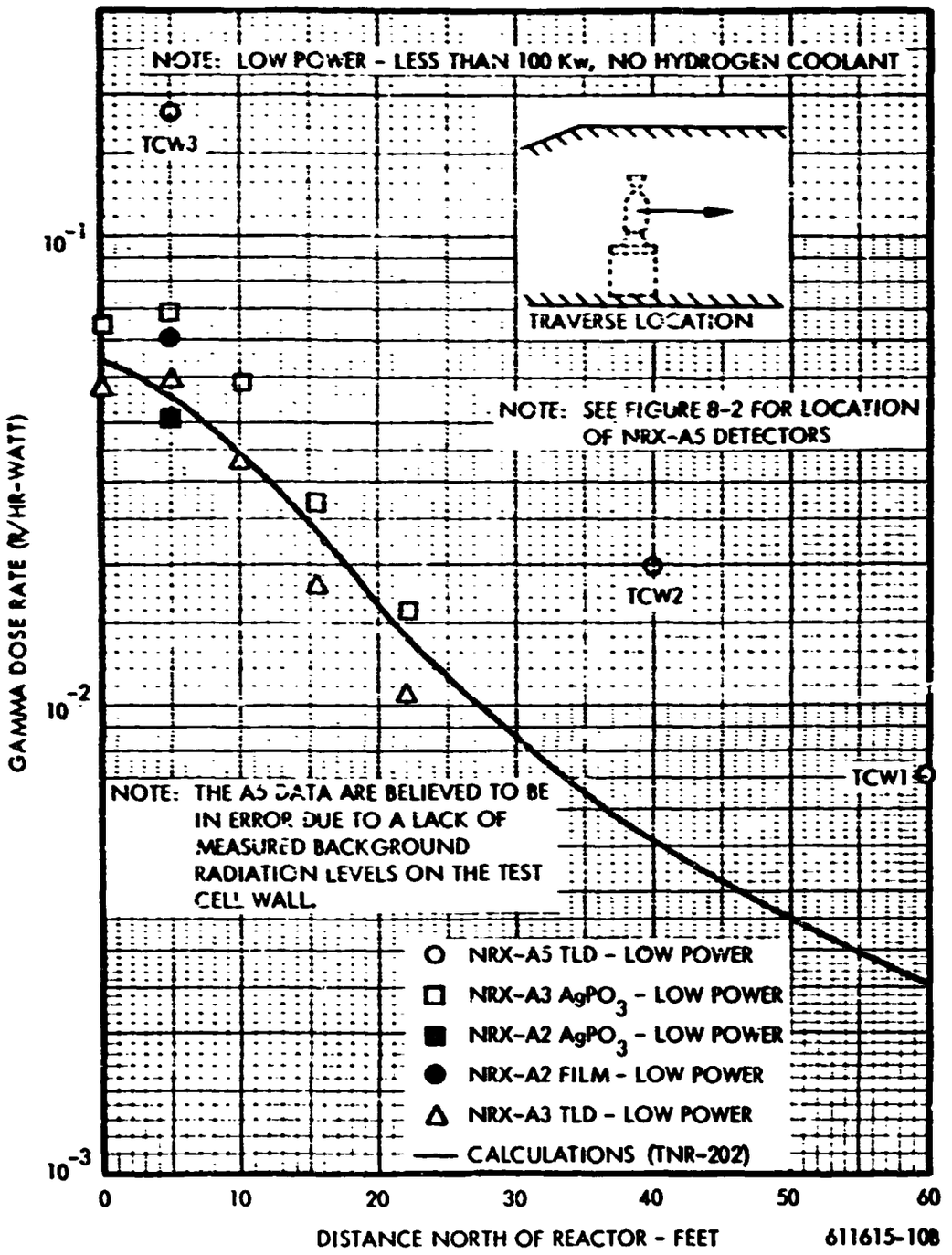

Figure 8-10. Gamma Ray Dose Rate Distribution on the Test Cell Wall (Horizontal Traverse in the Core Midplane)

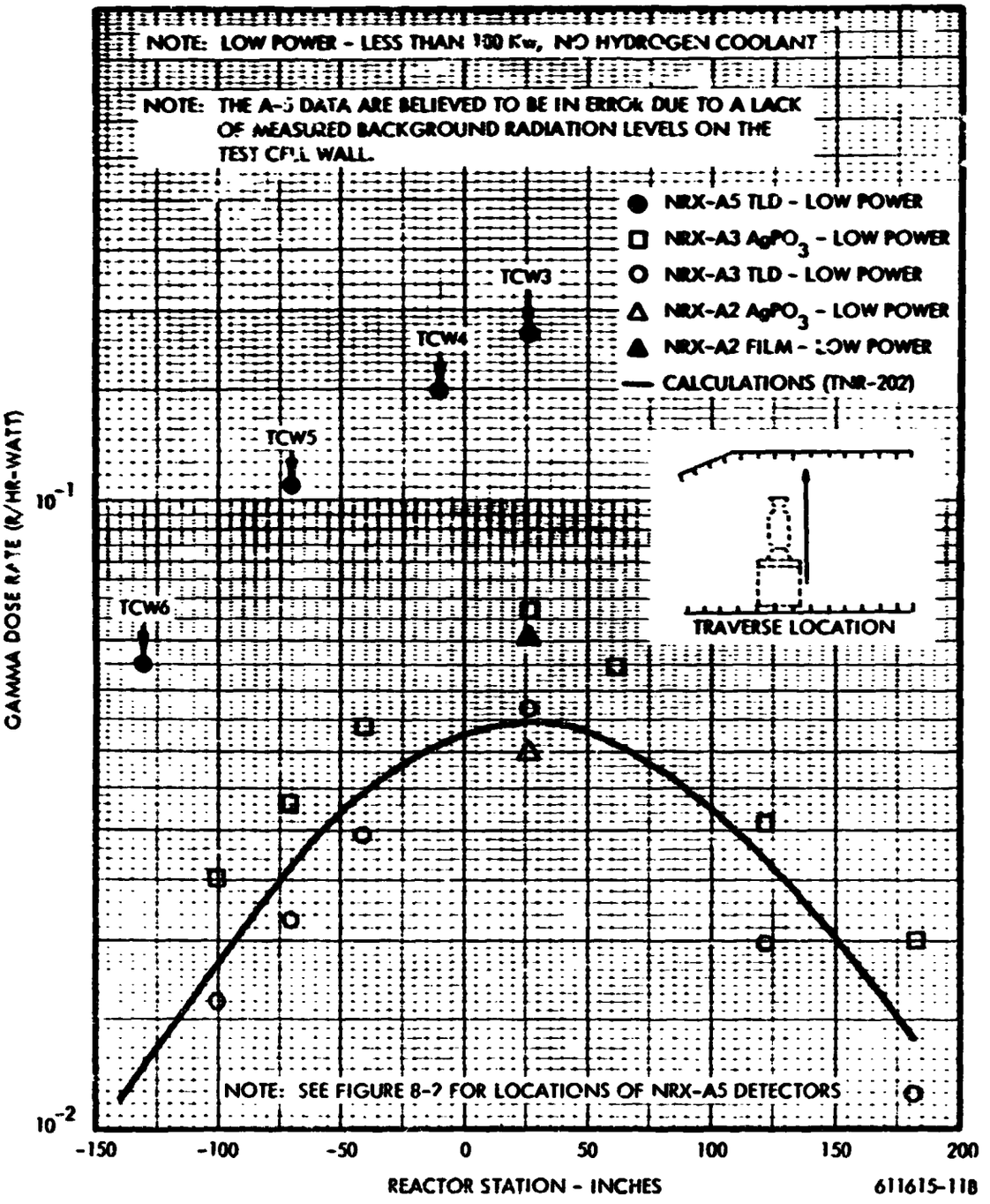

Figure 8-11. Gamma Ray Dose Rate Distribution on the Test Cell Wall (Vertical Traverse Five Feet North of Reactor)

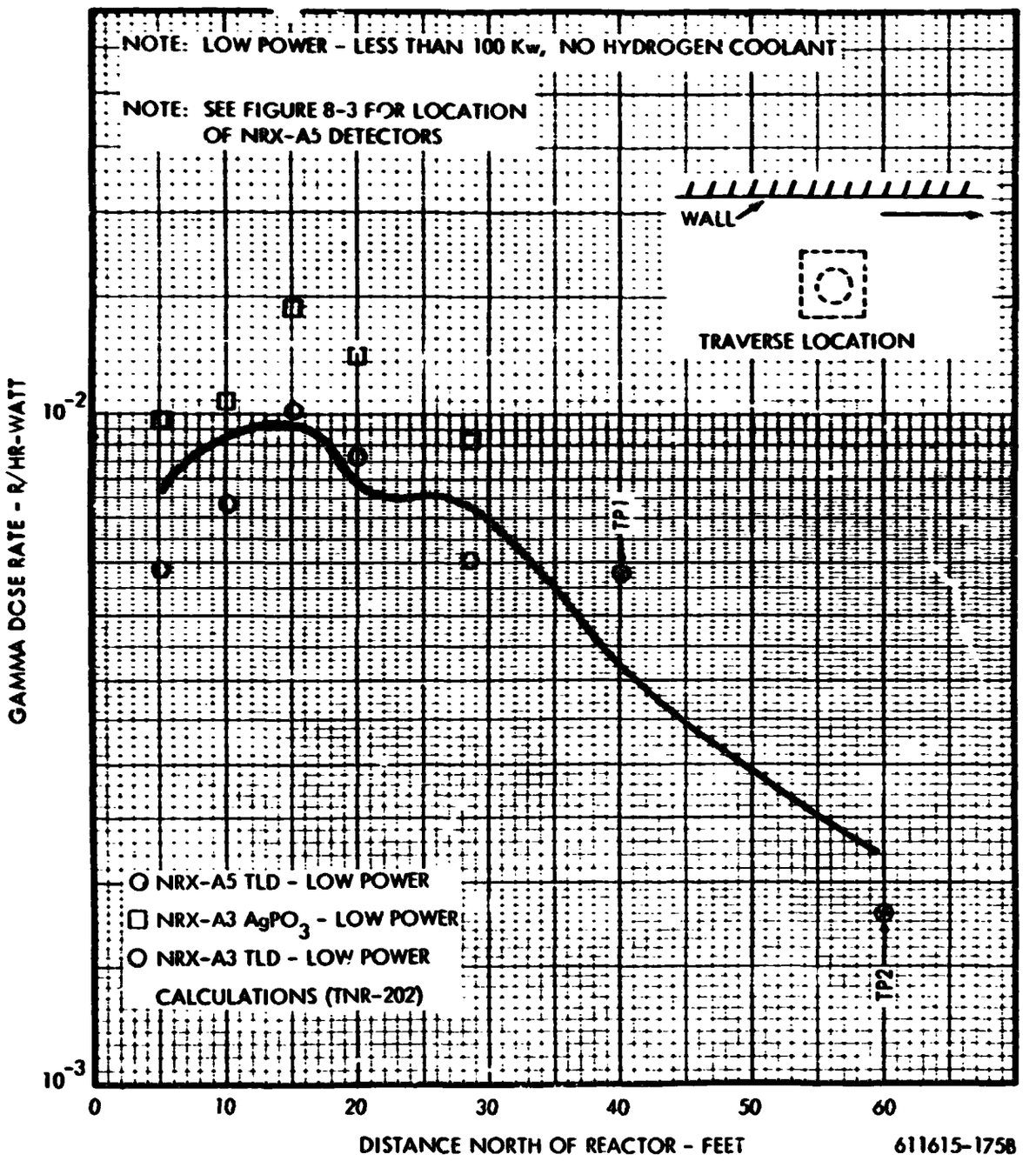

Figure 8-12. Gamma Ray Dose Rate on the Test Pad (Traverse Parallel to the Wall and 3 Feet from the Wall)

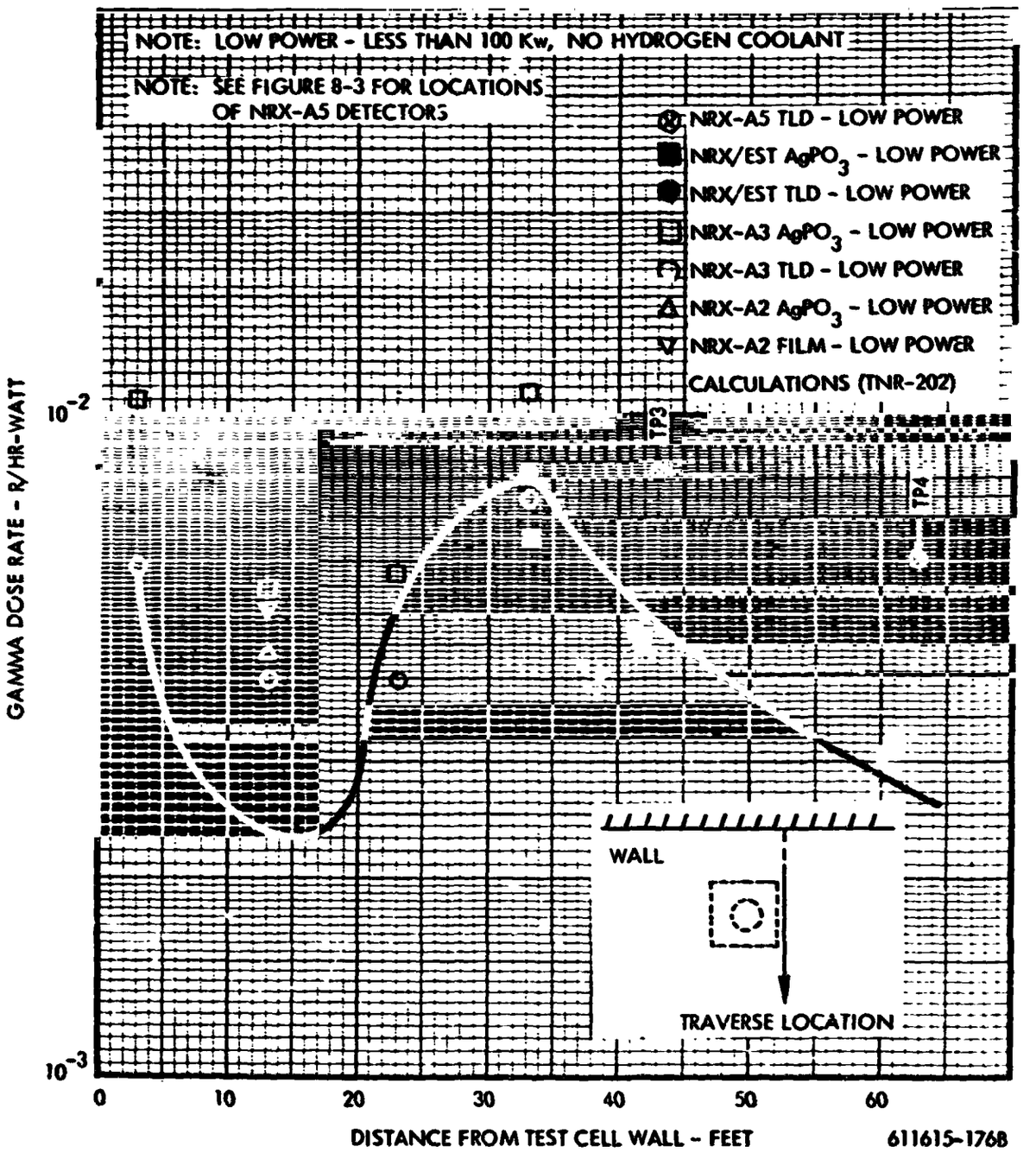

Figure 8-13. Gamma Ray Dose Rate Distribution on the Test Pad (Traverse Normal to Wall and 5 Feet North of Reactor)

locations that were much higher than the background count. (Specifically, this applies to detectors located in the shadow of the privy roof.) Therefore, the A5 gamma ray measurements did not reduce the uncertainties in the experimental data at many locations obtained during the previous reactor tests.

At most locations around the NRX facility, a scatter of about a factor of two can be observed in the measured (A2, A3, and A5) gamma ray data. The calculations generally fall within the spread of the experimental data. The calculated dose rates given in this report are based on those previously published in reference 10. It should be pointed out that the calculational techniques are semi-empirical for certain data. Specifically, in highly shielded areas, such as in the shadow of the privy roof; a significant source of gamma radiation is the (n,γ) reaction. This reaction occurs when neutrons are captured by materials and emit high energy gamma rays. Therefore, in order to calculate gamma ray dose rates from radiation sources under the roof, a knowledge of the neutron flux is required. At present WANL has no technique for computing the neutron flux in the thermal energy range at locations such as under the privy roof. Consequently measured thermal neutron fluxes from earlier reactor tests were used to calculate the gamma sources for the test car and associated hardware. These sources contribute most of the dose rate at locations in the shadow of the privy roof.

8.5 FAST NEUTRON FLUX DATA (E>2.9 Mer)

Fast neutron (E>2.9 Mer) fluxes were measured with sulfur pellets at 53 locations outside the NRX-A5 reactor. The measured data are compared with calculated data for each detector point in Table 8-3.

Data given in Table 8-3 are presented graphically in Figures 8-14 through 8-22 for most detector points. Experimental data from previous reactor tests (References 9, 10, 11) are included (where applicable) on Figures 8-14 through 8-22. Each figure is discussed in detail in the following sections

8.5.1 Pressure Vessel Surface

Experimental fast neutron fluxes obtained during low power tests of NRX-A2, NRX-A3, and NRX-A5 reactors on an axial transverse at the surface of the pressure vessel are given in Figure 8-14 as a function of reactor station. Also included in Figure 8-14 are some high power NRX-A3 data obtained with nickel foils.

The low power experimental data with the exception of the A5 data point at station 26 appear to be in good agreement from one reactor to another. The three A5 data points are all somewhat higher than previous reactor tests indicate. Although the A5 design is slightly different than the A2 and A3 designs, calculations do not indicate that the fast neutron fluxes for A5 should be that much higher than for A2 or A3 as the measurements show. Measurements show about a 50 percent higher flux for the A5 data. Part of this discrepancy can be explained by the differences in detector mounting configuration. The A5 detectors were mounted directly on this vessel while the A2 and A3 detectors were mounted on aluminum bands such that the detectors were about 1.5 inches from the vessel and there was about 0.25 inches of aluminum between the reactor and the detectors. Calculations incorporating these differences indicate that the A5 data should be about 16 percent higher than the A2 or A3 data.

TABLE 8-3

COMPARISON OF EXPERIMENTAL WITH CALCULATED NRX-A5
FAST NEUTRON FLUX (E>2.9 Mev) DATA

Neutron Flux (E>2.9 Mev) (n/cm^2-sec-watt)

Dosimeter Identification		Measured Sulfur Data (EP I and II)	Calculated Data	Ratio of Measured/Calculated
N	1	2.7 (3)	2.2 (3)	1.2
N	2	5.3 (3)	2.2 (3)	2.4
NF	1	5.2 (3)	3.8 (3)	1.4
NF	2	3.2 (3)	3.8 (3)	0.85
TB	1	5.8 (0)	8.2 (0)	0.71
TB	2	2.3 (0)	7.5 (0)	0.31
TB	3	2.8 (0)	7.5 (0)	0.37
TB	4	3.6 (1)	4.0 (1)	0.89
TB	5	4.9 (0)	8.0 (0)	0.61
TB	6	3.6 (0)	7.5 (0)	0.48
P	1	2.3 (2)	2.4 (2)	0.96
P	2	2.9 (2)	2.4 (2)	1.2
CA	1	2.1 (1)	2.7 (1)	0.78
CA	2	2.9 (1)	6.9 (1)	0.42
CA	3	7.3 (1)	8.8 (1)	0.83
CA	4	1.9 (2)	9.8 (1)	1.9
CA	5	1.5 (1)	2.4 (1)	0.63
CA	6	2.4 (1)	2.8 (1)	0.86
CA	7	5.6 (1)	1.1 (2)	0.51
CA	8	1.7 (2)	2.2 (2)	0.77
C	1	9.7 (1)	7.1 (1)	1.4
C	2	8.0 (2)	1.7 (3)	0.47
C	4	2.3 (2)	2.4 (2)	0.95
C	5	3.8 (2)	2.8 (2)	1.3

TABLE 8-3 (Continued)

Neutron Flux (E>2.9 Mev) (n/cm^2-sec-watt)

Dosimeter Identification		Measured Sulfur Data (EP I and II)	Calculated Data	Ratio of Measured/Calculated
IP	1	6.1 (0)	1.1 (1)	0.55
IP	2	5.2 (0)	1.2 (1)	0.43
IP	3	3.4 (0)	7.5 (0)	0.45
DP	1	3.9 (2)	4.4 (2)	0.89
DP	2	7.8 (2)	7.4 (2)	1.1
DP	3	1.4 (3)	1.2 (3)	1.2
DP	4	1.8 (3)	1.4 (3)	1.3
DP	5	2.0 (3)	1.4 (3)	1.4
DP	6	2.4 (3)	1.7 (3)	1.4
DP	7	3.2 (3)	2.7 (3)	1.2
DP	8	3.1 (3)	2.5 (3)	1.2
DP	9	2.3 (3)	1.7 (3)	1.3
DP	10	1.8 (3)	1.3 (3)	1.4
DP	11	1.9 (3)	1.4 (3)	1.4
DP	12	1.6 (3)	1.4 (3)	1.1
DP	13	1.5 (3)	1.3 (3)	1.2
DP	14	1.4 (3)	1.2 (3)	1.2
TCW	1	1.8 (1)	1.2 (1)	1.5
TCW	3	3.2 (2)	2.5 (2)	1.3
TCW	4	2.9 (2)	2.2 (2)	1.3
TCW	5	1.7 (2)	1.3 (2)	1.3
TCW	6	7.8 (1)	6.0 (1)	1.3
TP	1	3.2 (1)	2.2 (1)	1.5
TP	2	1.6 (1)	1.1 (1)	1.5
TP	3	4.2 (1)	3.2 (1)	1.3
TP	4	1.9 (1)	1.6 (1)	1.2
SPV	1	3.3 (3)	2.9 (3)	1.1
SPV	2	1.1 (4)	7.2 (3)	1.5
SPV	3	3.9 (3)	2.4 (3)	1.6
SD	1	1.7 (3)	1.3 (3)	1.3

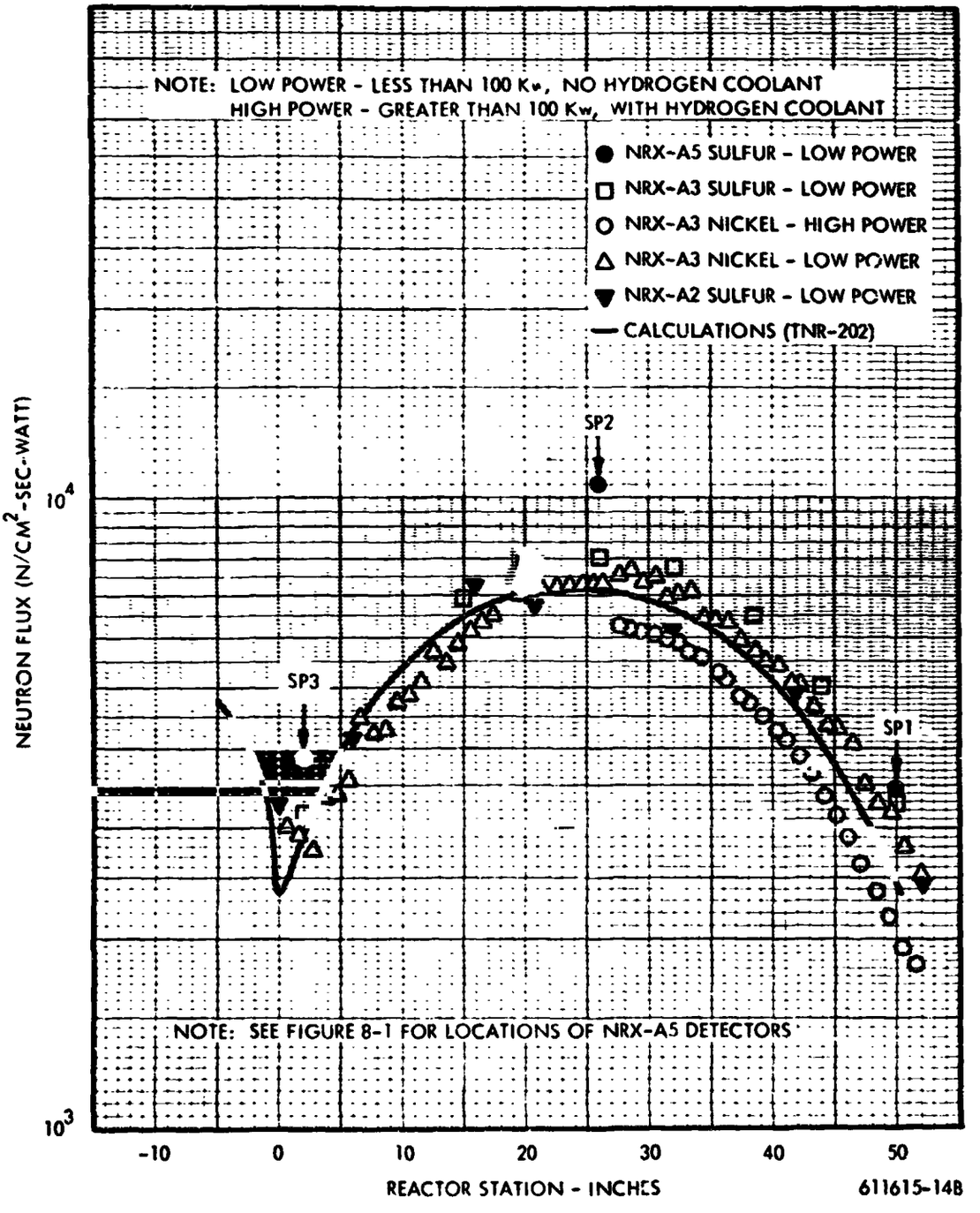

Figure 8-14. Axial Distribution of the Fast Neutron Flux (E > 2.9 Mev) on the Surface of the Pressure Vessel

A definite trend can be observed between the high and low power nickel data for NRX-A3 indicating that at high power with coolant in the reactor, the fast flux per unit power is reduced. The extent of this reduction is difficult to determine due to the uncertainty associated with the measured data.

Calculations (described in Reference 10) which were performed for high power conditions are in good agreement with the measured data. These calculations used the point kernel technique with carbon moments data for the neutron spectra.

8.5.2 Dosimeter Pole

NRX-A5 measured and calculated fast neutron flux (E>2.9 Mev) at locations on the dosimeter pole are shown in Figure 8-15 as a function of reactor station. The dosimeter pole is a vertical pole mounted on the privy roof at reactor angle (θ) equal to 323 degrees and 47 inches from the reactor axis. The dosimeter pole was not used in earlier reactor tests. However, data from interpolations of measurements on the meridian ring used in previous reactor tests are included for comparison in Figure 8-15. The NRX-A5 data are somewhat higher than data from other reactors. This trend was also noted for the data on the pressure vessel surface. The point kernel carbon moments data calculations agree well "shape" with the measurements and are generally lower. The maximum difference between calculations and measurements is only 40 percent.

8.5.3 Top of the Privy Roof Shield

Measured and calculated fast neutron fluxes are plotted in Figure 8-16 as a function of radial distance from the core axis on the top surface of the privy roof. A factor of two spread in low power sulfur data (A5 versus A3) is observed on the centerline. It is difficult to determine from the experimental data whether or not the fast flux increases as a function of radial position as indicated by calculations. The calculated data (point kernel carbon moments data) are in good agreement with the A5 measurements

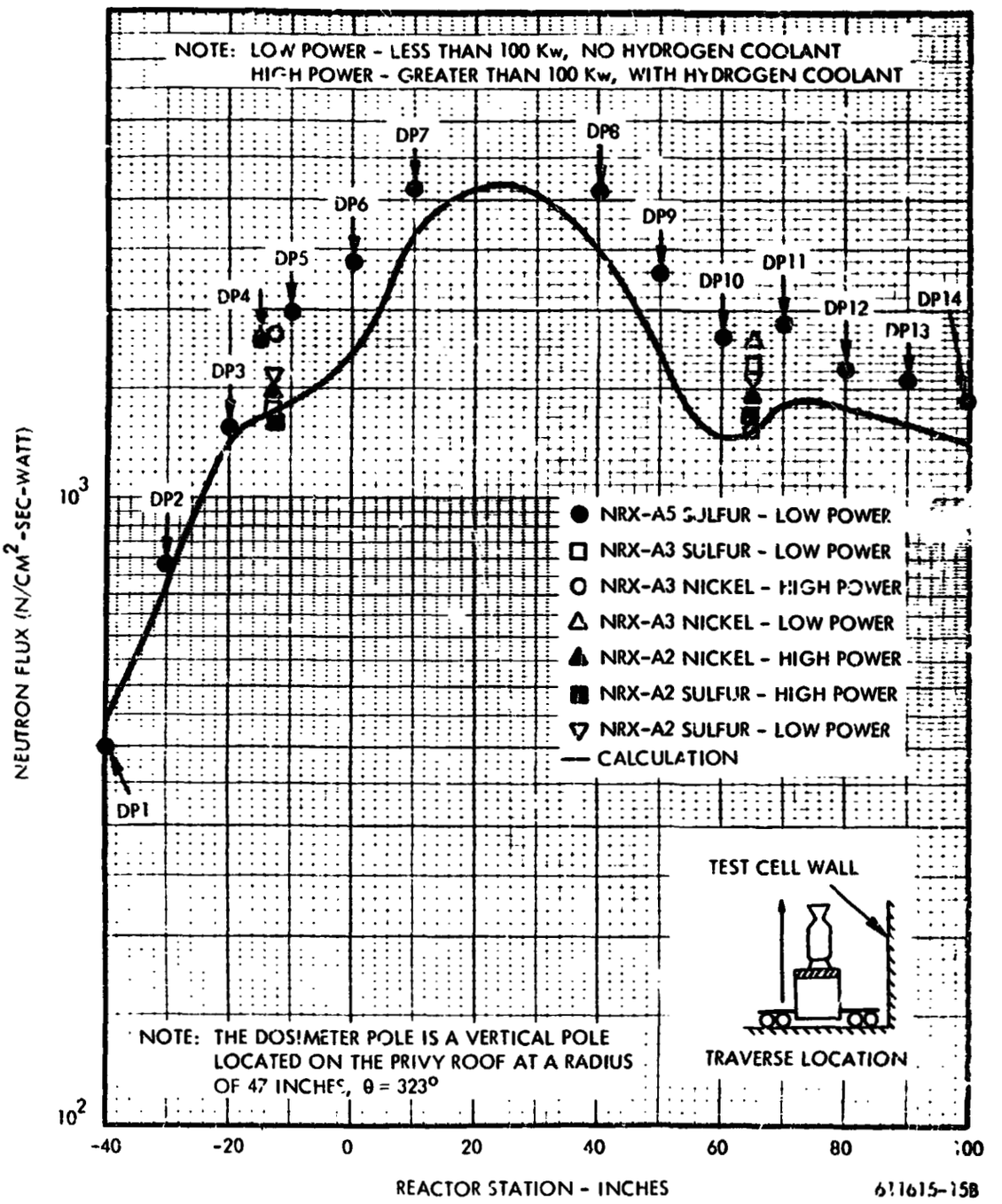

Figure 8-15. Fast Neutron Flux (E > 2.9 Mev) Distribution on the Dosimeter Pole

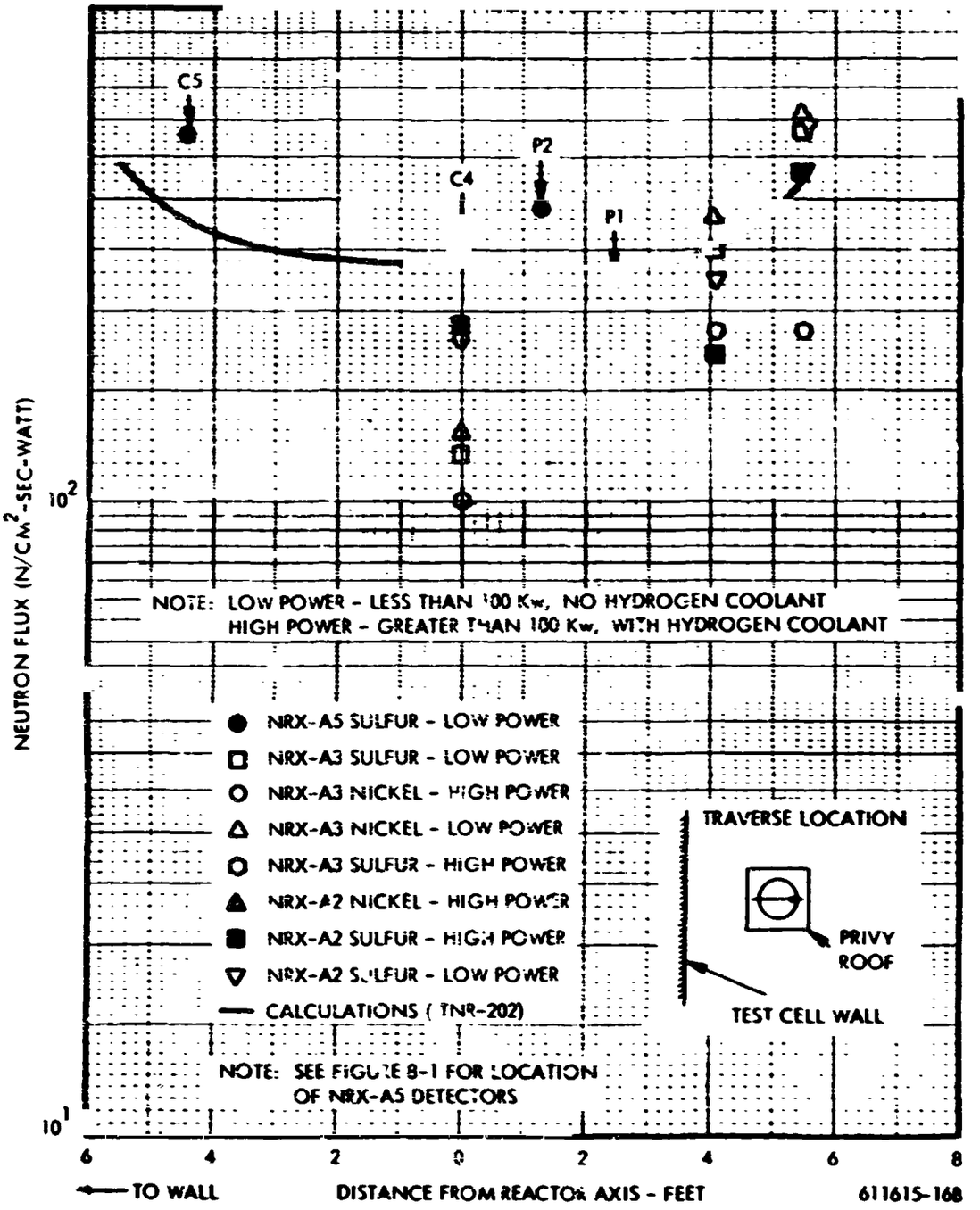

Figure 8-16. Fast Neutron Flux (E >2.9 Mev) Distribution on the Top Surface of the Privy Roof Shield

It is interesting to note the lack of consistency in the high and low power nickel measurements for NRX-A3. On the reactor axis the flux per unit power, determined from high power measurements, is higher than determined from low power measurements whereas at a radius of 5.5 feet the opposite is observed. There is no logical explanation for this discrepancy and merely points out the scatter in the data.

However, it should also be noted that the congestion of hardware on the privy roof under the reactor closure makes it very difficult to orient the detectors the same way for all reactor tests. In particular the NRX-A5 test had the INIS neutronic detector system mounted on the roof under the closure and this system itself would probably perturb the neutron levels.

8.5.4 Test Car

Fast neutron fluxes were measured at various locations on the test car (see Figure 8-1 for detector locations). A horizontal traverse, shown in Figure 8-17, extends approximately the length of the test car at an elevation of about 11 feet below the center of the core (station-108). The A5 sulfur data fall within the range of the previously measured data except at location CA4, where the A5 sulfur data is somewhat higher. At some locations on the test car, a spread of a factor of 4 or 5 is observed in the measured data. No correlation between low and high power flux per unit power can be noted since the sulfur high power data is generally higher than the sulfur low power data, whereas the opposite is true for the nickel data. The calculated data (Reference 10) have about the same "shape" as the experimental data.

Figure 8-18 shows a traverse of measured and calculated fast neutron flux in the privy. The A5 measurements are in reasonable agreement with the previous reactor test data. The calculated data are in reasonable agreement with the measurements considering the complexity of the geometry involved. However, the predicted fluxes are as much as a factor of 2 higher than the bulk of the data in this area. The predictions, described in Reference 10,

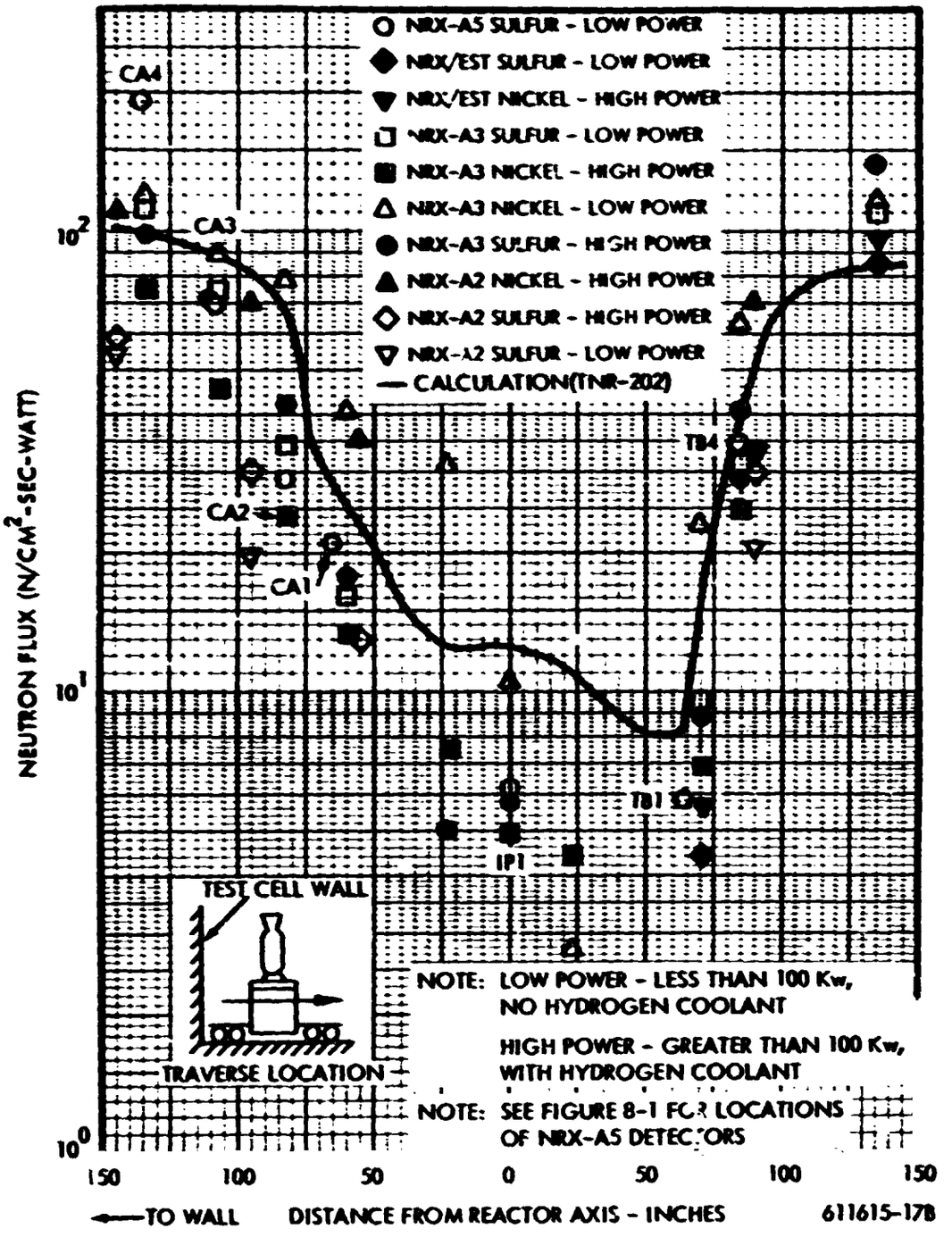

Figure 8-17. Fast Neutron Flux (E>2.9 Mev) Distribution under the Privy Roof (Horizontal Traverse-Station-108)

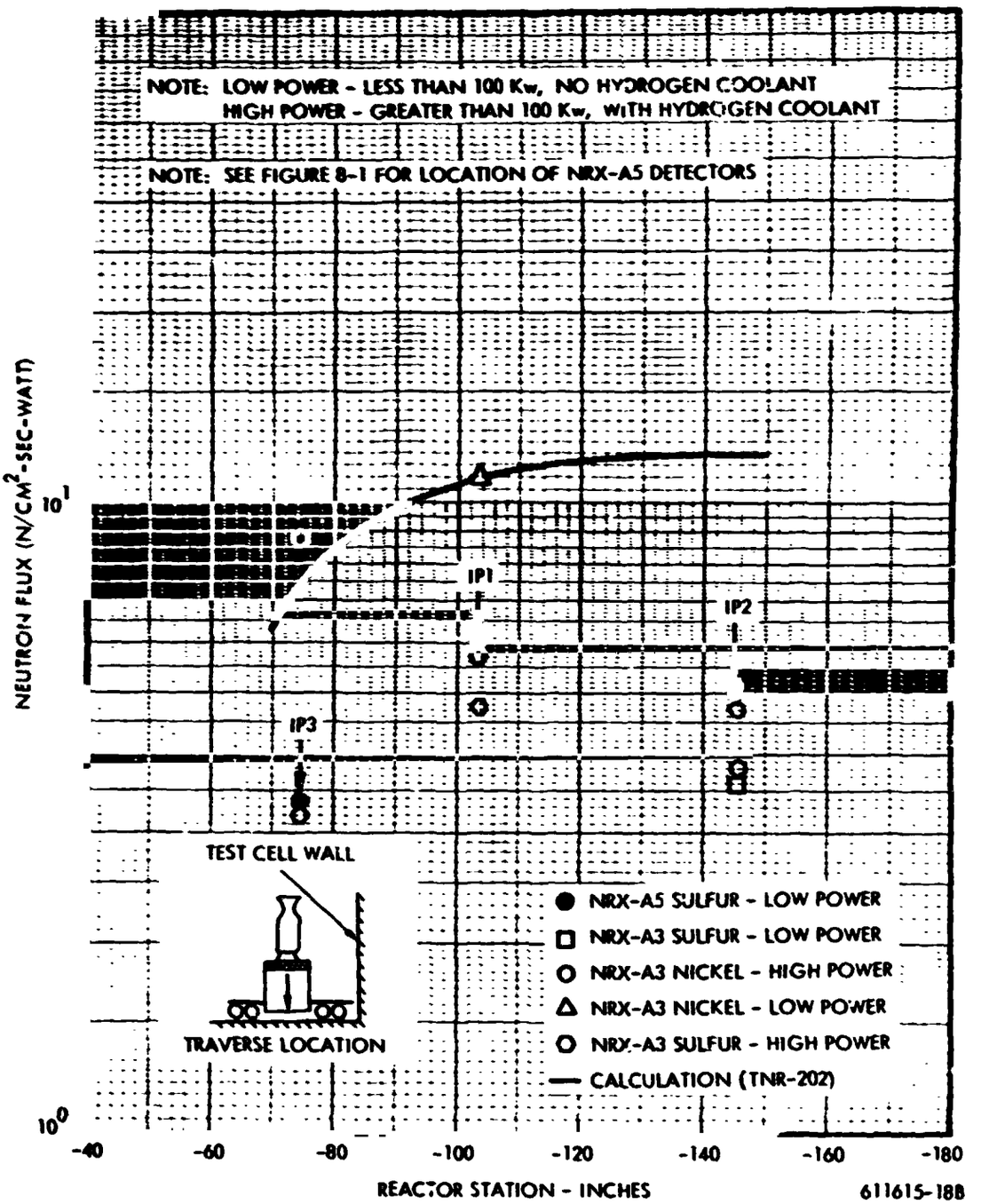

Figure 8-18. Fast Neutron Flux (E > 2.9 Mev) Distribution on the Reactor Axis under the Privy Roof

have as the chief component neutrons which scatter from the wall or pad into the area under the roof. The calculations do not take into account the attenuation of neutrons by the test car or privy and associated structure which probably is the main reason why the calculations are higher than measurements in this area.

8.5.5 Test Cell Wall

Figure 8-19 presents a horizontal traverse in the core midplane on the test cell wall. Figure 8-20 presents a vertical traverse on the wall 5 feet north of the normal projection of the core center. (See Figure 8-2 for detector locations.) In the horizontal traverse on the test cell wall, previous measurements were available only out to a distance of 20 feet north of the core. The A5 measurement at TCW-1 extended the traverse out to 60 feet north of the reactor. The A5 measured data shown in the vertical traverse in Figure 8-20 are in excellent agreement with previous measurements which lend confidence to the data at 60 feet on the horizontal traverse. The calculated data (Reference 10) for both the horizontal and vertical traverses agree very well both in shape and magnitude with the measurements.

8.5.6 Test Cell Pad

Four detectors were exposed on the test cell pad at locations not covered during previous reactor tests. The fast neutron fluxes are presented in Figures 8-21 and 8-22 along with previous reactor test data. Figure 8-21 is a traverse on the pad 3 feet from the wall and parallel to the wall, extending to 60 feet north of the core. Figure 8-22 is a traverse on the pad normal to the wall, 5 feet north of the reactor, extending to a distance of about 60 feet from the wall. The A5 measured data appear to be reasonable with respect to the previous measured data and with calculation results. The A3 low power sulfur fluxes per unit power on the pad (Figure 8-22) are higher than the high power sulfur data, which conflict with the observation of similar data on the test car (Figure 8-17). The calculated data (Reference 10) agree to within a factor of 2 with the measurements.

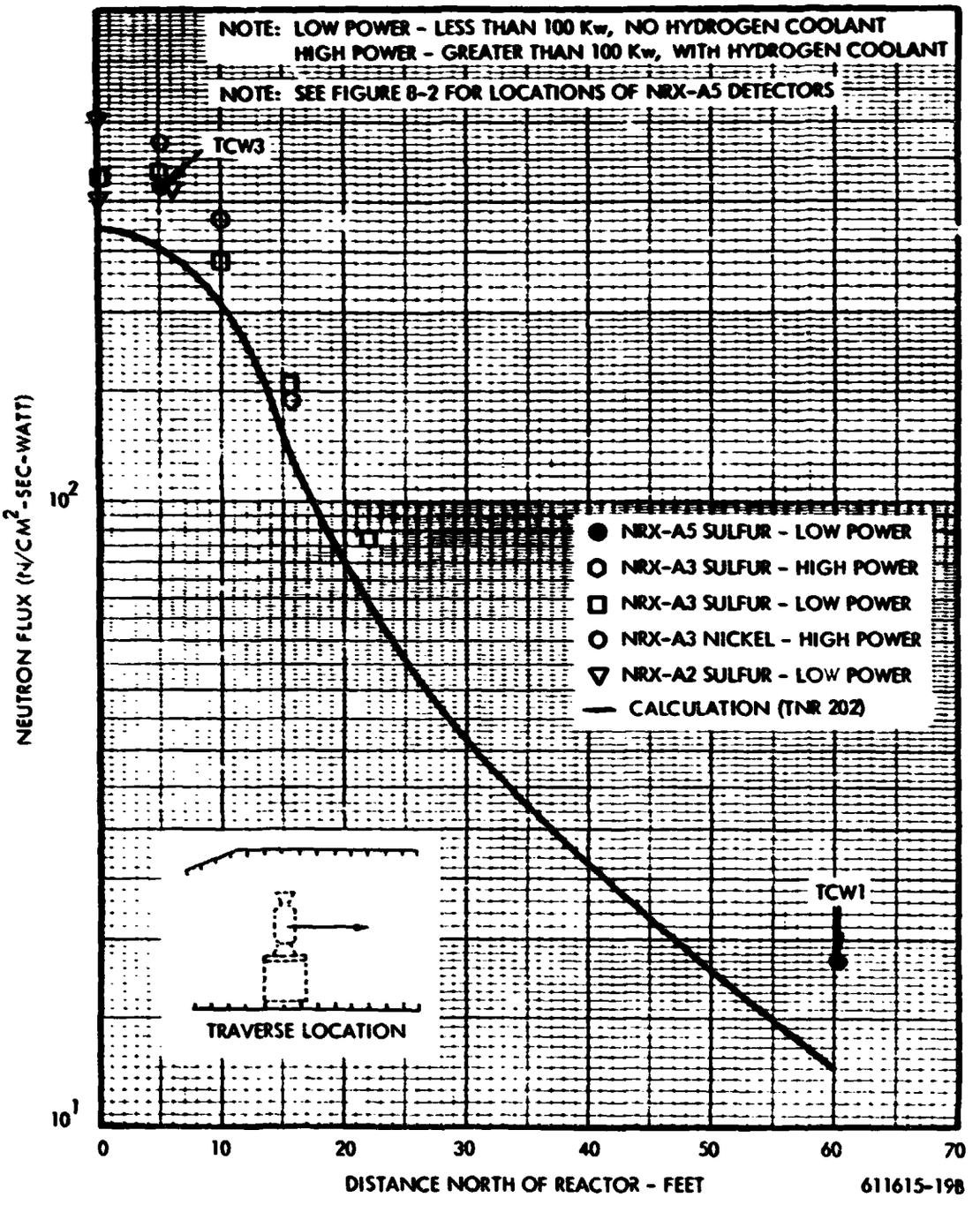

Figure 8-19. Fast Neutron Flux (E > 2.9 Mev) Distribution on the Test Cell Wall (Horizontal Traverse in the Core Midplane)

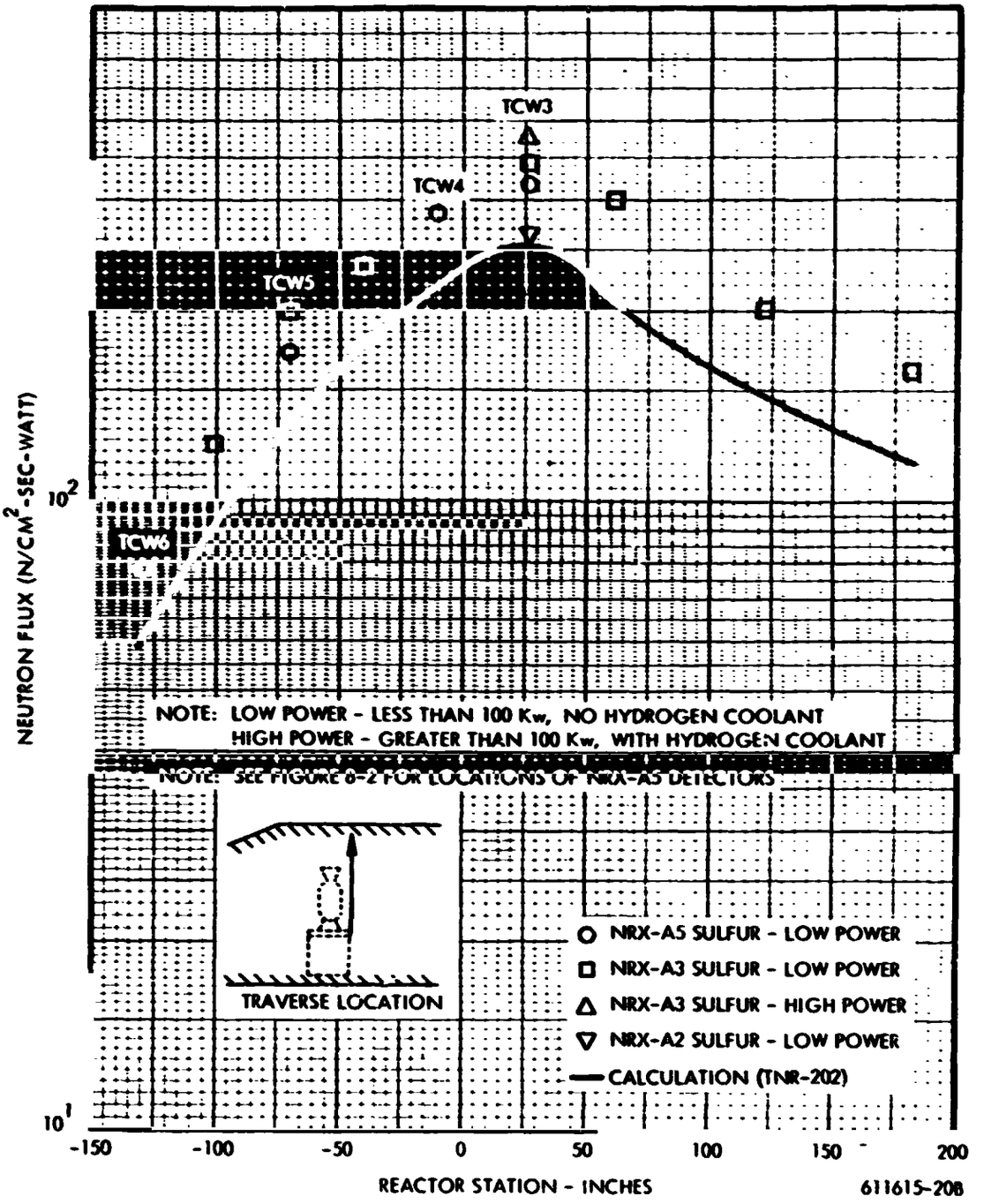

Figure 8-20. Fast Neutron Flux (E > 2.9 Mev) Distribution on the Test Cell Wall (Vertical Traverse Five Feet North of the Reactor)

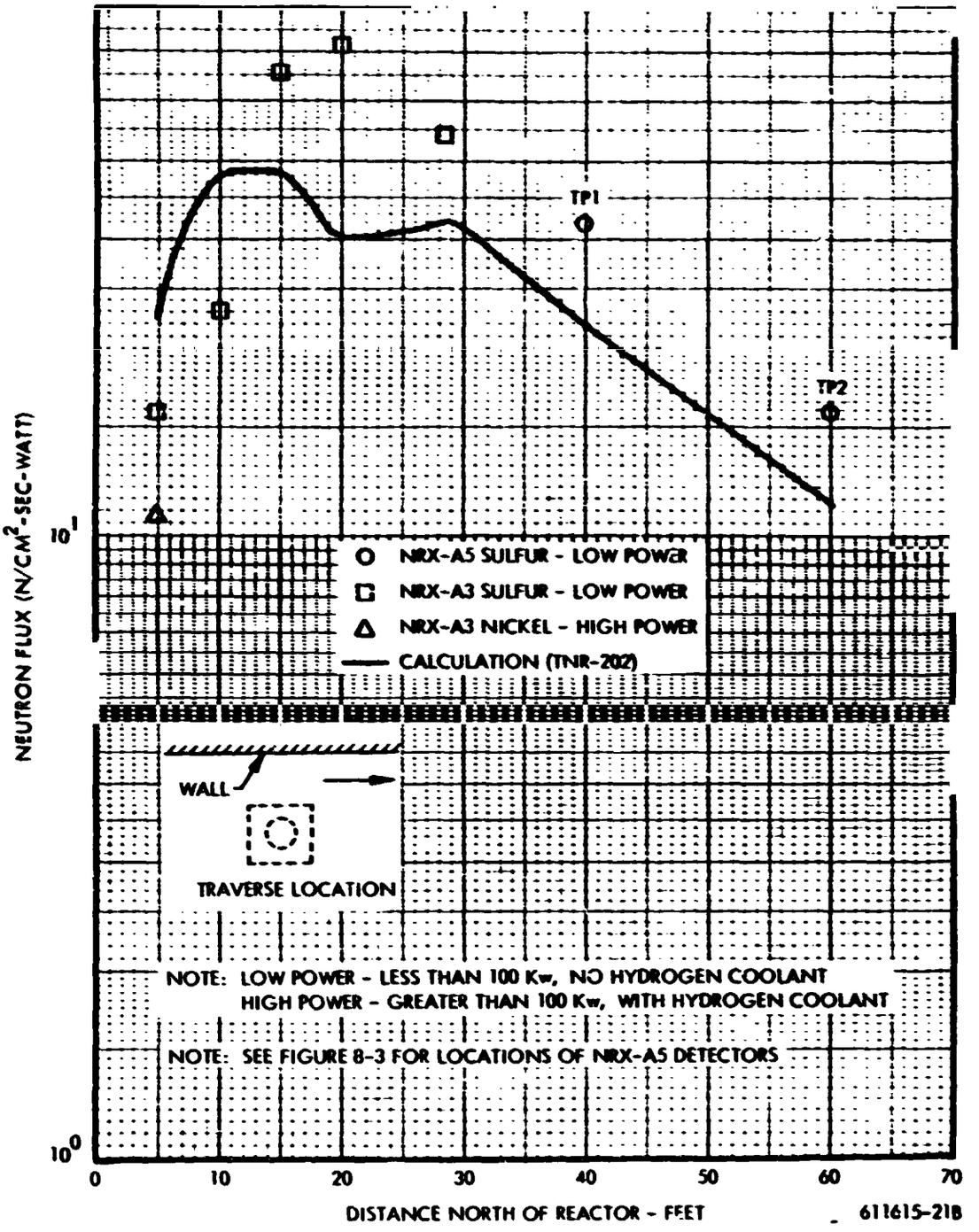

Figure 8-21. Fast Neutron Flux (E>2.9 Mev) Distribution on the Test Pad (Traverse Parallel to the Wall and 3 Feet from the Wall)

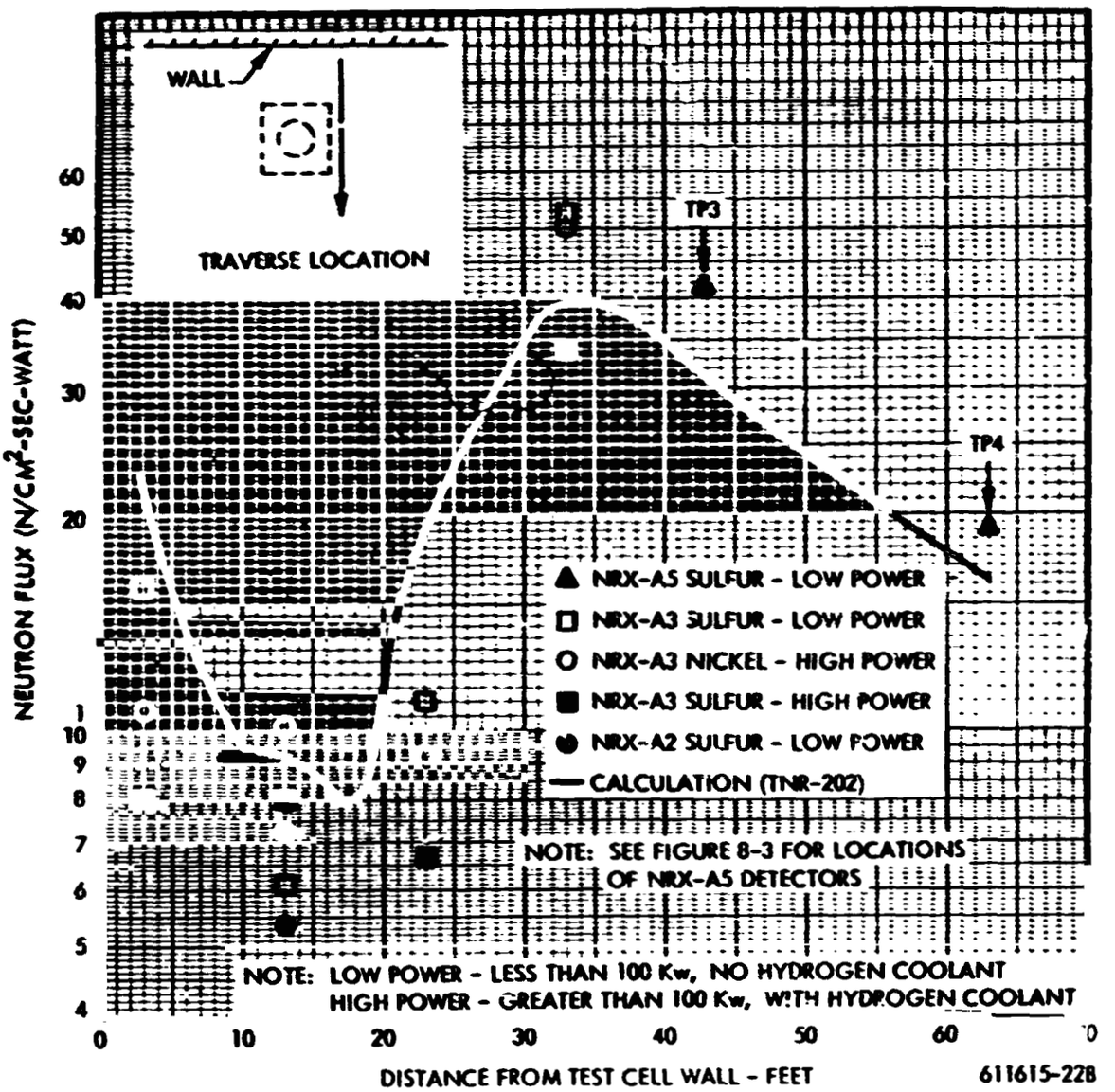

Figure 8-22. Fast Neutron Flux (E >2.9 Mev) Distribution on the Test Pad (Traverse Normal to the Wall and 5 Feet North of the Reactor)

8.5.7 Summary

The NRX-A5 fast neutron flux (E>2.9 Mev) measurements were in good agreement with previous reactor measurements. In addition, A5 data were obtained in areas not previously measured during the other NRX reactor tests. The A5 data extend the measured NRX fast neutron environment on the test cell wall from 20 feet to 60 feet north of the reactor. On the pad, previous fast flux traverses were extended by about 30 feet. These traverses were both parallel and perpendicular to the test cell wall.

The spread in the experimental data for three NRX reactors (A2, A3, and A5) was observed to be less than 50 percent except at locations in the shadow of the privy and on the top surface of the privy roof. On the surface of the roof the spread was about a factor of two. At locations in the shadow of the roof the spread in the experimental data was as much as a factor of five. These areas are very congested with hardware and the spread in the data is probably caused by differences in detector location from one reactor test to another and local perturbations caused by associated hardware in these areas. Neutron levels in these areas are also relatively low and are based on poorer counting statistics.

With the exception of the measured data on the pressure vessel surface it is not possible to establish any trend in fast neutron fluxes per unit power at high power versus low power conditions. On the pressure vessel surface, the measurements indicate that the fast neutron flux per unit power is somewhat higher for low power conditions than for high power.

Calculations of fast neutron flux (E>2.9 Mev) are within 50 percent of all measurements made at locations outside the shadow of the privy roof. One exception should be noted (i.e., at locations on top of the privy roof where the discrepancy is as much as a factor of two).

At locations within the shadow of the privy roof the calculations disagree with the measurements by as much as a factor of four. However, for these latter cases where the discrepancy between calculations and measurements is large, the calculations are conservative. The calculations of neutrons which scatter off the wall and pad into these highly shielded areas do not account for attenuation by the test car, privy, or associated hardware which causes the calculations to be conservative.

TABLE 8-4

NRX-A5 THERMAL NEUTRON FLUX MEASUREMENTS

Dosimeter Identification		Neutron Flux (n cm^{-2}-sec^{-1}) Bare Au	Cd Covered Au	Bare-Cd Covered	Cadmium Ratio **
N	1	4.002 (3)*	2.387 (3)	1.62 (3)	1.64
N	2	7.212 (3)	6.503 (3)	7.09 (2)	1.11
NF	1	7.553 (3)	4.695 (3)	2.86 (3)	1.61
NF	2	7.640 (3)	2.735 (3)	4.91 (3)	2.78
TB	1	4.022 (2)	1.829 (2)	2.19 (2)	2.20
TB	2	2.975 (2)	1.720 (2)	1.26 (2)	1.73
TB	3	3.332 (2)	1.966 (2)	1.37 (2)	1.69
TB	4	9.935 (2)	4.624 (2)	5.21 (2)	2.13
TB	5	4.305 (2)	2.082 (2)	2.22 (2)	2.08
TB	6	5.063 (2)	2.418 (2)	2.65 (2)	2.09
P	1	1.187 (4)	4.148 (3)	7.72 (3)	2.87
P	2	1.579 (4)	4.671 (3)	1.11 (4)	3.40
CA	1	2.152 (3)	6.889 (2)	1.46 (3)	3.12
CA	2	2.581 (3)	8.926 (2)	1.69 (3)	2.89
CA	3	3.053 (3)	1.069 (3)	1.98 (2)	2.84
CA	4	3.214 (3)	1.175 (3)	2.04 (3)	2.72
CA	5	1.739 (3)	6.235 (2)	1.12 (3)	2.79
CA	6	2.330 (3)	8.692 (2)	1.46 (3)	2.68
CA	7	2.999 (3)	1.002 (3)	1.99 (3)	2.99
CA	8	3.446 (3)	1.192 (3)	2.25 (3)	2.89
C	1	1.676 (3)	6.770 (2)	9.99 (2)	2.48
C	2	1.163 (4)	4.750 (3)	6.88 (3)	2.44
C	4	1.116 (4)	4.278 (3)	6.88 (3)	2.62
C	5	7.457 (3)	2.987 (3)	4.47 (3)	2.50
IP	1	8.084 (2)	3.240 (2)	4.84 (2)	2.49
IP	2	8.420 (2)	3.231 (2)	5.19 (2)	2.61
IP	3	6.484 (2)	2.019 (2)	4.47 (2)	3.20
DP	1	6.896 (3)	2.735 (3)	4.16 (3)	2.52
DP	2	8.477 (3)	3.688 (3)	4.79 (3)	2.31
DP	3	1.158 (4)	5.111 (3)	6.47 (3)	2.27
DP	4	1.383 (4)	6.131 (3)	7.69 (3)	2.25
DP	5	1.705 (4)	7.245 (3)	9.81 (3)	2.36
DP	7	3.836 (4)	1.575 (4)	2.26 (4)	2.44
DP	8	3.745 (4)	1.650 (4)	2.09 (4)	2.27
DP	9	2.577 (4)	1.185 (4)	1.39 (4)	2.17
DP	10	---	7.605 (3)	---	---
DP	11	1.012 (4)	5.054 (3)	5.07 (3)	2.00
DP	12	6.356 (3)	3.434 (3)	2.92 (3)	1.85
DP	13	4.684 (3)	2.661 (3)	2.02 (3)	1.76
DP	14	3.792 (3)	2.066 (3)	1.72 (3)	1.83
TCW	1	4.900 (2)	1.200 (2)	3.71 (2)	4.07
TCW	2	7.311 (2)	2.377 (2)	4.94 (2)	3.08
TCW	3	6.923 (3)	2.441 (3)	4.48 (3)	2.84
TCW	4	5.394 (3)	1.935 (3)	3.46 (3)	2.78
TCW	5	4.021 (3)	1.443 (3)	2.58 (3)	2.79
TCW	6	2.365 (3)	7.502 (2)	1.61 (3)	3.16
TP	1	7.719 (2)	2.471 (2)	5.25 (2)	3.13
TP	3	9.811 (2)	3.281 (2)	6.53 (2)	2.99
TP	4	4.624 (2)	1.563 (2)	3.06 (2)	2.96
SP	1	2.539 (4)	1.431 (4)	1.11 (4)	1.78
SP	2	1.572 (5)	5.928 (4)	9.79 (4)	2.65
SP	3	5.362 (4)	1.902 (4)	3.46 (4)	2.82
SD	1	8.544 (3)	5.210 (3)	3.33 (3)	1.64

Note * Numbers in Parentheses Indicate Powers of 10.

** Cadmium Ratio is defined as Bare Au / Cd Covered Au

8.6 THERMAL NEUTRON FLUX DATA (E<0.4 ev)

Bare and cadmium covered gold foils were exposed at 54 locations outside the NRX-A5 reactor. Table 8-4 gives both the measured bare and cadmium covered fluxes at each detector location. The thermal neutron fluxes for (E<0.4 ev) are also included in the table. These data were obtained by subtracting the cadmium covered foil data from the bare foil data. Also included at each location is the cadmium ratio which is defined as the ratio of the bare foil count rate to the cadmium covered foil count rate. The cadmium ratio indicates how thermal the spectrum is--i.e., a high cadmium ratio indicates a relatively high thermal flux. No calculated data are presented in Table 8-4 because, except at the surface of the pressure vessel, the analytical techniques employed here cannot be used to compute thermal fluxes in the complex geometries encountered at the test facility. Measured thermal flux data (bare minus Cd covered) from Table 8-4 are plotted graphically (where possible) in Figures 8-23 through 8-31 along with previous reactor test data.

8.6.1 Pressure Vessel Surface

Explerimental thermal neutron flux data obtained during low power tests of NRX-A3 and NRX-A5 on an axial traverse at the surface of the pressure vessel are presented in Figure 8-23 as a function of reactor station. The A5 data at detectors SP-2 and SP-3 are in good agreement with the A3 data. The A5 data at SP-1 is roughly a factor of 2 lower than indicated by previous measurements which is probably due to poor statistics.

The calculated data shown in Figure 8-23 are in reasonable agreement with measured data; the maximum deviation is 45 percent on the reactor midplane. These calculations were obtained from an (r, z) transport code (TDC) run for room temperature conditions with an S_6 approximation.

8.6.2 Dosimeter Pole

NRX-A5 measured thermal neutron fluxes at locations on the dosimeter pole are plotted in Figure 8-24 as a function of reactor station. The dosimeter pole is a vertical pole mounted on the privy roof at a distance of 47 inches from the core axis at a reactor angle (θ) equal to 323 degrees. A dosimeter pole was not employed during previous reactor tests. However, data from interpolations of measurements on the meridian ring employed in previous reactor tests, are included for comparison in Figure 8-24. The A5 data appear to be somewhat lower than previous reactor data on the meridian ring.

8.6.3 Top or the Privy Roof Shield

NRX-A5 and previously measured thermal neutron fluxes are plotted in Figure 8-25 as a function of radial distance on the top surface of the privy roof. A spread of almost a factor of two is observed in the experimental data at several locations on top of the roof. No correlation is evident between high and low power thermal neutron fluxes on a per unit power basis.

8.6.4 Test Car

Thermal neutron flux measurements were made at various locations on the test car (see Figure 8-1 for detector locations). A horizontal traverse, shown in Figure 8-26, extended approximately the length of the test car at an elevation of about 11 feet below the center of the core (station-108). The A5 measurements appear to be in good agreement with previously measured data. A spread of about a factor of 1.5 is evident at most locations in this traverse.

8.6.5 Under the Privy Roof

A vertical traverse on the core centerline under the privy roof is shown in Figure 8-27 as a function of reactor station. The NRX-A5 data is in very good agreement with previously measured data. The spread in all of the measurements is about 70 percent.

No trend is evident between low and high power fluxes (on a per watt basis) at these locations.

8.6.6 Test Cell Wall

Figure 8-28 presents a horizontal traverse in the core midplane on the test cell wall. Previous reactor tests provided thermal neutron fluxes only out to 22 feet north of the reactor on the wall. The A5 measurements extended the traverse out to 60 feet north of the reactor. The A5 data is in excellent agreement with the A3 gold data at detector location TCW-3. The maximum scatter in the data from all reactors on this traverse is about 70 percent. The three cobalt data points measured during the A3 high power test, are consistently higher on a per watt basis (by about 17 percent) than the A3 cobalt data measured during the low power test. However, since this difference is within the accuracy of the measurements, it is not possible to conclude with certainty that the change is caused only by changes in reactor operating conditions.

Figure 8-29 presents a vertical traverse of thermal neutron fluxes on the test cell wall, 5 feet north of the normal projection of the core center. (See Figure 8-2 for detector locations.) The A5 data are in close agreement with the A3 gold data. The scatter in the data is similar to that previously observed in Figure 8-28 on the test cell wall.

8.6.7 Test Cell Pad

Four detector packets employing gold foils (with and without cadmium covers) were exposed on the test cell pad during the A5 reactor test. (See Figure 8-3 for detector locations.) The detectors were located at positions not covered during previous reactor tests. The A5 measurements are given in Figures 8-30 and 8-31 along with previous reactor test data. Figure 8-30 is a traverse on the pad 3 feet from the wall and parallel to the wall, extending to 40 feet north of the core. (Unfortunately, the data for location TP-2 was lost and, hence, is not shown in this traverse.) Figure 8-31 is a traverse on the pad, normal to the wall, 5 feet north of the reactor, extending to a distance of about 60 feet from the wall. The maximum scatter in the low power measured data is 50 percent. The

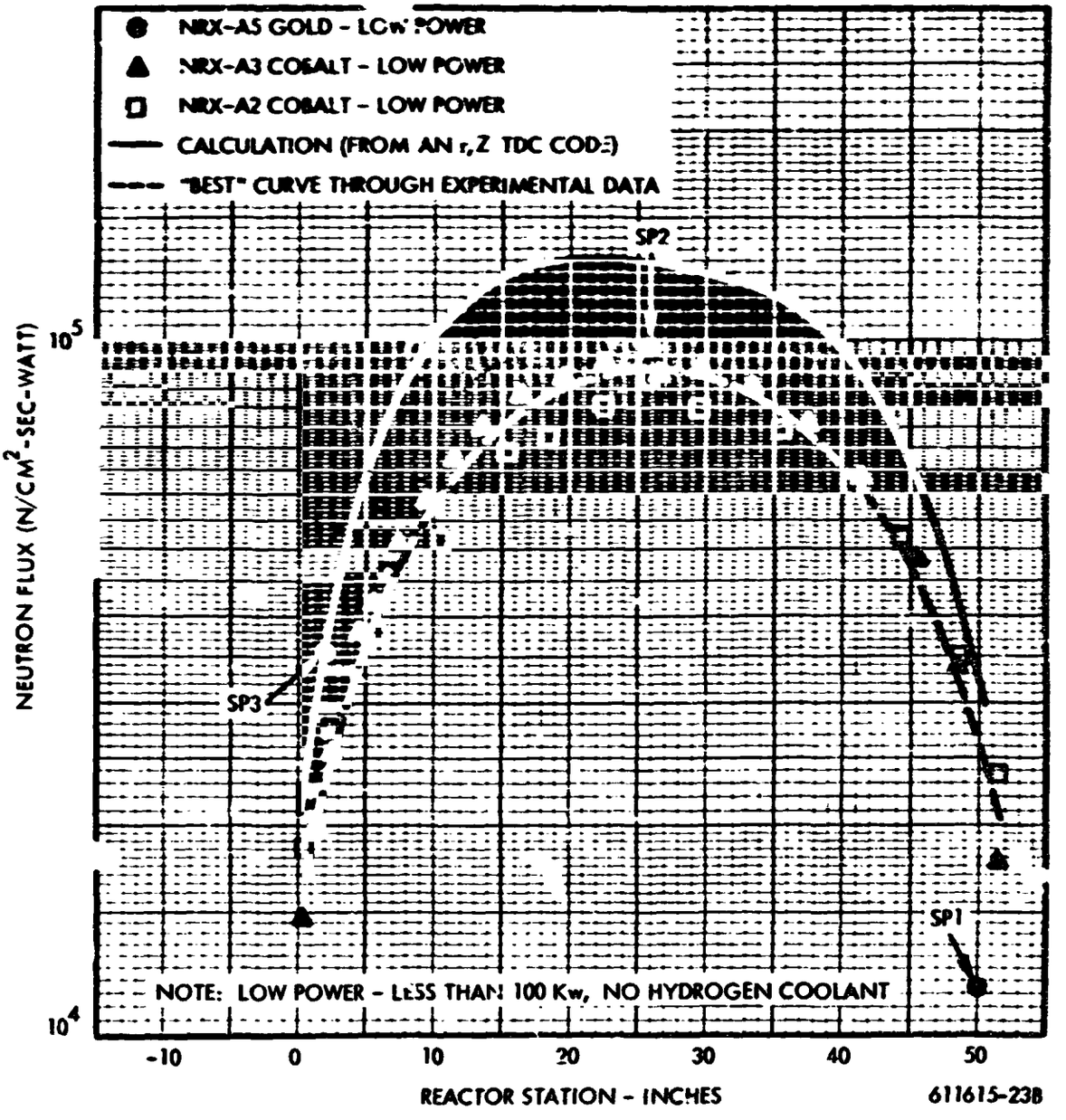

Figure 8-23. Axial Distribution of the Thermal Neutron Flux (E < 0.4 ev) on the Surface of the Pressure Vessel

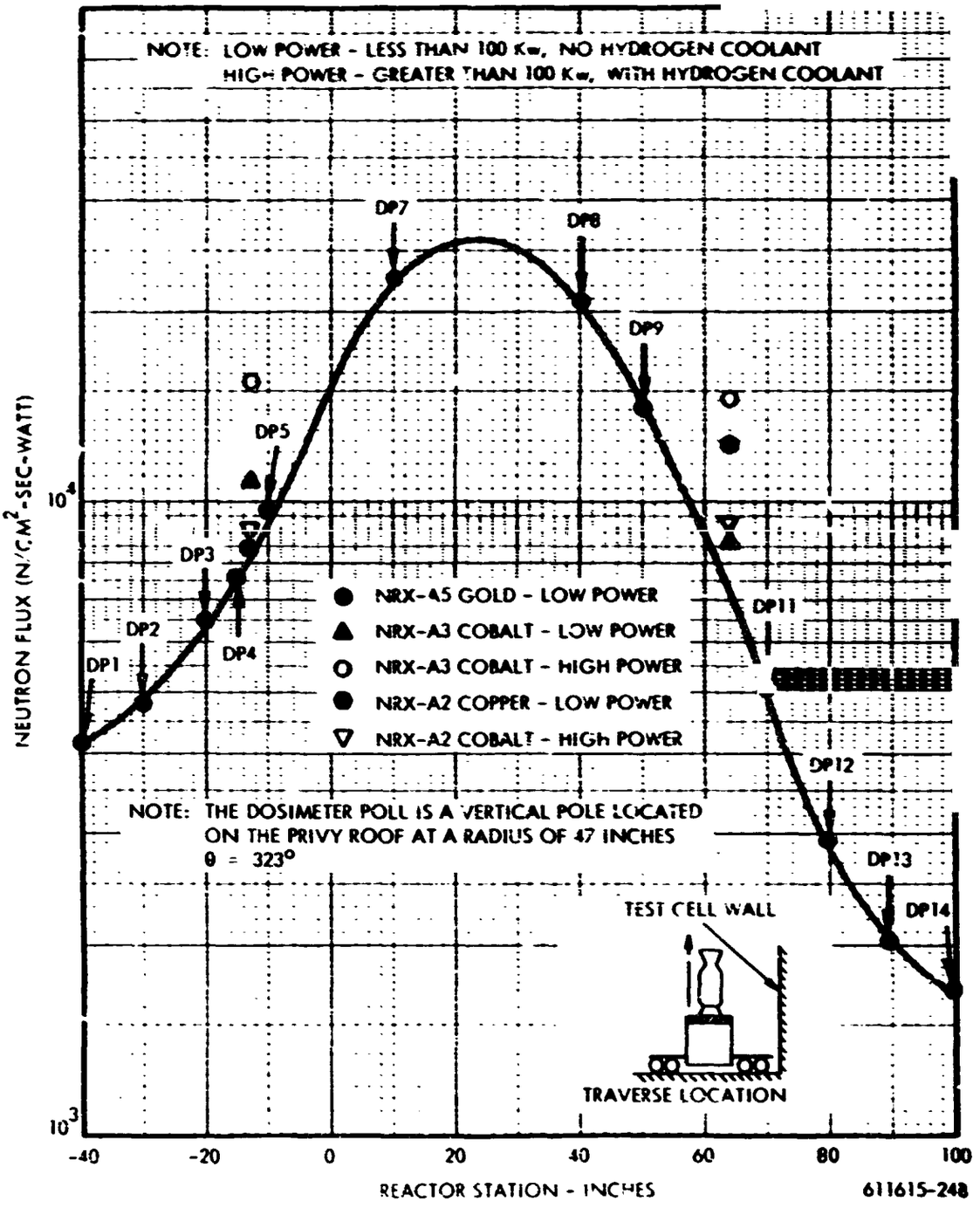

Figure 8-24. Thermal Neutron Flux (E<0.4 ev) Distribution on the Dosimeter Pole

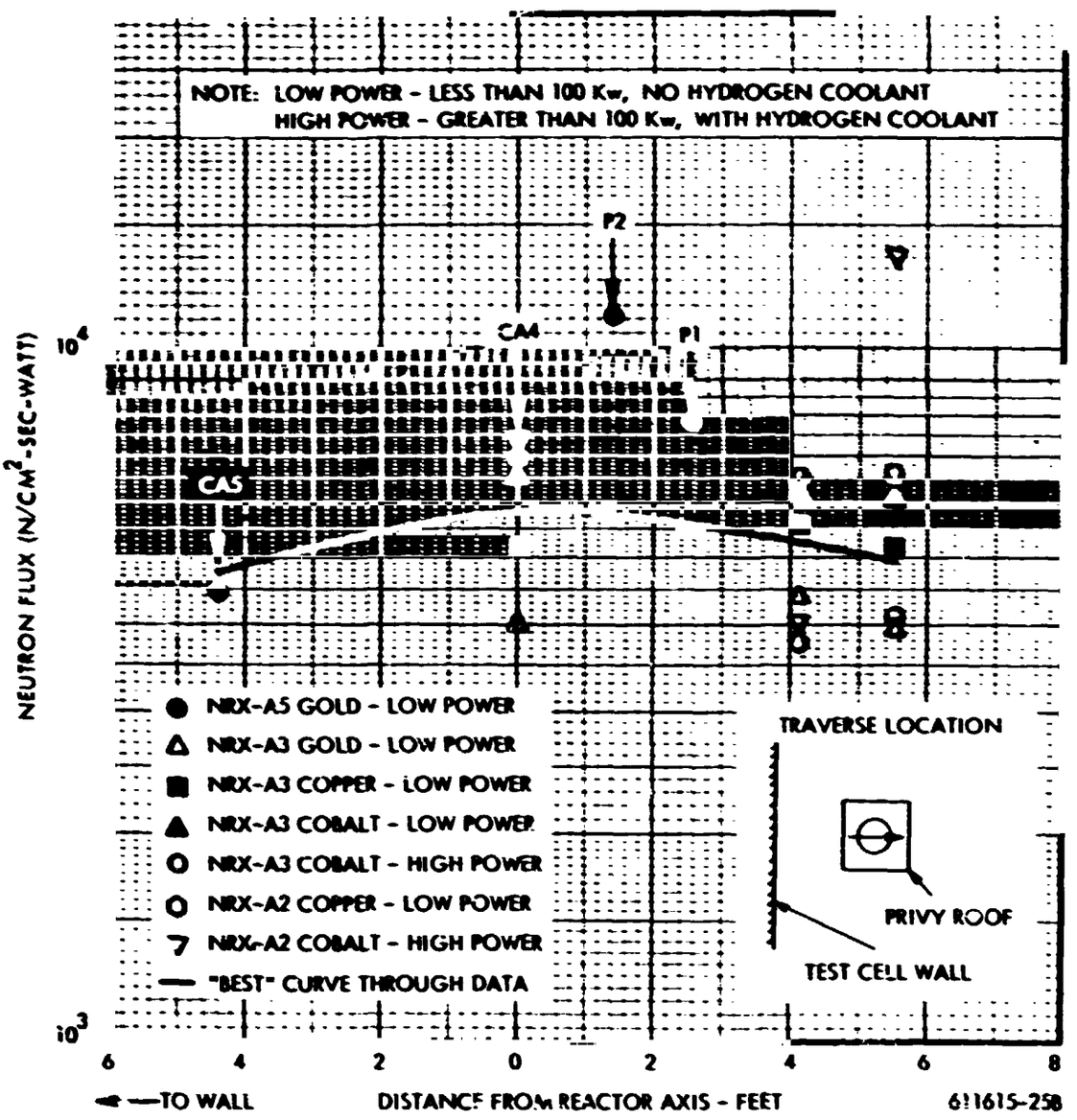

Figure 8-25. Thermal Neutron Flux (E<0.4 ev) Distribution on the Top Surface of the Privy Roof Shield

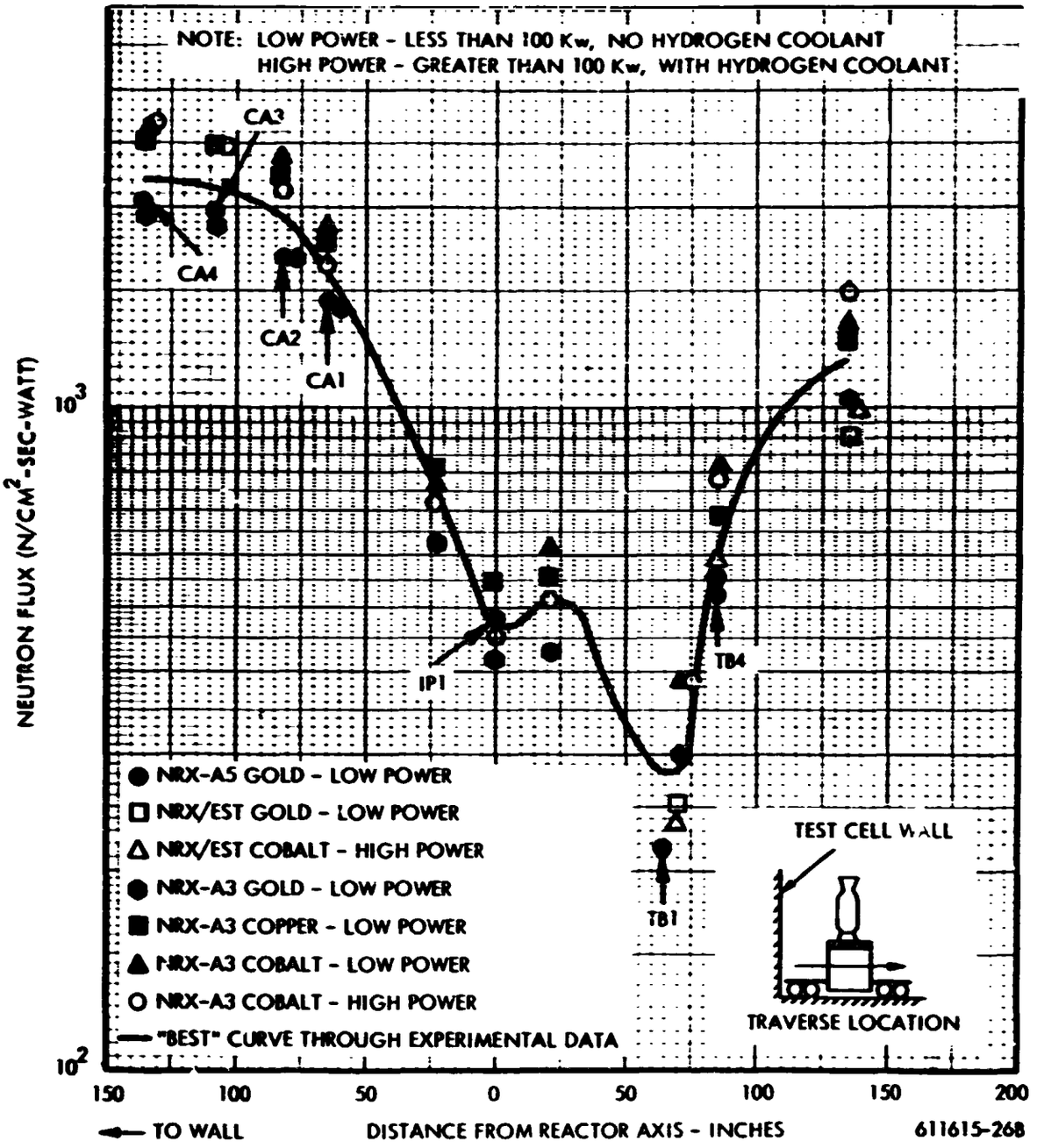

Figure 8-26. Thermal Neutron Flux (E <0.4 ev) Distribution under the Privy Roof (Horizontal Traverse-Station-108)

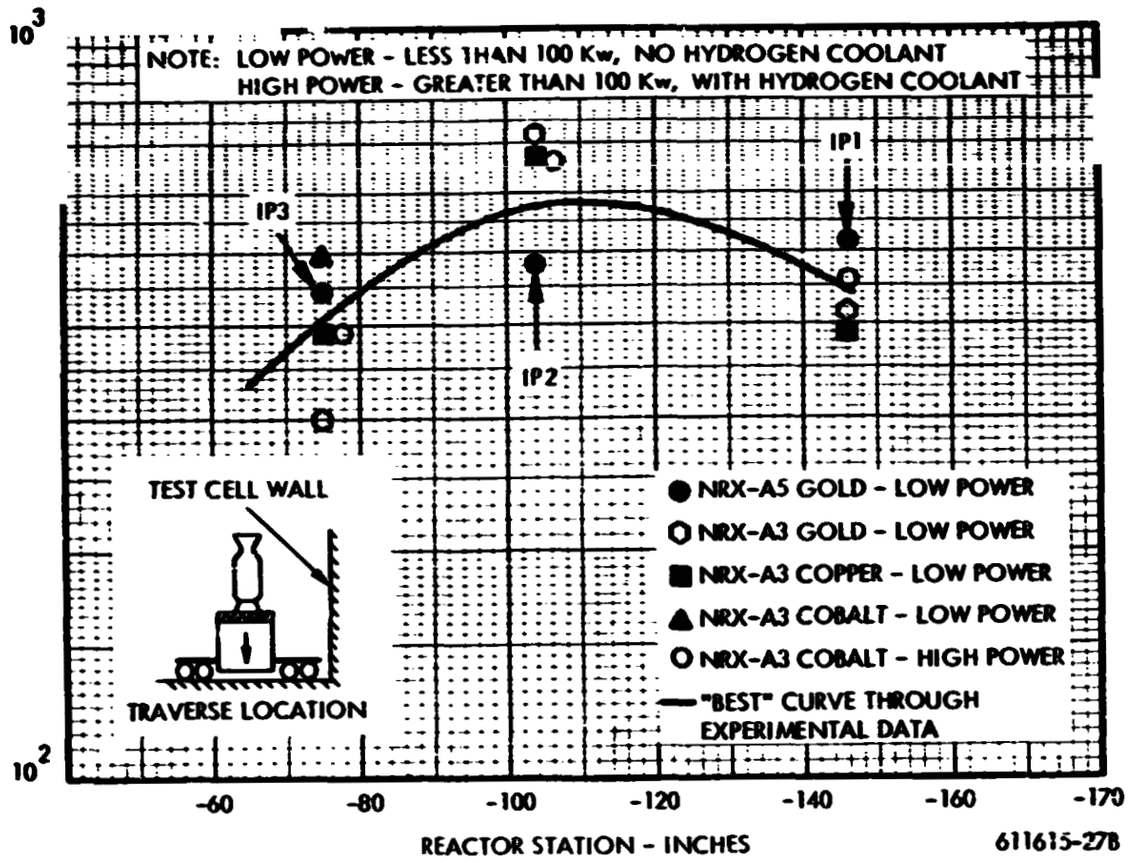

Figure 8-27. Thermal Neutron Flux (E < 0.4 ev) Distribution on the Reactor Axis under the Privy Roof

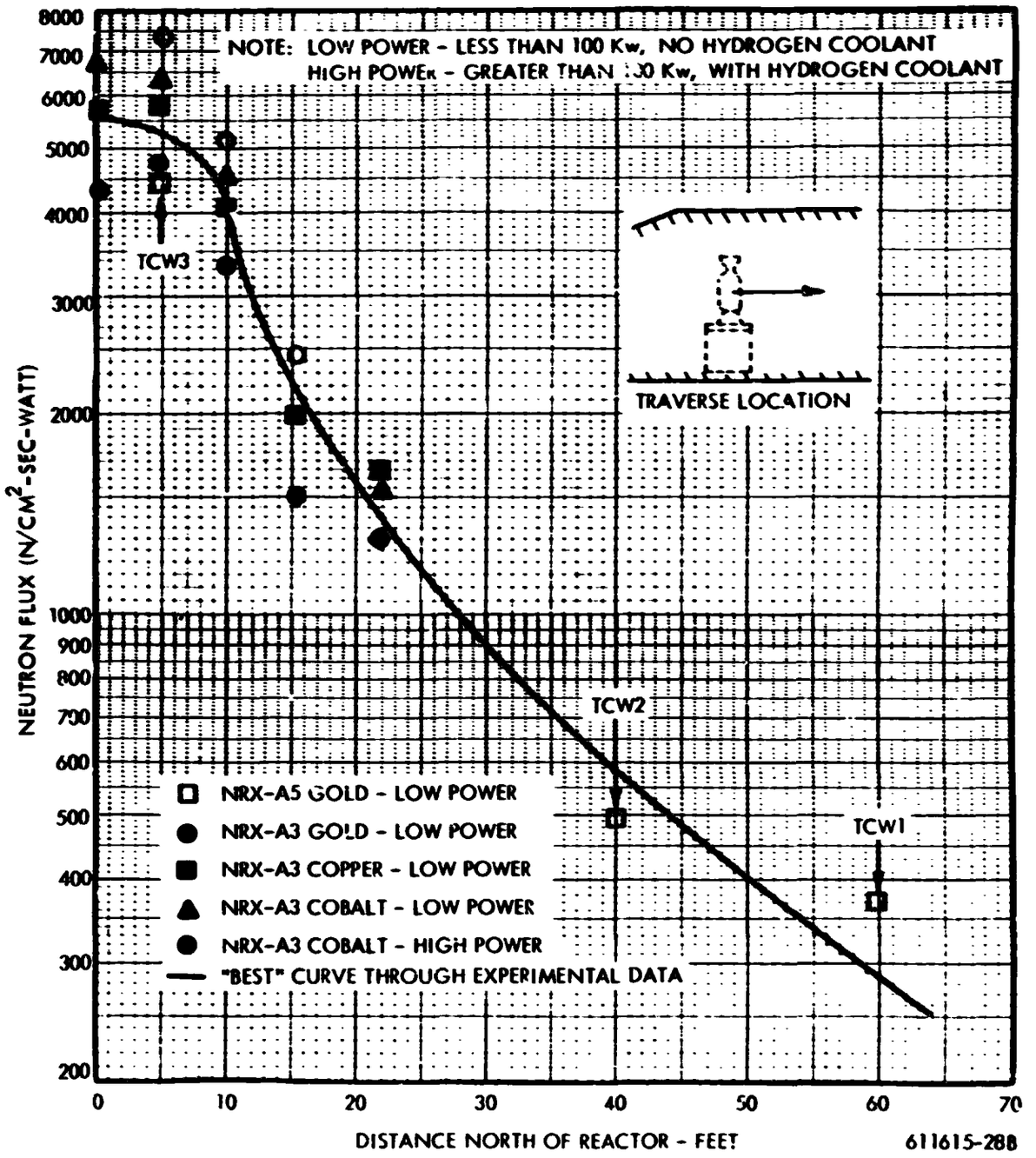

Figure 8-28. Thermal Neutron Flux (E <0.4 ev) on the Test Cell Wall (Horizontal Traverse in the Core Midplane)

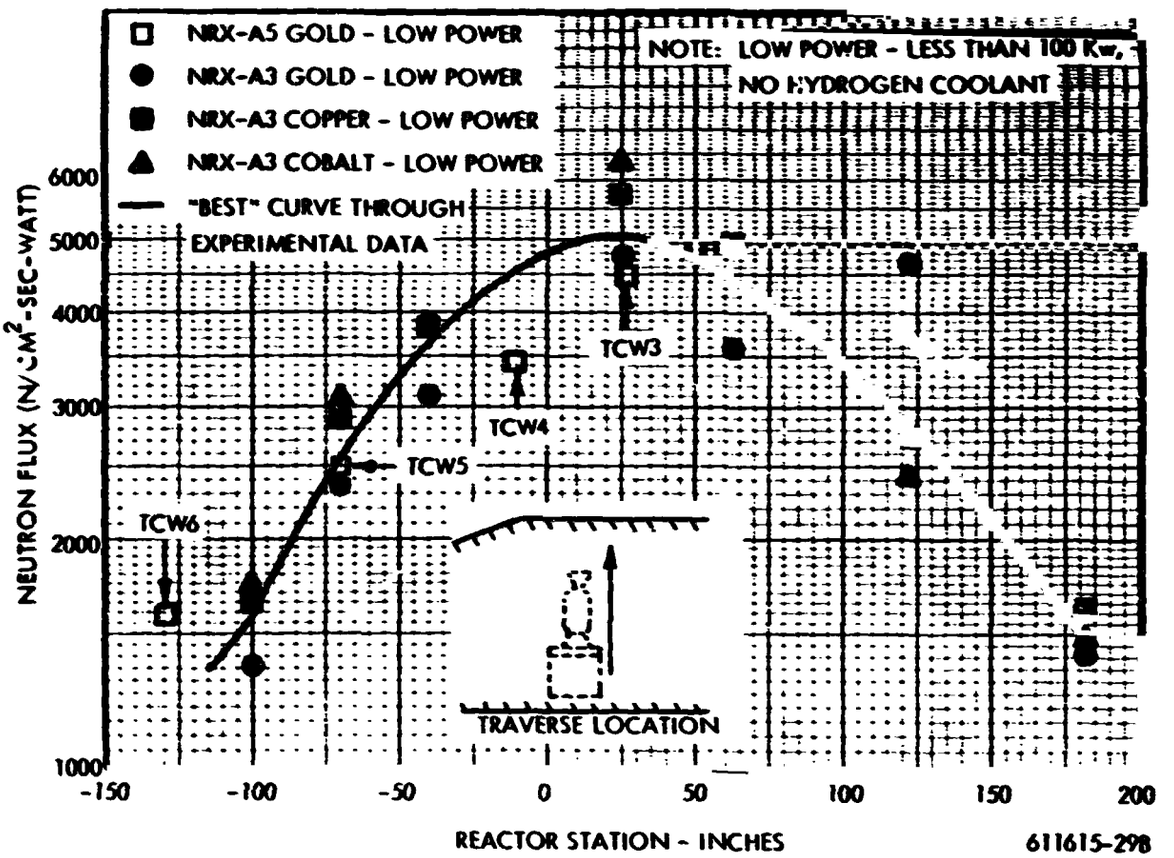

Figure 8-29. Thermal Neutron Flux (E <0.4 ev) Distribution on the Test Cell Wall (Vertical Traverse Five Feet North of the Reactor)

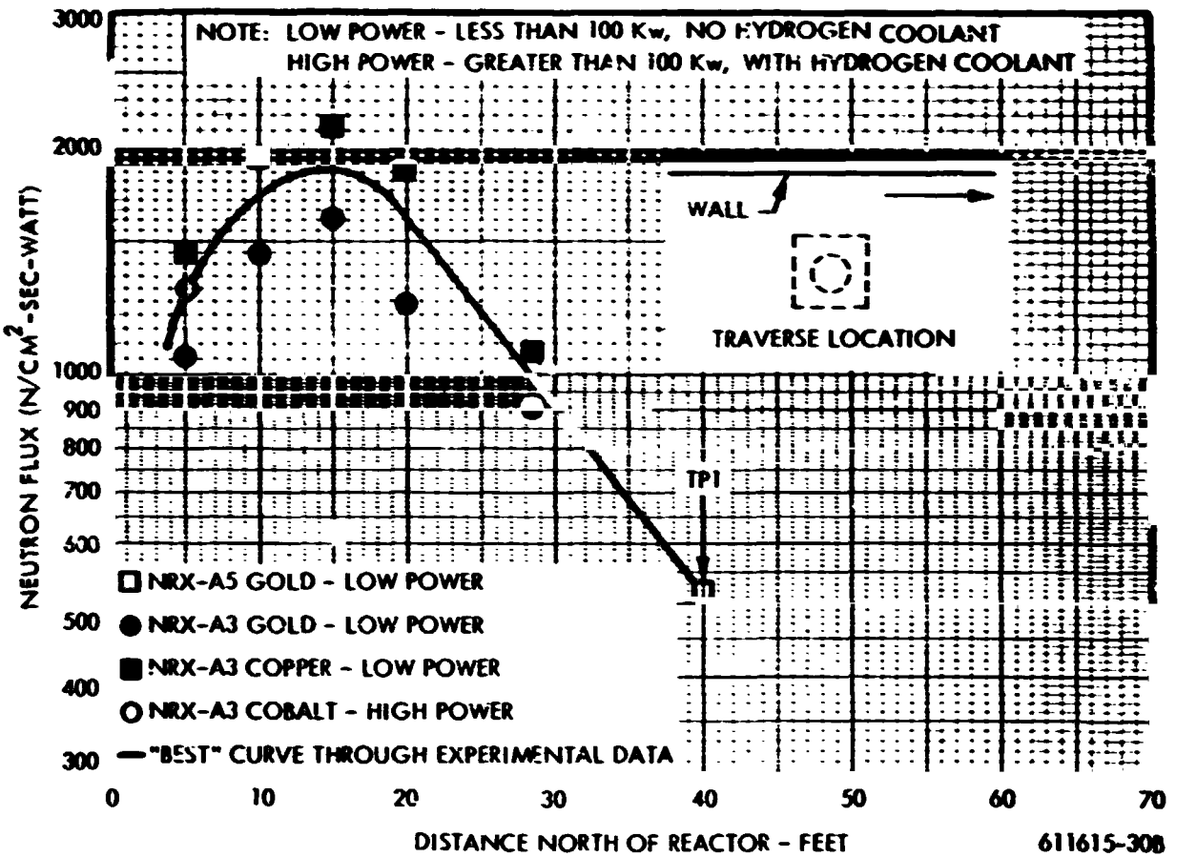

Figure 8-30. Thermal Neutron Flux (E<0.4 ev) Distribution on the Test Pad
(Traverse Parallel to the Wall and 3 Feet from the Wall)

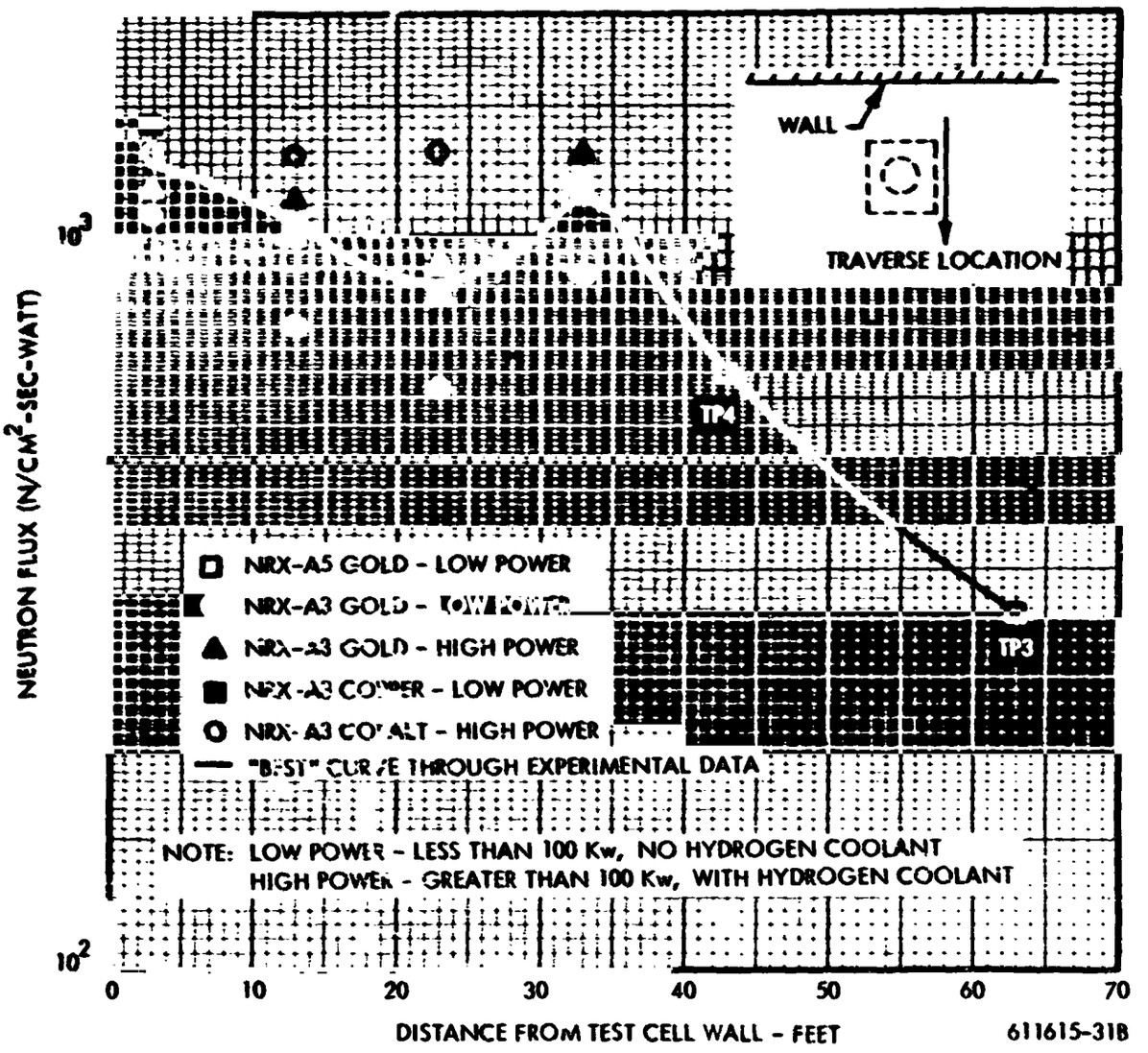

Figure 8-31. Thermal Neutron Flux (E<0.4 ev) Distribution on the Test Pad (Traverse Normal to Wall and 5 Feet North of the Reactor)

A3 cobalt data measured during the high power test are generally higher than any of the low power data, but no valid conclusion can be reached since no cobalt measurements were made during the low power A3 test.

8.6.8 Summary

Gold foil measurement of thermal neutron fluxes (E<0.4 ev) obtained during low power testing of NRX-A5 are in good agreement with data obtained during the NRX-A2 and NRX-A3 reactor tests. Considering data from all three reactors, the scatter in data is within a factor of two. This is good agreement considering that three types of foil (gold, copper, and cobalt) were used. There is better correlation between reactors for thermal neutron flux data than for either gamma ray data or fast neutron data. Similar to gamma ray and fast neutron data, it is not possible to see any differences on a per watt basis between measurements made at low power and measurements obtained at high power.

8.7 HEATING RATES FROM CALORIMETRIC DATA

8.7.1 General Discussion of the NRX-A5 Calorimeters

The NRX-A5 calorimeters were similar but not identical to those used in previous NRX reactor tests. Figure 8-32 is a schematic diagram showing the main components of the A5 calorimeters. The stand-off insulators shown in Figure 8-32 are the chief differences between the NRX-A5 calorimeters and those used in previous NRX tests. For the A5 calorimeters, the stand-offs connect the outer case directly to the sample core, whereas in the earlier design, the stand-offs did not pass through the inner shell. Another change in the A5 calorimeter design from the A2 through A4 calorimeters is in the material used for the stand-offs. The A5 calorimeter used alumina for the stand-offs, whereas the earlier calorimeters used steatite for the insulating material. Both design changes improved the calorimeters from a mechanical standpoint. However, these changes tend to impair the thermal performance of the detectors since: (1) the stand-offs now provide a more direct path for heat to flow from the outer case to the sample core, and (2) alumina has a higher thermal conductivity than steatite.

Three types of calorimeters (steel, aluminum, and beryllium) were exposed during the NRX-A5 test series. The outer case for all three types is made of steel and the inner shell and core are made of the sample material, except for the beryllium calorimeter which has a graphite inner shell. The inner shell is designed to act as a thermal shield for the core, and ideally, should operate at the same temperature as the calorimeter core if adiabatic conditions are achieved. In practice, however, the A5 calorimeters did not conform to the ideal standards. Except for the one steel calorimeter used in NRX-A5, the temperature of the inner shell was higher than that of the calorimeter core; and also, the temperature difference between the inner shell and the core increased with reactor operating time. Since the outer case of the calorimeters is made of steel which has a lower specific heat than either aluminum or beryllium, and since on a "per gram" basis the nuclear heating is expected to be similar for all three materials, it is obvious that the

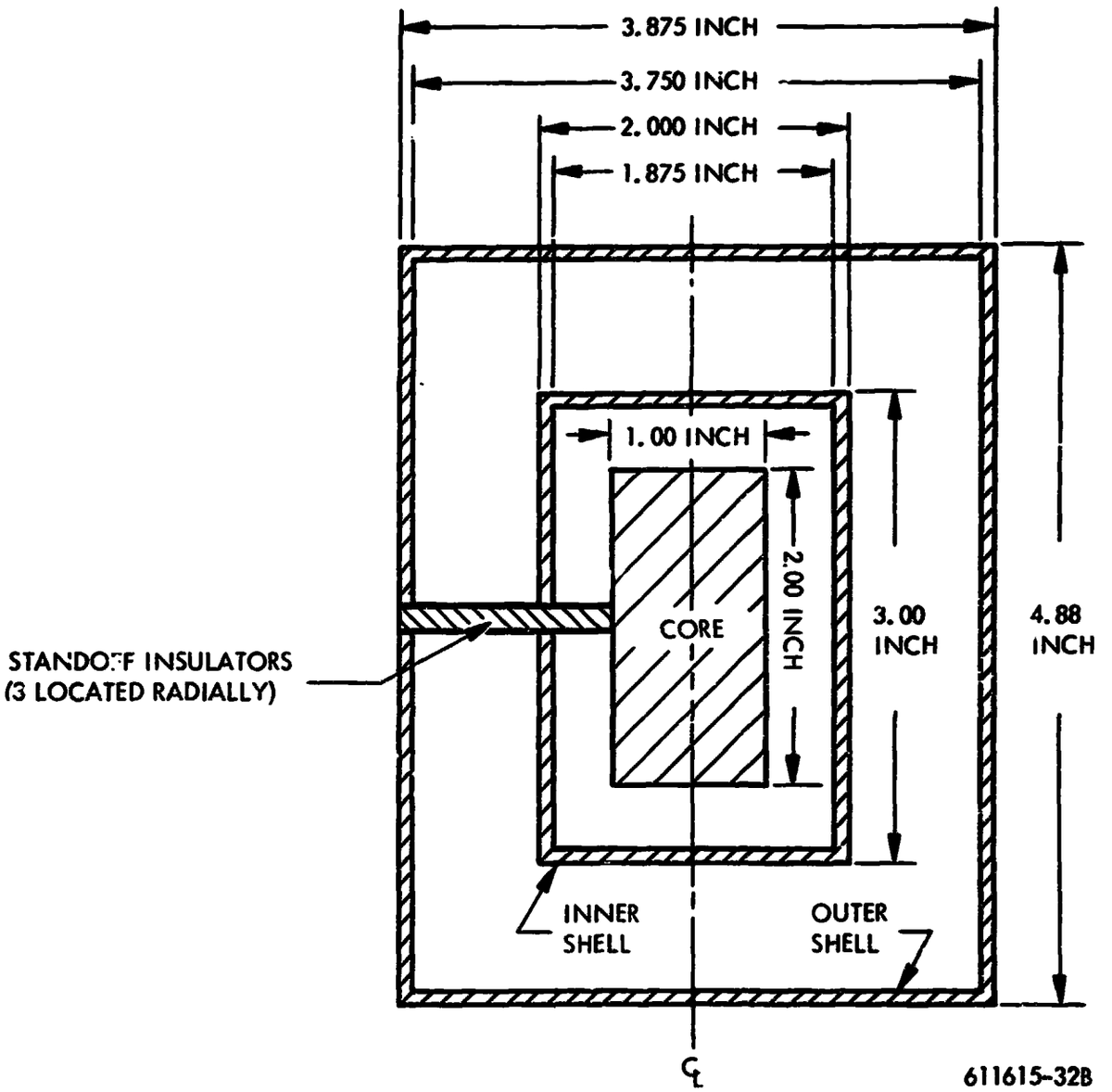

Figure 8-32. Schematic Diagram of NRX-A5 Calorimeter

temperature rise per unit time for steel should be steeper than for aluminum or beryllium provided that all three materials "see" the same nuclear radiation field. As discussed above, the alumina stand-off directly connects the outer case with the calorimeter core. Consequently, the temperature rise of the steel case is probably influencing the temperature rise of the core material. Unfortunately, the temperature of the calorimeter outer case is not monitored during the reactor tests. Consequently, no adjustment to the calorimeter data can be made to account for heat being added to the sample core from the outer shell which is of a different material for the aluminum or beryllium calorimeters.

In summary, the NRX-A5 calorimeters, although mechanically superior to the calorimeters used during the NRX-A2, NRX-A3 and NRX-A4 reactor tests, were slightly inferior from a thermal standpoint in that heat transfer from the case of the calorimeter to the sample material is more likely for the A5 calorimeter design. Without a temperature measurement of the outer calorimeter case, it is not possible to correct the sample data to account for heat leaking from the case to the sample. It will be noted later in the section that the NRX-A5 calorimeter heating rate data are slightly higher than measurements obtained with the previous type calorimeters during the A2, A3 and A4 tests at comparable locations.

8.7.2 NRX-A5 Calorimeter Heating Rate Data

Six calorimeters (4 aluminum, 1 steel, and 1 beryllium) were exposed during the NRX-A5 EP-III and EP-IV high power tests. Figure 8-33 shows a view of the reactor, test cell wall and privy roof shield, and gives the location of all calorimeters exposed during the four NRX reactor tests. Included in this figure is an outline (dashed line) of the privy roof mounted shield. This shield was mounted on the privy roof only during the NRX/EST test series. Figure 8-33 also gives the spatial locations of all the calorimeters in terms of reactor station, radius, and reactor azimuth angle θ. Calorimeters were placed at locations 1, 3, 5, 8, and 10 shown in Figure 8-33. For each of the six (NRX-A5) calorimeters, data were obtained for four data points during the EP-III and EP-IV tests. One point was obtained from EP-III and three points were obtained from EP-IV.

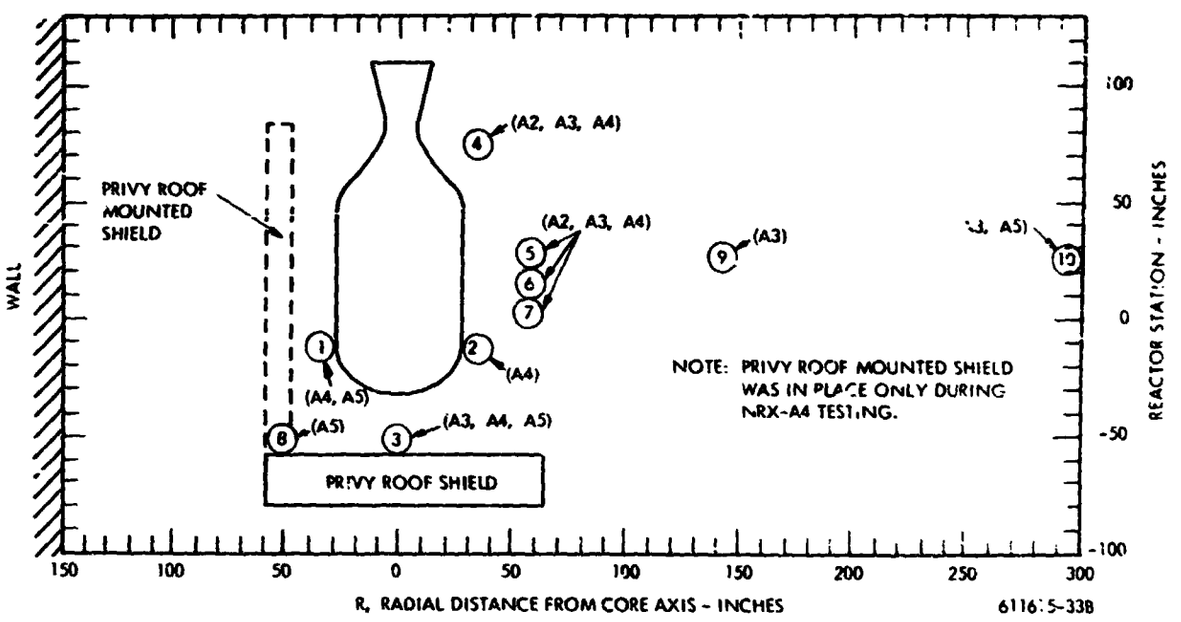

CALORIMETER LOCATION NO.	STA. (IN.)	R(IN.)	θ(DEG.)
1	-15.5	30.3	120
2	-15.5	30.3	300
3	-51	0	C
4	-76	33	-300
5	26	60	306
6	15	60	306
7	8.5	60	306
8	-51	52.4	126
9	26	144	345
10	26	300	345

NOTE: DATA IN PARENTHESES INDICATE THE REACTOR TESTS DURING WHICH CALORIMETERS WERE POSITIONED AT THE SPECIFIED LOCATIONS

Figure 8-33. View of Test Facility Showing Calorimeter Locations for the Various NRX Test Series

TABLE 8-5

NRX-A5 HEATING RATES FROM CALORIMETER MEASUREMENTS

Location Number *	Mat.	General Location	Reactor Test	Thermal Power (MW)	CRT t (sec.)	Temp. T (°R)	ΔP/Δt (°R/sec)	C_p (BTU/lb.-°R)	Heating Rate (W/Gm)
1	Al	Near Flange (θ = 120°)	EP-III	1042	25305	615	0.828	0.219	0.421
3	Al	Privy Roof (R = 0)				561	0.334	0.215	0.167
8	Al	Privy Roof (R = 52.4")				578	0.360	0.217	0.181
8	SS	Privy Roof (R = 52.4")				590	0.520	0.110	0.133
10	Al	Core Midplane (R = 25')				558	0.087	0.214	0.0433
10	Be	Core Midplane (R = 25')				556	0.055	0.439	0.0561
1	Al	Near Flange (θ = 120°)	EP-IV	1120	13050	693	0.950	0.223	0.492
3	Al	Privy Roof (R = 0)				610	0.420	0.218	0.213
8	Al	Privy Roof (R = 52.4")				603	0.370	0.218	0.187
8	SS	Privy Roof (R = 52.4")				651	0.660	0.114	0.174
10	Al	Core Midplane (R = 25')				571	0.103	0.215	0.0515
10	Be	Core Midplane (R = 25')				568.5	0.071	0.440	0.0726
1	Al	Near Flange (θ = 120°)	EP-IV	1100	13150	788	0.950	0.230	0.508
3	Al	Privy Roof (R = 0)				653	0.440	0.221	0.226
8	Al	Privy Roof (R = 52.4")				639	0.370	0.220	0.189
8	SS	Privy Roof (R = 52.4")				718	0.680	0.116	0.103
10	Al	Core Midplane (R = 25')				582	0.114	0.217	0.0575
10	Be	Core Midplane (R = 25')				576.5	0.091	0.450	0.0951
1	Al	Near Flange (θ = 120°)	EP-IV	1098	13270	882	0.940	0.235	0.513
3	Al	Privy Roof (R = 0)				697	0.440	0.223	0.228
8	Al	Privy Roof (R = 52.4")				677	0.370	0.222	0.191
8	SS	Privy Roof (R = 52.4")				783	0.610	0.120	0.170
10	Al	Core Midplane (R = 25')				594	0.120	0.218	0.0608
10	Be	Core Midplane (R = 25')				586	0.099	0.455	0.105

* See Figure 8-33 for calorimeter location and coordinates

In reducing the calorimeter measurements to heating rates, it is necessary to analyze the data at a steady state point on the reactor profile. For the EP-III test the only good steady state high power hold available before the calorimeter ranges were exceeded was between control room time (CRT) 25295 and 25310 seconds. (The reader is referred to Section 3.4.1 for a presentation of the reactor power profiles.)

For EP-IV, however, full power steady state conditions were available for a considerable time span (about 15 minutes) and consequently, calorimeter data were obtained at three points in time.

Table 8-5 gives the basic calorimeter data obtained from the Calcomp tracings of the temperature measurements made of the sample core of the six calorimeters. The following equation was used to reduce the basic data in Table 8-5 to heating rates for the calorimeters.

$$H = \frac{\frac{\Delta T}{\Delta t} \times C \times 1054.8 \frac{\text{watts}}{\text{Btu/sec}}}{454 \text{ gm/lb}}$$

where:

H = Heating rate, watts/gm

$\frac{\Delta T}{\Delta t}$ = °F/second from experimental data

C = Specific heat of material, Btu/lb-°F, as given in Table 8-5

Table 8-6 gives the measured heating rates adjusted to 100 percent power for comparison purposes. It gives the mean of the four data points for each calorimeter. Also presented in Table 8-6 is the root mean square deviation from the mean known as the standard deviation, defined by:

$$\sigma = \sqrt{\frac{\sum_{i=1}^{N} (x_i - \bar{X})^2}{N}}$$

where: σ = standard deviation

$\bar{X}$ = mean or average value (see below)

x_i = ith value

N = number of observations

$$\bar{X} = \frac{\sum_{i=1}^{N} X_i}{N}$$

In addition, Table 8-6 gives the standard deviation expressed as a percent of the mean, called the coefficient of variation, defined by:

$$\text{coefficient of variation} = \frac{\sigma}{\text{mean}} \times 100$$

One interesting observation can be made concerning the data in Table 8-6. During EP-IV, the measured heating rates increase with time for all calorimeters with the exception of the steel calorimeter which is mounted on the corner of the privy roof. Although a slight increase in the heating rate per watt of reactor power is expected due to the buildup of fission products (i.e. gamma sources) in the reactor, the increases shown in Table 8-6 are higher than expected. Furthermore, since the steel calorimeter does not show a continual increase during EP-IV, it does not seem reasonable to assume that the increase in the measurement for the aluminum or beryllium calorimeters can be attributed to the buildup of fission products. These increases, however, can be explained if the temperatures of the outer cases of the aluminum calorimeters are increasing at a faster rate than the calorimeter cores and are leaking heat to the sample cores. Since the outer case is steel for all the calorimeters, and, in fact does have a temperature rise which is steeper than either aluminum or beryllium, this explanation appears valid. However, without actual measurements of the outer case these arguments must remain qualitative.

TABLE 8-6

NRX-A5 CALORIMETER HEATING RATES ADJUSTED TO 100% POWER (1120 MW)

Calorimeter Designation			Heating Rate (W/gm)						
Location Number*	Material	General Location	EP-III CRT-25305 sec.	EP-IV CRT-13050 sec.	EP-IV CRT 13150 sec.	EP-IV CRT-13250 sec.	Average	Standard Deviation	Coefficient of Variation
1	Al	Near Flange (θ=120°)	0.453	0.492	0.517	0.523	0.496	0.0275	5.5%
3	Al	Privy Roof (R=0)	0.180	0.213	0.230	0.233	0.214	0.0211	9.9%
6	Al	Privy Roof (R=52.4")	0.195	0.187	0.192	0.195	0.192	0.0036	1.9%
8	SS1	Privy Roof (R=52.4")	0.143	0.174	0.187	0.173	0.169	0.0161	9.5%
10	Al	Core Midplane (R=25')	0.0465	0.0515	0.0585	0.0620	0.0546	0.0060	11.0%
10	Be	Core Midplane (R=25')	0.0603	0.0726	0.0969	0.107	0.0842	0.0186	22.0%

*See Figure 8-33 for calorimeter location and coordinates

8.7.3 Comparison of NRX-A5 Calorimeter Measurements with Calculations

Calculations of heating rates were made at the six detector locations for which NRX-A5 calorimeter data are available. The calculational techniques are discussed in detail in References 10 and 11. Table 8-7 gives a comparison of calculations with measurements for the NRX-A5 calorimeters. Except for the calorimeter located near the flange (location No. 1), all of the measurements are higher than calculations. As has been previously discussed, it is expected that the aluminum and beryllium calorimeters are giving higher heating rates than really exist due to heat leakage from a hotter steel case to the sample material. Although this argument is not supported by the data at the aluminum mockup shield flange, it should be pointed out that calculations near the flange indicate that there is a relatively steep gradient in the heating rate as a function of reactor station. Consequently the calculation at this location is very sensitive to axial location and the close agreement with the measurement may be fortuitous.

Table 8-8 gives a synopsis of the calorimeter data obtained for all four NRX reactor power tests. From Table 8-8 it can be seen that there really isn't a great deal of data upon which a good evaluation of the calorimeters can be based. The spread in the data is sufficiently large to demonstrate the need for improvement in the calorimeter design. However, at locations 3 and 10, where both NRX-A3 and NRX-A5 data are available, the A5 data are higher at both locations. One obvious improvement that can be made without too much difficulty is the addition of a thermocouple to the outer case of the calorimeter.

This design change is now being planned for future reactor tests. A better understanding of the calorimeter would be possible if more experimentation were performed on a basic level. More controlled experiments are required to determine the characteristics of the calorimeters themselves. Plans are being made at WANL to perform such experiments.

TABLE 8-7

COMPARISON OF CALCULATIONS WITH MEASUREMENTS OF CALORIMETER DATA FOR NRX-A5

Calorimeter Designation			Calculated (W/gm)					
Location Number*	Material	General Location	Neutron	Gamma+	N,γ Reaction in Calorimeter++	Total	Measured Average**	Ratio of Measured/Calculated
1	Al	Near Flange (θ=120°)	0.0511	0.452	0.0072	0.510	0.496	0.97
3	Al	Privy Roof (R=0)	0.00380	0.109	0.0072	0.120	0.214	1.79
8	Al	Privy Roof (R=52.4")	0.00263	0.0916	0.00469	0.0989	0.192	1.94
8	SS	Privy Roof (R=52.4")	0.000562	0.0882	0.0555	0.144	0.169	1.17
10	Al	Core Midplane (R=25')	0.000882	0.0315	0.00105	0.0334	0.0546	1.63
10	Be	Core Midplane (R=25')	0.0070	0.0283	0.0000306	0.0353	0.0842	2.38

+Gamma radiation from the reactor and privy roof shield.

++Secondary gamma radiation in the calorimeter.

*See Figure 8-37 for calorimeter locations.

**From Table 8-6.

Aerojet Nuclear Laboratory

TABLE 8-8

COMPARISON OF CALORIMETER DATA FROM ALL NRX REACTOR TESTS

Calorimeter Designation			Heating Rate (W/gm)			
Location Number*	Material	General Location	NRX-A2	NRX-A3	NRX/EST	NRX-A5
1	Al	Near Flange (θ=120°)	---	---	0.629**	0.496
2	Al	Near Flange (θ=300°)	---	---	0.453	---
3	Al	Privy Roof (R=0)	---	0.201	0.280**	0.214
4	SS	Near Nozzle	---	0.364	0.402	---
4	Al	Near Nozzle	---	0.418	0.469	---
4	Be	Near Nozzle	0.744	0.595	0.631	---
5	SS	Core Midplane (R=5')	0.832	0.877	0.897	---
6	Al	STATION 15 (R=5')	0.794	0.941	1.00	---
7	Be	STATION 8.5 (R=5')	1.05	1.06	1.15	---
8	Al	Privy Roof (R=52.4")	---	---	---	0.199
8	SS	Privy Roof (R=52.4")	---	---	---	0.169
9	Al	Core Midplane (R=12')	---	0.152	---	---
10	Al	Core Midplane (R=25')	---	0.0471	---	0.0546
10	Be	Core Midplane (R=25')	---	---	---	0.0842

*See Figure 8-33 for calorimeter Locations.

**NOTE: Heating rates at these locations during the NRX/EST test are higher than NRX-A3 or NRX-A5 data due to radiation scattered from or generated by the Privy Roof Mounted Shield (PRMS).

8.8 COMPILATION OF RADIATION ENVIRONMENT DATA FOR NRX REACTORS AT TEST CELL A

Since the NRX-A2, NRX-A3 and NRX-A5 reactors are very similar in design, the radiation environment in the test facility should be the same for all three reactors. The NRX/EST radiation environment is quite different due to test cell and facility modifications. The main modifications for NRX/EST consisted of the addition of a shadow shield mounted on the privy roof and a horizontal shield connecting the privy roof with the test cell wall. These shields were necessary primarily to protect engine components which were mounted on the test car near the test cell wall and to reduce test cell wall activation. Therefore, although this report is principally concerned with the NRX-A5, the radiation environment presented in this section is applicable to the NRX-A2 and NRX-A3 also.

This section combines all the measurements from the NRX-A2, NRX-A3, and NRX-A5 reactors, along with calculations where needed, to arrive at what is believed to be the most accurate representation of the radiation environment around reactors of this type operated in a test facility similar to Test Cell "A". The data are presented in the form of iso-flux contours for neutrons, iso-dose rate contours for gamma rays and iso-heating rate contours for radiation heating in aluminum.

Figure 8-34 gives the iso-dose rate contours for gamma rays in units of R/hr for full power (1120 MW) conditions. It is estimated that the data given in Figure 8-34 are accurate to within a factor of two. It should be remembered that these iso-plots can be severely perturbed by nearby components. For instance, massive test car components such as the counter weights on the back of the car would cause serious local perturbations within the component. Therefore, iso-contours of this type should be used with caution.

Figure 8-35 gives iso-flux contours for neutrons with energy (E>2.9 Mev) in units of neutrons per square centimeter per second for full power operation (1120 MW). The 2.9 Mev threshold is used here because most of the available measurements on which the plots are based were obtained using sulfur pellet activation. However, also included in Figure 8-35

is a factor which can be used to convert the data to fluxes for energy (E>1.0 Mev). This latter threshold is commonly used for specifying radiation damage criteria. The data given in Figure 8-35 are estimated to be accurate to within a factor of two.

Figure 8-36 gives similar radiation data in the form of heating rate in aluminum. The units for the data are watts per gram of aluminum and are based mainly on a combination of measured calorimetric heating rates, measured gamma dose rates and calculated data. Aluminum was chosen as the reference material because it is the most common material used throughout the facility. However, on a per gram basis, considering the accuracy of the data, the heating rates given in Figure 8-36 can be applied to any metal. These data also are considered to be only accurate to within a factor of two.

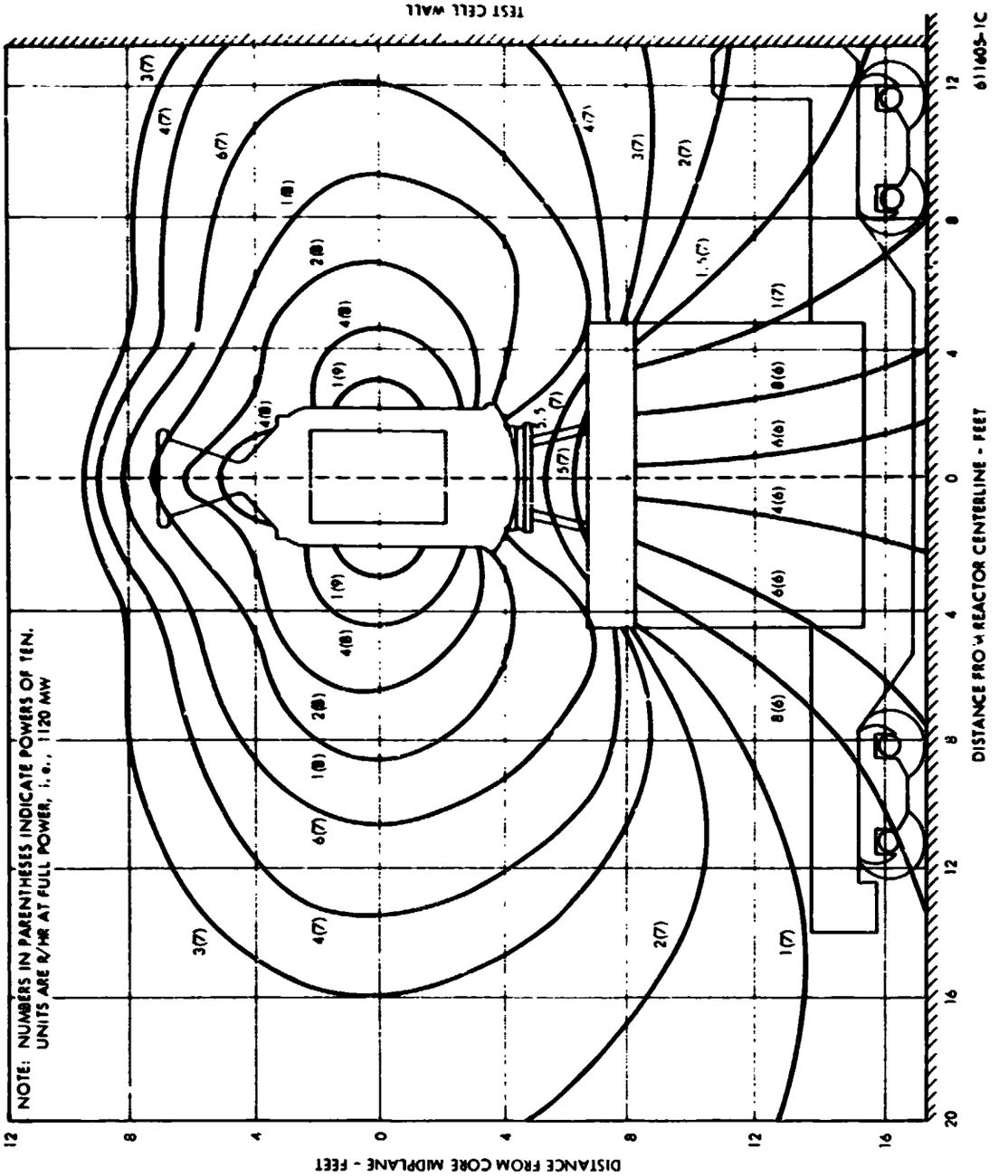

Figure 8-34. Gamma Ray Isodose Pattern Around a Typical NRX Reactor

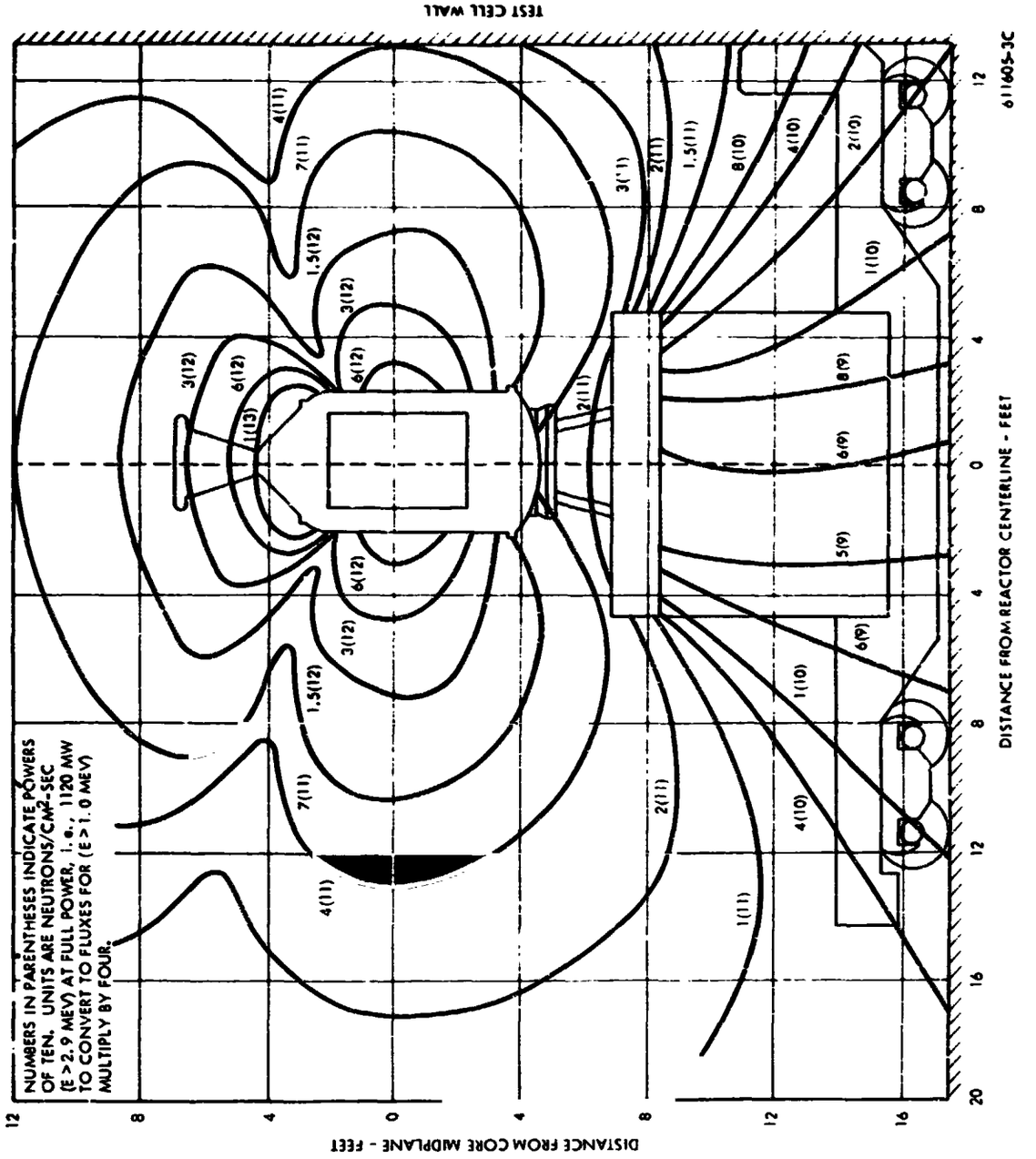

Figure 8-35. Fast Neutron (E > 2.9 Mev) Isoflux Pattern Around a Typical NRX Reactor

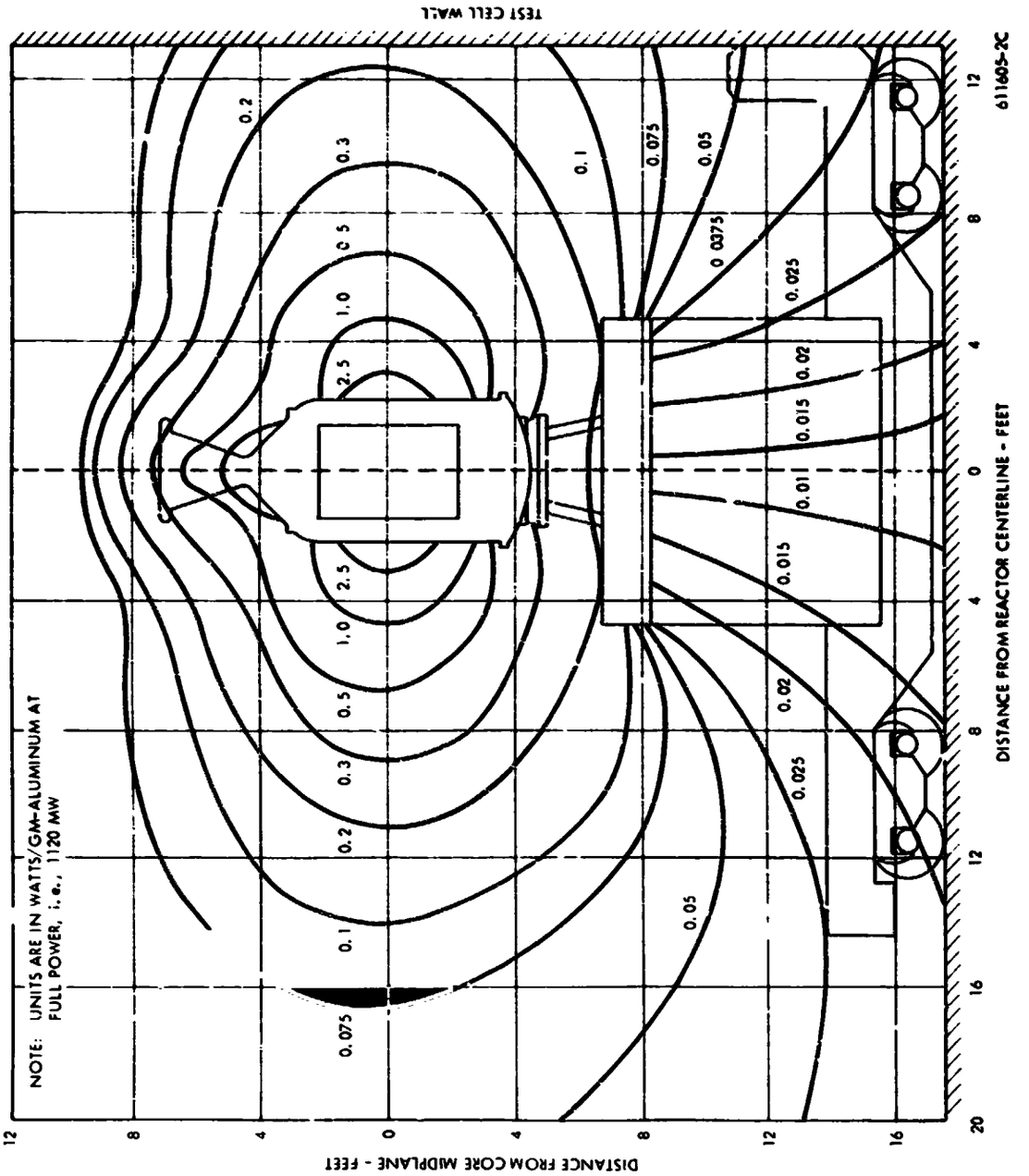

Figure 8-36. Isoheating Rate Contours for Aluminum Around a Typical NRX Reactor

8.9 CONCLUSIONS

8.9.1 Gamma Ray Data

1) Passive dosimeters are reliable only when used in tests where background radiation from preceding tests is small or where sufficient measurements of background radiation are available to correct the data. The background for the NRX-A5 test was not sufficiently mapped. Health Physics surveys of test cell activity were not extensive enough to provide adequate background data on the test cell wall. Gamma dose rate meters would help considerably in providing background radiation level data.

2) The A5 measurements were less reliable than previous tests and did not reduce the uncertainty in gamma ray levels in the test cell area.

3) At most detector locations a scatter of about a factor of two can be observed in the gamma ray data for the NRX-A2, NRX-A3, and NRX-A5 reactors.

4) Calculations generally lie within the spread of the experimental data.

5) No significant difference between low versus high power measurements of the gamma ray dose rate per unit power could be observed.

8.9.2 Fast Neutron Flux Data

1) The A5 fast neutron fluxes (E>2.9 Mev) were in good agreement at comparable locations with data obtained during tests of the NRX-A2 and NRX-A3 reactors.

2) The A5 measurements extended the flux traverses on the wall and the pad by an additional 30 feet out to a distance of 60 feet from the reactor.

3) Outside the shadow of the privy roof the measurements of fast neutron (E>2.9 Mev) flux for the NRX-A2, NRX-A3, and NRX-A5 reactors exhibited a scatter of less than 50 percent.

4) In the shadow of the roof, the scatter in experimental fast neutron data for the three reactors previously discussed was as much as a factor of 5.

5) Calculations of fast neutron flux (E>2.9 Mev) were within 50 percent of all measurements from the A2, A3, and A5 reactors at locations outside the shadow of the roof. At locations in the heavy roof shadow, discrepancies between measurements and calculations are as much as a factor of 4.

6) On a per unit power basis, considering all reactor tests, no significant trends could be observed between measurements made at low power and measurements taken at high power except on the pressure vessel lateral surface where the data is considered most accurate. On the pressure vessel, the fast neutron flux per unit power was somewhat higher for the low power measurements than for high power measurements. It is believed that rate meter fast neutron detectors would have provided a more consistent and accurate measurement of fast neutron leakage at external locations and thus would have provided a better basis of comparison of high and low power data.

8.9.3 Thermal Neutron Data

1) Thermal neutron fluxes (E<0.4 ev) measured during NRX-A5 low power testing were in good agreement with fluxes measured during NRX-A2 and NRX-A3 tests.

2) The scatter in thermal neutron flux data for the NRX-A2, NRX-A3, and NRX-A5 reactors is less than a factor of two for all detector locations.

3) Calculation of thermal neutron flux levels at the lateral surface of the pressure vessel are about 45 percent higher than measurements. However, these calculations are greatly dependent on representation of the control vane geometry. Techniques for calculating thermal neutron fluxes at external shielded locations are not at present available at WANL.

4) In comparing all the thermal neutron flux data from the NRX-A2, NRX-A3, and NRX-A5 reactors there is no perceptible trend on a per watt basis between data obtained at low power from that at high power.

8.9.4 Calorimeters

1) The design changes to NRX calorimeters from the A4 to the A5 improved the calorimeters from a structural standpoint but slightly impaired their thermal performance.

2) In order to get more accurate data from the calorimeters, the outer case temperature should be monitored and/or the calorimeters should be redesigned. Design changes are being incorporated in calorimeters for use with NRX-A6 and subsequent reactors.

3) Basic thermal data should be obtained with the calorimeters to better understand their performance.

4) The NRX-A5 calorimeters indicate higher heating rates than previous reactor tests at similar locations; probably due to the design changes in the A5 calorimeters.

5) Heating rate calculations are in most cases lower than measurements differing by as much as a factor of two at some locations with the A5 measurements, but are in closer agreement with measurements made during earlier reactor tests.

8.10 REFERENCES

1. NTO-R-0087, "NRX-A5 Dosimetry Data Report", Nevada Test Operations, J. R. Seibold, July, 1966.

2. NTO-M-5240, "NRX-A3 Dosimetry Data Report", Nevada Test Operations, J. W. Sadler, September, 1965.

3. WANL-TME-1061, "NRX-A2 Dosimetry Measurements", Westinghouse Astronuclear Laboratory, E. H. Brooks, September, 1963.

4. WANL-TME-1238, "Radiation Analysis of the NRX-A4/EST Configuration", Westinghouse Astronuclear Laboratory, Radiation and Shielding Group, October, 1965.

5. XDC-59-2-16, "Shielding Computer Program 14-0 and 14-1, Reactor Shield Analysis", General Electric Co., ANPD, W. E. Edwards, et al., January, 1959.

6. Unpublished, Los Alamos Scientific Laboratory.

7. LAMS 2346, "The DSN and TDC Neutron Transport Codes", Los Alamos Scientific Laboratory, B. G. Carlson, et al, February, 1960.

8. WANL-TME-1273, "SAP, A Neutron and Gamma Ray Albedo Model Scatter Shield Analysis Program", Westinghouse Astronuclear Laboratory, L. D. Stephenson, September, 1965.

9. WANL-TNR-199, "Analysis of NRX-A2 Reactor Test Results", Westinghouse Astronuclear Laboratory. L. Boman, April, 1965.

10. WANL-TNR-202, "NRX-A3 Reactor Final Test Report", Westinghouse Astronuclear Laboratory, Reactor Analysis Department, December, 1965.

11. WANL-TNR-216, "NRX/EST Reactor Test Analysis Report", Westinghouse Astronuclear Laboratory, Reactor Analysis Department, December, 1966.

12. NTO-R-0079, "NRX/EST Post Test Report", Nevada Test Operations, July, 1966.

13. WANL-TME-1389, "NRX-A5 Reactor Analysis Data", Westinghouse Astronuclear Laboratory, April, 1966.

CHAPTER 9*

POST-OPERATIVE RADIOCHEMISTRY

9.1 SUMMARY

Following the NRX-A5 power test at NRDS, the integrated radial and axial fission distribution was established by gross radiation measurements and radiochemical analysis**. As in the NRX/EST post-operative analysis, a comparison of these NRX-A5 measurements with predictions was more difficult than in NRX-A2 and NRX-A3 due to the high loss of material from the fuel elements during the test.

An effective drum angle of 119 degrees was obtained for the entire test profile enabling the calculated power distribution to be compared directly with that derived from the gross radiation measurements. Prior to comparison the activity measurement for each element was adjusted to account for the reduction in intensity associated with loss of fission products by corrosion. Three independent methods were used to derive this correlation. The first method had previously been used to estimate the effects of corrosion on the NRX/EST hot power measurements. This method utilized the change in activity as a function of weight loss for elements from a given location, but in different core sectors. The effects of corrosion were also estimated by analyzing individual element deviations from a trend in the ratio of the experimental to predicted fissions per gram values in the central core region. The third approach used the percent difference in the integrals of the measured and predicted axial power distributions in fuel elements with large weight losses.

---

* Major contributors to this chapter were R. A. Doncals and R. V. Rittenberger.

** NTO-R-0093, "NRX-A5 Chemical and Radiochemical Measurements Report", September 30, 1966.

A comparison of the adjusted experimental fission product activity per fuel element with the 119 degree predictions shows a maximum difference of 4.7 percent on a per element basis. The differences noted were due mainly to design differences between the NRX-A5 and NRX-A3 reactors, since the prediction was based on the NRX-A3 test results. PAX power measurements have since shown that the fuel loading differences between the two reactors will cause power changes by as much as 5 percent. Smaller errors than this were introduced by the code 32 element power perturbations that were applied to the predictions. Recent PAX-E* peripheral power measurements which mapped the complete core boundary, both with fueled and unfueled partial elements, have since shown that these perturbations were slightly underestimated.

The NRX-A5 predicted axial power distribution showed good overall agreement with the gamma scan measurements. This agreement was similar to that seen in the NRX-A3 Analysis.**

A comparison of the cold PAX-D power distribution and that derived from the NRX-A5 post-operative ionization measurements indicated little or no difference in the cold and hot power distributions except in the edge fuel elements where the observed cold-to-hot power change showed a definite rise. This cold-to-hot power swing is slightly more pronounced (approximately 2 percent) than that observed from the NRX/EST data.

---

* WANL-TME-1519, "WANEF Critical Experiments in Support of NERVA", 9/66

** WANL-TNR-202, "NRX-A3 Reactor Final Test Report", 12/65.

9.2 NRX-A5 POWER DISTRIBUTION PREDICTIONS

Three dimensional power distributions were predicted for the NRX-A5 for several drum angles.* These predictions were performed for operation at the design point. The radial power predictions were normalized to the NRX-A3 hot fission distribution as established by radiochemistry. NRX-A3 hot measurements were chosen rather than those of NRX-A2 since its loading distribution more closely simulated that of NRX-A5. Radiochemical measurements on the NRX/EST core which had a loading distribution identical to NRX-A5, were not available at the time of the predictions.

Normalization coefficients were obtained on an element-by-element basis by comparing NRX-A3 predictions adjusted to the effective drum angle during the test series with the actual fission density as established from ionization measurements of the gross fission product activity. The NRX-A5 predictions of fission fragment heating at all drum angles were adjusted by these normalization coefficients. Detailed power variations in each element were obtained from the ambient temperature power measurement in the PAX critical facility at Waltz Mills, Pa. The normalization of the NRX-A5 power predictions to the NRX-A3 post-test results and PAX-A experimental data were performed by means of the PFENCE computer program.** The heating throughout the core by fast neutrons and gamma rays were also included in the predictions by PFENCE.

The NRX-A5 power prediction was adjusted at the core periphery to reflect the local perturbations caused by the replacement of the Code 32 fueled partial elements with unfueled graphite partial elements. These perturbations were derived from PAX-E power measurements around a limited number of Code 32 elements with both fueled and solid graphite elements in the Code 32 positions. The power perturbations derived from these measurements were used to describe the peripheral design change between the NRX-A3 and NRX-A5 reactors.

---

* WANL-TME-1389, "NRX-A5 Reactor Analysis Data" 4/66.

** "Comparison of Analytical and Experimental Power Distribution of NERVA Reactors", R. Doncals, D. A. McCutchan, L. Ortenberg, J. Ravets, Trans. Amer. Nucl. Soc. II/65.

The NRX-A5 power predictions were considerably better than those used to orifice NRX-A2 and A3 since the NRX-A5 predictions were normalized to hot reactor test data. NRX-A2 and A3 predictions were normalized to a measured cold power distribution and utilized a calculated cold-to-hot power change. The NRX-A5 predictions were also an improvement over the NRX/EST values since the hot measurements used in the normalization scheme were obtained from a reactor, NRX-A3, which better represented its fuel loading distribution. Also, the code 32 power perturbations used in the NRX-A5 predictions were measured directly in a PAX power experiment; NRX/EST values were estimated by analyzing the local variation in the PAX-A fission distribution along the irregularities of the fuel/filler strip boundary.

The improvement in the NRX-A5 power distribution prediction is evident by the excellent uniformity observed in the temperature patterns at and near the orifice drum angle. This is discussed in Section 5.4.2.2 and shown graphically in Figures 5-2 and 5-3. Temperature uniformity as indicated by thermocapsule data (Section 5.4.9) was better in the NRX-A5 than any previous reactor tested. This is shown by the following measured three sigma temperature variations:

NRX-A3	259°R
NRX/EST	271°R
NRX-A5	141°R

9.3 EFFECTIVE DRUM ANGLE FOR THE NRX-A5 HOT TEST

The NRX-A5 test series included two experimental plans in which there was sufficient fission product buildup to affect the gross ionization measurements made at the end of the test series. The power-time weighted drum angles for each of these hot tests are listed below:

Experimental Plan	Power-Time Weighted Drum Angle (Degrees)
III	109.2
IV	124.3

In order to make a comparison of the NRX-A5 power predictions with measurements, it is necessary to define an effective average control drum angle for the entire test. In order to do this, the above angles were weighted by factors which took into account the total fission product buildup in each EP and the subsequent decay in gamma activity until the start of the power measurements. This resulted in an effective drum angle of 119 degrees for the entire NRX-A5 test series.

The effective drum angles for each NRX-A reactor tested to date are listed below:

Reactor	Effective Control Drum Angle (Degrees)
NRX-A2	99.7
NRX-A3	99.3
NRX/EST	120.0
NRX-A5	119.0

The small differences between the drum angles of NRX-A2 and A3 and likewise between NRX/EST and A5 allow a direct comparison of the experimental data from each of the respective hot tests. Of course, the slight differences in element fuel loadings must also be factored into this comparison. The comparison of the fissions per gram obtained from the NRX-A2 and NRX-A3 hot tests is reported in WANL-TNR-216, "NRX/EST Reactor Test

Analysis Report". This comparison showed that in the 78 elements of NRX-A3 which were downgraded in loading relative to A2, an increase in fission rate of as much as 5.5 percent was seen. PAX ambient power measurements also showed a similar dependence of the fission flux on the loading distribution. A comparison of the experimental hot data from the NRX/EST and NRX-A5 reactors is presented in this chapter.

9.4 COMPARISON OF THE NRX-A5 EXPERIMENTAL POWER DISTRIBUTION WITH PREDICTIONS

The NRX-A5 fission density distributions were constructed from gross radiation measurements made in a whole body ionization counter on all unbroken fueled elements. The gamma intensity reading for each fuel element was divided by its actual uranium loading as obtained by another gamma scan technique during fuel manufacture, giving a number which is assumed to be proportional to the total number of fissions per gram of uranium in that element. These values for each of the six sectors were averaged and normalized to unity in the central elements to produce the distribution shown in Figure 9-1.

The ratios of these experimental fission per gram values to the NRX-A5 predictions are plotted in Figure 9-2 as a function of radial position. The individual fuel element gamma intensity reading is a measure of the total energy generated in that element by fission fragments (i.e., not gamma and neutron heating) during the entire test series. This is based on the assumption of negligible fission product loss. A detailed inspection of the ratios of the experimental to calculated fissions per gram values shown in Figure 9-2 raises some question as to the validity of this assumption for the NRX-A5 elements. This is shown by the erratic variations which are exhibited by the experimental to predicted fission ratios in the central core region, a region of the reactor with little element to element power variation. The deviations in these ratios have since been found to be positively correlated with the individual fuel element weight losses. Similar reductions were observed in NRX/EST ionization measurements for elements with large weight losses. It was impossible to detect this phenomenon in the NRX-A2 and A3 data due to the relatively small weight losses exhibited by the elements during these tests.

The central normalization scheme used in reporting the experimental fission per gram data causes all the normalized intensity values to be in error if the central elements have unusually high fission product losses. Consequently, the NRX-A5 peripheral ionization measurements were erroneously increased due to the large conversion which took place in the central elements. In order to make an error analysis of the NRX-A5 predictions, it was necessary to develop from the hot experimental data a correlation of

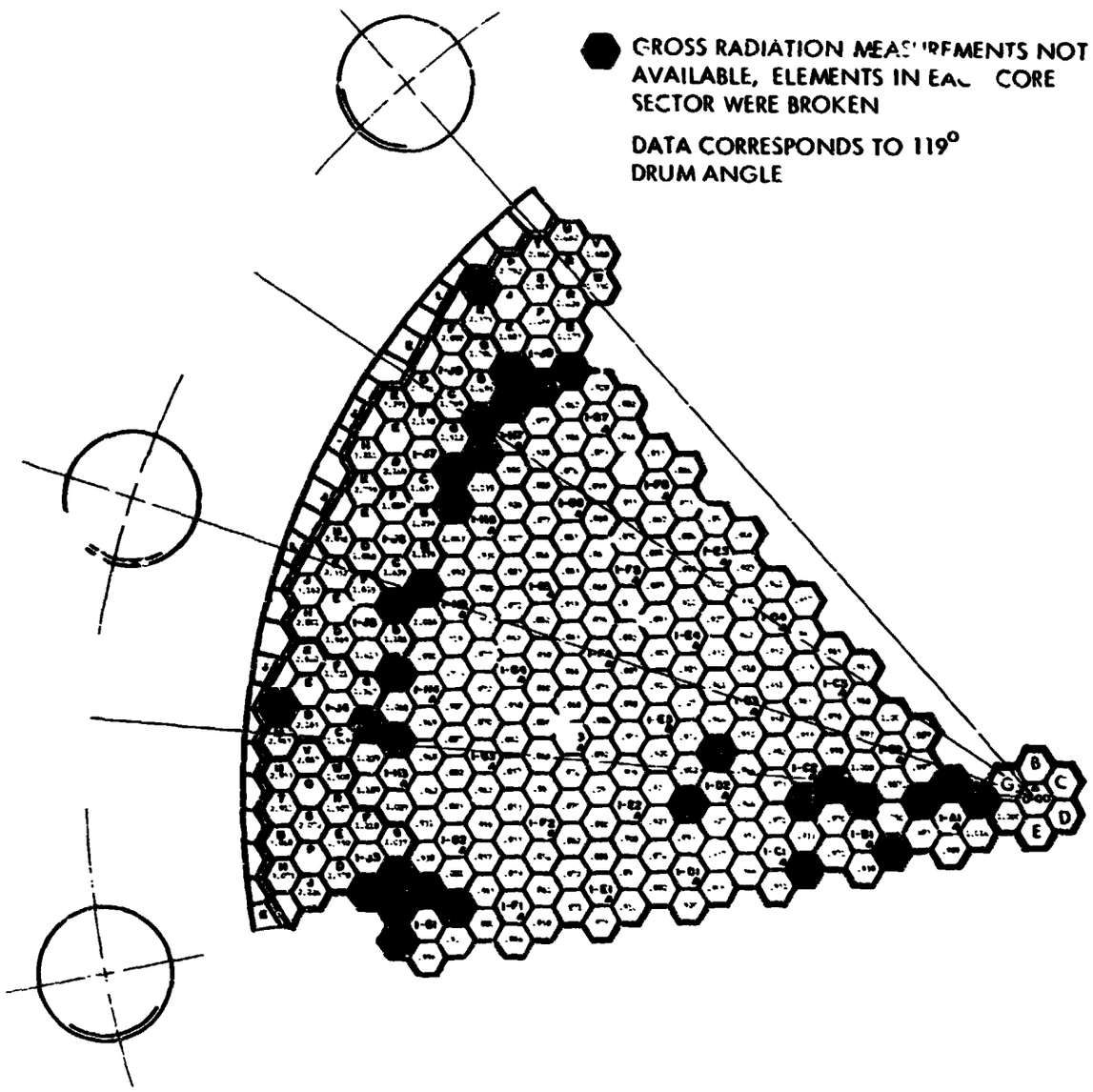

Figure 9-1. NRX-A5 Experimental Fissions per Gram Values as Derived from Gross Radiation Measurements, Uncorrection for Fission Product Loss

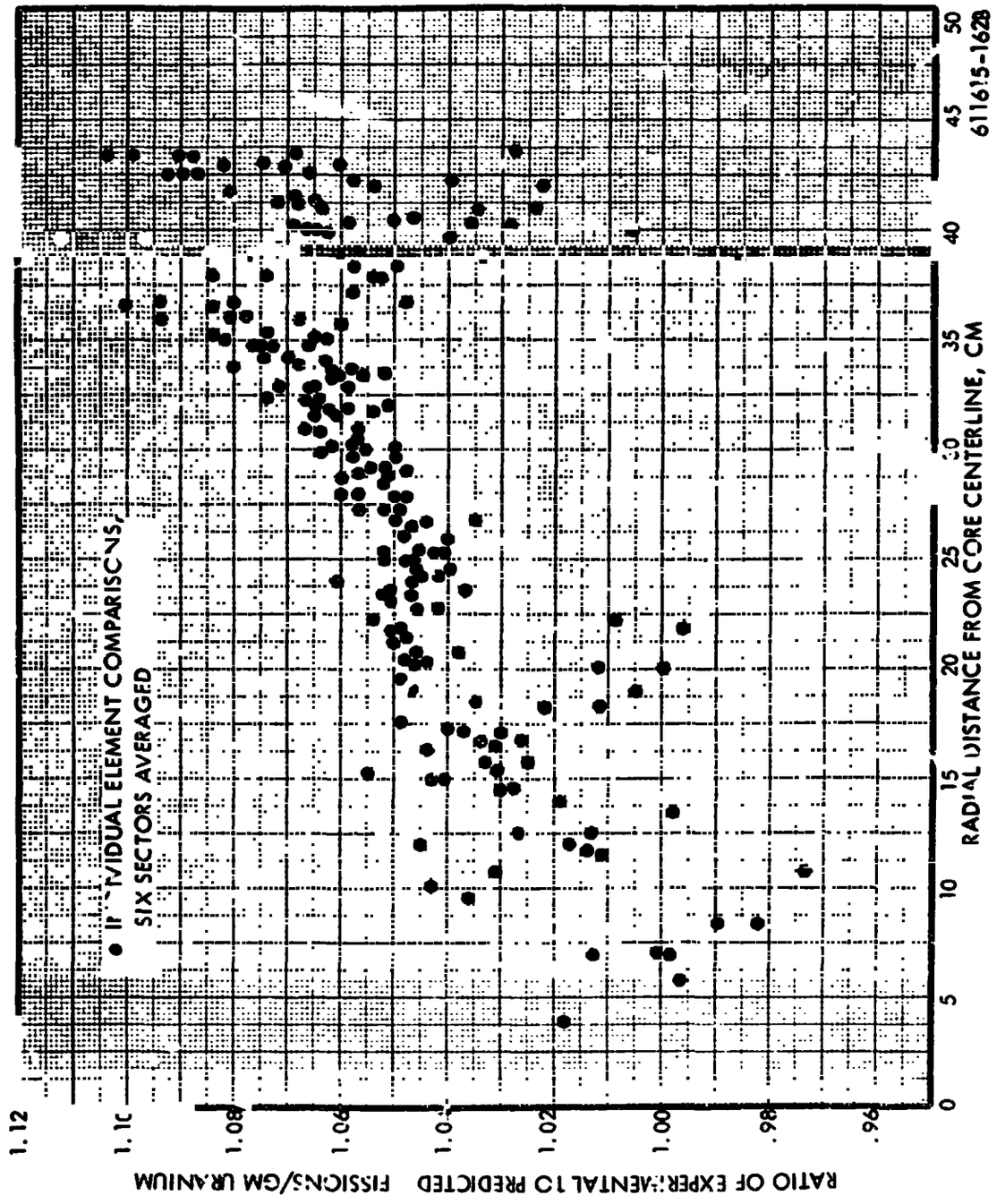

Figure 9-2. Comparison of Theoretical and Uncorrected Experimental Fissions/ Gram Uranium

ionization intensity loss with weight loss. This correlation was then used to correct the individual power measurements for fission product loss to provide a better estimate of the fission rate for comparison with predictions.

9.5 FISSION PRODUCT LOSS DURING TESTING

The two modes by which fission products could be lost during the NRX-A5 test series were diffusion and corrosion. The term diffusion is defined here as fission product migration through the pyrocarbon shell of the fuel bead to the coolant channel surface. Gamma spectra measured at intervals along the lengths of selected NRX-A5 fuel elements permitted a comparison of the intensity of the 1.60 Mev photopeak due to the migrating Ba^{140} - La^{140} fission products with the intensity of the 0.50 Mev photopeak due to the non-migrating isotope Ru^{103} at each axial station. The activity due to a second pair of migrating isotopes, Zr^{95} - Nb^{95}, was also compared with the Ru^{103} activity. These ratios of migrating to non-migrating isotopic pairs were relatively constant along the length of the fuel indicating that the activity loss due to diffusion of fission products could be neglected. Similar measurements on the NRX-A2, NRX-A3, and NRX/EST fuel elements also support the conclusion that fission product diffusion at the NRX operating temperatures is not great enough to appreciably change the fission product spatial distribution.

It is well known on the other hand that corrosion does cause fission product loss through gross removal of the fuel matrix, especially in the midband and hot end regions of the element. The effect of corrosion in the NRX-A5 elements was analyzed by correlating the weight loss of each element with its gross fission product activity as measured in the whole element ionization chamber. Three independent methods were used to derive this correlation.

The first method has previously been used to estimate the effects of corrosion on the NRX/EST hot power measurements (WANL-TNR-216, "Reactor Test Analysis Report", pages 9-4 to 9-10). Briefly, the method consists of establishing for each fuel element a correlation between the observed whole element ionization chamber reading and the element weight loss. Similar to the NRX/EST analysis, a statistically significant reduction in gross ionization intensity with increasing total element weight loss was found by analyzing the experimental fissions per gram values for the six fuel elements at the same location, but in different core sectors. Briefly, heavy weight loss elements exhibit

a lower activity. Plots of these values as a function of element weight loss indicates that there is only about 1 percent loss in gamma activity for a weight loss of 20 grams. This observation was used to extrapolate the intensity values back to zero weight loss, i.e., it was assumed that ionization readings for elements with weight losses below 20 grams represent essentially the original activity. Consequently, to determine the percent loss in ionization intensity as a function of element weight loss, it was necessary to find element locations which had a spread in weight loss, with at least one element below 20 grams. The results of this analysis are shown in curve (a) of Figure 9-3.

The effects of corrosion were also estimated by analyzing individual element deviations from a trend in the ratio of experimental to predicted fissions per gram values shown in Figure 9-2. Both the actual and calculated fission rates per gram of uranium in the central core region are necessarily smooth functions since they are based on continuous flux distributions. Consequently, significant local deviations in the experimental to predicted fission ratio in the central core region can only be attributed to inaccurate uranium loading values or to a loss in fission product intensity due to corrosion. In the central core region of 20 cm radius, unbroken element weight losses varied from 11 to 56 grams per element while in the region between 20 and 30 cm radius the weight loss per element averaged approximately 14 grams. As noted above, the elements with the 14 gram weight losses should have less than 1 percent loss of fission products due to corrosion. Consequently, it was assumed that differences in the 1.048 average ratio noted between 20 and 30 cm radii in Figure 9-2 and those calculated for the central core region, 0 to 20 cm, was the loss in gamma intensity due to corrosion. These differences are plotted in Curve (b) of Figure 9-3.

A third approach to the problem of establishing a correlation between weight loss and fission product activity loss was based on the axial variation in gross fission product gamma activity as measured with a scintillation detector. For this purpose, elements were selected with weight losses of 25 to 72 grams. Axial power distributions derived from the absolute count rate are compared with the corresponding predictions in

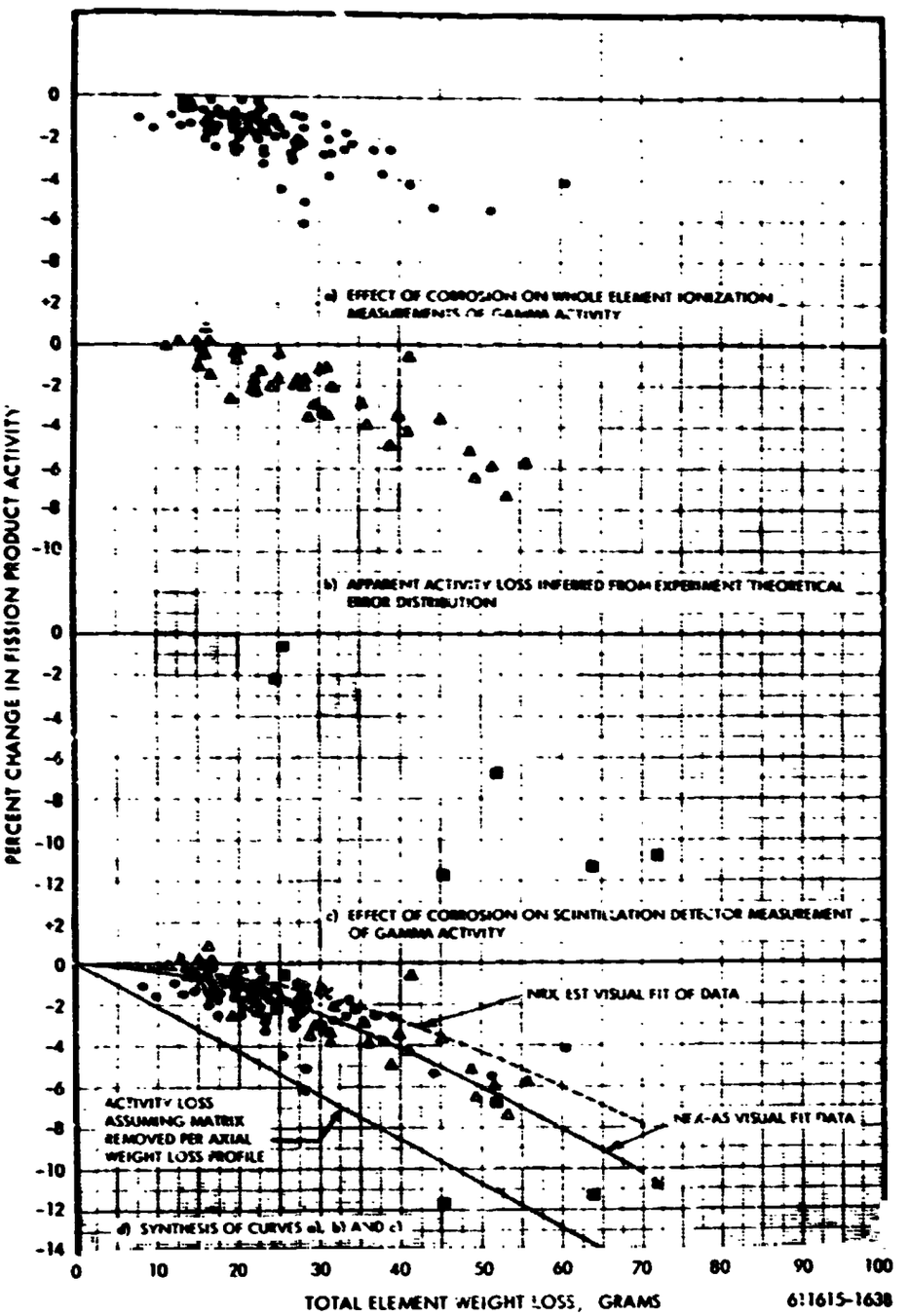

Figure 9-3. The Effect of Corrosion on Fission Product Activity by Various Methods

Figures 9-4 to 9-6. Since the axial fission distribution is known to closely resemble a cosine function from both room temperature experimental data and the NRX-A2 and A3 radiochemical measurements, the dips occurring near the 22 in. station must be attributed to loss of fission products. The predicted curve provides an indication of what the fission product distribution would have been in the absence of corrosion. Past comparisons of prediction and experimental measurements have been in good agreement where extensive corrosion was not present. In order to derive a fairly quantitative estimate of the activity loss, the prediction curves have been adjusted in amplitude to coincide with the measured distribution in the uncorroded inlet end of the element. The percent differences between the measured and the fitted theoretical (uncorroded) axial power distributions were computed at each axial station. The figures show the clear relation between these differences and the incremental weight losses obtained by sectioning the element. The agreement between weight and activity losses implies that uranium carbide and its associated fission products were lost in the midband region in addition to carbon.

The percent difference in the integrals of the measured and theoretically uncorroded axial power distributions is shown as a function of weight loss in curve (c) of Figure 9-3.

Curve (d) of Figure 9-3 is a composite of the results of the three methods described. Shown on the curve is a visual fit of all these NRX-A5 values and for comparison, a curve previously calculated from the NRX/EST gross ionization measurements. The significant difference between the two curves can be explained in terms of the difference in axial distribution of the weight loss in the two reactors. The major portion of corrosion in NRX-A5 elements was generally confined to the midband region while in NRX/EST both midband and hot end losses were significant. The fission product activity loss in NRX-A5 elements was found to be 27 percent greater than if the weight loss had been axially uniform, since corrosion occurred predominantly at the midband region where the fission rate is highest. The corresponding NRX/EST factor of 11 percent was considerably lower due to the corrosion on the outside surface at the hot end where the fission rate is lower.

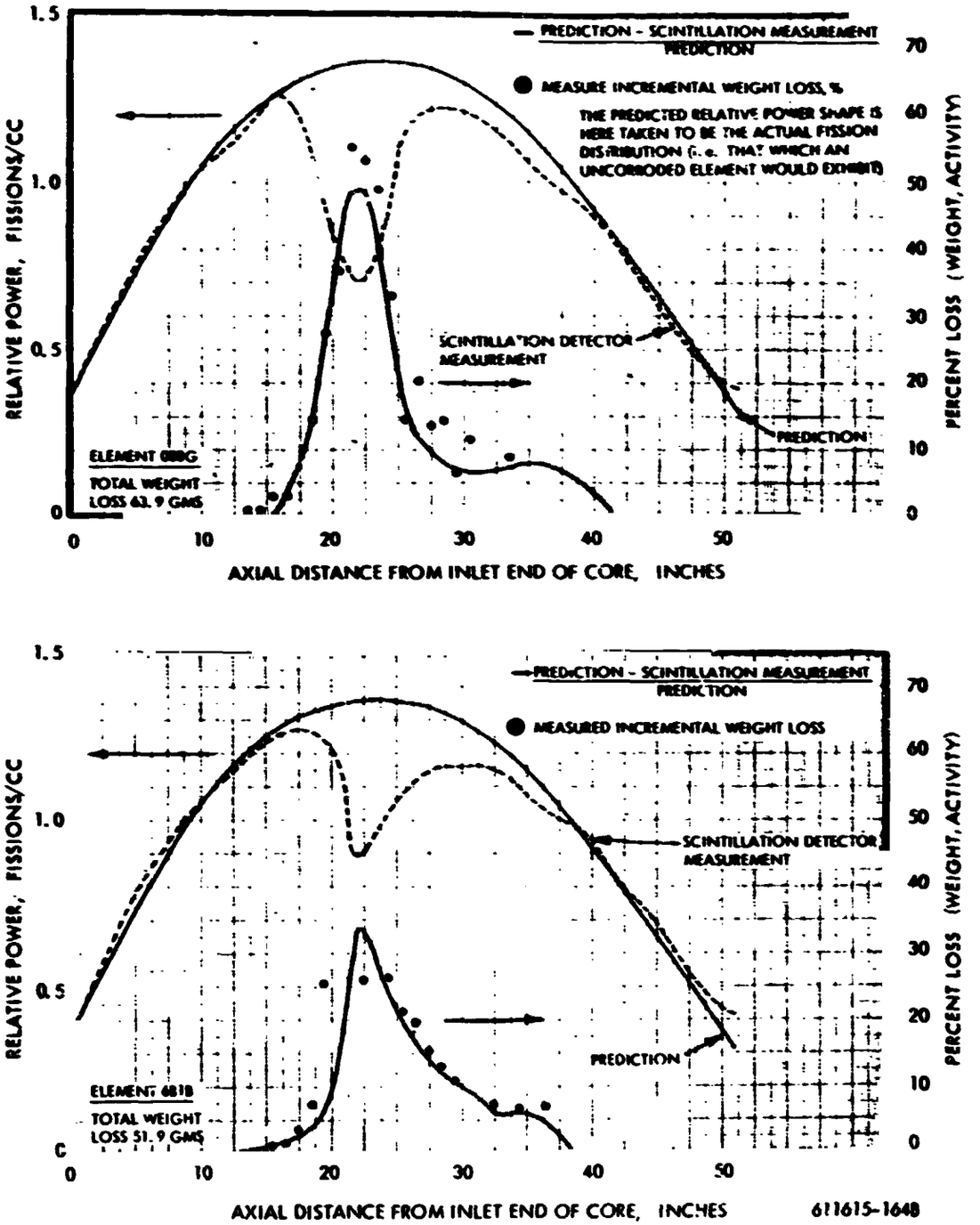

Figure 9-4. Loss of Fission Product Activity due to Corrosion (Scintillation Detector Measurements)

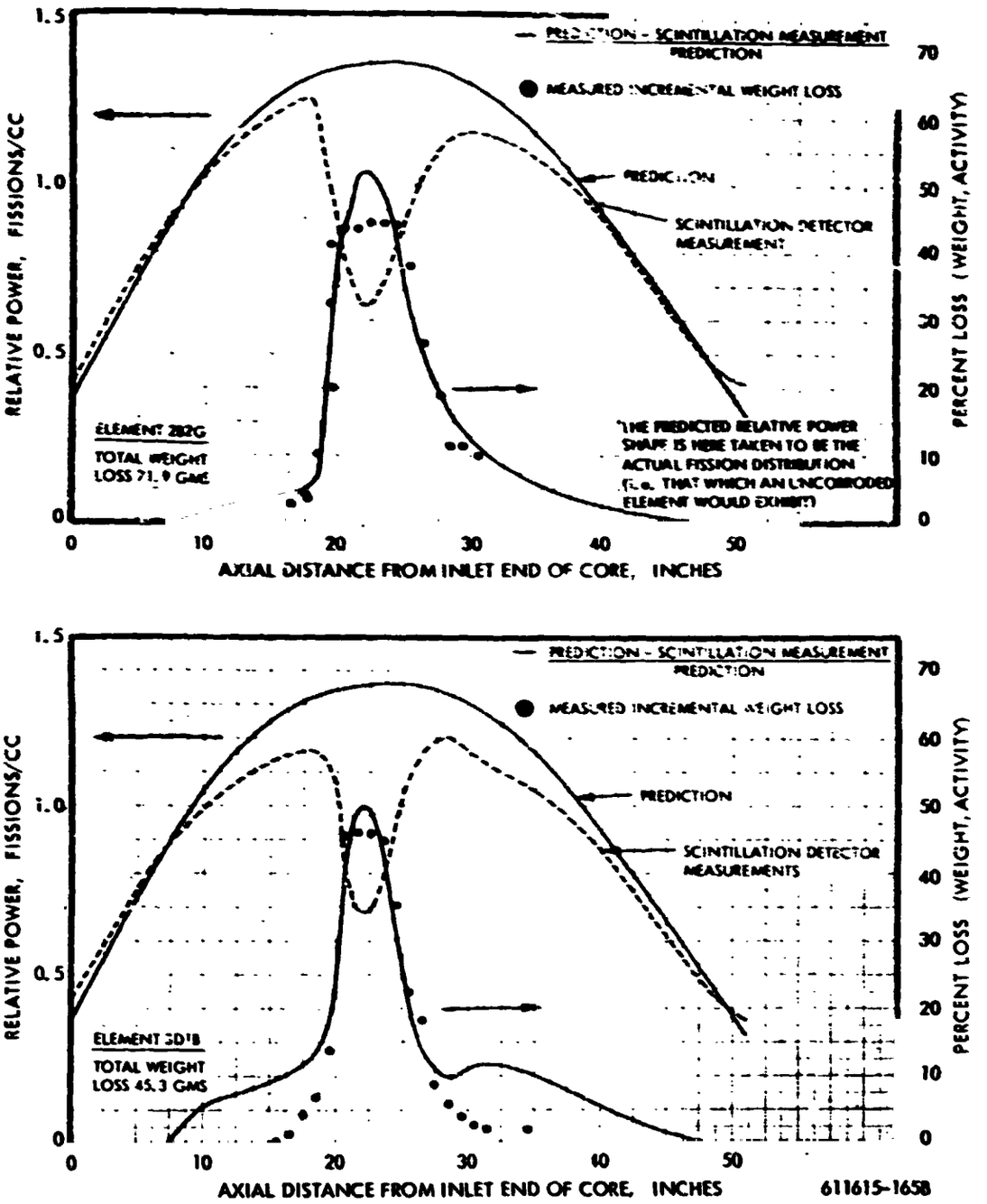

Figure 9-5. Loss of Fission Product Acrivity due to Corrosion (Scintillation Detector Measurements)

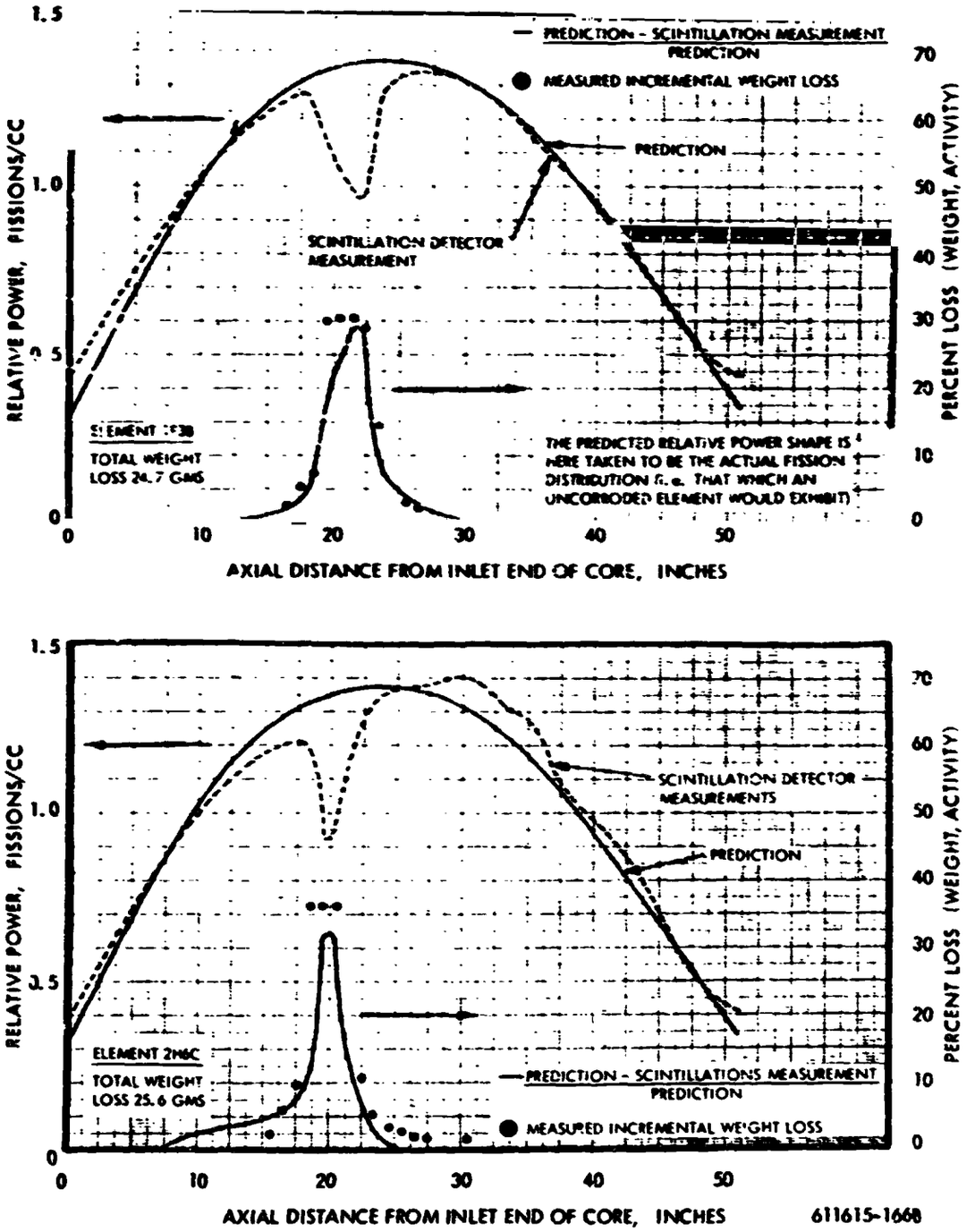

Figure 9-6. Loss of Fission Product Activity due to Corrosion (Scintillation Detector Measurements)

The straight line shown on Figure 9-3 is the activity loss which would occur if the fission product loss at each station is proportional to the weight loss using the 0.27 factor to account for the axial weight loss distribution. As in the NRX/EST analysis, the curve fit to the data shows very little activity change for a weight loss below 15 - 20 grams. Physically this is interpreted to mean that essentially only carbon is lost in the initial stages of the corrosion process. At higher losses the slope becomes more negative, until it agrees in slope with the straight line developed above. Thus, the data denotes a gradual transition toward the situation in which fission products and presumably uranium are removed in direct proportion to the weight loss.

9.6 COMPARISON OF ADJUSTED NRX-A5 EXPERIMENTAL POWER DISTRIBUTION WITH PREDICTIONS

The gross ionization measurement of the gamma activity of each unbroken element in NRX-A5 was adjusted to account for the loss of activity due to corrosion during the test. These corrections were obtained from the curve shown in Figure 9-3d using measured element weight losses. The corrected values of fissions per gram of uranium are shown in Figure 9-7.

The ratios of these adjusted experimental fissions per gram data to the 119° NRX-A5 predicted values for each element location are shown in Figure 9-8 as a function of radial position. These ratios are also noted on the core schematic in Figure 9-9. Note that the error in the predicted fissions per gram of uranium is now constant over the region within the 25 cm radius, in contrast to the apparent increase in error in Figure 9-2. The maximum ratio of approximately 6 percent occurs in a few elements in the J and H row clusters.

The convention of normalizing the fission rate per gram uranium to unity at the centerline both in theory and experiment suppresses any error in the prediction at the core centerline, while exaggerating the error at the edge. In order to determine the actual error in the predicted fission power per element, the ionization data was renormalized. The predicted element average power factor was divided by the nominal uranium loading of that element. A comparable measured quantity was derived by dividing the experimental gamma intensity reading for that element by the average gamma intensity reading for all elements and by the as-built uranium loading. Since the calculated power factors include not only energy from fission fragments, but also that from gamma and fast neutron interactions in the core, the calculation was adjusted to delete these effects. The results of this comparison are given in Figure 9-10 which shows that the power distribution was overpredicted by approximately 2 percent at the center and underpredicted by a maximum of 4.7 percent at the core periphery.

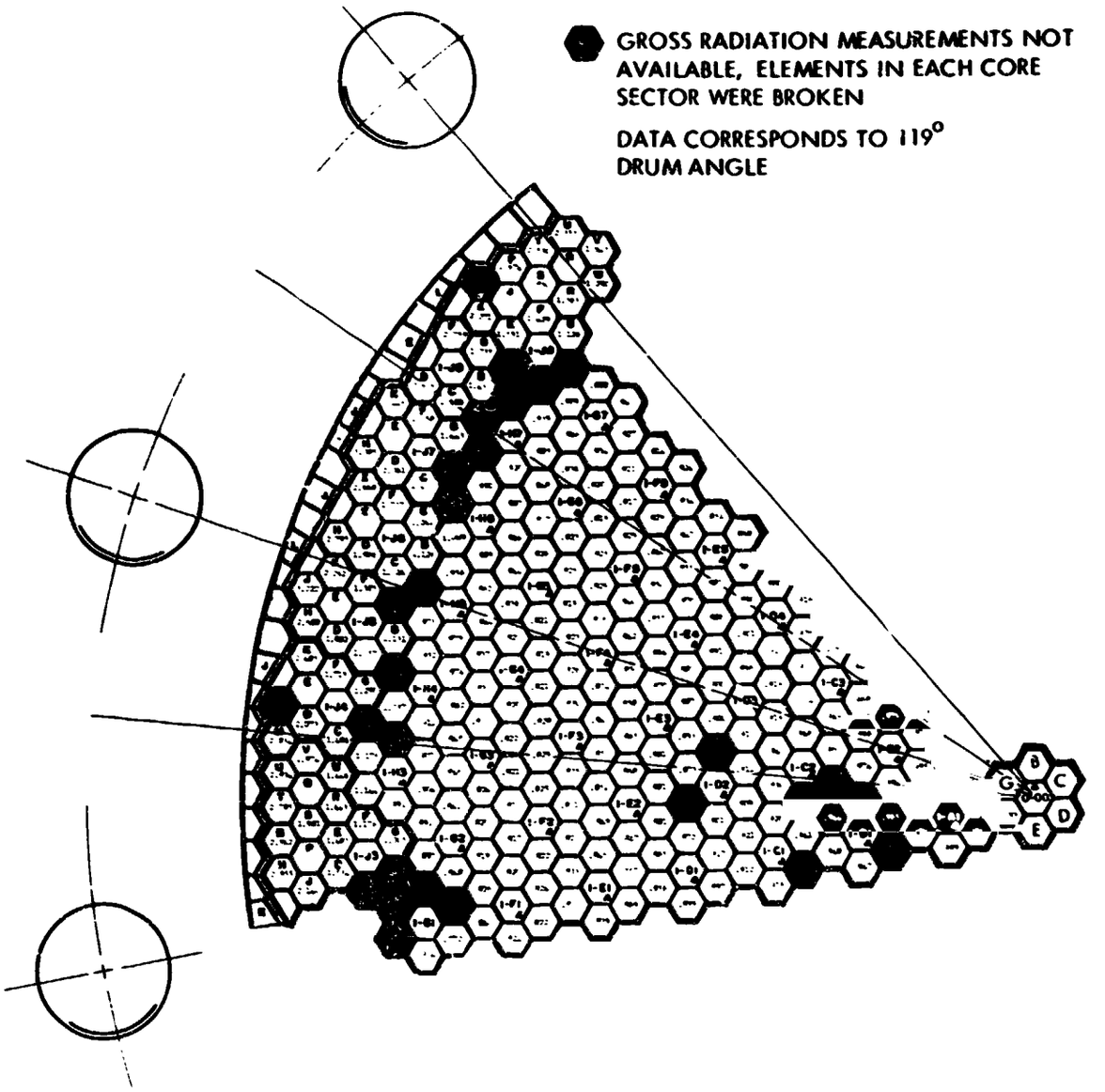

Figure 9-7. NRX-A5 Experimental Fission per Gram Values, Corrected for Fission Product Loss

Figure 9-8. Comparison of the Theoretical and Experimental Fissions/Gram Uranium (Experimental Values Adjusted for Corrosion Effects)

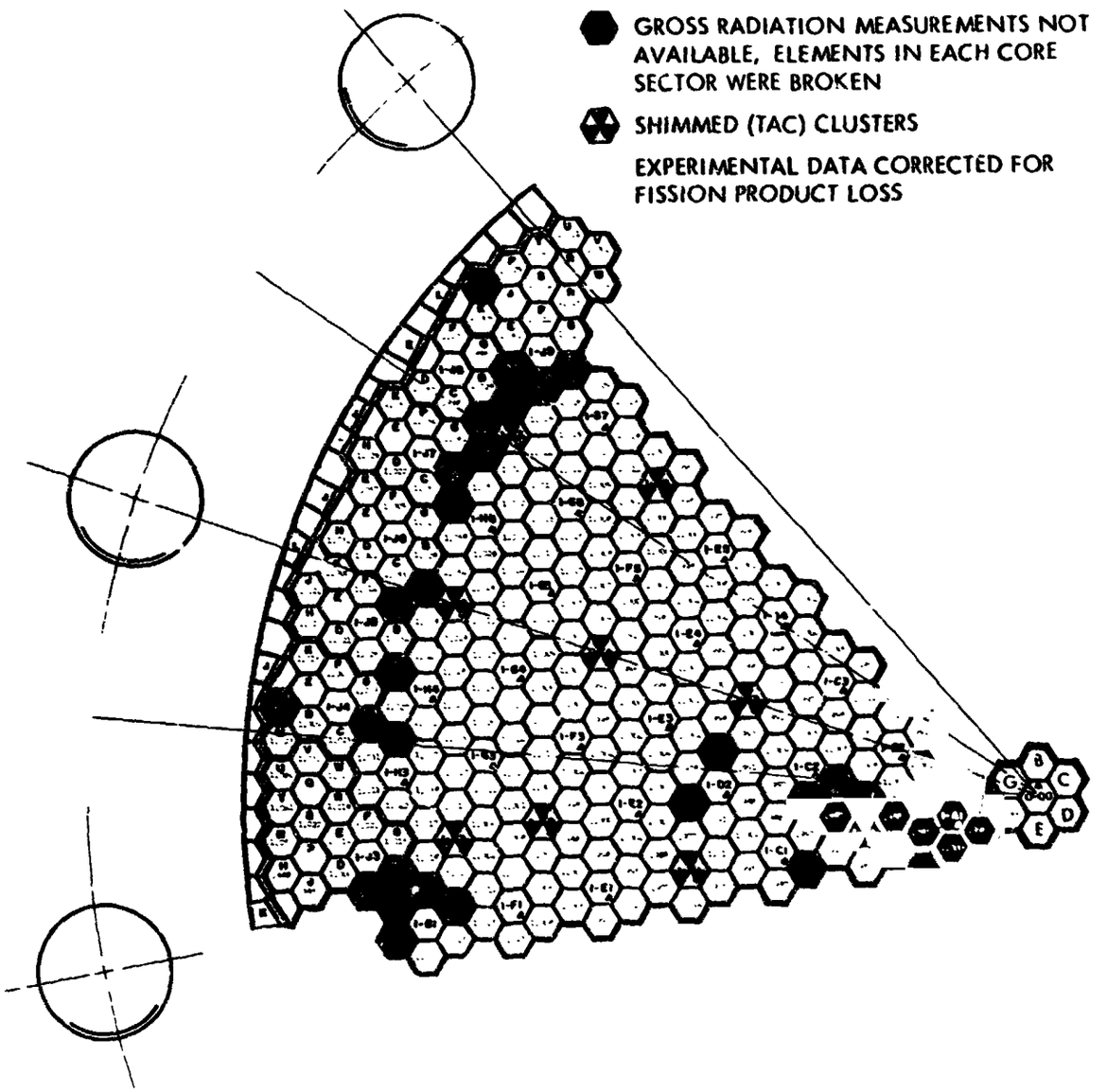

Figure 9-9. Ratio of the NRX-A5 Experimental (Adjusted for Fission Product Loss) to Calculated Fissions per Gram, Each Fission Distribution being Normalized to Unity in the Center-Most Cluster

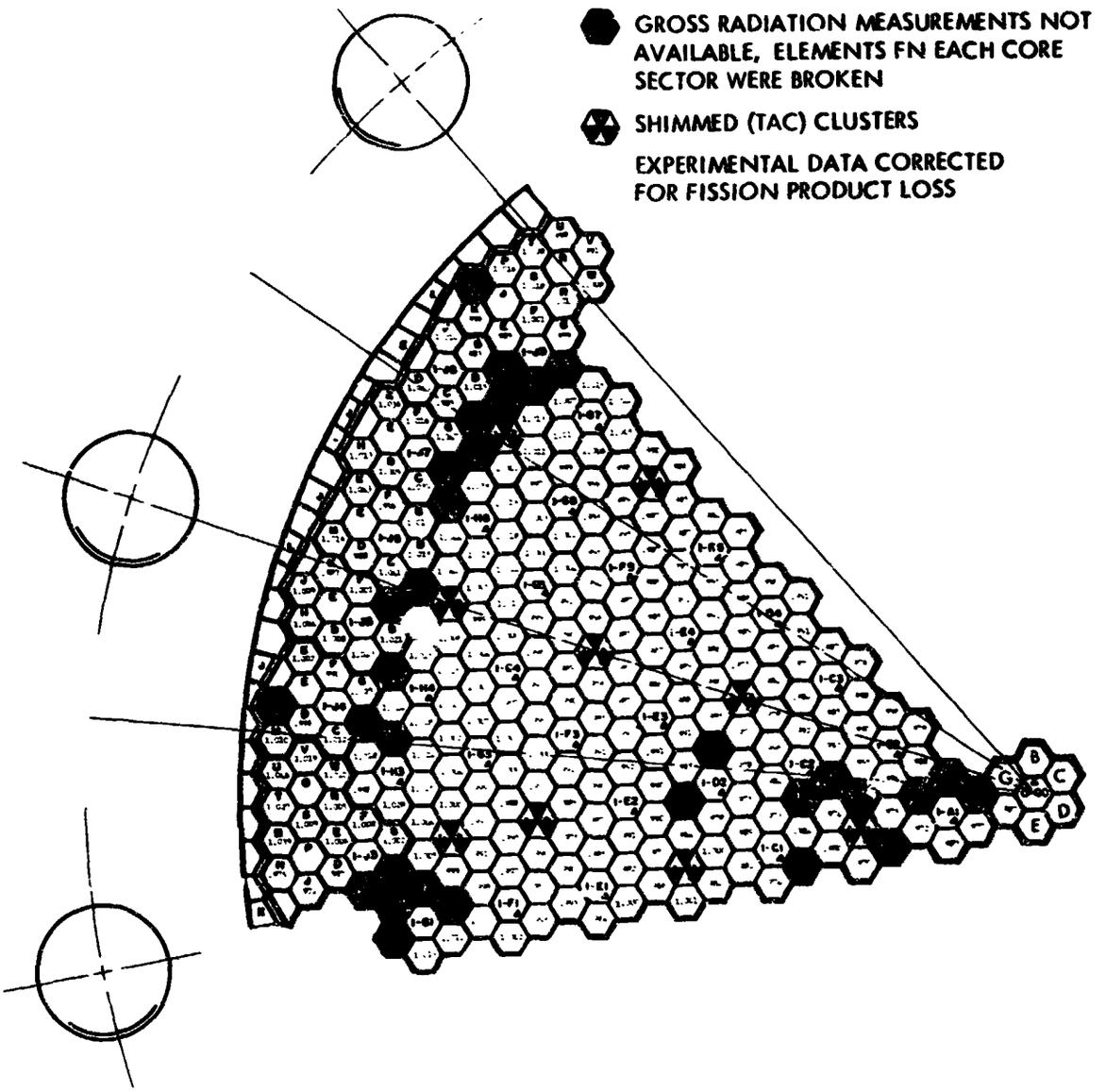

Figure 9-10. Ratio of the NRX-A5 Experimental (Adjusted for Fission Product Loss) to Calculated Fissions per Gram, Each Fission Distribution being Normalized to a Unity Average Factor in the Core

The errors noted in the power predictions can be understood in terms of the design changes made between the NRX-A5 and NRX-A3 reactors. As mentioned previously, the NRX-A5 power prediction was normalized to a power distribution derived from the NRX-A3 gross ionization measurements. A reduction in loading of 42 elements in NRX-A5 relative to the A3 loading distribution was found necessary in order to reduce the power factors slightly inward from the periphery which became excessive at the higher operating drum angles intended for NRX-A5. Calculations and experimental power measurements* at the Westinghouse Astronuclear Experimental facility have since shown that the fission flux in the downgraded elements would increase by as much as 2 to 5 percent, producing most of the higher errors in Figure 9-10. Smaller errors were also introduced in the core periphery by the power perturbations applied in the prediction to correct for the absence of fueled partial elements in NRX-A5. The available WANEF power measurements used to derive these A5 perturbations were made only in a limited number of coolant channels adjacent to selected partial elements. Recent PAX-E peripheral power measurements which mapped the complete core boundary, both with fueled and unfueled partial elements have since shown that these perturbations were slightly underestimated.

The next few paragraphs review briefly the experience in predicting the four NRX reactors tested up to this time. Further comparisons between the NRX-A2 and A3 reactors are made in WANL-TNR-202, "NRX-A3 Reactor Final Test Report," Chapter 8, while the NRX/EST results were compared to both of these reactors in WANL-TNR-216, "NRX/EST Reactor Analysis Test Report", Chapter 9.

Most of the errors noted in all the NRX-A power predictions made to date can be attributed either to design changes which were made between the various reactors or to the predicted cold-to-hot power swing. In the NRX-A2 and A3 analytical predictions the latter effect introduced a 1 percent increase in the central core region and a sharp

---

* WANL-TME-1474, "Critical Experiments in Support of NERVA", Quarterly Report - 3rd Quarter CY '66, 6/66

reduction of 7 percent at the core periphery at operating conditions. Deviations of this magnitude were accordingly seen in the actual power distribution relative to the prediction since no hot measurements were available at the time of these predictions. A comparison of the cold A2-PAX power distribution and that derived from NRX-A2 post-operative ionization measurements indicated little or no difference in the cold and hot power distributions, except in the edge fuel elements where the observed cold-to-hot power change showed an increase of 2 to 4 percent. The analysis of NRX-EST and NRX-A5 gross ionization measurements and ambient PAX data have confirmed that there is a localized but definite rise rather than a drop in the hot edge power distribution relative to the ambient case.

The various normalizing schemes used to predict the NRX-A3, NRX/EST and NRX-A5 power distributions did not properly account for localized increases in the fission flux due to reductions in individual fuel element loadings. This introduced errors of 2 to 5 percent in the various power predictions. The extent of these errors depended on the number and location of the elements whose loadings were reduced.

The power perturbations due to the replacement of fueled partial elements with unfueled graphite elements also introduced measurable errors in the NRX/EST predictions. While power perturbations were introduced in the NRX/EST calculations to account for this change, the correction was not based on a direct measurement, but was inferred from NRX-A2 PAX peripheral power changes as a function of core penetration and depth of peripheral irregularity. PAX power experiments have since shown that these power perturbations were underestimated by approximately 5 percent in those elements adjacent to the unfueled partial elements.

The design experience gained from analyzing all the hot NRX-A and ambient PAX power measurements has been utilized in predicting the XE-1 power distribution. It is believed that the error in these predictions will be of the order of the random variations in the hot experimental data. The XE-1 power predictions were normalized to the NRX-A2 gross ionization measurements which were not complicated by corrosion. A PAX power

map for a complete 90 degree sector was made to determine the perturbations due to loading change in XE-1 relative to NRX-A2. Additional peripheral power measurements were made to completely define the unfueled partial element power perturbations. Finally, the power measurements made at LASL with the test Cell "C" shield mockup were used to determine the effects of the shield on the power distribution.

9.7 MEASURED COLD-TO-HOT POWER CHANGE

Figure 9-11 shows the observed NRX-A5 cold-to-hot power change. The cold power distribution was determined by measurements of the fission product activity induced in uranium-aluminum detector wires irradiated throughout the PAX-D reactor. For this experiment the NRX-A5 loading distribution was mocked up in a 180 degree sector of the PAX core. These power measurements were made for a 90 degree control drum angle; an adjustment to the 119 degree angle was necessary for comparison with the hot NRX-A5 power distribution as derived from the corrosion corrected ionization measurements. The ratios of the NRX-A5 ionization measurements to the PAX-D experimental power distribution shown in Figure 9-11 reflects not only the power change due to operating conditions, but also a small change in the hot power distribution due to corrosion. The NRX-A5 peripheral cold-to-hot swing is slightly more pronounced than observed from the NRX/EST data, approximately 2 percent. This increase is believed to be attributable primarily to the different radial weight loss patterns in the two cores. A second possibility is the different hydrogen densities in the beryllium reflectors of the two reactors. Transport calculations do indicate, however, that this second effect should not be important.

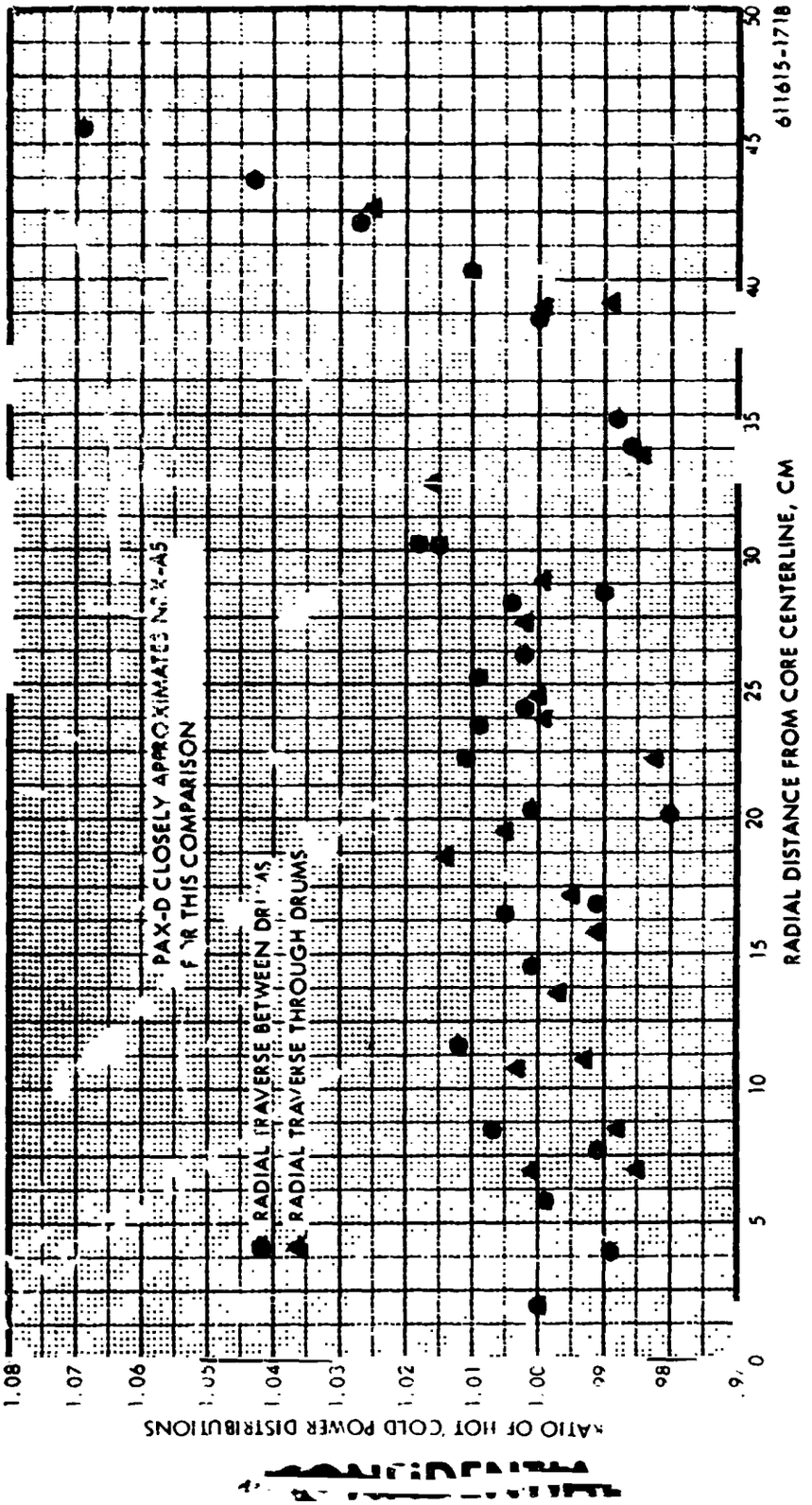

Figure 9-11. Ratio of NRX-A5 Hot to PAX-D Cold Experimental Fission Densities

9.8 COMPARISON OF THE NRX EXPERIMENTAL AND PREDICTED AXIAL POWER DISTRIBUTIONS

Figure 9-12 presents the measured and calculated axial fission power distributions at the core centerline and edge in NRX-A3, NRX/EST and NRX-A5 for elements with low weight losses. Both predictions were obtained from R - Z TDC calculations. The difference between these two predictions is the use of gadolinium - stainless steel cluster plates in NRX/EST and Ag - In - Cd in NRX-A3, NRX/EST, and NRX-A5. The corresponding prediction and measurements show good overall agreement for each cluster plate material.

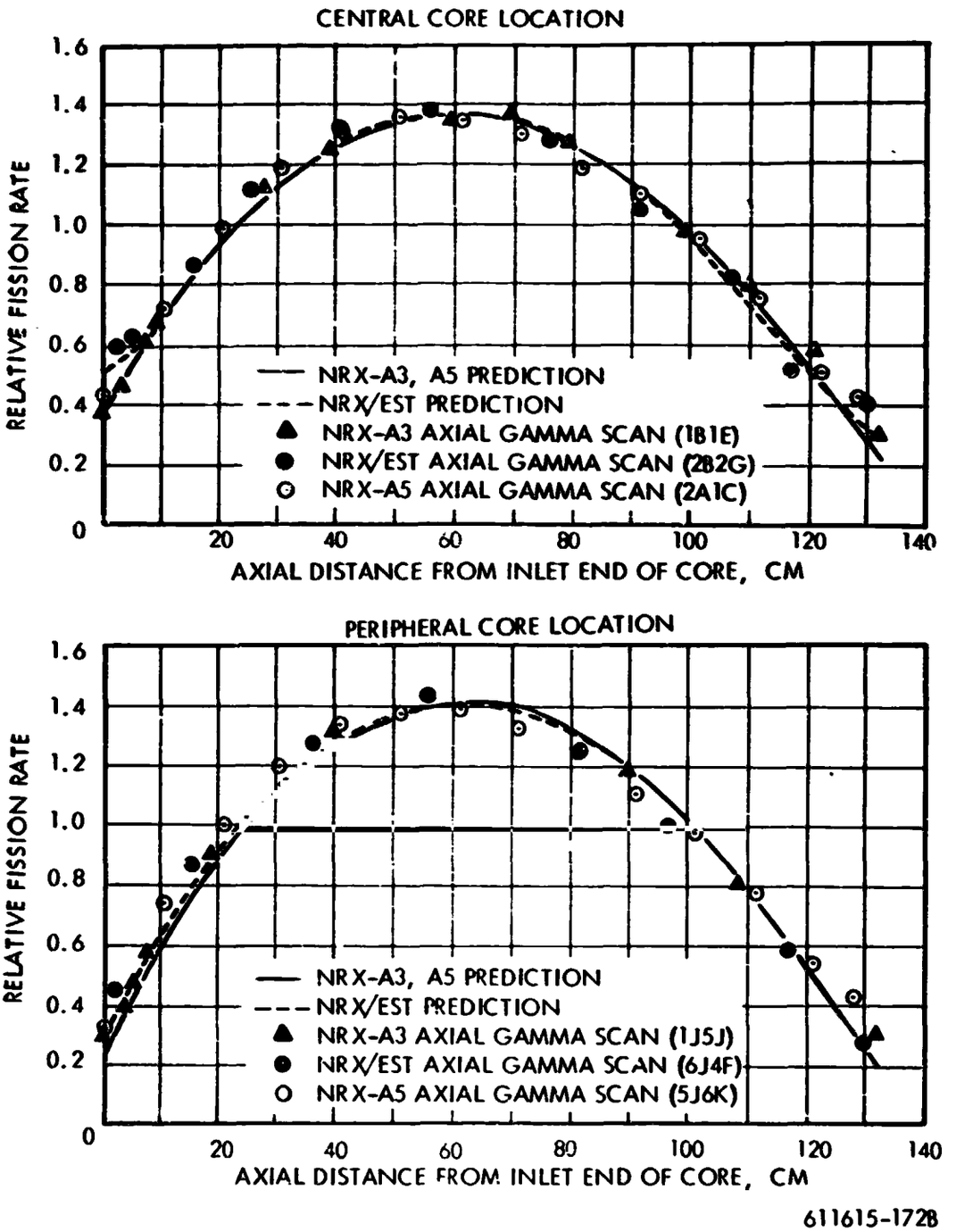

Figure 9-12. Comparison of the Measured and Predicted Axial Power Distributions for Low Weight Loss Elements in NRX-A5

9.9 COMPARISON OF THE NRX/EST AND NRX-A5 GROSS IONIZATION MEASUREMENTS

The small difference in the NRX/EST and NRX-A5 effective drum angles, 120 versus 119 degrees, permitted a direct comparison of the experimental data from each of the two hot tests, see Figure 9-13. Scatter in these ratios is primarily due to different shim patterns in each core, the experimental error, and the inability to eliminate all of the deviations in the measurements due to corrosion. The radial mean of these ratios deviates approximately 2 percent from unity in the central core locations and increases to 4 percent at the edge of the core. This observed gross difference in the two power distributions is believed to be caused by the different radial weight loss patterns in each core.

CONFIDENTIAL

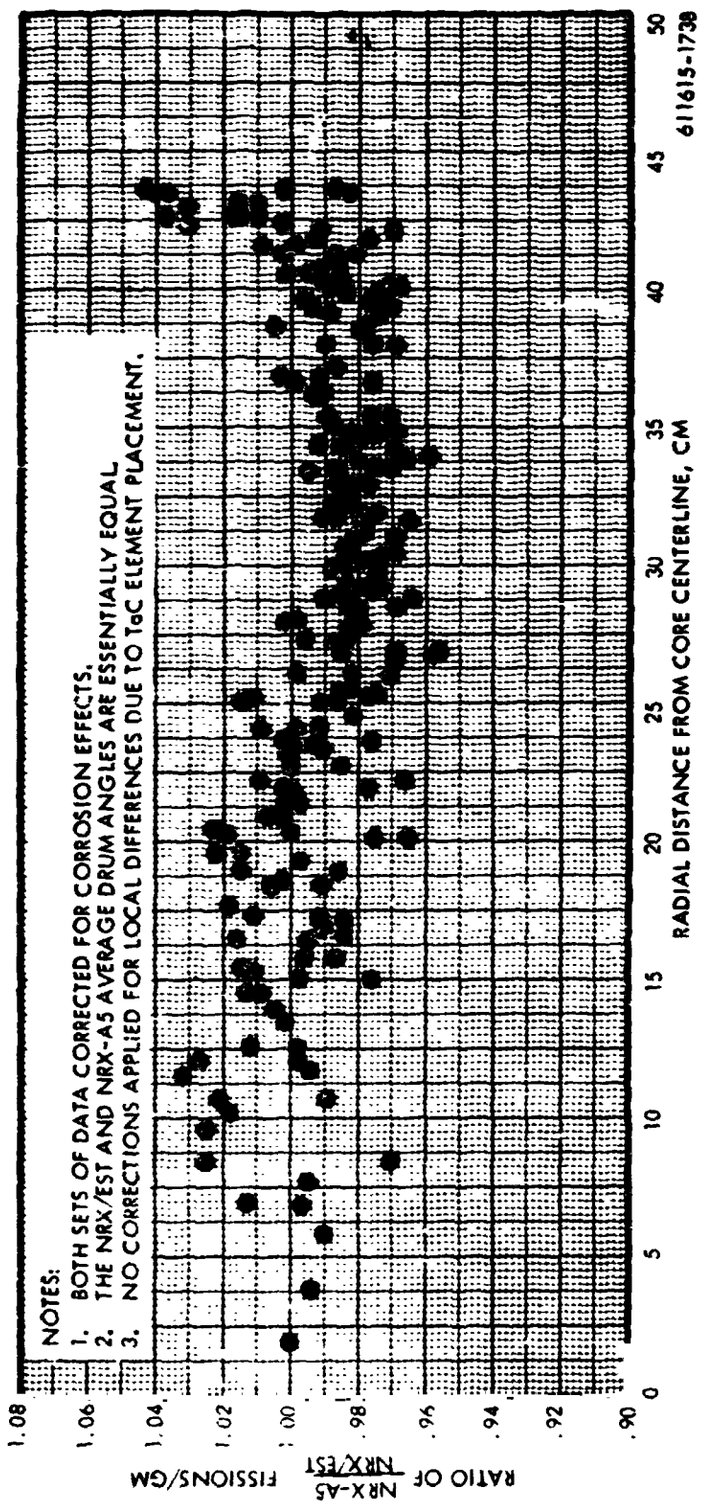

Figure 9-13. Comparison of NRX/EST and NRX-A5 Radiochemical Power Measurements

CONFIDENTIAL

APPENDIX A

REACTIVITY CALCULATIONS

A derivation of the methods used for reactivity calculations in this report appears in WANL-TME-936. A summary of the more significant effects and key nuclear parameters is shown in Table A-1. Note that during steady state operation the terms R_D, R_C, R_H, and R_T must sum to zero. The last three terms are determined by the fluid flow and temperature characteristics of a particular reactor condition. The term R_D permits the calculation of the drum angle for equilibrium operation.

67

TABLE A-1

SIMPLIFIED NRX-A5 REACTIVITY EQUATIONS

NRX-A5 Reactivity at Steady State $= R_D + R_C + R_H + R_T = 0$

Control Drum Position	R_D	$= -4.1\ (1 + \cos\theta) + 3.4$
Carbon Loss	R_C	$= 0.055\ M_{CL}$
Hydrogen Reactivity Contribution	R_H	$= (1 + A)\ (W_C + W_{LS} + W_{Be})$
Core Worth	W_C	$= 4.0\ \bar{\rho}_1 + 10.5\ \bar{\rho}_2 + 4.6\ \bar{\rho}_3$
Lateral Support Worth	W_{LS}	$= (0.968 - 10^{-4}\ \bar{T}_C)\ \bar{\rho}_{LS}$
Be Reflector Worth	W_{Be}	$= 0.040\ \bar{\rho}_{Be}$

Temperature Reactivity Contribution $R_T = \left[-1.039\ (\bar{T}_C - 528) + 0.943\ (\bar{T}_{Be} - 528)\right] \times 10^{-3}$

where

R_i	=	Reactivity, dollars (i is D, C, H or T)
θ	=	Control drum bank position, degrees
M_{CL}	=	Mass of carbon lost, kilograms
A	=	Fraction of diffused hydrogen (0.12 used)
ρ_1, ρ_2, ρ_3	=	Average hydrogen densities in the upper, middle, and lower thirds of the core, lb/ft^3
ρ_{LS}	=	Average hydrogen density in the lateral support, lb/ft^3
ρ_{Be}	=	Average hydrogen density in the beryllium reflector, lb/ft^3
$\bar{T}_C$	=	Average core temperature, ^oR
$\bar{T}_{Be}$	=	Average beryllium reflector temperature, ^oR